



TECHNISCHE UNIVERSITÄT MÜNCHEN
Fakultät für Physik

Planar titanium oxycarbide electrodes for electrocatalysis studies

Synthesis, characterization and application

Celine M. Rüdiger

Vollständiger Abdruck der von der Fakultät für Physik der Technischen Universität München zur Erlangung des akademischen Grades eines

Doktors der Naturwissenschaften (Dr. rer. nat.)

genehmigten Dissertation.

Vorsitzende: Prof. Dr. Nora Brambilla

Prüfer der Dissertation:

1. Prof. Dr. Julia Kunze-Liebhäuser
2. Prof. Dr. Aliaksandr Bandarenka

Die Dissertation wurde am 17.01.2018 bei der Technischen Universität München eingereicht und durch die Fakultät für Physik am 27.02.2018 angenommen.

Abstract

Carbon modified titania (TiOC) is a promising material that could substitute carbon based electrocatalyst supports in proton-exchange membrane fuel cells, whose durability is limited by corrosion of the carbon electrode. Planar TiOC model systems (TiOC films), that are meant to be used for fundamental electrocatalysis studies in low pH environment, have been synthesized *via* a carbothermal treatment of compact anodic TiO₂ films on polycrystalline Ti substrates in a gas flow reactor using acetylene as carbon source. Two parameter studies have been performed, in which TiOC films were prepared with two different acetylene flow fractions and at each four different synthesis temperatures between 550 and 1050 °C. Through combination of microscopic, (micro-)spectroscopic and diffractometric analysis tools, the influence of the annealing temperature and of the Ti substrate texture on the physicochemical properties of the prepared TiOC films has been investigated and a fundamental understanding of the conversion mechanism of compact anodic TiO₂ to oxycarbide (TiO_{1-x}C_x) phases and of their subsequent reoxidation in air has been obtained. TiOC electrodes, synthesized at different annealing temperatures, have been studied with electrochemical techniques to assess their electric conductivity at the electrode/electrolyte interface and their stability against passivation/corrosion under anodic polarization in acidic electrolytes. In a preliminary study, a set of TiOC electrodes has been tested as catalyst for the hydrogen evolution reaction (HER). Finally, Pt nanoparticles deposited on a glassy carbon (GC) electrode and on TiOC films have been investigated in terms of their activity towards the electrochemical ethanol oxidation reaction (EOR) and in terms of their electrochemical stability, both in 1.0 M HClO₄ supporting electrolyte at room temperature and in concentrated H₃PO₄ at temperatures between 25 and 80 °C.

The core insights of these studies are:

1. The most efficient conversion of anodic TiO₂ to a TiC-rich and crystalline oxycarbide phase is obtained through the carbothermal treatment at 750 °C.
2. The thus obtained TiOC₇₅₀ electrode is characterized by a high intrinsic stability in air, fast and stable outer sphere electron transfer kinetics during potentiodynamic cycling between 0.2 and 0.9 V_{SHE} in 0.1 M H₂SO₄ with the ferro-/ferricyanide redox couple, a comparably high activity towards the HER in 0.1 M H₂SO₄, and a high corrosion resistance in 1.0 M HClO₄ during anodic polarization until 0.74 V_{SHE}.
3. The Pt/TiOC₇₅₀ model system outperforms the Pt/GC catalyst in terms of its activity towards the EOR at temperatures between 25 and 80 °C and in terms of its stability in concentrated phosphoric acid at 80 °C.

In conclusion, TiC-rich oxycarbide materials constitute a promising alternative to carbon-based catalyst supports for electrocatalysis applications in low pH environment and at elevated temperatures.

Zusammenfassung

Mit Kohlenstoff versetztes Titandioxid (TiOC) ist ein vielversprechendes Material, welches die aus reinem Kohlenstoff bestehenden Träger von Elektrokatalysatoren in Protonenaustauschmembran-Brennstoffzellen ersetzen könnte, deren Lebensdauer durch die Korrosion der Kohlenstoffelektroden begrenzt ist. Ziel dieser Arbeit war die Entwicklung von TiOC Modellsystemen, die für grundlegende Studien elektrokatalytischer Prozesse in saurem Elektrolyten verwendet werden können. Dafür wurden TiOC Filme über eine carbothermische Umwandlung von kompakten anodischen Oxidfilmen auf polykristallinen Titansubstraten synthetisiert, wobei ein Gasflussreaktor verwendet wurde und Acetylgas als Kohlenstoffquelle diente. Zwei Parameterstudien wurden durchgeführt, bei denen TiOC Filme mit zwei unterschiedlichen Durchflussraten von Acetylgas, und bei je vier verschiedenen Synthesetemperaturen zwischen 550 und 1050 °C hergestellt wurden. Der Einfluss von Synthesetemperatur und Substratbeschaffenheit auf die physikalisch-chemischen Eigenschaften der hergestellten TiOC Filme wurde mittels mikroskopischer, (mikro-)spektroskopischer und diffraktometrischer Analysemethoden untersucht. Dabei konnte ein grundlegendes Verständnis des Umwandlungsprozesses von kompaktem anodischen TiO_2 zu Titanoxycarbid ($\text{TiO}_{1-x}\text{C}_x$) und von dessen anschließender Reoxidation an Luft gewonnen werden. Bei verschiedenen Synthesetemperaturen hergestellte TiOC Elektroden wurden mit elektrochemischen Methoden untersucht, um ihre elektrische Leitfähigkeit an der fest/flüssig Grenzfläche sowie ihre Stabilität gegenüber Passivierungs-/Korrosionsprozessen bei anodischer Polarisierung in sauren Elektrolyten zu testen. In einer vorläufigen Studie wurde ein Satz von TiOC Elektroden als Katalysator für die elektrochemische Wasserstoffentstehungsreaktion (HER) verwendet. Um zu überprüfen, ob die hergestellten TiOC Modellsysteme geeignete Katalysatorträger sind, wurden Platin-Nanopartikel auf den TiOC Filmen und auf Elektroden aus Glaskohlenstoff (GC), die als Referenzsystem dienten, abgeschieden. Anschließend wurde die elektrochemische Stabilität und die Aktivität der unterschiedlich geträgerten Elektrokatalysatoren gegenüber der elektrochemischen Oxidation von Ethanol (EOR) jeweils in 1.0 M HClO_4 Grundelektrolyt bei Raumtemperatur und in konzentrierter H_3PO_4 Säure bei Temperaturen zwischen 25 und 80 °C getestet. Die wesentlichen Erkenntnisse dieser Studien sind:

1. Die effizienteste Umwandlung von anodischem TiO_2 zu einer TiC-reichen und kristallinen Oxycarbidphase wurde durch eine carbothermische Synthese bei 750 °C erzielt.
2. Die so hergestellte TiOC_{750} Elektrode zeichnet sich durch eine hohe intrinsische Stabilität an Luft, schnelle und stabile „outer-sphere“ Elektronenübertragungskinetik bei Cyclovoltammetrie-Messungen zwischen 0.2 und 0.9 V_{SHE} in 0.1 M H_2SO_4 mit dem Ferro-/Ferricyanid Redoxpaar, eine vergleichsweise hohe Aktivität gegenüber der HER in 0.1 M H_2SO_4 , und einen hohen Korrosionswiderstand in 1.0 M HClO_4 bei anodischer Polarisierung bis 0.74 V_{SHE} aus.
3. Das Pt/ TiOC_{750} Modellsystem übertrifft den Pt/GC Katalysator hinsichtlich seiner Aktivität gegenüber der EOR bei Temperaturen zwischen 25 und 80 °C und hinsichtlich seiner Stabilität in konzentrierter Orthophosphorsäure bei 80 °C.

In Bezug auf elektrokatalytische Anwendungen in saurer Umgebung und bei erhöhter Temperatur lässt sich abschließend feststellen, dass TiC-reiche Titanoxycarbide eine vielversprechende Alternative zu Kohlenstoffbasierten Katalysatorträgern darstellen.

Acknowledgements

First of all I would like to thank Prof. Dr. Julia Kunze-Liebhäuser for having motivated this work and for having given me the possibility to conduct my PhD thesis in her developing junior research group and to participate in a European project. I am grateful for her guidance and for the freedom that she has given to me to develop and follow own research ideas and projects within the frame of the given topic, for her trust and patience and for letting me take over representative tasks which allowed me to gain early insight into the work of an independent research group leader.

Secondly, I would like to thank Prof. Dr. Aliaksandr Bandarenka for being the referee of this thesis.

I thank the International Graduate School for Science and Engineering (IGSSE) of the Technische Universität München (TUM) for the 3.5 years PhD grant and qualification program, and the EU RTD Framework Program FP7 (FP7-NMP-2012-SMALL-6, project title DECORE, project number 309741) for financial support during the last 3 years of my PhD.

The Treibacher Industrie AG (Austria) is acknowledged for providing titanium oxycarbide powders for my studies.

Furthermore, I would like to thank Dr. Oliver Schneider, who was my second mentor during my research at the TUM, for his valuable and helpful advices, and for his detailed lessons in electrochemistry. I am grateful to Dr. Odysseas Paschos for his scientific support during the first years of my PhD, and for his training at the scanning electron microscope. I thank Dr. Filippo Maglia for his lessons in X-ray diffraction techniques and solid state chemistry. I am grateful to Prof. Dr. Nathalie Bozzolo, who patiently replied to all my questions even during late Skype calls, for improving my knowledge of electron backscatter diffraction. Thanks to the assistance of Prof. Dr. Andreas Jentys and Jennifer Hein, I was introduced into the operation of a Raman microscope.

Among the other PhD students with whom I have shared the first years of my PhD at the E19 chair of the TUM, I want to thank in particular my office mates Tine Brülle, Cornelia Ostermayr and Christoph Traunsteiner, my lab mate Silvia Leonardi and my colleagues Jassen Brumbarov and Rianne Schöffler for the friendly, joyful and cooperative environment in the group, which was the basis for long lasting friendships. Thanks to Rianne, Tine and Cornelia, I was introduced into the basics of electrochemical and scanning probe techniques.

My special thanks are dedicated to Siegfried Schreier, who was available to help with any technical and engineering problem and became a dear friend and Salsa dance partner. At this point also Markus Haß should be acknowledged, who did a reliable job in the mechanical workshop and cut an uncounted number of Ti disks. Furthermore I thank Katarzyna Danielewicz of the Kristalllabor for patiently cutting the square Ti substrates by electrical discharge machining.

I am very grateful to Prof. Dr. Gaetano Granozzi for giving me the possibility to spend three months as visiting PhD in the *Surface Science and Catalysis Group* at the *Università degli Studi di Padova* (UNIPD) in Italy. During my stay in his group I had the chance to deeply improve my knowledge about XPS and to be introduced into UPS. In particular, I am grateful for the helpful assistance of Assoc. Prof. Dr. Stefano Agnoli, who was always willing to give me constructive (and critical) feedback and who inspired me to study the effect of the titanium substrate grains. Furthermore, I thank Assoc. Prof. Dr. Gian-Andrea Rizzi of the *Surface Science and Catalysis Group*, as well as Assoc. Prof. Dr. Alessandro Martucci and Dr. Marco Bersani of the *Nanomaterials Engineering Group* for having taught me sol-gel synthesis routes of titania powders. I am grateful for the friendly atmosphere, interest in my work and for the fruitful discussions that I have experienced during my stay at the UNIPD.

The person, however, who has made my stay in Padova an unforgettable event for the rest of my life, is Dr. Marco Favaro, who not only was the most patient photoelectron spectroscopy teacher and introduced me into the Italian culture, but who conquered my heart (with a lot of fruits, coffee and chocolate) and became my beloved husband.

The internship at UNIPD was followed by an ongoing strong collaboration between the two research groups of Prof. Dr. Gaetano Granozzi and Prof. Dr. Julia Kunze-Liebhäuser, in particular during the period of the common European project DECORE, when I had the chance to work with Dr. Laura Calvillo (UNIPD) and Dr. Carlos Valero-Vidal (TUM) that both became dear friends to me. Together with Dr. Marco Favaro, the four of us had a great time at the Elettra synchrotron in Trieste. I am particularly grateful to Carlos for his infinite will to support me and for giving me detailed lessons in corrosion and impedance spectroscopy.

In conclusion, I would like to express my deepest gratitude to my family, first of all to my dear parents, who always believed in me and who were always there for me, for their infinite support and love. I have received a lot of love and support from Enrica, Adri and Sere, too, which means a lot to me.

My final thoughts of gratitude are dedicated to Marco, the most important person in my life, who is always at my side, giving me a strong shoulder to lean on in good and in bad times. I thank him for showing so much interest in my work, for his patience and for his helpful and motivating advices. Every day I am grateful for having found real love and for the joy that he brings to my life.

Contents

1	Introduction	1
2	Fundamentals	7
2.1	Electrochemical methods	7
2.1.1	The electrode/electrolyte interface in equilibrium	7
2.1.1.1	The Nernst equation and the electromotive force	8
2.1.1.2	The metal/electrolyte and the semiconductor/electrolyte interface	10
2.1.2	Electrical current flow in an electrochemical cell	15
2.1.2.1	The kinetics of electrode reactions	16
2.1.2.2	Limiting currents due to mass transport	21
2.1.3	Electrochemical Techniques	22
2.1.3.1	The potentiostat and the three electrode electrochemical cell	22
2.1.3.2	Chronoamperometry	23
2.1.3.3	Linear sweep voltammetry and cyclic voltammetry	27
2.1.3.4	AC methods to measure impedance	30
2.1.4	Fuel cells and the electrocatalysis of the ethanol oxidation reaction	35
2.1.4.1	The polymer electrolyte fuel cell and the direct ethanol fuel cell	36
2.1.4.2	The Pt electrocatalyst	37
2.1.4.3	The ethanol oxidation reaction on Pt	39
2.2	Materials analysis	43
2.2.1	Diffraction of electromagnetic or material waves for structure analysis	43
2.2.1.1	X-ray diffraction and grazing incidence X-ray diffraction	44
2.2.2	Scanning electron microscopy and related methods	45
2.2.2.1	Electron backscatter diffraction	48
2.2.3	Atomic force microscopy	50
2.2.4	Raman spectroscopy	51
2.2.4.1	Analysis and interpretation of Raman spectra	55
2.2.5	X-ray photoelectron spectroscopy	58
2.2.5.1	The X-ray photoelectron spectrum	58
2.2.5.2	Qualitative and quantitative elemental analysis	62
2.2.5.3	Angle-resolved XPS	66
2.2.5.4	XPS at the synchrotron	66
2.3	The investigated materials	68
2.3.1	Titanium	68
2.3.2	Anodic oxide films on titanium	68
2.3.2.1	Growth modes and growth parameters	69
2.3.2.2	Growth mechanisms: the high-field and the low-field approach	70
2.3.2.3	Characteristics of anodic TiO ₂	72
2.3.2.4	Influence of anodization parameters	72
2.3.2.5	Electrochemical and chemical stability of anodic TiO ₂	73
2.3.3	Titania and reduced titanium oxides	74
2.3.4	Titanium oxycarbide and titanium carbide	76
2.3.4.1	Titanium carbide	77

3	Materials and Equipment	79
3.1	The used chemicals, materials and gases	79
3.2	Preparation of TiOC, Pt/TiOC and Pt/GC electrodes	80
3.2.1	Synthesis of planar TiOC films	80
3.2.1.1	Preparation of the Ti substrates	80
3.2.1.2	Preparation of compact anodic TiO ₂ films	82
3.2.1.3	Carbothermal treatment to obtain TiOC films	83
3.2.2	Glassy carbon electrodes	85
3.2.3	Deposition of Pt nanoparticles	85
3.3	Setups of the electrochemical experiments	87
3.3.1	The standard electrochemical cell	87
3.3.2	The elevated temperature electrochemical cell	89
3.3.3	The potentiostats	90
3.3.4	Experimental parameters of the electrochemical measurements	91
3.3.4.1	Outer sphere electron transfer and HER at TiOC films	91
3.3.4.2	Polarization resistance of TiOC films	92
3.3.4.3	Electrochemical investigation of the EOR at Pt/TiOC and Pt/GC electrodes	93
3.4	Microscopic measurements	94
3.4.1	The atomic force microscope	94
3.4.2	The scanning electron microscope	94
3.5	X-ray diffraction and electron backscatter diffraction experiments	95
3.6	Spectroscopic experiments	96
3.6.1	X-ray photoelectron spectroscopy (XPS)	96
3.6.1.1	The electron energy analyzer	96
3.6.1.2	The used equipment and experimental parameters	98
3.6.2	Micro-Raman spectroscopy	100
3.6.3	Scanning photoelectron microscopy at the Elettra synchrotron light source in Trieste	101
4	Synthesis and investigation of planar TiOC films	103
4.1	Preparation of compact anodic TiO ₂ on smooth titanium surfaces	103
4.1.1	Preparation of anodic films on square Ti sheets	103
4.1.2	Preparation of anodic films on round Ti disks	106
4.2	TiOC films prepared on square substrates at temperatures between 750 and 1050 °C	108
4.2.1	Preparation of the first TiOC series	109
4.2.2	TiOC surface topography and morphology	109
4.2.3	TiOC surface composition and structure	111
4.2.3.1	XPS analysis	111
4.2.3.2	GID characterization	116
4.2.4	Conductivity of TiOC at the solid/liquid interface	116
4.2.5	Interpretation of the carbothermal conversion based on a thermodynamic model	120
4.3	TiOC films prepared on round substrates at temperatures between 550 and 850 °C	121
4.3.1	Preparation of the second TiOC series	122
4.3.2	TiOC appearance and surface morphology	122
4.3.3	TiOC surface composition	124
4.3.4	Conductivity of TiOC at the solid/liquid interface	128
4.3.5	Electrochemical stability of TiOC under polarization in acidic electrolyte	131
4.4	The effect of aging in air on the chemical and electrochemical properties of TiOC films	137
4.4.1	XPS analysis before and after prolonged exposure of TiOC to air	137
4.4.2	The effect of air aging on the conductivity of TiOC at the solid/liquid interface	139
4.4.3	The effect of air aging on the electrochemical stability of TiOC in acidic electrolyte	142

5	Ti substrate grain effects on physicochemical properties of TiOC	149
5.1	Preparation of TiOC films and a TiO ₂ ^{ref} reference system	149
5.2	Ti substrate grain dependent C/TiO ₂ composites through carbothermal treatment of anodic TiO ₂ at 550°C	150
5.2.1	Identification of substrate grain orientations from EBSD maps and optical appearance of anodic TiO ₂ and thermally treated oxide films	151
5.2.2	Potentials and limitations of micro-Raman spectrometry for chemical and structural analysis of thermally treated TiO ₂ on polycrystalline Ti	153
5.2.2.1	Effect of preferential orientation of crystalline phases in C/TiO ₂ and TiO ₂ ^{ref} on band intensities	153
5.2.3	Thermal treatment of anodic TiO ₂ with acetylene at 550°C	155
5.2.4	Thermal treatment of anodic TiO ₂ at 550°C without acetylene	159
5.2.5	Origin of the grain-dependent crystallinity of thermally treated anodic TiO ₂	165
5.2.6	Origin of the grain-dependent carbon content in the C/TiO ₂ composite film	166
5.3	Ti substrate grain-dependent physicochemical properties of carburized anodic TiO ₂ films prepared at different temperatures	167
5.3.1	Ti substrate grain-dependent surface morphology of TiOC	167
5.3.2	Ti substrate grain-dependent surface chemistry of TiOC	168
5.3.3	Ti substrate grain-dependent phase composition of TiOC	170
5.3.4	Representation of the cross-sectional composition of TiOC on differently oriented substrate grains	172
5.3.5	Effect of annealing temperature and Ti substrate texture on the crystallization of anodic TiO ₂ , and on the reactive decomposition of C ₂ H ₂	174
5.3.6	Effect of annealing temperature and Ti substrate texture on the conversion of anodic TiO ₂ to TiC, and on the material transport in TiO ₂ and Ti	174
5.3.7	Effect of TiO _{1-x} C _x surface reoxidation on the final composition of TiOC films	175
6	Ethanol electro-oxidation on Pt/TiO_{1-x}C_x	177
6.1	Preparation of the TiOC and GC electrodes	177
6.2	EOR at room temperature using different TiOC supports	177
6.3	EOR on Pt/TiOC ₇₅₀ and Pt/GC at elevated temperatures and in concentrated H ₃ PO ₄	181
6.3.1	Origin of the enhanced EOR activity of the Pt/TiOC system	186
6.4	Electrochemical stability of Pt/TiOC and Pt/GC in hot H ₃ PO ₄	187
6.4.1	Electrochemical stability of Pt/TiOC in hot H ₃ PO ₄	189
6.4.2	Chemical stability of TiOC powders in concentrated boiling H ₃ PO ₄	195
6.4.3	The degradation mechanism of Pt/TiOC during the EOR in concentrated H ₃ PO ₄ at elevated temperatures	197
7	Summary and Conclusions	199
7.1	Synthesis and characterization of TiOC films	199
7.1.1	Understanding the carburization and reoxidation mechanisms of anodic TiO ₂	199
7.1.2	Understanding the interplay between synthesis conditions and electrochemical characteristics of TiOC films	200
7.2	The effect of the Ti substrate texture on the carbothermal conversion of anodic TiO ₂	201
7.3	Application of TiOC films as Pt catalyst supports for the EOR	202
7.3.1	Performance of the Pt/TiOC catalyst towards the EOR	202
7.3.2	Electrochemical stability of TiOC in hot phosphoric acid	203
A	Additional figures	205
A.1	Chapter 4	205
A.2	Chapter 5	206

B Abbreviations	209
C List of Publications	213

1. Introduction

Future challenges in energy conversion

Since the industrial revolution in the western European countries during the late 19th century, the human demand for energy has grown exponentially. The sophisticated industrialized societies and in particular emerging nations, whose population is still growing, critically depend on a reliable supply of energy. According to the World Energy Outlook 2015, published by the International Energy Agency (IEA), the world energy demand grows by nearly one-third between 2013 and 2040, with all of the net growth coming from non-OECD countries.¹ Up to now, the highest fraction of this demand is covered by combustion of natural resources of fossil fuels, such as oil, gas and coal. Besides the accompanying accumulation of greenhouse gases in the atmosphere which are widely believed to have a harmful influence on earth's climate, these natural resources are limited and predicted to be consumed approximately by the mid of this century.² Facing these problems, the necessity of renewable energy resources is indisputable to provide a high standard of living for mankind. A transformation of the energy sector, which is urged by the IEA to limit global warming to an average of no more than 2 °C, also involves the development of efficient energy conversion and storage technologies. Electrochemical energy production is under serious consideration as an alternative energy/power source, as long as this energy consumption is designed to be more sustainable and more environmentally friendly.³ In this context, electrochemical devices such as fuel cells and batteries, have experienced a revival, in particular in electromobility, and are seen as an important part of the future energy framework.

Proton-exchange membrane fuel cells

Thermodynamically, fuel cells clearly outperform any combustion engine in efficiency, because they allow for a direct conversion of chemical into electrical energy thereby avoiding the Carnot-process. In practice, commercial fuel cell systems do not yet compete with traditional fossil combustion-based systems in terms of energy efficiency, material costs and durability. In the past decades, significant research efforts have been undertaken to tackle these issues. Depending on the aimed application, different types of fuel cell systems exist. For electromobility applications, low temperature proton exchange membrane fuel cells (PEMFC), fueled with hydrogen, are the state of the art and commercially available. For local, decentral energy supply or for low power electric devices, alcohol-run fuel cells, operated at intermediate temperatures (up to 200 °C) can potentially substitute currently employed, less sustainable energy converters (e.g. the diesel-generator). In recent years, there has been increasing interest in the development of direct ethanol fuel cells (DEFC).⁴ Ethanol, with its relatively high energy density of 8 kWh kg⁻¹, good availability from renewable sources, non-toxicity, and easy storage and transportation, is almost the ideal fuel.⁵ To convert the chemical energy stored in a fuel into electrical energy using a PEMFC, a catalyst is required. Up to now, platinum (Pt) or platinum group noble metals are the best materials known for that purpose. Due to the finite resources of noble metals and the resulting high costs, significant efforts are undertaken to limit the catalyst loading in PEMFC and to maintain high energy conversion efficiency at the same time. The amount of generated electricity scales with the active surface area, where the reactions take place on a molecular scale. Therefore, PEMFC catalysts typically consist of metal nanoparticles supported on a high surface area support, the basic role of which is

to maintain the catalytically active phase in a highly dispersed state and to provide the electric conductivity of the electrode. In commercial PEMFC systems carbon based materials are commonly used as support. These have the disadvantage of being prone to corrosion, in particular at elevated operating temperatures, which causes catalyst dissolution and agglomeration, and therewith limits the fuel cell durability.⁶ Considerable research efforts are dedicated to the development of suitable PEMFC catalyst support materials.⁶⁻⁸ The situation is somewhat more complex in case of proton exchange membrane DEFCs, because there is still a lack of catalysts that can completely oxidize ethanol into CO₂ at a high rate.⁹ Here, the catalytic performance can be significantly improved by shifting towards higher operating temperatures,¹⁰ which brings about new challenges concerning the stability of the catalyst, the support materials and the polymer electrolyte.¹¹ In PEMFCs that are operated at intermediate temperatures, acid doped polybenzimidazole (PBI) is proposed as alternative proton conducting membrane due to its thermal stability.^{12,13} The consequent harsh operating conditions, being a low pH environment plus elevated temperatures, emphasize the necessity of chemically and electrochemically stable catalyst supports that ensure electrical conductivity and an intimate contact with the catalyst.

Titania based catalyst supports

Metal oxides are particularly interesting in this respect because they are expected to be more stable than carbon supports at medium and high temperatures as well as at higher anodic potentials in acidic electrolyte.⁶ Titanium dioxide (TiO₂) has a broad field of applications that is based on its semiconducting nature. TiO₂, in its anatase or rutile form, is a wide band gap semiconductor ($E_g \sim 3.0-3.2$ eV) and, as such, particularly suitable for applications based on UV or X-ray induced interactions. That is why this material is frequently used in photo-catalysis¹⁴⁻¹⁶ and dye sensitized solar cells.^{17,18} Furthermore, it is well known for its biocompatibility^{19,20} and its ability to form self-organized anodic nanotube layers of highly defined morphology.^{21,22} Crystalline TiO₂ has been studied extensively for decades.²³ Being n-type semiconductors, TiO₂ electrodes behave similar to diodes, which block any current flow if electrons are drawn from them, as it is the case under anodic polarization of TiO₂ in an electrolyte. However, TiO₂'s electronic properties can be significantly changed through a reduction treatment which opens new perspectives concerning its application in catalysis and electrocatalysis. In reduced form, it has been used as a support material in heterogeneous catalysis studies. Chen and Goodman reported that Au catalysts supported on a reduced rutile TiO₂(110) surface show a remarkable activity for CO oxidation that can be attributed to interesting substrate effects.²⁴ As a reducible oxide, TiO₂ strongly interacts with group VIII noble metal nanoparticles, which is known as the strong metal-support interaction (SMSI) and can have significant effects on the activity of the supported catalyst, also for other reactions than the CO oxidation.²⁵

To expand the utilization of TiO₂ to applications that require a fast electron transport in electrolytic environments, such as electrocatalyst supports in fuel cells, the conductivity of the oxide must be enhanced while keeping the material inert toward reoxidation. A known method to achieve enhanced conductivity is by high temperature annealing in a reducing atmosphere such as H₂. This causes a phase transition from TiO₂ to stable Magnéli-type phases which are a homologous series of substoichiometric oxides of titanium with the general formula Ti_nO_{2n-1}, where n is between 4 and 10.²⁶ Their relatively high electrical conductivity at room

temperature, exceptional chemical stability in corrosive environments and large overpotentials toward gas evolution in aqueous electrolytes make them an attractive material for electrochemical applications.^{27,28} Pt catalysts supported on Ti_nO_{2n-1} are reported to show promising performances when employed as PEMFC cathode.²⁹ Another way to reduce titania in order to make it conductive is the use of a carbothermal treatment, which produces hybrid or mixed materials consisting of carbon and reduced titania species. Such materials are characterized by functional properties that are highly attractive for electrocatalysis applications.

Hybrid materials of carbon and titania in electrocatalysis

Novel hybrid materials made of TiO_2 , TiO_x , TiC and C (from now on termed TiOC) are particularly appealing for applications in PEMFC catalysis because they may provide (electro-)chemical stability, due to the presence of TiO_2 , and electrical conductivity, through TiO_x , TiC and graphite-like C phases, at the same time. Furthermore, synergistic effects due to the close proximity between suitable titania species and supported catalysts can lead to an enhancement of the overall catalytic activity.³⁰⁻³² Pt catalysts supported on TiC@ TiO_2 and TiO_2 @C core-shell particles have shown improved electrochemical stability with respect to Pt/C or Pt/TiC, when tested for their activity towards the oxygen reduction reaction (ORR).^{33,34} In full cell experiments, the performances of a H_2/O_2 -PEMFC with a Pt- TiO_2 /C catalyst were reported to increase with increasing added oxide content,³⁵ on the other hand, an excellent durability and the ability of water retention could be achieved with Pt TiO_x /C electrocatalysts.³⁶ Depending on the synthesis conditions, Pt/ TiO_x /C composite catalysts exhibited a higher catalytic activity towards the ORR and a better methanol tolerance than Pt/C.³⁰ TiOC based catalyst supports have also been investigated for reactions at the PEMFC anode, such as the electrochemical oxidation of primary alcohols. The CO-tolerance of Pt during the methanol oxidation reaction (MOR) could be improved by using a TiC support.³⁷ The activity of TiC supported Pt nanoparticles towards the MOR was shown to be enhanced by electrochemical surface oxidation of TiC, which was attributed to an electronic catalyst-support interaction combined with a bifunctional effect, where TiO_2 supplies OH groups for the CO-oxidation.³² Pt/Ru catalysts supported on anodic titania nanotubes (TNT), that have been converted into carbon-rich titanium oxycarbide ($TiO_{1-x}C_x$, a solid solution of TiO in TiC), have shown promising performance for the electrochemical oxidation of methanol.³⁸

Synthesis of TiOC materials

Biphasic C/ TiO_2 or mixed $TiO_{1-x}C_x$ -containing materials (rich in TiC/TiO) can be prepared using a carbothermal treatment. The final composition, structure and morphology is empirically tailored *via* the synthesis parameters, in particular the annealing temperature and the chosen precursors. To obtain $TiO_{1-x}C_x$ nanoparticles with a high fraction of TiC, numerous approaches have been performed in the past via both solid state synthesis³⁹⁻⁴³ and reaction in the gas phase.⁴⁴ In these synthesis routes, titania powders are typically used as precursor, whose reduction to titanium oxycarbide requires high temperatures of at least 1000 °C, which is very energy-intensive and leads to a loss of surface area due to particle agglomeration and growth. Anodic TiO_2 films on titanium substrate are particularly appealing titania precursors due to their tunable morphology, which can be varied from compact films⁴⁵ to high aspect ratio self-organized nanotubes.⁴⁶ A very flexible synthesis route, which can be used to produce TiOC materials of different morphologies, such as planar films, nanotubes or nanoparticles, and which provides realistic process conditions for large scale production, is a carbothermal

treatment of initially prepared titania precursors with reactive acetylene (C_2H_2) in a gas flow reactor. In 2009, Hahn et al. employed a high temperature carbothermal reduction with C_2H_2 gas to convert nanotubular anatase TiO_2 layers into carbon-rich $TiO_{1-x}C_x$ -nanotubes already at 850 °C. The nanotubes retained their structural integrity upon annealing, and a stable semi-metallic conductivity together with a substantial overpotential for oxygen evolution have been observed.³⁸

Planar TiOC model electrodes for electrocatalysis studies

The development of efficient catalyst/TiOC materials for the (intermediate temperature) PEMFC requires a detailed understanding of the intrinsic physicochemical and electrochemical properties of the TiOC support alone as well as of the interplay between the support properties and the activity and stability of thereon deposited catalysts. In order to perform systematic electrocatalysis studies and investigate potential catalyst–support interactions on a microscopic scale, e.g. by means of *in situ* methods involving electrochemistry, microscopy, chemical and structural analysis, it is considered useful to prepare *model systems* consisting of well-defined catalyst nanoparticles on a planar TiOC support of controllable composition, morphology and structure. In this context, planar compact anodic titania films on Ti substrates provide an attractive TiO_2 precursor material, because many of their properties, such as crystallinity, doping and film thickness can be modified in a facile and controlled way through the anodization parameters.^{47–50} Furthermore, as demonstrated for TNT,³⁸ anodic films can be converted into the desired TiOC materials *via* a facile carbothermal treatment employing the acetylene route. Anodically grown compact TiO_2 films on Ti metal substrates have been investigated for decades with respect to the oxide growth mechanism,^{51,52} as well as their physical and chemical properties.^{45,53,54} It is well known that the crystallographic orientation of the Ti substrate has a strong influence on the thickness, morphology, electrochemical, electrocatalytic, electronic and crystallographic properties of the anodic TiO_2 film grown on top.^{55–62} This effect needs to be taken into account when studying TiOC materials that have been prepared from such films. On the other hand, with the emergence of experimental methods that combine microscopy with complementary analysis tools such as photoelectron or vibrational spectroscopy, diffractometry or electrochemistry, the investigation of planar polycrystalline materials opens up new perspectives in materials research.

Aim of this work

The aim of this work is the synthesis, analysis and characterization of planar TiOC model electrodes and their application as catalyst supports for the ethanol oxidation reaction (EOR) at elevated temperatures. As a precursor material, planar compact TiO_2 films that are produced *via* a facile and reproducible electrochemical anodization of titanium sheets are chosen due to their simple morphology and easy handling. To convert these films into TiOC, the carbothermal route with acetylene as carbon source is employed, because it has proven suitable for the conversion of anodic TiO_2 into $TiO_{1-x}C_x$.³⁸ Pt nanoparticles are used as catalyst, because they are the best studied material for PEMFC reactions and provide a well-accepted benchmark. Chapter 2 provides the reader with the fundamentals and theoretical background that is needed to understand the performed experiments and data analysis. The experimental details and used materials are given in Chapter 3. In Chapters 4, 5 and 6 the results of the performed experiments are presented and discussed. A major part of the presented work was dedicated to the controlled synthesis of TiOC films of different

chemical composition and structure and their detailed characterization using microscopic, diffractometric and spectroscopic analysis tools. Prior to their application as electrocatalyst support, the electrochemical characteristics of the stand-alone planar TiOC materials, such as interfacial electron transfer kinetics and electrochemical stability window, were investigated with the appropriate electrochemical methods. Here, also the intrinsic stability of the TiOC films during aging in air was taken into account. The results of these studies are shown and discussed in Chapter 4.

Special focus was put on the influence of the substrate grain orientations of the polycrystalline Ti substrate on the physicochemical properties of carburized compact anodic TiO₂, which was investigated with spectro-microscopic techniques. The related studies are presented in Chapter 5.

To validate the applicability of planar TiOC systems for electrocatalysis studies, Pt catalysts were deposited and the activity and stability of Pt/TiOC was investigated for the electrochemical oxidation of ethanol up to 90 °C in concentrated phosphoric acid. This study is presented in Chapter 6. In a side project, the chemical stability of commercial TiO_{1-x}C_x powders in hot, concentrated phosphoric acid was investigated to address the issue of corrosion resistance of support materials for elevated temperature PEMFC that are equipped with an acid doped PBI membrane. This study is included at the end of Chapter 6. Chapter 7 provides the conclusion of the performed work and an outlook for future experiments.

2. Fundamentals

2.1 Electrochemical methods

This section will introduce some important basics of electrochemistry and the electrochemical methods that were employed in this work to study TiOC electrodes. Detailed treatments of the presented concepts can be found in the relevant literature, for example in references [63–66].

2.1.1 The electrode/electrolyte interface in equilibrium

If a solid electrode, i.e. an electronic conductor, is immersed into a liquid electrolyte, i.e. an ionic conductor, an electrified interface forms. Two types of processes occur at the electrode/electrolyte interface:⁶⁴ *faradaic* and *non-faradaic* processes. The former comprise charge transfer across the electrode/electrolyte interface, e.g. the transfer of electrons in the course of an oxidation or reduction reaction, which is governed by Faraday's law. The latter include processes such as adsorption and desorption of charged species, reorientation of dipoles or accumulation of charge at the interface, which are not accompanied by a charge transfer.

To understand the properties of an electrified solid/liquid interface at equilibrium, some thermodynamic considerations about the energy states of species on either side of the interface are required. The solid and the liquid phases can be treated as mixtures consisting of different components whose energies are determined by the chemical environment in each phase. The chemical potential of the i^{th} component in phase α is given by:

$$\mu_i^\alpha = \mu_i^{0\alpha} + RT \ln a_i^\alpha \quad (2.1)$$

with the activity being the *effective* concentration $a_i = \gamma_i c_i$ (γ_i is the *activity coefficient*, and c_i the concentration), and the chemical potential μ_i^0 at standard conditions, that is $a_i = 1$. Thermodynamically, the chemical potential μ_i is defined by the differential change of the Gibbs free energy G upon addition of a small amount of the species i to the phase α :

$$\mu_i^\alpha = \left(\frac{\partial G}{\partial n_i} \right)_{T,p,n_j \neq n_i} \quad (2.2)$$

where n_i is the number of moles of i . If a solid electrode is immersed into an aqueous electrolyte solution, the chemical potential of component i is usually different on either side of the interface. To minimize the overall free energy G , the chemical potentials of both phases will try to equilibrate. This can be achieved by several electrochemical processes, such as dissolution of metal ions, electrochemical solvent decomposition reactions, electron transfer reactions of a redox couple in electrolyte or specific adsorption of ions from solution at the electrode surface. All of these processes lead to the accumulation of charge on either side of the interface, which brings about the formation of electrical potentials. The electrical potential within a phase is termed *Galvani potential*. To bring a z -valent charged particle from a non-interacting position into a phase α in which a Galvani potential φ exists, the work $zF\varphi$ needs to be done (where F is the Faraday constant). This additional contribution to the energy state of the phase is taken into account by the electrochemical potential of species i in phase α :

$$\tilde{\mu}_i^\alpha = \mu_i^{0\alpha} + RT \ln a_i^\alpha + z_i F \varphi^\alpha \quad (2.3)$$

An electrochemical reaction at an electrode/electrolyte interface is in equilibrium, if the change in *electrochemical* free energy, $\Delta\tilde{G}$ is zero:

$$\Delta\tilde{G} = \sum_i \nu_i \tilde{\mu}_i^{0\alpha} = 0 \quad (2.4)$$

with the stoichiometric coefficients ν_i being positive for the products and negative for the reactants of the reaction. It needs to be emphasized that an electrochemical equilibrium is a *dynamic* steady state of the solid/liquid interface, in which the Gibbs free energy is constant over time.

For a given electrochemical reaction, the Galvani potential difference $\Delta\varphi$ between electrode and electrolyte can be derived from equations 2.3 and 2.4, which yields the Nernst equation for a single electrode (see below). In electrochemistry, a solid/liquid interface, at which an electrochemical reaction is taking place, is also referred to as an *electrode* or as an (*electrochemical*) *half cell*. The latter derives from the fact that it is not possible to measure the Galvani potential difference of an electrode without inserting into the same electrolyte a second electrode as probe. On the other hand, this introduces an additional solid/liquid interface and a Galvani potential difference. To be able to attribute potential values to a given electrode of interest, the *working electrode*, the electrochemistry community has introduced *reference electrodes* with well defined and stable Galvani potential differences. The common standard is the so-called *standard hydrogen electrode* (SHE), whose potential is set to zero by convention. It consists of a Pt electrode in an aqueous electrolyte solution at 25 °C containing protons (H^+) of unit activity and gaseous hydrogen (H_2) at 1 atm (i.e. standard conditions).

2.1.1.1 The Nernst equation and the electromotive force

To determine $\Delta\varphi$ of an electrochemical half cell, the cell reaction needs to be taken into account. A straightforward example is a redox electrode, which consists of a metal electrode immersed into an electrolyte solution containing a substance that can exist in oxidized (OX) or reduced (RED) form through the loss or gain of n electrons to/from the electrode. The simplest redox reaction takes the form:



At equilibrium one obtains with equations 2.4 and 2.3:

$$\begin{aligned} \tilde{\mu}_{\text{OX}}^{\text{El}} + n\tilde{\mu}_{\text{e}^-}^{\text{Me}} &= \tilde{\mu}_{\text{RED}}^{\text{El}} \\ \mu_{\text{OX}}^0 + RT \ln a_{\text{OX}} + (z+n)F\varphi^{\text{El}} + n\mu_{\text{e}^-}^0 + RT \ln a_{\text{e}^-} - nF\varphi^{\text{Me}} &= \mu_{\text{RED}}^0 + RT \ln a_{\text{RED}} + zF\varphi^{\text{El}} \end{aligned} \quad (2.6)$$

From this, the Galvani potential difference between the metal (Me) and electrolyte (El) can be derived and yields the *Nernst equation* for the redox electrode:

$$\Delta\varphi = \varphi^{\text{Me}} - \varphi^{\text{El}} = \Delta\varphi^0 + \frac{RT}{nF} \ln \left(\frac{a_{\text{OX}}}{a_{\text{RED}}} \right) \quad (2.7)$$

where $\Delta\varphi^0$ contains the Galvani potential differences at standard conditions, which are defined as $a_{\text{OX}} \equiv a_{\text{RED}}$. Experimentally, the Galvani potential difference of the redox electrode can only be measured versus a reference electrode, such as the SHE. The resulting equilibrium electrode potential is then given by:

$$E_{\text{eq}} = E^0 + \frac{RT}{nF} \ln \left(\frac{a_{\text{OX}}}{a_{\text{RED}}} \right) \quad (2.8)$$

Now, E^0 determines the thermodynamic equilibrium potential of the electrode at standard conditions. From equation 2.8 one can see that at 25 °C the electrode potential varies by $-0.059/nV$ per decade decrease in the activity ratio. It is important to note that a true equilibrium with a potential given by equation 2.8 can only be established if a redox couple is present, whose oxidized and reduced form are linked *via* a redox reaction at the electrode. The standard potentials E^0 of electrochemical redox reactions can be derived from thermodynamic data, and their values (referenced to the SHE) are tabulated for the reduction reaction (notation like in equation 2.5). The higher the value of E^0 , the more favored is the reduction reaction. In other words, the more noble a species that is involved in a redox reaction, the more likely it will be reduced. Since the activity coefficients are almost always unknown, it is convenient to define the equilibrium electrode potential for the concentrations in the bulk electrolyte solution, which are labeled by an asterisk (c_{OX}^* and c_{RED}^*):⁶⁴

$$E_{\text{eq}} = E^{0'} + \frac{RT}{nF} \ln \left(\frac{c_{\text{OX}}^*}{c_{\text{RED}}^*} \right) \quad (2.9)$$

Here, $E^{0'}$ incorporates the activity coefficients (γ_{OX} and γ_{RED}) and is called the *formal potential*. It can be determined experimentally.

When two electrochemical half cells are electrically connected, e.g. through a common electrolyte (ionic conductor) into which two electrodes of different equilibrium potentials are immersed, and through an electric conductor that closes the circuit externally, one obtains an electrochemical cell. The overall cell reaction is electrically neutral and given as the combination of the two half cell reactions with the stoichiometric coefficients chosen so that the number of exchanged electrons, n , is equal for both half reactions. Electrochemical cells in which faradaic currents are flowing are classified as either *galvanic* or *electrolytic* cells, respectively, depending on whether the electrode reactions occur spontaneously or not. In a galvanic cell, chemical energy is converted into electrical energy. The most important commercial galvanic cells are batteries (during discharge) and fuel cells. In an electrolytic cell, electrical energy is supplied by an external voltage source to drive electrochemical reactions, which is used for example for electrolytic syntheses. Independent of the type of cell, the electrode, where oxidation reactions are taking place is defined as the *anode*, and the electrode, where reduction reactions are taking place, as the *cathode*. Accordingly, the current associated with oxidation is an anodic current and the one associated with reduction a cathodic one. In a galvanic cell, the cathode will be the electrode that has the higher standard reduction potential, since here the reduction reaction is favored and the cell reaction will proceed spontaneously.

The overall cell voltage at open circuit (i.e. no net current), also termed *open circuit potential* (OCP), is given by the difference in equilibrium potentials of the cathode and the anode. For a given spontaneous cell reaction, the Nernst equation of the complete (galvanic) cell is then:

$$\begin{aligned} \Delta E_{\text{cell,eq}} &= E_{\text{cathode}} - E_{\text{anode}} \\ &= \Delta E_{\text{cell}}^0 - \frac{RT}{nF} \ln \prod_{i = \text{products, reactants}} (a_i)^{\nu_i} \end{aligned} \quad (2.10)$$

where the stoichiometric coefficients ν_i are positive for the products and negative for the reactants.

With an exchange of n electrons during the transformation of one mole of reactants at each electrode, at maximum, an electrical work equal to $nF\Delta E_{\text{cell,eq}}$ can be performed in the external electrical circuit. This must correspond to the maximum useful work that can be obtained from the chemical reaction, that is the molar

Gibbs free energy change of the reaction, $\Delta_r G$. With that, the electrical work done by the electrochemical cell is given by the fundamental expression:

$$\Delta_r G = -nF\Delta E_{\text{cell,eq}} \quad (2.11)$$

where $\Delta E_{\text{cell,eq}}$ is the so-called *electromotive force* (EMF) of the electrochemical cell. The EMF of a galvanic cell has a positive value, since the cell reaction is spontaneous. If the reactants and products of the cell reaction are in their standard states (gases at unit atmospheric pressure, soluble species at unit mean activity), the free energy change is denoted by the standard value, $\Delta_r G^0$, and the corresponding standard cell voltage is ΔE_{cell}^0 . The standard molar free energy change of a given cell reaction can be calculated from thermodynamic data, using the expression

$$\Delta_r G^0 = \Delta_r H^0 - T\Delta_r S^0 \quad (2.12)$$

where the standard enthalpies of formation, $\Delta_r H^0$ and the standard entropies $\Delta_r S^0$ of the reactants and products are tabulated.

From the relation between cell voltage and Gibbs free energy change, the temperature dependence of the cell voltage can be derived according to:

$$\frac{\partial \Delta E_{\text{cell,eq}}}{\partial T} = -\frac{1}{nF} \frac{\partial \Delta_r G}{\partial T} = \frac{\Delta_r S}{nF} \quad (2.13)$$

which means that the EMF of a galvanic cell will increase with temperature, if the entropy change of the overall reaction is positive, and decrease with temperature, if the entropy change of the overall reaction is negative.

2.1.1.2 The metal/electrolyte and the semiconductor/electrolyte interface

The microscopic structure of the potential drop across the solid/liquid interface depends on the physical properties of both phases. Upon immersion of an electrode into the electrolyte, charge accumulates on the electrode side of the interface to adjust the electrochemical potentials of both phases. In response to this charging, ions of opposite charge accumulate and water dipoles reorientate in the vicinity of the surface on the solution side of the interface. The whole array of charged species and oriented dipoles existing at the electrode/electrolyte interface is called the *electrical double layer* (EDL), because it was initially thought of as a plate capacitor. Accordingly, at a given potential, the electrode-solution interface is characterized by a double layer capacitance, C_{EDL} , typically in the range of 10 to 40 $\mu\text{F cm}^{-2}$.⁶⁴ However, the potential drop across the solid/liquid interface is usually not simply linear like in a plate capacitor. Its shape depends on the density and distribution of charge in the electrode and in the electrolyte. On the solution side, the potential drop is determined by the structure of the EDL, which in turn depends on the concentration and the valency of the ions in solution. The potential drop inside the electrode depends on the electronic properties of the material. In the following, two cases will be considered: a metal electrode and a semiconductor electrode immersed into a dilute aqueous electrolyte solution.

The electrical double layer

Due to the high electrical conductivity of a metal, the charge that accumulates, when it is immersed into an electrolyte solution, is located at the very surface of the metal. Any inhomogeneous distribution of charge inside the bulk of the metal is immediately compensated by the free electrons that are available in high concentration (typically in the order of 10^{23} cm^{-3}). This is not the case on the electrolyte side of the interface, where the charge is carried by ions, having a significantly larger size and lower mobility. Therefore, the potential does not drop instantly across the solid/liquid interface but extends into the EDL. The structure of the EDL which forms on the solution side of the interface can be described in good approximation by the Gouy-Chapman-Stern model, which is schematically shown in Fig. 1.

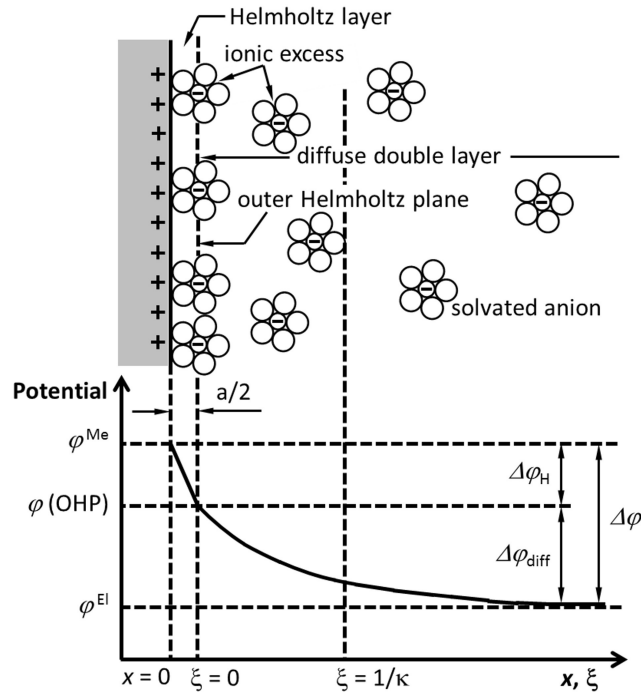


Fig. 1: Gouy-Chapman-Stern model of the EDL and according potential drop. Based on Fig. 3.16 in [65].

According to this model, the EDL consists of the Helmholtz layer and the diffuse layer. The Helmholtz layer contains specifically adsorbed ions and oriented water molecules on the metal surface (compact or inner Helmholtz plane, IHP, not shown in Fig. 1) and solvated ions in contact with the metal surface (outer Helmholtz plane, OHP). The thickness of the Helmholtz layer is determined by the distance $a/2$ between the metal surface and the center of charge of the largest present solvated ions, and is of the order of $\sim 100 \text{ \AA}$. Using the one-dimensional Poisson equation and assuming that there is no charge density ρ within the Helmholtz layer (as depicted in Fig. 1),

$$\frac{d^2 \varphi}{dx^2} = -\frac{\rho}{\epsilon_r \epsilon_0} = 0 \quad (2.14)$$

the potential drop across the Helmholtz layer is found to be constant. In the diffuse layer, the concentration of the excess charge decreases exponentially with the distance $\xi = x - a/2$ from the OHP due to thermal motion of the ions in solution, which is described by the Maxwell-Boltzmann distribution:⁶⁵

$$c_{\text{ion}}(\xi) = c_{\text{ion}}^* \exp \left[\frac{-ze_0 (\varphi(\xi) - \varphi^{\text{El}})}{k_B T} \right] \quad (2.15)$$

where c_{ion}^* is the ion concentration of the bulk electrolyte solution, ze_0 the charge carried by each ion, $\varphi(\xi)$ the potential at position ξ (see Fig. 1), φ^{El} the potential in the bulk electrolyte solution, k_{B} the Boltzmann constant and T the absolute temperature (in K). To calculate the potential drop, the according charge density $\rho = ze_0c_{\text{ion}}$ needs to be inserted into the Poisson equation 2.14, which can be solved for dilute electrolyte solutions and yields an exponential drop of the potential from the OHP into the bulk electrolyte solution:⁶⁵

$$\varphi(\xi) - \varphi^{\text{El}} = (\varphi(\text{OHP}) - \varphi^{\text{El}}) e^{-\kappa\xi} \quad (2.16)$$

A measure of the thickness of the diffuse double layer is given by the Debye-length κ^{-1} , at which the diffuse layer potential has dropped to $1/e$ of its value at the OHP.^{63,65} The Debye-length inversely depends on the square root of the total ionic concentration in the solution. The overall potential drop across the diffuse layer is also known as the zeta-potential, $\zeta = \varphi(\text{OHP}) - \varphi^{\text{El}}$. Due to its layered structure, the EDL behaves like a capacitor that consist of two capacitive contributions in parallel: the Helmholtz capacitance C_{H} and the diffuse layer capacitance C_{diff} . The total capacitance is given by

$$\frac{1}{C_{\text{EDL}}} = \frac{1}{C_{\text{H}}} + \frac{1}{C_{\text{diff}}} \quad (2.17)$$

In dilute electrolytes, e.g. 0.01 M ionic solutions, the thickness of the diffuse double layer may extend over more than 10 nm; however already at a concentration of 0.1 M, it is less than 1 nm thick, which is of the order of the compact Helmholtz layer thickness.^{63,65} Hence, for concentrated electrolyte solutions, C_{diff} can be neglected. The capacitance of the interface characterizes its ability to store charge q in response to a perturbation in potential E . Due to the complex microscopic structure of the EDL, its capacitance is generally a function of electrode potential and the process of double layer charging is usually described using the *differential capacitance* $C_{\text{EDL}}(E) = \partial q_{\text{EDL}} / \partial E$.

The Mott-Schottky equation and its limitations

If the metal is exchanged by a semiconductor (SC), the situation is different due to the significantly lower concentration of available charge carriers in the electrode (typically 10^{15} – 10^{18} cm^{-3} at room temperature in moderately doped semiconductors), that is typically lower than the concentration of ions in dilute electrolyte solutions. Depending on the type of semiconductor doping, the majority charge carriers are electrons (n-type semiconductor) or holes (p-type semiconductor). To understand what happens when a semiconductor is immersed into an electrolyte solution, one needs to consider the changes in the energy band structure. The semiconductor/electrolyte contact can be described using the theoretical framework that is used for semiconductor/metal interfaces, also known as Mott-Schottky model. Fig. 2 depicts the schematic energy diagrams for an n-type semiconductor before and after contact with an electrolyte that contains a redox couple.

In the presented case of an n-doped semiconductor, the initial Fermi level of the semiconductor is higher than the Fermi level of the redox couple Fig. 2a. When the electrode is brought into contact with the electrolyte solution, both energy levels equilibrate which causes a charging of the interface (Fig. 2b). Due to the low concentration of charge carriers in the semiconductor, the charging can only be accomplished through ionization of states in a certain volume from the surface to the bulk of the electrode. As a consequence, a

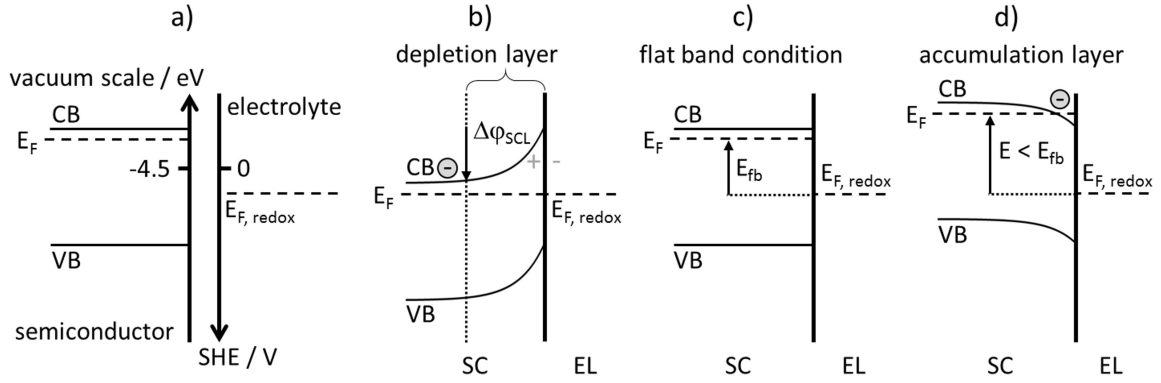


Fig. 2: Interface between n-type semiconductor (SC) and an electrolyte (EL) with redox couple. a) Before contact with indicated vacuum scale and electrochemical scale. b) After contact: depletion layer conditions, potential drop across space charge layer and accumulation of charge at interface. Applied potentials: c) flat-band conditions at $E = E_{fb}$, and d) accumulation layer conditions at $E < E_{fb}$ so that E_F lies within the conduction band. The donor level is not shown. Based on the theoretical treatments in [63, 67, 68].

space charge layer (SCL), which is a depletion layer in the presented case, is built up which accounts for most of the potential drop. The extraction of electrons from this volume is accompanied by a down-shift of the electrode Fermi level. At the same time, the band edges of the conduction band (CB) and of the valence band (VB) remain fixed at the surface and bend into the bulk of the electrode, where the relative band configuration resembles the situation of the semiconductor without contact with the electrolyte. The position of the electrode Fermi level and therewith the band bending can be influenced by the application of an external potential. There exists one potential which completely compensates for the band bending. This is the so-called *flat-band potential* E_{fb} (Fig. 2c). At potentials that are more negative than E_{fb} , the bands bend down towards the interface and electrons accumulate on the electrode surface (Fig. 2d). As the Fermi level enters the conduction band, the semiconductor's behavior can be compared to that of a metal and if an acceptor state of a redox active species is present, electrons can be transferred from the conduction band of the electrode to the species in solution. In contrast, the semiconductor blocks any current flow at potentials more positive than E_{fb} due to the energy barrier of the depletion layer, also called Schottky barrier. The space charge q_{SCL} that is present in the SCL under depletion layer conditions causes a capacitance inside the electrode, C_{SCL} , that contributes to the overall capacitance of the semiconductor/electrolyte interface:

$$\frac{1}{C} = \frac{1}{C_{EDL}} + \frac{1}{C_{SCL}} \quad (2.18)$$

To obtain the differential capacitance of the SCL, $C_{SCL} = \partial q_{SCL} / \partial \Delta \varphi_{SCL}$, a relationship between the excess charge in the semiconductor and the potential needs to be derived.

The relationship between the charge density, ρ_{SCL} , and the potential drop inside the SCL is given by the Poisson equation 2.14. Using the Boltzmann distribution to approximately describe the density of electrons in the SCL of an n-type semiconductor, and Gauss' law to relate the electric field through the interface to the charge contained within the interfacial region, the Poisson equation can be solved and yields the Mott-Schottky equation for the differential capacitance of the space charge under depletion layer conditions ($E > E_{fb}$):⁶⁹

$$\frac{1}{C_{SCL}^2} = \frac{2}{\epsilon_r \epsilon_0 A^2 e_0 N_D} \left(E - E_{fb} - \frac{k_B T}{e_0} \right) \quad (2.19)$$

where ε_r is the relative permittivity (dielectric constant) of the semiconductor, ε_0 the vacuum permittivity, A the electrode area, e_0 the elemental charge, N_D the donor density (in cm^{-3}), E the applied potential, E_{fb} the flat-band potential, k_B the Boltzmann constant and T the absolute temperature (in K). According to equation 2.19, a plot of the inverse square capacitance of an n-type semiconductor versus the applied potential, that is termed Mott-Schottky plot, gives a straight line with positive slope. For a given dielectric constant, the slope is determined by the donor density and its intersection with the abscissa yields the flat-band potential. The extension of the space charge layer is given by:⁶³

$$d_{\text{SCL}} = \sqrt{\frac{2\varepsilon_r\varepsilon_0\Delta\varphi_{\text{SCL}}}{e_0N_D}} \quad (2.20)$$

where $\Delta\varphi_{\text{SCL}}$ is the potential drop across the SCL. At potentials more negative than the flat-band potential, an accumulation layer is present and as soon as the Fermi level of the electrode reaches the lower band edge of the conduction band (or lies within the conduction band as in Fig. 2d) the capacitance of the space charge layer becomes independent of potential. In case of a thin semiconducting film on a conducting substrate, the thickness of the space charge layer d_{SCL} may exceed the film thickness d_{film} at sufficiently positive potentials ($E \gg E_{\text{fb}}$) and low donor concentration. Then, the SCL behaves like a dielectric between the electrolyte and the conducting substrate and the corresponding capacitance is the constant capacitance of a plate capacitor:

$$C_{\text{SCL}} = C_{\text{film}} = \varepsilon_r\varepsilon_0\frac{A}{d_{\text{film}}} \quad (2.21)$$

The Mott-Schottky plot of measured capacitance values is frequently used to characterize the electronic properties of semiconductors and in particular to extract values for N_D and E_{fb} . However, there are several cases, in which equation 2.19 is not valid or needs modification. In particular, the differential capacitance of an electrochemical cell, which contains a semiconductor electrode can only be set equal to the space charge capacitance C_{SCL} , if the capacitance of the EDL, that is determined by the compact Helmholtz layer at sufficiently high ionic concentrations, C_H , is much larger than C_{SCL} and if the predominant fraction of the potential drop occurs inside the semiconductor. This may not be the case for high concentrations of ionized donors (typically more than 10^{20}cm^{-2}). Theoretical treatments that account for the contributions of the compact Helmholtz layer to the overall capacitance and potential drop reveal that the slope of the Mott-Schottky curve will not be affected. However, the intersection with the potential axis suffers from a negative shift that needs to be taken into account to extract the flat-band potential:⁷⁰

$$\Delta E_{\text{error}} = -\frac{\varepsilon e_0 N_D}{8\pi C_H^2} \quad (2.22)$$

If the value of C_H is unknown, determination of the correct E_{fb} is difficult. Furthermore, a linear relationship between the squared inverse electrode capacitance and the applied potential, as predicted by equation 2.19, can only be found when all donors are ionized at the flatband potential. This implies the presence of a single donor level and sharp band edges, characteristic of the density of states function, $D(E)$, in ideal crystalline semiconductors. In non-crystalline or amorphous semiconductors this is usually not the case due to the distorted long-range order which brings about a distribution of localized electronic states below the conduction band edge and above the valence band edge. As the electrode potential is varied, these states may be ionized yielding a potential dependent charge density, that is given by the potential dependent

concentration of ionized donor states $N_D(E)$. As a consequence, one often encounters non-linear Mott-Schottky plots for noncrystalline materials, such as anodic TiO_2 .⁷¹⁻⁷³ From such plots, only the differential donor density can be extracted and a determination of the flatband potential is not accurate. Also a high concentration of surface states (SS) on non-ideal semiconductors can have an important impact on the effective band structure. Surface states can be caused by dangling covalent bonds or by a surface lattice potential that is different from the bulk potential in ionic compounds. The consequent excess energy at the surface can be minimized by surface reconstruction or by the adsorption of species from solution, which causes electronic states that are localized on the surface and usually lie in the band gap. For a high density of surface states, any charging current can be absorbed by these so that the Fermi level is effectively pinned to the according energy level, $E_F = E_{SS}$. In this case, the predominant potential drop will occur in the EDL and the electrode capacitance will be independent of potential.

2.1.2 Electrical current flow in an electrochemical cell

If an equilibrium potential is defined according to equation 2.8, any departure of the electrode potential from this reference point is termed *polarization* and the extent of polarization is measured by the *overpotential*,

$$\eta = E - E_{\text{eq}} \quad (2.23)$$

At cell potentials different from the equilibrium potential, the redox reactions at each electrode are proceeding in a preferred direction causing a net current to flow through the electrochemical cell. Besides currents from such faradaic processes, a polarization of an electrode/electrolyte interface from its equilibrium gives rise to currents associated with the non-faradaic adjustments of the excess charges at the interface to the new potential drop, a process which is often described as charging of the EDL.

Non-faradaic currents

Under some conditions, e.g. the absence of a redox couple, a given electrode/solution interface will show a range of potentials where non-faradaic processes are possible, but no charge transfer reactions occur. In this potential range, or potential window, the electrode is *polarizable*. When a potential step is applied to such an electrode, charge accumulates at or leaves from the interface until a new equilibrium is attained. The interface can be described by the ohmic resistance R_Ω of the electrolyte in series with the capacitance C_{EDL} of the EDL, and the potential step will cause a capacitive charging current that decays exponentially to zero,

$$I_{\text{EDL}} = \frac{E}{R_\Omega} e^{-t/R_\Omega C_{\text{EDL}}} \quad (2.24)$$

with the characteristic time constant of the RC circuit, defined as $\tau = R_\Omega C_{\text{EDL}}$. The EDL of an electrode/electrolyte interface does usually not behave like an ideal plate capacitor, and its capacitance generally depends on the applied potential. However, some electrodes have an extended potential range in which the EDL capacitance does not significantly change. When a linear potential sweep with the sweep rate $v = dE/dt$ is applied to such an electrode in this potential range, the current attains a steady-state value of vC_{EDL} .

Faradaic currents

A faradaic electrode reaction consists of several steps so that the electric current is governed by the rates of the corresponding processes, which are:

1. Mass transport between bulk electrolyte and interface;
2. Electron transfer across the interface;
3. Homogeneous or heterogeneous chemical reactions preceding or following the electron transfer;
4. Other surface reactions, such as adsorption, desorption, or crystallization.

The simplest reactions involve only mass transport and heterogeneous electron transfer and follow an *outer-sphere* mechanism, where the reactant does not adsorb on the electrode surface but is located in the outer Helmholtz plane during the electron transfer. An example for such an electron transfer is the redox reaction of the ferricyanide/ferrocyanide redox couple. In a general reaction, one or more of the above listed processes may be the *rate-determining steps* and limit the obtainable current at a given overpotential.

In the following, the two important cases of electron transfer controlled and mass transport controlled current will be discussed.

2.1.2.1 The kinetics of electrode reactions

Chemical reactions are thought to proceed along a reaction coordinate, along which the potential energy (or free energy) of the participants of the reaction changes as it is illustrated in the simplified scheme in Fig. 3. From a microscopic point of view, the reaction coordinate represents changing nuclear configurations in the reactants and the surrounding phase (e.g. the solvent of an electrolyte) in the course of the transformation to the product state.

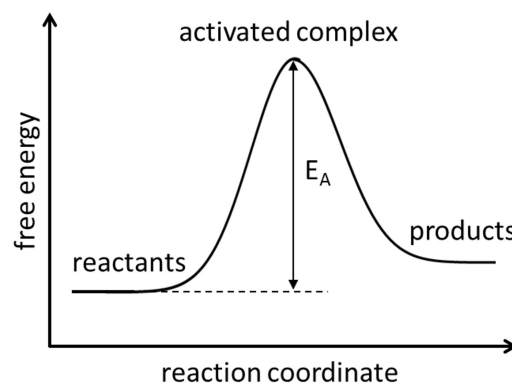


Fig. 3: Scheme of the free energy change along the reaction coordinate.

In order to be transformed to products, the reactants have to surmount a potential energy barrier, which requires a certain activation energy E_A that is defined as the difference between the potential barrier height and the potential energy of the reactants.

This picture derives from the observation that most reactions follow the empirically found Arrhenius law that relates the reaction rate with the temperature T :

$$k = Ae^{-E_A/RT} \quad (2.25)$$

where A is known as the *frequency factor*, which gives the frequency of attempts on the energy barrier and R is the universal gas constant.

According to the *transition state theory*, also known as the *activated complex theory*, the reactants need to go through a transition state in the course of a reaction, where they form an activated complex that has a higher potential energy than the reactants and the products. To apply this model for electron transfer reactions at the electrode/electrolyte interface, it is convenient to substitute the activation energy in equation 2.25 by the free energy of activation ΔG^\ddagger . From a microscopic point of view, the frequency factor of an electrode reaction is generally associated with bond vibrations and solvent motion in an electrolyte solution.

For a redox reaction of the form given in equation 2.5 the reaction can proceed in both directions and equilibrium is characterized by the Nernst equation. The reaction rates of the forward and backward reaction are determined by the associated rate constants, which in turn depend on the corresponding free energies of activation. The forward reaction is the reduction (red) of OX, and is associated with a cathodic current, $I_c < 0$. Accordingly, the backward reaction is the oxidation (ox) of RED and yields an anodic current, $I_a > 0$. For an electrode of area A it is useful to consider the current density $j = I/A$ rather than the absolute current. The relationship between the current densities and the rate constants is given by:

$$\begin{aligned} j_c &= \frac{I_c}{A} = -nFk_{\text{red}}c_{\text{OX}}(x=0, t) \\ j_a &= \frac{I_a}{A} = nFk_{\text{ox}}c_{\text{RED}}(x=0, t) \end{aligned} \quad (2.26)$$

where c_{OX} and c_{RED} denote the generally time dependent concentrations of the oxidized and reduced species at the electrode surface ($x = 0$).

The net current density at the redox electrode is then defined as

$$j = j_a + j_c = nF [k_{\text{ox}}c_{\text{RED}}(0, t) - k_{\text{red}}c_{\text{OX}}(0, t)] \quad (2.27)$$

where the rate constants are determined by the free energy changes during the reduction and oxidation reaction according to:

$$\begin{aligned} k_{\text{red}} &= A_{\text{red}}e^{-\Delta G_{\text{red}}^\ddagger/RT} \\ k_{\text{ox}} &= A_{\text{ox}}e^{-\Delta G_{\text{ox}}^\ddagger/RT} \end{aligned} \quad (2.28)$$

Under equilibrium conditions, the net current density is zero and $k_{\text{ox}}c_{\text{RED}} = k_{\text{red}}c_{\text{OX}}$.

The Butler-Volmer equation

Under certain restrictions, equation 2.27 can be used straight forwardly to derive an expression for the current density as a function of electrode overpotential. For this, the following conditions need to be fulfilled:

- the electrode has metallic conductivity, so that there is no potential drop inside the electrode;
- the electrolyte solution contains a high concentration of salt, so that the potential drop across the diffuse layer of the EDL is negligible, and the potential of the bulk electrolyte is fixed to a constant value;

- the redox reaction involves the transfer of n electrons in a single step, so that only one reaction path with one energy barrier needs to be considered;
- the electrons are transferred *via* an outer-sphere mechanism, which means that the redox species in solution remain outside the Helmholtz layer during the electron transfer.

Under these conditions, a change in electrode potential will only modify the energy of the electrons resident on the electrode and the entire potential drop will be accommodated within the Helmholtz layer. The redox species in solution on the other hand will not feel the potential drop in the Helmholtz layer and remain at the constant potential of the bulk electrolyte.

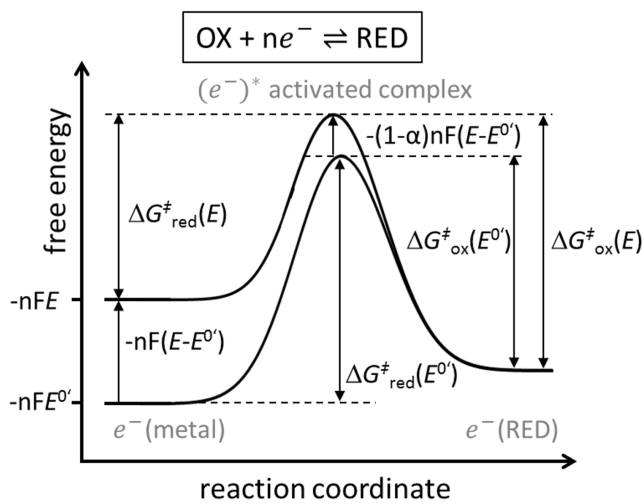


Fig. 4: Scheme showing the modification of the free energy diagram caused by a change of the potential. Based on the theoretical treatments in [64] (Fig. 3.3.2) and [65] (Fig. 4.5).

Fig. 4 shows schematically how the free energy difference of the reaction is affected by the application of a potential to the electrode. On the left hand side of the diagram is the free energy of the reactants OX + ne^- and on the right hand side the free energy of the products RED. It is sufficient to consider only the free energy of the involved electrons. Without loss of generality, the initial potential of the electrode is chosen as the formal potential $E^{0'}$, where the reaction is in equilibrium (equation 2.9) and $c_{\text{OX}}^* = c_{\text{RED}}^*$. If the initial potential of the electrode is changed by $\Delta E = E - E^{0'} < 0$ to the new value E , the free energy of the electrons resident on the electrode increases by $-nF\Delta E$ and the left side of the curve moves up by that value. Since the free energy of the electrons in solution (on RED) remains unaltered, only a fraction of the total free energy change $-(1 - \alpha)nF\Delta E$ actually appears for the activated complex. Thus one obtains for the free energy change of the reduction and oxidation reaction, respectively:

$$\begin{aligned}\Delta G_{\text{red}}^{\ddagger}(E) &= \Delta G_{\text{red}}^{\ddagger}(E^{0'}) + \alpha nF(E - E^{0'}) \\ \Delta G_{\text{ox}}^{\ddagger}(E) &= \Delta G_{\text{ox}}^{\ddagger}(E^{0'}) - (1 - \alpha)nF(E - E^{0'})\end{aligned}\quad (2.29)$$

When equation 2.29 is inserted into equation 2.28 for the rate constants, one obtains:

$$\begin{aligned}k_{\text{red}} &= A_{\text{red}} e^{-\Delta G_{\text{red}}^{\ddagger}(E^{0'})/RT} \cdot e^{-\alpha nF(E - E^{0'})/RT} \\ k_{\text{ox}} &= A_{\text{ox}} e^{-\Delta G_{\text{ox}}^{\ddagger}(E^{0'})/RT} \cdot e^{(1 - \alpha)nF(E - E^{0'})/RT}\end{aligned}\quad (2.30)$$

The first two factors in each of these expressions form a product that is independent of potential E and equal to the rate constant at $E = E^{0'}$. For an interface at equilibrium, there is no net current and equation 2.27 yields $k_{\text{ox}}c_{\text{RED}}(0, t) = k_{\text{red}}c_{\text{OX}}(0, t)$. Taking into account that the equilibrium potential E_{eq} assumes the value of the formal potential $E^{0'}$, if $c_{\text{OX}}^* = c_{\text{RED}}^*$ (Nernst equation 2.9), one obtains $k_{\text{red}} = k_{\text{ox}} = k^0$, which is the *standard rate constant*. The rate constants at other potentials can then be expressed in terms of k^0 :

$$\begin{aligned} k_{\text{red}} &= k^0 e^{-\alpha n F (E - E^{0'}) / RT} \\ k_{\text{ox}} &= k^0 e^{(1-\alpha) n F (E - E^{0'}) / RT} \end{aligned} \quad (2.31)$$

Using the Nernst equation 2.9 for general values of c_{OX}^* and c_{RED}^* , and the definition of the overpotential, $\eta = E - E_{\text{eq}}$, the potential difference $E - E^{0'}$ can be substituted by

$$E - E^{0'} = E - \left(E_{\text{eq}} - \frac{RT}{nF} \ln \frac{c_{\text{OX}}^*}{c_{\text{RED}}^*} \right) \quad (2.32)$$

and the rate constants in equation 2.31 can be expressed as a function of overpotential.

$$\begin{aligned} k_{\text{red}} &= k^0 \left(\frac{c_{\text{OX}}^*}{c_{\text{RED}}^*} \right)^{-\alpha} e^{-\alpha n F \eta / RT} \\ k_{\text{ox}} &= k^0 \left(\frac{c_{\text{OX}}^*}{c_{\text{RED}}^*} \right)^{(1-\alpha)} e^{(1-\alpha) n F \eta / RT} \end{aligned} \quad (2.33)$$

Insertion of these rate constants into equation 2.27 and introduction of the *exchange current density*, j_0 , yields the current density-overpotential equation, which is also known as the *Butler-Volmer equation*:

$$j = j_a + j_c = j_0 \left[\frac{c_{\text{RED}}(0, t)}{c_{\text{RED}}^*} e^{(1-\alpha) \frac{nF}{RT} \eta} - \frac{c_{\text{OX}}(0, t)}{c_{\text{OX}}^*} e^{-\alpha \frac{nF}{RT} \eta} \right] \quad (2.34)$$

where $0 \leq \alpha \leq 1$ is called the *transfer coefficient* or *asymmetry parameter* and is a measure of the symmetry of the energy barrier, with $\alpha = 0.5$ for the totally symmetric case. In the present derivation, the asymmetry parameter is defined such that for α near unity, the cathodic branch ($\eta < 0$) of the current density-overpotential curve (equation 2.34) would rise much more steeply than the anodic branch ($\eta > 0$). The exchange current density is defined by $j_0 = nF k^0 c_{\text{OX}}^{*(1-\alpha)} c_{\text{RED}}^{*\alpha}$ and yields the current density in equilibrium. It is a measure of the reaction kinetics for a given electrochemical system and depends on the physicochemical properties of the electrode and of the redox active species in solution, as well as on the reaction mechanism. Equation 2.34 contains the time-dependent concentrations at the electrode surface and therewith takes into account that the current density can be not only controlled by the electron transfer kinetics but also by mass transport processes. If mass transport does not limit the overall reaction rate, the overpotential associated with any given current density solely serves to provide the activation energy required to drive the heterogeneous process at the rate reflected by the current. The lower the exchange current density j_0 , the more sluggish the kinetics; hence, the larger this *activation overpotential* must be for any particular net current. If the exchange current density j_0 is very large, only insignificant activation overpotentials are required to supply large currents, even the mass-transport-limited current. In that case, any observed overpotential is associated with changing surface concentrations of the species OX and RED. This overpotential is called a *concentration overpotential* and can be viewed as an activation energy required to drive mass transport at the rate needed to support the current.⁶⁴

For small overpotentials and $c(0, t) = c^*$ for OX and RED, i.e. a purely electron transfer controlled reaction, the Butler Volmer equation simplifies to a linear relation between current and overpotential, which is independent of α :

$$j = -j_0 \frac{nF}{RT} \eta \quad (2.35)$$

Taking into account Ohm's law $j = \eta/R_{ct}$, where R_{ct} has units of $\Omega \text{ cm}^2$, the so-called *charge transfer resistance* R_{ct} can be defined:

$$R_{ct} = \frac{RT}{nFj_0} \quad (2.36)$$

At large anodic (cathodic) overpotentials and $c(0, t) = c^*$ for OX and RED, the cathodic (anodic) current density becomes negligible and the Butler Volmer equation simplifies to:

$$\eta = \frac{RT}{\alpha nF} (\ln j_0 - \ln |j|) \quad (2.37)$$

A plot of the logarithmic current density versus overpotential is called *Tafel plot* and can be used to determine E_{eq} as well as the kinetic parameters j_0 and α .^{64,65}

Charge transfer at a semiconductor electrode

In case of a doped n-type semiconductor electrode with a large band gap, where the density of mobile minority charge carriers, i.e. holes, is very small, the exchange current density for electrons is significantly higher than that for holes, and the measured current density becomes dominated by electron transfer between the conduction band and the redox species in solution. The current density-overpotential relation for the transfer of one electron from the conduction band of the electrode onto an acceptor state on the redox species in solution is given by:⁶³

$$j = j_0 \left(1 - e^{-\frac{e_0 \eta}{k_B T}} \right) \quad (2.38)$$

Here, the overpotential is defined by the shift of the Fermi level in the semiconductor with respect to the flat-band level through application of a potential $\eta = E - E_{fb}$, and equation 2.38 describes a rectifying behavior, with a cathodic current flowing for $E < E_{fb}$. For $E > E_{fb}$, the current density is small and essentially independent of potential.

Charge transfer by tunneling through blocking films

If a metal electrode is covered by a thick blocking film, such as an oxide, a direct electron transfer between the species in solution and the metal is inhibited or at least strongly hampered. An indirect transfer process is possible if the film is semiconducting and under accumulation layer conditions (see Fig. 2 and equation 2.38). However for very thin films, electrons can tunnel through the film and cause faradaic reactions. The effect of tunneling on the electron-transfer rate constant can be expressed by the modified standard rate constant:⁶⁴

$$k^0(x) = k^0(x=0)e^{-\beta x} \quad (2.39)$$

where x denotes the tunneling distance, and β is a factor that depends on the height of the energy barrier and the nature of the medium between the states. Due to the exponential decrease of the tunneling rate with distance, and with magnitudes of β of the order of 1 \AA^{-1} , electron tunneling will only be important for

electrodes with blocking films thinner than about 1.5 nm.

2.1.2.2 Limiting currents due to mass transport

The modes of mass transfer in an electrochemical cell are

1. Diffusion: movement of a species under the influence of a gradient of chemical potential (i.e. a concentration gradient);
2. Migration: movement of a charged species under the influence of a gradient of electrical potential (i.e. an electric field);
3. Convection: natural convection occurs due to density gradients, forced convection e.g. by stirring.

General mass transfer to an electrode is then described by the Nernst-Planck equation, which is for a one-dimensional problem:

$$J_i(x) = -D_i \frac{\partial c_i(x)}{\partial x} - \frac{z_i F}{RT} D_i c_i \frac{\partial \varphi}{\partial x} + c_i v(x) \quad (2.40)$$

where $J_i(x)$ is the flux of species i in $\text{mol s}^{-1} \text{cm}^{-2}$ at a distance x from the surface. The first term is *Fick's first law* and describes the flux due to diffusion with the diffusion coefficient D_i (in $\text{cm}^2 \text{s}^{-1}$) and the concentration gradient $\frac{\partial c_i(x)}{\partial x}$ at distance x . The second term is the flux due to migration, where z_i is the charge number, c_i the concentration in mol cm^{-3} of species i , and $\frac{\partial \varphi}{\partial x}$ the potential gradient. Finally, convection is defined by the last term, where $v(x)$ is the velocity with which a volume element in solution moves along x .

By a thorough design of the electrochemical experiment, overpotentials due to mass transport can be minimized or at least controlled. Using an inert supporting electrolyte with high ionic conductivity, the effect of migration can be neglected. To avoid uncontrolled (natural) convection or diffusion, the electrolyte can be stirred or a rotating disk electrode can be used (creating a laminar flow towards the electrode), both of which ensure sufficient transport of reactant species to the electrode surface. Under some conditions, it can be useful to allow for diffusion processes, e.g. to distinguish between kinetically controlled and diffusion controlled (i.e. nernstian) electrode reactions.

In case of a diffusion controlled electrode reaction, the current density is determined by the rate of diffusion of the electroactive species to the electrode. As soon as electron transfer reactions set in, the concentration of the reactants at the electrode surface, c^S , assumes very low values with respect to the concentration, c^* , in the bulk electrolyte, thereby causing a concentration gradient. Using Fick's first law for one-dimensional diffusion, the current density becomes:

$$j = I/A = -nFJ(x)_d = nFD \frac{\partial c}{\partial x} = nFD \frac{c^* - c^S}{\delta_N} \quad (2.41)$$

where δ_N is the *Nernst diffusion layer thickness*, which is generally time-dependent. When the solution is stirred, a steady state can be attained within seconds and δ_N takes on a constant value (of the order of μm). For constant δ_N , in any case $c^S \rightarrow 0$ with time, yielding the diffusion limited current density $j_{\text{lim}} = nFDc^*/\delta_N$. For the condition that the electron transfer rate is very fast, which is fulfilled at high activation overpotentials, the current density is limited by diffusion. The associated diffusion overpotential, η_d is defined by:

$$\eta_d = \frac{RT}{nF} \ln \left(1 - \frac{j}{j_{\text{lim}}} \right) \quad (2.42)$$

and describes the current density-overpotential characteristics in the diffusion limited regime.

At a constant potential, the diffusion layer thickness will increase with time until a steady state is reached, that is defined by natural or forced convection. The current-time behaviour at a constant potential and constant surface concentration can be derived from *Fick's second law*:

$$\frac{\partial c}{\partial t} = D \frac{\partial^2 c}{\partial x^2} \quad (2.43)$$

For semi-infinite diffusion, the boundary conditions are:

$$\text{initial condition: } t = 0, x \geq 0, \quad c(x, 0) = c^* \quad (2.44)$$

$$\text{semi-infinite condition: } t > 0, x \rightarrow \infty, \quad c(x, t) = c^* \quad (2.45)$$

$$t > 0, x = 0, \quad c(0, t) = c^S \quad (2.46)$$

With that, equation 2.43 can be solved to obtain the concentration profile $c(x, t)$.^{64,65} For small distances and long times, the slope of the concentration profile $\partial c/\partial x$ at the surface ($x = 0$) yields the time-dependent Nernst diffusion layer thickness:

$$\delta_N = (\pi Dt)^{\frac{1}{2}} \quad (2.47)$$

The according time dependent current density at a constant potential is obtained by insertion of equation 2.47 into equation 2.41:

$$j = nF \left(\frac{D}{\pi} \right)^{\frac{1}{2}} \cdot \frac{c^* - c^S}{t^{\frac{1}{2}}} \quad (2.48)$$

When electron transfer rates are high, $c^S \rightarrow 0$, and equation 2.48 simplifies to the so-called *Cottrell equation*.

2.1.3 Electrochemical Techniques

2.1.3.1 The potentiostat and the three electrode electrochemical cell

To study electrochemical (EC) processes at a single electrode/electrolyte interface, a three electrode EC cell is usually employed together with a potentiostat/galvanostat. The EC cell consists of the *working electrode* (WE), which is the electrode under investigation, the *reference electrode* (RE), and the *counter or auxiliary electrode* (CE), which are all immersed into an electrolyte.

The RE is an electrode which has a stable and well-known potential that is used as a point of reference in the EC cell for the potential control and measurement. The high stability of the RE potential is reached by ensuring constant concentrations of the potential determining redox species. Moreover, the current flow through the RE is kept close to zero. This is achieved by using the CE to close the current circuit in the EC cell, together with a very high input impedance ($> 100 \text{ G}\Omega$) on the electrometer in the potentiostat/galvanostat instrument, to which the RE is connected. The CE is usually made of a material with high electrical conductivity that does not cause electrochemical reactions which disturb the reactions at the WE, such as Pt, Au, graphite or glassy carbon. Since the current in the EC cell is flowing between the WE and the CE, the total surface area of the CE must be higher than the area of the WE to not be a limiting factor in the kinetics of the EC process at the WE.

Due to the ohmic resistance of the electrolyte between WE and RE, a potential drop occurs across this distance which causes an error in the measurement of the potential. This error can be kept small by using

a separate compartment for the RE, usually filled with the same electrolyte as the main EC cell, and by connecting the RE compartment with the main cell *via* a so-called *Luggin-Haber capillary*, which can be positioned close to the WE (see Fig. 38 in Chapter 3).

In an electrochemical experiment, a well defined (constant or time-dependent) potential or current is applied to the WE and the resulting current or potential response is measured, e.g. as a function of time or of the applied signal. Precise potential and current control and measurement is accomplished using a potentiostat/galvanostat.

Working principle of a potentiostat/galvanostat

In potentiostatic mode a potentiostat/galvanostat accurately controls, by a negative feedback mechanism, the potential of the CE against the WE so that the potential difference between the WE and the RE corresponds to the value specified by the user (i.e. applied potential or current). In galvanostatic mode, the current between WE and CE is controlled. Fig. 5 depicts a simplified circuit of a potentiostat in potentiostatic mode for the three electrode configuration.

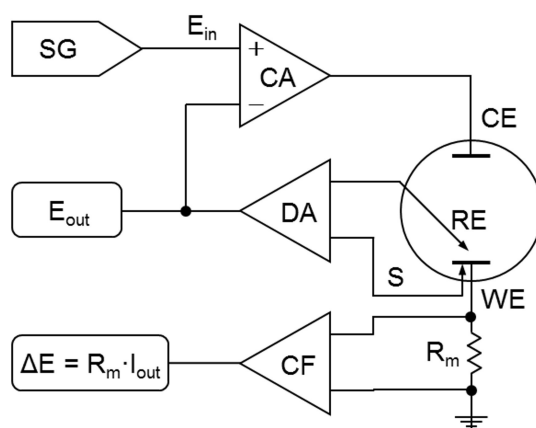


Fig. 5: Simplified scheme of a potentiostat. Based on schemes in [74, 75].

The CE is connected to the output of a *control amplifier* (CA), which forces current to flow through the EC cell. A *signal generator* (SG) creates the signal form requested from the user (e.g. linear ramp, triangular or sinusoidal wave) and sends it to the CA, which applies the signal form to the CE and adjusts its amplitude so that it corresponds to the chosen input value. The potential difference is measured between the RE and a sensing electrode (S), using a differential amplifier (DA) (i.e., the electrometer). The measured voltage signal is sent back to the CA, where it is compared to the desired voltage value. In case of deviation, the CA output signal is adjusted and counteracts to the initial perturbation. To obtain a three electrode configuration, where the potential difference is measured between the WE and the RE, S needs to be connected to the WE.

The current flow through the cell is measured by a current follower (CF, i.e., a current-to-voltage converter). For this, the current signal is converted to a voltage signal (ΔE) using the measurement resistance R_m in the converter.

2.1.3.2 Chronoamperometry

In chronoamperometry, an instantaneous potential step is applied to the working electrode and the current response measured as a function of time. The resultant current-time profile (also referred to as current

transient) yields information both about the rate of electron transfer and the rate of diffusion of material to the surface during electrode reactions. When the electrode is initially in equilibrium, the height of the potential step is identical with the overpotential.

If the overpotential is sufficiently high, so that only the anodic or only the cathodic electron transfer is relevant and also rapid (in the Tafel regime, equation 2.37), the current density is immediately diffusion controlled and its time dependency described by the Cottrell equation (see equation 2.48). A similar relation is obtained already for small overpotentials, if the electron transfer reaction is reversible and determined by the Nernst equation.⁶⁴ In case of arbitrary overpotentials and finite exchange current densities, at very short times the limiting processes will be electron transfer rather than diffusional in nature. However, immediately after the step, the current density is usually determined by the capacitive charging of the EDL and decays exponentially according to equation 2.24, where the time scale of the decay is given by the time constant $\tau = R_{\Omega}C_{EDL}$ and is of the order of 1 ms.

For a simple one-step, n -electron transfer reaction as in equation 2.5, neglecting adsorption and desorption steps and coupled chemical reactions, and without forced convection, the diffusion equations 2.43 can be written in the form:⁶⁵

$$\frac{\partial c_{OX}}{\partial t} = D_{OX} \frac{\partial^2 c_{OX}}{\partial x^2}; \quad \frac{\partial c_{RED}}{\partial t} = D_{RED} \frac{\partial^2 c_{RED}}{\partial x^2}, \quad (2.49)$$

and the electron transfer rate is determined by the concentration dependent Butler-Volmer equation 2.34.

The boundary conditions for a potential step from the stationary state ($\eta = 0$) to an overpotential η are:

$$t = 0, x \geq 0, \quad c_{OX}(x, 0) = c_{OX}^*; \quad c_{RED}(x, 0) = c_{RED}^* \quad (2.50)$$

$$t > 0, x \rightarrow \infty, \quad c_{OX}(x, t) = c_{OX}^*; \quad c_{RED}(x, t) = c_{RED}^* \quad (2.51)$$

$$t > 0, x = 0, \quad c_{OX}(0, t) = c_{OX}^S; \quad c_{RED}(0, t) = c_{RED}^S \quad (2.52)$$

In addition, the flux balance at the electrode surface requires that:

$$j = -nFD_{OX} \left(\frac{\partial c_{OX}(x, t)}{\partial x} \right)_{x=0} = nFD_{RED} \left(\frac{\partial c_{RED}(x, t)}{\partial x} \right)_{x=0} \quad (2.53)$$

Solving equations 2.49, the overpotential- and time-dependent current density can be expressed as:⁶⁵

$$j(\eta, t) = j_0 \left\{ \exp \left[\frac{(1-\alpha)nF\eta}{RT} \right] - \exp \left[-\frac{\alpha nF\eta}{RT} \right] \right\} e^{\lambda^2 t} \operatorname{erfc}(\lambda\sqrt{t}), \quad (2.54)$$

where

$$\operatorname{erfc}(\lambda\sqrt{t}) = 1 - \frac{2}{\sqrt{\pi}} \int_0^{\lambda\sqrt{t}} e^{-x^2} dx; \quad \lambda = \frac{j_0}{nF} \left\{ \frac{\exp \left[\frac{(1-\alpha)nF\eta}{RT} \right]}{c_{RED}^* \sqrt{D_{RED}}} + \frac{\exp \left[-\frac{\alpha nF\eta}{RT} \right]}{c_{OX}^* \sqrt{D_{OX}}} \right\} \quad (2.55)$$

Apparently, the current density is given as the product of two functions, $j_{et}(\eta) \times g(\eta, t)$. The first term corresponds to the electron transfer-limited current density and the second term accounts for the effect of diffusion, where $g(\eta, t) \rightarrow 1$ as $t \rightarrow 0$. Since at very short times $\lambda\sqrt{t} \ll 1$ equation 2.54 simplifies to

$$j(\eta, t) = j_{et}(\eta) \left(1 - \frac{2\lambda}{\sqrt{\pi}} \sqrt{t} \right) \quad (2.56)$$

a plot of $j(\eta, t)$ vs. \sqrt{t} allows to determine the electron transfer-limited current density $j_{et}(\eta)$ for a given

overpotential by extrapolation to $t = 0$. Doing this for several overpotentials, a Tafel plot can be generated and the kinetic parameters j_0 and α extracted. At long times, $g(\eta, t) \rightarrow 1/(\lambda\sqrt{\pi t})$, a purely diffusion-limited current density is recovered. Without forced convection, the diffusion-limited current density eventually drops to zero.

Fig. 6 shows a typical current transient after a potential step and the above discussed time-regimes. The non-faradaic currents due to charging of the EDL are only relevant at very short times (black segment). A plot of the current *versus* \sqrt{t} allows to extrapolate the faradaic current density at short times to $t = 0$ and to determine the kinetically controlled value j_{et} .

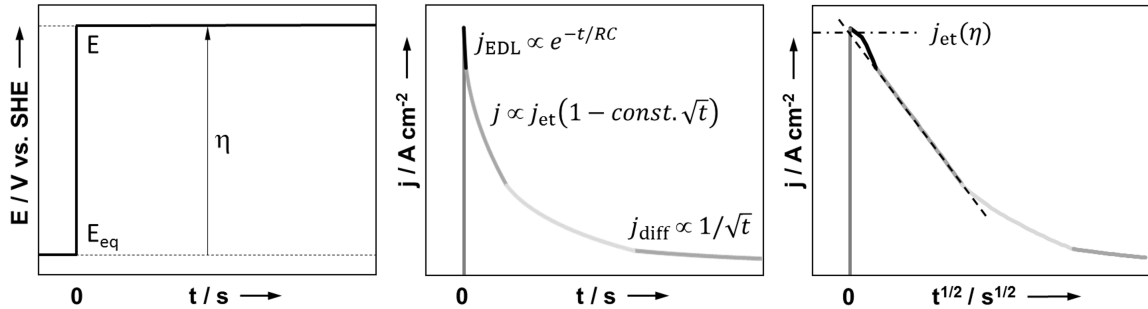


Fig. 6: Potential step, current transient with indicated electrode processes at different times, and determination of electron transfer-limited current density from the plot of the current density versus \sqrt{t} .

Limiting effects due to diffusion can be reduced or even eliminated experimentally by forced convection, evoked e.g. by stirring the electrolyte or rotating the electrode. Under these conditions, the current density does not decay to zero at long times but approaches a steady-state value which is determined by the now constant diffusion layer thickness δ_N (see equation 2.41). Sufficiently high enforced material transport rates can ensure that the concentration of reactants at the electrode surface is equal to the bulk concentration at the potentials of interest. Under these conditions, the diffusion layer vanishes and the reaction rate is entirely kinetically controlled, yielding constant current-time curves after the initial capacitive charging regime. Multi-step electron transfer reactions that comprise ad- and desorption of reactants, intermediates and products, as well as coupled chemical reactions, or electrochemical reactions that occur in parallel, lead to more complex current-time behaviors during a potential step experiment. Blocking adsorbates for example can cause also purely kinetically controlled current densities to decrease with time.^{76,77}

Activation energies from current transients

An alternative expression for equation 2.54 is:⁶⁴

$$j(t) = nF (k_{\text{ox}}c_{\text{RED}}^* - k_{\text{red}}c_{\text{OX}}^*) e^{H^2 t} \text{erfc}(H\sqrt{t}) \quad (2.57)$$

with

$$H = \frac{k_{\text{red}}}{\sqrt{D_{\text{OX}}}} + \frac{k_{\text{ox}}}{\sqrt{D_{\text{RED}}}} \quad (2.58)$$

At high anodic overpotentials, only the oxidation reaction is relevant, and the terms that are proportional to the reduction rate constant k_{red} become zero. For long times, the anodic current density is diffusion controlled

and equation 2.57 simplifies to:

$$j(t)_{\text{diff}} = nFk_{\text{ox}}c_{\text{RED}}^* \frac{\sqrt{D_{\text{RED}}}}{k_{\text{ox}}\sqrt{\pi t}} \quad (2.59)$$

which shows that the diffusion-limited current density is independent of the electron transfer rate constant.

At short times, the current density is given by:

$$j(t) = nFk_{\text{ox}}c_{\text{RED}}^* \left(1 - \frac{2k_{\text{ox}}}{\sqrt{\pi D_{\text{RED}}}}\sqrt{t} \right) \quad (2.60)$$

and for $\sqrt{t} \rightarrow 0$, inserting k_{ox} from equation 2.28:

$$j(t=0) = j_{\text{et}} = nFc_{\text{RED}}^*k_{\text{ox}} = nFc_{\text{RED}}^* \cdot A_{\text{ox}}e^{-\Delta G_{\text{ox}}^\ddagger/RT} \quad (2.61)$$

This relation provides the possibility to determine the potential dependent activation energy $\Delta G_{\text{ox}}^\ddagger$ (see equation 2.29) of a simple one-step, n -electron transfer reaction from a measurement of current transients at a given overpotential η and at different temperatures. Since equation 2.61 can be written in the form

$$\ln j(t=0) = \ln(nFc_{\text{RED}}^*A_{\text{ox}}) - \frac{\Delta G_{\text{ox}}^\ddagger}{R} \cdot \left(\frac{1}{T} \right) \quad (2.62)$$

the value of the potential dependent activation energy can be extracted from the slope of the *Arrhenius plot*, that displays $\ln(j(t=0))$ versus $1/T$, as shown in Fig. 7.

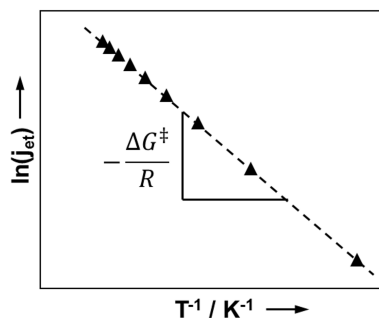


Fig. 7: Arrhenius plot of the electron transfer-limited current density and extraction of the activation energy from the slope.

For a specific (over)potential, $\Delta G_{\text{ox}}^\ddagger$ is linked to the exchange current density j_0 of the electron transfer reaction at a given electrode material (see equations 2.29–2.34), which provides information on the material's catalytic activity for that reaction. A low $\Delta G_{\text{ox}}^\ddagger$ value indicates a high exchange current density and therewith a high catalytic activity at the applied (over)potential. Activation energies that are determined from apparent current densities that are measured at a given (over)potential, and not from the exchange current density, are referred to as *apparent activation energies*.⁶⁵ In a real potential step experiment it is sometimes difficult to extract the true kinetically controlled current density, j_{et} , in particular if the region of capacitive charging extends to longer times and if material transport limitations cannot be completely excluded. Fortunately, diffusion coefficients in aqueous solution show a much lower temperature dependence than normal chemical reactions, increasing only at the rate of 2–3 % per degree K, and entirely diffusion controlled electrochemical reactions show little temperature sensitivity.⁶⁵ Therefore, a pronounced dependence of measured current densities on temperature indicates that, at the respective potentials, the electrochemical reaction rate is mainly controlled by charge transfer kinetics. When it comes to the interpretation of apparent activation

energies, particular care needs to be taken if complex multi-step electron transfer reactions are studied, which comprise several parallel reaction paths and the adsorption of blocking intermediates or anions from the supporting electrolyte.⁷⁸ In that case, the apparent activation energy, determined from the faradaic current densities, is a combination of the activation energies of different reaction steps occurring at the studied potential.⁷⁹ However, if the overall rate of the electrochemical reaction at a specific potential is limited by a single reaction step, independent of temperature, linear Arrhenius plots can be observed and the apparent activation energy provides information about this rate determining step.⁷⁸

2.1.3.3 Linear sweep voltammetry and cyclic voltammetry

In potential sweep voltammetry, a time-dependent linearly changing potential $E_i + dE/dt \cdot t$ is applied to the working electrode, and its current response is measured simultaneously as a function of potential, $j(E)$. The variation of the applied potential is constant and given by the *scan rate* $v = dE/dt$, that is positive for an anodic potential sweep and negative for a cathodic sweep. There are two important types of voltammetry: *linear sweep voltammetry* and *cyclic voltammetry*. In linear sweep voltammetry (LSV), starting from an initial value E_i , the potential is varied with time in one direction and then interrupted at a final potential E_f . In cyclic voltammetry, a time-dependent potential of triangular waveform is applied to the electrode: starting from an initial value E_i , e.g. the OCP of the cell, the potential is varied with a constant scan rate in anodic direction until a chosen switching potential $E_{s,a}$ is reached, where the potential sweep is reversed and varied with the same scan rate in cathodic direction until the second switching potential $E_{s,c}$, and so on. Just as well, the CV can be cycled with the cathodic direction first. The obtained current-potential curve is called *cyclic voltammogram* (CV) and provides an electrochemical spectrum of anodic and cathodic electrode processes. In the following, some important aspects of cyclic voltammetry will be discussed.

Generally, the current measured during cyclic voltammetry is a superposition of several non-faradaic and faradaic processes. There are always capacitive charging currents due to the formation of the EDL:

$$j = \frac{dQ}{dt} = C \frac{dE}{dt} = C_{\text{EDL}} v \quad (2.63)$$

where Q is the charge and C_{EDL} the area specific EDL capacitance, and v the scan rate in V s^{-1} . A potential range, in which only capacitive charging is observed, is called the double layer region of the CV. These non-faradaic currents increase linearly with the scan rate v and any faradaic current needs to be measured from this baseline. It should be noted, that C_{EDL} generally depends on potential. In the absence of redox active species, the observed current-potential behaviour in aqueous solution corresponds to the formation and dissolution of chemisorbed hydride and oxide layers on the electrode surface and yields electrochemical spectra that are often characteristic for the material and surface structure of the electrode. One of the most studied CVs is the one of a polycrystalline Pt surface, which causes a unique electrochemical fingerprint. A typical Pt CV will be described below. At high enough anodic and cathodic polarization potentials, any aqueous solution becomes electrochemically active due to the hydrolysis of water to hydrogen and oxygen gas, which defines the potential window, in which CVs can be acquired. The corresponding reactions are called *hydrogen evolution reaction* (HER), which causes an exponential increase of the cathodic current, and *oxygen evolution reaction* (OER), that is accompanied by a strong increase of the anodic current.

In combination with a redox couple in the electrolyte solution, that undergoes a simple outer sphere one-step,

n -electron transfer reaction (equation 2.5), cyclic voltammetry can be used to study reaction kinetics at a given electrode. An often used probe for such experiments is the ferro-/ferricyanide redox couple, where $n = 1$. With bulk concentrations $c_{\text{OX}}^* = c_{\text{RED}}^*$ and without electrolyte agitation, one may obtain a stable CV as depicted in Fig. 8 after several cycles. Due to the coupling of diffusion of reactants to the electrode and an electron transfer process at the surface, an anodic and a cathodic current maximum is observed. As soon as the oxidation of RED is initiated during the anodic scan, the current density will increase and the surface concentration $c_{\text{RED}}^{\text{S}}$ will start to decrease from c_{RED}^* to zero. This initially increases the concentration gradient and therewith the flux of RED to the electrode. At higher potentials, the mass transport limited current density will be reached, which drops with time due to the increasing diffusion layer thickness (equations 2.47 and 2.48), causing the observed anodic current density peak. An according discussion explains the cathodic current density peak. The shape of the CV, in particular the peak separation ΔE_p and the anodic and cathodic peak current densities $j_{p,a}$ and $j_{p,c}$, provide qualitative information about the kinetics of the electron transfer reaction.

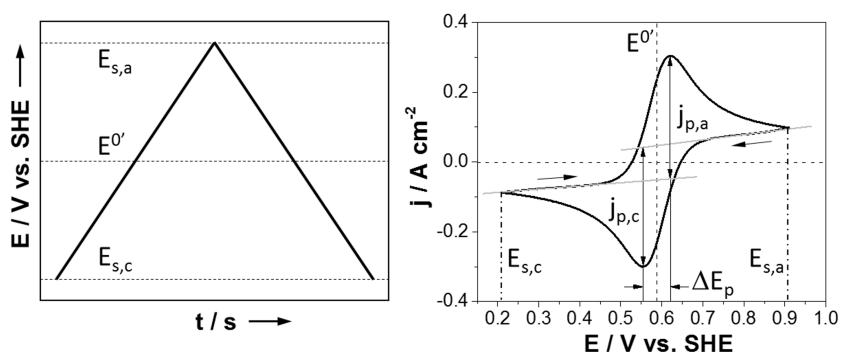


Fig. 8: Triangular voltage signal at working electrode and typical cyclic voltammogram of a reversible redox reaction. The scan direction is indicated by arrows.

In general, the anodic (cathodic) current density-potential curve of a CV like the one depicted in Fig. 8 can be calculated by invoking the concentration-dependent Butler-Volmer equation 2.34, where the time-dependent overpotential $\eta(t) = E_i + vt - E_{\text{eq}}$ ($v > 0$ for the anodic scan and $v < 0$ for the cathodic scan) needs to be inserted, in conjunction with Fick's laws (equations 2.49), which can give the time-dependent surface concentrations $c_{\text{RED}}^{\text{S}}$ and c_{OX}^{S} . To do this, appropriate boundary conditions need to be defined, which is difficult if the initial potential E_i is not the equilibrium potential, where no net current flows. Therefore, usually only the current density-potential curve for the very first anodic or cathodic CV scan is calculated in the literature.^{64,65} Given that the electrode is initially in equilibrium (boundary condition 2.50), the time dependence of the surface concentrations, $c_{\text{OX}}(0, t)$ and $c_{\text{RED}}(0, t)$, and therewith the boundary condition 2.52 is dictated by the rate of the electron transfer process. In the following, three cases will be considered: reversible (fast), irreversible (slow) and quasi-reversible electron transfer. Since even for simple boundary conditions for a planar electrode in equilibrium and semi-infinite diffusion a throughout analytical solution of this problem is not possible,⁶⁴ the derivation will be kept short.

Case (a): reversible (fast) electron transfer. At all potentials, electron transfer is sufficiently rapid, so that the Nernst equation always applies and relates the concentration ratio at the surface with the momentary

potential $E(t) = E_i + vt$. This yields the following boundary condition:

$$t > 0, x = 0, \quad \frac{c_{\text{OX}}^{\text{S}}}{c_{\text{RED}}^{\text{S}}} = \exp \left[\frac{nF(E_i + vt - E^{0'})}{RT} \right] \quad (2.64)$$

and one obtains for the anodic peak current density during the very first anodic scan:⁶⁴

$$j_{\text{p,a}} = 0.4463 \left(\frac{F^3}{RT} \right)^{1/2} n^{3/2} D_{\text{RED}}^{1/2} c_{\text{RED}}^* v^{1/2} \quad (2.65)$$

The theory predicts that the peak current density increases linearly with the square root of the scan rate, \sqrt{v} , which is confirmed experimentally. When starting a cyclic voltammogram, the current density is initially zero. Therefore, the base-line for the peak current density during the first anodic scan is $j = 0$. The shape of the current density curve on reversal depends on the distance between the anodic peak potential and the anodic switching potential. If the switching potential, $E_{\text{s,a}}$ is at least $35/n$ mV past the anodic peak, the cathodic peak will have the same general shape as the very first anodic peak, but with the decaying anodic current upon reversal as baseline. The same is true for the reversal from the cathodic back to the anodic scan direction, so that upon cycling the anodic and cathodic peak current densities are defined as shown in Fig. 8. For a redox couple with $D_{\text{OX}} = D_{\text{RED}}$ and $c_{\text{OX}}^* = c_{\text{RED}}^*$ the peak current density ratio is $j_{\text{p,a}}/j_{\text{p,c}} = 1$, regardless of scan rate, as soon as a stable CV is established. In that case, the center potential between the two peaks $E_{1/2}$ is identical with the formal redox potential $E^{0'}$ of the chosen redox couple. For a redox couple with $D_{\text{OX}} \neq D_{\text{RED}}$, the center potential is $E_{1/2} = E^{0'} + (RT/nF) \ln(D_{\text{RED}}/D_{\text{OX}})^{1/2}$. A clear identification of a nernstian electron transfer is given by the peak separation. If the distance between the switching potentials is sufficiently large, the peak separation is predicted to be $\Delta E_{\text{p}} = 57/n$ mV and independent of the scan rate.⁶⁴

Case (b): irreversible (slow) electron transfer. Is the electron transfer slow, there will be still current peaks in the CV, but the peak separation will be no longer independent of scan rate. Instead, an increase of the peak separation is observed with increasing scan rate, which is a qualitative measure for an inhibited electron transfer. The boundary condition for a totally irreversible one-step, n -electron transfer reaction during the anodic scan is now:

$$t > 0, x = 0, \quad \frac{j}{nF} = D_{\text{RED}} \left(\frac{\partial c_{\text{RED}}(x, t)}{\partial x} \right)_{x=0} = c_{\text{RED}}(0, t) k_{\text{ox}}(t) \quad (2.66)$$

where the rate constant is time-dependent due to the potential sweep,

$$k_{\text{ox}}(t) = k_0 \exp \left[- \frac{(1 - \alpha)nF(E_i + vt - E^{0'})}{RT} \right] \quad (2.67)$$

With these boundary conditions the anodic peak current density during the very first scan can be calculated:⁶⁴

$$j_{\text{p,a}} = 0.4958 \left(\frac{(1 - \alpha)F^3}{RT} \right)^{1/2} n^{3/2} D_{\text{RED}}^{1/2} c_{\text{RED}}^* v^{1/2} \quad (2.68)$$

It is proportional to \sqrt{v} , as in the reversible case. For a symmetric electron transfer, $\alpha = 0.5$, and a given scan rate, the irreversible peak current density is 79 % of the reversible peak current density of the same redox reaction.

The peak potential can be shown to be:⁶⁴

$$E_{p,a} = E^{0'} + \frac{RT}{(1-\alpha)nF} \left[0.780 + \ln \left(\frac{D_{RED}^{1/2}}{k^0} \right) + \ln \left(\frac{(1-\alpha)nFv}{RT} \right)^{1/2} \right] \quad (2.69)$$

Due to the dependence on k^0 , which is small for slow electron transfer, the peak separation will be larger than the one of the reversible reaction for any scan rate. Furthermore, the peak potential in equation 2.69 depends on the scan rate. For $\alpha = 0.5$, $n = 1$, and at 25 °C, this leads to an additional increase of peak separation by ~ 30 mV for every tenfold increase in v .

Case (c): quasireversible electron transfer. The term *quasireversible* is used for reactions that show electron-transfer kinetic limitations where the reverse reaction has to be taken into account as well. As in the irreversible case, the peak separation will be always larger than $57/n$ mV and increase with increasing scan rate. But in contrast to reversible or irreversible electron transfer kinetics, the peak current densities are not proportional to \sqrt{v} , which allows identification of the quasireversible case.⁶⁴

2.1.3.4 AC methods to measure impedance

An alternative approach to study the dynamics of electrochemical processes is based on the perturbation of a steady state (e.g. the electrochemical equilibrium) with an alternating signal of small amplitude and the measurement of the system response. In a typical experiment, a dc potential with a superimposed sinusoidal ac signal of defined frequency $\omega = 2\pi f$ and amplitude δE , as shown in Fig. 9, is applied to the working electrode, and the output current density measured as a function of frequency or as a function of potential. The amplitude δj and phase shift ϕ (with respect to the phase of the ac potential signal) of the alternating current response are determined by the impedance of the electrochemical cell, which is essentially the impedance of the induced faradaic and non-faradaic processes towards the perturbation. An analysis of the cell impedance in combination with appropriate models that relate interfacial phenomena with electrical quantities, such as resistances and capacitances, yields quantitative information about electrode processes.

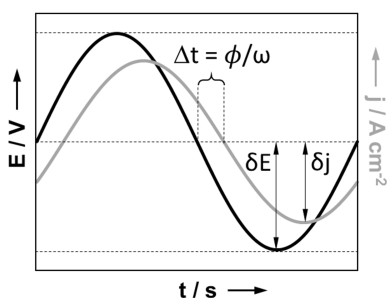


Fig. 9: Sinusoidal potential signal that is applied to an electrochemical cell and sinusoidal current response with phase shift ϕ .

Such methods depend on the fact that current-overpotential relationships are virtually linear at low overpotentials (equation 2.35). Under these conditions, the frequency of the response signal is identical to the one of the excitation signal, and the proportionality "factor" between current density and potential is given by the

complex, frequency-dependent (area specific) impedance $Z(\omega)$:

$$\begin{aligned} E(t) &= \delta E \sin(\omega t) \\ j(t) &= \delta j \sin(\omega t + \phi) \\ E(t) &= Z(\omega)I(t) \end{aligned} \quad (2.70)$$

The area specific complex impedance is defined by:

$$\begin{aligned} \mathbf{Z} &= Z_{\text{Re}} + iZ_{\text{Im}} = |Z|e^{i\phi} \\ \tan(\phi) &= \frac{Z_{\text{Im}}}{Z_{\text{Re}}} \\ |Z|^2 &= Z_{\text{Re}}^2 + Z_{\text{Im}}^2 \end{aligned} \quad (2.71)$$

where i is the complex number. The experimental requirements for the measurement of cell impedances are a potentiostat that is equipped with a function generator, to produce sinusoidal signals, and with a frequency response analyzer (FRA) or lock-in amplifier, to measure the amplitude and phase shift of the ac current signal.

Electrochemical impedance spectroscopy

Electrochemical impedance spectroscopy (EIS) involves the study of the variation of the impedance of an electrochemical system as a function of the frequency of an applied small-amplitude ac perturbation. Its main advantage is the capability of studying different processes occurring simultaneously, such as charge accumulation at the interface, electron transfer across the interface and mass transport in the bulk electrolyte close to equilibrium conditions. Therewith it provides a complementary approach to potential sweep voltammetry, which requires large-voltage perturbations to extract the same information. In an EIS experiment, the frequency of the alternating voltage signal is varied over several orders of magnitude, usually going from high to low frequencies, and the current response is measured to determine the impedance of the electrochemical cell as function of frequency. The obtained data are usually presented in form of so-called *Nyquist* and *Bode plots*, which both allow to extract some quantitative information about the studied system at one glance. In a Nyquist plot, or complex plane plot, the negative imaginary part of the impedance $-Z_{\text{Im}} = -Z''$ is plotted versus the real part $Z_{\text{Re}} = Z'$. The Bode plot shows the *Bode modulus* (i.e. the absolute value of the impedance $|Z|$) and the *Bode phase* (i.e. the negative phase shift $-\phi$ of the current signal with respect to the voltage perturbation) versus the frequency $f = \omega/2\pi$. Fig. 10 shows typical Nyquist and Bode plots that would be obtained from EIS of an electrode in an electrolyte that contains a redox couple with $c_{\text{OX}}^* = c_{\text{RED}}^*$, where the equilibrium potential is defined by the Nernst equation.

The ohmic resistance of the EC cell, which is predominantly the uncompensated resistance of the electrolyte solution (between working and reference electrode), R_{Ω} , as well as the charge transfer resistance, R_{ct} (defined by equation 2.36) can be immediately read off from the intersections of the semicircle with the real axis in the Nyquist plot and from the plateaus in the Bode modulus. The area specific capacitance of the EDL can be determined from the frequency, where the top of the semicircle in the Nyquist plot is reached and where the Bode phase has a maximum. At low frequencies, the cell impedance is increasing further due to the growing relative importance of mass transport limitations. This causes a characteristic straight line of 45° in

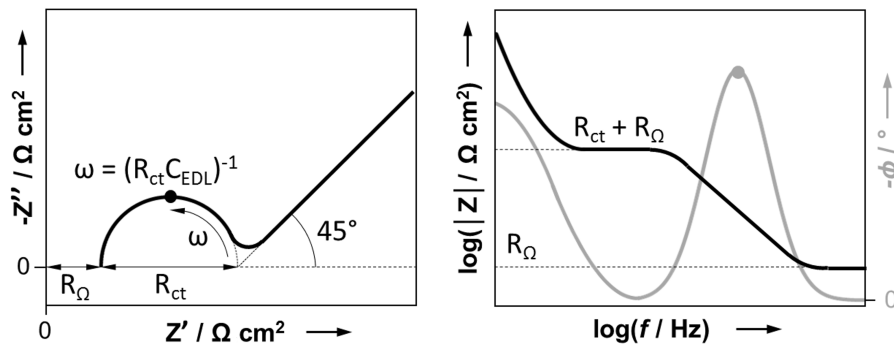


Fig. 10: Nyquist plot (left) and Bode plot (right) qualitatively presenting the impedance of an electrode reaction in presence of a redox couple. In the Nyquist plot, the frequency ω increases along the arrow. The plots are based on measured spectra reported in [80].

the Nyquist plot and an increase of the Bode modulus and phase towards low frequencies. The assignment of electrochemical processes to different parts of the measured impedance spectra and the extraction of electrical quantities requires a model that allows to calculate the total impedance of the electrochemical (half) cell.

Equivalent circuit models

The phenomenological behavior of an electrode/electrolyte interface is mathematically described in terms of electrical equivalent circuit (EEC) models, that consist of serial or parallel connected simple electronic components, such as resistors and capacitors. If an appropriate model is found, the total impedance of an electrochemical system can be calculated and a least squares fit of the model to the measured impedance spectra enables the determination of the impedances of individual electrochemical processes. In the following, the EEC models and the associated impedances of some relevant non-faradaic and faradaic electrochemical processes will be introduced.

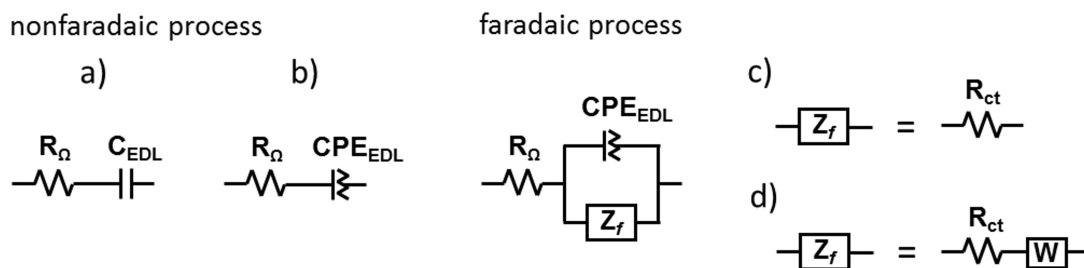


Fig. 11: EEC models representing typical non-faradaic and faradaic electrochemical processes: Charging of a) an ideal and b) a non-ideal EDL; faradaic process with c) irreversible charge transfer or d) charge transfer and mass transport control. The symbols denote: R = resistor, C = capacitor, CPE = constant phase element, Z_f = faradaic impedance, W = Warburg element. The labels denote: Ω = ohmic, EDL = electrical double layer, ct = charge transfer.

Charging of the EDL and the constant phase element: A blocking electrode, where the charging of the EDL *via* the electrolyte is the only electrochemical process at the electrode/electrolyte interface, can be represented by a series circuit of the ohmic resistance of the EC cell R_Ω and the EDL capacitance C_{EDL} , as shown in Fig. 11a. This EEC model produces a straight line in the Nyquist plot, perpendicular to the real axis

and intersecting it at R_Ω . However, in particular with solid electrodes, one often encounters a straight line that is tilted by less than 90° with respect to the real axis, suggesting that the EDL does not behave like an ideal capacitor. This can be explained by a distribution of time constants $\tau = RC$ along the area of the electrode and/or along the axis normal to the electrode surface due to inhomogeneous physicochemical properties, which brings about a frequency dispersion of the complex dielectric constant.^{66,80,81} A lateral distribution of time constants is proposed to arise from surface heterogeneities such as grain boundaries, crystal faces on a polycrystalline electrode, chemical inhomogeneities and the like.^{66,80} A distribution of time constants perpendicular to the electrode surface may be related with porosity, surface roughness or to changes in the conductivity of oxide layers.⁶⁶

To take into account a distribution of time constants in EEC models a so-called *constant phase element* (CPE) can be used. Its impedance is defined by:⁶⁶

$$Z_{\text{CPE}} = \frac{1}{Q(i\omega)^n} \quad (2.72)$$

where Q is the CPE constant, ω the angular frequency and $0 \leq n \leq 1$ the CPE exponent, which is related to the angle of rotation β of a purely capacitive line on the complex plane plot, with $\beta = 90^\circ(1 - n)$. Both Q and n , as well as the phase angle associated with a CPE are independent of frequency. In general, equation 2.72 can describe ideal capacitive or resistive behavior as well as a distribution of time constants, depending on the exponent value. For $n = 1$, $Q = C$ and the impedance is the one of a pure capacitor, and for $n = 0$, it corresponds to a pure resistor $Q = 1/R$. When $0 < n < 1$, Q has units of $\text{s}^n \Omega^{-1} \text{cm}^{-2}$. Deviation of n from unity characterizes the degree to which the capacitor is not ideal.⁶⁶ With equation 2.72, the total impedance associated with the charging of the EDL at a blocking electrode is given by:⁶⁶

$$Z(\omega) = R_\Omega + \frac{1}{Q(i\omega)^n} \quad (2.73)$$

and the corresponding EEC model is depicted in Fig. 11b.

Irreversible electron transfer and the charge transfer resistance: When the electrolyte contains a redox couple and the electrode allows for charge transfer, the total current derives from the sum of two processes: inert ions and redox active species move from the bulk electrolyte to the electrode surface, where the former accumulate and charge the EDL and the latter undergo a faradaic reaction with charge transfer across the interface. Since both processes occur in parallel, the according EEC model consists of a parallel circuit of the faradaic impedance Z_f and a CPE impedance for the EDL, Z_{EDL} , that are both in series with the electrolyte resistance, as depicted in Fig. 11. In case of a totally irreversible charge transfer, diffusion does not limit the reaction rate and the faradaic impedance is determined by the charge transfer resistance, $Z_f = R_{\text{ct}}$, which is defined by equation 2.35. The according EEC model is shown in Fig. 11c, and the total impedance is given by:⁶⁶

$$Z(\omega) = R_\Omega + \frac{R_{\text{ct}}}{1 + R_{\text{ct}}Q(i\omega)^n} \quad (2.74)$$

In case of $n = 1$ and $Q = C$, the parallel RC -circuit yields a semicircle in the Nyquist plot, similar to the one shown in Fig. 10. Taking into account the ohmic resistance of the EC cell (i.e. basically the solution resistance), the center of the semicircle on the real axis is shifted from zero by $R_\Omega + R_{\text{ct}}/2$. In case of inhomogeneous

electrode properties, the impedance of the EDL behaves like the one of a CPE. The consequence is a semicircle in the Nyquist plot that is depressed along the imaginary impedance axis.

The contribution of diffusion and the Warburg impedance: In general, the kinetics of faradaic electrode reactions are determined by the electron transfer rate and by the rate of mass transport to the electrode, where diffusion is the dominating mechanism in most electrochemical systems. Using the boundary conditions for semi-infinite diffusion in an unstirred electrolyte (equations 2.50 and 2.51) and solving

$$j(t) = -nFD_{\text{OX}} \left(\frac{\partial c_{\text{OX}}(x,t)}{\partial x} \right)_{x=0} = nFD_{\text{RED}} \left(\frac{\partial c_{\text{RED}}(x,t)}{\partial x} \right)_{x=0} = \delta j \sin(\omega t) \quad (2.75)$$

to obtain the alternating surface concentrations $c_{\text{OX}}(0,t)$ and $c_{\text{RED}}(0,t)$, it can be shown that the faradaic impedance is given by:⁶⁴

$$\mathbf{Z}_f = R_{\text{ct}} + \mathbf{Z}_W = R_{\text{ct}} + R_W - i/(\omega C_W) \quad (2.76)$$

Replacing the faradaic impedance in Fig. 11 by the sum in equation 2.76 yields the EEC model depicted in Fig. 11d, where the symbol W denotes the so-called *Warburg element*. The corresponding *Warburg impedance*, \mathbf{Z}_W , is the impedance of the system due to linear semi-infinite diffusion. It is defined by:

$$\mathbf{Z}_W = \frac{\sigma}{\omega^{1/2}} - i \frac{\sigma}{\omega^{1/2}} \quad (2.77)$$

where the area specific Warburg coefficient is given by:

$$\sigma = \frac{RT}{(nF)^2 \sqrt{2}} \left[\frac{1}{D_{\text{OX}}^{1/2} C_{\text{OX}}^*} + \frac{1}{D_{\text{RED}}^{1/2} C_{\text{RED}}^*} \right] \quad (2.78)$$

Since $-Z''_W/Z'_W = 1$, the Warburg impedance yields a straight line of slope one in the Nyquist plot. If one compares Z''_W of equation 2.77 with the CPE impedance in equation 2.72, it becomes clear that for $n = 0.5$, the CPE represents the imaginary part of the Warburg impedance.

With the introduced correlations between electrical circuit elements and electrochemical processes, a least-square fit of the electrochemical impedance spectra in Fig. 10 can be performed with the EEC model in Fig. 11d and will yield values for the solution resistance, the charge transfer resistance, the EDL capacitance and the Warburg coefficient.

Potential step EIS and Mott-Schottky analysis

In potential step EIS, the dc potential is changed from an initial value E_i to a final value E_f with a constant step size, and electrochemical impedance spectra are acquired at each step. Since it allows to study impedances as a function of potential, this technique is particularly interesting for Mott-Schottky analysis of electrochemically stable semiconducting electrodes. In an inert aqueous electrolyte solution and within the stability window of water, the only electrochemical process will be the capacitive charging of the interface. Therefore, the system can be described with the EEC model in Fig. 11a or b. However, the C_{EDL} needs to be replaced by the capacitance given in equation 2.18 to take into account the capacitance of the space charge layer, C_{SCL} , that is in series with the EDL. For sufficiently concentrated ionic solutions, the extension of the diffuse double layer in the electrolyte is negligible and the EDL consists essentially of the compact Helmholtz layer. Furthermore, the capacitance of the Helmholtz layer is usually much larger than the one

of the space charge layer, unless the semiconductor is highly doped, so that the total capacitance will be dominated by C_{SCL} . Under these conditions, the imaginary impedance that is measured during a potential step EIS experiment, is $-Z'' = 1/(\omega C_{\text{SCL}})$ and yields, for a chosen frequency, the potential-dependent space charge layer capacitance. This capacitance may be used for Mott-Schottky analysis (equation 2.19) to obtain information about the doping level of the semiconductor.

2.1.4 Fuel cells and the electrocatalysis of the ethanol oxidation reaction

A fuel cell is a galvanic cell consisting of an anode and a cathode that are separated by an ion conducting electrolyte. When a fuel is fed to the anode and an oxidant to the cathode, electron transfer reactions are taking place and a current can be extracted to run an external load. In principle, a fuel cell can continuously produce electrical energy if the fuel supply is not interrupted. However, the fuel is often stored in a container, which imposes limits to the volume and mass of available fuel and is particularly problematic for electromobility applications. Therefore, fuels of high energy density, such as primary alcohols, are in the focus of fuel cell research. The electric power of a fuel cell $P = I \cdot V$, with current I and voltage $V = \Delta E$, is determined by its current-voltage characteristics. When a current is drawn, the corresponding operating voltage will be lower than the EMF of the galvanic cell due to activation overpotentials, concentration overpotentials and ohmic drops.⁸² It is desired to keep the overpotential, at which a usable current can be drawn from the cell, as low as possible. The highest potential drop is usually associated with the activation overpotential, which is linked with the current density *via* the Butler Volmer equation 2.34. To extract high currents at low overpotentials, the free energy of activation of a given reaction must be reduced.

The kinetics of heterogeneous reactions depend on the temperature, the reactant concentration, the physical state of the reactants (liquid or gaseous) and on the used catalyst. Electrocatalytic processes involve physisorption or chemisorption of reactants and/or products on the electrode surface. In complex multi-step electrochemical reactions also homogeneous or heterogeneous chemical reactions may occur. Since processes that are based on an interaction of the reacting species with the electrode strongly depend on the physicochemical properties of the latter, an appropriate choice of the catalyst can increase the reaction kinetics significantly.

Fig. 12 shows the general effect of a suitable catalyst on the activation energy for a particular reaction.

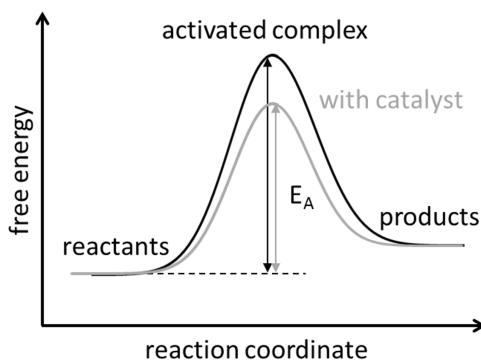


Fig. 12: Effect of a catalyst on the activation energy of a reaction.

2.1.4.1 The polymer electrolyte fuel cell and the direct ethanol fuel cell

A very important type of fuel cell, which can be operated at low to intermediate temperatures using hydrogen or primary alcohols as fuel, is the *polymer electrolyte membrane fuel cell* (PEMFC). In a PEMFC, the electrolyte is a polymer, which has a high conductivity for protons and behaves insulating for electrons. That is why such fuel cells are also called proton exchange membrane fuel cells. Fig. 13 shows a sketch of a PEMFC that is run with hydrogen gas or ethanol (EtOH). The H₂ fuel is supplied to the anode and oxidized at the catalyst to protons that release electrons to the external circuit. The protons cross the polymer membrane - up to operating temperatures of 80 °C typically Nafion[®] - and at the cathode, which is fed with molecular oxygen or air, they react with oxygen to form water.

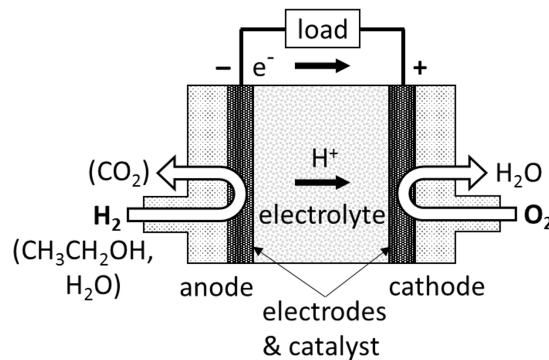
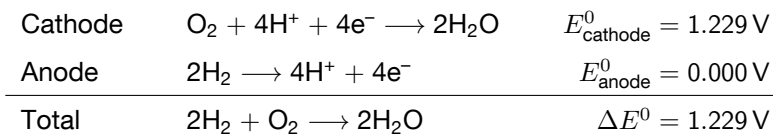
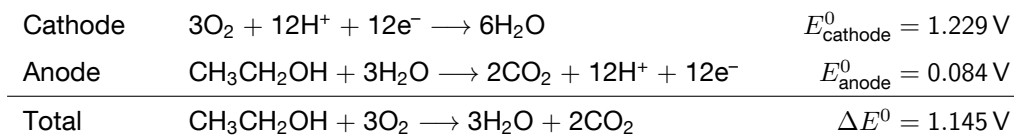


Fig. 13: Sketch of a PEMFC fed with hydrogen gas or alcohols.

In acidic environment, as present in a PEMFC, and using hydrogen fuel, the electrochemical half cell reactions are:^{65,83}



As mentioned in the introduction, the use of ethanol fuel instead of hydrogen is very appealing due to its high mass specific energy density. Principally, the chemical energy stored in ethanol can be converted into electric energy by using a *direct ethanol fuel cell* (DEFC). The electrochemical reactions in a PEM-DEFC are given by:^{84,85}



One can see that the expected reaction products are only water and carbon dioxide. This anticipates that ethanol is fully oxidized to CO₂. Upon full oxidation, 12 electrons can be extracted per molecule, leading to the high specific energy density. In contrast to the hydrogen oxidation reaction, the oxidation of ethanol requires a sufficient amount of water at the anode, which needs to be taken into account when optimizing the water management in DEFC stacks.⁵

The performance of the H₂-O₂ PEMFC is limited by the sluggish reaction kinetics of the oxygen reduction reaction (ORR) at the cathode, while the main overpotential loss of DEFCs is attributed to the slow reaction kinetics of the ethanol oxidation reaction (EOR) at the anode.^{84,86} The EOR is a complex multi-step reaction

that comprises ad-/desorption of reactants, intermediates and products, as well as a C-C bond-cleavage step. There is more than one possible reaction path, but only one of them leads to the complete oxidation of ethanol, which is associated with the maximum electron yield. To achieve a high electron yield at low overpotentials, highly active catalysts are required, that are at the same time selective towards the most favorable reaction path.⁹ Furthermore, the operating conditions of the DEFC, such as reaction temperature and water management, are parameters that need to be optimized.⁵

2.1.4.2 The Pt electrocatalyst

The most studied and commercially used PEMFC electrocatalyst material is platinum (Pt). It is an efficient catalyst for the electrochemical hydrogen evolution reaction (HER) and hydrogen oxidation reaction (HOR), as well as for the C-C bond cleavage of ethanol.^{84,89} Pt belongs to the noble transition metals and is highly corrosion resistant. It crystallizes in the hexagonal system with an fcc lattice. Fig. 14 shows top views of the most stable surfaces (111), (100) and (110).

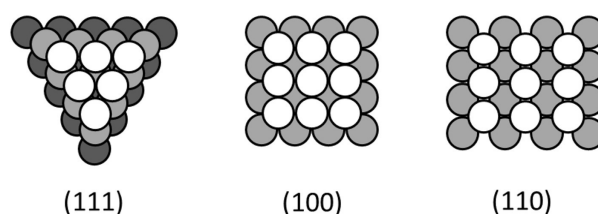


Fig. 14: Top views of the fcc crystal surfaces (111), (001) and (110) of Pt.

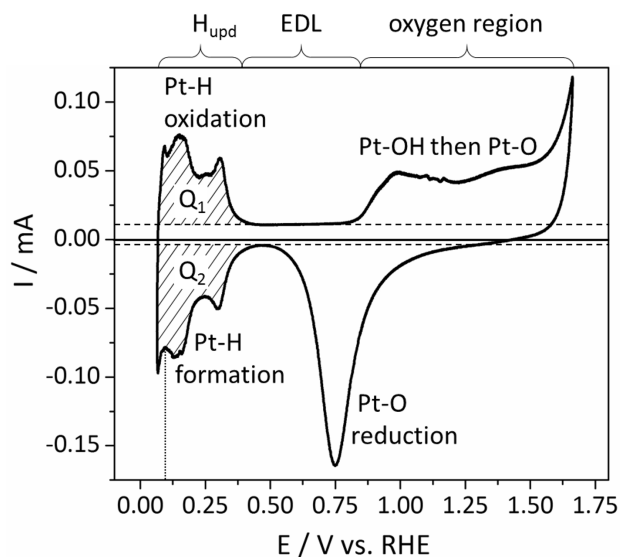


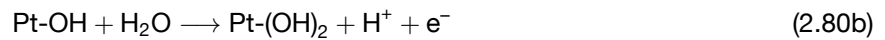
Fig. 15: CV of polycrystalline Pt wire in 0.1 M H_2SO_4 , scan rate 100 mV s^{-1} .

Fig. 15 shows the electrochemical fingerprint of a polycrystalline Pt electrode, obtained by cyclic voltammetry in 0.1 M H_2SO_4 electrolyte. The cathodic potential limit is chosen before the onset of high cathodic currents, which are caused by the hydrogen evolution reaction (HER, below 0.0 V). The rising anodic currents beyond 1.5 V are ascribed to the onset of the oxygen evolution reaction (OER). The dashed lines in Fig. 15 denote the anodic and cathodic current densities that originate from capacitive processes (i.e. charging of the EDL). Current densities beyond this level arise from faradaic processes. There are several characteristic features

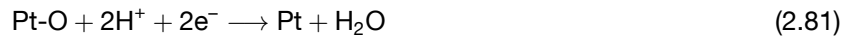
in the cathodic and anodic branches of the CV curve. During the positive-going potential scan, two distinct anodic peaks are observed between ~ 0.1 V and 0.40 V that correspond to the dissociative adsorption of H_2 and the oxidation of H to produce H^+ . This process can be expressed as:⁸⁸



Between ~ 0.40 V and ~ 0.82 V, i.e. the double-layer region, the current density takes on a constant value which is ascribed to the capacitive charging of the EDL. Above ~ 0.82 V the current density is rising until it reaches a peak at ~ 1.00 V, which is followed by a plateau. Here, oxidation of the Pt surface takes place in several steps:⁸⁸



During the reverse (negative-going) CV scan, the PtO on the surface is reduced again, leading to the cathodic current peak at 0.75 V. The according reaction can be expressed as:⁸⁸



After a small double-layer region, the (negative) current density is increasing again, and two cathodic peaks are observed between 0.40 V and ~ 0.1 V. They can be ascribed to the adsorption of hydrogen induced by the reduction of protons on the Pt surface. The according process is⁸⁸



Since this reaction occurs at potentials that are less cathodic than the thermodynamic potential for the HER (0.0 V), it is referred to as underpotential deposition of hydrogen (H_{upd}).

Electrochemically active surface area

Real Pt-based PEMFC catalysts consist of supported metal nanoparticles, where the effective catalyst area that is accessible for an electrochemical reaction is determined by the size and shape of the nanoparticles and depends on how they are embedded into the high surface area support. Furthermore, many Pt-catalyzed electrochemical reactions are sensitive to the structure of the catalyst surface, which is characterized by the exposed Pt(*hkl*) facets and by the number and kind of surface defects.^{87,90} To be able to compare the activities of differently prepared Pt catalysts for the same electrochemical reaction, it is therefore necessary to know the number of available active sites, and to normalize reaction currents to the electrochemically active surface area (ECSA) rather than to the geometric area of the catalyst or electrode. A widely recognized procedure for the determination of the ECSA of Pt catalysts is based on the electroadsorption and -desorption of hydrogen on Pt.

The hatched areas of the anodic and cathodic peaks in the H_{upd} potential region of the Pt CV in Fig. 15 represent the amounts of charge exchanged during the electroadsorption (Q_2) and desorption (Q_1) of atomic

hydrogen on the active Pt sites. The charge can be calculated by the integration of the cathodic and anodic current I in the respective potential range dE , and subtraction of the double-layer charge Q_{EDL} :

$$Q = \frac{1}{v} \int_{E_{min}}^{E_{max}} I dE - Q_{EDL} \quad (2.83)$$

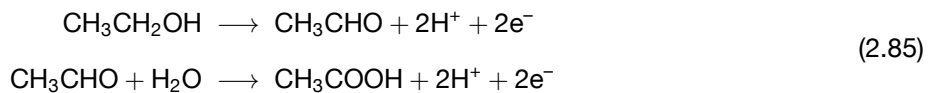
where $v = dE/dt$ is the scan rate of the CV. From the charge Q_H , which is the arithmetic average of Q_1 and Q_2 , the ECSA of any Pt (impregnated) electrode can be determined, using the formula:

$$ECSA = \frac{Q_H [\mu C]}{210 \mu C cm^{-2}} \quad (2.84)$$

It has been commonly accepted, that the charge that corresponds to a monolayer of adsorbed hydrogen on a planar Pt surface can be assumed to be $210 \mu C cm^{-2}$, which has become the conventional standard for the determination of the ECSA of Pt from the H_{upd} charge.⁹¹ This value is based on the assumption that a polycrystalline Pt surface is characterized by an equal distribution of the three low index planes (100), (111) and (110), and that each surface atom can adsorb one hydrogen atom, which is accompanied by the transfer of one electron. It should be noted that, when scanning towards cathodic potentials, the HER sets in before full coverage of the Pt surface with monoatomic hydrogen is achieved, so that the current density close to the cathodic potential limit in Fig. 15 is a superposition of hydrogen adsorption and hydrogen evolution. To obtain a reliable value for the hydrogen adsorption charge, it has been recommended to integrate the current between the anodic potential limit of the H_{upd} and the potential, where the cathodic current reaches the second minimum, denoted by the dotted line in Fig. 15. At this potential the hydrogen coverage has been determined to be 77%.⁹¹

2.1.4.3 The ethanol oxidation reaction on Pt

It is known that the EOR follows a multistep reaction mechanism with a number of intermediates and possible pathways that lead to the formation of undesired by-products, which diminish the total electron yield. Furthermore, the oxidation of intermediates requires the activation of water (OH_{ads}) to provide oxygen. On Pt catalyst and in acidic media, the main products of EOR are acetaldehyde and acetic acid, that result from partial ethanol oxidation without C-C bond breaking:⁷⁹



where the intermediate acetaldehyde is easily desorbed and lost for further oxidation, while the strongly adsorbing acetic acid (acetate anion) cannot be further oxidized and constitutes a catalyst poison, blocking active sites for the EOR.

For an optimal conversion of the chemical energy stored in EtOH into electricity by a DEFC, it is required to enhance the current efficiency for complete EtOH electrooxidation to CO_2 per one carbon atom (CO_2 current efficiency), and to minimize the overpotentials and maximize the reaction rate of the related reaction steps. The key step in the EOR is the electrooxidation of adsorbed CO and it is necessary to remove CO_{ads} from the electrode surface through its electrooxidation at a lower potential.⁸⁶ This can be achieved

by the use of binary or ternary catalysts, where Sn (or Sn oxide) and/or Ru are added to or alloyed with Pt to facilitate water activation which is required to oxidize the adsorbed intermediates during ethanol dissociation.^{9,84,86,89,92-96} The efficiency for the splitting of the C-C bond in EtOH at low potentials and for the subsequent deprotonation can be enhanced by addition of Rh to Pt-based catalysts.^{89,96-99} Furthermore, and independent of the chosen Pt-based catalyst, a clear reduction of the EOR overpotential, increased current densities and an enhancement of the CO₂ current efficiency is achieved by an increase of the cell temperature.^{9,10,76,86,93,99,100}

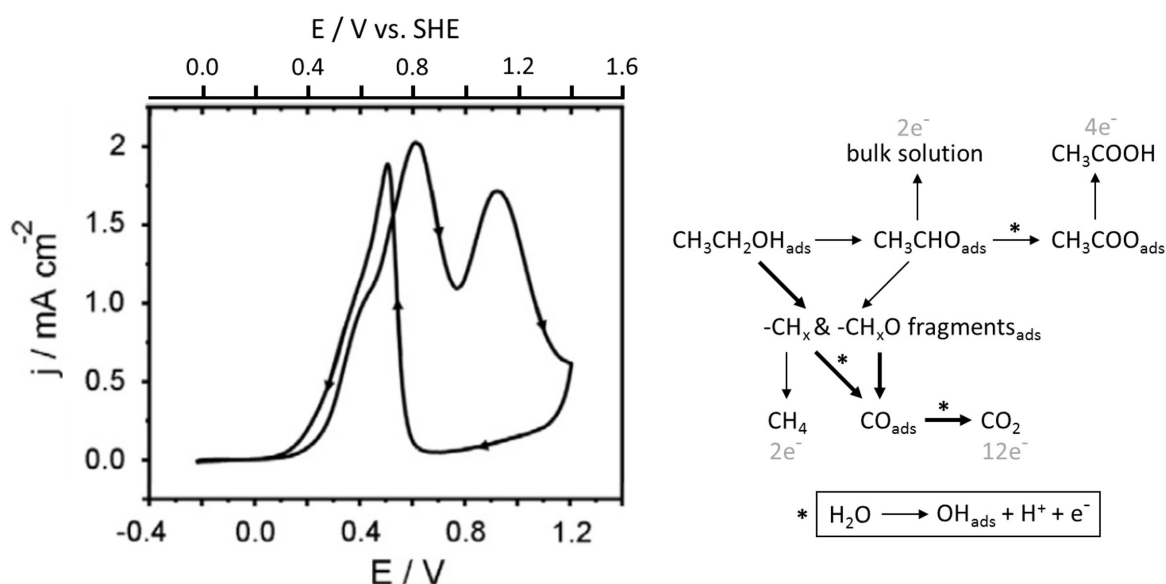


Fig. 16: Left: CV of polycrystalline Pt in 0.1 M HClO₄ with 0.5 M of ethanol, taken at a scan rate of 5 mV s⁻¹ (reprinted from [101] © 2010, with permission from Elsevier Inc.). The potential of the original graph is reported vs. a saturated Ag/AgCl electrode. The corresponding SHE potential scale has been added on top of the graph. Right: Scheme of the EOR reaction pathways including the activation of water (box) (based on the considerations in [79, 101]).

The reaction mechanism of the EOR on Pt was investigated by a number of research groups that used *in situ* spectroelectrochemical techniques such as *in situ* Fourier transform infrared spectroscopy (FTIR) and related methods to identify adsorbed reaction intermediates and products, and differential electrochemical mass spectroscopy (DEMS) to detect volatile reaction products (see for example [76, 85, 92, 95, 101–103] and references therein). Fig. 16 shows a CV of a polycrystalline Pt electrode in ethanol containing acidic electrolyte, which was reported by Kutz et al.,¹⁰¹ and a scheme of the EOR pathways that is based on the considerations reported in [101] and [79]. The bold arrows indicate the desired path, which corresponds to the complete oxidation of ethanol to CO₂. The shape of the CV results from the superposition of different electrochemical reactions.

On Pt, the C-C bond of EtOH can be broken already at ~ 0.0 V_{SHE},¹⁰¹ leading to an increasing coverage of the surface with strongly adsorbed CO and -CH_x fragments,¹⁰³ which constitute an electrode poison and lower the active surface area for adsorption and oxidation of EtOH until they are oxidatively removed. If the electrode is initially covered by hydrogen (H_{upd}), dissociative adsorption of EtOH is prevented until slightly higher anodic potentials, where active sites are freed from H_{ads}.¹⁰³ The transformation of the -CH_{x,ads} fragments to CO_{ads} becomes possible above ~ 0.4 V_{SHE}, but is less efficient than the formation of CO_{ads} from

adsorbed $-\text{CH}_x\text{O}$ fragments, which happens instantaneously upon dissociative adsorption of EtOH.⁹⁵ The subsequent oxidation reactions of the adsorbates to the desired CO_2 require relatively high overpotentials and are therefore the rate limiting steps for the EOR at Pt at low potentials.¹⁰ These overpotentials are in parts related to an impeded activation of water on the (blocked) Pt surface, i.e. the formation of OH_{ads} , which is required to provide oxygen for the adsorbate oxidation (see box in Fig. 16). During the anodic potential sweep, prior to the oxidation of CO_{ads} and $-\text{CH}_{x,\text{ads}}$, bulk electrooxidation of EtOH to acetaldehyde sets in at $\sim 0.35 V_{\text{SHE}}$ and causes the current to rise.^{10,92,99,102} The oxidative stripping of the adsorbed CO to CO_2 initiates $\sim 0.2 \text{ V}$ after the onset of faradaic current.^{10,92,99,101} The current related to the formation of CO_2 reaches a maximum at $\sim 0.65 V_{\text{SHE}}$, where a shoulder is observed in the CV, and drops to negligible values above $\sim 0.9 V_{\text{SHE}}$, where the surface is completely freed from CO_{ads} .^{10,92,101} Direct oxidation of $-\text{CH}_{x,\text{ads}}$ to CO_2 happens at negligible rates below $\sim 0.85 V_{\text{SHE}}$, so that this adsorbate constitutes a severe poison during EOR on Pt.^{76,103} After the shoulder in the CV, the faradaic current is further increasing and originates mainly from incomplete oxidation of EtOH to acetaldehyde and acetic acid, which prevails at high potentials.^{76,92} Above $\sim 0.8 V_{\text{SHE}}$, the EOR current drops at first due to the adsorption of blocking acetate, whose coverage reaches a maximum at $\sim 0.95 V_{\text{SHE}}$, where the CV shows a minimum.¹⁰¹ After the minimum, the acetate desorbs as acetic acid into the electrolyte, allowing the EOR current to increase again, and is completely removed at $\sim 1.1 V_{\text{SHE}}$, where the CV shows the second maximum.¹⁰¹ Finally, the formation of a passive oxide film causes the deactivation of the Pt catalyst and therewith a decrease of the EOR current towards higher potentials.^{104,105}

During the cathodic potential scan, the EOR is inhibited until $\sim 0.8 V_{\text{SHE}}$, where the reductive dissolution of Pt oxide starts, and active sites for EtOH adsorption become available again.^{92,99,101} At room temperature, no CO_2 is detected with DEMS during the cathodic scan,^{10,76,92,99} which can be explained by a low C-C bond splitting rate at potentials positive of $\sim 0.5 V_{\text{SHE}}$, where CO oxidation becomes possible, due to the presence of OH_{ads} on the surface.⁷⁶ Consequently, the EOR during the negative going potential scan is based on incomplete oxidation to acetaldehyde and acetic acid. With decreasing potential, re-poisoning with CO_{ads} and $-\text{CH}_{x,\text{ads}}$ due to dissociative EtOH adsorption causes the EOR current to decrease again between ~ 0.6 and $\sim 0.3 V_{\text{SHE}}$.^{92,99,101} Below $\sim 0.2 V_{\text{SHE}}$, entering the H_{upd} region, the adsorbed $-\text{CH}_x$ fragments can be reductively desorbed as methane and be lost for further oxidation during succeeding positive potential scans.^{76,92,102}

Due to the complexity of the reaction mechanism and the structure sensitivity of the EOR, the preferred reaction path and the related kinetics depend on several parameters, such as the composition and structure of the catalyst and electrode material, the pH and the anions of the supporting electrolyte, the ethanol concentration in the electrolyte and the reaction temperature.^{10,76,84–86,90,93,96,99,100}

The exact shape of the EOR CV on Pt is affected by the used supporting electrolyte due to possible co-adsorption of the supporting anions and their interaction with intermediate species of the EOR.^{100,101} In H_2SO_4 , for example, the co-adsorbed sulfuric acid anion blocks active sites for EOR intermediates, and stabilizes adsorbed acetate, decreasing the electron yield.¹⁰¹ Adsorbed anions decrease the active surface area of the electrode and therewith the EOR current density. In concentrated H_3PO_4 , the onset of EOR during the positive going potential sweep is shifted to considerably higher anodic potentials due to (electrochemical) adsorption of impurities and anions from the supporting electrolyte, which block the electrode.¹⁰⁰

The faradaic EOR current densities are enhanced for higher concentrations of EtOH in the electrolyte, which however originates mainly from an enhanced reaction rate for incomplete EtOH oxidation to acetaldehyde and acetic acid.^{10,76,99}

When the cell temperature is increased, the total reaction activity and the selectivity towards complete EtOH oxidation are enhanced, which results in higher faradaic current densities, decreased EOR onset potentials, and smaller separations between the anodic and cathodic current peaks (i.e. less hysteresis).^{10,76,99,100} The decrease in current peak separation is ascribed to kinetically activated CO_{ads} oxidation (shift to lower potentials) and PtO reduction (shift to higher potentials).^{10,100,106,107} While at room temperature, incomplete oxidation of EtOH to acetaldehyde and acetic acid prevails, the CO_2 current efficiency increases with increasing temperature,^{10,99} and at $T \geq 60$ °C, using a thin-layer flow cell, CO_2 is detected during the negative going potential scan as well.^{10,76}

2.2 Materials analysis

Scanning probe microscopy, electron microscopy, diffractometry and spectroscopy belong to the most important analysis tools in materials science. By means of these tools, the morphology and topography, the crystalline structure and crystallographic orientation, and the chemical composition of the bulk and surface of a material can be studied. The materials of the present work were studied with atomic force microscopy (AFM), scanning electron microscopy (SEM), grazing incidence X-ray diffraction (GID), micro-Raman spectroscopy and X-ray photoelectron spectroscopy. This section gives an overview of the fundamental physical processes that provide the basis for these techniques.

2.2.1 Diffraction of electromagnetic or material waves for structure analysis

The phase composition, crystal structure and orientation of crystalline solids can be studied by elastic scattering of material waves or electromagnetic waves at the atoms in the specimen. Radiation with wavelengths λ smaller than the distances between the atoms in the solid undergoes diffraction and interference at the lattice planes. Constructive interference of the scattered waves, and therewith reflection of the incident ray, is only obtained if the Laue-condition is fulfilled, which states that the change in the wave vector \vec{k} equals a reciprocal lattice vector:^{108,109}

$$\Delta\vec{k} = \vec{G} \quad (2.86)$$

Two waves that are elastically scattered at two adjacent atomic layers, which belong to a family (hkl) of lattice planes and have the distance d_{hkl} , undergo constructive interference if their path difference is an integer multiple n of the wavelength λ . Therefore, reflection occurs for those angles ϑ_B between the incident beam and the lattice planes that fulfill the Bragg condition,^{108,109}

$$2d_{hkl} \cdot \sin \vartheta_{\text{Bragg}} = n\lambda, \quad (2.87)$$

where n denotes the order of diffraction. Figure Fig. 17 shows the diffraction of monochromatic radiation at parallel lattice planes in a crystal and the path difference of two partial waves.

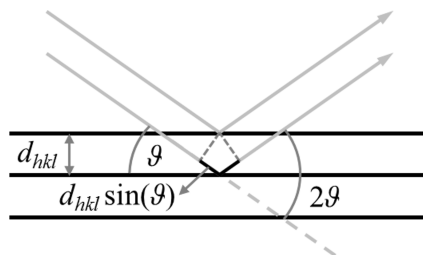


Fig. 17: Bragg diffraction. A reflection is only observed at angles $2\vartheta_{\text{Bragg}}$ with respect to the incident X-ray beam. Based on the treatment in [108].

The intensity of the resulting reflections that belong to a family (hkl) of lattice planes is determined by the arrangement and type of atoms in the unit cell (there can be more than one atom per lattice point), by the spatial distribution of the electrons in the unit cell and by the vibration of the atoms in the solid. In the case of non-primitive lattices, such as bcc or fcc, some reflections that are allowed according to equation 2.86 can

be cancelled due to destructive interference between partial waves that are diffracted at two adjacent lattice planes within the unit cell, which are spanned by identical atomic or molecular units in each lattice point. This brings about characteristic spatial diffraction patterns for a material of given chemical composition and crystal structure and, through comparison with reference data, can be used to obtain structural and compositional information about an unknown material. Depending on the chosen probe and scattering geometry, structural information can be obtained for the surface layers or for a larger volume of the material.

2.2.1.1 X-ray diffraction and grazing incidence X-ray diffraction

The penetration depth of X-rays in a material is of the order of mm, and therewith allows for the analysis of the structure and phase composition of a considerably large volume that is often representative for the bulk of a crystalline solid material. In polycrystalline solids or crystalline powders, the microcrystals and their lattice planes are randomly oriented. When irradiated with a monochromatic X-ray beam, only those crystals, whose lattice orientation fulfills the Bragg-condition (equation 2.87), contribute intensity to the observed diffraction pattern. The reflected light produces intense rings at angles $2\vartheta_{\text{Bragg}}$ with respect to the incident beam. Conventional powder diffraction experiments are conducted in the Bragg-Brentano (ϑ - 2ϑ) configuration, where the X-ray tube and the detector are rotated so that the angle between X-ray beam and specimen surface is ϑ and that between detector axis and incident X-ray beam 2ϑ . With this geometry, a section across the generated Debye-Scherrer rings is recorded and yields a one-dimensional X-ray diffraction pattern, in which the diffraction intensity is plotted versus 2ϑ .

For homogeneous solid solutions of two constituents A and B that have the same crystal structure in their pure form, but different lattice parameters a_A and a_B , the approximate concentration of each constituent in the solid solution ($A_{1-x}B_x$) can be calculated using Vegard's law:¹¹⁰

$$a_{A_{1-x}B_x} = (1 - x)a_A + xa_B \quad (2.88)$$

The lattice constant of the mixture, $a_{A_{1-x}B_x}$, can be calculated from the separation d_{hkl} of neighboring lattice planes, which can be determined from the position 2ϑ of the peak in the diffraction pattern, that is produced by the respective lattice plane (hkl), using the Bragg equation.

For cubic crystals, the relation between lattice constant and lattice plane separation is given by:

$$d_{hkl} = \frac{a}{\sqrt{h^2 + k^2 + l^2}} \quad (2.89)$$

The structure of thin polycrystalline films or surface layers can be studied with grazing incidence X-ray diffraction (GID) (also known as glancing angle X-ray diffraction (GAXRD), glancing-incidence X-ray diffraction (GIXRD), or low incidence X-ray diffraction) in the asymmetric out-of-plane scattering geometry.^{111,112} In this configuration, the incident X-ray beam falls on the sample surface at a fixed, low glancing angle, α , which is typically between 1° and 3° , and therewith slightly larger than the critical angle for total reflection. Diffraction profiles are recorded by rotation of the detector arm in the plane spanned by the surface normal of the planar sample and the incident X-ray beam. Because of the asymmetric scattering geometry, the detected diffraction pattern is produced by lattice planes that are inclined with respect to the sample surface. The surface sensitivity is significantly enhanced compared to the ϑ - 2ϑ geometry due to a prolonged path of the

X-ray beam through the surface-near layers. It can be shown that the maximum depth of analysis (X-ray penetration depth) is controlled by the angle of incidence.¹¹¹

2.2.2 Scanning electron microscopy and related methods

In a scanning electron microscope (SEM), a sample is scanned in x and y direction with a highly focussed energetic electron beam, and the signals produced by the sample are detected as a function of beam position to obtain an image of its topography, composition, crystal orientation and other properties. With a high-resolution field emission scanning electron microscope (FE-SEM), the size, shape and fine structure of 3D particles can be analyzed at the micrometer to nanometer scale. When a focused beam of energetic electrons impinges on the surface of a solid, the incident (primary) electrons interact with the atoms in the material through elastic and inelastic scattering and produce various signals, such as back-scattered electrons (BSE), secondary electrons (SE), Auger electrons and X-rays, that contain different information about the investigated sample.

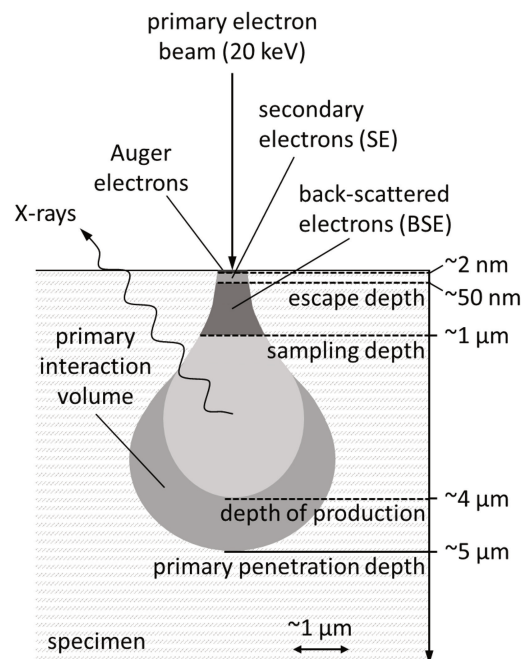


Fig. 18: Interaction volume of energetic electrons in a low-density, low-atomic-number specimen, and depths from which Auger, secondary and backscattered electrons, and X-rays emerge. Based on the treatment in [113]. The escape depth of Auger electrons was taken from [114].

Fig. 18 shows a typical interaction volume of the incident electrons in a low-density, low-atomic-number target for the case of normal incidence, and the depths from which the generated signals emerge. The size and shape of the interaction volume, which has dimensions in the micrometer range, is determined by the elastic scattering efficiency, the electron energy loss per traveled distance due to inelastic scattering events, and by the sample tilt with respect to the incident beam. During an elastic scattering event, the electron is scattered into a direction that is tilted with respect to its initial direction of travel by the elastic scattering angle ϕ . The most probable scattering angle is typically in the range 3° – 5° .¹¹³ The cross section for elastic scattering Q (in cm^2) at scattering angles greater than ϕ depends on the atomic number Z and the electron

beam energy E (in keV) as

$$Q(>\phi) \propto \frac{Z^2}{E^2} \cot^2(\phi), \quad (2.90)$$

and the elastic scattering mean free path is given by

$$\Lambda_{\text{elastic}} = \frac{A}{N_A \rho Q} \quad (2.91)$$

with Avogadro's number N_A , and the atomic weight A (in g mol^{-1}) and density ρ (in g cm^{-3}) of the specimen. Due to inelastic scattering events, the incident beam gradually loses its energy by dE with distance traveled ds , which depends on the atomic number Z and the electron beam energy E as

$$\frac{dE}{ds} \propto \frac{\rho}{A} \cdot \frac{Z}{E} \ln\left(\frac{E}{J}\right) \quad (2.92)$$

where J is the average loss in energy per event. Hence, the interaction volume increases with increasing beam energy and decreases with increasing average atomic number of the target. For samples that are tilted with respect to the incident beam, it becomes asymmetric and less deep, since the penetration depth of the electrons is reduced.

As a consequence of the electron-matter interaction, several signals are emitted by the sample, of which the following are usually used to generate topographic images in SEM.

1. **Backscattered electrons (BSEs).** After several inelastic and elastic scattering events in the sample, a fraction of the incident electrons can eventually reach the surface and escape the sample as backscattered electrons. For conventional beam energies (5–50 keV), the number fraction of BSEs increases with the atomic number of the target atoms, yielding higher signal intensities for sample areas with a larger average atomic number than for areas with a lower average atomic number. This allows to obtain compositional contrast images, where regions of high average atomic number appear bright relative to regions of low atomic number. Due to the dominant tendency of elastic scattering to be in the forward direction (equation 2.90), the number fraction of backscattered electrons is increased when the surface normal of a mapped sample feature is inclined with respect to the incident beam. This effect is used to produce topographic contrast in an BSE image, by which the shape of objects is recognized. Besides specimen composition and topography, also its crystallography or internal magnetic fields affect the contrast of BSE images. The primary electrons penetrate to a significant sample depth before reversing their course and returning to the surface to escape as a backscattered electron. Therefore, the sampling depth of backscattered electrons is of the order of $1 \mu\text{m}$, and BSEs may be influenced by subsurface features of the specimen structure. The BSE signal is known to be sensitive to bulk and surface composition at conventional SEM beam energies.
2. **Secondary electrons (SE).** Secondary electrons are loosely bound outer shell valence electrons or conduction band electrons from the specimen which receive sufficient kinetic energy during inelastic scattering of the beam electrons to be ejected from the atom and set into motion. SEs are generated isotropically and when propagating through the solid, some of them will intersect the surface and escape. Directly after ejection, the secondary electrons have only a low kinetic energy, so that they

are strongly attenuated with distance traveled due to inelastic scattering and energy loss (equation 2.92). The resulting mean free path Λ_{SE} of SEs is rather small ($\Lambda_{SE} = 1\text{--}10\text{ nm}$, depending on the material), and only secondary electrons that are generated within a depth of $5\Lambda_{SE}$ underneath the surface are able to escape from the sample and to be detected (see Fig. 18). Such surface-near secondary electrons are generated on the one hand where the incident beam enters the sample surface (SE_1), and on the other hand where BSEs exit the surface (SE_2), giving rise to two different signals of secondary electrons. Because a considerable fraction of BSEs leave the sample remote from the incident beam (not shown in Fig. 18), the SE_2 signal lowers the spatial resolution of SE images. Furthermore, the sample information contained in the SE_2 signal is significantly less surface sensitive than that of the SE_1 signal, since the BSE that produce SE_2 have traveled through deeper lying layers of the sample. The SE_2 contribution to the overall SE signal intensity depends on the number of BSE generated per incident electron, which is determined by sample properties such as composition and topography. Nevertheless, the total number of SEs per incident electron is relatively insensitive to the atomic number. This can be ascribed to the fact that under conventional experimental conditions, the sample surface is always covered by a layer of surface contamination from deposited hydrocarbons, which determines the emission of SEs. When, using conventional beam energies, the surface normal of a mapped sample area is tilted with respect to the incident beam, the path length of the incident beam within the surface layer of thickness $5\Lambda_{SE}$ is greater, and more SE_1 are generated than under normal incidence condition. Since the number fraction of BSEs increases with increasing surface tilt, the fraction of SE_2 is enhanced as well. This effect is used in an SEM to obtain a topographic contrast image from the SE signal.

There is a third class of secondary electrons, SE_3 , which are produced through the collision of the emitted BSE with the SEM chamber walls. They provide an indirect measure for the number of emitted BSE, and therefore contain compositional and topographic information.

To obtain a topographic image, a beam of electrons is accelerated with a high voltage onto a sample, and thereby collimated and focused by a series of apertures and electromagnetic lenses to form a well defined electron probe on the sample plane. The electron probe is then scanned across the sample plane, while the emitted backscattered and secondary electrons are detected at every image pixel. The achievable image resolution is determined by the minimum spot size of the electron beam at the sample plane and the electron current in this spot, which limits the maximum intensity of the detected signals. A very small electron probe size (of the order of few nm), without loss in probe current, can be achieved in FE-SEMs, which therefore provide a higher resolution compared to other SEM instruments. In a FE-SEM, the beam is generated through field emission of electrons from a metallic cathode, typically tungsten, shaped as a sharp tip. The mostly used detector for the generation of topographic images in SEM is the Everhard-Thornley detector, which is a combined SE/BSE signal detector. It collects the low energy SE with an attractive electric field, and can therefore detect the SE_1 and SE_2 signals, emitted by the sample, and the SE_3 signal, which is an indirect measure of the BSE intensity. Back-scattered electrons, whose trajectories fall within the solid angle of the detector, are detected directly. Other commonly used detectors are selective towards the BSE signal and are used to obtain compositional contrast images. FE-SEM chambers can be equipped with an in-lens detector, which has an enhanced detection efficiency for SE_1 electrons and therefore provides the possibility to obtain

topographic images with an enhanced surface sensitivity and lateral resolution.

Further details on topographic imaging with SEM can be found in the respective literature, such as [113].

2.2.2.1 Electron backscatter diffraction

Electron backscatter diffraction (EBSD) provides quantitative microstructural information about the crystallographic nature of metals and other solids. It reveals grain size, grain boundary character, grain orientation, texture (i.e. overall preferred orientation), and phase identity of the investigated substrate.

When a focussed beam of energetic electrons strikes the surface of a highly tilted crystalline solid, back-scattered electrons, which have lost only a small fraction of their energy (so-called low-loss BSE), are channeled in and out of the crystal due to Bragg diffraction and wide-angle scattering events, and are subject to path differences that lead to constructive and destructive interference. If a phosphor screen is placed at a short distance from the tilted sample, a diffraction pattern can be seen, which is known as electron backscatter pattern (EBSP), also called Kikuchi pattern. The condition for the diffraction of electrons at the atomic planes in a crystal is given by equation 2.87, and requires the electrons to have sufficiently high kinetic energies $E_{\text{kin}} = eV$ so that their de Broglie wavelength $\lambda_e = 2\pi\hbar/p = 2\pi\hbar/\sqrt{2m_e eV}$ (\hbar is the reduced Planck constant, p the electron momentum, m_e the electronic mass, e the elementary charge and V the voltage applied to accelerate the electrons) is of the order of the interatomic distances.

In an EBSD experiment, the electron beam of an SEM is directed on a flat, highly polished sample at an angle of typically 70° with respect to its surface normal, and the BSE are collected on a nearby positioned phosphor screen, where they produce a visible EBSP which illuminates a CCD chip. The large sample tilt is required to produce a high amount of BSE and therewith obtain a sufficiently high intensity in the diffraction pattern, and to enhance the surface sensitivity. The channeled low-loss BSEs emerge from the sample surface very near the initial beam impact point, which brings about an enhanced spatial resolution of EBSD compared to conventional BSE intensity detectors. Typical values for the acceleration voltage and currents of the incident beam are 10–30 kV and 1–50 nA, respectively.¹¹⁶ The detected Kikuchi pattern is uniquely defined by the lattice parameters of the particular crystal under the beam, the crystal's orientation in space, the de Broglie wavelength of the incident electron beam and the proximity of the EBSP. With appropriate analysis software, the crystalline phase of the investigated substrate can be identified, and the Euler angles of the crystal lattice, which define its orientation with respect to the substrate surface, can be extracted from the EBSP. According to the Bunge convention,¹¹⁷ the three Euler angles φ_1 , Φ and φ_2 define the following rotations in space (see Fig. 19):

1. A rotation by φ_1 about the z -axis followed by
2. a rotation by Φ about the rotated x -axis followed by
3. a rotation by φ_2 about the z -axis.

By scanning the incident beam across the sample surface, a 2D orientation map can be generated, which contains information about the microstructure of the surface. A given set of Euler angles results in a particular crystallographic direction $\langle hkl \rangle$ being normal to the mapped sample surface, or a particular lattice plane $(h'k'l')$ being parallel to that surface (note that only in the cubic lattice system the direct lattice vector

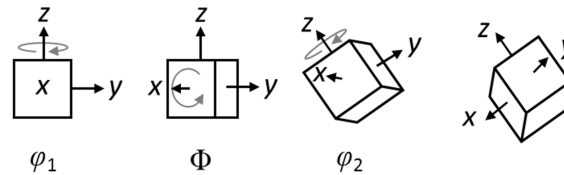


Fig. 19: Definition of the Euler angles according to the Bunge convention. Based on the representation in [116].

$\langle hkl \rangle$ is normal to the lattice plane that is defined by the same Miller indices). On the other hand, a given crystallographic direction $\langle hkl \rangle$ normal to the substrate surface is described by various sets of Euler angles, since any rotation about the corresponding axis is not taken into account by the Miller indices. This relation is used to create an inverse pole figure (IPF)-based orientation map, which depicts the projected orientation of a 3D crystal lattice, whose orientation in space is described by the three Euler angles, onto a 2D plane along a chosen projection direction. An IPF assigns a RGB color code to the crystallographic directions $\langle hkl \rangle$ of the mapped substrate grains, that are parallel to the chosen projection direction, typically the direction of the surface normal of the planar substrate. Alternatively, the RGB color code can be assigned to the lattice planes $(h'k'l')$ that are perpendicular to the projection direction.

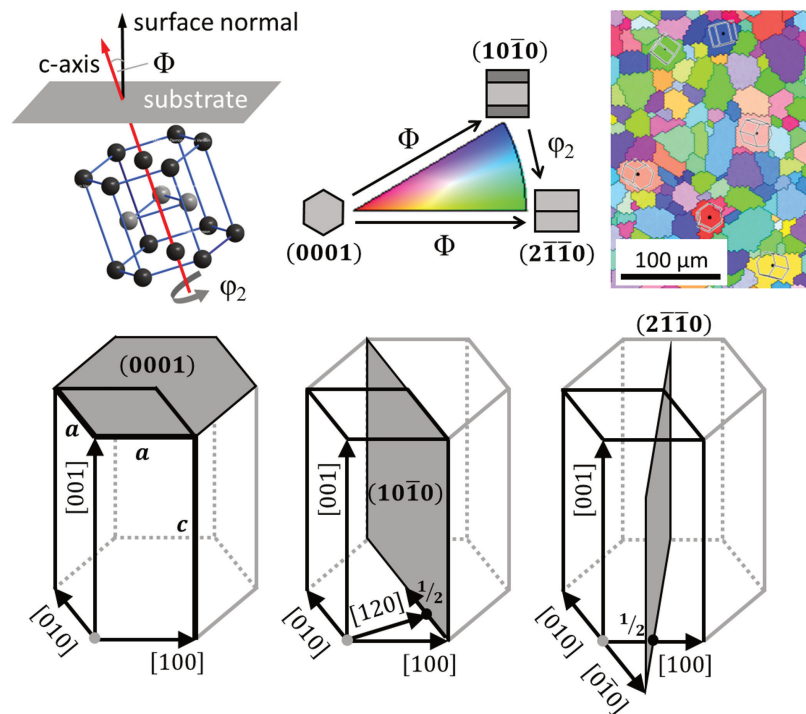


Fig. 20: Top-left to bottom-right: Orientation of hexagonal lattice with respect to surface normal (adapted from [118] - Published by the PCCP Owner Societies, and based on a similar sketch in [58]), standard triangle of surface-normal projected IPF orientation map with Euler angles, EBSD map with hexagonal lattice cells, and relation between low index directions and planes in the hexagonal system.

Fig. 20 illustrates the relation between the Euler angles and a surface-normal projected IPF orientation map for a polycrystalline metal sheet with hexagonal crystal structure, such as titanium. The sketch at the left top depicts the orientation of the hexagonal lattice¹ with respect to the substrate surface: Φ gives the tilt angle

¹The lattice cell was drawn with the software Diamond 4.0 (demonstration version).

of the unit cell c-axis with respect to the surface normal and φ_2 gives the azimuthal rotation of the hexagonal unit cell around its c-axis. A rotation of the substrate around its surface normal is described by the angle φ_1 (not shown). In the surface-normal projected IPF orientation map (from now on referred to as EBSD map), the color code provides no information about the Euler angle φ_1 . Due to the symmetry of the hexagonal lattice, the two Euler angles Φ and φ_2 can be restricted to $0^\circ \leq \Phi \leq 90^\circ$ and $0^\circ \leq \varphi_2 \leq 30^\circ$. For the azimuthal rotation the zero point is chosen to coincide with the $(10\bar{1}0)$ plane for $\Phi = 90^\circ$, while $\varphi_2 = 30^\circ$ and $\Phi = 90^\circ$ yield the $(2\bar{1}\bar{1}0)$ plane. The IPF with projection parallel to the surface normal assigns full red, blue and green to the crystal planes (0001) , $(10\bar{1}0)$ and $(2\bar{1}\bar{1}0)$, respectively, and mixed RGB colors to intermediate orientations. Fig. 20 shows an EBSD map of a polycrystalline titanium sheet together with the standard triangle, which defines its color code. To visualize the crystal orientation of some grains, thereby taking into account the Euler angle φ_1 , sketches of projected hexagonal lattice cells are added to the corresponding grains in the EBSD map.

Detailed treatments of EBSD can be found in the respective literature, such as [113, 115, 116]

2.2.3 Atomic force microscopy

Atomic force microscopy (AFM) is a scanning probe microscopy technique that allows to image planar surfaces of conducting and insulating solids with atomic resolution. It takes advantage of the separation-dependent attractive and repulsive forces that an atom on a sharp probing tip experiences when it approaches the atoms on a solid surface. At relatively large distances, the predominant force between two neutral atoms is the weakly attractive van der Waals force between their mutually induced dipole moments. When the two atoms approach each other so that their atomic orbitals start to overlap, the Pauli-exclusion principle causes a strong repulsive force that quickly grows to infinity with decreasing interatomic distance. The overall force-distance curve can be approximated by

$$F(r) = 12 \frac{B}{r^{13}} - 6 \frac{D}{r^7} \quad (2.93)$$

which is the derivative of the Lennard-Jones potential. B and D are constants. The first term describes the repulsive force and the second term the attractive van der Waals force. Depending on the properties of tip and sample, also other forces, such as electrostatic or magnetic, may affect their interaction and lead to a modified force-distance curve.

The scheme in Fig. 21 shows the basic working principle of AFM. The probe consists of a sharp tip that is attached to a bendable cantilever. If it is brought close to the surface of a planar sample, the tip feels attractive or repulsive forces, which cause a deflection of the cantilever. Physical contact with the surface is achieved at distances, where the repulsive force dominates the interaction. The deflection is measured by means of a laser beam that is focused onto the top of the cantilever, from where it is reflected onto a position sensitive detector (quadrant photodiode). A deflection of the cantilever causes the laser spot to impinge on a different vertical position (C/D) on the photodiode array with respect to the initially calibrated position, where the forces between tip and surface are negligible (high tip-surface separation). By keeping the force constant through an electronic feedback which adjusts the distance between tip and surface *via* a piezoelectric drive, a xy -scan of the AFM probe over the sample surface yields a topographic map. AFM can be operated in different modes. In contact mode, the measuring tip has constant physical contact with the

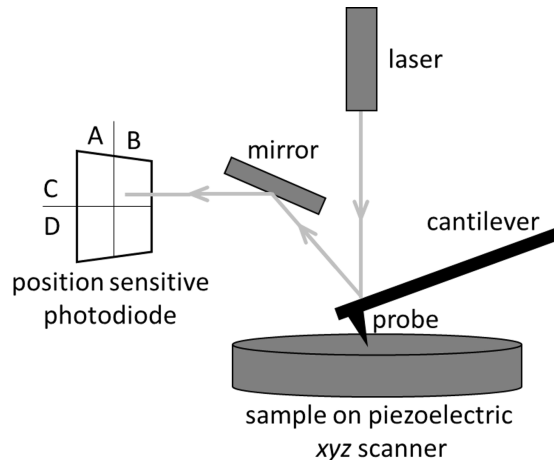


Fig. 21: Working principle of AFM.

surface (repulsive force regime), while it is traced across the sample. Here, the cantilever deflection is used as feedback signal. This mode provides a high resolution for topographic height differences due to the rapid decay of the repulsive force term in equation 2.93. To keep sample damage low, in particular soft materials should be imaged with tapping mode AFM. Here, the tip is excited by a piezo element to vibrate close to its resonant frequency, where it has a defined oscillation amplitude. In proximity to the surface, the oscillating tip hits the surface which reduces the root mean square (RMS) amplitude of the tapping motion. To ensure interaction with the surface, the RMS amplitude is set to a value below that of the freely vibrating tip and kept constant *via* an electronic feedback.

AFM images provide information about the surface morphology, roughness and the topographic area. The relative height of surface features can be analyzed by taking cross-sections along a line of the image. The root mean square height (h_{RMS}) provides a statistical parameter for the roughness and is determined by the averaged height and depth variations of surface features with respect to the zero-plane. The RMS height value of an image of N image points (pixels) is given by

$$h_{\text{RMS}} = \sqrt{\frac{\sum_i (z_i - z_0)^2}{N}}, \quad (2.94)$$

where the z_i are the height values measured at each pixel, and z_0 is the average absolute z -value which defines the zero-plane. The topographic area, i.e. the area of the three dimensional surface mapped with AFM, is the sum of the areas of each three adjacent pixels, which can be calculated with AFM analysis softwares. The roughness factor (RF) is then defined as

$$RF = \frac{A_{\text{AFM}}}{A_{\text{proj}}} \quad (2.95)$$

with the topographic area A_{AFM} , and the projected area A_{proj} of the AFM image. Further details on AFM can be found in the respective literature, e.g. in [119, 120].

2.2.4 Raman spectroscopy

Raman spectroscopy is a type of vibrational (and rotational) spectroscopy of molecules and solids that is based on the Raman effect. In combination with reference data, a Raman spectrum provides information

about the chemical compounds and structural phases present in a specimen. Under well defined experimental conditions, quantitative chemical analysis is possible and crystal orientations can be determined. To obtain a Raman spectrum, a Raman active specimen is excited with intense and monochromatic (visible or near UV) light, commonly provided by a laser, and the intensity of the scattered light is detected as a function of its frequency change. Detailed treatments of the theory of Raman spectroscopy can be found in the respective literature, such as [114, 121, 122, 124, 126, 127]. The basic concepts, that are necessary for the analysis and interpretation of Raman spectra of solids, will be presented in the following. When intense monochromatic light (visible to near UV regime) impinges on a molecule or solid, most of the photons undergo elastic scattering (Rayleigh-scattering) with unchanged photon energy $\hbar\omega_0$. A small fraction of the light experiences Raman scattering, which is an inelastic scattering process that involves vibrational (and rotational) transitions in a molecule or the excitation (de-excitation) of optical phonons in a solid. The inelastically scattered photons are detected as intensity lines (Raman bands) at frequencies that are lower (Stokes-lines) or higher (anti-Stokes-lines) than the frequency of the incident light. The change in photon frequency corresponds to quanta of the vibrational normal modes of the investigated molecule or of the phonons in the case of a solid. In a Raman spectrum, the detected light intensity is plotted *versus* the wavenumber $\Delta\tilde{\nu} = 1/\lambda_0 - 1/\lambda_s$ (Raman shift), which is the difference between the inverse wavelengths of the excitation laser (λ_0) and the scattered radiation (λ_s).

The energy level diagram in Fig. 22 illustrates the fundamental processes that may occur, when visible to near UV light interacts with a Raman active molecule.

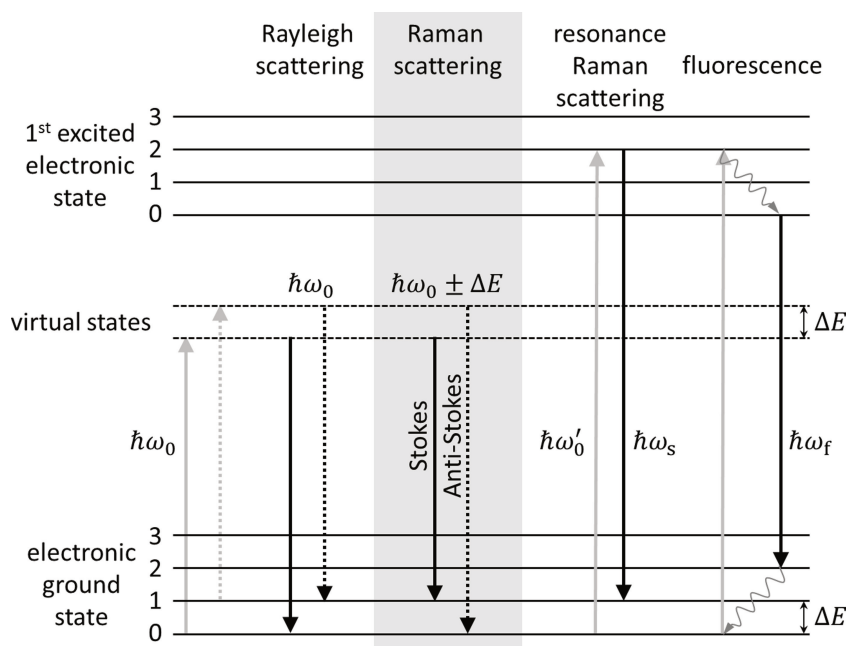


Fig. 22: Energy level diagram for elastic, inelastic and resonant scattering processes of photons (visible to near UV regime) in a Raman active molecule, as well as absorption followed by fluorescence. The wavy arrows indicate radiation-less transitions. Based on [128].

During non-resonant scattering processes, the specimen is lifted from its initial state (which can be the ground state or an excited vibrational state) into a virtual state. When the system is returning to the initial state, the photons are emitted without energy loss, which is the Rayleigh scattering process. In the inelastic Raman scattering process, the final state has a higher or lower energy than the initial state, and the energy difference

corresponds to a vibrational transition. Resonance Raman scattering can be achieved if the specimen is excited with photons of wavelengths that closely approach that of an electronic absorption peak (i.e. photon energy $\hbar\omega'_0$ in Fig. 22) and results in greatly enhanced Raman line intensities with enhancement factors of 10^2 – 10^6 .¹²⁴ A competing resonant process is fluorescence, which involves an electronic transition and radiation-less transitions between vibrational states (i.e. internal conversion), so that the emitted light has a lower frequency than the excitation light.

The classical description of the Raman effect is based on the coupling between electromagnetic waves and induced electrical dipole moments in a molecule or solid. The incident electromagnetic wave of electric field strength $\vec{E} = \vec{E}_0 \cos \omega_0 t$ induces an electrical dipole moment that is superimposed to any permanent electrical dipole moment present in a molecule or in the unit cell of a crystal lattice:¹⁰⁸

$$\vec{p}_{\text{el}} = \vec{p}_{\text{el}}^0 + \tilde{\alpha} \cdot \vec{E} \quad (2.96)$$

where $\tilde{\alpha}$ is the electrical polarizability tensor of the interatomic bonds in a molecule or in the unit cell of the crystal lattice of a solid. Due to the fast motion of the electrons, the time-dependent total dipole moment depends only on the time-dependent displacements Q_n of the nuclei, which are represented by the normal coordinates of the vibrational normal modes. In a crystalline solid with N nuclei, there are $3N - 6 \approx 3N$ (for $N \gg 1$) possible normal modes. For small displacements from the equilibrium positions, the permanent electrical dipole moment and the components α_{ij} ($i, j = x, y, z$) of the polarizability tensor can be expanded in a Taylor series around the equilibrium ($Q_n = 0$), and the normal displacements can be described by harmonic oscillations of amplitude Q_{n0} and frequency ω_n . With that, one obtains for the time-dependent electrical dipole moment the expression:¹⁰⁸

$$\begin{aligned} \vec{p}_{\text{el}} = & \vec{p}_{\text{el}}^0 + \sum_n \left(\frac{\partial \vec{p}_{\text{el}}}{\partial Q_n} \right)_{Q_n=0} Q_{n0} \cos \omega_n t \\ & + \tilde{\alpha}^0 \vec{E}_0 \cos \omega_0 t + \left(\sum_n \left(\frac{\partial \alpha_{ij}}{\partial Q_n} \right)_{Q_n=0} Q_{n0} \cos (\omega_0 \pm \omega_n) t \right) \cdot \frac{\vec{E}_0}{2}. \end{aligned} \quad (2.97)$$

The first term is the permanent electrical dipole moment (if present) of the molecule or of the atoms in a lattice unit cell and the second term the part of the electrical dipole moment that is oscillating when vibrational normal modes (i.e. phonons in a solid) are excited. If $(\partial \vec{p}_{\text{el}} / \partial Q_n)_{Q_n=0} \neq 0$, the oscillating dipole moment may allow for a coupling between vibrational modes and electromagnetic radiation and cause electric dipole transitions between adjacent vibrational states. These transitions require the absorption or emission of photons whose energy corresponds to the vibrational transition energies, which are in the infrared (IR) regime. Molecules or solids that yield an absorption spectrum when excited with IR radiation are called IR-active. The third term represents the induced dipole moment related to Rayleigh scattering and the last term the induced dipole moments related to the Stokes ($\omega_0 - \omega_n$) and anti-Stokes ($\omega_0 + \omega_n$) processes of Raman scattering. As can be seen from equation 2.97, Raman scattering is only possible, if the vibrational normal modes bring about a variation in the local polarizability of the interatomic bonds. Raman active molecules and solids fulfill this requirement. The energies of visible light are too high to allow for transitions between adjacent vibrational states through photon absorption/emission, which is a one-step process. However, vibrational transitions may be evoked through inelastic scattering, which involves the formation of an intermediate excited state. The

Raman process can be separated into three interaction steps:¹²¹ (1) electron-photon interaction to produce an excited state, (2) electron-phonon scattering event where a phonon is created or absorbed (vibrational transition), and (3) emission of the scattered photon in an electron-photon interaction.

Since Raman active solids contain a high amount of atomic bonds, Raman scattering at solids can be described macroscopically in terms of the material's polarization density, which is determined by the material's electric susceptibility $\tilde{\chi}_{\text{el}}$. The relation between the macroscopic polarization density \vec{P}_{el} and the locally induced dipole moment \vec{p}_{el} in one interatomic bond of a solid is given by:¹⁰⁸

$$\begin{aligned}\vec{P}_{\text{el}} &= N\vec{p}_{\text{el}} = N\varepsilon_0\tilde{\alpha}\vec{E}_{0,\text{local}} \\ &= \varepsilon_0\tilde{\chi}_{\text{el}}\vec{E}_{0,\text{external}}\end{aligned}\quad (2.98)$$

where N is the number of locally induced dipole moments, $\tilde{\alpha}$ the polarizability tensor of an interatomic bond, ε_0 the electric permittivity of free space, $\vec{E}_{0,\text{local}}$ the local and $\vec{E}_{0,\text{external}}$ the externally applied electric field, and $\tilde{\chi}_{\text{el}}$ the electric susceptibility tensor. A solid is Raman active, if the electric susceptibility varies with the atomic displacements of the normal vibrational modes (i.e. phonons).

To predict whether or not a Raman scattering event occurs, energy and momentum conservation laws need to be taken into account, which requires a quantum mechanical treatment. The probability for a Raman transition between two vibrational states with wavefunctions ψ_l and ψ_m is given by the squared amplitude of the expectation value of the according transition moment. Using the Dirac notation, the expectation value can be written as:¹²⁶

$$\langle \vec{p}_{lm} \rangle_{\text{Raman}} = \sum_n \left(\frac{\partial \alpha_{ij}}{\partial Q_n} \right)_{Q_n=0} \langle \psi_l | Q_n | \psi_m \rangle \cdot \vec{E}_0. \quad (2.99)$$

With that, the condition for Raman scattering becomes

$$\left(\frac{\partial \alpha_{ij}}{\partial Q_n} \right)_{Q_n=0} \langle \psi_l | Q_n | \psi_m \rangle \neq 0. \quad (2.100)$$

The first term is the gross selection rule, which states that only solids or molecules whose polarizability depends on the relative atomic displacements Q_n can be Raman active. The second term expresses the specific selection rule for vibrational transitions. Since the wavefunctions are solutions of the Schrödinger equation for a given potential, the specific selection rule depends on the shape of the potential-curve as a function of interatomic displacement. For the harmonic oscillator approximation, the transition moment is non-zero when the vibrational quantum number changes by $\Delta\nu = l - m = \pm 1$ during the transition.

The tensor properties of the polarizability bring about a dependency of the Raman transition probability on the direction and polarization of the incident and scattered light with respect to the normal interatomic displacements in a molecule or solid. The Raman active vibrational modes, which are all modes for which equation 2.100 is fulfilled, can be deduced from the symmetry properties of the molecule or of the crystal lattice, which requires group theoretical examinations.¹²³

In free molecules, also rotational transitions can be excited by Raman scattering, which give rise to Raman spectra with a rotational fine structure (see e.g.¹¹⁴ for Raman spectroscopy of molecules) while there are no rotational degrees of freedom for the atoms in a solid. The possible states (energy $\hbar\Omega$ and momentum $\hbar\vec{K}$) of phonons in a solid are fully described by the phonon dispersion relation $\Omega(|\vec{K}|)$ in the first Brillouin zone along a given crystal axis, which extends from $K = -\pi/a$ to $K = \pi/a$, with the lattice constant a (note that a

is the distance between lattice points in the primitive unit cell, which is not necessarily the distance between neighboring atoms). For a crystal with N lattice points, there are N allowed states of wave vectors \vec{K} in the Brillouin zone. IR absorption and Raman scattering in solids is only possible if optical vibrational modes can be excited in the lattice. Optical phonons can be generated in crystals with two or more atoms per lattice point in the primitive unit cell, and are longitudinal or transversal oscillations where the atoms move out of phase with respect to each other. For first-order Raman scattering in a solid, i.e. only one vibrational mode (Ω, \vec{K}) is involved, the selection rules are¹⁰⁸

$$\omega_0 = \omega_s \pm \Omega, \quad \vec{k}_0 = \vec{k}_s \pm \vec{K} \quad (2.101)$$

where ω_0, \vec{k}_0 are the frequency and wavevector of the incident photon, and ω_s, \vec{k}_s the corresponding values of the scattered photon. These are directly deduced from the conservation of energy and momentum in a scattering process. Second order Raman scattering involves two phonons at once and the selection rules require the two phonons to travel in opposite directions. The frequency Ω of the phonons that are excited/de-excited in a Raman process is generally very small compared to the light frequency (visible to near UV regime). The maximum momentum transfer occurs when the light is scattered backwards, so that $\vec{k}_s = -\vec{k}_0$. For light of wavelength λ , the corresponding magnitude of the scattering wavevector is $|\vec{K}|_{\max} = 4\pi/\lambda$. Since the wavelength of visible light ($\lambda \approx 500$ nm) is long compared to typical lattice constants ($a \approx 0.1$ – 1.0 nm), the magnitude of \vec{K}_{\max} is very small compared to the Brillouin zone dimensions ($2\pi/a$). Therefore, Raman scattering mainly excites phonons from the center of the first Brillouin zone ($\vec{K} \approx 0$),^{108,127} which is often referred to as the Γ -point. The selection rule $\vec{K} \approx 0$ applies only to Raman modes in (infinitely extended) perfect single crystals. In polycrystalline solids or in crystalline nanoparticles, the dimensions of the crystalline domains may be in the submicron range. The consequent three-dimensional confinement of the phonons causes an asymmetric broadening and a shift of the Raman bands. This effect is described by phonon confinement models which take into account that in a finite size microcrystalline domain the selection rule 2.101 is relaxed due to the uncertainty principle, and allows the participation of phonons near the Γ -point, with $\Delta\vec{K} \approx 2\pi/L$, where L is the dimension of the domain.^{127,129–132} Since now phonons with wavevectors $\vec{K} \neq 0$ are involved in the Raman scattering, the phonon dispersion relation becomes relevant and causes a broadening and a shift of the Raman lines, which both depend on the particular shape of $\Omega(\vec{K})$ near the Brillouin zone center. In amorphous materials with no long range order, the wave vector uncertainty is $\Delta\vec{K} \approx 2\pi/a$, where a is the bond length (lattice constant), so that all optical phonon modes in the Brillouin zone contribute to the first-order Raman scattering. The resulting Raman spectra are determined by the phonon density-of-states, and may contain prominent humps or broad Raman bands, but no sharp and well-defined peaks.

2.2.4.1 Analysis and interpretation of Raman spectra

Every Raman-active material produces a characteristic fingerprint. Hence, the comparison of a given Raman spectrum with reference data allows the identification of the crystalline phases and chemical species present in an investigated sample. Additional information can be obtained from a detailed analysis of the intensity, position and width of the individual Raman bands in a spectrum.

Line intensity The intensity of Raman bands depends on sample-related and instrument-related parameters. The latter comprise the excitation laser intensity, the analyzed volume and instrument-dependent factors, such as the measurement geometry and detector efficiency. On the other hand, the intensity of Raman signals is directly related to the probability of vibrational transitions during light scattering at a material, which depends on the wavelength of the incident light, the material's polarizability and symmetry properties, the number density of Raman scatterers, and the temperature.

Based on the Beer-Lambert law for the attenuation of light in matter, a qualitative value for the optical penetration depth, d_{optical} , of the excitation laser into the studied material, and therewith the interaction volume, can be estimated with equation 2.102:¹³³

$$d_{\text{optical}} \approx \frac{1}{\beta} = \frac{\lambda_0}{2\pi\kappa} \quad (2.102)$$

where β is the absorption coefficient, λ the wavelength of the excitation source and κ the extinction coefficient of the material (i.e. the imaginary part of the complex refractive index).

The intensity of the electric dipole radiation that is emitted by a Raman scatterer depends on the intensity of the incident light, I_0 , and scales with the fourth power of the frequency:^{124,126,134}

$$I_{\text{Raman}} \propto I_0 (\omega_0 \pm \omega_n)^4. \quad (2.103)$$

Hence, the intensity of Raman lines can be expected to increase with increasing light frequency. On the other hand, competing processes, such as fluorescence, become relevant at increasing photon energies, and in practice, mostly lasers in the frequency regime of visible light are used for Raman spectroscopy.

The dipole transitions in the Raman process depend on the orientation of the scattering (induced) dipole moment with respect to the polarization and direction of the incident and scattered light. For a Raman active vibrational normal mode with normal coordinate Q_n , the corresponding Raman polarizability tensor ($(\partial\tilde{\alpha}_{ij}/\partial Q_n)_{Q_n=0} = \tilde{\alpha}'$), which represents the vibrational modulation of the polarizability with Q_n , is fixed relative to the positions of the atoms and the directions of the bonds between them. Therefore, for a crystal fixed in space, the Raman scattering intensity depends on the crystal symmetry (which is described by its point group) and the orientation of the sample relative to the direction and polarization of the incident and collected light.

The Raman scattering intensity is proportional to the square of the dot product of the incident electric field vector, the Raman polarizability tensor, and the scattering vector:^{122,125,127}

$$I_{\text{Raman}} \propto |\vec{e}_s^* \cdot \tilde{\alpha}' \cdot \vec{e}_0|^2. \quad (2.104)$$

where \vec{e}_0 is the polarization of the incident light, \vec{e}_s the polarization of the scattered light, and $\tilde{\alpha}'$ the Raman polarizability tensor, associated with the Raman active n^{th} vibrational normal mode of the studied crystal. Even for unpolarized incident light, the scattered light may show a direction-dependent polarization and intensity, in particular if the specimens are oriented single crystals. The directions of incident and collected light are defined by the scattering geometry of the measurement. The two most common geometries are the detection of the backscattered light and the detection perpendicular to the incident laser beam. In the backscattering geometry, the incident and scattered light propagate along the z -direction to and from a solid

surface in the xy -plane. If no polarizer is used, the incident light has electric field amplitudes E_x and E_y . With an arbitrary Raman polarizability tensor $\tilde{\alpha}'$, whose components are expressed with respect to the cartesian coordinates of the experimental geometry, and $\langle \psi_l | Q_n | \psi_m \rangle = \text{const.} \neq 0$, one obtains for the expectation value of the induced electrical dipole moment (see equation 2.99):

$$\langle \vec{p} \rangle_{\text{Raman}} = \begin{pmatrix} p_x \\ p_y \\ p_z \end{pmatrix} = \text{const.} \cdot \begin{pmatrix} \alpha'_{xx} & \alpha'_{xy} & \alpha'_{xz} \\ \alpha'_{yx} & \alpha'_{yy} & \alpha'_{yz} \\ \alpha'_{zx} & \alpha'_{zy} & \alpha'_{zz} \end{pmatrix} \cdot \begin{pmatrix} E_x \\ E_y \\ 0 \end{pmatrix} = \text{const.} \cdot \begin{pmatrix} \alpha'_{xx}E_x + \alpha'_{xy}E_y \\ \alpha'_{yx}E_x + \alpha'_{yy}E_y \\ \alpha'_{zx}E_x + \alpha'_{zy}E_y \end{pmatrix} \quad (2.105)$$

Since the scattered light is detected in z -direction, it can have polarizations in x and y direction. If no polarization is selected for analysis, both the p_x and p_y components of the induced dipole moment contribute to the intensity of the scattered light:

$$I_{\text{Raman}} \propto p_x^2 + p_y^2 = \text{const.} \cdot \left[(\alpha'_{xx}E_x + \alpha'_{xy}E_y)^2 + (\alpha'_{yx}E_x + \alpha'_{yy}E_y)^2 \right]. \quad (2.106)$$

Whether or not the components α'_{ij} are nonzero depends on the orientation of the crystal with respect to the scattering geometry. The analysis of the polarization and intensity of the scattered light as a function of the orientation of an unknown sample with respect to the directions and polarizations of the incident and scattered light provides information about the crystallinity and preferential orientation (texture) of the sample.¹²⁵

The relative intensity of Stokes and anti-Stokes lines depends on the population of the different vibrational levels, which is described by the Boltzmann distribution. The intensity of a Stokes-line that corresponds to a vibrational transition $n \rightarrow n + 1$ (i.e. selection rule in the harmonic oscillation approximation) is affected by the total number density N of Raman scatterers and the temperature T (in K), yielding the relation¹³⁴

$$I_{\text{Raman}} \propto \frac{N}{1 - \exp(-\hbar\omega_n/k_{\text{B}}T)} \quad (2.107)$$

At room temperature, the population of the vibrational ground state is usually higher than that of the excited states, and the Stokes lines are considerably more intense than the anti-Stokes lines, so that often only the Stokes spectrum is analyzed. The fact that the intensity of the scattered light depends on the number density of Raman scatterers, provides the possibility to do quantitative chemical analysis based on Raman spectra, which can be, for example, used to determine the fractions of the components in a mixture. In practice, however, care needs to be taken in controlling all other parameters, in particular the instrument-related parameters, to obtain reliable values for N .^{134,135} Often, a continuous background signal, caused by fluorescence, is superimposed to the Raman response and affects the intensity of the Raman lines or may even obscure some lines. To obtain the original Raman spectrum, the background can be subtracted from the data by fitting an appropriate curve to its signal.

Line position The position of a Raman band in the (Stokes) spectrum is determined by the energy difference between the ground state ($\nu = 0$) and the first excited vibrational state ($\nu = 1$). In the harmonic oscillator approximation, the energy levels are defined as $E_n = (n + 1/2)\hbar\omega_n$ ($n = 0, 1, 2, \dots$), and the vibrational frequency can be expressed as $\omega_n = \frac{1}{2\pi} \sqrt{\frac{\kappa}{\mu}}$, with the force constant κ of the involved bond, and the reduced mass $\mu = (1/m_1 + 1/m_2)^{-1}$ of the involved atoms with masses m_1 and m_2 . Therefore, the Raman

band position is determined by the force constant and the type of vibration (κ) and by the reduced mass (μ).^{114,124,126} As a consequence, weak bonds that involve light atoms are found at high wavenumbers. Since the hybridization state of the considered atoms affects the bond energy, it affects the force constant and therewith the position of the Raman line as well. Experimentally observed shifts of Raman lines with respect to the theoretically predicted position provide information about the local environment of the Raman scatterer. For example, internal stress or dopants (such as foreign atoms or point defects) in solid materials influence the force constants (e.g. by modifying the electron density of a bond) and cause shifted wavenumbers. As described above, small crystallites cause phonon-confinement effects, which in turn produce shifted Raman lines. Raman spectra of mixed phases may contain broadened and shifted peaks if the Raman lines that are produced by the individual constituents lie too close together to be resolved by the spectrometer but are at the same time sufficiently separated to be superposed to an effectively shifted peak.

Linewidth In general, Raman bands have Gaussian-Lorentzian profiles which result from several factors related to the studied material (e.g. gas or solid), the environment (e.g. pressure and temperature) and to instrumental factors (spectral resolution of the spectrometer).^{126,136} The natural linewidth is determined by the finite lifetime of the excited state, which brings about a purely Lorentzian line profile. In solids, the exact vibrational frequency of a particular bond is controlled by its local environment, which in turn determines the relaxation time, and therewith the lifetime of an excited vibrational mode. Due to the statistical distribution of the local environments, the line shape of the Raman bands is predominantly Gaussian, and the linewidth, defined by the full width at half maximum (FWHM), is inversely proportional to the effective lifetime of the phonon. Broad Raman peaks are related to short phonon lifetimes, which is often an indication for disorder. Therefore, broad peaks can be observed in the spectra of amorphous materials and nanocrystals (phonon confinement).¹³⁷ An enhanced peak width may as well originate from the superposition of nearby lying lines of different phases in a mixture.

2.2.5 X-ray photoelectron spectroscopy

X-ray photoelectron spectroscopy (XPS) is a type of photoelectron spectroscopy (PES), which is based on the photoelectric effect that was first described by A. Einstein in 1905 using a quantum mechanical treatment. Since it allows for qualitative and quantitative elemental analysis of the surface of solid materials, it is also called electron spectroscopy for chemical analysis (ESCA). For a detailed treatment of photoelectron spectroscopy the reader may be referred to the respective literature, such as [138–140]. Fig. 23 illustrates the involved fundamental processes. Irradiation of an atom with X-rays causes the ejection of an electron from a core level orbital leaving behind an ionized atom. As a result of relaxation of the excited ion, the generated hole is filled afterwards by an outer shell electron and a second electron is simultaneously emitted, carrying off the excess energy. This is the so-called Auger electron. The competing emission of a fluorescent X-ray photon is a minor process in this energy range.

2.2.5.1 The X-ray photoelectron spectrum

In the basic XPS experiment, a solid sample is irradiated by X-rays under ultra-high vacuum (UHV) conditions to minimize interaction of the X-rays and the emitted photoelectrons with the ambient gas molecules, and the

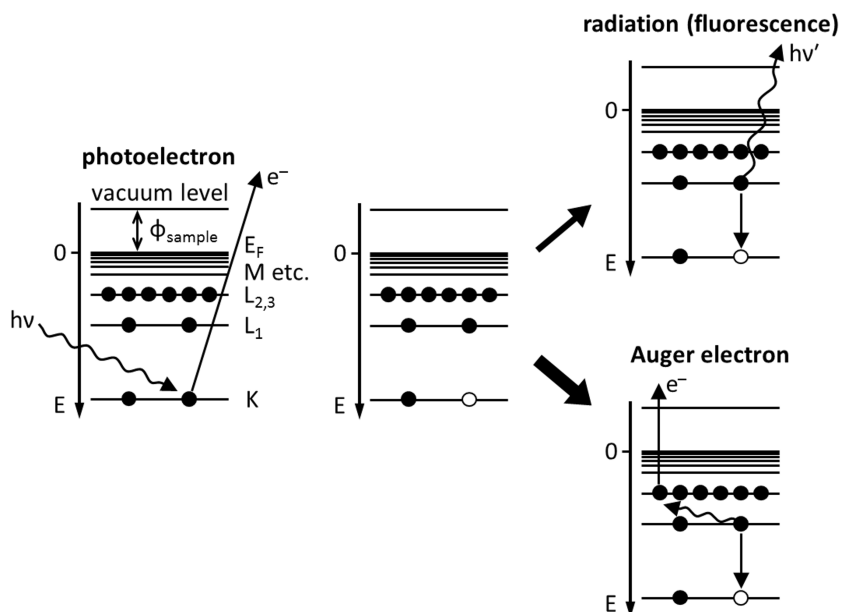


Fig. 23: Scheme of core level photoelectron emission and the two de-excitation channels that cause the emission of radiation (fluorescence) or of an Auger electron (based on the treatments in [141] and [114]).

number of photoelectrons that are emitted from the surface of the sample is measured as a function of their kinetic energy using an electron energy analyzer. Typical X-ray sources for home-lab XPS equipment are Al or Mg anodes that are bombarded with high energetic electrons to produce an X-ray spectrum consisting of the continuous Bremsstrahlung and a set of characteristic lines. The characteristic X-ray lines of these anode materials which are used for XPS are the Al K_α ($h\nu = 1486.6$ eV, linewidth (non-monochromatized) = 0.8 eV) and the Mg K_α ($h\nu = 1253.6$ eV, linewidth (non-monochromatized) = 0.7 eV) line, respectively. Fig. 24 shows the energy diagrams of the irradiated solid and the spectrometer.

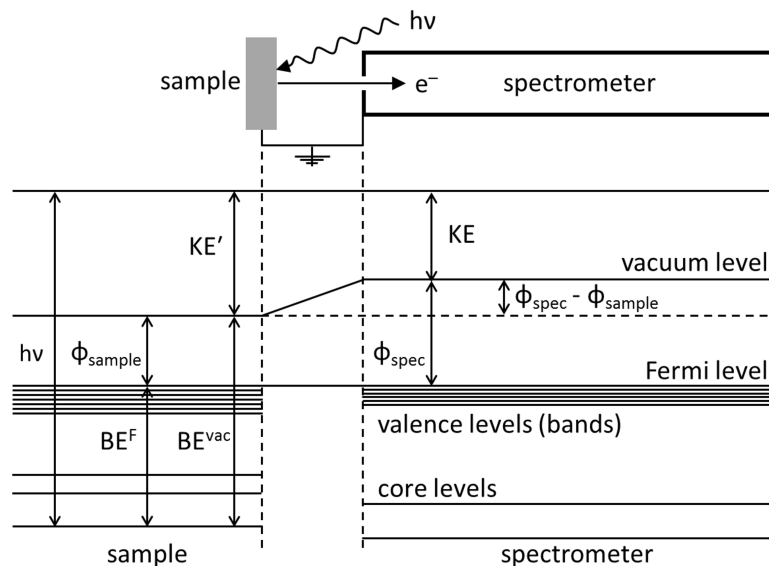


Fig. 24: Energy diagram of the sample and the spectrometer. Based on Fig. 3 in [138].

In a typical spectrometer setup, the (conducting) sample and analyzer are both grounded, so that their Fermi energies are on the same level and the binding energies of the photoelectrons can be referenced to the Fermi level ($BE = BE^F$). Then, the kinetic energy (KE) of a photoelectron, that is ejected during irradiation with a

photon of energy $h\nu$ and measured by an electron spectrometer with work function ϕ_{spec} can be converted into binding energy (BE) according to the relation:

$$\text{BE} = h\nu - \text{KE} - \phi_{\text{spec}} \quad (2.108)$$

The X-ray photoelectron (XP) spectrum as a function of binding energy yields a set of discrete sharp peaks that are characteristic for each element, which allows for elemental analysis. The positions of the core electron peaks are directly related with the discrete BE values of these electrons that originate from atomic levels of the solid, i.e. levels that are not involved in chemical bonds. Their relative intensities depend primarily on the photoemission cross-sections of the corresponding core levels, which give the probability for the photoionization process.

The measured BE of the ejected electron is equal to the energy difference between the initial N -electron state and the final (singly ionized) $(N - 1)$ electron state of the many-electron system (i.e. a single atom with more than one electron, a molecule or a solid).

$$\text{BE} = E_{\text{ini}}(N) - E_{\text{fin}}(N - 1)$$

Hence the position of an XPS peak originates from a superposition of initial state contributions and final state contributions. Some of them will be explained in the following.

Initial state effects *Spin orbit coupling* is an example of an initial state effect. Core level electrons that originate from atomic levels of non-zero angular momentum (all states but s-states), such as p , d or f orbitals, produce double peaks due to the spin-orbit coupling, with a peak separation that is directly related to the energy separation of the corresponding two atomic levels. The spin-orbit interaction energy is given by

$$E_{l,s} = \frac{\xi_{n,l}}{2} [j(j+1) - l(l+1) - s(s+1)] \quad (2.109)$$

For orbital angular momenta $l > 0$, the atomic levels split into two states with different total angular momentum ($j_{\pm} = l \pm s$, with spin quantum number s). The energy separation of the two states is directly proportional to the spin-orbit coupling constant $\xi_{n,l}$, which in turn depends on the expectation value $\langle 1/r^3 \rangle$ of the corresponding orbital. Hence, the experimentally observed peak separation is expected to increase with the atomic number Z for constant (n, l) and with decreasing l for constant n . The intensity (i.e. XPS peak areas) ratio of the doublet components equals the ratio of the respective degeneracy (occupancy) of the two levels:

$$R = \frac{2j_+ + 1}{2j_- + 1}$$

This yields an intensity ratio of 2 for the $p_{3/2}$, $p_{1/2}$ doublet, 3/2 for the $d_{5/2}$, $d_{3/2}$ doublet and 4/3 for the $f_{7/2}$, $f_{5/2}$ doublet.

Another important initial state effect is a consequence of the chemical environment of an element in a molecule or solid in the ground state and causes the so-called *chemical shift* of the BE of few electron volts. The chemical environment is determined by the actual bonding situation, e.g. electronegativity or oxidation state of an atom or fraction of covalency or ionicity of a bond, which are associated with a certain valence electron density at the atom emitting the photoelectron. Typically, lower electron densities at the

local position of the core electron lead to a higher binding energy. This explains the positive chemical shift observed in XP spectra of oxidized transition metals, with respect to the peak position that corresponds to the pure metal. Higher electron densities at the local position of the core electron lead to a lower binding energy. This situation can be found in compounds with elements of high electron affinity. The chemical shifts can be used to identify the chemical states of the materials being analyzed.

Final state effects Final state effects occur only during the photoemission process and can have many causes. A typical final state effect is atomic *relaxation*, a rearrangement of the $(N - 1)$ other electrons, in particular of outer shell electrons, in the presence of the core hole in the ionized state, which leads to a lowering of the total energy of the final state. In solids, interatomic relaxations can occur, where also the electrons on neighbouring atoms undergo rearrangements as a reaction on the sudden presence of the core hole. Depending on the electronic conductivity, such relaxations can be a charge transfer of freely moving valence electrons to the ionized atom (metals), or a polarization of immobile neighboring electrons (insulators). Both relaxation processes result in a screening of the core hole, which is more efficient in conductors. Relaxation gives rise to small shifts in BE often superimposed to chemical shifts, or asymmetric peak shapes (due to differential shifts).

Other final state effects can cause additional peaks in the spectra, which complicate the interpretation of the XPS data but often provide additional information on the chemical state of a material. Among these are the *final state configuration interactions*, which involve the excitation of an electron into a higher energy state in the course of relaxation processes in a solid. If the higher energy state is a bound state, the process is called *shake up* and yields a distinct satellite peak, if it is an unbound state in the continuum above the vacuum level, the process is called *shake off* and causes broad features. Both effects reduce the kinetic energy of the photoelectron. Many metallic materials (e.g. Pt, Pd, Ti or graphite) exhibit a considerable electronic density of states (DOS) above the Fermi level (in the conduction band), which provides a continuous distribution of possible energy levels for shake up electrons. Therefore, instead of individual peaks, a characteristic tail on the high BE side of each XPS peak is observed, which causes an asymmetric peak shape typical for these metals.

Another final state effect worth to mention here, is the coupling between unpaired spins in core and valence levels, which causes the so-called *multiplet splitting* in the case of paramagnetic materials. This creates an ion with several possible final state configurations and results in a PE line which is split asymmetrically into several components.

Experimentally, one always measures the superposition of all initial and final state effects and they are often very difficult to separate. However, for simple chemical analysis and fingerprinting a thorough understanding of the two contributions is often not required and peak assignments are mostly done by considering the effective shift. In most cases, elements and chemical states can be identified using experimental data from standard materials, which are published in handbooks or online databases.¹⁴¹⁻¹⁴³

Instrumental effects and sample charging Instrumentally caused XP lines occur for example if a non-monochromatic X-ray source is used: one or more minor peaks are observed at lower binding energies, which originate from electrons that are produced by minor X-ray components (at higher photon energies) of the used source. The intensity and spacing is characteristic of the X-ray anode material. These peaks are called

X-ray satellites. X-ray ghost lines occur if the sample is impinged by a photon from an element other than the X-ray source, e.g. due to impurities in the source anode. Insulating samples, such as transition metals with a thick oxide layer, tend to acquire a steady state charge when irradiated with X-rays, which causes a rigid positive shift of the binding energy of the whole spectrum.

2.2.5.2 Qualitative and quantitative elemental analysis

For qualitative elemental analysis, identification of chemical states can be made from exact measurements of peak positions and separations, as well as from certain spectral features, e.g. shake up lines or multiplet splitting.

A precise identification of peak positions requires a sufficient energy resolution, in particular, if two peaks are very close to each other, which is often the case in the presence of small chemical shifts. The possibility to separate two adjacent peaks depends on their respective widths. The intense core electron lines are relatively symmetrical (only XPS peaks of some metallic materials exhibit a certain asymmetry) and are typically the narrowest lines observed in the spectra. The peak width, defined by the full width at half maximum (FWHM), is a convolution of the natural linewidth Γ , the width $\Delta E_{\text{X-ray}}$ of the exciting X-ray line, and the energy resolution $\Delta E_{\text{analyzer}}$ of the analyzer. The natural linewidth is the irreducible width in XPS because it is inversely related to the core hole lifetime, τ , through the Heisenberg uncertainty relation, $\Gamma \sim \hbar/\tau = 6.58 \times 10^{-16} \text{ eV s}/\tau(\text{s})$, where \hbar is the reduced Planck constant. Typical lifetime values are between 10^{-15} and 10^{-14} s, giving rise to lifetime broadening contributions (natural linewidths) of between 0.1 and 5 eV.¹³⁹ Under the assumption of pure Gaussian peak shapes, the FWHM can be approximated by:

$$\Delta E = \sqrt{\Gamma^2 + \Delta E_{\text{X-ray}}^2 + \Delta E_{\text{analyzer}}^2} \quad (2.110)$$

However, only the instrumental energy resolution is based on a Gaussian profile, while the characteristic X-ray line and the intrinsic lifetime broadening exhibit a Lorentzian profile. In an insulator, the intrinsic Lorentzian is hard to observe because of the tendency for differential charging which adds a Gaussian (symmetric) contribution to the linewidth. The overall peak shape can be approximated by a convolution (Voigt function) or linear combination (pseudo-Voigt function) of Lorentzian and Gaussian curves. In metals, on the other hand, the creation of electron-hole pairs during the photoemission process causes a lineshape given by the asymmetric Doniach-Sunjic or Mahan function. With a monochromator, the linewidths of the Al K_{α} and Mg K_{α} X-ray sources can be reduced to below 0.5 eV. The analyzer energy resolution has values of typically 0.25–0.3 eV.

One of the great strengths of XPS is that it can be used for quantitative analysis. A quantitative interpretation of photoemission peak intensities requires the development of a model that is able to predict their magnitude from the properties of the incident X-ray, the sample, the analyzer and the data acquisition system. The differential intensity dI_k of an XPS peak (number of counts registered per unit time and energy interval) produced by electrons from the atomic subshell k ($k = \text{K, L}_1, \text{L}_{2,3}, \text{M}_1$ etc.) of atoms in a volume part of the

sample can be expressed as a product of several contributions:¹³⁸

$$dI_k = [\text{X-ray flux at } x, y, z] \times [\text{Number } N \text{ of atoms in } dx dy dz] \\ \times [\text{Differential cross-section for subshell } k] \times [\text{Acceptance solid angle of electron analyzer}] \quad (2.111) \\ \times [\text{Probability for no-loss escape from specimen}] \times [\text{Instrumental detection efficiency}]$$

To integrate equation 2.111, some simplifying assumptions are needed. Fig. 25 shows an idealized spectrometer geometry that can be used to calculate XPS peak intensities from solid specimens.

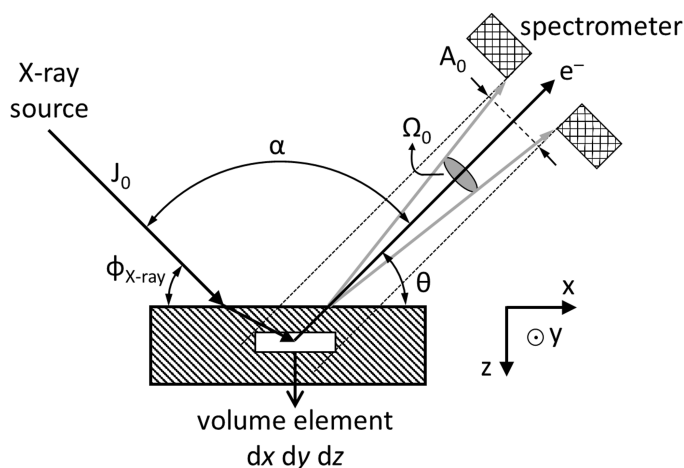


Fig. 25: Idealized geometry of X-ray source, solid sample and spectrometer. Based on Fig. 17 in [138].

If no highly focused X-ray beam is used, the incident X-ray flux can be assumed to be constant over the accessible specimen surface area, that is equal to or larger than the projection of the analyzer aperture. Except for grazing-incidence experiments, the attenuation of the X-rays in the specimen can be usually neglected with respect to the attenuation of the emitted photoelectrons, which permits the assumption of a constant X-ray flux of J_0 throughout the entire specimen volume that is active in producing detectable photoelectrons. For a given kinetic energy it is assumed that a mean solid acceptance angle Ω_0 is applicable over all the specimen volume included in the projection of an effective aperture A_0 (i.e. effective specimen area) along the mean electron emission direction (dotted lines). The mean emission direction is assumed to be at an angle θ with respect to the surface, which may be variable, depending on the instrument. The exciting radiation is incident at an angle $\phi_{\text{X-ray}}$ with respect to the surface. Due to refraction, the internal angle between incident X-ray and sample surface may be smaller than this external angle. The angle α between the mean X-ray incidence and electron take-off directions is held fixed.

Quantitative analysis of XP spectra of solids usually aims at the determination of concentrations of chemical elements in the surface near region of the material. The number N of atoms of a particular element in the investigated specimen volume $dx dy dz$ can be determined from the integrated XPS peak area (intensity), if all other contributions are known.

First of all, the intensity of XP lines is determined by the physics behind the photoionization process. The intensity depends on the probability for the transition of the system from its initial state to a final state that is accompanied by photoemission, when it is excited by an X-ray photon. The probability that a photoelectron from an atomic core level with quantum numbers (n, l) and with a KE of E_{kin} is emitted into the solid

acceptance angle Ω of the analyzer is proportional to

$$\frac{d\sigma_{nl}}{d\Omega} \cdot \Omega(E_{\text{kin}}, \theta, x, y).$$

The *differential photoemission cross-section* can be calculated under assumption of an amorphous or polycrystalline specimen with an atomically flat surface, and non-polarized incident X-ray photons according to:

$$\frac{d\sigma_{nl}}{d\Omega} = \frac{\sigma_{nl}(E_{\text{kin}})}{4\pi} \cdot \left[1 - \frac{1}{2} \cdot \beta_{nl}(E_{\text{kin}}) \cdot \left(\frac{3}{2} \cdot \cos^2(\alpha) - \frac{1}{2} \right) \right] \quad (2.112)$$

where

$$\sigma_{nl}(E_{\text{kin}}) = \int_{\Omega} \frac{d\sigma_{nl}}{d\Omega} d\Omega \quad (2.113)$$

is the *total photoemission cross-section*, which is defined as the transition probability per unit time (in s) for exciting an atom from its ground state to an excited state, that is accompanied by the emission of an electron, with a unit incident photon flux of $1 \text{ cm}^{-2} \text{ s}^{-1}$ and has the unit barn. James H. Scofield has calculated the total cross-sections for each element and several typical photon energies (e.g. Al K_{α} and Mg K_{α}) from quantum mechanical scattering theory.^{144,145} $\beta_{nl}(E_{\text{kin}})$ is termed the *asymmetry parameter*, which gives the preferential photoemission direction relative to the incident photon direction, with $\beta_{nl}(E_{\text{kin}}) = 0$ corresponding to an isotropic angular distribution. Values of $\sigma_{nl}(E_{\text{kin}})$ and $\beta_{nl}(E_{\text{kin}})$ are tabulated for a wide energy range of soft X-rays on the website of the Elettra Synchrotrone in Trieste.¹⁴⁶

In case of solid specimens, the photoelectron that has been excited somewhere below the solid surface needs to be transported to the surface, during which elastic and inelastic scattering events may occur. Inelastic scattering events play the most significant role. They involve processes such as one-electron excitations (interband transitions), phonon excitations (collective vibrations of atoms) or plasmon excitations (collective vibrations of electrons), which limit no-loss emission to a mean depth of only few atomic layers. The number intensity of photoelectrons with a KE of E_{kin} , that reach the surface after being generated at a depth of z can be described by an exponential decay law:¹³⁹

$$I_e(z) = I_0 \exp \left[\frac{-z}{\Lambda_e(E_{\text{kin}}, Z) \cdot \sin(\theta)} \right] \quad (2.114)$$

where Λ_e is termed the *inelastic mean free path* (IMFP). The well-defined (sharp) peaks in the XP spectrum are produced by the core photoelectrons that leave the surface without energy loss. All electrons that undergo inelastic loss processes generate the background signal. The IMFP of electrons in a solid depends on the KE of the electrons in a manner that does not depend too strongly on the chemical identity (atomic number Z) of the solid, as shown in Fig. 26. Therefore, the curve in Fig. 26 is known as the *universal curve*.¹⁴⁷ For a given E_{kin} and chemical species, the values of the IMFP can be calculated from the Tanuma, Powell and Penn TPP2M formula.¹⁴⁸

Finally, the instrumental detection efficiency $D_0(E_{\text{kin}})$ affects the measured intensity of photoelectron signals. It is defined to be the probability that a no-loss electron escaping from the specimen in a direction encompassed by the acceptance solid angle will yield a single final count.

For a homogeneous (i.e. constant atomic density $\rho = dN/dV = N/V$), semi-infinite (i.e. thickness $d \gg \Lambda_e$) substrate, an atomically clean surface, and under assumption of the idealized spectrometer geometry in Fig. 25, the differential XPS peak intensity in equation 2.111 for photoelectrons with a KE of E_{kin} that originate

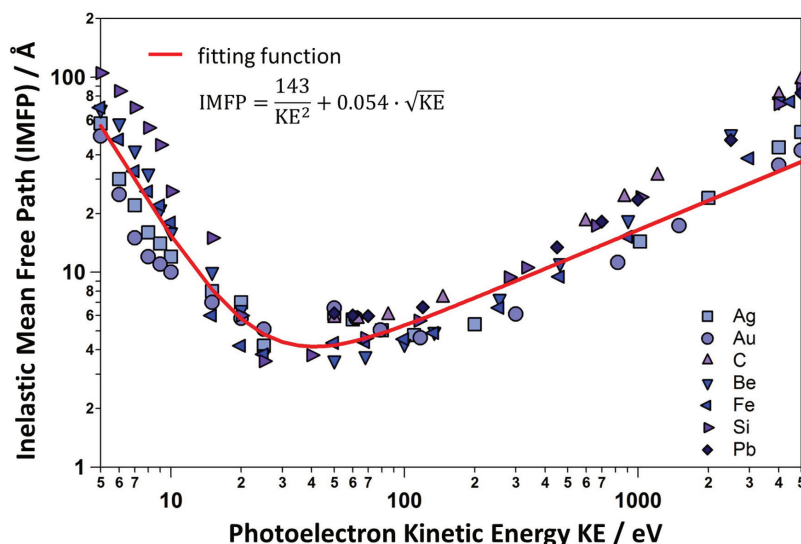


Fig. 26: Inelastic mean free path of electrons as a function of their kinetic energy (printed with kind permission of M. Favaro).

from the atomic subshell k can be integrated and yields¹³⁸

$$I_k = J_0 \cdot \Omega_0(E_{\text{kin}}) \cdot D_0(E_{\text{kin}}) \cdot A_0(E_{\text{kin}}) \cdot \frac{d\sigma_k}{d\Omega} \cdot \Lambda_e(E_{\text{kin}}) \cdot \rho. \quad (2.115)$$

The first four terms are the *instrumental response function* $R = J_0 \cdot T(E_{\text{kin}})$ at normal acquisition ($\theta = 90^\circ$), with the *analyzer transmittance* $T(E_{\text{kin}})$.

To obtain quantitative information on the chemical composition, firstly, one must obtain a value for the peak intensity I_j (i.e. peak area following background subtraction) of the principle spectral feature of each element j detected in the XP spectrum. The fractional atomic concentration c_i of element i is then given by

$$c_i = \frac{N_i}{\sum_j N_j} = \frac{I_i/S_i}{\sum_j I_j/S_j} \quad (2.116)$$

where N_i is the number of atoms of element i in the analyzed volume, and S_i is the *atomic sensitivity factor* of element i which is defined as:

$$S_i = R \cdot \frac{d\sigma_k}{d\Omega} \cdot \Lambda_{e,i} \quad (2.117)$$

For the calculation of atomic concentrations in percent (at%), only *relative sensitivity factors* (RSF) are required (see equation 2.116). RSF are usually the ratio between the sensitivity factor corresponding to a particular chemical species (and electron KE) and the sensitivity factor of adventitious or graphitic carbon. Quantitative data can thus be obtained from peak areas, utilizing the according RSF. To facilitate XPS peak integration, a background signal needs to be subtracted from the spectra first. The most simple background correction is achieved by a linear fit to the low and high energy sides of a spectrum. More physical fundament has the method of Shirley, which takes into account that the background of inelastically scattered electrons is increasing with increasing signal intensity. The Shirley background is hence proportional to the integrated signal intensity. However, the contribution of elastically scattered photoelectrons to the background is neglected. This is included in the background correction by Tougaard. Here, under the assumption of a particular distribution of the element of interest in the solid, the background is calculated from elastically and inelastically scattered

electrons, which makes this method the most accurate but also the most CPU-intensive. In most cases, the Shirley-type background is a good choice, in particular if only intensity (peak area) ratios are considered, where possible errors of the background correction are eliminated. If only a part of a spectrum can be acquired, without the spectral ranges on the high and low BE sides of an XPS peak that show the bare background signal, the subtraction of a constant background is required.

In practice, the shape of an XPS peak of a particular core level can be very complex, e.g. a superposition of several components belonging to different chemical states (chemical shift), satellites or multiplet splitting peaks. This can make interpretation of XP spectra very challenging, in particular if the studied material is a layered composite, mixture of different phases or of inhomogeneous composition. To identify and quantify different chemical states of an element of interest, one usually performs a component fit of the corresponding XP signal. A good fit is based on a well-chosen number of components which are characterized by physically reasonable BE values, intensity ratios (in case of spin-orbit splitting), line shapes (e.g. mixed Gaussian-Lorentzian, or Doniach-Sunjic) and FWHM values. For transition metal spectra, with prominent shake up lines, it is best to include the entire $2p$ region when measuring peak area.

2.2.5.3 Angle-resolved XPS

Angle-resolved XPS can be used to study the surface near chemical composition of an inhomogeneous specimen, e.g. an overlayer on top of a substrate or a sample with a vertical gradient in composition. The photoelectron *escape depth* is defined as the depth z for which I_e in equation 2.114 is 95 % of I_0 , which is the case for

$$d_e = 3\Lambda_e(E_{\text{kin}}, Z) \sin \theta \quad (2.118)$$

The small values of Λ_e in the KE range between 10 and 1100 eV (see Fig. 26) bring about the relatively high surface sensitivity of XPS and the requirement of UHV conditions for such measurements. As shown in Fig. 27, the surface sensitivity can be enhanced if the escaping electrons are detected at an angle θ between sample surface and the mean electron emission direction of less than 90° . So will the detection at small angles provide information of the chemical composition at the very surface, while the bulk contribution of the specimen is maximal at normal acquisition. This method can be used to ascertain if a specimen is homogeneous, because it would then yield identical relative XPS peak intensities for all detection angles.

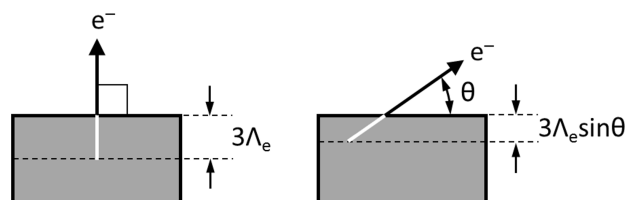


Fig. 27: Escape depths of photoelectrons from a solid for normal emission (left) and tilted emission (right). Based on Fig. 43 in [138].

2.2.5.4 XPS at the synchrotron

Some experiments require a source of intense radiation with a continuously tunable photon energy of very high energy resolution. This is provided by a synchrotron light source. In a synchrotron, electrons are accelerated

to near-relativistic velocities *via* pulsed electromagnetic fields in a circular ring that is typically between tens and hundreds of meters in diameter, giving rise to radiation tangential to the electron orbit. The electrons emit intense light with a continuous energy spectrum, which can be guided into a monochromator for energy selection. The adjustable photon energy has several advantages: (i) the energy can be chosen so that the photoionization cross sections for the core levels of interest are maximal; (ii) through appropriate choice of the photon energy, the IMFP and therewith the surface sensitivity of the measurement can be tuned.

2.3 The investigated materials

2.3.1 Titanium

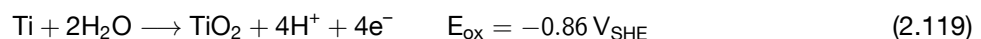
At atmospheric pressure and low annealing temperatures, pure titanium (Ti) crystallizes in the hexagonal lattice system with hcp crystal structure (α Ti), and undergoes an allotropic phase transformation to β Ti, with bcc crystal structure, at 882 °C.¹⁴⁹ The room temperature lattice parameter ratio of the α Ti hexagonal unit cell is $c/a = 1.587$ (see hexagonal unit cells in Fig. 20). Bulk metal Ti is usually polycrystalline, and the texture and average grain size depend on its processing parameters, such as the recrystallization temperature.^{150,151} Also, the phase transition from α Ti to β Ti is accompanied by rapid grain growth.¹⁵²

The high reactivity of Ti with oxygen (O) and the high solid solubility of O in Ti ($\sim 14.5\%$) lead to the immediate formation of a stable protective oxide layer, also called passive film, on the metal surface when exposed to air or water, which brings about a superior corrosion resistance of Ti in various kinds of aggressive environments, in particular aqueous acidic solutions. The thermal stability of Ti in oxygen containing atmosphere is limited to ~ 600 °C, above which oxygen diffusion through the surface oxide layer becomes too fast, resulting in thermal oxide film growth. This air-formed TiO₂ layer on Ti has a rutile crystal structure and is n-type semiconducting due its oxygen deficiency.¹⁴⁹ The native oxide layer on Ti (formed in air at room temperature) is typically 1.3–5.4 nm thick.⁵²

2.3.2 Anodic oxide films on titanium

The large driving force to form a surface oxide layer, which prevents further oxidation, is characteristic for the so-called valve metals, to which Ti belongs. When exposed to an aqueous electrolyte, the oxide film on valve metals constitutes a barrier to the flow of ions and electrons, reducing the rate of further oxidation to very low values. The application of anodic currents or potentials to a valve metal electrode in an electrochemical cell increases the oxide film thickness, which is determined by the final (formation) potential. Electrochemically grown oxide films are therefore called anodic (oxide) films.

The oxidation of Ti in aqueous solution takes place according to the following reaction:⁵³



where E_{ox} is the standard potential of the reaction.

Valve metals owe their name to the fact that they do not pass current in both directions. This rectification effect is interpreted in two manners:⁵²

1. The cathodic current is almost zero, and an anodic current is possible when the potential exceeds about 50 % of the formation potential. This is true for thick oxide layers.
2. The anodic current is low for potentials lower than the formation potential, but a strong (cathodic) hydrogen evolution is possible.

The latter is especially true for very thin insulating films, which allow for electron transfer *via* tunneling, or for doped (i.e. oxygen deficient) n-type semiconducting films, which behave like a diode and become electrically conducting at sufficiently cathodic potentials.

According to Lohrengel, an ideal valve metal is characterized by the following properties.⁵²

1. The surface of an (electro-) polished electrode is covered with 2–5 nm of oxide from air or electrolyte passivation. This corresponds to an open circuit potential of about 0.0 V (vs. a hydrogen electrode in the same solution).
2. During anodization, the thickness of the oxide layer increases with a constant growth rate dd_{oxide}/dE and is proportional to the exchanged charge. This results in a constant current during potentiodynamic anodization or in a linearly increasing potential during galvanostatic anodization.
3. The oxide layer is not reduced by (moderate) cathodic currents, and further oxide growth requires the potential to exceed the previous formation potential.
4. The ionic conductivity is small under steady state conditions or at potentials smaller than the formation potential. The electronic conductivity (of undoped oxides) and, hence, oxygen evolution are negligible. An addition of redox systems to the electrolyte causes no additional currents. Corrosion is small at moderate pH values.
5. The oxide grows independently of the composition of the electrolyte. A (possible) incorporation of e.g. anions from the electrolyte causes no fundamental changes of the layer properties.

A detailed review on the anodization of titanium has been written by J. Vanhumbecq and J. Proost.⁵⁴ Based on their paper and on Vanhumbecq's thesis,¹⁵³ some important aspects about the preparation of anodic films in general and about the characteristics of anodic TiO₂ in particular will be outlined in the following. If not given here, references to the respective literature reports can be found in the review paper.

2.3.2.1 Growth modes and growth parameters

Anodisation is carried out in an electrochemical cell by forcing a current to flow from the cathode to the anode, which is the metal substrate, using an external power source. Several growth modes can be chosen, which have an influence on the final structural and electronic properties of the film.

In the potentiostatic growth mode, a constant potential is instantaneously applied to the cell and held for a defined duration. Under these conditions, the oxide film grows rapidly during the first seconds of the anodization. As a result, a very high current flows through the cell at the beginning of the experiment, which then decays exponentially. By holding the potential for a prolonged period of time, the film eventually attains a constant thickness, associated with the formation potential.

In the galvanostatic growth mode, a constant current is applied to the cell and held until the desired formation potential is reached. When there are no side-reactions or structural transformations of the film throughout the growth, the oxide film grows at a constant rate. Under such ideal conditions, the cell voltage increases proportionally with the thickness of the oxide film to maintain a constant electric field in the film.

A similar growth mode is the potentiodynamic case. By scanning the cell voltage at a constant rate, a constant current is forced to flow through the cell, ideally giving rise to a constant growth rate.

Fig. 28 depicts the expected evolution of the cell potential E and current I as well as of the oxide film thickness d_{oxide} with time during a potentiostatic anodization experiment, as it is described in [54].

Under galvanostatic and potentiostatic conditions and assuming a maximum growth efficiency (i.e. the entire current is used to form the oxide film), the cell voltage E is proportional to d_{oxide} at any time of the experiment.

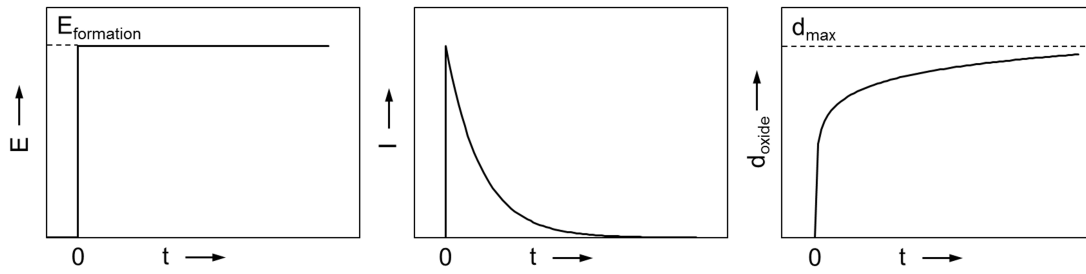


Fig. 28: Evolution of a) the cell potential, b) the cell current, and c) the oxide film thickness with time during potentiostatic anodization. Based on Fig. 3 in [54].

Under potentiostatic conditions, a linear relationship exists between the formation potential and the film thickness for a constant anodization time. The related oxide formation factor, $k = dd_{\text{oxide}}/dE$ is between 1.3 and 3.3 nm V⁻¹ for Ti, depending on the detailed experimental parameters.⁵³

2.3.2.2 Growth mechanisms: the high-field and the low-field approach

Once the first monolayer of oxide is formed on the metal substrate, the rate of the anodization process, i.e. the oxide growth rate, is limited by solid-state mass transport of ions through the oxide film. To promote ionic migration, very large electric fields must be sustained in the oxide film. Typically, the field in a growing anodic oxide film is of the order of 0.1 to 1×10^9 V m⁻¹. There are two main classes of models describing the kinetics of anodization, corresponding to a high-field and a low-field treatment of the ionic migration. At the time of the review of J. Vanhumbecq and J. Proost,⁵⁴ there was no general agreement as to which approach should be used. Both models have been reported to be coherent with some series of experimental data. In the high-field approach, the ionic current associated with the migration of one type of ion, e.g. Ti cations, through the film depends in an exponential manner on the electric field strength within the film:

$$I_{\text{Ti}} = I_0 \exp(\beta \cdot E) \tag{2.120}$$

where I_0 is the primary ionic current and β the field factor. Both these parameters are constants for a given set of experimental conditions and substrate properties. For homogeneous oxide films, the field strength in the oxide is constant and given by the potential drop $\Delta\varphi$ across the oxide and the layer thickness d_{oxide} as $E = \Delta\varphi/d_{\text{oxide}}$.

A detailed review on the high-field model has been written by M. Lohrengel.⁵² The model is based on the consideration that any type of charge carriers in the oxide, such as interstitial metal cations or oxygen vacancies, move through the film by jumping to neighboring sites in the atomic lattice. To do so, their activation energy needs to be sufficiently high to overcome the barrier between the initial and final state. The probability for a jump in a particular direction is described by an Arrhenius-type law. When an electric field is applied, the initially symmetric activation barrier is lowered for the jump in the direction of the field and increased in the opposite direction, giving rise to an effective flux of charge carriers through the film. This requires the assumption that the electric field inside the film is high and can therefore affect the energy barriers experienced by the charge carriers. Furthermore, the contribution from diffusion to the ionic current is postulated to be negligible as compared to that of migration.

Using Faraday’s law, and assuming that the entire anodic current (equation 2.120) is used for oxide layer

growth, the increase of the layer thickness d_{oxide} with time is given by

$$\frac{dd_{\text{oxide}}}{dt} = \frac{m}{\rho_{\text{oxide}} z F} I_0 \exp\left(\beta \frac{\Delta\varphi}{d_{\text{oxide}}}\right) \quad (2.121)$$

where m and ρ_{oxide} are the molecular weight and the density of the oxide, respectively, z is the number of electrons needed to form one molecule of oxide, and F is the Faraday constant. This differential equation has no exact solution, but rough approximations are given by an inverse logarithmic growth law under potentiostatic conditions, which is in accordance with experimental observations (see Fig. 28).

The high-field model does not require any assumption as to the rate-limiting step of the oxide film growth, such as the transfer of charge carriers through the bulk film or the injection of cations from the metal into the oxide. Nor does the model make any *a priori* assumption as to the type of charge carriers involved in the growth process. From experimental studies it is now well established that, for most valve metals including Ti both anions and cations are mobile and contribute to the oxide growth.

In contrast, low-field models consider that the effective electric field in the film is low due to shielding effects at the interfaces. Then, diffusion needs to be taken into account, which is described by Fick's law (first term in equation 2.40), and the ionic migration in the low electric field is described by the second term in equation 2.40. With the Nernst-Einstein equation, which relates the ionic diffusion coefficient D with the ionic mobility μ ,¹⁵⁴ the following differential equation for the total cationic current (e.g. in titanium) is obtained:⁵⁴

$$I_{\text{Ti}} = -zFD_{\text{Ti}} \frac{\partial c_{\text{Ti}}}{\partial x} - zF\mu_{\text{Ti}}c_{\text{Ti}} \frac{\partial \varphi}{\partial x} \quad (2.122)$$

where z is the charge of the cations, F is Faraday's constant, c the concentration and φ the potential.

The main model developed with the low-field approach is the point-defect model (PDM) introduced by D. D. Macdonald and coworkers.^{155,156} It is based on the following hypotheses:

- The ionic current through the film is carried by oxygen and metal vacancies (i.e. point defects).
- The oxide film grows at the metal/oxide interface only, by migration of oxygen anions from the electrolyte into the film. Cationic transport leads to the ejection of metal cations into the electrolyte.
- The diffusion of anions (or vacancies) through the film is the rate-limiting step.
- The reactions taking place at the metal/oxide and the oxide/electrolyte interfaces can be understood in terms of a creation and annihilation of point defects.
- The electric field in the film is buffered by electron/hole pair generation at the film/electrolyte interface, where the entire potential drop occurs, so that the field strength within the film is independent of the applied potential and of the film thickness. The potential drop at the film/electrolyte interface is assumed to vary linearly with pH and applied potential, as it is the case for a polarizable interface.

Under potentiostatic conditions, the PDM predicts an inverse logarithmic rate law for the oxide film growth as a function of time, which is in accordance with experimental observations (see Fig. 28). However, analytical predictions of the influence of the various parameters in the PDM equations, such as the externally applied potential, are not straightforward.

Typical valve metals, such as aluminum, form homogeneous insulating oxide films according to the high-field law (equation 2.120).¹⁵⁷ Also the growth of anodic TiO₂ obeys the high-field law.¹⁵⁸ However, titanium is not an ideal valve metal, since it does not fulfill all of the requirements listed by M. Lohrengel.⁵²

2.3.2.3 Characteristics of anodic TiO₂

Most differences of Ti in comparison with ideal valve metals, such as aluminum, arise from the n-type semiconducting character of anodic TiO₂. A high number of stoichiometric defects, in particular oxygen vacancies, generate donor states in the bandgap, giving rise to a comparably high electronic conductivity. Typical donor concentrations for anodic TiO₂ are of the order of 10¹⁸ to 10²¹ cm⁻³. The high concentration of electrons in the film allows electronic currents, associated with electrochemical side-reactions taking place at the surface of the oxide film, to flow through the film. The presence of side-reactions during Ti anodization strongly affects the kinetics of the growth process and the shape of the corresponding characteristic chronopotentiometric or chronoamperometric curves. The main side-reaction is the oxygen evolution reaction (OER), which starts at potentials above 3.0 V.¹⁵⁷ Since it is competing with film growth, it can to a large extent lower the oxide formation efficiency under galvanostatic conditions. Under potentiostatic conditions, side-reactions as the OER can significantly increase the steady-state current. Oxygen evolution can influence the growth process as well, both from the mechanical and morphological point of view. It has been reported that oxygen can evolve inside the oxide film, giving rise to the formation of blisters and therewith rough surface morphologies.^{159–162}

2.3.2.4 Influence of anodization parameters

The experimental parameters of Ti anodization can considerably affect the structure, morphology and electronic properties of the oxide film. They comprise the chosen electrolyte, temperature, growth rate, anodization time, formation potential and the condition of the Ti substrate itself. Some selected aspects of Ti anodization shall be mentioned here.

For example, foreign ions like protons, anions or impurities can be incorporated from the electrolyte into the passive film during or after anodization, which can then affect the electronic properties of the oxide, since they may cause donor, acceptor or trap states in the band gap. Films grown at a high rate are usually observed to be more insulating than slowly grown ones.

Anodic TiO₂ films prepared at moderate growth rates are initially amorphous and crystallize progressively to some extent in the course of the growth process. Under appropriate anodization conditions, a fully polycrystalline microstructure can be obtained. Film crystallization is promoted by low growth rates, long anodization times, potentiostatic aging and elevated temperatures. It can be delayed if the electrolyte is incorporated into the film. Specific ions in the electrolyte, such as F⁻, can directly influence the crystallization process, e.g. in favor of the rutile phase.¹⁶³

The used electrolyte can also modify the growth process of anodic films. Each electrolyte has the ability to chemically dissolve the oxide film at a given rate, which depends on the pH and on the presence of specific ions. F⁻ ions in the electrolyte for example trigger the self-organized electrochemical formation of TiO₂ nanotubes due to three processes: i) ion migration induced formation of a fluoride rich layer at the oxide metal interface (bottom of the tube); ii) displacement of this layer towards the cell boundaries by a

flow mechanism; iii) dissolution of the fluoride rich cell boundaries and formation of a nanotubular (instead of nanoporous) morphology.^{22,164} Generally speaking, TiO_2 is very stable in neutral electrolytes and its dissolution rate increases slightly with decreasing pH, also in the absence of aggressive ions. When chemical dissolution takes place at a considerable rate, it reduces the effective growth rate and growth efficiency during anodization and lowers the film thickness during prolonged exposure of the oxide to the electrolyte at OCP. Blackwood et al. report a dissolution rate on the order of 2.5 nm h^{-1} in $3.0 \text{ M H}_2\text{SO}_4$.¹⁶⁵

A strong effect on the local properties of anodic films has been found for the Ti micro-texture.^{48,55,57-62,161} Anodic films grown on electropolished polycrystalline Ti sheets, exhibit a substrate grain-dependent thickness, morphology, donor concentration, photoelectrochemical response and activity towards electron transfer reactions. Also film crystallization appears to be facilitated on particular grain orientations of the Ti substrate.⁶² However, there is evidence that a high growth rate, typical for potentiostatic anodization, can suppress the influence of the Ti-microtexture on the thickness and electrochemical properties of the oxide film.^{56,166}

2.3.2.5 Electrochemical and chemical stability of anodic TiO_2

This section provides a brief overview on selected aspects concerning the stability and corrosion of passive films on Ti. More detailed review papers on the passivity of metals and the stability of passive films were published e.g. by Schultze and Lohrengel, as well as Schultze and Hassel.^{53,157}

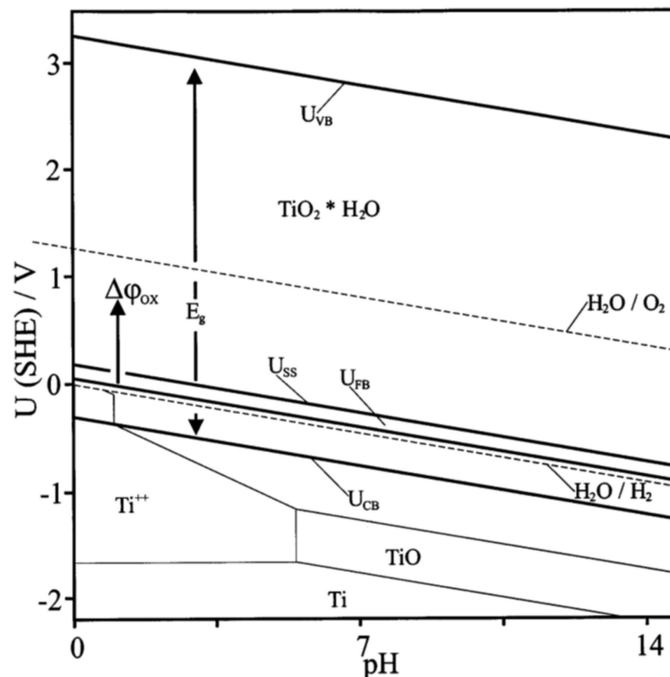


Fig. 29: Pourbaix diagram for Ti, extended by electronic data: U_{VB} : valence band potential, U_{CB} : conduction band potential, U_{FB} : flat band potential, U_{SS} : potential of surface states. E_g : band gap energy of anatase TiO_2 (3.2 eV). $\Delta\phi_{\text{ox}} = U - U_{\text{FB}}$: potential drop in the oxide film. Reprinted from [53] © 2000, with permission from Elsevier Science Ltd..

An understanding of the corrosion behavior of Ti can be obtained by considering the conditions under which the passive oxide film is thermodynamically stable. The Pourbaix diagram for the titanium-water system, shown in Fig. 29, depicts the potential-pH range over which the passive TiO_2 film is predicted to be

stable, based on thermodynamic considerations. Within the entire pH scale, the oxide is stable over a wide range of highly oxidizing to mildly reducing potentials. Oxide film breakdown and the resultant corrosion of titanium occur under reducing acidic conditions. Consequently, the corrosion resistance of Ti is rather low in reducing environments, such as warm or concentrated solutions of hydrochloric, sulfuric, oxalic or phosphoric acids.^{167,168}

Since the steady state electronic properties of the semiconducting oxide film, such as the flatband potential and the positions of the conduction and valence band, depend on the pH and potential as well, they can be included in Fig. 29. Typical values for the band gap E_g of anodic TiO_2 are 3.2–3.4 eV.⁵² The application of a potential $U > U_{\text{FB}}$ causes the depletion of majority charge carriers and the formation of a space charge layer in the semiconductor, which is accompanied by a potential drop $\Delta\varphi_{\text{ox}}$ from the electrode/electrolyte interface into the oxide film (see Fig. 2).

Despite the information provided by thermodynamic considerations, in practice, the stability of a passive film in aqueous solutions is determined by the kinetics of the involved processes. Depending on the electrolyte composition and pH, and on the applied potential, the following electrochemical processes may take place:⁵³

- oxide growth (transfer of oxygen ions from the electrolyte into the oxide);
- corrosion (transfer of metal ions through the oxide into the electrolyte);
- electrochemical reduction;
- chemical dissolution at OCP (no net current), whereby the oxide film thickness decreases;
- electron transfer reactions (e.g. HER, OER);
- capacitive charging.

Usually, several of these processes are taking place in parallel.

Anodic corrosion in the steady state (passive corrosion) involves the movement of metal ions at a constant rate from the metal/oxide interface through the oxide film, and their transfer into solution *via* an ion transfer reaction (ITR) at the oxide/electrolyte interface. Under these conditions, the thickness of the passive film remains constant. The rate of passive corrosion depends on the local potential drop at the interface, the pH and the activity of the metal ions at the metal/oxide interface. The ejection of metal cations can, depending on the electrolyte, lead to the formation of a porous precipitated oxide layer on top of the compact barrier layer.⁵⁴ Anodic films on Ti can be completely dissolved electrochemically upon cathodic polarization. According to D. Arsov, the rate of reductive dissolution in 0.5 M H_2SO_4 is maximum when the electrode is polarized at $-0.6 \text{ V}_{\text{SCE}}$.¹⁶⁹ Furthermore, as already mentioned above, anodic TiO_2 may be chemically dissolved in aqueous electrolytes, where the dissolution rate depends on the pH and the ions present in solution.

2.3.3 Titania and reduced titanium oxides

Titanium dioxide, TiO_2 , is the naturally occurring oxide of titanium. In its stoichiometric form, it is a wide-band gap semiconductor and its most important crystalline polymorphs, from a technical point of view, are the anatase and the thermodynamically more stable rutile phase. In nature it occurs also as the mineral brookite. The thermodynamically stable faces of anatase and rutile TiO_2 single crystals are shown in Fig. 30.

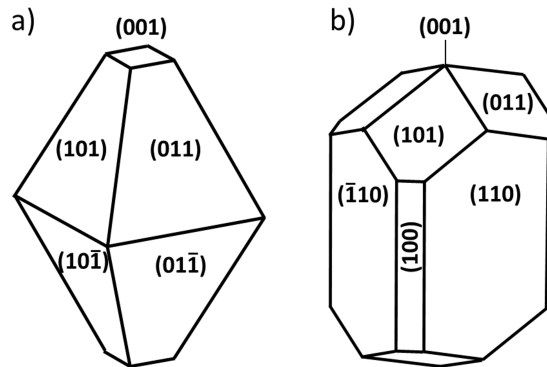


Fig. 30: Equilibrium shape of a macroscopic TiO_2 crystal in the a) anatase and b) rutile phase, according to the presentation in [23].

Both, anatase and rutile crystals are formed by chains of distorted TiO_6 octahedra, where each Ti atom is surrounded by six oxygen atoms. The tetragonal structures of anatase (space group: $D_{4h}^{19}-I4_1/amd$) and of rutile (space group: $D_{4h}^{19}-P4_2/mnm$) are illustrated in Fig. 31. In the anatase phase, the conventional unit cell contains four TiO_2 units, while the conventional unit cell of rutile contains two TiO_2 units. In both, each O atom is coordinated to three Ti atoms.

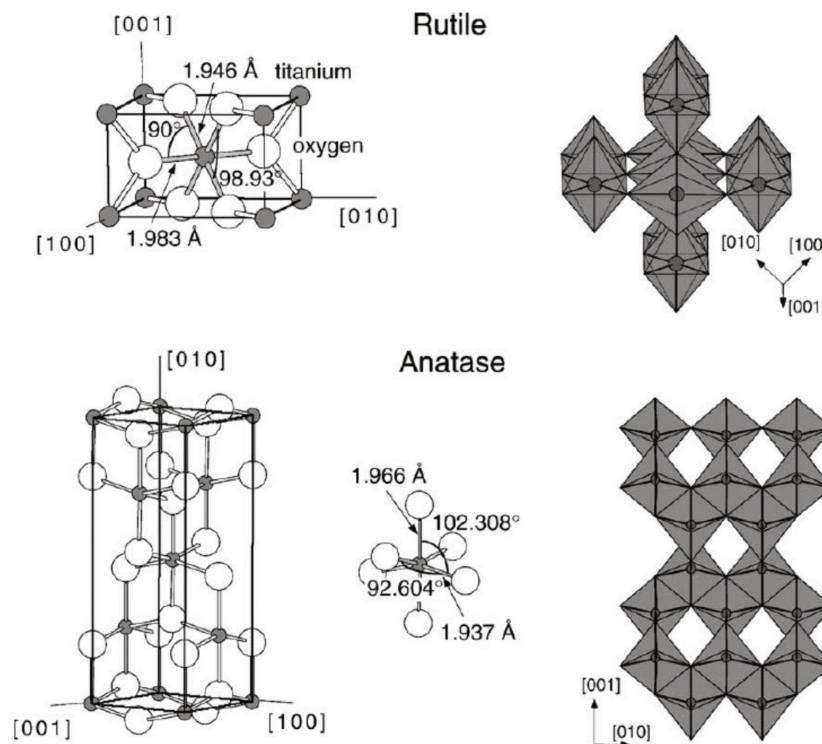


Fig. 31: Bulk structures of anatase and rutile. Reprinted from [23] © 2002, with permission from Elsevier Science B.V..

As typical for metal oxides, the valence band of TiO_2 derives from the O $2p$ levels and the conduction band from the Ti $3d$ states of the constituting ions O^{2-} and Ti^{4+} . Anatase and rutile TiO_2 have an indirect optical bandgap of 3.2 eV and 3.0 eV, respectively.¹⁷⁰ Being a reducible metal oxide, TiO_2 can form several types of structural defects, such as crystallographic shear planes, substitutional defects (oxygen vacancies) and Ti interstitial defects, which significantly alter the physicochemical properties of the material.²³ Particularly

important are oxygen vacancies and Ti^{3+} states, which dominate to a large extent the optical appearance and electronic structure of nonstoichiometric TiO_2 . The defects cause n-type doping states in the band gap and can even modify the energetic positions of the existing bands. Oxygen vacancies create F-centers, which are localized electrons that can undergo optical absorption processes thereby giving a blue color to the reduced oxide.¹⁷¹

According to the Ti–O phase diagram,^{172,173} several stable reduced TiO_2 phases exist, such as the so-called Magnéli-type phases which are a homologous series of substoichiometric oxides of titanium with the general formula $\text{Ti}_n\text{O}_{2n-1}$, where n is between 4 and 10.²⁶ These phases are made up of two dimensional chains of titania octahedra, with every n^{th} layer having oxygen atoms missing to accommodate the loss in stoichiometry. As a result, they consist of ordered and regular arrays of crystallographic shear planes along which the transport of electrons is facilitated. This leads to the relatively high room temperature electrical conductivity of some Magnéli-phases, in particular Ti_4O_7 and Ti_5O_9 , which exhibit conductivities comparable to the one of graphite.^{27,28} Oxygen vacancy point defects can be created already through a mild reduction treatment, while the generation of Magnéli-phases from TiO_2 requires high temperature treatments in reducing atmosphere such as hydrogen gas.

2.3.4 Titanium oxycarbide and titanium carbide

Titanium oxycarbide ($\text{TiO}_{1-x}\text{C}_x$) is a solid solution of the isostructural TiO and TiC . As the individual pure TiO and TiC phases, crystalline $\text{TiO}_{1-x}\text{C}_x$ has a cubic NaCl-type structure, where the oxygen and carbon atoms occupy the octahedral interstitial sites in a fcc titanium lattice. The lattice constant a varies with x from $a = 0.4177$ nm ($x = 0$, pure TiO)^{174,175} to $a = 0.4331$ nm ($x = 1$, pure TiC)^{175,176}. Titanium oxycarbide can be produced by carbothermal reduction of TiO_2 , in an inert atmosphere or vacuum, with a solid (e.g. graphite, carbon black) or gaseous (e.g. hydrocarbons, CO) carbon precursor.^{38–40,43,44,177,178} Through the reduction of TiO_2 to $\text{TiO}_{1-x}\text{C}_x$, the electrical and optical properties undergo a transition from a semiconducting and optically transparent oxide to a material, which shows a metallic-like electrical conductivity and reflectance in the UV, visible and near IR wavelength range.^{175,179,180} The nature of the interatomic Ti–O and Ti–C bonds changes from a mixed covalent-ionic character in TiO_2 to a mainly ionic character in TiC and TiO .^{181,182} The bulk reduction of TiO_2 involves solid-state diffusion of oxygen, titanium and carbon.

Diffusion of foreign atoms in a given crystal lattice is described by *Fick's first law* (see first term in equation 2.40). The temperature-dependence of the diffusion coefficient D is determined by the activation energy $\Delta G_{\text{diff}}^\ddagger$ for diffusion in the solid, and is described by the Arrhenius equation:¹⁸³

$$D = D_0 \cdot \exp\left(-\frac{\Delta G_{\text{diff}}^\ddagger}{k_{\text{B}}T}\right) \quad (2.123)$$

Here, D_0 is the frequency factor of the diffusion coefficient and k_{B} the Boltzmann constant. Lattice diffusion takes place through the transport of point defects, such as interstitial atoms or vacancy sites. In anisotropic crystals, such as titanium (hcp) and crystalline TiO_2 (tetragonal), the diffusion coefficient of a given species (foreign atom or intrinsic defect) depends on the direction with respect to the lattice vectors.^{184–186} Grain boundaries or dislocations, which are always present in polycrystalline materials, can have a significant effect on the introduction of foreign species *via* diffusion. In metallic materials the grain boundary diffusion

coefficient is typically larger than the lattice diffusion coefficient because of the more open structure of the grain boundaries. However, the overall diffusion process might be lattice or grain boundary diffusion controlled, depending on the temperature at which the experiments are conducted and the relative concentration of the defects present.¹⁸³

2.3.4.1 Titanium carbide

Pure TiC is a ceramic with a high melting point (3067 °C) and low electrical resistivity (100 $\mu\Omega$ cm).^{187,188} Similar to $\text{TiO}_{1-x}\text{C}_x$, it can be produced through a solid-state reaction between carbon and titanium or titanium oxides at high temperatures, or by gas-solid reactions *via* thermal decomposition of gaseous precursors (such as C_2H_2) at the surface of Ti or TiO_2 .¹⁸⁹ During an isothermal reaction, TiC forms initially at the surface and the thickness of this phase increases with reaction time due to chemical diffusion of carbon from the surface into the bulk of the solid precursor.¹⁹⁰ The rather low solubility of carbon in titanium is increased in the presence of oxygen, which explains why TiC is mostly prepared through a carbothermal reduction of titania.¹⁸⁷ According to the Ti-C phase diagram, titanium carbide exists over a very wide compositional range, which includes the substoichiometric phases TiC_x , with $0.47 < x < 0.97$.^{187,190}

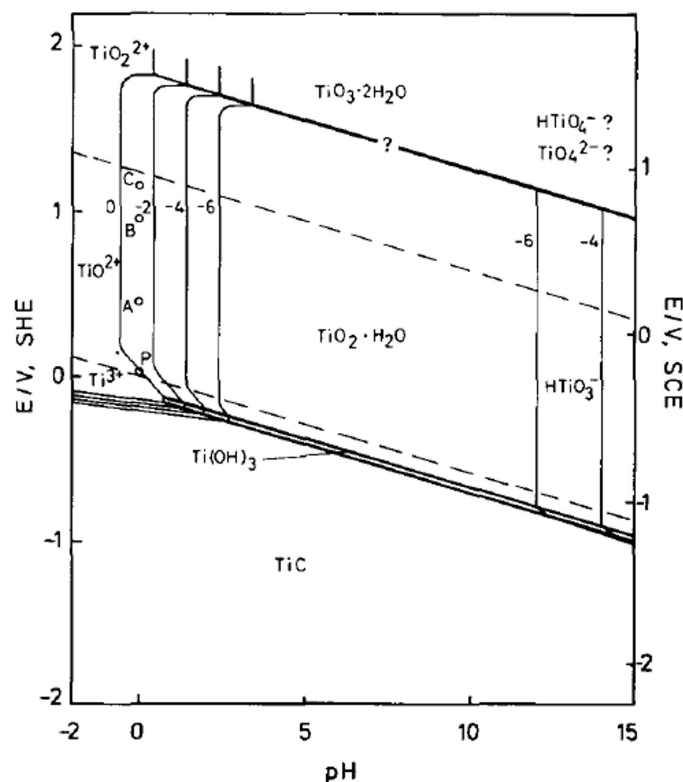
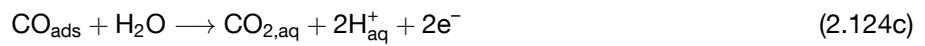
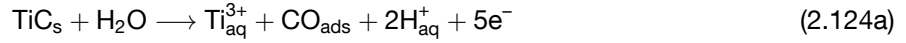


Fig. 32: Calculated Pourbaix-diagram for the TiC-H₂O system at 25 °C. The border lines are drawn for 10⁰, 10⁻², 10⁻⁴, and 10⁻⁶ M solutions respectively. The points in the graph indicate: (P) theoretical passivation potential; measured (A) corrosion potential, (B) passivation potential and (C) passive potential during potentiodynamic anodic polarization in deaerated 1.0 M HCl at a scan rate of 0.1 mV s⁻¹. Reprinted from [191] © 1990, with permission from Elsevier Sequoia.

The thermodynamic stability of TiC under polarization in aqueous solution is represented by the Pourbaix-diagram in Fig. 32. At a pH of zero and at potentials between ~ 0.2 and ~ 1.8 V vs. SHE, the most stable species is TiO_2^{2+} . Hintermann et al. studied the corrosion and passivation of TiC in aqueous 2.0 N (i.e. 1.0 M)

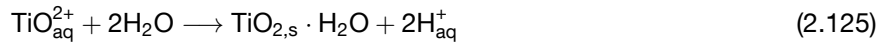
H_2SO_4 solution at $23\text{ }^\circ\text{C}$.¹⁹² From anodic polarization curves at a scan rate of 10 mV min^{-1} , they identified the potential ranges in which TiC undergoes corrosion at a considerable rate, and those in which it forms a passive film. They found that the formation rate of TiO^{2+} is very low at potentials below $\sim 0.8\text{ V}_{\text{SHE}}$.

During slow polarization, notable anodic currents started at $\sim 0.8\text{ V}_{\text{SHE}}$, reached a maximum and dropped to very low values at $\sim 1.0\text{ V}_{\text{SHE}}$. This current peak was attributed to TiC corrosion, which involves the dissolution of titanium as TiO^{2+} , with Ti^{3+} as an intermediate, followed by either the evolution of CO_2 or of CO:

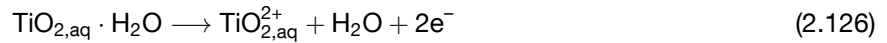


With increasing pH, the onset and the anodic current peak associated with these reactions shifted to cathodic potentials, in accordance with the Pourbaix-diagram.

Passivation of the surface started at $\sim 1.0\text{ V}_{\text{SHE}}$, evidenced by a constant (low) current, and was attributed to the formation of the hydrated oxide $\text{TiO}_2 \cdot \text{H}_2\text{O}$, which only occurs after a critical concentration of TiO^{2+} ions has been formed on the surface:



At potentials above $\sim 1.8\text{ V}_{\text{SHE}}$, a strong increase of the anodic current was observed, which was attributed to severe corrosion due to the oxidation of Ti(IV) to Ti(VI):



As a consequence of the release of $\text{TiO}_{2,\text{aq}}^{2+}$ ions into the solution, it turned yellow.

During the positive going scan of CVs performed with TiC powder electrodes in $0.5\text{ M H}_2\text{SO}_4$ at a scan rate of 20 mV s^{-1} , Roca-Ayats et al. observed similar oxidation peaks, starting at $\sim 0.8\text{ V}$ vs. RHE, due to the irreversible oxidation (corrosion) of TiC.³²

3. Materials and Equipment

3.1 The used chemicals, materials and gases

Table 3.1 lists all chemicals, materials and gases that were used for the presented experiments. Electrolyte solutions were prepared with de-ionized (DI) water from a Millipore-Milli-Q system with 18.2 M Ω resistivity. Prior to a measurement, electrodes and crystals were rinsed with DI water and dried in an Ar stream to remove dirt.

Table 3.1: List of chemicals and raw materials.

<i>application</i>	<i>chemical/material</i>	<i>quality, concentration</i>	<i>provider</i>
chemicals: cleaning	sulfuric acid	p.a., 95–97 %	Merck, Germany
	hydrogen peroxide	stabilized, 30 %	Merck, Germany
	hydrochloric acid (HCl)	p.a., 37 %	Merck, Germany
	nitric acid (HNO ₃)	p.a., 65 %	Merck, Germany
	acetone	technical	TUM Chemie Department
	ethanol	technical	TUM Chemie Department
	2-propanol	GC grade, 99.7 + %	Alfa Aesar, Germany
chemicals: synthesis/ electro- chemistry	sulfuric acid (H ₂ SO ₄)	suprapure, 96 %	Merck, Germany
	perchloric acid (HClO ₄)	suprapur, 70 %	Merck, Germany
	orthophosphoric acid (H ₃ PO ₄)	p.a., 85 %	Merck, Germany
	chloroplatinic acid hydrate (H ₂ PtCl ₆ ·xH ₂ O)	≥ 99.9 % (trace metals basis)	Sigma-Aldrich, Germany
	potassium ferricyanide (K ₃ [Fe(CN) ₆])	p.a.	Merck, Germany
	potassium ferrocyanide (K ₄ [Fe(CN) ₆]·3H ₂ O)	p.a.	Merck, Germany
	potassium chloride (KCl)	Suprapur [®] , 99.999 %	Merck, Germany
	2-n-butoxyethanol	99 %	Alfa Aesar, Germany
	ethanol (C ₂ H ₅ OH)	absolute, ≥ 99.8 %	Sigma-Aldrich, Germany
	methanol	analytical reagent, 99.8 %	Sigma-Aldrich, Germany
gases: synthesis/ electro- chemistry	argon (Ar)	4.8	Linde, Germany
	acetylene (C ₂ H ₂)	solvent-free	Linde, Germany
	hydrogen (H ₂)	99.999 %	Westfalen AG, Germany
	liquid nitrogen (N ₂)		TUM Physik Department
materials: substrates/ electrodes	titanium (Ti) sheet/rod	99.6 %, temper annealed	Advent Ltd., England
	glassy carbon (GC) disks	Sigradur [®]	HTW GmbH, Germany
	platinum (Pt) wire	99.99 %	Carl Schaefer GmbH, Germany
	gold (Au) wire	99.99 + %	Sigma-Adrich, Germany

3.2 Preparation of TiOC, Pt/TiOC and Pt/GC electrodes

The aim of the herein presented work was the design of model systems, based on carbon containing reduced titania materials (TiOC), for electrocatalysis studies on thereon deposited Pt catalysts. To prepare TiOC catalyst supports of simple morphology and geometry, planar compact anodic TiO₂ films on Ti metal disks were chosen as precursor material, into which carbon species were introduced through a carbothermal treatment with acetylene. Throughout this thesis, the carbothermally treated anodic films will be denoted by TiOC. For electrocatalysis studies, Pt nanoparticles (NPs) were deposited on TiOC films as well as on glassy carbon (GC) disks. In this section it is described how the TiOC films as well as the Pt/TiOC and Pt/GC electrodes were prepared.

3.2.1 Synthesis of planar TiOC films

Planar TiOC films were prepared in four steps: mechanical polishing and electrochemical polishing of the Ti substrate, anodic growth of a compact oxide film, and carbothermal conversion of the anodic film into a carbon containing TiOC film.

3.2.1.1 Preparation of the Ti substrates

Square Ti platelets of 1 mm thickness and an edge length of 12 mm were cut by electrical discharge machining from large metal sheets. Punching was not possible because it caused bent edges. Disks of 7, 10 or 15.5 mm diameter and 1 mm thickness were cut from a 20 mm diameter Ti rod using a turning machine. One side of the Ti substrates was mechanically polished in three steps using SiC wet abrasive paper and ethanol (technical grade). Water could not be used for cooling because it led to an oxidation of the Ti surface, which strongly impeded a homogeneous removal of material and resulted in brown stains. The best polishing results were achieved with abrasive papers from BUEHLER (ITW Test & Measurement GmbH, Germany), which are listed in table 3.2. After each polishing step, the samples were sonicated in ethanol and dried with an Ar stream. After the final step, they were rinsed with DI water and dried in an Ar stream.

Table 3.2: Abrasive SiC papers from BUEHLER

<i>product</i>	<i>grit size / ANSI [FEPA]</i>	<i>approx. grain size</i>	<i>diameter</i>
CarbiMet	600 [P1200]	15 μm	305 mm
MicroCut	1200 [P2500]	8 μm	305 mm
MicroCut (or BuehlerMet)	[P4000]	5 μm	305 mm

To remove the Beilby layer,¹⁹³ which forms upon mechanical polishing, the polished side of the substrates was electrochemically polished in a mixture of 270 mL methanol 175 mL 2-n-butoxyethanol and 30 mL of 40 % aqueous perchloric acid solution, following a recipe of Arsov.¹⁶⁹ The electropolishing setup is shown in Fig. 33. It consists of a glass beaker for the solution, which is dipped into a styrofoam container filled with liquid nitrogen. The electrolyte solution was continuously stirred and kept at a temperature between –37 and –30 °C, using the vapor of the liquid nitrogen bath, to increase the ionic solution resistance and hence keep the current density low. At the same time, the liquid nitrogen ensured cooling of the explosive solution. The temperature was monitored with a TJ-USB: Type-K thermocouple (OMEGA, Germany) connected to a PC

with the respective read-out software. The mechanically polished Ti substrates were contacted from the back side with a gold wire and wrapped into a Teflon[®] coated adhesive tape (CMC 75100, CMC Klebetechnik, Germany) with a punched round hole in the front, exposing a defined surface area of the substrate, as shown in Fig. 39. With an alligator clip soldered to a coated copper wire, the substrate was connected to the positive pole of a power supply and dipped into the solution. A sufficiently large Au or Ti CE was positioned parallel to the substrate surface in the same solution and connected to the negative pole of the power supply. The beaker was open to the surrounding air and no reference electrode was used.

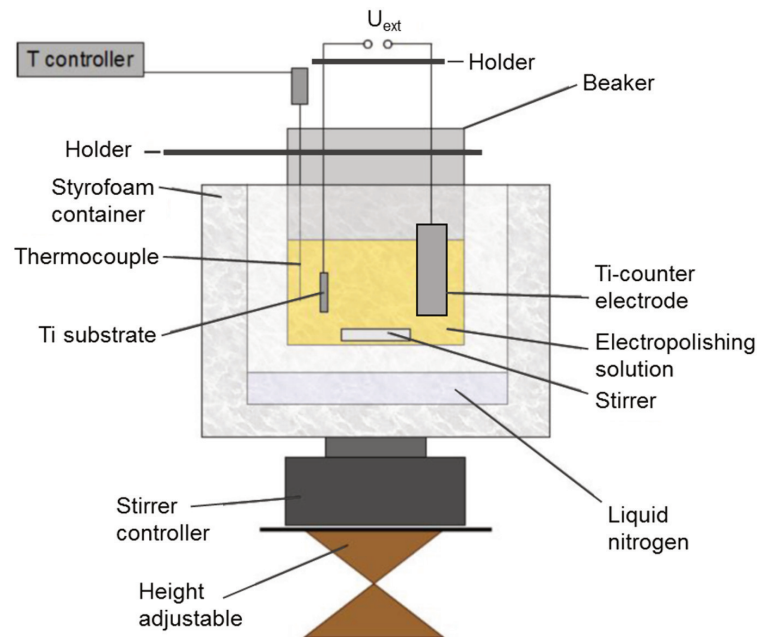


Fig. 33: Electropolishing setup. Adapted from [194] with kind permission of F. Wiesinger.

Depending on the Ti substrate size, different experimental parameters were used for electropolishing to achieve optimal results. In the first period of this thesis, a square Au sheet of $10 \times 10 \text{ mm}^2$ served as CE, and the Ti substrates (square sheets of $12 \times 12 \text{ mm}^2$ or round disks of 15.5 mm^2 diameter) were electropolished for five times at $-32 \pm 5^\circ\text{C}$, by applying a constant voltage of 60 V for 5 min each time. These samples were used for the studies presented in section 4.2 of Chapter 4 and in Chapter 6. After that, the electropolishing procedure was further optimized and for all following studies, in particular those discussed in sections 4.3 and 4.4 of Chapter 4 as well as in Chapter 5, the temperature during electropolishing was kept at $-35 \pm 2^\circ\text{C}$. In addition, a Ti sheet of at least twice the surface area of the substrate was used as counter electrode, to ensure a more efficient collection of the electropolishing current. The finally used electropolishing parameters are listed in table 3.3.

In the case of the 10 mm diameter substrates, two samples were wrapped in parallel into a mask of Teflon[®] tape with two holes to increase the surface area and keep the current density similar to that of the 15 mm diameter substrate. During each electropolishing step, a constant potential was applied for 5 min and after each step the sample was rinsed thoroughly with DI water to remove the milky layer of complexed Ti^{4+} ions, and then dried in an Ar stream.

At the end of the electropolishing procedure, the Teflon[®] tape was immediately removed to avoid contamination of the electropolished surface with glue. The samples used for local studies of the substrate grains

Table 3.3: Parameters used for electropolishing

Ti dimension	holes per mask	repetitions and potential
15 mm diameter	1 × 14 mm	3–4 times at 60 V
10 mm diameter	2 × 8 mm	3 times at 60 V
12 mm × 12 mm	1 × 10 mm	3 times at 60 V
8 mm × 8 mm	1 × 6 mm	2 times at 60 V

were marked with a cross scratch using a tungsten needle. Finally, the samples were cleaned in an ultrasonic bath with ethanol and then with DI water, and dried in an Ar stream. Of some electropolished and marked Ti substrates, EBSD maps were acquired. After these measurements, the Ti sheets were consecutively cleaned in an ultrasonic bath with ethanol, isopropanol and DI water.

3.2.1.2 Preparation of compact anodic TiO₂ films

A thin compact oxide film was prepared on the electropolished Ti substrates by potentiostatic electrochemical anodization for 10 min in 0.1 M H₂SO₄ and at room temperature. A home-built Teflon[®] electrochemical cell, depicted in Fig. 34a, was used with a two-electrode configuration, where a Pt-mesh served as counter electrode. The desired potential was applied using a DC power supply (PE 1540, 40 V/3 A, Philips), monitored by a multimeter (Voltcraft Dual Display M-3650D). The anodic films were rinsed with DI water and dried in an Ar stream.

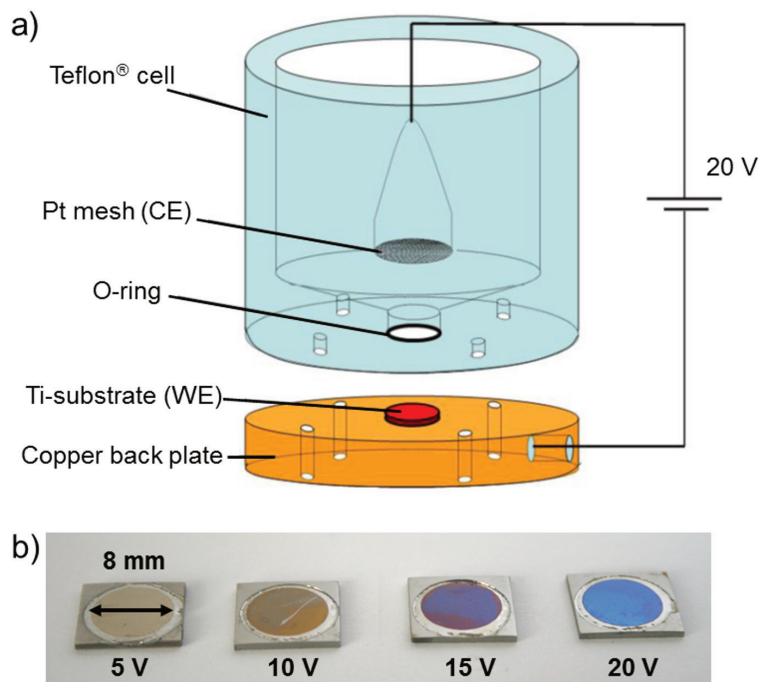


Fig. 34: a) Anodization cell (adapted from [194] with kind permission of F. Wiesinger). b) Anodic TiO₂ prepared at different potentials.

As can be seen from Fig. 34b, different anodization potentials yield films of different thickness, which can be

distinguished by their characteristic interference colors. For most of the studies, presented in the following chapters, anodic films were prepared at 20V, which corresponds to a thickness of 45–60 nm.^{61,195} The potentials used for the anodization will be given in the respective sections.

3.2.1.3 Carbothermal treatment to obtain TiOC films

Carbothermal treatments of the anodic films were conducted in a horizontal quartz tube reactor in a tube furnace (HST 12/600 from Carbolite, England, equipped with an Eurotherm 3216 temperature controller) under controlled gas flow. Fig. 35 depicts the quartz boat with anodized Ti sheets, a simplified sketch of the annealing station, the applied temperature profile and a typical gas flow program. The gas flow was controlled with appropriate mass flow controllers (MFC), which were mounted in the respective gas lines and connected to a control unit (MKS Instruments, Germany). The gas flow was measured in standard cubic centimeters per minute (sccm, at 0 °C and 1 atm pressure). The Ar gas flow was controlled with an MFC dedicated for a maximum flow of 500 sccm N₂ gas, which was calibrated for Ar gas. The C₂H₂ gas flow was controlled with an MFC calibrated for a maximum flow of 5 sccm C₂H₂. The exhaust gas was guided through a gas bubbler, filled with water, which allowed for a visual validation of an uninterrupted gas flow through the reactor.

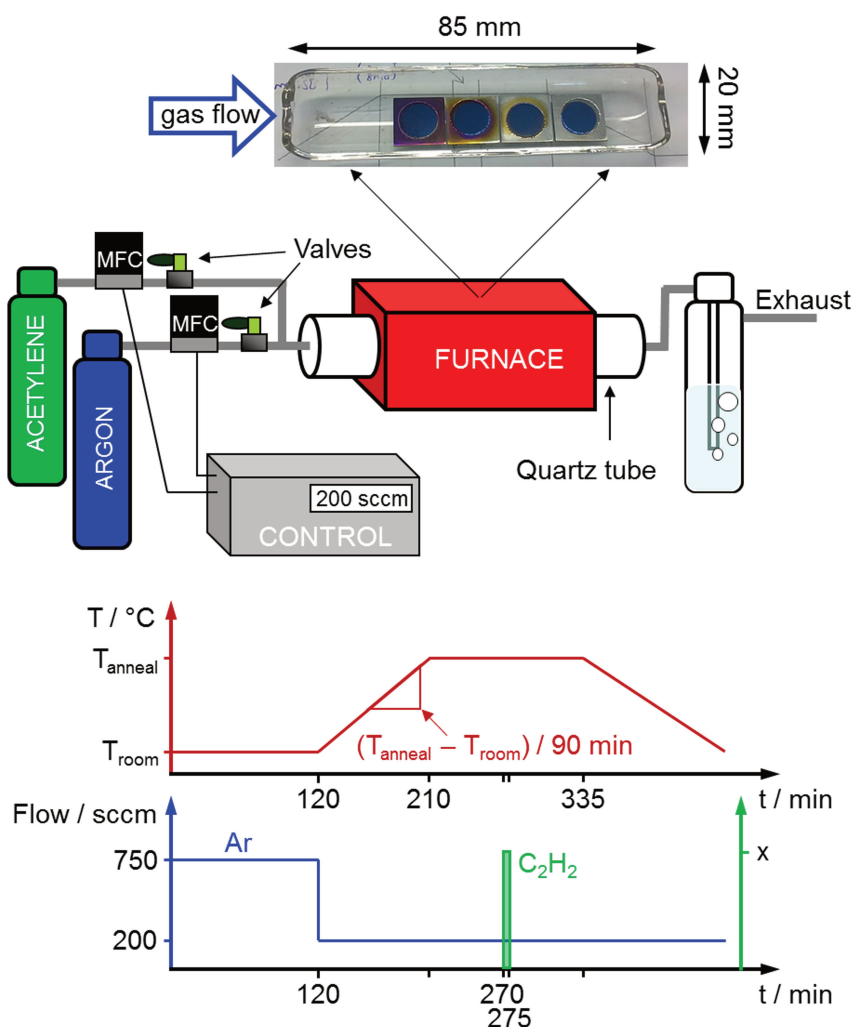


Fig. 35: Top: photograph of quartz boat with anodized Ti sheets; center: schematic of annealing setup; bottom: temperature and mass flow programs.

To connect the reactor with the stainless steel gas tubings, home-built stainless steel flanges were glued to both openings of the quartz tube using a heat resistant silicone adhesive/sealant (ELASTOSIL[®] E14, red, Wacker Silicones, distributed by DRAWIN Vertriebs-GmbH, Germany). The flange connections were sealed by stainless steel centering rings with Viton[®] O-rings and locked with aluminum clamping rings (vacuum parts available e.g. from Dekont Vakuum Service, Germany). Each gas supply line was equipped with appropriate flame arrester/rebound protection elements (WITT-Gasetechnik GmbH & Co KG, Germany).

Before a new annealing process was started, the inner walls of the reactor tube were wiped with an acetone soaked paper towel to remove residual carbon dust from previous processes. Then, three to four samples were placed in a quartz boat (Fig. 35), which was previously cleaned with acetone. The boat was inserted into the reactor tube and positioned in the zone of constant temperature of the furnace. To take into account the shift of the zone of constant temperature in the presence of gas flow, the sample boat was positioned a few cm right from the center position, when the gas entered the reactor from the left side.

For the carburization processes, the following protocol was applied (see Fig. 35):

- (i) The reactor tube was purged for 1-2 hours with a high flow of Ar to remove air;
- (ii) the carrier gas flow was set to the desired value for the carburization process and the reactor was heated at a constant rate within 90 min to the desired annealing temperature T ;
- (iii) the samples were pre-annealed for about one hour;
- (iv) x flow% of C_2H_2 were added for y min to the Ar flow;
- (v) after switching off the C_2H_2 gas flow, the samples were post-annealed for 60 min;
- (vi) the furnace was switched off and the reactor was allowed to cool down to room temperature.

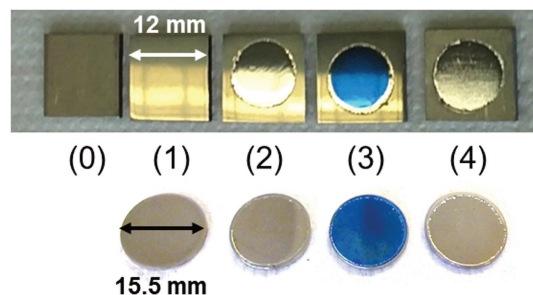


Fig. 36: Preparation steps of TiOC films: (0) raw Ti platelet/disk, (1) mechanically polished Ti surface, (2) electropolished Ti surface, (3) TiO_2 film on anodized Ti (4) carbothermally treated oxide film (TiOC). Top: square Ti platelets with an edge length of 12 mm; bottom: round Ti disks with a diameter of 15.5 mm.

If not stated otherwise, a reactor tube of 40 mm diameter was used for the carbothermal treatments. Then, the tube was initially purged for 2 h with 750 sccm Ar, which was set to 200 sccm for the synthesis. During the annealing at T , acetylene was added for 5 min to the Ar gas. The employed C_2H_2 gas flows were 0.1, 0.5 or 1.0 % of the Ar carrier gas flow during the annealing, which corresponds to 0.2, 1.0 and 2.0 sccm. The employed annealing temperatures were 550, 650, 750, 850, 950 and 1050 °C. The specific parameters used for different syntheses, in particular when a smaller reactor tube was used, will be given with the respective

results presented in the following chapters. Independent of the acetylene concentration, anodic films that were carburized and annealed at a temperature T will be termed TiOC_T throughout this thesis.

Fig. 36 depicts the sample surfaces after each of the described preparation steps for two different Ti substrate geometries.

3.2.2 Glassy carbon electrodes

GC electrodes with a thickness of 1 mm and a diameter of 15.5 mm were used to prepare a Pt/GC reference system for the electrocatalysis studies. Prior to the deposition of Pt NPs, the GC was freshly polished in three steps of each ~ 5 min, using diamond polishing dispersions of 1, 0.25 and 0.1 μm grain size (cloth and dispersions from ESCIL, France). After each polishing step the surface was rinsed with DI water and the disk was cleaned by ultrasonication in ethanol and in DI water. To reuse the GC disks, the Pt was chemically dissolved after the EC tests by immersing the Pt/GC surface for several hours into fresh aqua regia (i.e. a mixture of HCl and HNO_3 in a molar ratio of 3:1). After that, the GC surface was rinsed with DI water and polished for the next experiment.

3.2.3 Deposition of Pt nanoparticles

Different attempts were done to impregnate TiOC films with Pt NPs. In the frame of the Bachelor thesis of J. Landensfeind, which was co-supervised by myself, Pt NPs were deposited electrochemically.¹⁹⁶ Thereby, TiOC films were immersed as working electrode into an electrolyte solution of 1.0 M HClO_4 with 5 mM K_2PtCl_6 in a three electrode glass EC cell. A potentiostatic double-pulse of defined pulse amplitudes and durations was applied to electro-reduce Pt on the TiOC surface. Unfortunately, the impregnation of TiOC with Pt catalyst did not yield the desired results, that are a homogeneous surface coverage, NPs in the nm-range with a narrow particle size distribution, high electrochemical stability of the NPs, and a high reproducibility of the impregnation procedure, so that we did not follow up on this preparation route. During the last period of this thesis, an attempt was done to deposit Pt NPs on TiOC films using physical vapor deposition (PVD). Although well dispersed small NPs were obtained, the electrochemical stability of the deposited catalyst was very poor, so that also this preparation route had to be discarded.

The best results were obtained using an aerosol assisted deposition (AAD) setup as described in [197]. AAD is a modified spray pyrolysis technique, which allows the direct deposition of active species on the substrate without any further treatment.

Fig. 37a shows a sketch of the employed AAD setup. The reactor consisted of a 760 mm long quartz tube with a diameter of 48 mm, which was wrapped with a heating collar (Horst GmbH, Germany). The TiOC or GC substrates were put with the prepared surface upside down into the quartz sample holder, inserted into the reactor tube from the top and positioned in the center of the heated zone. A type-K thermocouple wire was inserted from the top into a channel in the sample holder rod, which was sealed at its bottom part to avoid corrosion of the sensor. Reaching the back of the substrate disk, the thermocouple allowed to monitor the temperature at the sample during the entire deposition procedure. The heating rate of the collar was controlled with an Eurotherm 2132 temperature controller (Invensys Systems GmbH, Germany), which used the sample temperature as feedback.

An ultrasonic nebulizer (12–15 W, 241T 241V Nebulizer, Sonaer Ultrasonics, USA) with a working frequency of

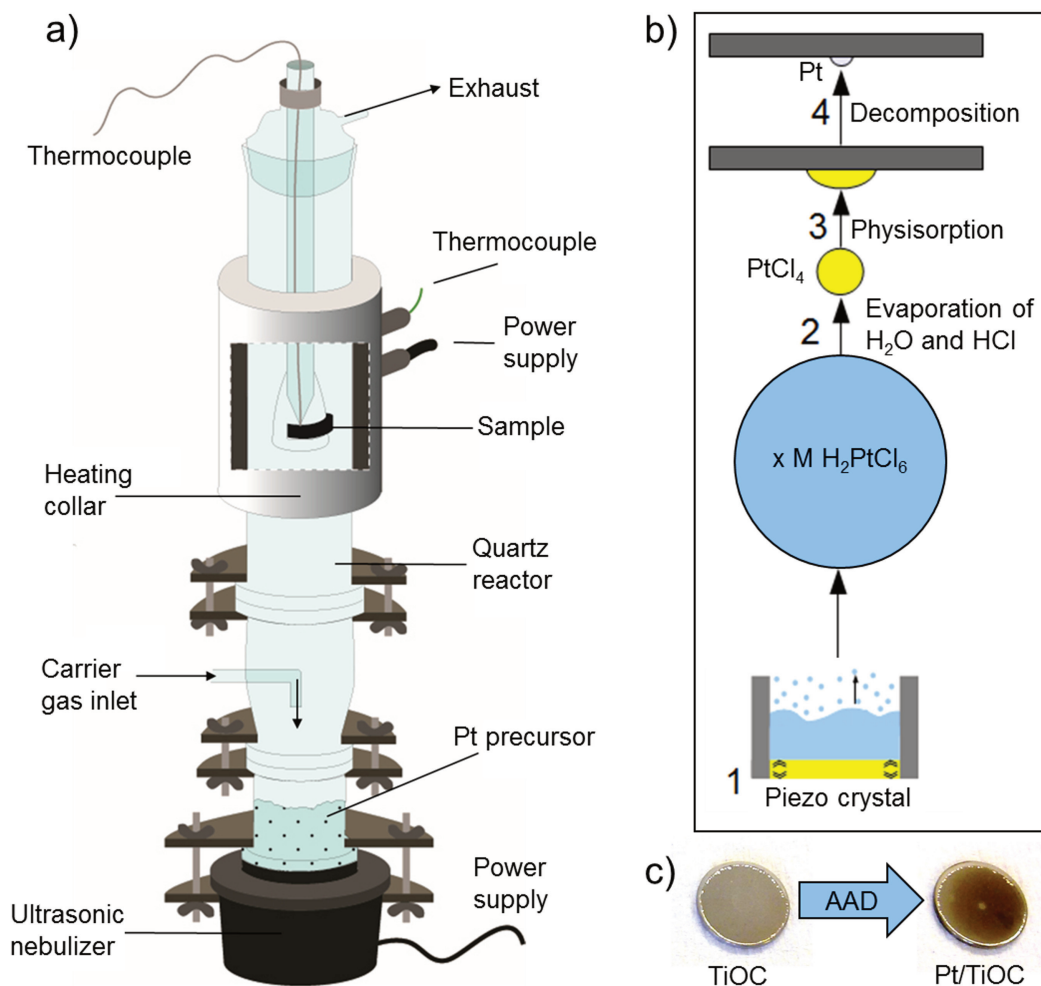


Fig. 37: a) Scheme of AAD setup; b) physical and chemical processes during AAD of Pt using a H_2PtCl_6 precursor solution; c) TiOC film before and after impregnation with Pt *via* AAD. a) and b) are adapted from [198] with kind permission of J. Brumbarov.

2.40 ± 0.05 MHz was mounted at the bottom of the vertical quartz cylinder. A dilute solution of chloroplatinic acid ($\text{H}_2\text{PtCl}_6 \cdot 6\text{H}_2\text{O}$) in DI water served as the Pt precursor and was filled in the container on top of the piezo crystal. When switched on, the high frequency vibrations of the nebulizer created a fine mist (aerosol) of the precursor above the solution. The small droplets were transported upwards into the heated zone by a defined flow of Ar carrier gas (controlled with a Bronkhorst EL-FLOW mass flow controller) that was fed into the reactor from the side at the bottom part. A bubbler filled with water was connected to the exhaust tube of the reactor to visually monitor the gas flow.

The molecular processes taking place during the AAD are illustrated in Fig. 37b. As soon as the precursor droplets that are carried by the inert Ar gas reach the heated zone, the solvent water and HCl are evaporated. The remaining PtCl_4 particles are transported further upwards towards the substrate, where they are physisorbed on the surface. At sufficiently high reaction temperatures, the PtCl_4 particles are instantaneously decomposed to volatile Cl_2 and solid Pt on the substrate surface. If the temperatures are too low to allow for the complete decomposition of the precursor salt, hydrogen gas may be added to the gas flow after the deposition of physisorbed PtCl_4 to facilitate the removal of the chloride as HCl.¹⁹⁹

The deposition parameters are the precursor concentration, the carrier gas flow, the deposition temperature,

the deposition duration and, if required, the hydrogen gas flow. They were optimized by J. Brumbarov, who has built an AAD setup for the deposition of Pt NPs on GC and TiOC in the frame of his Master thesis.¹⁹⁸ F. Wiesinger took over the procedure with slight modifications during his Master thesis.¹⁹⁴

The general protocol was as follows:

Before heating up and starting the AAD procedure the reactor tube was flushed with 1000 sccm Ar for up to 30 min to ensure an inert gas atmosphere and prevent a reoxidation of the sample by remaining oxygen. Then the Ar gas flow was set to the flow rate chosen for the deposition process and the heating collar was switched on to heat the reactor to the desired reaction temperature. After reaching a stable temperature, the nebulizer, that has been previously filled with a defined amount of the chosen chloroplatinic acid solution, was switched on for a defined duration. The heating collar was switched off after ~ 2 min, when no mist was left in the reactor tube, to cool the sample down to room temperature in Ar atmosphere. If required, a defined flow of H₂ gas was added to the Ar gas flow 2–6 min after switching off the nebulizer, and the heating collar was switched off after another 10 min. In this procedure, the hydrogen gas flow was kept on during cool down.

The deposition parameters used for the EOR study presented in Chapter 6 are given in table 3.4. They were optimized for both kinds of supports to obtain Pt coverages in the range of more than 10%. In the case of TiOC, lower deposition temperatures were required to avoid extensive oxidation of the support. To ensure complete reduction of the metal salt on the TiOC substrate, 9 flow% of H₂ was added to the gas flow while cooling down to room temperature. Fig. 37c depicts photographs of a TiOC film before and after AAD of Pt NPs.

Table 3.4: Precursor concentrations and AAD parameters used for deposition of Pt NPs on GC and TiOC.

support	H ₂ PtCl ₆ ·6H ₂ O	Ar flow	temperature	deposition duration
GC	0.01 M	500 sccm	400 °C	7 min
TiOC	0.02 M	500 sccm	350 °C	14 min

3.3 Setups of the electrochemical experiments

Electrochemical measurements were performed in the three electrode configuration, with electrochemical cells containing a working electrode (WE), a counter electrode (CE) and a reference electrode (RE). To monitor the potential close to the WE, the RE was put in an external compartment, connected *via* a Luggin-Haber capillary that was placed in front of the exposed area of the WE with a distance of less than about 10 mm. The CE was placed opposite to the WE and had a larger total surface area than the WE. A gas could be fed into the EC cells through two capillaries, where one was immersed into the electrolyte. Before starting EC experiments, the electrolytes were generally deaerated for 30 min with Ar gas, and an Ar blanket was maintained in the cell during the experiments.

3.3.1 The standard electrochemical cell

For electrochemical measurements at room temperature and in aqueous electrolyte solutions, a custom-made three electrode glass electrochemical (EC) cell (glass blowing workshop J. Höhn, Garching, Germany),

furnished with ground joint fittings for gas-capillaries, CE and WE, and with a fitting for the Luggin-Haber capillary, connecting the RE compartment with the main cell, was employed. Fig. 38 depicts a sketch and a photograph of the used glass EC cell.

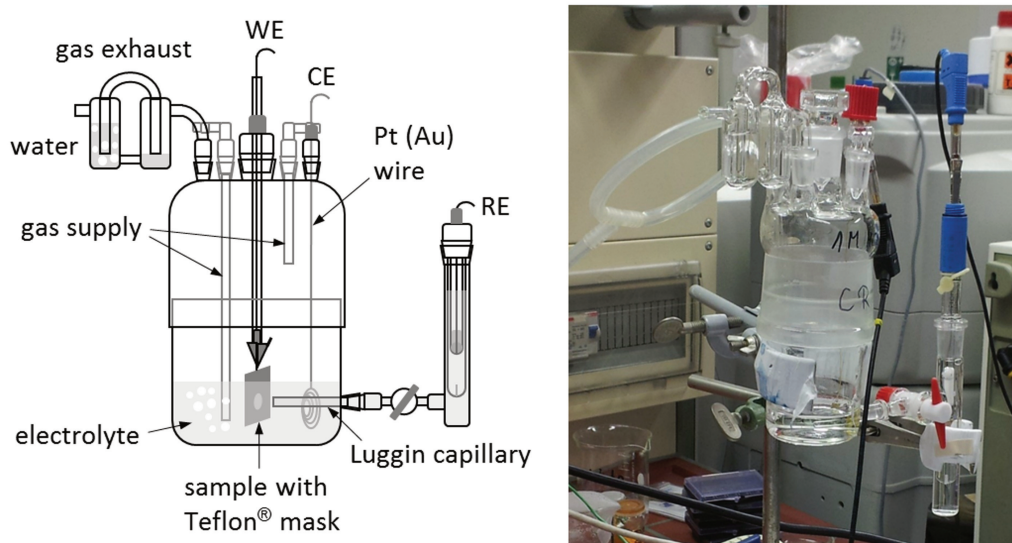


Fig. 38: Left: Sketch of the three electrode glass EC cell; right: photograph of one of the used EC cells.

A gas could be fed into the main cell compartment through two glass capillaries, where one was immersed into the electrolyte solution to saturate it with the gas prior to EC measurements. The second capillary was placed above the electrolyte and was used during EC measurements to saturate the atmosphere of the EC cell without causing vibrations due to gas bubbles in the electrolyte. The exhaust gas was guided through a water filled bubbler, which allowed to monitor the gas flow and ascertain that the cell was air-tight.

The WE was clipped to an alligator clamp, which was soldered to a coated copper wire. The wire was inserted into a glass tube to avoid corrosive attack and the bottom part, where the clamp stuck out of the tube, was wrapped with PTFE thread seal tape (Klingerflon). A Pt or Au wire, wound to a flat coil to enhance the surface area, was used as a CE. Both, WE and CE were inserted in the cell through rubber sealings in the screw caps attached to the respective glass lids. The metal wires outside the cell were used to connect the WE, CE and RE to the potentiostat. Mercury-sulfate or saturated calomel electrodes (SCE) were used as reference electrodes. The former were prepared with a 0.1 M H_2SO_4 solution, and their potential *versus* the standard hydrogen electrode (SHE) was determined by measuring their potential in a beaker with 0.1 M H_2SO_4 solution against the SCE or a saturated silver-silver chloride (Ag/AgCl) electrode using a multimeter. According to literature reports, the potentials of the SCE and the saturated Ag/AgCl electrode are 0.24 V_{SHE} and 0.20 V_{SHE} , respectively.⁶⁵ The potential values of the mercury-sulfate electrodes used throughout this work varied by ~ 0.01 V and will be therefore given when the respective experiments are described. The error in potential is ascribed to variations in the electrolyte concentrations of the reference electrodes. If not stated otherwise, all potentials throughout this thesis are reported versus SHE.

Prior to each electrochemical experiment, all glass components of the EC cell as well as the wire of the CE were cleaned in Caro's acid (i.e a mixture of concentrated H_2SO_4 and H_2O_2 with a molar ratio of 2:1) over night and then first thoroughly rinsed with DI water and after that soaked for two times in fresh boiling DI water. The Pt (Au) wire of the CE was furthermore cleaned by flame annealing using a Bunsen burner.

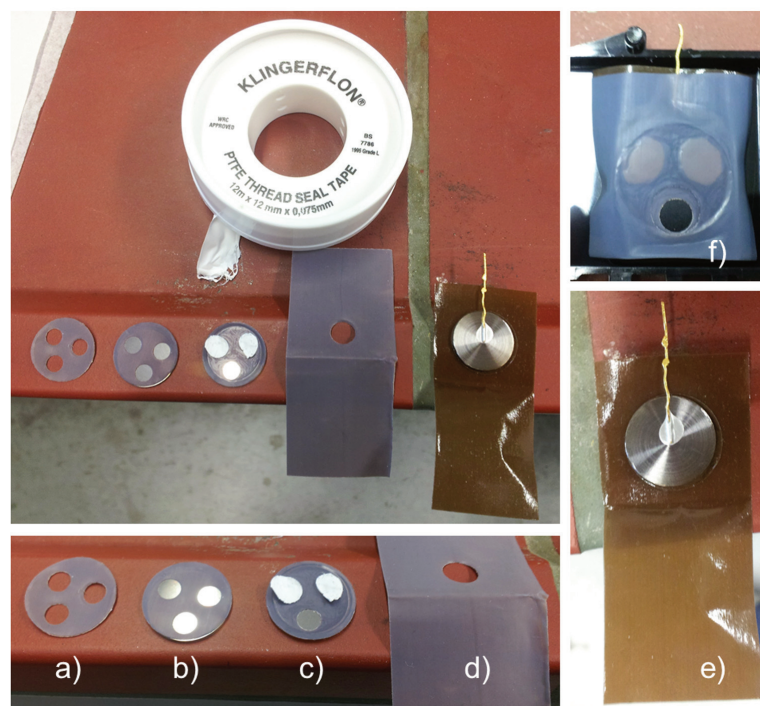


Fig. 39: Preparation of a working electrode for the room temperature EC cell, shown for a 15.5 mm diameter sample. See description in the text.

The WE was contacted from the backside with a Au wire and wrapped into a Teflon[®] coated adhesive tape with a punched hole of 3, 4 or 6 mm diameter on the front side, which was then exposed to the electrolyte. Fig. 39 depicts the preparation steps of the 15 mm large TiOC samples for electrochemical characterizations. To allow for the EC investigation of several zones on the same sample, a Teflon[®] mask was prepared which had the same diameter as the substrate disk and comprised three holes, each having a diameter of 4 mm (Fig. 39a). The mask was gently positioned on the substrate and pressed onto it with the flat tip of plastic tweezers. By sweeping the tweezer tip over the tape, air bubbles could be removed and it was ensured that no electrolyte could creep underneath the mask. After sticking the mask on the electrode (Fig. 39b), two of the holes were covered with punched pieces of PTFE seal tape (Fig. 39c and top) to protect these zones and reserve them for later EC investigations. A larger piece of the Teflon[®] coated adhesive tape was prepared with a hole of 6 mm diameter (Fig. 39d), which was placed on top of the open electrode area thereby covering the two other reserved zones of the electrode to protect them from the electrolyte. A Au wire was attached to the backside of the substrate disk with silver conductive paint (e.g. from Ferro GmbH, Germany, sold by Conrad) (Fig. 39e). When the contact was dry, the entire electrode was wrapped in the Teflon[®] coated adhesive tape, and after sweeping over the tape with the flat tip of plastic tweezers, the edges of the wrapping were cut straight to avoid contact between the glue of the tape and the electrolyte (Fig. 39f). Just before immersion into the electrolyte, the WE was rinsed thoroughly with DI water and dried in an Ar stream.

3.3.2 The elevated temperature electrochemical cell

A cylindrical electrochemical cell made from Teflon[®] was designed in the frame of the Master thesis of F. Wiesinger¹⁹⁴ to perform EOR experiments in concentrated H₃PO₄ supporting electrolyte at temperatures of up to 90 °C without pressurizing the cell. Fig. 40 depicts a schematic drawing of the cell.

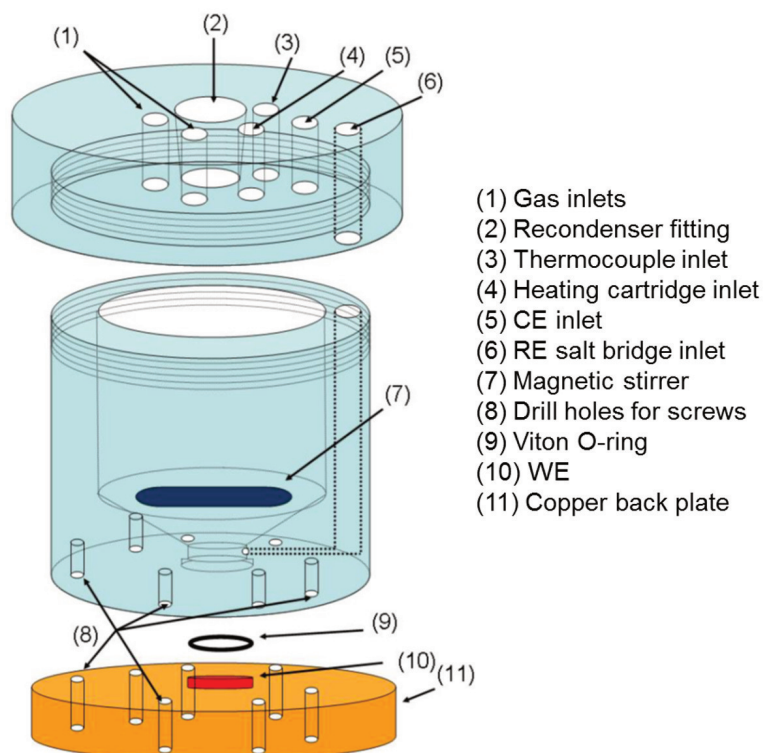


Fig. 40: Teflon[®] electrochemical cell for measurements at elevated temperatures. Adapted from [194] with kind permission of F. Wiesinger.

The electrolyte was heated with a heating cartridge (65 W, Maxi watt, Spain) and its temperature was monitored with a type-K thermocouple that was inserted into a glass capillary and then immersed into the electrolyte. The temperature was controlled with an Eurotherm 2132 temperature controller (Invensys Systems GmbH, Germany). To ensure a homogeneous temperature and ethanol distribution, the electrolyte was stirred with a magnetic stirrer during all measurements. Evaporating electrolyte was recovered by a reflux condenser mounted on top of the cell. The WE was put in contact with the electrolyte through a round hole at the bottom of the Teflon[®] cell. For the electric contact and sealing, a copper plate was screwed to the bottom of the cell, which pressed the WE against an O-ring (Viton[®]) in the hole. A Hg|Hg₂SO₄|0.1 M H₂SO₄ RE with a potential of 0.66 V_{SHE} was used. It was kept at room temperature in an external glass container with 0.1 M H₂SO₄, which was connected to the main cell compartment *via* an electrolyte bridge. The glass capillary of the electrolyte bridge, that was filled with concentrated H₃PO₄, was inserted into a cylindrical channel of the Teflon[®] cell. The potential was measured through a Luggin-Haber capillary at the side of the WE with a vertical distance of 2 mm. A coiled Au wire served as CE.

3.3.3 The potentiostats

Electrochemical measurements were performed with fast rising Autolab potentiostats (Metrohm Autolab B.V., Netherlands) equipped with frequency analyzer modules (FRA2) which allowed to perform electrochemical impedance spectroscopy. A PGSTAT 302N and a PGSTAT 30 instrument were used with the NOVA and with the FRA/GPES data acquisition softwares, respectively. Fig. 41 depicts photographs of both potentiostats. The PGSTAT 302N potentiostat was furthermore equipped with an ultrafast analog-to-digital converter (ADC10M) and with the SCAN250 module. The ADC10M module is an ultrafast sampling module

that increases the sampling rate to 10×10^6 samples per second, providing the possibility to acquire fast transients with intervals of as short as 100 ns. The SCAN250 module has the capability of applying a true analog potential sweep to the WE, instead of a potential staircase, enabling the measurement of capacitive as well as faradaic processes at the same time. The SCAN250 module in combination with ADC10M allows for the measurement of EC processes that exhibit rapid transient behavior such as hydrogen adsorption on Pt, which therefore allows an accurate determination of the ECSA of Pt catalysts.²⁰⁰

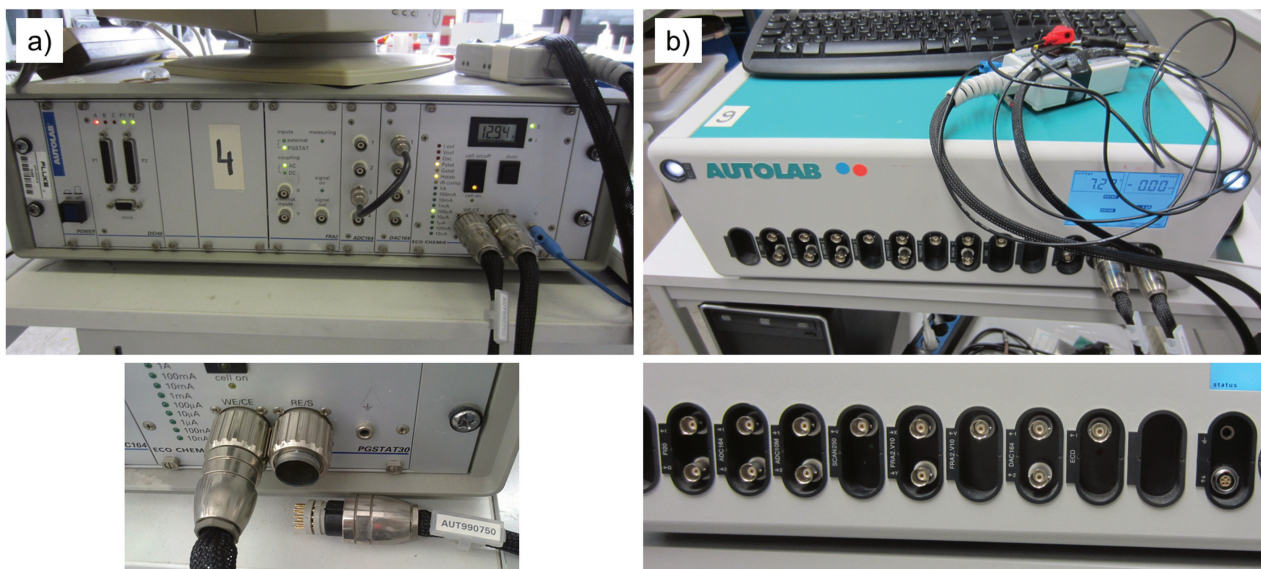


Fig. 41: Photographs of the used Autolab potentiostats. a) PGSTAT 30, b) PGSTAT 302N.

3.3.4 Experimental parameters of the electrochemical measurements

The processes at the electrode/electrolyte interface were studied with cyclic voltammetry, linear sweep voltammetry, chronoamperometry (i.e. current-time profiles at various potential steps) or (potential step) electrochemical impedance spectroscopy. The measured electrochemical impedance spectra were fitted with appropriate electrical equivalent circuit (EEC) models composed of combinations of simple circuit elements, which describe best the physical behavior of the system and provide the lowest χ^2 value. Data analysis was performed with OriginPro,²⁰¹ and the NOVA software²⁰² was used to perform EIS data fitting.

3.3.4.1 Outer sphere electron transfer and HER at TiOC films

The interfacial electron transfer at TiOC electrodes was investigated at room temperature in 0.1 M H_2SO_4 with each 2.5 mM of $\text{K}_4[\text{Fe}(\text{CN})_6] \cdot 3\text{H}_2\text{O}$ and $\text{K}_3[\text{Fe}(\text{CN})_6]$.

For the first parameter study, shown in section 4.2 of Chapter 4, the measurement protocol was:

- (i) Measure open circuit potential (OCP) for 120 s;
- (ii) Acquire 100 CV cycles at a scan rate of 10 mV s^{-1} and with a step size of 5 mV; potential staircase: OCP – 0.2 V – 0.9 V – OCP;
- (iii) Apply the equilibrium potential E_{eq} of the redox reaction, determined from the CVs, for 20 s;

- (iv) Perform EIS at E_{eq} with a superimposed sinusoidal wave of 5 mV amplitude and with frequencies ranging from 100 kHz to 1 mHz, thereby collecting 39 datapoints (equally distributed over the decades).

For the second parameter study and the study on the air aging behavior of TiOC electrodes, shown in sections 4.3 and 4.4 of Chapter 4, the measurement protocol was:

- (i) Measure open circuit potential (OCP) for 120 s;
- (ii) Acquire 20 CV cycles at a scan rate of 50 mV s^{-1} and with a step size of 1 mV; potential staircase: OCP – 0.9 V – 0.2 V – OCP;
- (iii) Acquire 20 CV cycles as above at a scan rate of 10 mV s^{-1} ;
- (iv) *Optional*: Acquire 20 CV cycles as above at a scan rate of 20 mV s^{-1} ;
- (v) *Optional*: Acquire 20 CV cycles as above at a scan rate of 100 mV s^{-1} ;
- (vi) Apply the equilibrium potential E_{eq} of the redox reaction, determined from the CVs, for 300 s;
- (vii) Perform EIS at E_{eq} with a superimposed sinusoidal wave of 5 mV amplitude and with frequencies ranging from 10 kHz to 20 mHz, thereby collecting 6 datapoints per decade.

The HER was studied in the frame of the first parameter study (section 4.2 of Chapter 4) by linear polarization in 0.1 M H_2SO_4 . Negative going linear sweep voltammograms with a scan rate of 10 mV s^{-1} and a step size of 2.44 mV were started at 0.0 V and reversed at cathodic potentials, where the HER current density assumed a value of about -4 mA cm^{-2} .

The EC measurements shown in section 4.2 of Chapter 4, were performed with the PGSTAT 302N potentiostat and with a coiled Pt wire as CE and a $\text{Hg}|\text{Hg}_2\text{SO}_4|0.1 \text{ M H}_2\text{SO}_4$ RE, whose potential was determined to be $0.66 \text{ V}_{\text{SHE}}$. The diameter of the exposed WE area was 6 mm.

The EC measurements presented in sections 4.3 and 4.4 of Chapter 4 were performed with the PGSTAT 30 potentiostat and with a coiled Au wire as CE and a $\text{Hg}|\text{Hg}_2\text{SO}_4|0.1 \text{ M H}_2\text{SO}_4$ RE, whose potential was determined to be $0.67 \text{ V}_{\text{SHE}}$. In the case of the pristine TiOC films, the diameter of the exposed WE area was 4 mm and in the case of the air aged TiOC films it was 3 mm.

3.3.4.2 Polarization resistance of TiOC films

In the frame of the second parameter study (sections 4.3 and 4.4 of Chapter 4) the polarization resistance of TiOC electrodes against passivation/corrosion and their electronic properties at the solid/liquid interface were studied with potential step EIS at room temperature in 1.0 M HClO_4 . A coiled Pt wire served as CE and a SCE ($0.24 \text{ V}_{\text{SHE}}$) as RE. For these EC measurements, the PGSTAT 302N potentiostat was used. The exposed diameters of the WE were 4 mm for the pristine TiOC films and 3 mm for the air aged films. C. Valero-Vidal assisted in the EC measurements and EIS data analysis, for which he helped to develop appropriate EEC models.

Potential step EIS was carried out between -0.16 and 0.94 V with a step size of 0.1 V according to the following measurement protocol:

- (i) Apply the dc potential $E_{\text{step } 1}$, used for the first EIS measurement, and record the current-time profile for at least 15 min with a time resolution of 1 s;
- (ii) Perform EIS at $E_{\text{step } 1}$ with a superimposed sinusoidal wave of 5 mV amplitude and with frequencies ranging from 20 kHz to 10 mHz, thereby collecting 7 datapoints per decade;
- (iii) Apply the dc potential $E_{\text{step } 2}$, used for the second EIS measurement, and record the current-time profile as above;
- (iv) Perform EIS at $E_{\text{step } 2}$ as above;
- (v) continue as above until the final potential step.

3.3.4.3 Electrochemical investigation of the EOR at Pt/TiOC and Pt/GC electrodes

The activity of Pt/TiOC and Pt/GC electrodes towards the EOR was electrochemically investigated in EtOH containing acidic supporting electrolytes at room temperature and at elevated temperatures. The results of the EOR experiments will be presented in Chapter 6. EC measurements were conducted with the PGSTAT 302N potentiostat. A coiled Au wire served as CE and a Hg|Hg₂SO₄|0.1 M H₂SO₄ RE (kept at room temperature) was employed. The EOR experiments at room temperature were performed by J. Brumbarov. The other EC measurements were carried out by F. Wiesinger in the frame of a Master thesis, which was co-supervised by myself.

A standard three electrode glass EC cell with 0.1 M HClO₄ (supporting) electrolyte was used for measurements at room temperature. The ECSA of the supported Pt catalyst was determined at room temperature from the hydrogen ad- and desorption charge in 0.1 M HClO₄. Therefore, 200 CV cycles were acquired between 0.0 and 1.2 V (starting at 0.46 V) at a scan rate of 400 mV s⁻¹ and with potential steps of 4 mV. The hydrogen ad-/desorption charge was evaluated using the 200th CV scan. The Pt ECSA, which was determined for the as-prepared electrodes, was used to convert the measured EOR currents into an effective current density. To test the electrochemical stability of the Pt catalyst, equivalent CVs were acquired between 0.0 and 1.2 V, as well as between 0.0 and 1.35 V, and the ECSA was determined from every 20th CV cycle. For the EOR experiments at room temperature, 30 CV cycles were acquired in 0.1 M HClO₄ supporting electrolyte with 0.5 M EtOH between 0.0 and 1.2 V (starting at 0.06 V) with a scan rate of 10 mV s⁻¹ and potential steps of 1.5 mV.

The EOR experiments at elevated temperatures were conducted in the home-built Teflon[®] EC cell. EC measurements were performed in 14.6 M H₃PO₄ electrolyte with 1.0 M EtOH at 25, 30, 40, 50, 60, 70, 80 and 90 °C.

At each temperature, the following measurement protocol was applied, where the first measurement was conducted at 25 °C:

- (i) Acquire 20 CV cycles (which was found to be sufficient to obtain stable CV curves) at a scan rate of 50 mV s⁻¹ and with a step size of 1.5 mV; potential staircase: 0.1 V – 1.16 V – 0.06 V – 0.1 V;
- (ii) Hold the final potential of 0.1 V for 300 s, to allow for an initial electrode coverage with EtOH adsorbates;⁷⁶

- (iii) Subsequently step the potential to 0.4, 0.5, 0.6, 0.7, 0.8 and 0.9 V, and record the current-time profiles for each 7 min with a time resolution of 0.2 s.

For the cyclic voltammetry measurements, the anodic switching potential was set to below 1.2 V to avoid possible electrooxidation of the carbon support, which becomes more severe at elevated temperatures.¹⁰ The graphs of the EOR CVs were smoothed by a ten-point-average method to reduce the noise generated by the magnetic stirring.

EOR simulation experiments were performed at 50 and 80 °C in the absence of EtOH. At each temperature, 30 CVs were acquired between 0.0 and 1.2 V (starting at 0.06 V) with a scan rate of 10 mV s⁻¹, followed by four current transient measurements at potentials of 0.5, 0.6, 0.7 and 0.8 V.

3.4 Microscopic measurements

3.4.1 The atomic force microscope

For topographic imaging with atomic force microscopy (AFM) a Bruker (previously Veeco) MultiMode 8 scanning probe microscope (SPM) with a NanoScope V controller and the accompanying NanoScope 8 software package was employed. In this instrument, the AFM probe is stationary and the sample is scanned back and forth beneath the probe. Fig. 42 depicts photographs of the SPM with AFM head and some key components of the instrument.

The sample substrate was glued to a round magnetic metal disk with double-sided adhesive tape or silver conductive paint, and magnetically attached to the top of the scanner tube (see Fig. 42). An AS-12 (type E) scanner was used, which allowed to scan an area of 15 × 15 μm². The images consisted of raster-scanned, electronic renderings of the sample surface at a maximum resolution of 5120 × 5120 points per image. AFM was conducted in tapping mode (TM) or in contact mode (CM) using antimony doped silicon (MPP-11120-10, RTESP, BRUKER AFM Probes) or silicon nitride (SNL-10, BRUKER AFM Probes) probes, respectively. Analysis of the AFM micrographs was performed with the WSxM 5.0,²⁰⁴ or with the NanoScope Analysis 1.5 software packages. The images were pre-processed with plane fit and zero-order flattening procedures.

3.4.2 The scanning electron microscope

Scanning electron microscopy (SEM) was carried out to analyze morphological characteristics of the herein prepared films. In the frame of this thesis, two similar Zeiss SEM instruments were used. For the first parameter study, where TiOC films were prepared on square Ti substrates (section 4.2 of Chapter 4), SE micrographs were taken with a Zeiss SUPRA™40 field emission SEM based on the 3rd generation GEMINI® column. The instrument belonged to the *Department of Energy and NEMAS – Center for NanoEngineered Materials and Surfaces, Politecnico di Milano* in Italy, and the measurements were performed by S. Leonardi. The acceleration voltage of the electron beam was 5 kV, the working distance was 3 mm and the SE micrographs were collected with the InLens detector.

All other samples (TiOC films on round Ti substrates, Pt/TiOC and Pt/GC electrodes) were investigated with a field emission SEM based on a GEMINI column in a Zeiss CrossBeam® NVision 40 system. The instrument belonged to the group of A. Holleitner (E24) at the *Center for Nanotechnology and Nanomaterials (ZNN) of the Walter Schottky Institute (WSI) at the Technical University of Munich (TUM)* in Germany, and was available for

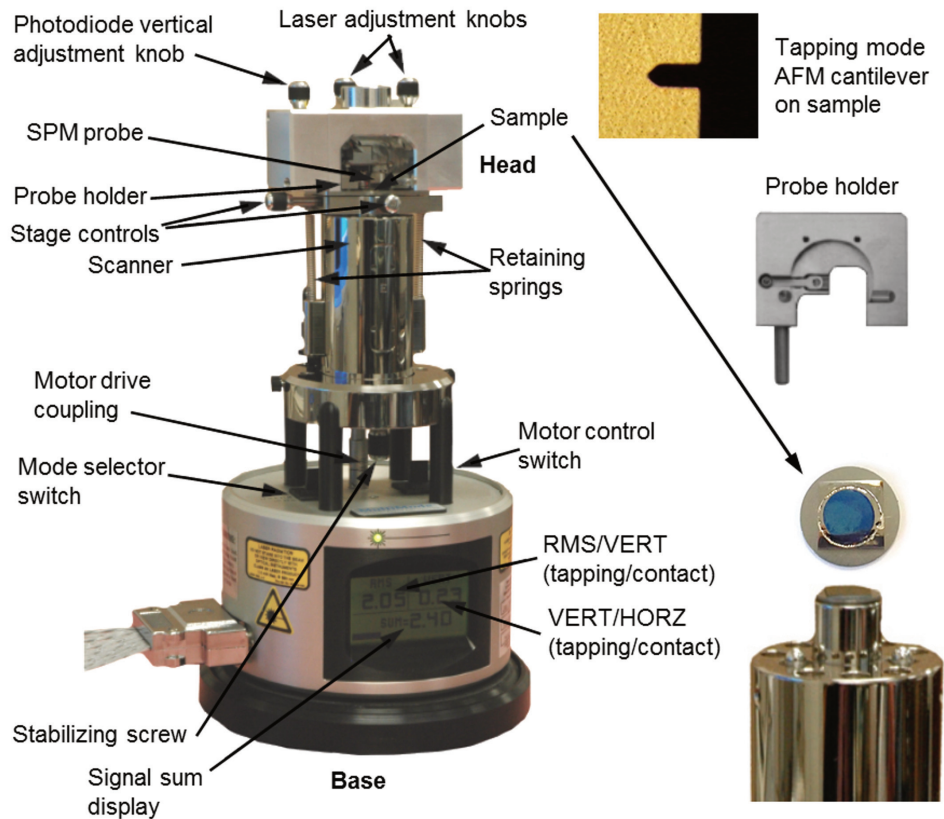


Fig. 42: Photographs of the Bruker (previously Veeco) MultiMode 8 SPM with AFM head, the sample holder on the scanner, a sample attached to the magnetic disk, the AFM probe holder, and the top view of a tapping mode cantilever on top of a sample surface (seen through the optical microscope with camera, which was mounted on top of the AFM head). The pictures of the equipment are taken from [203], with permission of the Bruker Corporation.

external users. SE micrographs were taken with the InLens SE detector, using electron beam acceleration voltages of between 4 and 6 kV and working distances of between 3 and 7 mm. The sample stage of the SEM could accommodate up to 9 samples, which were attached to individual metal disk holders with conductive double sided adhesive carbon tape (Fig. 43).

3.5 X-ray diffraction and electron backscatter diffraction experiments

Structural and compositional information about the reduced titania films was obtained by grazing incidence diffraction (GID) measurements (shown in section 4.2 of Chapter 4). The GID analysis was performed on a Bruker D8 Advance Diffractometer, equipped with a Göbel Mirror as primary optics and a Soller Slit on the detector. The optimal incidence angle was found to be 2° . Diffractograms were acquired between 20° and 60° (2 theta) with a step size of 0.02° and an acquisition time of 60 s per step. The GID measurements were carried out by F. Maglia at the *Department of Chemistry, IENI - Institute for Energetics and Interphases, CNR - National Research Council, Pavia University* in Italy.

Powder diffraction measurements on commercial TiO₂ powders (shown in section 6.4.2 of Chapter 6) were performed by M. Bersani in the *Nanomaterials Engineering Group of the Industrial Engineering Department, University of Padova (UNIPD)* in Italy. A Bruker Advance D8 diffractometer was employed in the Bragg-Brentano (θ - 2θ) configuration and using a Cu K _{α} X-ray source and a monochromator ($\lambda = 1.541874 \text{ \AA}$).

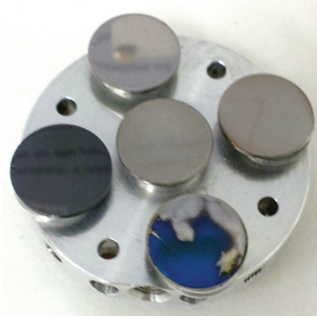


Fig. 43: Photograph of the sample stage of the Zeiss CrossBeam[®] NVision 40 system with five attached samples of each 15.5 mm diameter.

The crystallographic orientation of the electropolished Ti substrates was mapped with EBSD using a FEI XL30 scanning electron microscope operated at a 20 kV accelerating voltage and equipped with a TSL-EDAX EBSD system. The instrument was operated by S. Jacomet in the *Metallurgy, Structure, Rheology (MSR) Team* of N. Bozzolo at the *CEMEF – Centre de Mise en Forme des Matériaux, MINES ParisTech, PSL – Research University* in France. The step size of the EBSD map was set to 2 μm , which led to a suitable spatial resolution of the microstructure. The accuracy of orientations determined by EBSD is typically in the range 0.5°–1° when considered in the acquisition reference frame (which is linked to the microscope). When analyzed in the sample frame, additional uncertainty associated with the positioning of the sample in the SEM chamber has to be taken into account. The actual accuracy of the given angular values can be considered to be in the range of 2°–3°. The acquired EBSD data are shown in Chapter 5.

3.6 Spectroscopic experiments

3.6.1 X-ray photoelectron spectroscopy (XPS)

X-ray photoelectron spectroscopy (XPS) measurements were carried out to analyze the surface chemistry of TiOC films.

3.6.1.1 The electron energy analyzer

Fig. 44 shows a schematic drawing of a typical XPS setup with photon source, sample, electron optics, an energy dispersive analyzer and a detector. Most state of the art XP spectrometers are equipped with a hemispherical electron analyzer. An electrostatic field between hemispherical electrodes forces the entering electrons on spherical trajectories and guides them through the exit slit onto the detector. The analyzer is usually operated in the fixed analyzer transmission (FAT) mode, also known as the constant analyzer energy (CAE) mode to maintain the absolute energy resolution constant over the investigated spectral range. In this mode, a fixed potential is applied across the concentric hemispheres inside the analyzer, and a transfer lens (electron optics in Fig. 44), placed between the sample and the analyzer input slit is used to decelerate or accelerate electrons to a selected pass energy ($PE = E_p$). The analyzer acts as an energy window, accepting only those electrons having a kinetic energy within the range of this window (usually $\pm 0.1E_p$). Scanning for different energies is accomplished by applying a variable electrostatic field to the transfer lens, which retards the given kinetic energy channel to the range accepted by the analyzer. With a fixed PE, the absolute energy resolution of the analyzer remains constant over the whole spectral range. The detector itself is usually a

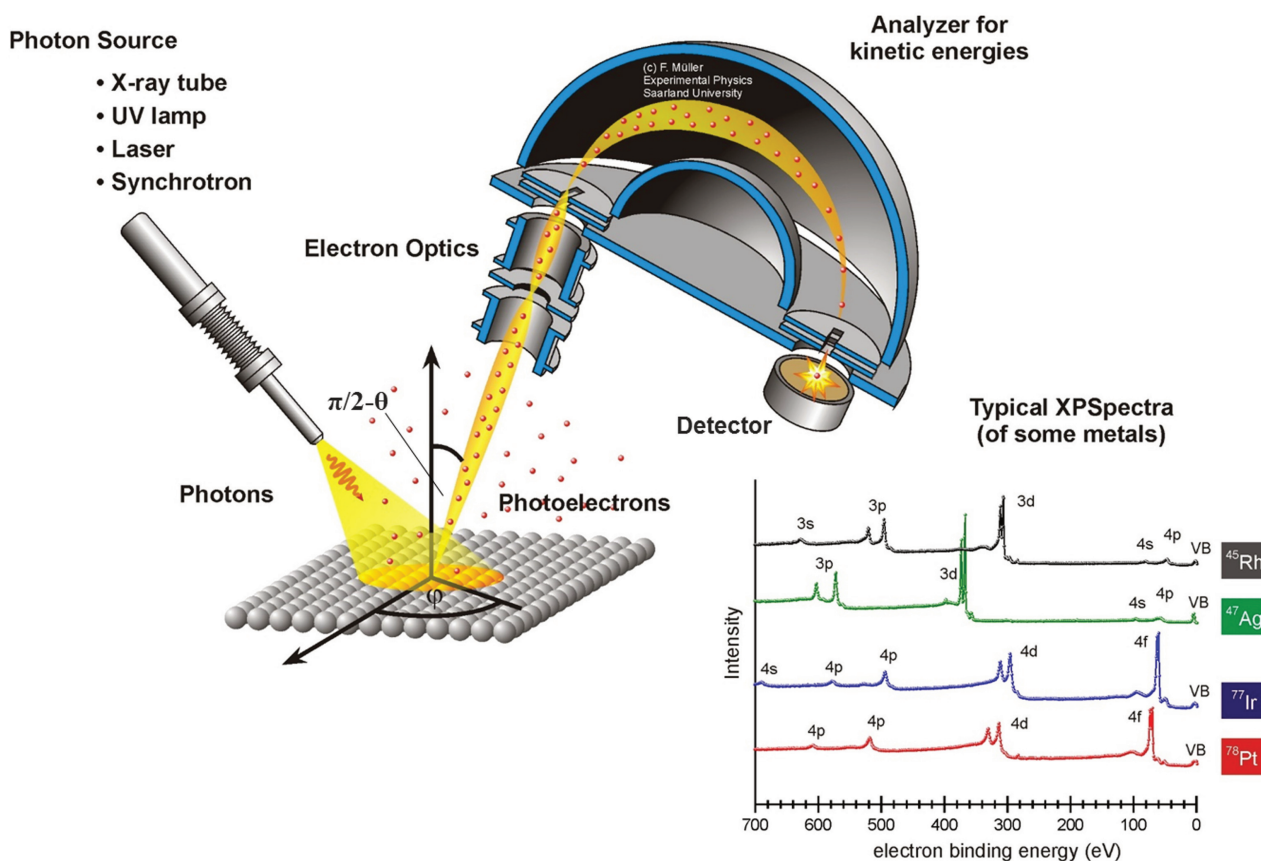


Fig. 44: Schematic drawing of a typical XPS setup with photon source (X-rays, UV-light, laser or Synchrotron radiation), a sample manipulation with different linear and rotational degrees of freedom, electron optics, an energy dispersive analyzer and detector. XP spectra (intensity vs. binding energy) are shown for four different metals with their element specific distribution of core level photoemission. Adapted from [205], with kind permission of F. Müller.

multichannel electron multiplier in the focal plane of the analyzer, which allows simultaneous collection of electrons with a range of energies.

In CAE, the analyzer energy resolution ΔE is determined by the instrumental parameters analyzer radius, entrance slit (aperture) width and pass energy. The absolute resolution can be improved by using a hemispherical analyzer with a larger radius, by decreasing the aperture width, or by decreasing the PE. Calibration of the energy scale, i.e. determination of and correction for the analyzer work function, is usually accomplished by using the Au $f_{7/2}$ peak of a clean Au surface at 84.0 eV (also the Cu $2p$ and $3p$ or the Ag $3d$ lines are suitable references). Adventitious hydrocarbon (CH_x) at 284.8 eV is often used as internal reference for charge correction. If the carbon C $1s$ signal is more complex and itself scope of the analysis, other unambiguous internal standards, such as easily distinguishable peaks of particular oxidation states of the material, can be used.

The noise in an XP spectrum is the consequence of the collection of single electrons as counts randomly spaced in time. The standard deviation for n collected counts is \sqrt{n} , so the signal to noise ratio (SNR) improves through signal averaging by a factor of $n/\sqrt{n} \propto \sqrt{t_{\text{sampling}}}$. Besides an enhanced sampling time per energy interval, the SNR can be improved by averaging several spectra of the same energy range. The latter method is more effective, because it avoids sample damage.

3.6.1.2 The used equipment and experimental parameters

To perform XPS, one needs to operate in *ultra-high vacuum* (UHV, i.e. $< 10^{-8}$ mbar)²⁰⁶ to reduce scattering and loss of the photoelectrons, that are emitted from the surface, with ambient gas molecules. The UHV environment is obtained using high density stainless steel chambers and several pumping stages, including ion and turbomolecular pumps.

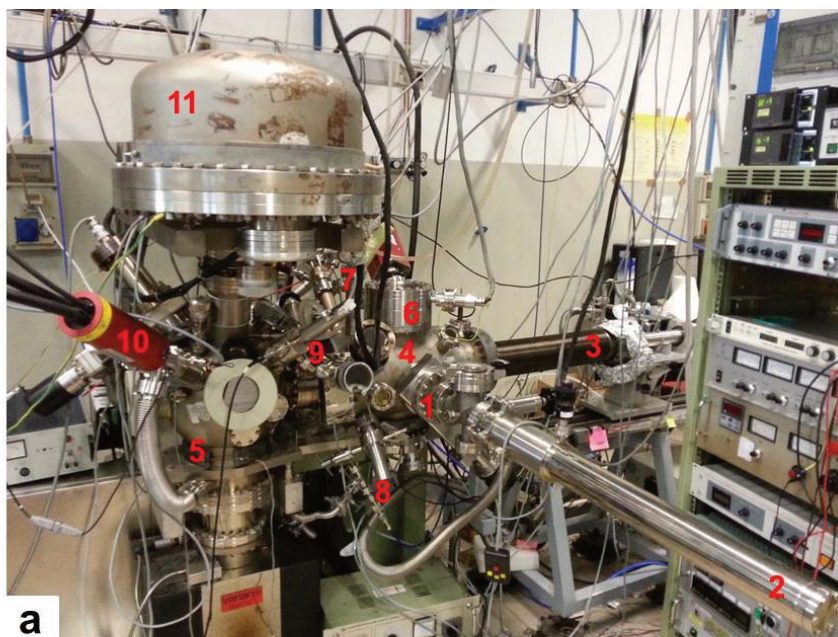
In the frame of this work, XPS was performed within two collaborations. The initially used UHV system belonged to the group of M. Stutzmann (E25) of the *Walter Schottky Institute and Department of Physics* at the *Technical University of Munich (TUM)* in Germany. The analysis chamber of the UHV system was equipped with a Specs Phoibos 100 hemispherical electron energy analyzer and a MCD-5 detector. For the presented data, the take off angle was 90° relative to the sample surface and a non-monochromatized Al K_α X-ray source (1486.6 eV) was used. The pass energy was set to 25 eV for all measurements. Survey spectra were recorded with a step size of 1 eV and a dwell time of 0.5 s. High resolution spectra were recorded for the Ti 2p, C 1s and O 1s regions with a step size of 0.025 eV and a dwell time of 0.5 s. Two scans were taken for each spectrum. The measurements were performed by M. Sachsenhauser under supervision of I. D. Sharp. These XPS data are discussed in section 4.2 of Chapter 4 and in section 6.4.1 of Chapter 6.

The later on used XPS equipment belonged to the *Surface Science and Catalysis Group* of G. Granozzi in the *Department of Chemical Sciences* of the *University of Padova (UNIPD)* in Italy. Their multitechnique UHV chamber was equipped with a 5 degree of freedom (x, y, z, polar angle θ and azimuthal angle φ) manipulator, allowing for angle resolved XPS. A twin anode (Mg/Al) X-ray source (PSP TX 400) provided non-monochromatized Mg K_α ($h\nu = 1253.601$ eV and FWHM = 0.711 eV) or Al K_α ($h\nu = 1486.712$ eV and FWHM = 0.861 eV) radiation. A 5 channeltron VG MK II hemispherical photoelectron analyzer was available for XPS. The angle between X-ray source and analyzer axis was 75° . Fig. 45 shows a photograph of the UHV system and of the manipulator head with sample holder.

Angle resolved XPS was performed at take off angles θ of between 30° and 90° relative to the sample surface. The angular acceptance of the analyzer was about 8° . Under normal emission configuration ($\theta = 90^\circ$, the diameter of the X-ray beams on the sample surface was of the order of mm. Survey spectra were acquired at a pass energy of 50 eV with a step size of 0.25 eV and a dwell time of 0.25 s (2 scans). High resolution spectra of the Ti 2p, C 1s and O 1s (as well as P 2p and Pt 4f) regions were recorded at a pass energy of 20 eV with a step size of 0.1 eV and a dwell time of 0.5 s (6 scans). In the studied BE range (between 0 and 600 eV) the instrumental response function R (see equation 2.115) was approximately constant. The measurements were conducted by myself, M. Favaro or L. Calvillo, assisted by S. Agnoli and supervised by G. Granozzi, and are shown in sections 4.3 and 4.4 of Chapter 4, and in Chapter 6.

Qualitative analysis of the XP spectra was performed using Igor Pro (version 6.37).²⁰⁸ (Quantitative) chemical analysis was carried out based on multi-peak fits of the high resolution core level spectra, performed with the CasaXPS software (version 2.3.14dev38).²⁰⁹ Shirley-type or linear backgrounds were used for baseline correction. Component fits were performed using product Gaussian-Lorentzian line shapes (GL(m) function of CasaXPS, $m = 100$ yields a pure Lorentzian peak shape) to determine the core level peak areas associated with the individual chemical bonds. As shown in Fig. 27, the photoelectron escape depth $d_e = 3\Lambda_e \sin \theta$ is determined by the IMPF of the respective materials and by the electron take off angle (equation 2.118). Values for the IMFP (Λ_e) were calculated using the QUASES-IMFP-TPP2M software.²¹⁰ To determine atomic

1. Load lock
2. Load lock manipulator (2 DOF)
3. Main manipulator (5 DOF)
4. Preparation chamber
5. Analysis chamber
6. LEED (*Omicron SpectraLEED*)
7. Evaporators (*Tetra*)
8. Ion Gun (*Omicron ISE 5*)
9. Helium UV source (*VG MK II*)
10. X ray source (*PSP TX 400*)
11. Photoelectron analyzer (*VG MK II*)



12. Azimuthal angle handling
13. Manipulator (x, y, z and θ DOF)
14. Manipulator head and filament housing
15. Sample holder

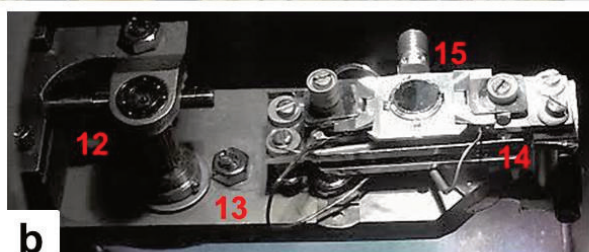


Fig. 45: Photograph of the UHV system of the *Surface Science and Catalysis Group* at UNIPD and of the manipulator head with attached sample. Reprinted from [207] with kind permission of M. Favaro.

sensitivity factors for a given X-ray energy and core level, the differential photoemission cross-section needs to be calculated with equation 2.112, which requires values for the total photoemission cross-section and for the asymmetry parameter. For the present thesis, these values were taken from a table provided on the homepage of the Elettra synchrotron light source in Trieste (Italy).¹⁴⁶

Table 3.5 summarizes some values of d_e determined for graphitic carbon, TiC and TiO₂ for the X-ray sources and spectrometer geometries employed in this work.

Table 3.5: Escape depths determined for graphite, TiC and TiO₂ for three photon energies and two emission angles θ_e . The last X-ray energy was used in the ESCA microscopy beamline at the Elettra synchrotron light source, Trieste (Italy).

X-ray source	$h\nu / \text{eV}$	$\theta_e / ^\circ$	$d_e (\text{sp}^2\text{-C, C } 1s) / \text{\AA}$	$d_e (\text{TiC, Ti } 2p) / \text{\AA}$	$d_e (\text{TiO}_2, \text{Ti } 2p) / \text{\AA}$
Al K _{α}	1486.6	90	98.0	72.5	66.6
		30	49.0	36.3	33.3
Mg K _{α}	1253.6	90	78.2	59.9	54.8
		30	39.1	29.9	27.4
Synchrotron	756	30	23.1	15.4	13.9

Table 3.6 summarizes the values of the total photoemission cross-sections σ and asymmetry parameters β for the Ti 2p and C 1s core level electrons and for the X-ray sources employed in this work.

Table 3.6: Values for σ and β , taken from tables provided on [146] for the Ti 2p and C 1s core level electrons for three photon energies. The last X-ray energy was used in the ESCA microscopy beamline at the Elettra synchrotron light source, Trieste (Italy).

X-ray source	$h\nu / \text{eV}$	$\sigma(\text{C } 1s)$	$\beta(\text{C } 1s)$	$\sigma(\text{Ti } 2p)$	$\beta(\text{Ti } 2p)$
Al K_α	1486.6	0.01366	2	0.1069	1.397
Mg K_α	1253.6	0.02228	2	0.1746	1.436
Synchrotron	756	0.09087	2	0.6873	1.43

3.6.2 Micro-Raman spectroscopy

Micro-Raman spectroscopy was applied to investigate the local crystalline phase composition of the carbothermally treated anodic films. The used Raman spectrometers were equipped with a microscope, and allowed to work in a backscattering geometry, as illustrated in Fig. 46. In the frame of this work, micro-Raman spectroscopy was performed within two collaborations.

For the study presented in section 5.2 of Chapter 5, a Jobin Yvon Horiba HR800 instrument was used, which belonged to the equipment of the *Institute of Mineralogy und Petrography, Leopold-Franzens-University Innsbruck* in Austria, and was operated by C. Hejny. The spectrometer was equipped with a Nd:YAG laser (532 nm) and was used in a non-focal operation mode and without a polarizer to analyze the average chemical composition and structure of the films on top of individual Ti substrate grains. The size of the focused laser spot on the sample was about 5 μm , when the 50 \times magnification of the optical microscope was used. Back-scattered Raman signals were recorded with a resolution of less than 2 cm^{-1} (as determined by measuring the Rayleigh line) in a spectral range from 80 to 2000 cm^{-1} . The laser power and acquisition time were adjusted starting from low values and increasing both until a good signal to noise ratio was achieved while no sample damage occurred. The exposure time for one spectrum was ~ 205 s. To compensate for instrumental drift in wavenumber, the spectrometer was re-calibrated several times during a set of measurements using a clean Si(111) surface.

In the same study, Raman measurements were conducted on two natural anatase TiO_2 crystals (SurfaceNet GmbH, Germany) with polished surfaces oriented parallel to the (001) and to the (100) plane, respectively, so that the incoming laser was perpendicular to one of these planes. For these experiments a filter was employed to reduce the laser intensity by a factor of 0.1; the Raman response was detected in the spectral region from 80 to 800 cm^{-1} using the 100 \times magnification of the microscope and with an acquisition time of 2 \times 1 s. Two spectra were taken of the (100) oriented anatase crystal, where the sample was positioned under the microscope with two azimuthal orientations differing from each other by about 90 $^\circ$.

For the study shown in section 5.3 of Chapter 5, Raman spectra were acquired at the *Chair of Chemical Technology II* of J. A. Lercher in the *Department of Chemistry* of the *Technical University of Munich (TUM)* in Germany. A. Jentys and J. Hein assisted during the measurements that were performed by myself.

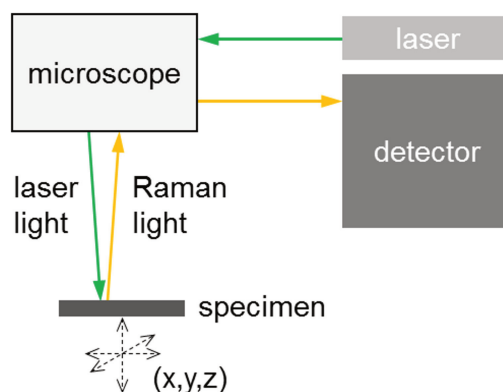


Fig. 46: Scetch of the backscattering geometry of the used Raman equipment.

A dispersive Renishaw Raman Microscope (Type 1000) equipped with a CCD detector, a Leica DM LM microscope, and a multiline argon-ion gas laser (Stellar-Pro Select 150 of MODU-Laser) set at 514 nm was used. The laser was unpolarized, the size of the focused laser spot on the sample was about $5\ \mu\text{m}$ (using the $50\times$ magnification of the optical microscope), and the excitation energy of the laser was set to $\leq 20\ \text{mW}$, which was low enough to avoid chemical modifications or sample damage during the selected exposure times. Backscattered Raman signals were recorded with a resolution of about $1\ \text{cm}^{-1}$ from 2000 to $146\ \text{cm}^{-1}$ (lower wavenumbers were cut off by the notch filter), with an acquisition time of $1 \times 50\ \text{s}$, and from 800 to $146\ \text{cm}^{-1}$, with an acquisition time of $2 \times 100\ \text{s}$. For baseline correction (background fluorescence), a fourth-order polynomial function was subtracted from the raw data of the extended spectra²¹¹ and the small-range spectra were only shifted to a common background level.

3.6.3 Scanning photoelectron microscopy at the Elettra synchrotron light source in Trieste

Scanning photoelectron microscopy (SPEM) was performed at the *ESCA microscopy* beamline of the *Elettra Synchrotron Facility* in Trieste (Italy), which is described in detail on the respective webpage.²¹² The measurements were carried out by M. Favaro, C. Valero-Vidal, L. Calvillo and myself during a beamtime in 2014 and are shown in Chapter 5. Technical support was given by M. Amati and L. Gregoratti. The X-ray photon beam was demagnified by a Zone Plate to a sub-micron spot of about $150\ \text{nm}$ onto the sample surface. The SPEM microscope can operate in two modes: imaging and spectroscopy. In the first mode the sample surface is mapped by synchronized-scanning the sample with respect to the focused photon beam and collecting photoelectrons with a selected kinetic energy.²¹³ The second mode is an XPS from the sub-micron spot. The incident X-ray beam was normal to the sample surface while the angle between the hemispherical electron analyzer (HEA) and the sample surface was 30° , providing high surface sensitivity. The HEA was equipped with a multichannel electron detector which simultaneously acquires 48 maps (channels), each tuned at a specific photoelectron energy within a selected energy window. This allowed the (i) extraction of XP spectra from a selected area of the acquired photoelectron micrograph with an energy window of $7.8\ \text{eV}$ and a step of $0.164\ \text{eV}$ and (ii) removal of the topographic contributions to the photoelectron micrographs and extraction of the chemical contrast. Chemical contrast micrographs (chemical maps) were obtained by selecting two sets of maps from the recorded 48 maps, that were each acquired in different binding energy ranges, integrating them to obtain two effective maps corresponding to the photoelectron signal in the two spectral ranges, and determining their ratio.²¹⁴ The two spectral ranges were selected so that at least one

of them comprised a photoelectron peak, and the second spectral range comprised another photoelectron peak or the background signal.

For the SPEM experiments with TiOC films, the photon energy was set to 756 eV to detect the C 1s and Ti $2p_{3/2}$ core level electrons. Photoelectron maps of $50 \times 50 \mu\text{m}^2$ were recorded by sampling the film surface with a step of 200 nm and a dwell time of 60 ms per pixel. If no reduced titania species were detected in the Ti $2p_{3/2}$ core level spectra, TiO₂/BG chemical maps were generated by dividing the integrated map obtained in the binding energy range 459.85–456 eV by the integrated map obtained in the binding energy range 456–452.15 eV. If reduced titania species were detected, TiC/TiO₂ (i.e. Ti(II)/Ti(IV)) or TiO_x/TiO₂ (i.e. Ti(III)/Ti(IV)) chemical maps were generated by dividing the integrated map obtained in the spectral range 456–452.15 eV by the integrated map obtained in the spectral range 459.85–456 eV. C/BG chemical maps were generated from the C 1s core level spectra by dividing the integrated map obtained in the binding energy range 286.85–283 eV by the integrated map obtained in the binding energy range 283–279.15 eV.

For the elemental analysis of the C/TiO₂ composite films (section 5.2 of Chapter 5), the uncorrected absolute peak area was used as a qualitative measure, which was obtained from integration of the spectra from the SPEM image after subtraction of a constant background.

4. Synthesis and investigation of planar TiOC films

The aim of this thesis was the design of model systems based on carbon containing reduced titania materials (referred to as TiOC) for electrocatalysis studies on thereon deposited electrocatalysts, such as Pt. To allow for systematic electrocatalysis studies on catalyst/TiOC systems and to investigate potential catalyst–support interactions on a microscopic or even atomic scale, e.g. by means of *in situ* scanning probe microscopy, it is necessary to provide sufficiently smooth planar TiOC supports of a defined surface morphology. Therefore, planar and compact anodic TiO₂ films on Ti metal disks were chosen as precursor materials, into which carbon species were introduced by a carbothermal treatment with acetylene. The broad parameter space of this synthesis route was expected to provide a wide variety of TiOC films with different chemical composition, crystallographic structure and surface morphology, which can then be related to the performance of catalyst/TiOC systems for a specific electrochemical reaction. This requires to first gain control of the synthesis procedure and to map the available parameter space. Here, the focus was on the preparation of TiOC supports that contained both TiC and TiO₂ species at the surface. While TiC species are expected to enhance the electrical conductivity of the converted anodic films, TiO₂ at the TiOC support surface is expected to improve the electrochemical stability and may furthermore give rise to interesting catalyst-support interactions or to co-catalytic effects in electrocatalytic reactions.

This chapter shows the results of two detailed parameter studies, in which the influence of the synthesis temperature (T_{anneal}), employed for the carbothermal treatments, on the average physicochemical and electrochemical properties of the carburized anodic films was investigated. The difference between the two studies was the chosen Ti substrate, the used acetylene concentration, as well as the range of annealing temperatures.

In the first section, the used Ti substrate surfaces and the thereon prepared compact anodic films are characterized. The second section comprises the findings of a detailed investigation of TiOC films prepared at annealing temperatures between 750 and 1050 °C. Based on their chemical composition and structure, a thermodynamic model describing the carbothermal conversion process is proposed. In a following study, TiOC films were prepared at annealing temperatures between 550 and 850 °C, and special focus was on their electrochemical stability under anodic polarization in acidic aqueous electrolyte and their intrinsic stability in air. These results will be presented in sections 4.3 and 4.4. First, the effect of the lower annealing temperatures on the surface composition, the conductivity at the solid/liquid interface and the electrochemical stability is analyzed. Second, the effect of air aging on the electrochemical properties is addressed. From both parameter studies, the most promising TiOC model systems for electrocatalysis studies are identified.

4.1 Preparation of compact anodic TiO₂ on smooth titanium surfaces

4.1.1 Preparation of anodic films on square Ti sheets

To obtain planar TiOC films, smooth Ti substrate surfaces had to be prepared, which was accomplished through several mechanical and electrochemical polishing steps, as described in Chapter 3. In the first period of this thesis, Ti sheets were electropolished at ~ -30 °C in five repetitive steps by applying 60 V for each 5 min. As it can be seen in Fig. 47, about 100 μm of material were removed from the surface by the electropolishing procedure, thereby exposing the individual grains of the polycrystalline Ti sheet. For the

square Ti sheet precursor material, the average substrate grain size was determined to be $8.8 \pm 3.8 \mu\text{m}$.

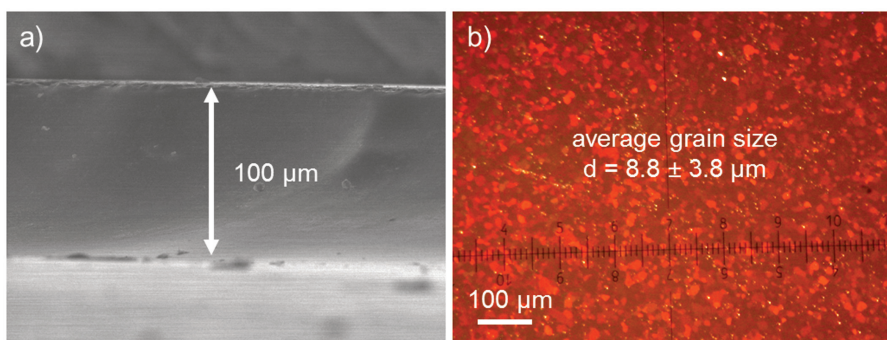


Fig. 47: Square Ti platelet (cut from metal sheet) after electropolishing at -30°C by applying five times 60 V for each 5 min. a) SE micrograph taken at a tilt angle of 2° , b) optical micrograph taken with crossed polarizers.

For a collaboration with the *Surface Science and Catalysis Group* of G. Granozzi at the *Università degli Studi di Padova* in Italy, a set of anodic films with different thicknesses was prepared on square Ti substrates with an edge length of 8 mm. These substrates were electropolished individually each for two times 5 min at 60 V at a temperature of $\sim -30^\circ\text{C}$, thereby exposing a round area of 6 mm diameter. TiO₂ films of 4 mm diameter were prepared on the substrates by anodization for 10 min at 5 V and 10 V, which provided the possibility to perform the anodization with a potentiostat (voltage range: $\pm 10\text{V}$). A modified anodization cell made from Teflon[®] was used, which exhibited a separated cylindrical channel, into which a RE could be inserted. This RE compartment was connected with the main cell compartment by a thin capillary in the Teflon[®] cylinder, positioned few mm above the Ti substrate. For this measurement, a Hg|Hg₂SO₄|0.1 M H₂SO₄ RE was used. Like all other Ti substrates prepared for this thesis, the metal sheets were anodized at room temperature in 0.1 M H₂SO₄. Chronoamperometry with potential steps from 0 to 5 or 10 V was performed with an Autolab PGSTAT 30 instrument. Current transients were acquired with time steps of 0.2 s. Fig. 48 depicts the measured current-time profiles.

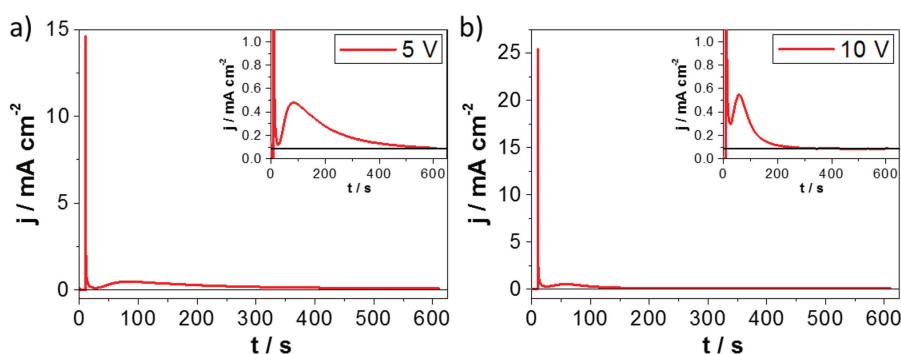


Fig. 48: Current transients during potentiostatic anodization of electropolished Ti substrates at a) 5 V and b) 10 V using a potentiostat. Insets: magnification of the current transients after the initial decrease.

As soon as the potential is stepped to the desired value, very high current densities are measured, which decay rapidly within the first $\sim 16\text{ s}$. The higher the potential step, the higher is the initial current. After the initial decrease, the current density increases again slightly and reaches a maximum at 75 s (inset in Fig. 48a) or at 48 s (inset in Fig. 48b), after which it decreases with a slower rate and reaches $\sim 0.085\text{ mA cm}^{-2}$ after $\sim 600\text{ s}$ (Fig. 48a) or after $\sim 300\text{ s}$ (Fig. 48b).

The high initial current is the typical response to the sudden potential step during potentiostatic anodization.^{54,215} The general evolution of the current density with time reminds to that observed during the anodic growth of self-organized titania nanotubes (TNT) in fluoride-containing aqueous electrolytes. From the current transients recorded during TNT growth, three stages of anodic film growth in presence of fluoride ions were identified.²¹⁶ At the first stage, the anodization process begins and the initially high current quickly decreases to a minimum value due to the formation of a highly resistive barrier oxide layer, which impedes the motion of the ions (O^{2-} , OH^- , Ti^{4+}) that are required for the oxidation process. At the same time, porosity is induced by the presence of F^- . After sufficiently long time (the second stage), pore nucleation progresses and the number of paths in the film that are available for ionic species in the electrolyte, that contribute to the oxide growth, is increasing. This process gives rise to a decreasing resistance of the initially formed barrier layer, and the current rises again (after the initial drop) until it reaches a maximum. During the final stage, the current drops and attains a constant value at long anodization times, which is attributed to the establishment of a steady state, where the rate of oxide formation and the rate of its (electrochemical or chemical) dissolution are equal.

Most of these processes can explain the current-time profiles measured in the present work during anodization in 0.1 M H_2SO_4 (Fig. 48). But since no fluoride ions are present in the electrolyte, the increasing current during the second stage cannot be related to a decreasing oxide film resistance due to F^- induced pore nucleation. However, very similar current transients like those in Fig. 48 were observed by Fahim et al. during the potentiostatic anodization of degreased unpolished titanium sheets in 2.0 M H_2SO_4 at 20 V.²¹⁵ Interestingly, they obtained titania nanotubes (TNT) on some spots of the substrate, which is considered unusual for anodization in H_2SO_4 aqueous solutions without aggressive ions, such as fluorides.²¹⁶ Based on their observations, they explained the current increase during the second stage by localized oxide film break down, induced by the used electrolyte and anodization potential.

During the first seconds of the potentiostatic anodization, not only the anodic oxidation of Ti to TiO_2 , but also the oxygen evolution reaction (OER) contributes to the measured current density, until a sufficiently resistive barrier oxide has formed. The instantaneous onset of the OER and the parallel oxide film growth are evidenced by considerable gas bubble formation on the electrode surface and by a visible color change of the substrate, respectively. The latter is caused by interference effects in the thin transparent TiO_2 film. It should be noted that the initial partial coverage of the surface with oxygen gas bubbles and their removal after some time may provide an alternative explanation for the current increase during the second stage of anodization.

The same anodization experiment shown in Fig. 48 was repeated for each of the two potential steps and yielded very similar current-time transients, evidencing a high reproducibility of the anodization process. For the studies presented in the following, anodic TiO_2 films were prepared by applying 20 V for 10 min using a power supply without measuring the current (see Chapter 3). It can be expected that the initial current densities are even higher under this condition. From a comparison between the insets in Fig. 48a and b it can be inferred that the steady state current is reached at shorter times for higher anodization potentials.

Anodic films prepared at 20 V on square Ti substrates as that shown in Fig. 47 were characterized with optical microscopy, AFM and SEM. The respective images are shown in Fig. 49 and suggest that the thickness, roughness and morphology of the oxide films are strongly affected by the crystallographic orientation of the individual Ti substrate grains. The substrate grain-dependent anodic film thickness is a well-known

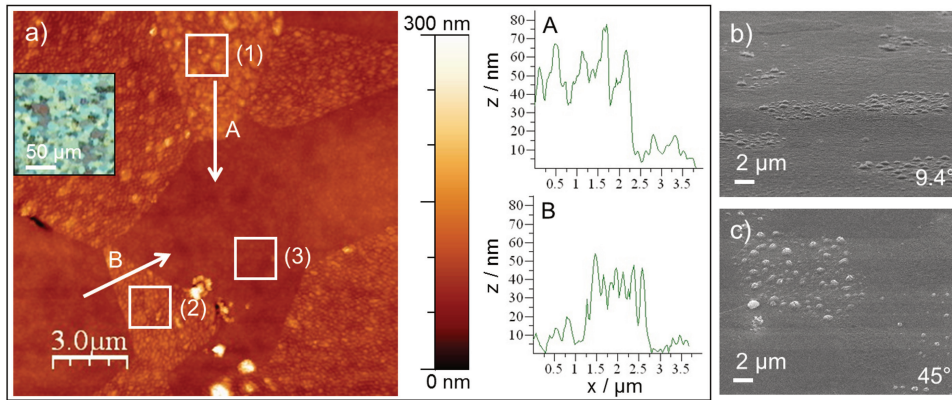


Fig. 49: Oxide film on a square Ti platelet as that shown in Fig. 47, synthesized by anodization at 20 V for 10 min. a) Topographic contrast map acquired with tapping mode AFM, and line profiles A and B. Roughness analysis in the indicated boxes yields the following RMS height values: (1) 20 nm, (2) 15 nm, (3) 6 nm. SE micrograph taken at a tilt angle of b) 9.4°, and c) 45°. The AFM image shown in a) has been published in [217].

phenomenon and is ascribed to the different atomic surface densities on differently tilted Ti grains, which have a great influence on ion transfer reactions and therewith the oxide growth rate.^{58–61} A visible evidence for the substrate grain-dependent film thickness are the substrate grain-dependent interference colors that can be seen in the optical micrograph in Fig. 49a. However, it should be pointed out that the relative height differences between the oxide films on different substrate grains that are observed in the AFM line profiles (Fig. 49a) may not reflect according variations in oxide film thickness. This is related to the fact that also the rate of Ti dissolution during electropolishing is affected by the substrate grain orientations, causing height differences between different substrate grains after long electropolishing times.⁶⁰

The substrate orientation-dependence of the oxide film morphology and roughness was shown to originate from different rates of the OER within TiO₂ films formed on differently oriented Ti grains.^{160–162} Oxygen can be evolved inside the oxide film and form high-pressure gas-filled cavities, which progressively coalesce and lead to a roughening of the film, blistering and eventually rupture when the gas is released. This provides an explanation for the blisters in the film on some substrate grains, as observed with SEM (Fig. 49b). Since the OER rate is known to be considerably higher on the densely packed planes of the Ti substrate (i.e. with orientations similar to Ti(0001)),^{56,57} a notably different roughness can be expected for the anodic film on these grains. In addition, impurities in the substrate may locally enhance the reactivity towards OER inside the growing oxide film,¹⁵⁹ so that the morphology and roughness of the anodic film may vary for Ti substrates of different quality. It should be noted that no nanotubular features are found on the anodic films, so that the current increase during the second stage of anodization (Fig. 48) cannot be ascribed to the growth of titania nanotubes.²¹⁵ However, a possible explanation for the evolution of the anodization current with time could be the rupture of the blisters that are visible in Fig. 49b, and a concomitant local increase of film conductivity. From the depicted AFM image, a roughness factor (RF = topographic/projected area) of 1.040 has been determined.

4.1.2 Preparation of anodic films on round Ti disks

The electropolishing procedure of the round Ti substrates (cut from a metal rod) was optimized for the EBSD studies, which required very smooth and clean surfaces. To track the progress of electropolishing, AFM

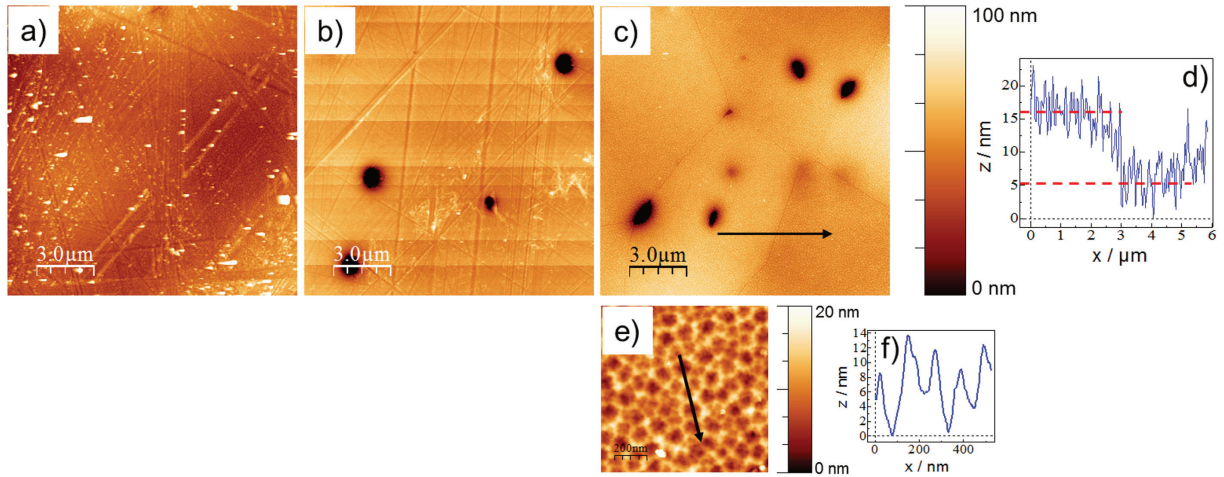


Fig. 50: AFM analysis of a round Ti disk after each electropolishing step. Electropolishing was performed at $-33\text{ }^{\circ}\text{C}$ by repeatedly applying 60 V for 5 min. Topographic images after the a) first, b) second and (c,e) third repetition, and (d,f) height profiles along the respective arrows in c) and e).

was done after each electropolishing step. Fig. 50 depicts AFM images of a Ti disk of 15.5 nm diameter. After the first and second electropolishing step, the scratches of the SiC grinding paper are still visible. The scratches have vanished after the third electropolishing step and the grain boundaries are well exposed. There are some $\sim 100\text{ nm}$ deep holes, which may originate from the mechanical polishing. The section across the grain boundary in Fig. 50c reveals a height difference of $\sim 10\text{ nm}$ between the two grains, which suggests a substrate grain-dependent metal dissolution rate during electropolishing, as mentioned above. From Fig. 50e,f it can be seen that the electropolished surface is characterized by up to $\sim 14\text{ nm}$ deep dimples with a diameter of $\sim 100\text{ nm}$, which reminds of a Ti substrate from which a previously grown layer of titania nanotubes has been removed.²¹⁸ This may be related to the high anodic potentials that are applied during electropolishing and to the used electrolyte, which contains perchloric acid. It was reported that, at sufficiently high anodic voltages, TNT can be grown in perchlorate containing aqueous electrolytes, which

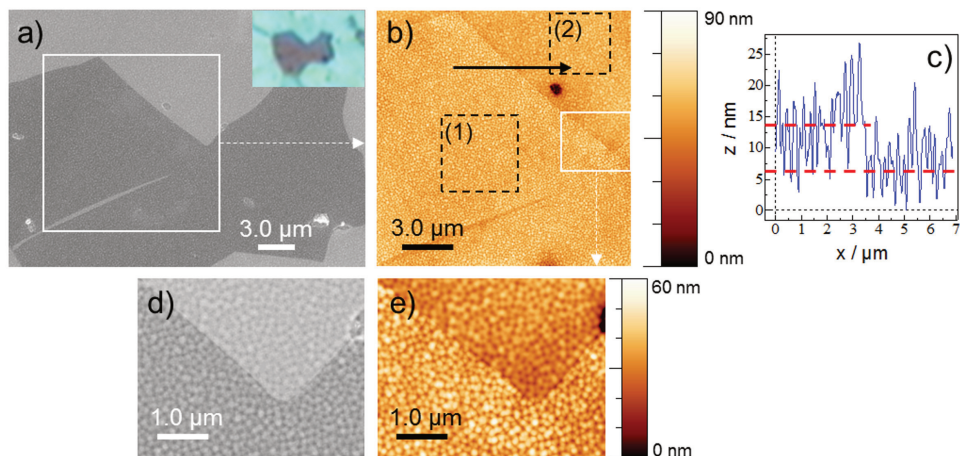


Fig. 51: Morphology and topography of anodic TiO₂ on a round Ti substrate. (a,d) SE micrographs acquired with the inlens detector using an acceleration voltage of 4.0 kV and a working distance of 4.0 mm. Inset in a): optical micrograph of the analyzed film area. (b,e) Topographic images acquired with AFM and c) height profile along the arrow in b). Roughness analysis in the indicated boxes yields the following RMS height and RF values: (1) 5 nm, 1.016; (2) 4 nm, 1.007.

was ascribed to localized anodic breakdown events.²¹⁹ Similar processes may cause the dimples in the electropolished Ti substrates. The area shown in Fig. 50e has an RMS height value of 3 nm and a roughness factor of 1.024.

Anodic oxide films were prepared by anodization at 20 V for 10 min as in the case of the square Ti sheets. Fig. 51 shows SEM and AFM images of an anodic film on selected substrate grains of a round Ti disk similar to that in Fig. 50. From the interference colors of the oxide in the optical micrograph, different film thicknesses and therewith different substrate grain orientations can be inferred. These affect the electron backscattering efficiency and cause the grain-dependent contrast in the depicted SEM images. Both the SEM and the AFM images show that the anodic film follows the topography of the underlying substrate, which is characterized by almost regularly arranged small dimples. Roughness analysis reveals slightly different depths of the dimples in the film on differently oriented substrate grains. Moreover, the line profile across the grain boundary shows an (apparent) height difference of ~ 5 nm between the oxide on the two depicted grains.

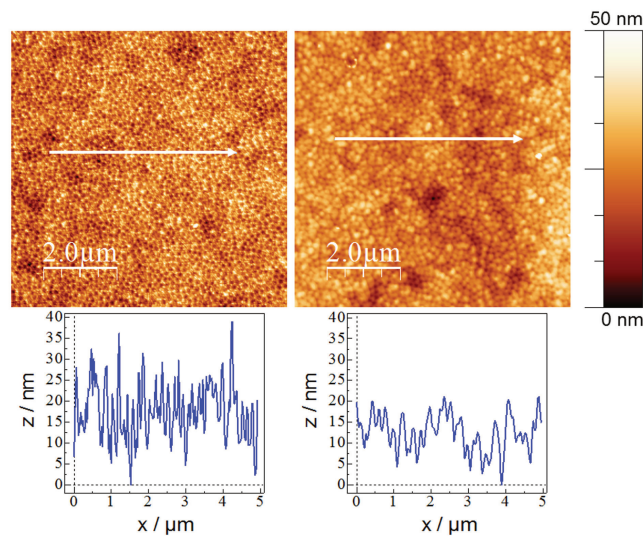


Fig. 52: AFM analysis of a) electropolished Ti substrate, and b) oxide film prepared by anodization at 20 V for 10 min.

Sometimes it was required to electropolish the substrates four times to entirely remove residual scratches from the grinding paper. In Fig. 52, the surface topography of such an electropolished Ti disk is compared with that of the anodic film prepared on the same substrate. The depicted electropolished surface is characterized by an RMS value of 8 nm and a roughness factor of 1.061, and is therewith slightly rougher than the three times electropolished substrate shown in Fig. 50. After anodization, the surface is significantly smoother with an RMS height (roughness) of 5 nm and a roughness factor of 1.007, which are similar to the values of the anodic film on the three times electropolished Ti substrate (Fig. 51).

4.2 TiOC films prepared on square substrates at temperatures between 750 and 1050 °C

This section contains the results that have been published by C. Rüdiger et al. in 2012.²¹⁷ Aim of the study was to understand the carbothermal reduction process and its interdependence with annealing temperature, in particular the effect of the annealing temperature on the films' physicochemical and electrochemical properties. The topography, morphology, chemical composition and crystallographic structure of the TiOC

films were studied with AFM, SEM, XPS and GID (see Chapter 3 for experimental details). A thermodynamic model is proposed based on these investigations for the carbothermal conversion mechanism of compact anodic titania films, showing that the film thickness and the carbon content in the carburized film decrease with increasing annealing temperature due to thermally activated diffusion. The electrochemical activity of TiOC towards outer sphere charge transfer was investigated using electrochemical impedance spectroscopy (EIS), which revealed an increase in charge transfer resistance with increasing annealing temperature. First studies of the hydrogen evolution reaction (HER) on TiOC indicate that the electrocatalytic properties directly depend on the chemical, structural and electronic properties of the surface since the overpotential of the HER shifts to higher values for increasing annealing temperature.

4.2.1 Preparation of the first TiOC series

TiOC films were prepared *via* carbothermal treatments at 750, 850, 950 and 1050 °C. The following procedure was applied:

- (i) purging for two hours with 750 sccm Ar to remove air,
- (ii) heating to the desired annealing temperature T during 90 min at a constant rate in 200 sccm Ar,
- (iii) dwelling for 60 min at T ,
- (iv) addition of 0.1 flow% (i.e. 0.2 sccm) of acetylene for 5 min,
- (v) dwelling for 60 min at T in Ar, and
- (vi) switching off the oven to let it cool down to room temperature.

A TiC-rich reference film was prepared following the protocol:

- (i) purging for two hours with 750 sccm Ar to remove air,
- (ii) heating to 850 °C during 60 min at a constant rate in 198 sccm Ar,
- (iii) dwelling for 29 min at T ,
- (iv) addition of 1.0 flow% (i.e. 2.0 sccm) of acetylene for 3 min,
- (v) dwelling for 29 min at T in Ar, and
- (vi) switching off the oven to let it cool down to room temperature.

4.2.2 TiOC surface topography and morphology

Fig. 53 shows topographic images and height profiles of TiOC₇₅₀, TiOC₈₅₀ and TiOC₁₀₅₀ obtained with AFM. It can be clearly seen that the annealing temperature as well as the Ti substrate grains affect the surface topography. In Fig. 53a and b areas of different topography and roughness are observed which are framed by pronounced ridges or step edges that can be related to the Ti substrate grain boundaries. The grain areas are larger and the grain boundaries are more emphasized compared to the as-grown anodic TiO₂ (Fig. 49). This can be ascribed to substrate grain growth and to the chemical and structural transformations of the

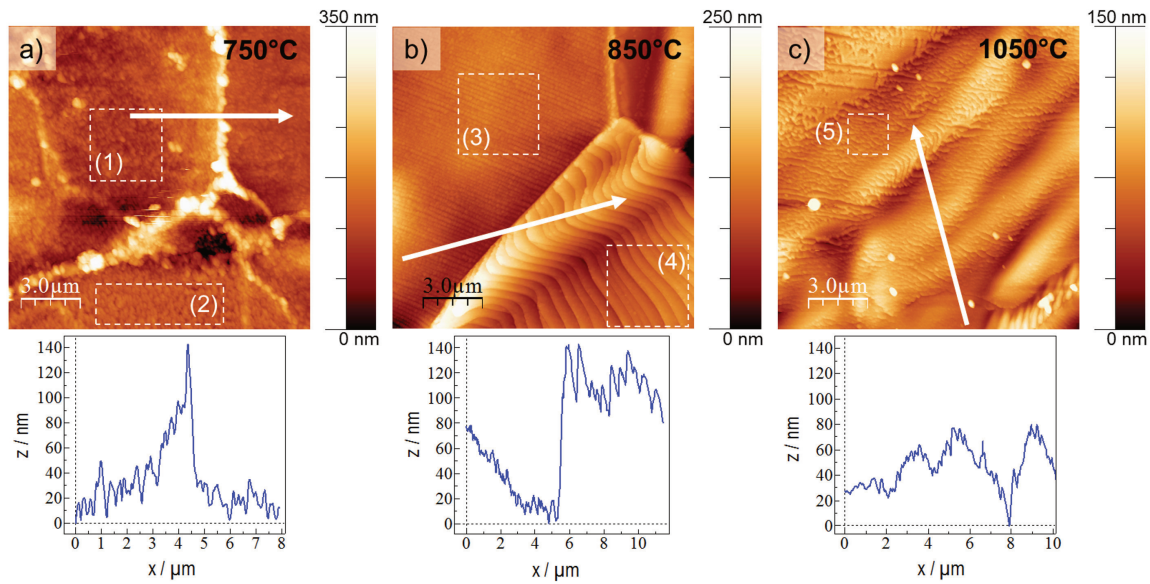


Fig. 53: AFM analysis of TiOC films on square substrates prepared at a) 750, b) 850 and c) 1050 °C. Top: height contrast images, bottom: height profiles along the arrows. Roughness analysis in the indicated boxes yields the following RMS height and RF values: (1) 14 nm, 1.024; (2) 11 nm, 1.025; (3) 8 nm, 1.011; (4) 14 nm, 1.012; (5) 6 nm, 1.012. The AFM image shown in b) has been published in [217].

oxide film that are accompanied by internal strains. After annealing at very high temperatures, no clear grain boundaries attributable to the substrate are visible (Fig. 53c). The RMS height values of the TiOC films on top of different substrate grains, determined from the AFM images, are between 6 nm and 14 nm and therewith comparable with the RMS height values determined for the as-grown anodic TiO₂ (Fig. 49). A pronounced change of the surface topography of the anodic film is observed after annealing at 850 °C, where faceted ordered structures of different frequency have formed.

SEM allowed to study variations of the surface morphology on a larger scale and revealed grain growth and the formation of ordered morphological structures with increasing annealing temperature. From the low magnification SE micrographs in Fig. 54 one can deduce that the average grain size is increasing with increasing T_{anneal} . At this low magnification, almost no difference in morphology is visible when comparing TiOC₇₅₀ and TiOC₈₅₀. Both films have clearly defined grain boundaries with grain sizes in the range of several ten to hundred μm. The most obvious change occurs when the annealing temperature is raised to 950 °C. Anodic films carburized at the two highest annealing temperatures are characterized by large areas with differing morphologies, and the initial substrate grain boundaries cannot be identified anymore due to intensive substrate grain growth.^{150,152} From the SE micrographs in Fig. 54 that were acquired at higher resolutions, one can see that the TiOC₇₅₀ film is characterized by rough grains with frayed boundaries and several bright blister-like spots distributed over the surface. No ordered morphological structures can be observed. In contrast, TiOC₈₅₀ has a much more regular and structured surface morphology. Clearly defined areas of differently oriented ordered lamella have formed, where the lamella orientation depends on the grain orientation. On some areas, interlaced terraces are visible, which indicate the onset of ordering. With increasing T_{anneal} , further homogenization of the surface morphology is observed. Films carburized at 950 and 1050 °C show wavy surface morphologies on large areas. In accordance with the AFM roughness analysis (Fig. 53), the SE micrographs suggest a smoothening of the surface with increasing annealing temperature.

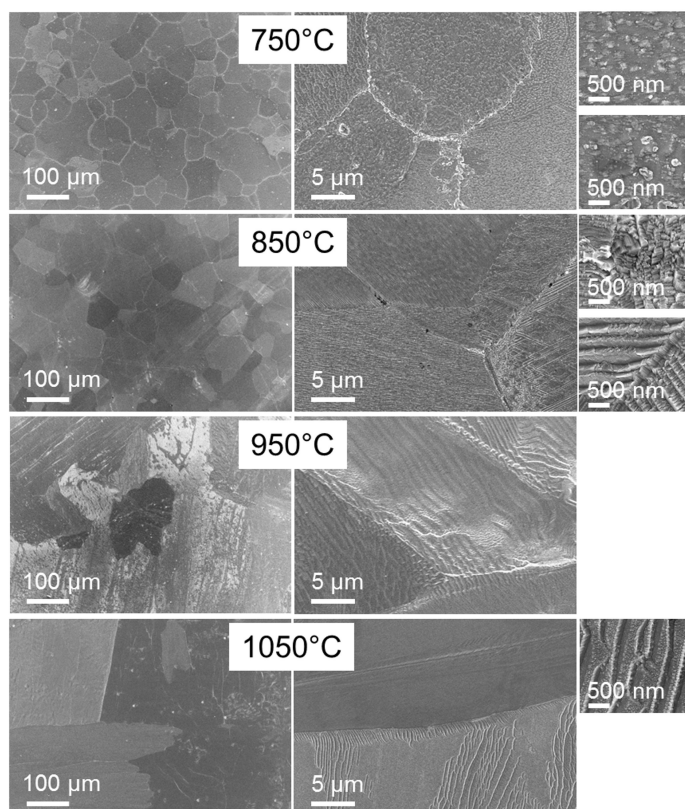


Fig. 54: SE micrographs of TiOC films on square substrates prepared at different annealing temperatures. High magnification micrographs of different film areas are shown for TiOC₇₅₀, TiOC₈₅₀, and TiOC₁₀₅₀. Similar SE micrographs have been published in [217].

4.2.3 TiOC surface composition and structure

4.2.3.1 XPS analysis

The chemical surface composition of the carbothermally reduced titania films was analyzed with XPS. An as-grown anodic oxide film served as a reference for the composition prior to the carbothermal treatments. An anodic film that was carburized with 1.0 flow% acetylene for 3 min at 850 °C served as a reference for a highly reduced TiC-rich film.

Fig. 55 depicts the high resolution spectra of the Ti 2*p*, O 1*s* and C 1*s* regions with multi-peak fits for the four samples annealed with 0.1 flow% acetylene at different temperatures, along with the spectra obtained for the two reference films. For this thesis, the XPS data analysis was harmonized with the measurements and analyses that were performed later in the *Surface Science and Catalysis Group* of G. Granozzi at the *Università degli Studi di Padova* (UNIPD) in Italy. Therefore, the results shown here vary slightly from those published in [217], but lead to the same conclusions. To correct for sample charging effects due to a considerable fraction of poorly conducting oxide on the surface of the as-grown anodic TiO₂ film and the TiOC films that were synthesized with 0.1 flow% C₂H₂ at different temperatures, the Ti 2*p*_{3/2} peak of the Ti(IV) component was shifted to a binding energy (BE) of 459.0 eV. For the highly reduced TiC-rich film, the XP peak of carbidic carbon (C-Ti) at a BE of 282.0 eV in the C 1*s* spectrum was used as internal reference to calibrate the BE scale. Table 4.1 lists the BE and full width at half maximum (FWHM) values used for the fits, and the associated chemical compounds or functional groups.

As can be deduced from the Ti 2*p* and O 1*s* spectra, the as-grown anodic film predominantly consists of fully

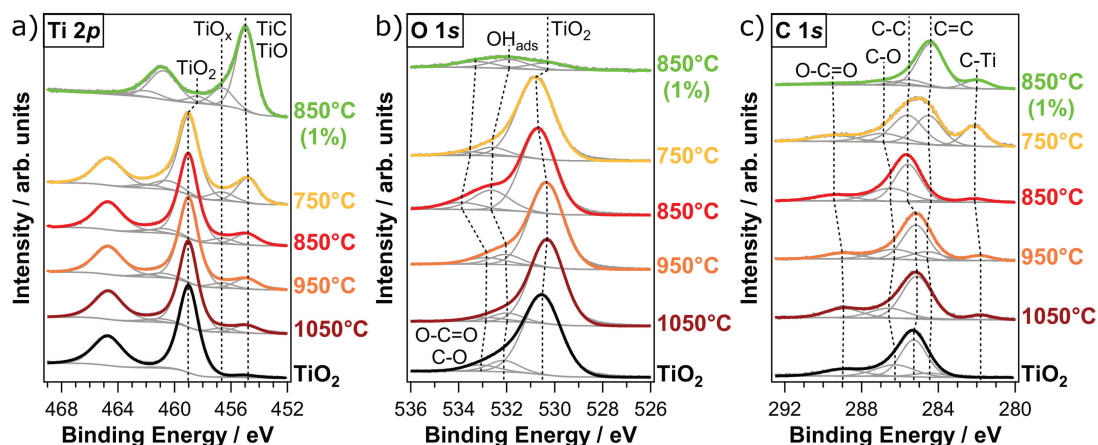


Fig. 55: XPS spectra of TiOC films on square substrates prepared at different annealing temperatures. Reference spectra: as-grown anodic TiO_2 (black) and a TiC-rich film, that was prepared at 850°C with a ten times higher flow fraction of C_2H_2 (green). High resolution spectra of the a) Ti $2p$, b) O $1s$ and c) C $1s$ core level regions with multi-peak fits. The spectra in a) and b) are scaled to a common Ti $2p_{3/2}$ peak height of the TiO_2 component; the spectra in c) are scaled to a common height of the peak maximum, which originates from sp^2 (C=C) and/or sp^3 (C-C) carbon. For clarity, the spectra are shifted vertically. X-ray source: Al K_{α} , normal emission. a) and c): re-analyzed spectra that have been published in [217].

oxidized TiO_2 , and all carburized films contain a considerable fraction of Ti(II) and Ti(III) species at the surface, which can be ascribed to TiC and/or TiO, and TiO_x suboxides, respectively. The low BE peak in the C $1s$ spectra confirms the presence of TiC. Furthermore, there are graphite-like carbon (GLC), diamond-like carbon (DLC), adsorbed carbon-oxygen species and adsorbed OH on the surface. The carbothermal treatment with 1.0 flow% acetylene at 850°C yields a significantly higher content of Ti(II) and TiO_x at the film surface than the carbothermal treatment with 0.1 flow% acetylene at the same temperature. The low signal intensity at BEs related to Ti-O bonds in the O $1s$ region, relative to the signal intensity associated with adsorbed OH, suggests that the Ti(II) component is mainly due to TiC species. From the C $1s$ spectra it can be seen that the higher acetylene concentration gives rise to an enhanced fraction of excess carbon (GLC and DLC) on the surface relative to TiC. The comparison of the Ti $2p$ spectra of the TiOC films that were synthesised with 0.1 flow% acetylene at different temperatures shows that the TiC (TiO) component decreases with increasing annealing temperature.

Evaluation of the multi-peak fitting procedure The Ti $2p$ spectrum of TiO_2 consists of a spin-orbit doublet, Ti $2p_{3/2}$ and Ti $2p_{1/2}$. For the least-squares multi-peak fits of the Ti $2p$ spectral range, it was taken into account that the respective degeneracy of the two $2p$ levels causes the area of the $2p_{1/2}$ to be half the area of the $2p_{3/2}$. Ti compounds are usually mixed valent systems with unpaired $3d$ electrons giving rise to multiplet (final state) effects. As a consequence, the $2p_{1/2}$ is considerably broader than that of the $2p_{3/2}$ peak.²²⁰ Pure TiC and TiO both correspond to an oxidation state of Ti(II), but their different chemical environment causes the chemical shift of TiC, relative to metallic Ti, to be ~ 0.3 eV higher than that of TiO.²²¹ Since this difference in BE is lower than the experimental energy resolution, which was limited by the 0.8 eV linewidth of the Al K_{α} X-ray source, only one doublet was used to fit the spectral component associated with Ti(II) species. Titanium suboxides, in particular TiO, were reported to give rise to a chemical shift of the O $1s$ singlet associated with Ti-O bonds to a higher BE relative to the O $1s$ peak of oxygen in TiO_2 (see table 4.1). For the herein

investigated films, the O 1s core level spectra could be satisfactorily reproduced without using an additional singlet peak for Ti-O bonds in titanium monoxide, which indicates that no extended TiO phase has formed. Differently from the XPS fits in [217], here the two most common hybridization states of carbon in chemical compounds, namely the sp^2 and sp^3 -hybridization, were taken into account to fit the C 1s spectra, as was done in following studies.

The line shape, spin-orbit splitting and the respective FWHM values of the Ti(IV) (i.e. TiO_2) spin-orbit doublet were determined from the fit of the Ti 2p spectrum of the as-grown anodic film. Both the Ti $2p_{3/2}$ and Ti $2p_{1/2}$ core level peaks of the anodic film could be best fit with the GL(69) line shape available in the CasaXPS software, and had a peak separation of 5.7 eV, which is in line with literature reports.²²² The FWHM values of the fitted TiO_2 spin-orbit doublet were 1.67 eV for the Ti $2p_{3/2}$ peak and 2.45 eV for the Ti $2p_{1/2}$ peak. Typical values for the experimental FWHM are ~ 1 –1.6 eV for the $2p_{3/2}$ peak and ~ 2 –2.3 eV for the $2p_{1/2}$ peak of TiO_2 ,^{222,223} which are comparable to the values obtained here. Based on these results, the FWHM values of the Ti(IV) doublet were restricted to 1.6 ± 0.1 eV and 2.4 ± 0.1 eV, respectively, to fit the Ti 2p spectra of the carburized films.

The fit parameters for the Ti(II) doublet were determined from the Ti 2p spectrum of the highly reduced reference film. A satisfactory fit was obtained by using GL(30) line shapes, which yielded FWHM values of 1.61 eV for the Ti $2p_{3/2}$ peak and 2.31 eV for the Ti $2p_{1/2}$ peak. These FWHM values are similar to those obtained for TiO_2 , as it was reported by Pouilleau et al.²²³ However, the Ti 2p spectra of the other films could only be fit by allowing for FWHM values of up to 2.0 eV for the Ti $2p_{3/2}$ peak of the Ti(II) state. This may be an indication of $TiO_{1-x}C_x$ ($0 \leq x \leq 1$) patches or defects present within a matrix of TiO_2 . In accordance with literature reports,²²² the spin-orbit splitting of the Ti(II) doublet was 5.8 eV in the case of the TiC-rich reference film. This value was allowed to vary between 5.7 and 6.1 eV to fit the Ti 2p spectra of the other films. Since none of the reduced films showed an individual Ti(III) doublet, no reference for a determination of its FWHM values was available. The best fit results for the Ti 2p spectra of the carburized films were obtained by restricting the corresponding FWHM to ~ 1.8 –2.0 eV for the $2p_{3/2}$ peak and to ~ 2.1 –2.5 eV for the $2p_{1/2}$ peak. The Ti 2p spectrum of the as-grown anodic TiO_2 film could be fit without a Ti(III) doublet. From the relatively intense Ti(III) doublet present in the Ti 2p spectrum of the highly reduced reference film (green spectrum in Fig. 55a), the line shape could be determined to be GL(30) as in the case of the Ti(II) doublet, and a spin-orbit splitting of 5.4 eV was extracted, which is supported by the results of other research groups,²²² and which proved to be a suitable value to fit this doublet in the Ti 2p spectra of all TiOC films.

As proposed by Biesinger et al.,²²² the multi-peak fits of the C 1s and O 1s spectra were performed using GL(30) line shapes. XP peaks in the C 1s spectrum that are associated with (hydrogenated) graphite-like carbon or diamond-like carbon species are reported to have a FWHM in the range of 1.0–2.2 eV.^{224–228} Higher FWHM values are attributed to structural defects or disorder, indicating an amorphous nature of the respective carbon phase.^{224,225} The relatively large linewidths of up to 2.5 eV required to fit the XP peaks associated with carbon-oxygen groups suggests that different chemical compounds with similar functional groups are present on the surface. Since those species are detected prior to and after the carbothermal treatment, they can be mainly ascribed to organic carbon contamination adsorbed on the films during their exposure to air.

Table 4.1: Chemical compounds with the respective XP binding energies (BE) and full width at half maximum (FWHM) values obtained from multi-peak fits of the Ti 2*p*, O 1*s* and C 1*s* core level spectra (Fig. 55) and BE values reported in the literature.

core level	chemical compound	BE (fit) [eV]	FWHM (fit) [eV]	BE (literature) [eV]
Ti 2 <i>p</i> _{3/2}	Ti(IV), TiO ₂	458.4, 459.0	1.5–1.7	458.4–459.2 ^{221–223,229–233}
Ti 2 <i>p</i> _{1/2}		BE(Ti 2 <i>p</i> _{3/2}) + (5.69 ± 0.03)	2.3–2.5	BE(Ti 2 <i>p</i> _{3/2}) + (5.66 ± 0.08), ²²² BE(Ti 2 <i>p</i> _{3/2}) + 5.8, ²²⁹ BE(Ti 2 <i>p</i> _{3/2}) + 6.0 ²³⁰
Ti 2 <i>p</i> _{3/2}	Ti(III), TiO _x	456.6	1.8–2.0	456.6–457.6 ^{222,230–234}
Ti 2 <i>p</i> _{1/2}		BE(Ti 2 <i>p</i> _{3/2}) + (5.36 ± 0.05)	2.1–2.5	BE(Ti 2 <i>p</i> _{3/2}) + (5.60 ± 0.36), ²²² BE(Ti 2 <i>p</i> _{3/2}) + 5.0 ²³⁰
Ti 2 <i>p</i> _{3/2}	Ti(II), TiC or TiO	454.8–455.1	1.6–2.0	454.4–455.8 ^{221,222,230,232–239}
Ti 2 <i>p</i> _{1/2}		BE(Ti 2 <i>p</i> _{3/2}) + (5.93 ± 0.16)	2.2–2.5	BE(Ti 2 <i>p</i> _{3/2}) + (5.73 ± 0.15), ²²² BE(Ti 2 <i>p</i> _{3/2}) + 5.5 ²³⁰
O 1 <i>s</i>	O–C=O (carbonates), C=O, C–O–C, C–OH groups	532.8–533.9	1.7–2.0	532.8–534.9 ²⁴⁰
	OH _{ads} at TiO ₂	531.9–532.6	1.5–1.8	531.9–532.9 ^{223,231}
	TiO _{0.9}	none	none	531.8 ²³⁴
	TiO	none	none	531.6 ²³⁷
	TiO _{1<x<2}	none	none	531.3–531.5 ^{230,234}
	TiO ₂	530.3–530.8	1.6–1.9	530.0–530.8 ^{223,231,233,234,241}
C 1 <i>s</i>	O=C–O (carbonates)	289.0–289.5	2.2–2.5	288.8–289.5 ^{222,240}
	C–OH, C–O–C, C=O groups	286.3–286.9	2.3–2.5	286.2–288.2 ^{222,240}
	C–C, <i>sp</i> ³ or diamond-like C	285.1–285.6	1.6–1.9	285.0–285.6 ^{224,226–228,242}
	C=C, <i>sp</i> ² or graphite-like C	284.4–284.6	1.6–1.9	284.2–284.6 ^{224–228,238,243}
	C–Ti, titanium carbide	281.8–282.1	1.4–1.7	281.6–282.4 ^{235,236,239}

The singlet signal of TiO_2 in the O 1s core level spectrum was reported to have a FWHM of 1.5–2 eV,^{223,237} and the singlet assigned to adsorbed OH on titania a FWHM of 2.3 eV. Similar values were found suitable for the three singlet peaks that were used to fit the O 1s spectra of the as-grown anodic film and the carburized films in the present work.

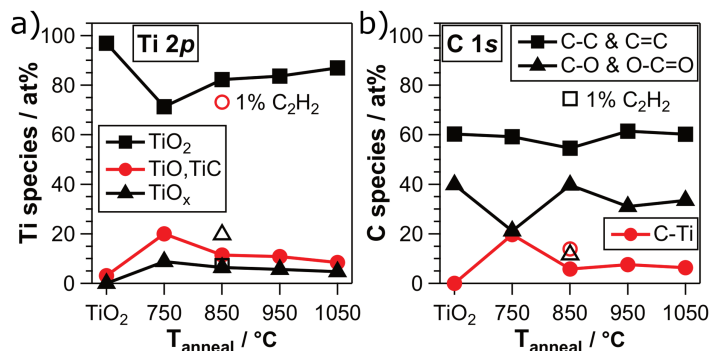


Fig. 56: Fractions of photoelectrons from a) TiO_2 , TiO_x and TiC (TiO) species in the $\text{Ti } 2p$ spectral range and of those from b) carbidic carbon (C-Ti), carbon-carbon bonds (C=C , C-C) and carbon-oxygen groups (C-O , O-C=O) in the $\text{C } 1s$ spectral range. Solid symbols: as-grown anodic TiO_2 and TiOC films prepared at different annealing temperatures with 0.1 flow% acetylene; open symbols: reference film, prepared at 850 °C with 1.0 flow% acetylene.

The results from XPS data fitting were used to extract quantitative information on the chemical composition of the film surfaces. The film composition was evaluated in terms of the fractions of titanium species in the $\text{Ti } 2p$ peak and those of carbon species in the $\text{C } 1s$ peak, respectively. Fig. 56 depicts the fractions of Ti and C species in the two reference films and in the TiOC films as a function of annealing temperature. There is no TiO_x , no TiC and only 3% of TiO in the as-grown anodic film. After the carbothermal treatment at 750 °C, the $\text{Ti } 2p$ spectra contain 22% TiC and/or TiO species and 9% TiO_x species, and the respective fractions steadily decrease with increasing annealing temperatures, reaching 9% and 5% for TiOC_{1050} (Fig. 56a). In the $\text{C } 1s$ spectra, the highest fraction of carbidic carbon, namely 20%, is detected for TiOC_{750} . Only 6% C-Ti are detected in the $\text{C } 1s$ spectrum of TiOC_{850} , and similar values are found for TiOC_{950} and TiOC_{1050} . This trend is in line with the decreasing fraction of Ti(II) in the $\text{Ti } 2p$ spectra with increasing annealing temperature. The fraction of sp^2 and sp^3 carbon relative to the other carbon species shows almost no dependency on annealing temperature and has a value of $59 \pm 3\%$. The fraction of functional groups with carbon-oxygen bonds scatters between 21% (TiOC_{750}) and 40% (TiOC_{850} , as-grown anodic TiO_2), but shows no correlation with increasing annealing temperature. This suggests a random contamination of the film surfaces with organic carbon species. It can, however, not be excluded that some carbon-oxygen species are generated by the carbothermal treatment.

An increase of the acetylene flow to 1.0 flow% during the carbothermal treatment at 850 °C yields a ~ 16 percentage points higher fraction of sp^2 and sp^3 carbon compared to the films prepared with the lower acetylene flow. Although the oxide of the carburized reference film contains 75% of Ti(II) oxidation states at the surface (open circle in Fig. 56a), the relative contribution of carbidic carbon to the $\text{C } 1s$ signal is only 14% (open circle in Fig. 56b), and therewith lower than that of TiOC_{750} . These results suggest that there is a high amount of excess carbon on the surface of a TiC -rich reduced oxide film. It should be pointed out that the results obtained from the revised XPS fits agree well with those published in [217]. From the present data, it

is not possible to understand whether or not the surface chemistry of the carburized films is influenced by the orientation of the Ti substrate grains. A detailed study on the substrate grain-dependent surface chemistry will be presented in Chapter 5.

4.2.3.2 GID characterization

The crystallographic structure of the TiOC films was analyzed with grazing incidence diffractometry (GID). The GID patterns for anodic films that have been carburized with 0.1 flow% acetylene at 750, 850, 950 and 1050 °C are depicted in Fig. 57. For an incidence angle of 2°, the penetration depth of the diffracted X-rays is estimated to be between 500 nm and 1 μm depending on the film composition. Since the anodic film is only 50–60 nm thick,¹⁹⁵ the most intense peaks in all patterns arise from the Ti substrate. The relative intensities of the different Ti reflections vary notably for each sample. This may be ascribed to substrate grain growth, as observed with SEM (Fig. 54), and concomitant changes of the texture as the annealing temperature is varied. Noteworthy, there are no reflections associated with βTi in the substrates that have been annealed at 950 and 1050 °C, which indicates that no phase transformation has occurred within the analyzed volume. As regards the TiOC film composition, the most intense reflections observed in the pattern of TiOC₇₅₀ correspond to TiC and/or its solid solution with TiO (titanium oxycarbide). In TiOC₈₅₀, the TiC reflections are no longer detectable and different titanium oxide phases appear. These comprise rutile TiO₂, TiO and Ti₆O where the latter is clearly visible as a tail at the low angle side of the Ti peaks. Finally, for TiOC₉₅₀ and TiOC₁₀₅₀ only the substrate peaks are present.

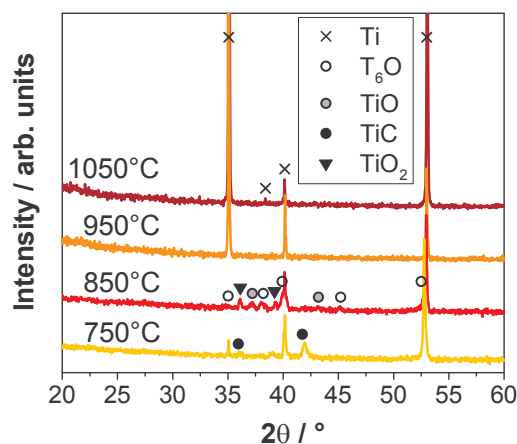


Fig. 57: Grazing incidence X-ray diffraction patterns of TiOC films on square substrates prepared at different annealing temperatures. Assignment of the phases was done using the PDF-2 database. The XRD patterns of TiOC₇₅₀, TiOC₈₅₀ and TiOC₁₀₅₀ have been published in [217].

4.2.4 Conductivity of TiOC at the solid/liquid interface

The conductivity at the solid/liquid interface of TiOC electrodes was studied with cyclic voltammetry and electrochemical impedance spectroscopy (EIS) in an 0.1 M H₂SO₄ electrolyte solution containing the ferro-/ferricyanide redox couple. If a chemical modification of the redox active species can be excluded, the oxidation and reduction reaction of the [Fe(CN)₆]⁴⁻/[Fe(CN)₆]³⁻ couple at the solid/liquid interface can be well described by a one-step outer-sphere mechanism, where one electron is transferred.²⁴⁴ In that mechanism, the electroactive species is located in the outer Helmholtz plane, with its coordination sphere remaining intact

during the electron transfer process. As expected for an outer-sphere charge transfer process, the reaction kinetics of the ferro-/ferricyanide system were found to be almost independent of the electrode material in the case of conducting Pt and Au metal electrodes.²⁴⁴ On the other hand, the electroactivity of carbon-based electrodes towards the heterogeneous redox reaction of $[\text{Fe}(\text{CN})_6]^{4-}/[\text{Fe}(\text{CN})_6]^{3-}$ was shown to be directly related to the intrinsic conductivity of the electrode surface, that was measured with conductive AFM.²⁴⁵ In the case of semiconducting electrodes, the electron-transfer process at the semiconductor/electrolyte interface is strongly affected by the density of available charge carriers in the semiconductor at the interface.⁶⁴ Differently from conducting electrodes, not only the rate constant of the reduction/oxidation reaction but also the charge carrier concentration at the interface can be affected by the applied potential, since the latter depends on the amount of band-bending inside the semiconducting electrode. For an n-type semiconductor, such as TiO_2 , at all potentials positive of the flat band potential E_{fb} the concentration of electrons at the surface is lower than the concentration of electron donors N_{D} . As a consequence, moderately doped n-type materials can carry out reductions but not oxidations. Due to these correlations, the redox reaction rate of the ferro-/ferricyanide redox couple has been chosen as a qualitative measure for the (interfacial) conductivity of the TiOC films. In particular a considerable fraction of poorly doped semiconducting TiO_2 on the TiOC surface can be expected to reduce the charge transfer rate because of the low conductivity at the solid/liquid interface.

EIS was performed at the formal redox potential determined from CVs (0.54 V) with a superimposed sinusoidal amplitude of ± 5 mV and with frequencies ranging from 100 kHz to 5 mHz. To extract the electron transfer resistance, which quantifies the redox reaction kinetics at a specific electrode and therewith its interfacial conductivity, the obtained EIS spectra were fitted using an electrical equivalent circuit (EEC) model that describes the redox reaction of the $[\text{Fe}(\text{CN})_6]^{4-}/3-$ couple under mixed kinetic and diffusion control.^{64,66} Fig. 58 shows Nyquist and Bode plots of the fitted EIS spectra, the CVs and the charge transfer resistances of the studied electrodes. As references served an as-grown anodic TiO_2 film and a polished glassy carbon (GC) electrode. The EEC model used for the fit is depicted in Fig. 58a. R_{sol} is the uncompensated ohmic resistance of the electrochemical cell and R_{ct} the charge transfer resistance. The constant phase element CPE_{EDL} represents the (non-ideal) capacitive impedance response of the EDL, and the Warburg element W the impedance of diffusion of reactants and products to and from the electrode surface. A close comparison between the fit curves and the spectra, in particular those of TiOC_{850} and TiOC_{950} depicted in the Nyquist plot (Fig. 58a), show that this simple model is not sufficient to completely reproduce the data. A possible reason for this discrepancy may be additional electrochemical processes related with the electrode itself, such as reoxidation of reduced titania species to TiO_2 or release of Ti^{4+} ions into the electrolyte (corrosion). In the frame of the second parameter study, presented below, a revised EEC model has been developed which takes these processes into account.

As expected from the semiconducting electronic properties of anodic TiO_2 ,⁵⁴ the as-grown anodic TiO_2 is completely blocking electron transfer within the investigated potential window (Fig. 58c). After the carbothermal treatments with different annealing temperatures, the electron transfer rate is significantly enhanced, yielding pronounced redox peaks in the CVs. From the data shown in Fig. 58 it becomes apparent that the annealing temperature employed for the synthesis of the TiOC films has a strong impact on the electron transfer kinetics and therewith the conductivity of the electrodes at the interface with the electrolyte.

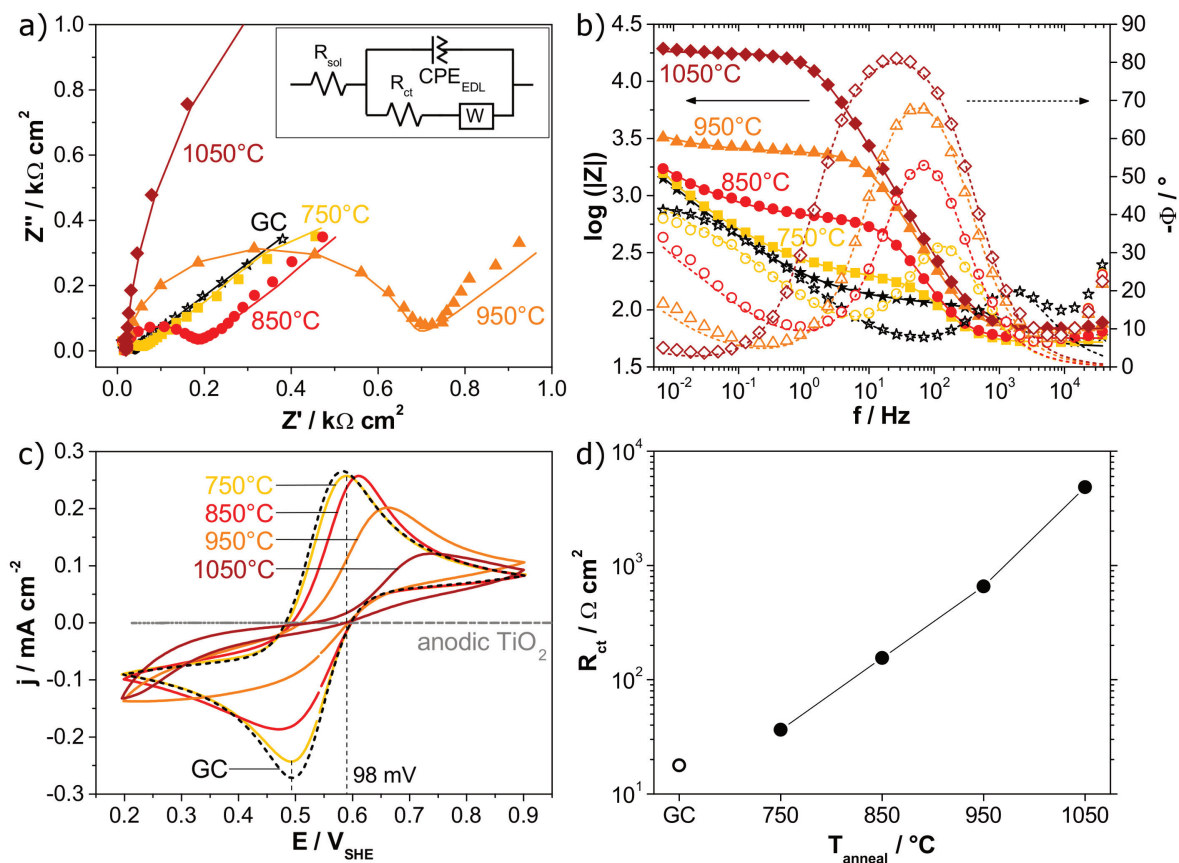


Fig. 58: Electrochemical oxidation and reduction of the ferro-/ferricyanide redox couple at TiOC films, and GC and anodic TiO_2 references. EIS spectra and EEC fits, represented in a) a Nyquist and b) a Bode plot. EIS was performed at the formal equilibrium potential $0.54 \text{ V}_{\text{SHE}}$ in a frequency range of $100 \text{ kHz} - 1 \text{ mHz}$. Inset in a): EEC used to fit the spectra. c) Last CVs of 100 potentiodynamic cycles at 10 mV s^{-1} prior to EIS. The indicated peak separation belongs to TiOC_{750} . d) Electron transfer resistance extracted from the EIS fits as a function of TiOC annealing temperature. Electrolyte: $0.1 \text{ M H}_2\text{SO}_4$ with each $2.5 \text{ M K}_3[\text{Fe}(\text{CN})_6]$ and $\text{K}_4[\text{Fe}(\text{CN})_6]$. Currents and resistances are normalized to the geometric surface areas of the electrodes. The data have been published in [217].

The redox peak separations and peak current densities of the CVs, as well as the impedance responses and in particular the extracted charge transfer resistances evidence a markedly decreasing reaction rate, and therewith interfacial conductivity, with increasing annealing temperature. Among the TiOC films, the highest interfacial conductivity is obtained for TiOC_{750} , which allows for a reaction rate that is only slightly lower than that at the GC electrode. The peak separation of 98 mV in the CV suggests irreversible or quasi-reversible charge transfer kinetics at TiOC_{750} (Fig. 58c).⁶⁴

The ohmic resistance obtained from the EIS fits varied from between 15 and $19 \Omega \text{ cm}^2$ for the different measurements, and can therewith be attributed to the electrolyte solution. Ohmic contributions from the cable connections and the electrodes were negligible. The obtained values of the CPE exponents ranged from 0.95 for TiOC_{750} to 0.98 for TiOC_{1050} , suggesting a non-ideal capacitive behavior, which is most pronounced for the sample annealed at 750°C . Based on the SEM (Fig. 54) and AFM (Fig. 53) analyses, the non-ideal capacitive behavior may be ascribed to the grain boundaries and the substrate grain orientation-dependent morphology and roughness of the TiOC films, which brings about a lateral distribution of time constants for the capacitive charging of the EDL.^{66,80,81} In Chapter 5 it will be shown that the substrate grain orientations

affect also other physicochemical properties of the TiOC films, such as their local chemical composition, which in turn can contribute to the non-ideal capacitive response. With increasing annealing temperature, however, the capacitive impedance response appears to become more ideal, which is in line with the observed substrate grain growth and concomitant homogenization of film properties (Fig. 54, Fig. 53).

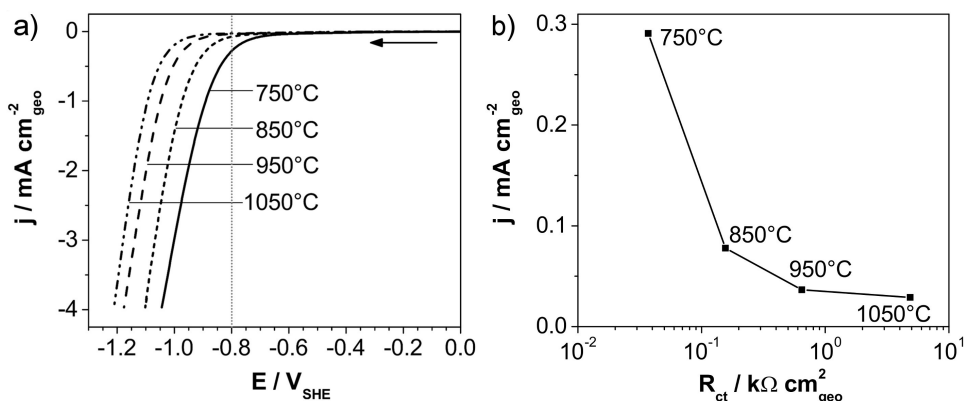


Fig. 59: HER activity of TiOC prepared at different annealing temperatures. a) LSV in 0.1 M H_2SO_4 , starting from 0.0 V and going cathodic with a scan rate of 10 mV s^{-1} until a cathodic current density of $\sim 4 \text{ mA cm}^{-2}$ is reached. b) HER current density at -0.8 V taken from a) vs. the area specific charge transfer resistance r_{ct} of the respective TiOC (determined by EIS with the ferro-/ferricyanide redox couple). The data in a) have been published in [217]; b) is adapted from [246] © 2013 WILEY-VCH Verlag GmbH & Co. KGaA, Weinheim.

To obtain a first idea on the electrocatalytic properties of TiOC surfaces, their activity towards the hydrogen evolution reaction (HER) was studied with linear sweep voltammetry (LSV) in 0.1 M H_2SO_4 , the results of which are presented in Fig. 59. The HER has been chosen as one of the best investigated cathodic electrocatalytic reactions. With increasing TiOC annealing temperature, the HER onset clearly shifts cathodic, evidencing higher overpotentials (Fig. 59a). As it can be seen in Fig. 59b, the HER current density at -0.8 V decreases significantly for an increasing outer sphere electron transfer resistance of the TiOC surfaces, which indicates that the electrocatalytic behavior is linked to the interfacial conductivity of the TiOC films and thus depends on the annealing procedure applied. For Magnéli-type titanium oxides it is reported that the onset of proton reduction shifts to more cathodic potentials for less reduced phases, which can be related to their lower electric conductivity. For example, during CVs in 1.0 M H_2SO_4 a current density of 10 mA cm^{-2} is reached at $-0.6 \text{ V}_{\text{RHE}}$ in the case of a Ti_4O_7 electrode and at $-0.7 \text{ V}_{\text{RHE}}$ in the case of a Ti_5O_9 electrode.²⁸ In comparison, at the TiOC_{750} electrode, which shows the highest HER activity of all investigated TiOC films and has an electron transfer resistance similar to that of glassy carbon, a proton reduction current density of 1 mA cm^{-2} is measured at a potential of $-0.9 \text{ V}_{\text{SHE}}$. The high HER overpotentials of the four TiOC electrodes compared to that of the mentioned Magnéli-type titanium oxides shows that not only the electrode's conductivity but also the surface chemistry and structure have an impact on the activity towards the HER. This is reasonable since inner-sphere electrocatalytic reactions as the HER involve adsorption processes on the electrode surface. Although the performance of the investigated electrodes towards the HER is comparably poor, the strong relation between the electrochemical/electrocatalytic properties of TiOC films and their annealing temperature demonstrates that the TiOC system offers a wide parameter space with room for an optimization in view of specific electrocatalytic applications. The results of these first experiments give insight into the behavior of the TiOC system toward an inner-sphere electrocatalytic reaction and thus deliver important information for

other electrocatalytic reactions of interest like the ethanol oxidation reaction (EOR) (see Chapter 6).

4.2.5 Interpretation of the carbothermal conversion based on a thermodynamic model

From the XPS and GID results, a strong impact of the annealing temperature employed during the carbothermal treatment on the final film composition is deduced. In particular the fraction of TiC (TiO) species at the surface and in the carburized anodic film is decreasing with increasing annealing temperature. The phase evolution of the anodic film during the different stages of the carbothermal treatment (heating in argon, carburization and post annealing) can be interpreted on the basis of the Ti-O-C equilibria, as illustrated in Fig. 60.

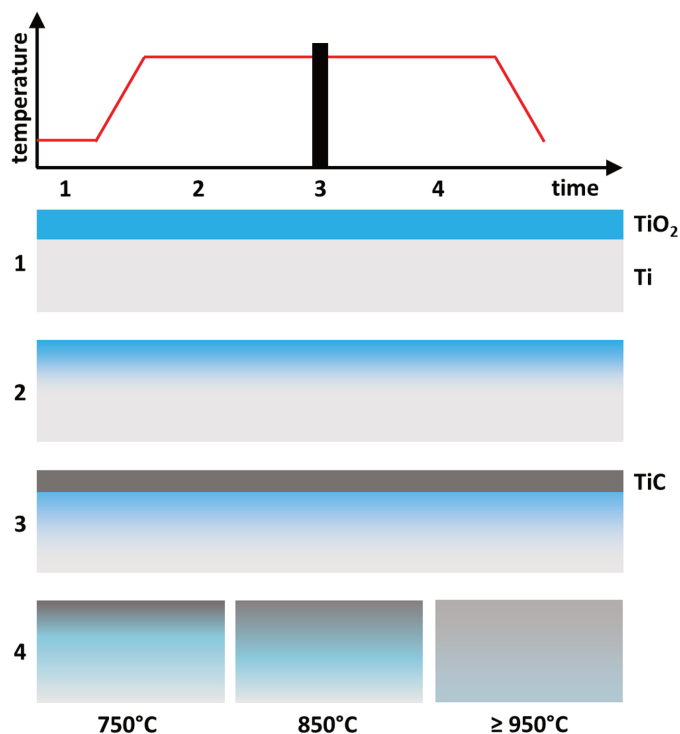


Fig. 60: Thermodynamic model of the phase evolution and temperature program of the annealing procedure. Adapted from [217].

After the anodization step (step 1 in Fig. 60) the sample is heated up in Ar and annealed for 60 min at high temperature (step 2 in Fig. 60). During this stage, and for the employed annealing temperatures, crystallization of the oxide layer to the rutile phase is expected.^{247,248} Moreover, due to the high solubility of oxygen in titanium, it is likely that some in-diffusion of oxygen from the surface oxide into the bulk of the metallic Ti substrate takes place. Immediately after carburization (step 3 Fig. 60), TiC or $\text{TiO}_{1-x}\text{C}_x$ is expected to be the dominant phase on the outermost layer of the film. Residual surface carbon from the decomposition of acetylene, which has not been consumed for the formation of TiC species, is not considered in the model. The evolution of the film during the subsequent annealing stage (step 4 in Fig. 60) is highly dependent on the annealing temperature. Since no further oxygen or carbon is supplied to the film surface during the final 60 min of annealing, the drive to equilibrium requires a redistribution of C and O within the anodic film and/or the Ti substrate *via* diffusion of both species inside the sample where the C and O diffusion coefficients depend exponentially on the annealing temperature. After annealing at 750 °C the GID results show that both $\text{TiO}_{1-x}\text{C}_x$ and TiO_2 (rutile) are still present, indicating that inward diffusion was limited at this temperature. At 850 °C only rutile TiO_2 and various Ti suboxides are detected, indicating that both oxygen and, in particular,

carbon have diffused into the substrate. Finally, for the two highest annealing temperatures the GID patterns show no indication of Ti carbide or oxide phases, which suggests that C and O are present as solutes inside the Ti structure and do not form an extended (and therewith detectable) $\text{TiO}_{1-x}\text{C}_x$ phase. The O and C solutes in the Ti substrate may be responsible for the observation that no phase transformation to the beta phase of titanium has occurred within the studied sample volume. The XPS results evidence the presence of TiO_2 and a small amount of $\text{TiO}_{1-x}\text{C}_x$ species at the very surface of TiOC_{950} and TiOC_{1050} . This indicates that, due to the diffusion of C and O into the bulk of the Ti substrate, only a very thin layer of $\text{TiO}_{1-x}\text{C}_x$ species remains at the surface when high annealing temperatures are used for the film synthesis. It has to be mentioned that an out-diffusion of C and O upon annealing cannot be excluded. Furthermore, the role of surface reoxidation during exposure of the films to air at room temperature cannot be accessed based on the results presented so far. The effect of air aging on the electrochemical and chemical properties of TiOC will be addressed in section 4.4.

Based on the proposed thermodynamic model, the origin of the observed increase of the electron transfer resistance for the outer sphere reaction of the ferro-/ferricyanide redox couple and the increase of the overpotential for the HER with increasing annealing temperature can be explained. At low temperatures, the outermost film is dominated by a carbide phase, which is expected to have a good electrical conductivity ($\sigma(\text{TiC}) = 56 \times 10^{-8} \Omega \text{ m}$,²⁴⁹ $\sigma(\text{rutile TiO}_2) = 10 \times 10^{20} \Omega \text{ m}^{250}$). With increasing temperature, carbon and oxygen diffuse into the bulk and TiO_2 is the dominant phase at the surface (as proven by the XPS data) which leads to a reduced electrical conductivity due to its intrinsic semiconducting nature.

4.3 TiOC films prepared on round substrates at temperatures between 550 and 850 °C

The first parameter study has shown that $\text{TiO}_{1-x}\text{C}_x$ -containing films can be produced through a carbothermal treatment of compact anodic TiO_2 films on Ti substrates with acetylene at annealing temperatures between 750 and 1050 °C. For a given acetylene flow fraction during the synthesis process, carburization at the lowest tested annealing temperature (i.e. 750 °C) yielded TiOC films with the highest fraction of TiC at the surface, the highest interfacial conductivity and the highest activity towards the HER. This section shows the results of a second parameter study, in which the range of annealing temperatures was extended to lower values to identify the threshold temperature for the conversion of TiO_2 to $\text{TiO}_{1-x}\text{C}_x$. Since the overall fraction of TiC appears to be beneficial for the film's electrochemical conductivity/activity, the acetylene flow used to prepare this set of TiOC films was enhanced from 0.2 sccm to 1.0 sccm.

In the first parameter study, a slight discrepancy has been found between some EIS data and the EEC model used to fit the data. This finding suggests that the overall electrochemical process did not only comprise the oxidation and reduction of the hexacyanoferrate redox probe in solution but also faradaic reactions of the TiOC electrode itself, in particular passivation and corrosion. Therefore, the electrochemical stability of the TiOC electrodes against passivation/corrosion under anodic polarization in acidic electrolyte (at room temperature) were carefully evaluated in the frame of the second parameter study. The simple EEC model used for the EIS fits shown in Fig. 58 was revised to take these processes into account.

A scientific report comprising the presented XPS and electrochemistry results has been published by Rüdiger et al. in 2017.²⁵¹

4.3.1 Preparation of the second TiOC series

For this study a set of anodic films was prepared on round disk Ti substrates with 15.5 mm diameter, which underwent carbothermal treatments at 550, 650, 750 and 850 °C. The following procedure was applied:

- (i) purging for two hours with 750 sccm Ar to remove air,
- (ii) heating to the desired annealing temperature T during 90 min at a constant rate in 200 sccm Ar,
- (iii) dwelling for 60 min at T ,
- (iv) addition of 0.5 flow% (i.e. 1.0 sccm) of acetylene for 5 min,
- (v) dwelling for 60 min at T in Ar, and
- (vi) switching off the oven to let it cool down to room temperature.

A reference sample (termed TiO_{2-x}) was thermally treated at 550 °C in 200 sccm Ar without C_2H_2 according to the sequence (i)-(ii)-(v)-(vi).

4.3.2 TiOC appearance and surface morphology

Fig. 61 depicts photographs of an as-grown anodic TiO_2 film and of TiOC films prepared at the four different annealing temperatures. The optically transparent anodic oxide film on the metallic substrate generates a blue interference color, which corresponds to a film thickness of 50–60 nm.¹⁹⁵ The TiOC films that have been synthesized at 650, 750 and 850 °C have a metallic appearance, which indicates a complete conversion of the oxide film to a conducting oxycarbide phase or a complete in-diffusion and redistribution of O and C in the matrix of the metal substrate. In contrast, TiOC_{550} has a blue color, darker than that of the anodic film, and shows only few metallic spots. The blue appearance indicates a comparably high content of residual TiO_2 in the film and therewith an incomplete conversion to oxycarbide at 550 °C. The difference in apparent color between the as-grown anodic film and TiOC_{550} can be ascribed to color centers in the latter due to oxygen vacancies that are generated in the oxide film during the annealing in reducing atmosphere.²³ Fig. 62 shows SE micrographs of an anodic film prior to and after the carbothermal treatment at 550 °C. The images have been acquired with the inlens detector to obtain chemical contrast. Both films yield a very similar substrate grain-dependent image contrast, which supports the conclusion of an incomplete conversion and the presence of unconverted TiO_2 .

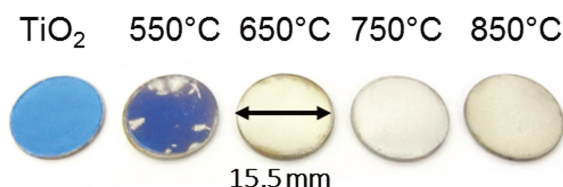


Fig. 61: Photographs of as-grown anodic TiO_2 and TiOC films on round disk substrates prepared at different annealing temperatures.

SE micrographs of all four types of TiOC films, acquired with the Everhart-Thornley detector and with the inlens detector at different magnifications, are shown in Fig. 63. From the low magnification micrographs

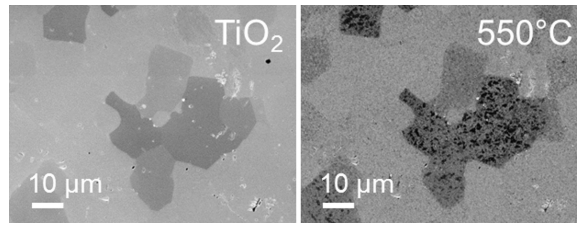


Fig. 62: SE micrographs of an anodic TiO_2 film prior to and after carbothermal treatment at 550°C . Detector: inlens; acceleration voltage: 4 kV; working distance: 4 mm (TiO_2) and 5 mm (TiOC_{550}).

(Fig. 63a-d, images 1 and 2) it can be seen that substrate grain growth can be completely neglected in films prepared at 550°C and 650°C , but becomes highly relevant at 850°C . For comparison, when using the square substrates, significant substrate grain growth was observed only in TiOC_{950} and TiOC_{1050} (Fig. 54), which can be ascribed to the different texture and purity of the two different substrates. In the case of TiOC_{550} , TiOC_{650} and TiOC_{750} , the grain boundaries of the polycrystalline substrate are visible in the micrographs acquired with the Everhart-Thornley detector, which provides mainly morphological contrast, and in those acquired with the inlens detector, which provides mainly chemical contrast. In particular the contrast variations observed in Fig. 63a2-c2 suggest a substrate grain-dependent film composition. The chemical contrast image of TiOC_{850} (Fig. 63d2) shows large areas of homogeneous gray shade across several deeper lying substrate grains, that are only visible in the morphological contrast image (Fig. 63d1). This suggests that extended areas of similar composition have formed during the carbothermal treatment at 850°C .

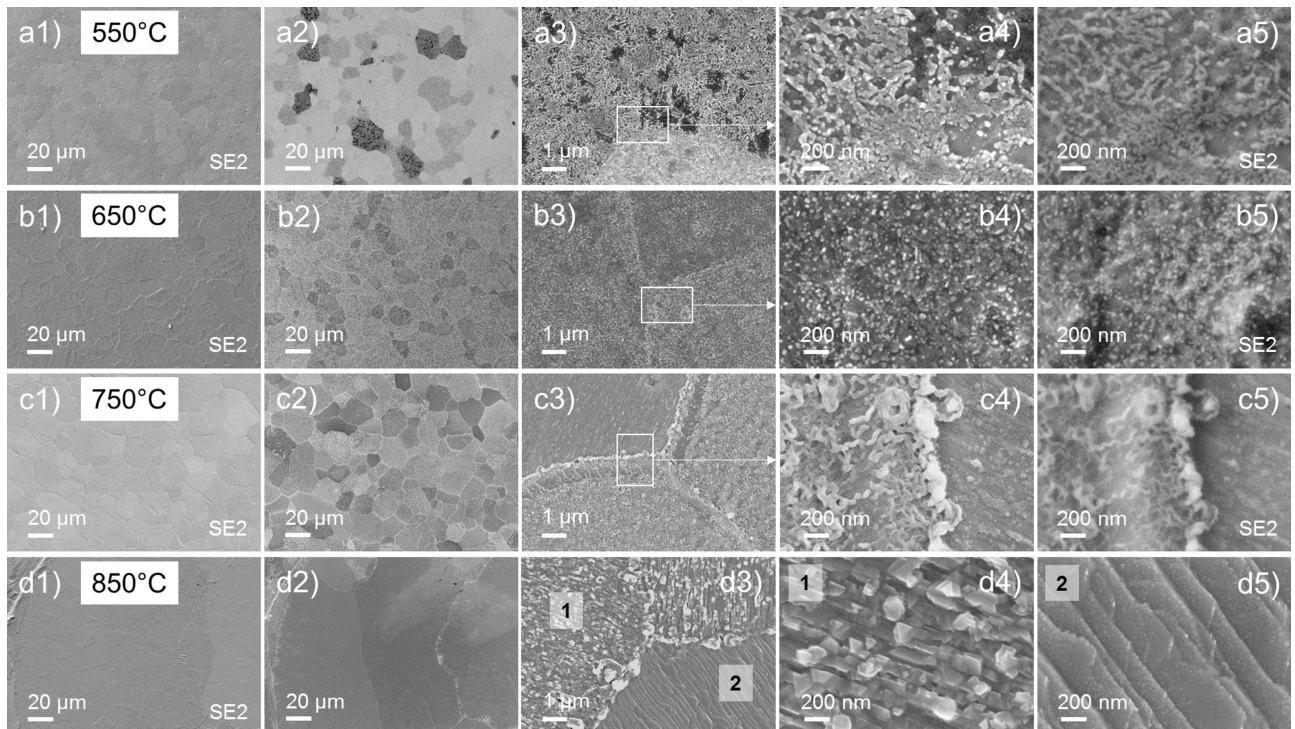


Fig. 63: SE micrographs of TiOC films on round disk substrates prepared at different annealing temperatures, as indicated. SE2: Everhart-Thornley detector, all others: inlens detector. For TiOC_{850} , high magnification micrographs are shown for two zones of different morphology.

From the micrographs acquired at higher magnifications (Fig. 63a-d, images 3 to 5), a substrate grain-dependent morphology can be clearly observed for TiOC_{550} , TiOC_{650} and TiOC_{750} , and the image contrast

suggests a substrate grain-dependent composition and/or structure, which will be confirmed in Chapter 5. Moreover, TiOC₅₅₀ seems to have a patched layer of a material on the surface which has a different chemical composition than the film underneath. Compared to TiOC₅₅₀ and TiOC₇₅₀, the surface morphology and chemical contrast of the film prepared at 650 °C seem to vary less from grain to grain. The morphology of TiOC₈₅₀ appears to depend on the substrate properties as well, which can, however, not be correlated with the substrate texture prior to the annealing due to grain growth. In agreement with the first parameter study (Fig. 54), the order of the surface structures is increasing with increasing annealing temperature, leading to the stepped terraces and triangular shapes observed on TiOC₈₅₀.

4.3.3 TiOC surface composition

The chemical composition of the TiOC films was analyzed with XPS using a Mg K α X-ray source. Fig. 64 depicts high resolution XP spectra with multi-peak fits of the Ti 2*p* and C 1*s* core-level regions of the TiOC films and of an as-grown anodic TiO₂ reference. The spectra were acquired in normal emission geometry (angle between sample surface and detector axis: $\theta = 90^\circ$). Prior to the fitting procedure, Shirley-type backgrounds were computed. In the case of the Ti 2*p* spectra of TiOC₆₅₀ and TiOC₇₅₀, the background correction was performed in two steps: first a linear function was subtracted from the spectra and then a Shirley-background was computed for the modified spectra. As described in section 4.2.3.1, the Ti 2*p* spectra were fitted taking into account three oxidation states of Ti: Ti(IV), Ti(III) and Ti(II). The C 1*s* spectra were fitted taking into account five carbon species: O-C=O, C-O/C-OH, *sp*³-hybridized carbon (C-C), *sp*²-hybridized carbon (C=C) and C-Ti. The peak positions and FWHM values agree well with those reported in table 4.1. The multi-peak fits were used to extract quantitative information about the chemical surface composition. To determine atomic fractions of individual species, the corresponding peak areas were corrected with the respective atomic sensitivity factors (ASF). The atomic sensitivity factors were calculated based on the assumption of a homogeneous mixture of the detected species. For this study, the concentrations of carbon species on the very surface, i.e. O-C=O, C-O/C-OH, C-C and C=C, relative to the amount of detected Ti species was determined. Therefore, the corrected area of the respective peak in the C 1*s* spectrum was divided by the sum of the corrected areas of the four considered carbon peaks and the corrected area of the entire Ti 2*p* signal.

To access the average depth-dependent chemical composition of the film surfaces, XP spectra were acquired at two photoelectron take off angles. The depth of the probed volume can be estimated by the photoelectron escape depth, which is $3\lambda_e \sin \theta$ in the respective material. Under normal emission (NE, $\theta = 90^\circ$), the detected electrons originate from a $3\lambda_e$ depth of $\sim 5.5\text{--}7.8$ nm, while under grazing emission (GE, $\theta = 30^\circ$), the accessible depth of the films is reduced to $\sim 2.7\text{--}3.9$ nm. These values were calculated for anatase TiO₂ and graphite, respectively. In the case of the TiOC films, the actual accessible depth depends on the true chemical composition and layered structure.

Fig. 65 shows the Ti 2*p* and C 1*s* core level spectra, acquired at the two take off angles, of the TiOC films together with reference spectra of as-grown anodic TiO₂. The relative contributions of the different Ti and C species to the Ti 2*p* and C 1*s* core level spectra, respectively, are depicted in Fig. 65c,d as function of the annealing temperature. Fig. 65e shows the relative concentrations of carbon species detected in the C 1*s* spectral region that are not bound to Ti, where their sum is denoted by surface C, and of all titanium-species

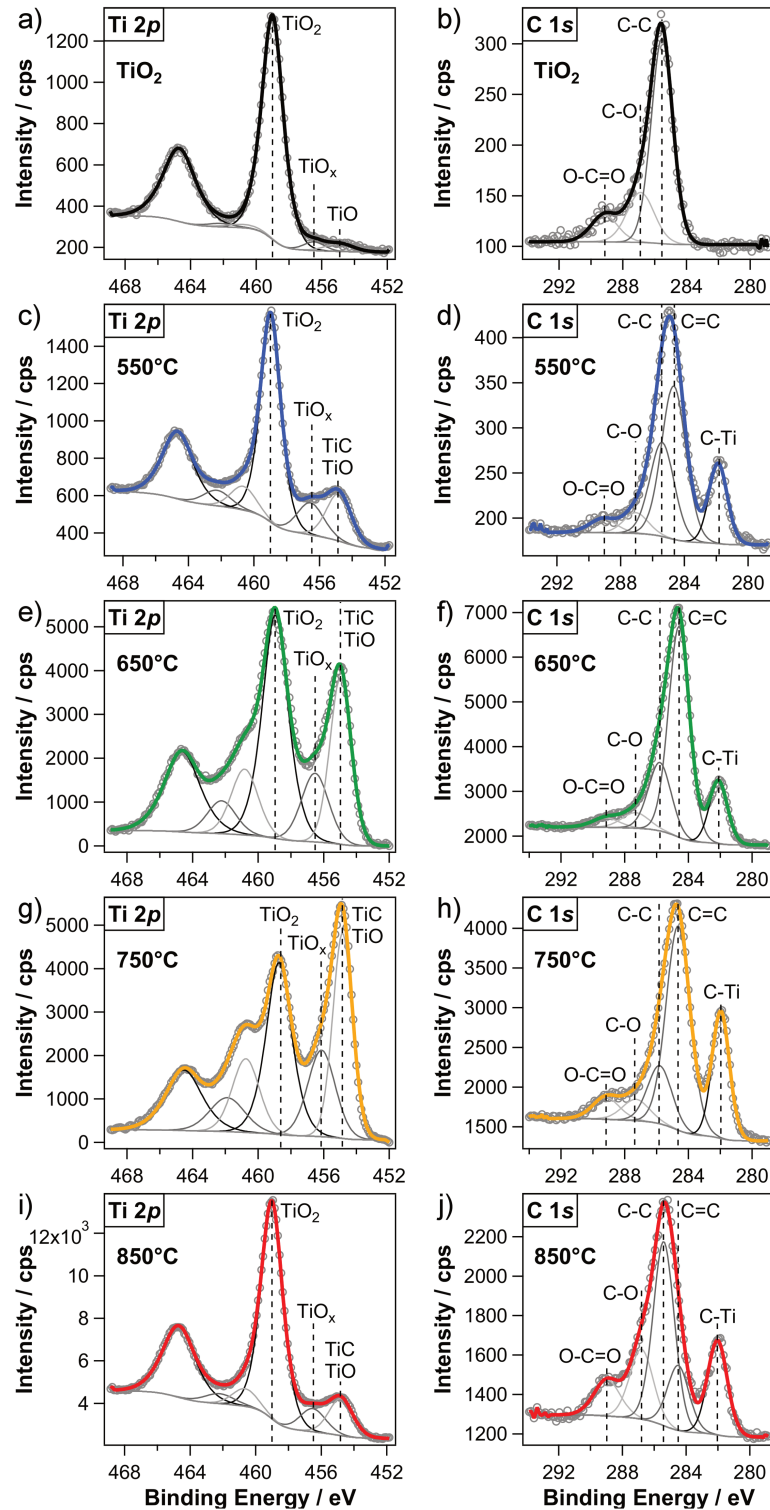


Fig. 64: XPS of TiOC films and of an as-grown anodic TiO_2 reference, prepared on round disk substrates. High resolution spectra with Shirley-type backgrounds and component fits (a,c,e,g,i) of the Ti 2p and (b,d,f,h,j) of the C 1s core levels. (a,b) As-grown anodic film, (c,d) TiOC_{550} , (e,f) TiOC_{650} , (g,h) TiOC_{750} and (i,j) TiOC_{850} . X-ray source: Mg $K\alpha$, normal emission. The spectra with analysis have been published in the supporting information of [251].

detected in the Ti 2p spectral region.

From Fig. 65a,c one can infer that the as-grown anodic oxide film mainly consists of stoichiometric TiO_2 and only contains minor fractions of TiO_x and TiO (in total 7.3 at% at NE, see also Fig. 64a). Compared to the

previously studied anodic film, that was prepared on a square substrate (Fig. 56), the oxide film on the round substrate appears to have a higher oxygen deficiency. This may be ascribed to differences in the substrate texture and purity, which both affect anodic film growth, or to different (unregistered) aging times of the two oxide films in air.

After carbothermal treatment, the fractions of Ti(II) and Ti(III) in the oxide are significantly enhanced. Between annealing temperatures of 550 °C and 750 °C, the amount of TiC (TiO) species in the TiOC continuously increases and then at 850 °C drops to a lower value than that observed at 550 °C. The overall highest content of Ti(II) and Ti(III) species is found in TiOC₇₅₀, while TiOC₈₅₀ shows the lowest grade of oxide film reduction. On as-grown anodic TiO₂, besides carbon-oxygen groups, only *sp*³ carbon is detected (C-C) (Fig. 65b,d). After the carbothermal treatments, also graphite-like carbon (C=C) is present at the surface. Its fraction increases from 550 °C to 650 °C, where it is at a maximum, and decreases again for higher annealing temperatures to a value at 850 °C, that is lower than that at 550 °C. At the same time, the fraction of *sp*³ carbon decreases to a minimum on the surface of TiOC₇₅₀ and is enhanced on the surface of TiOC₈₅₀. Carbide carbon is detected in the C 1s spectra of all TiOC, and its fraction reaches a maximum at 750 °C. This confirms the presence of TiC and/or oxycarbide (TiO_{1-x}C_x) compounds in all the TiOC, where the highest grade of conversion of TiO₂ to TiO_{1-x}C_x is obtained at 750 °C.

The comparison between NE and GE acquisition configurations in Fig. 65a,c reveals a higher fraction of TiO₂ and a lower fraction of TiC (TiO) and TiO_x at the very surface (GE) of TiOC₆₅₀, TiOC₇₅₀ and TiOC₈₅₀. The variation in the fraction of TiC (TiO) is stronger than that of TiO_x, and the largest difference between detection under GE and detection under NE configuration is found for TiC (TiO) species in TiOC₆₅₀. In TiOC₅₅₀, the fraction of TiO₂ is the same for GE and NE, but the TiC (TiO) content is diminished and the fraction of TiO_x slightly enhanced at the surface. These observations suggest a reoxidation of the reduced titania species, in particular the TiO_{1-x}C_x compounds, in the TiOC films at the surface, which is known to happen during air exposure.²⁵² The decreased fraction of C-Ti and higher relative amount of carbon (in particular C-C), observed at GE (Fig. 65b,d) evidences that the carburized films are covered by a layer of carbon.

As it can be seen in Fig. 65e, the amount of surface C species (relative to Ti species) is similar on as-grown anodic TiO₂ and TiOC₅₅₀, reaches a maximum on TiOC₆₅₀, and decreases with further increasing annealing temperature to a value at 850 °C that is lower compared to that of the as-grown anodic TiO₂. Carbon-oxygen groups and *sp*³ carbon species are present on the film surface before and after carbothermal treatment, and their surface concentrations show no pronounced correlation with the annealing temperature (Fig. 65e). Most likely, these carbon species predominantly originate from adventitious carbon contamination, which adsorbs when the films are exposed to air. This explanation is in line with XPS data reported for *in situ* prepared TiOC films.²⁵² In contrast, a strong correlation between graphite-like carbon species and the annealing temperature is observed, which is responsible for the trend of the overall surface C concentration on the TiOC films. The initial increase of the C=C concentration from 550 °C to 650 °C suggests an improving efficiency for the decomposition of acetylene to graphite-like carbon with increasing annealing temperature. The decrease with further increasing annealing temperature can be explained by thermally activated diffusion of carbon from the surface into the bulk of the film (see Fig. 60).

Taking into account the optical appearance of the TiOC films, the chemical analysis provides insight into the conversion mechanism of anodic TiO₂ during the carbothermal treatments in the studied range of

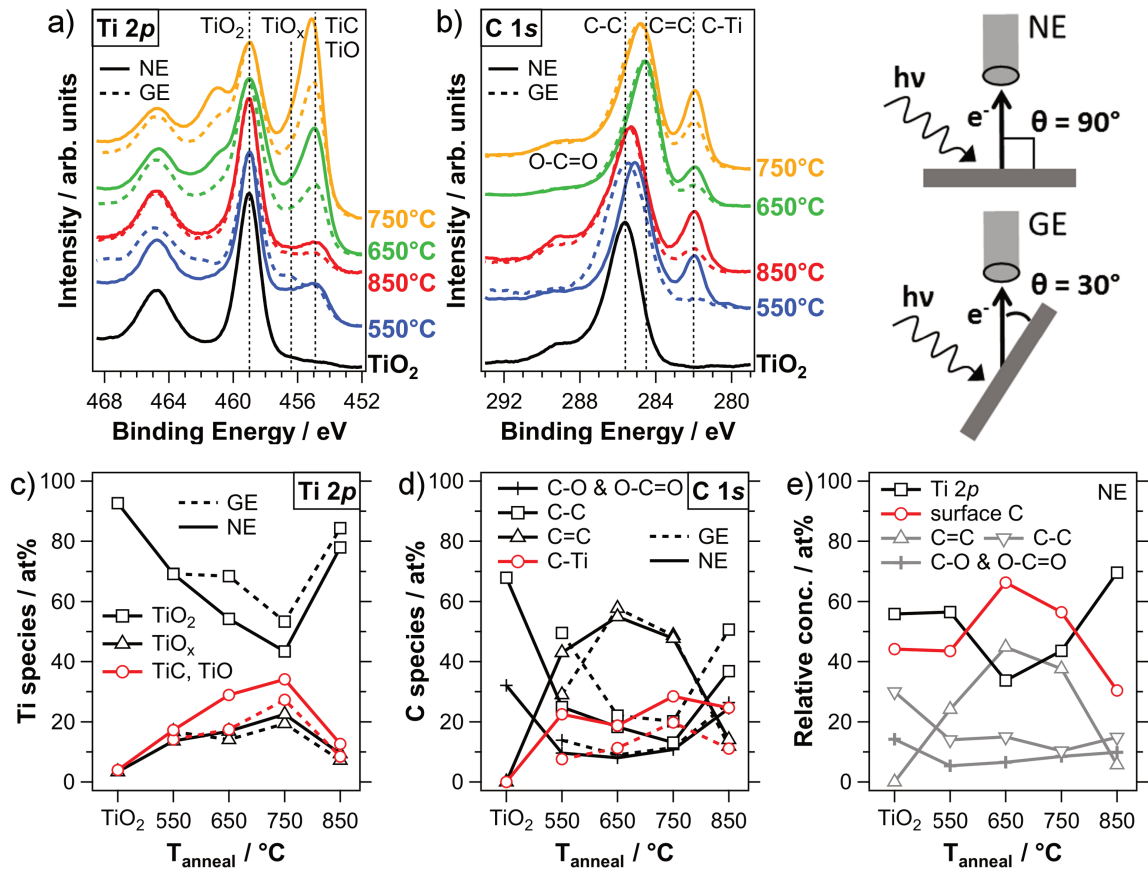


Fig. 65: XPS analysis of TiOC films prepared on round disk substrates. a) Ti 2p and b) C 1s core level spectra acquired at $\theta = 90^\circ$ (solid lines: NE) and at $\theta = 30^\circ$ (broken lines: GE) of TiOC, and of an as-grown anodic TiO₂ reference (black, $\theta = 90^\circ$). Ti 2p spectra are scaled to a common TiO₂ peak height and C 1s spectra to a common height of the peak maximum. For clarity, the spectra are shifted vertically. Results of multi-peak fitting for c) Ti 2p and d) C 1s spectra. e) Relative concentrations of C=C, C-C, C-O and O-C=O species on the film (surface C), and of the detected Ti species (Ti 2p) versus annealing temperature (NE). Adapted from [251] © 2017 Wiley-VCH Verlag GmbH & Co. KGaA, Weinheim.

annealing temperatures. The chemical composition of TiOC depends on the annealing temperature due to a temperature-dependent carbon deposition and film conversion efficiency. The metallic appearance of TiOC₆₅₀, TiOC₇₅₀ and TiOC₈₅₀ substantiates that the deposition and in-diffusion rate of carbon is sufficiently high at annealing temperatures between 650 and 850 °C to promote the conversion of the entire oxide film into a conducting oxycarbide phase. In fact, an extended TiO_{1-x}C_x phase in these TiOC films has been detected with Raman spectroscopy measurements, which will be presented in Chapter 5. The highest fraction of TiO_{1-x}C_x at the surface, and in particular TiC, is detected in TiOC₇₅₀ and the lowest in TiOC₈₅₀. Based on the insights obtained by the first parameter study on TiOC, the decreased TiO_{1-x}C_x content in TiOC₈₅₀ can be explained by thermodynamic considerations (Fig. 60): at 850 °C, carbon species diffuse deeper into the oxide film and even into the titanium substrate, leaving behind a higher fraction of TiO and TiO₂ near the surface and a lower concentration of graphite-like carbon (Fig. 57, Fig. 65c,e).

On the other hand, the chemical surface composition and the bluish optical appearance of TiOC₅₅₀ suggest that the carbothermal treatment at 550 °C yields only a superficial conversion of the compact anodic oxide film, resulting in TiO_{1-x}C_x species at the surface (Fig. 65) and some TiO_x species in the bulk oxide, which act as color centers (Fig. 61). Apparently, both the carbon deposition rate and the rate of carbon diffusion into

the bulk film, which initiates the conversion to oxycarbide, are very low at this temperature.

4.3.4 Conductivity of TiOC at the solid/liquid interface

As previously explained, a qualitative measure for the conductivity of the TiOC films at the electrode/electrolyte interface is provided by the films' activity towards outer sphere electron transfer across this interface. To investigate the electron transfer kinetics at TiOC electrodes, CVs and electrochemical impedance spectra have been acquired in 0.1 M H_2SO_4 with $\text{Fe}(\text{CN})_6^{3-}/\text{Fe}(\text{CN})_6^{4-}$.

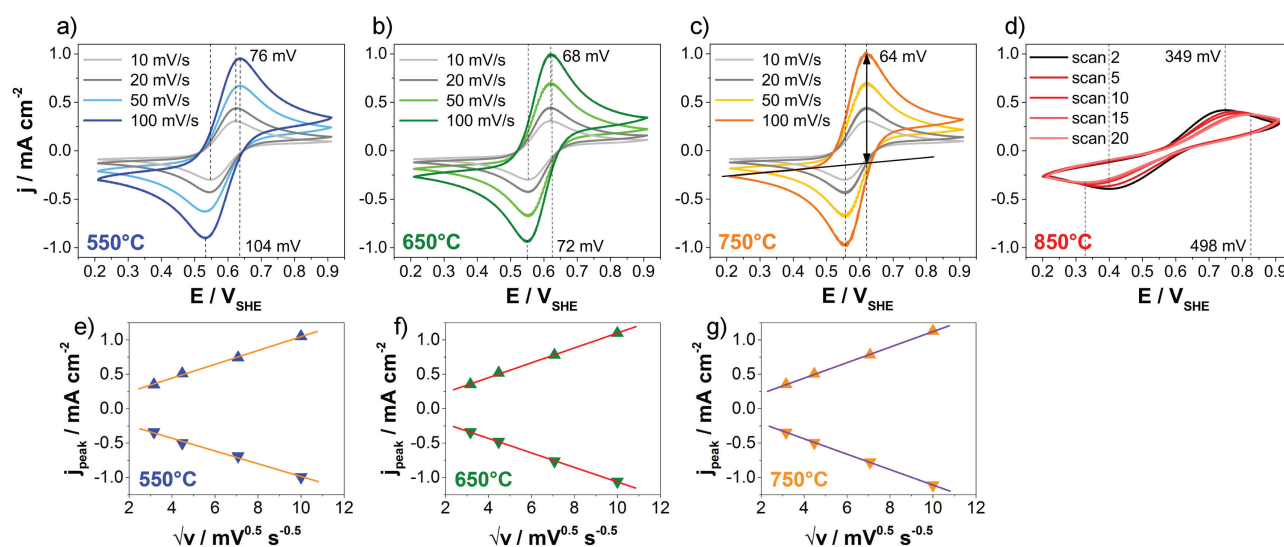


Fig. 66: Cyclic voltammetry of TiOC films prepared on round disk substrates. (a-c) Each 20th CV scan of TiOC₅₅₀, TiOC₆₅₀ and TiOC₇₅₀ acquired with different scan rates, and d) evolution of CV scans of TiOC₈₅₀ at a scan rate of 50 mV s^{-1} . Peak separations are indicated in the graphs. (e-g) Peak current densities of CVs in (a-c), determined as shown in c), versus square root of scan rate v . Electrolyte: 0.1 M H_2SO_4 with each 2.5 M $\text{K}_3[\text{Fe}(\text{CN})_6]$ and $\text{K}_4[\text{Fe}(\text{CN})_6]$. Adapted from [251] © 2017 Wiley-VCH Verlag GmbH & Co. KGaA, Weinheim, and the associated supporting information.

A first estimation of the electron transfer kinetics is given by the redox peak separations and peak current densities measured during CVs at different scan rates. Fig. 66 shows the analyzed CVs. The scan rate independent anodic and cathodic current peak separation of 64 mV, observed in Fig. 66a, evidences electrochemically reversible (i.e. nernstian) electron transfer kinetics at TiOC₇₅₀.⁶⁴ At TiOC₆₅₀, electron transfer is still relatively fast and almost reversible; the peak separation of 68 mV obtained at 10 mV s^{-1} increases only slightly with increasing scan rate, being 72 mV at 100 mV s^{-1} (Fig. 66b). In the case of TiOC₅₅₀, the peak separation at 100 mV s^{-1} is almost 30 mV larger than that at 10 mV s^{-1} , suggesting irreversible kinetics (Fig. 66c).⁶⁴ As it can be seen in Fig. 66e-g, the peak current densities of TiOC₅₅₀, TiOC₆₅₀ and TiOC₇₅₀ are proportional to the square root of the scan rate v , which proves that the charge transfer kinetics are not quasi-reversible.⁶⁴ At a scan rate of 50 mV s^{-1} the anodic peak current density is $0.78 \pm 0.05 \text{ mA cm}^{-2}$ for TiOC₆₅₀ and TiOC₇₅₀, suggesting similar activities, and $0.74 \pm 0.05 \text{ mA cm}^{-2}$ for TiOC₅₅₀. The CVs of TiOC₈₅₀ show a comparably high peak separation, indicating irreversible kinetics, and low peak current densities, attributable to a low activity towards electron transfer (Fig. 66d). For example, the anodic peak current density obtained in the second CV scan at 50 mV s^{-1} is only $0.32 \pm 0.01 \text{ mA cm}^{-2}$ and therewith less than half of that observed for the other TiOC films. In contrast to the other TiOC electrodes, the CVs of TiOC₈₅₀ are not

stable: upon potential cycling at a constant scan rate, the peak separation is increasing and the peak current densities are decreasing (Fig. 66d). This observation can be explained by a steady surface reoxidation during potential cycling between 0.2 and 0.9 V, which leads to the formation of a more resistive TiO_2 layer on TiOC_{850} that inhibits the outer sphere charge transfer. From the CVs it can be concluded that TiOC_{750} and TiOC_{650} have the highest activity for an outer-sphere electron transfer, closely followed by TiOC_{550} , and TiOC_{850} has the lowest activity and undergoes reoxidation during the electrochemical measurements.

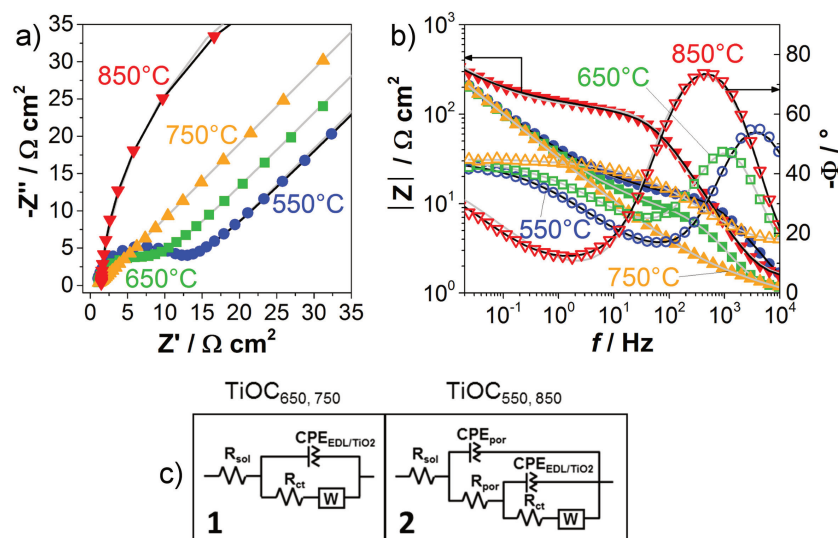


Fig. 67: EIS of outer sphere electron transfer at TiOC. a) Nyquist and b) Bode plots from EIS data, and c) EEC models **1** and **2** used for the least squares fits plotted in a) and b). Gray lines: EEC **1**, black lines: EEC **2**. Electrolyte: 0.1 M H_2SO_4 with each 2.5 M $\text{K}_3[\text{Fe}(\text{CN})_6]$ and $\text{K}_4[\text{Fe}(\text{CN})_6]$. Potential: 0.59 ± 5 mV; frequency range: 10 kHz–20 mHz. (a,c) Adapted from [251] © 2017 Wiley-VCH Verlag GmbH & Co. KGaA, Weinheim.

Fig. 67 shows Nyquist and Bode plots obtained from EIS of the redox reaction at TiOC electrodes together with least squares fits using the depicted electrical equivalent circuit (EEC) models. EIS was performed at the formal redox potential of 0.59 V, which was determined from the CVs. EEC **2** is used as the main circuit to fit the EIS spectra. It is simplified to EEC **1** in the case of TiOC_{650} and TiOC_{750} . Comparison of the gray and black fit curves in Fig. 67a,b confirms that the impedance spectra of TiOC_{550} and TiOC_{850} can be better reproduced with the more complex model EEC **2**. Both EEC models comprise the uncompensated ohmic resistance of the electrolyte solution, R_{sol} , and the charge transfer resistance R_{ct} of the TiOC films (against the outer sphere electron transfer) in parallel with a constant phase element ($\text{CPE}_{\text{EDL}/\text{TiO}_2}$) that describes the (non-ideal) capacitive behavior of the electrical double layer (EDL) and/or the capacitive impedance contribution of the electrode itself, that may become relevant for a high fraction of semiconducting TiO_2 on the surface of TiOC.^{64,157} A Warburg element (W) in series with R_{ct} is required to account for the impedance of diffusion of reactants and products to and from the electrode surface. The elements R_{por} and CPE_{por} in the outer circuit of EEC **2**, that are required to reproduce the spectra of TiOC_{550} and TiOC_{850} , can be ascribed to a thin nanoporous and resistive TiO_2 layer on the very surface of TiOC, that is reported to form on oxide covered titanium during passivation/corrosion processes when the electrodes are exposed to neutral or acidic aqueous electrolytes.^{253–256} Since R_{por} is in series with the charge transfer resistance, it acts like an additional resistance against the heterogeneous reaction of the redox couple. The overall resistance of TiOC against the redox reaction, which is a measure for the electrical resistance of the TiOC films at the

electrode/electrolyte interface, is then given by the polarization resistance $R_{p,\text{redox}} = R_{\text{ct}} + R_{\text{por}}$.

Through combination of the EIS results with the chemical surface analysis, a relationship between the surface composition and the charge transfer kinetics at TiOC electrodes is obtained. Fig. 68 shows the polarization resistance $R_{p,\text{redox}}$ of the TiOC electrodes *versus* the fraction of reduced titania and TiO_2 species in the films (deduced from the Ti $2p$ core level spectra), and *versus* the concentrations of sp^2 - and sp^3 -hybridized carbon as well as of carbon-oxygen species (all relative to the amount of detected Ti species) on the film surfaces. From the trend in Fig. 68a, a clear correlation between the grade of oxide film reduction at the surface of TiOC and the electrode activity can be inferred. This is in accordance with the results obtained during the first parameter study (Fig. 58), and confirms that a high fraction of TiC (TiO) and TiO_x enables fast outer sphere electron transfer. As it can be seen in Fig. 68b, there is no clear correlation between the amount of carbon-oxygen species nor between that of sp^3 -hybridized carbon species and the resistance against the redox reaction, which shows that these species do not affect the interfacial electrode conductivity. This result supports the statement that these species originate from organic contamination that is adsorbed on the film surfaces after the carbothermal treatment. Although an enhanced fraction of graphite-like carbon, which is clearly generated during the carbothermal treatment, is likely to contribute to an enhanced electric conductivity of the film surface,²⁵⁷ there is no clear dependence of the TiOC activity on the concentration of sp^2 -hybridized carbon (Fig. 68b). Interestingly, TiOC_{650} contains ~ 10 percentage points less Ti(II) and Ti(III), and ~ 7 percentage points more graphite-like carbon (C=C) than TiOC_{750} , but has a more than three times higher electron transfer resistance. This suggests that the enhanced content of graphite-like carbon on the surface does not compensate for a lower degree of film reduction in terms of activity.

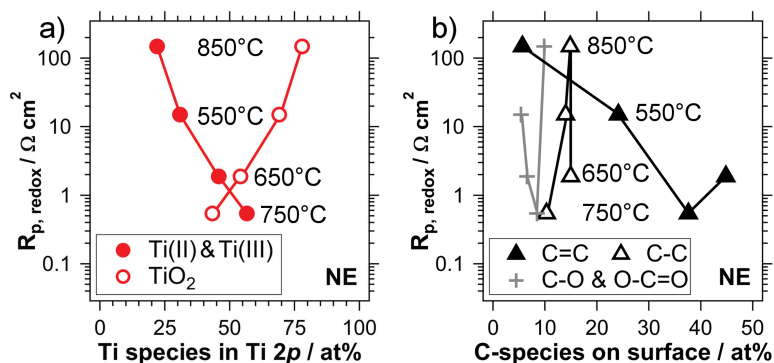


Fig. 68: Polarization resistance of TiOC against the $\text{Fe}(\text{CN})_6^{3-}/\text{Fe}(\text{CN})_6^{4-}$ redox reaction, *versus* chemical surface composition. a) Fraction of Ti species in the oxide film (from Ti $2p$ spectra). b) Concentration of sp^2 , sp^3 carbon and carbon-oxygen species on the surface (relative to all Ti species). XP spectra were acquired at NE. Adapted from [251] © 2017 Wiley-VCH Verlag GmbH & Co. KGaA, Weinheim.

A comparison between the XPS and EC results obtained for TiOC_{750} and TiOC_{850} films that have been prepared on different Ti substrates and with different flow fractions of acetylene during the carbothermal treatment reveals that not only the acetylene concentration but also the substrate properties determine the physicochemical and electrochemical characteristics of the TiOC films. At an annealing temperature of 750 °C, mainly the chosen acetylene concentration determines the chemical composition and charge transfer resistance of the obtained TiOC_{750} films. From Fig. 56 and Fig. 65 it can be seen that the converted oxide of TiOC_{750} prepared with 0.1 sccm (0.5 sccm) C_2H_2 contains 21.8 % (34.1 %) of Ti(II) species and 8.6 % (22.5 %) of Ti(III) species. These chemical compositions correlate well with the respective polarization resistances

against the redox reaction, which are determined to be $36.5 \Omega \text{ cm}^2$ for TiOC_{750} (0.1 sccm C_2H_2) and $0.5 \Omega \text{ cm}^2$ for TiOC_{750} (0.5 sccm C_2H_2).

In contrast, there seems to be a discrepancy between the chemical composition and charge transfer kinetics observed for TiOC_{850} prepared with different acetylene concentrations and on different substrates. Firstly, both TiOC_{850} films contain almost the same amount of reduced titania species, although they were prepared with significantly different acetylene concentrations: The film prepared with 0.1 sccm (0.5 sccm) C_2H_2 contains 12.6% (12.6%) of Ti(II) species and 6.3% (9.4%) of Ti(III) species. This discrepancy can be explained by the obviously different properties of the respective Ti substrates, which become apparent through their different grain growth kinetics. From the respective SE micrographs in Fig. 54 and Fig. 63 it can be seen that the grains of the square substrate are almost unaltered after the annealing treatment at 850°C (compared to the annealing treatment at 750°C), whereas the round substrate suffers from significant grain growth. Secondly, the TiOC_{850} that was prepared on the round substrate and with the higher amount of acetylene is not electrochemically stable during potential cycling between 0.2 and 0.9 V, while the respective film that was prepared on the square substrate and with less acetylene shows stable redox CVs even after 100 cycles. Moreover, the redox peak separation observed for TiOC_{850} (0.5 sccm C_2H_2) during the second CV scan is by a factor of 2.5 larger than the redox peak separation observed for TiOC_{850} (0.1 sccm C_2H_2) after 100 CV cycles. Clearly, the electrochemical stability of TiOC_{850} films is affected by other synthesis parameters as well, such as the substrate texture and purity. Despite the different electrochemical stability at high anodic potentials, the respective polarization resistances against the redox reaction, determined with EIS at the formal equilibrium potential, are very similar, namely $155.2 \Omega \text{ cm}^2$ ($147.9 \Omega \text{ cm}^2$) for the TiOC_{850} film prepared with 0.1 sccm (0.5 sccm) C_2H_2 . Since both electrodes are electrochemically stable at the formal redox potential, the charge transfer resistance at this potential seems to be determined by the chemical composition, in particular the fraction of reduced titania species, which are similar for both types of TiOC_{850} films.

4.3.5 Electrochemical stability of TiOC under polarization in acidic electrolyte

In the so far presented EIS analysis of TiOC, the overall current density and therewith the impedance response was dominated by the redox reaction of the $\text{Fe}(\text{CN})_6^{3-}/\text{Fe}(\text{CN})_6^{4-}$ probe, which makes it difficult to extract information about parallel passivation/corrosion processes occurring at the TiOC films in this electrolyte. In the case of TiOC_{850} the electrode appears to suffer from passivation and a concomitant activity loss during potential cycling in acidic electrolyte between 0.2 and 0.9 V (Fig. 66d). The EIS results provide additional indirect evidence that the TiOC electrodes suffer from a passivation/corrosion process during the electrochemical measurements, which affects the impedance response of TiOC_{550} and TiOC_{850} (Fig. 67).

A measure for the stability of the TiOC films against passivation/corrosion is given by their polarization resistance in absence of a redox probe in the electrolyte solution. The potential-dependent polarization resistance R_p has been determined with potential step EIS experiments in 1.0 M HClO_4 . Prior to each EIS measurement, the electrodes were stabilized at the applied dc potential for at least 15 min to reach steady state conditions, and the current-time transients were recorded (Fig. 69). Steady state currents close to zero indicate that ionic and electronic charge transfer processes are inhibited due to a high polarization resistance of the electrode. High initial cathodic currents at the beginning of a potential step, followed by a decay with time, can arise from an electrochemical reduction of surface TiO_2^{258} or from proton intercalation into the

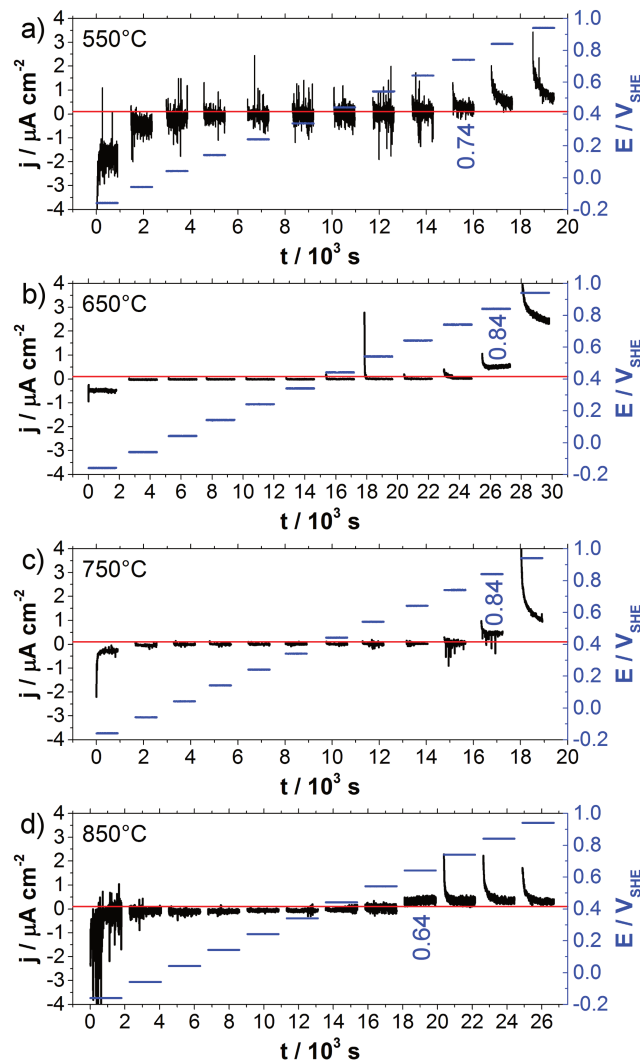
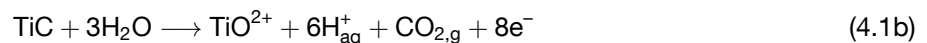
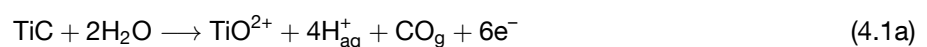


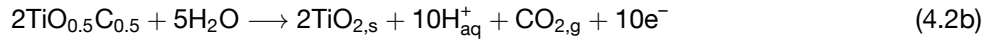
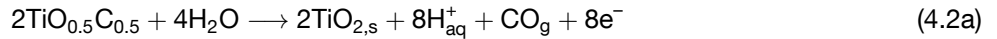
Fig. 69: Current density-time profiles of a) TiOC₅₅₀, b) TiOC₆₅₀, c) TiOC₇₅₀ and d) TiOC₈₅₀ acquired at each potential step prior to EIS. The values of the approximate onset potentials of corrosion are given in the graphs. Electrolyte: 1.0 M HClO₄. Adapted from the supporting information of [251].

oxide layer on the electrode.⁵³ Cathodic steady state currents can be ascribed to proton discharge at the electrode surface with a constant rate (HER)⁵³ and/or to a continuous reductive dissolution of surface TiO₂.¹⁶⁹ At sufficiently high anodic potentials, reduced titania species are reoxidized which gives rise to anodic growth of TiO₂, similar to the passivation of metal titanium.^{53,54,258} Under potentiostatic polarization, the onset of anodic oxide growth at a potential step is evidenced by high initial anodic currents prior to an exponential decay with time.^{54,258} Pure TiC is reported to be oxidized in 0.5 M H₂SO₄ at potentials above $\sim 0.7 V_{RHE}$.³² The authors of the cited article suggest the following reactions which presumably lead to the formation of oxycarbide species at the surface:



The oxycarbide compounds can then be further oxidized to titania according to reactions such as the

following:²⁵⁸



Without initial surface reoxidation in air, electrochemical reoxidation of the $\text{TiO}_{1-x}\text{C}_x$ species near the surface is reported to start between ~ 0.35 and $0.5 \text{ V}_{\text{RHE}}$ in $0.5 \text{ M H}_2\text{SO}_4$.²⁵⁸

As can be seen in Fig. 69, notable anodic current peaks, and thus electrochemical surface reoxidation of the TiOC films, start to be observed during the first seconds of the potential steps at $\sim 0.74 \text{ V}$ in the case of TiOC_{550} , TiOC_{650} and TiOC_{850} , and at $\sim 0.84 \text{ V}$ in the case of TiOC_{750} (note, that the high current peak detected for TiOC_{650} at 0.54 V is most likely related to the oxidation of surface contamination). In addition to surface passivation, corrosion processes such as the transfer of Ti^{4+} ions from the electrode (through the TiO_2 layer on the surface) into the electrolyte can become relevant at anodic potentials.⁵³ These faradaic processes give rise to non-zero steady state currents. Anodic steady state current densities of $j > 0.1 \mu\text{A cm}^{-2}$, due to continuous passivation/corrosion of the TiOC electrodes, start to be first observed at $\sim 0.64 \text{ V}$ for TiOC_{850} , at $\sim 0.74 \text{ V}$ for TiOC_{550} , and at $\sim 0.84 \text{ V}$ for TiOC_{650} and TiOC_{750} (Fig. 69), evidencing a superior electrochemical stability of the latter two films at 0.74 V . Noteworthy, corrosion of the TiOC_{850} sample appears to set in $\sim 0.1 \text{ V}$ earlier than surface passivation. At 0.94 V , TiOC_{650} and TiOC_{750} produce the highest current densities, which do not reach steady state conditions during the chronoamperometric measurement.

Fig. 70 depicts the impedance spectra of TiOC electrodes acquired at three selected dc potentials, and the EEC models used for fitting the data. The EIS spectra of TiOC_{850} , TiOC_{750} and TiOC_{650} can be successfully fitted using the model EEC 3, whereas EEC 4 provides the better model to fit the impedance spectra of TiOC_{550} over the entire investigated potential range. The presence of an additional time constant in the impedance spectra of TiOC_{550} can be clearly deduced from the exceptional frequency dependence of the Bode phase (Fig. 70a-c). Both EEC models are reported to reproduce the impedance behavior of multi-layered oxide films on titanium electrodes that consist of an outer nanoporous layer (R_{por} , CPE_{por}) on top of an inner compact layer (R_{ct} , $\text{CPE}_{\text{EDL/TiO}_2}$).²⁵³⁻²⁵⁶ The schemes in Fig. 70 illustrate the proposed relation between the EEC models and the layered structure of the surface oxide on TiOC, for which it is sufficient to consider a single pore of the outer oxide layer. Here, R_{ct} represents the resistance against electronic and ionic charge transfer across the film/electrolyte interface, associated with passivation/corrosion processes, and R_{sol} , R_{por} , C_{por} and $\text{CPE}_{\text{EDL/TiO}_2}$ correspond to the respective elements in EEC 2 (Fig. 67).

In Ref. [255], an additional parallel circuit of R and CPE is used to model the impedance response of an inner compact oxide layer with heterogeneous (cross-sectional) chemical composition, which gives rise to an additional time constant. Following this interpretation and taking into account the incomplete carburization of anodic TiO_2 at $550 \text{ }^\circ\text{C}$, the third time constant in the impedance spectra of TiOC_{550} (represented by R_{TiO_x} and $\text{CPE}_{\text{TiO}_x}$ in EEC 4) is assigned to the impedance contribution of the interface between the conducting oxycarbide-rich layer near the surface and the semiconducting oxide in the bulk of the TiOC_{550} film, which contains some TiO_x species only, as deduced from the optical appearance (Fig. 61).

The polarization resistance R_p is given by the sum of all serial resistances in the EEC models apart R_{sol} and follows a similar trend with potential for all TiOC, as can be seen in Fig. 71: it first increases, reaches

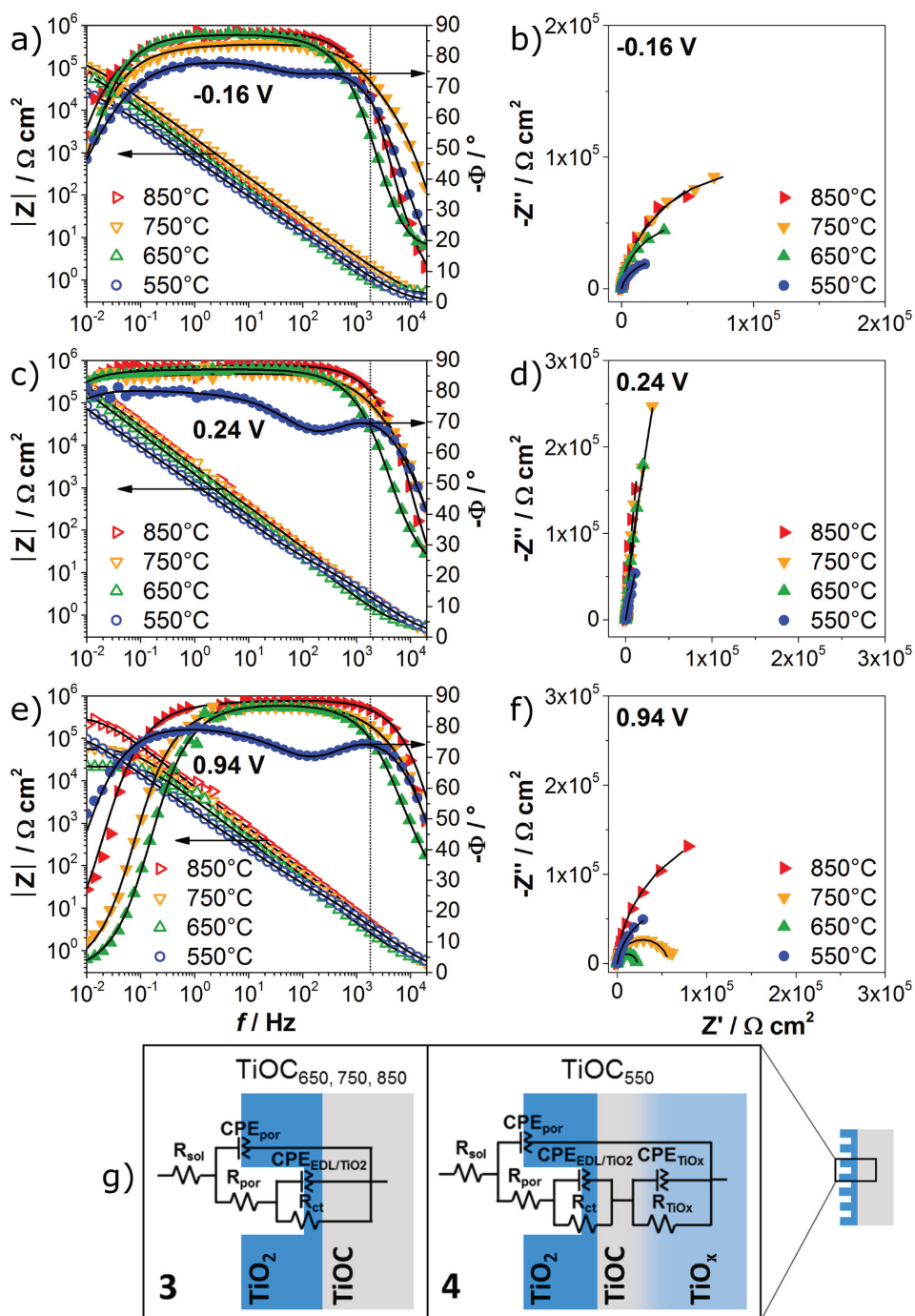


Fig. 70: EIS analysis of TiOC in 1.0 M HClO_4 . Bode (left) and Nyquist (right) diagrams of EIS data acquired at (a,b) -0.16 V , (c,d) 0.24 V and (e,f) 0.94 V with fit curves. Dotted lines in (a,c,e): $f = 1.8\text{ kHz}$, at which $-Z''$ was extracted to generate Mott-Schottky plots. g) EEC models used for the fits and schemes of the multi-layered film structure showing one nanopore of the outer oxide layer. Adapted from [251] © 2017 Wiley-VCH Verlag GmbH & Co. KGaA, Weinheim, and the associated supporting information.

a maximum and decreases again towards the anodic potential limit. Since a low polarization resistance is directly related to non-zero steady state currents (Fig. 69), low R_p values at cathodic potentials can be ascribed to the HER and/or to the electro-reduction of TiO_2 at the film surface. At sufficiently high anodic potentials, increasing TiOC corrosion rates cause the polarization resistance to decrease again. In the intermediate potential range, where the highest R_p values are measured, steady state faradaic reaction rates are very low. The dashed vertical lines in Fig. 71 denote the approximate threshold potentials, up to which

anodic steady state current densities are $\leq 0.1 \mu\text{A cm}^{-2}$, and hence TiOC corrosion processes are to a good approximation negligible (Fig. 69).

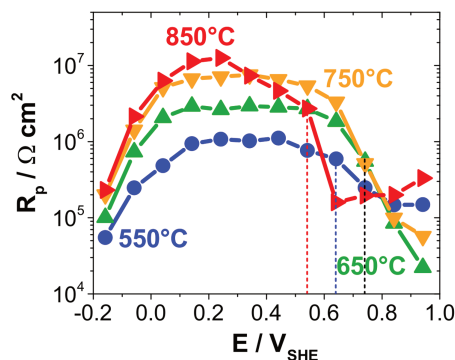


Fig. 71: Area specific polarization resistance of TiOC in 1.0 M HClO_4 versus dc potential, determined from EIS fits. Vertical dashed lines: threshold potentials up to which anodic current densities are $\leq 0.1 \mu\text{A cm}^{-2}$. Adapted from [251] © 2017 Wiley-VCH Verlag GmbH & Co. KGaA, Weinheim.

In parallel with the onset of anodic steady state currents, the polarization resistances of the TiOC films drop to values below $\sim 4 \times 10^5 \Omega \text{ cm}^2$. With further increasing potential, the polarization resistances of TiOC_{650} and TiOC_{750} strongly decrease and assume values below $\sim 6 \times 10^4 \Omega \text{ cm}^2$ at 0.94 V, a potential at which comparably high anodic current densities are observed that do not reach steady state conditions (Fig. 69). This indicates that both TiOC_{650} and TiOC_{750} suffer from passivation/corrosion above the threshold potential and that any passive film that has formed according to reactions 4.1 and/or 4.2 is only poorly protective at 0.94 V. The polarization resistance of TiOC_{550} decreases at a significantly slower rate and takes on a higher value than that of TiOC_{650} and TiOC_{750} at 0.94 V. In contrast, R_p of TiOC_{850} increases again between ~ 0.64 V and the anodic potential limit, where it reaches the highest value of all TiOC. This trend evidences the anodic formation of an increasingly more protective oxide film that inhibits further oxidation and/or corrosion of the electrode. It is worth to note that the polarization resistance of TiOC_{850} starts to considerably decrease already above ~ 0.24 V, a potential similar to that reported for the electrochemical oxidation of Ti^{3+} , i.e. titanium sub-oxides in the oxide layer, to TiO_2 .²⁵⁸

The polarization resistance-potential curves and current-time transients can be correlated with the electron transfer kinetics observed during the CVs in presence of $\text{Fe}(\text{CN})_6^{3-}/\text{Fe}(\text{CN})_6^{4-}$ (Fig. 67). An early onset of passivation under anodic polarization and the formation of a comparably protective oxide film lowers the electron transfer kinetics at TiOC. In particular, the activity loss of TiOC_{850} towards the redox reaction observed during potential cycling between 0.2 and 0.9 V (Fig. 67d) can be ascribed to the steady formation of a protective passive film that inhibits faradaic reactions. The stagnating decrease of the polarization resistance of TiOC_{550} toward the anodic potential limit suggests the formation of a passive layer, which is less protective than that on TiOC_{850} at 0.94 V. Although the redox CVs measured at TiOC_{550} between 0.2 and 0.9 V are stable (Fig. 67a), the formed multi-layered passive film affects the impedance response of TiOC_{550} in presence of the redox probe, so that EEC 2 provides the better fit of the EIS data. The very low polarization resistances measured for TiOC_{650} and TiOC_{750} between 0.84 and 0.94 V are in line with the high and stable activity towards the redox reaction of the $\text{Fe}(\text{CN})_6^{3-}/\text{Fe}(\text{CN})_6^{4-}$ couple during potential cycling between 0.2 and 0.9 V. Apparently, neither the oxide generated in air nor any anodic TiO_2 generated on TiOC_{650} and TiOC_{750} between ~ 0.74 and 0.9 V have a major impact on the electrodes' activities (Fig. 66, Fig. 67).

In contrast to the polarization resistance against the oxidation and reduction of the $\text{Fe}(\text{CN})_6^{3-}/\text{Fe}(\text{CN})_6^{4-}$ couple, there is no obvious correlation between the polarization resistance against passivation/corrosion and the films' chemical surface composition. Only at a potential of 0.64 V, an increasing polarization resistance is found for an increasing fraction of Ti(II) and Ti(III) species in the films. But until ~ 0.24 V, the R_p values of TiOC show a correlation with the annealing temperature: the higher the annealing temperature, the higher is the polarization resistance. This result suggests that also other physicochemical properties of the films, such as their crystallinity or the number of grain boundaries, determine their electrochemical stability.

Sufficiently thick and closed films of poorly doped TiO_2 on the TiOC electrodes are expected to dominate the capacitive response of the electrode/electrolyte interface due to the formation of a space charge layer in the semiconductor. Therefore, the impact of TiO_2 species on the electronic properties of TiOC at the solid/liquid interface has been further evaluated using the Mott-Schottky approach, which allows to identify semiconducting properties. To generate Mott-Schottky diagrams, capacitance values have been calculated from the imaginary impedance, measured at each potential step, *via* the formula $C^{-2} = (-\omega Z'')^2$. The Z'' values have been extracted from the impedance spectra at a frequency of $f = 1.8$ kHz (note that $\omega = 2\pi f$), which is sufficiently high for the imaginary impedance to have contributions from the capacitance of the solid/liquid interface (see dotted lines in the Bode diagrams of Fig. 70).

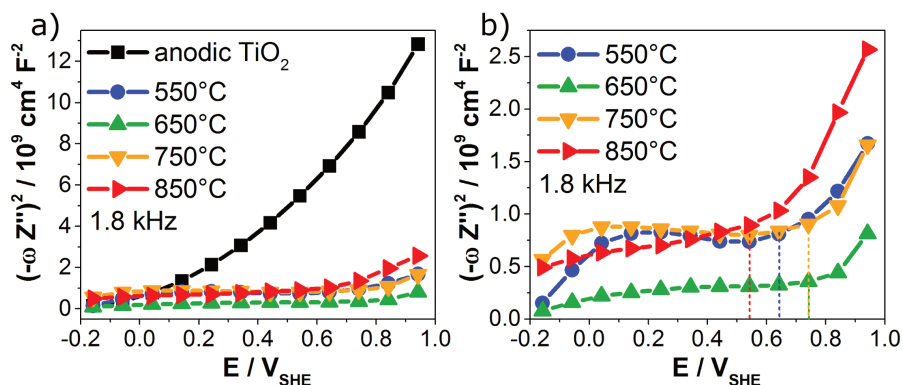


Fig. 72: Mott-Schottky diagrams of anodic TiO_2 and of TiOC. Area specific $(-\omega Z'')^2$ values extracted from potential step EIS in 1.0 M HClO_4 at a frequency of 1.8 kHz (see dotted lines in Fig. 70), *versus* dc potential. b) Enlargement of a), showing only the data of TiOC. Vertical dashed lines in b): threshold potentials up to which anodic current densities are $\leq 0.1 \mu\text{A cm}^{-2}$.

Fig. 72 shows the Mott-Schottky diagrams of the interfacial capacitances obtained for an as-grown anodic TiO_2 film and for the four TiOC films. The high positive slope of the black curve evidences a relatively low donor concentration in the n-type semiconducting anodic TiO_2 , which is in line with the XPS results (Fig. 65c). The non-linear shape of the Mott-Schottky curve is typical for amorphous or polycrystalline TiO_2 films, and is commonly attributed to a continuous distribution of localized donor states inside the band-gap.⁷¹⁻⁷³ Compared to the capacitance-potential relation found for the as-grown anodic TiO_2 , the Mott-Schottky curves of all four TiOC films are flat, attesting a comparably high electrical conductivity at the interface. This is in agreement with the observation of pronounced redox peaks in the CVs shown in Fig. 66.

In Fig. 72b it can be seen that the inverse square capacitance of the TiOC films is rising when the potential is increased beyond the onset of considerable anodic steady state currents (Fig. 69). This trend indicates a growing thickness of the multi-layered oxide film on the surface at sufficiently high anodic potentials.

Due to the relatively early onset of passivation of TiOC_{850} , namely above ~ 0.64 V (Fig. 71), the respective Mott-Schottky curve becomes comparably steep already at potentials above 0.64 V. At potentials, where the rate of faradaic reactions at TiOC is very low, the inverse square capacitance is almost independent of potential for all TiOC, which indicates that, prior to the anodic polarization, the TiOC electrodes are at the most covered by a very thin layer of TiO_2 species, in accordance with the XPS analysis. The results obtained from the EIS measurements in HClO_4 confirm that all TiOC undergo passivation/corrosion in acidic electrolyte solutions, which is accompanied by the formation of a nanoporous oxide layer on top of a compact oxide layer on the surface. The protection and resistivity of this layer up to 0.94 V, however, depends on the physicochemical properties of the TiOC films prior to their immersion into the electrolyte, and therewith on the synthesis parameters. Taking into account the XPS analysis, the comparison between the redox reaction kinetics and the potential-dependent polarization resistances reveals that TiOC electrodes initially consisting of a thin oxide layer (generated in air) on top of a TiC-rich film that is fully converted to $\text{TiO}_{1-x}\text{C}_x$ in the bulk, exhibit the highest electrochemical stability up to ~ 0.74 V, and the highest interfacial conductivity, even after polarization to 0.9 V.

4.4 The effect of aging in air on the chemical and electrochemical properties of TiOC films

Within the frame of the parameter study on TiOC films prepared at annealing temperatures between 550 and 850 °C, special focus was on the films' intrinsic stability in air, and the impact of air aging on their conductivity and electrochemical stability at the electrode/electrolyte interface. Most of the results shown in the following have been published by Rüdiger et al. in 2017,²⁵¹ together with the parameter study presented in the previous section.

4.4.1 XPS analysis before and after prolonged exposure of TiOC to air

To gain insight into the material's intrinsic stability against reoxidation, XPS analysis has been performed of pristine TiOC and of TiOC that have been exposed to air for two months at room temperature. Fig. 73 depicts the high resolution Ti 2p and C 1s core level spectra recorded at normal emission (NE, $\theta = 90^\circ$) of the pristine TiOC and of the air aged TiOC together with quantitative results obtained from multi-peak fits of the respective spectra. The corresponding spectra recorded with grazing emission (GE, $\theta = 30^\circ$) configuration are given in Fig. 111 in Appendix A. Comparison of the Ti 2p spectra reveals an enhanced content of TiO_2 in all TiOC films after prolonged air exposure, which suggests a progressing surface reoxidation. From Fig. 73c,d, a considerable loss of TiC species due to reoxidation can be deduced. This process appears to be fastest for TiOC_{550} , where no TiC species and only a small fraction of reduced oxide states are detected after exposure to air for 12 days only. A similar oxide film composition is found for as-grown anodic TiO_2 (see also Fig. 64). If the air exposure is longer than 12 days, the surface chemistry of TiOC_{550} remains essentially constant.

TiOC that are prepared at higher annealing temperatures still contain a relatively high fraction of TiC (TiO) and TiO_x species after air exposure for two months, which indicates that reoxidation of these films happens at a significantly slower rate. In TiOC_{650} , a comparably high fraction of Ti(II) is reoxidized, yielding a notably enhanced amount of TiO_2 in the aged film. On TiOC_{750} and TiOC_{850} the fraction of TiO_2 increases significantly less during the same air exposure time. Considering only the Ti species, the overall trend of the chemical surface composition with annealing temperature is preserved after exposure of TiOC to air for two

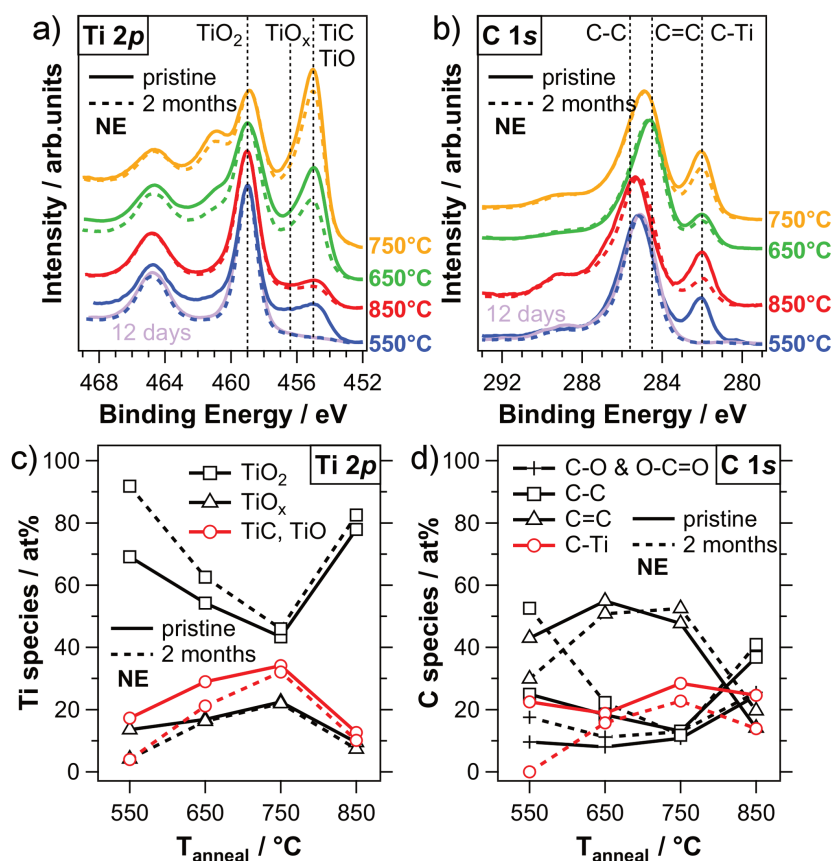


Fig. 73: XPS analysis of TiOC after different air exposure times. a) Ti 2p core level spectra, scaled to a common TiO₂ peak height, and b) C 1s core level spectra, scaled to a common height of the peak maximum, acquired at normal emission (NE, $\theta = 90^\circ$). Solid lines: pristine TiOC, broken lines: two months old TiOC, violet spectra: 12 days old TiOC₅₅₀. For clarity, the spectra are shifted vertically. Results of multi-peak fitting for c) Ti 2p and d) C 1s spectra. Adapted from [251] © 2017 Wiley-VCH Verlag GmbH & Co. KGaA, Weinheim.

months, and reveals the highest content of reduced titania in TiOC₇₅₀ (Fig. 73c). The C 1s spectra show an enhanced fraction of sp^3 carbon and carbon-oxygen species on the aged films, indicating a higher surface contamination, which is particularly marked in the case of TiOC₅₅₀. In accordance with the Ti 2p spectra, the highest fraction of C-Ti is detected in TiOC₇₅₀ (Fig. 73d).

The chemical analysis of pristine and air-aged TiOC films provides insights into the relation between the annealing temperature used for the synthesis and the intrinsic chemical stability of these materials. Due to the superficial conversion of the compact anodic film at 550 °C, the thin carburized layer at the surface of TiOC₅₅₀, and in particular the TiC species, are oxidized within a short time when the film is exposed to air (Fig. 73). This process yields a C/TiO₂ composite film, with a thin layer of (sp^2 and sp^3) carbon on a still slightly reduced oxide (the optical appearance did not change upon aging). Exposure to air causes also the TiOC₆₅₀, TiOC₇₅₀ and TiOC₈₅₀ films to reoxidize from the surface towards the bulk (Fig. 73), but at a considerably slower rate compared to the superficially converted TiOC₅₅₀. A possible reason for the enhanced stability of TiOC₆₅₀, TiOC₇₅₀ and TiOC₈₅₀ is the absence of unconverted oxide in the bulk, which demonstrates the benefit of a complete conversion. In addition, higher annealing temperatures generally improve the film crystallinity, which enhances the stability against reoxidation in air. The GID data of TiOC prepared at 750 °C and 850 °C with a lower amount of acetylene revealed the presence of crystalline TiC in TiOC₇₅₀ and of crystalline TiO and

TiO₂ (rutile) in TiOC₈₅₀ (Fig. 57). In the case of TiOC₈₅₀, also the high initial amount of TiO₂ on the surface is likely to enhance the film's intrinsic stability in air. The observation that, after prolonged aging in air, TiOC₆₅₀ experiences a higher increase of TiO₂ than TiOC₇₅₀ and TiOC₈₅₀, which is mainly at the cost of Ti(II) species, may be related to a different average stoichiometry of the TiO_{1-x}C_x compounds in TiOC₆₅₀, which most likely contains less TiC than TiOC₇₅₀, since there is more residual graphite-like carbon on the surface of TiOC₆₅₀, and/or to a different crystalline phase composition. The high amount of (mainly graphite-like) carbon on the surface of TiOC₆₅₀, seems to have no protective effect against oxidation of TiO_{1-x}C_x. It should be noted that XPS provides the average chemical surface composition of TiOC within a spot of a few mm diameter. Due to substrate grain effects, which will be discussed in the next chapter, the chemical composition locally varies on a μm scale, and it is likely that TiOC films on different substrate grains show a different aging behavior.

4.4.2 The effect of air aging on the conductivity of TiOC at the solid/liquid interface

As described in the previous sections, the conductivity at the solid/liquid interface of pristine and aged TiOC electrodes was studied through the outer sphere electron transfer kinetics of the ferro-/ferricyanide redox couple, which was analyzed with CVs, and with EIS at the formal equilibrium potential.

Fig. 74 depicts electrochemical impedance spectra and fit curves of pristine TiOC and of TiOC that have been exposed to air for up to ~ 9 months. The least squares fits of the EIS data have been performed with the models EEC 1 and EEC 2 shown in Fig. 67c. As the EIS data of pristine TiOC₅₅₀ and TiOC₈₅₀, those of the respective aged films can be best reproduced by the model EEC 2. This takes into account the formation of a resistive multi-layered oxide film on the surface during the EC measurements, which affects the redox reaction kinetics of the ferro-/ferricyanide probe. The impedance spectra of pristine and 9 months old TiOC₇₅₀ can be fit straightforward with the more simple model EEC 1, indicating that also on the aged electrode the formation of nanoporous surface oxide and/or its additional impedance against the outer sphere redox reaction can be neglected. In contrast, passivation/corrosion and the concomitant formation of a resistive nanoporous oxide film appear to become relevant after sufficiently long aging of TiOC₆₅₀, where the model EEC 2 is required to fit the EIS data of 6 and 9 months old TiOC₆₅₀ (see inset in Fig. 74c).

Noteworthy, the exponents of the two constant phase elements CPE_{EDL,TiO2} and CPE_{por} used for the EIS fits were smaller than unity for all pristine and aged TiOC, indicating a non-ideal capacitive behavior of both the EDL and the (multi-layered) surface oxide. As previously mentioned, this is typically explained by a distribution of time constants, which can be caused by inhomogeneous physicochemical properties of the surface (e.g. roughness, chemistry) and/or bulk (crystallinity, chemical composition) of the electrode.^{66,80,81} Thus, the non-ideal capacitive behavior of the TiOC films can be ascribed to their substrate grain-dependent surface roughness, morphology and chemical contrast (see Fig. 53 and Fig. 63). SPEM and micro-Raman spectroscopy analyses, the results of which will be presented in Chapter 5, have revealed that the investigated TiOC films are characterized by a substrate grain orientation-dependent surface chemistry, phase composition and crystallinity, which can give rise to a distribution of time constants as well.

From the least squares fits of the impedance spectra, the polarization resistance against the redox reaction, $R_{p,redox} = R_{ct} + R_{por}$, has been determined. The CVs and the polarization resistances of the investigated films are depicted in Fig. 75. An as-grown anodic TiO₂ film and an TiO_{2-x} electrode have been investigated as reference systems. As will be shown in Chapter 5, the as-grown anodic TiO₂ film is amorphous, whereas

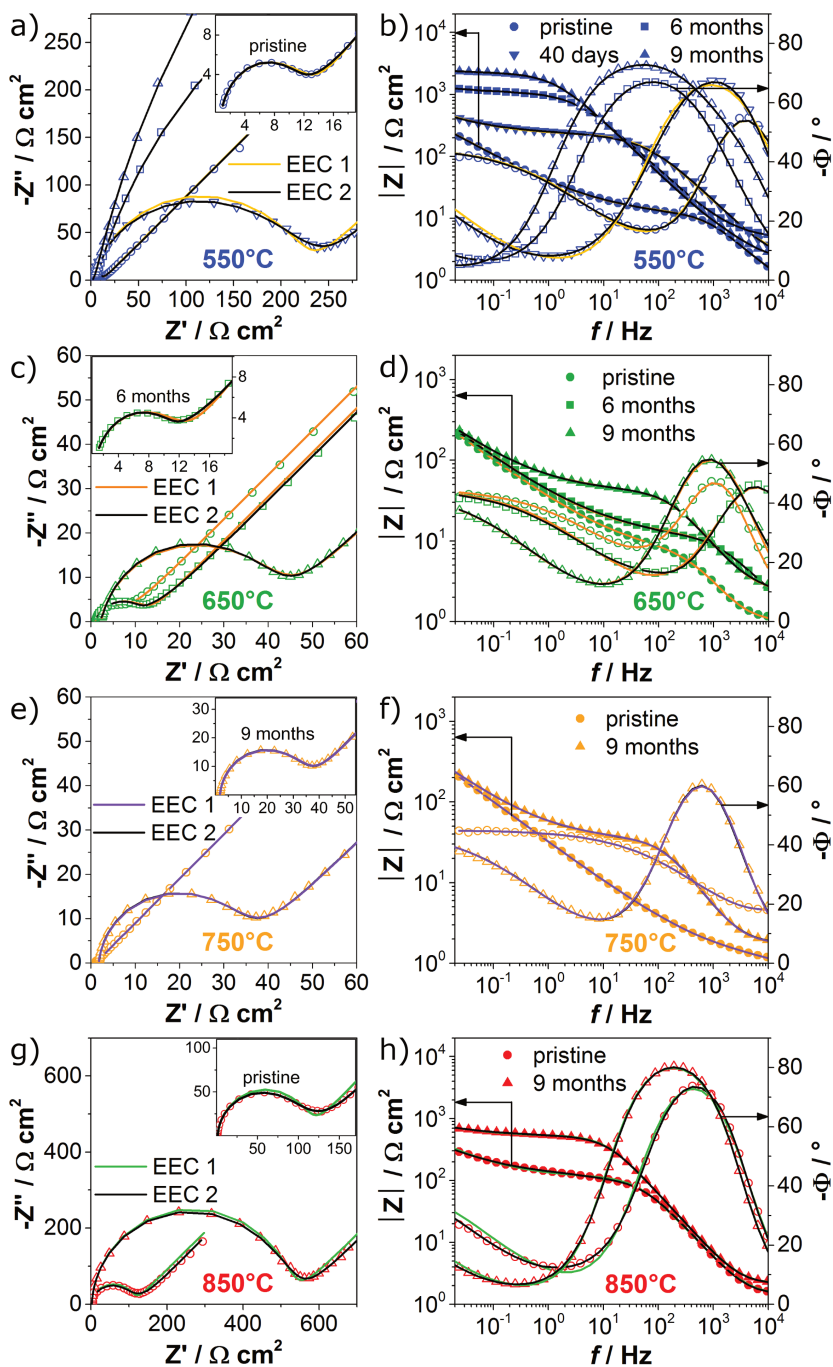


Fig. 74: EIS of outer sphere electron transfer at pristine and air aged TiOC. Nyquist (left) and Bode (right) diagrams of EIS data acquired for (a,b) TiOC₅₅₀, (c,d) TiOC₆₅₀, (e,f) TiOC₇₅₀ and (g,h) TiOC₈₅₀ with fit curves. The data were fitted using the models EEC 1 (colored) and EEC 2 (black) shown in Fig. 67c. The duration of air aging is indicated in the legend of the Bode plots. Insets on the left: Nyquist plot of a) pristine TiOC₅₅₀, c) 6 months aged TiOC₆₅₀, e) 9 months aged TiOC₇₅₀ and g) pristine TiOC₈₅₀. Electrolyte: 0.1 M H₂SO₄ with each 2.5 mM K₃[Fe(CN)₆] and K₄[Fe(CN)₆]. Potential: 0.59 ± 5 mV; frequency range: 10 kHz–20 mHz. Adapted from the supporting information of [251].

the thermally treated TiO_{2-x} film contains a considerable fraction of anatase TiO₂. The semiconducting electronic properties of amorphous TiO₂ are generally described using the concept of a mobility gap with a trail of localized states within the bandgap, which is larger than the well-defined bandgap in crystalline TiO₂.⁵⁴ Due to the large band gap, the as-grown anodic TiO₂ is completely blocking electron transfer within

the potential window of the CVs (Fig. 75a). Besides having most likely sharper band edges and a slightly reduced bandgap,⁵⁴ the partially crystalline TiO_{2-x} appears to be sufficiently oxygen deficient to allow for electron transfer in both directions of the redox reaction in the investigated potential range. However, the large separation of the anodic and cathodic current peaks in the CVs indicates sluggish electron transfer kinetics. The reaction kinetics are significantly enhanced through the carbothermal treatments, as inferred from the smaller peak separations and higher peak current densities in the CVs of the pristine TiOC films. In fact, the polarization resistance of all pristine TiOC is more than one order of magnitude lower than that of the TiO_{2-x} film, demonstrating the effectiveness of the carbothermal treatment regarding an improvement in conductivity and activity of anodic TiO_2 (Fig. 75e). $R_{p,\text{redox}}$ of pristine TiOC is lowest for TiOC_{750} , followed by TiOC_{650} , and highest for TiOC_{850} , which is in accordance with the CVs.

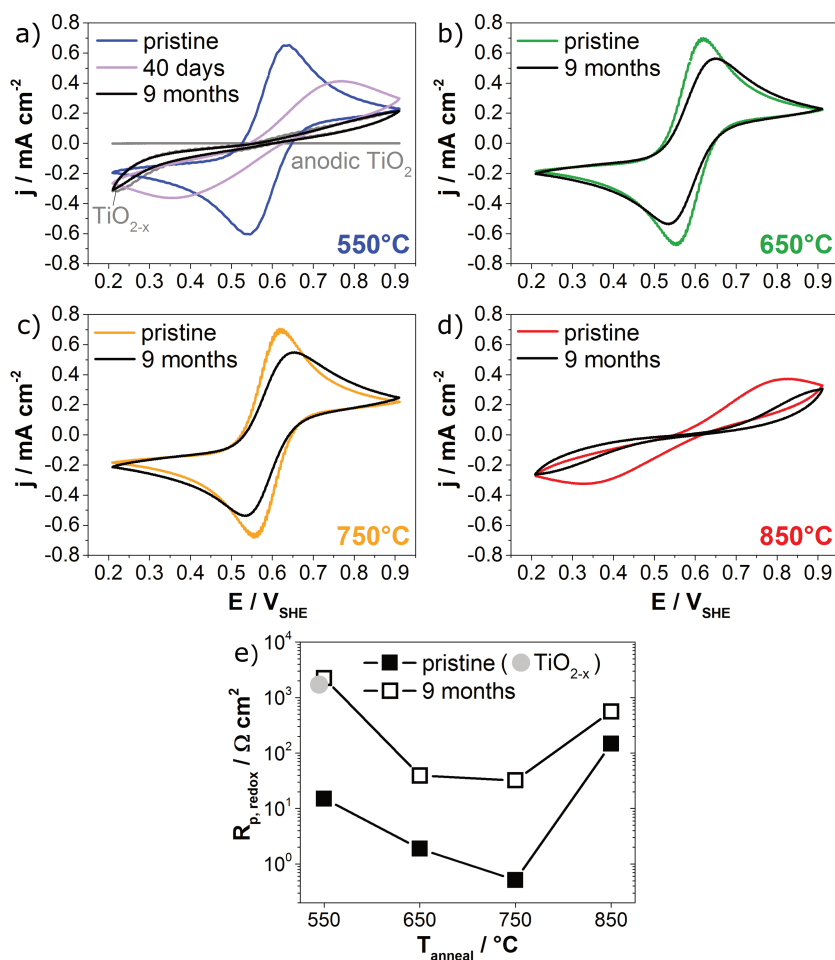


Fig. 75: Outer sphere charge transfer kinetics at pristine TiOC, air aged TiOC and reference films. Each 20th CV scan acquired at a scan rate of 50 mV s^{-1} for a) TiOC_{550} , as-grown anodic TiO_2 and TiO_{2-x} , b) TiOC_{650} , c) TiOC_{750} and d) TiOC_{850} . The duration of air aging is indicated in the legends. e) Area specific polarization resistance against the redox reaction, $R_{p,\text{redox}} = R_{\text{ct}} + R_{\text{por}}$, versus TiOC annealing temperature. $R_{p,\text{redox}}$ is determined from EIS fits using the models EEC 1 and EEC 2 shown in Fig. 67. Electrolyte: 0.1 M H_2SO_4 with each 2.5 M $\text{K}_3[\text{Fe}(\text{CN})_6]$ and $\text{K}_4[\text{Fe}(\text{CN})_6]$. Adapted from [251] © 2017 Wiley-VCH Verlag GmbH & Co. KGaA, Weinheim.

After TiOC aging in air for 9.0 ± 0.1 months, the reaction kinetics of $\text{Fe}(\text{CN})_6^{3-}$ and $\text{Fe}(\text{CN})_6^{4-}$ are clearly reduced, as can be deduced from the enhanced peak separations and lower anodic and cathodic peak current densities in the black CVs shown in Fig. 75. The anodic peak current densities measured for aged

TiOC₆₅₀ and TiOC₇₅₀ drop to $79.6 \pm 0.3\%$ and $76.9 \pm 0.3\%$ of the respective initial values, and the peak separation is almost twice as large as that found for the pristine films, evidencing a lower electrode activity and irreversible electron transfer kinetics at the aged electrodes. In the case of TiOC₅₅₀, the anodic peak current density drops to $64.5 \pm 0.7\%$ of the initial value at an age of 40 days. Therewith, aging of TiOC₅₅₀ for 40 days yields already a significantly lower electrode activity than aging for ~ 9 months does in the case of TiOC₆₅₀ and TiOC₇₅₀. From a comparison of the CVs of pristine and aged TiOC, the lowest electron transfer activities are deduced for TiOC₅₅₀ and TiOC₈₅₀ that have been exposed to air for ~ 9 months. Moreover, also after aging in air, TiOC₈₅₀ is not electrochemically stable in the investigated potential range. These findings are in line with the changes observed for the polarization resistance against the redox reaction upon aging (Fig. 75e). For all TiOC, $R_{p,\text{redox}}$ is significantly enhanced after aging for ~ 9 months, and experiences the strongest change for TiOC₅₅₀, namely by a factor of 150. The lowest $R_{p,\text{redox}}$ values after aging are measured for TiOC₇₅₀ and TiOC₆₅₀, followed by TiOC₈₅₀. The highest value is found for TiOC₅₅₀, and it exceeds the one of pristine TiO_{2-x} which indicates a significant loss of TiO_x species in the TiOC₅₅₀ film.

In summary, the EC results show that aging of TiOC in air leads to an inhibition of the electron transfer across the electrode/electrolyte interface, which appears to be most severe for TiOC₅₅₀. Based on the previously found correlation between electrode activity and concentration of reduced titania species at the surface (Fig. 68a), the decreased electron transfer rates at air aged TiOC electrodes can be mainly ascribed to the enhanced fraction of TiO₂ (Fig. 73). Noteworthy, 40 days old TiOC₅₅₀ has a higher interfacial conductivity than as-grown anodic TiO₂, although XPS reveals essentially identical surface compositions already after 12 days aging of TiOC₅₅₀. This indicates that the 40 days aged TiOC₅₅₀ film is still sufficiently conductive and at the most covered by a very thin resistive oxide layer. The steadily increasing polarization resistance against the redox reaction with prolonged air exposure of TiOC₅₅₀ can then be ascribed to an increasing thickness and/or resistivity of this oxide layer.

4.4.3 The effect of air aging on the electrochemical stability of TiOC in acidic electrolyte

As in the case of the pristine TiOC (section 4.3), the stability of the aged TiOC films against passivation/corrosion has been studied with potential step EIS experiments in combination with chronoamperometry in 1.0 M HClO₄. From fits of the EIS data, the potential-dependent polarization resistance R_p has been determined. In addition, the measured capacitive impedance has been used to perform Mott-Schottky analysis.

Fig. 76 shows the current density-time profiles of 9 months old TiOC, obtained by chronoamperometry at each potential step prior to an EIS measurement. Electrochemical surface oxidation is indicated by an anodic current peak prior to an exponential decay with time during the first seconds of a potential step. As can be seen in the current-time transients of aged TiOC₅₅₀, there is a more or less pronounced current peak at every potential step between -0.06 and 0.94 V, which makes it difficult to identify the onset of surface reoxidation. Latest with the detection of anodic steady state currents at ~ 0.74 V, passivation of the surface becomes relevant. In the case of the other aged films, surface reoxidation appears to start first on aged TiOC₈₅₀, at ~ 0.54 V, and later on aged TiOC₆₅₀ and TiOC₇₅₀, at ~ 0.74 V. Comparison with the current-time transients of the pristine films in Fig. 69 suggests that surface reoxidation of the 9 months old TiOC initiates at lower anodic potentials, which points to a lower electrochemical stability of the aged films.

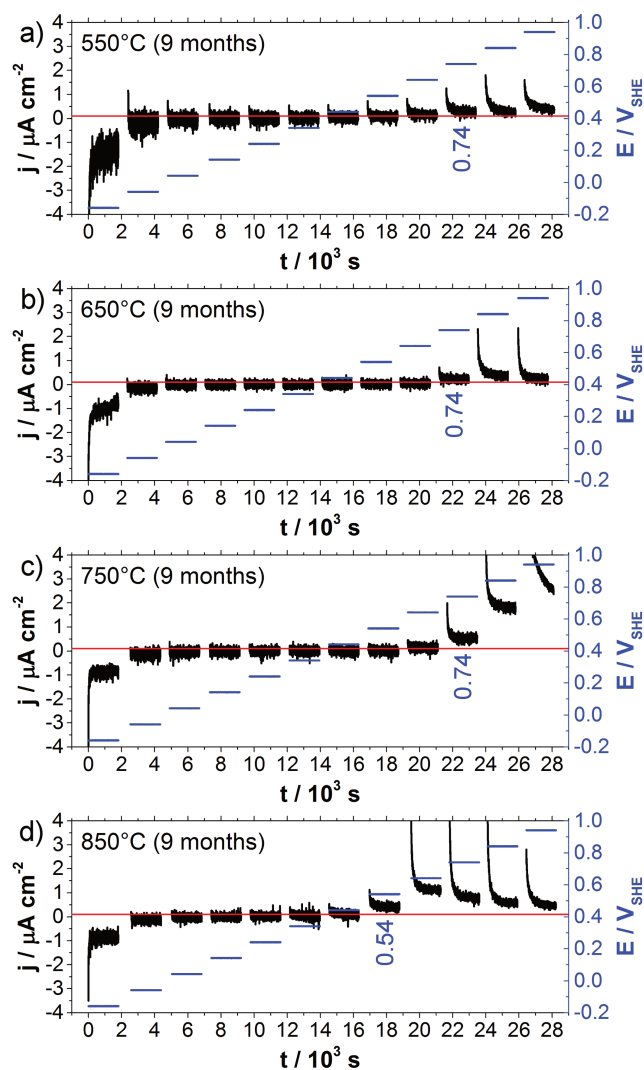


Fig. 76: Current density-time profiles of 9 months old a) TiOC_{550} , b) TiOC_{650} , c) TiOC_{750} and d) TiOC_{850} acquired at each potential step prior to EIS. The values of the approximate onset potentials of corrosion are given in the graphs. Electrolyte: 1.0 M HClO_4 . Adapted from the supporting information of [251].

Anodic steady state current densities of $j > 0.1 \mu\text{A cm}^{-2}$, ascribed to continuous passivation and/or corrosion of the TiOC electrodes, start to be first observed at $\sim 0.54 \text{ V}$ for TiOC_{850} , and at $\sim 0.74 \text{ V}$ for TiOC_{550} , TiOC_{650} and TiOC_{750} . Compared to the findings made for the pristine films prepared at 650, 750 and 850 °C, the threshold potentials up to which corrosion of the respective aged TiOC films is negligible, are about $\sim 0.1 \text{ V}$ lower. This result suggests that reoxidation in air does not improve the corrosion stability of these films. In the case of TiOC_{550} , aging in air does not notably alter the threshold potential. At 0.94 V, only TiOC_{750} produces very high current densities, which do not reach steady state conditions during the chronoamperometric measurement.

The EIS spectra of the TiOC films that have been exposed to air for 9 months are plotted in Fig. 77, together with the EEC models used for the fits. As in the case of the pristine TiOC electrodes (Fig. 70), the EIS data of aged TiOC_{650} , TiOC_{750} and TiOC_{850} can be best reproduced by a fit based on the model EEC 3, and that of aged TiOC_{550} by a fit using the model EEC 4. Apparently, also the aged TiOC_{550} film is characterized by a cross-sectional heterogeneity in electronic properties, which gives rise to an additional time constant in the impedance spectra, as evidenced by the exceptional trend in the Bode phase (Fig. 77d-f). Since after

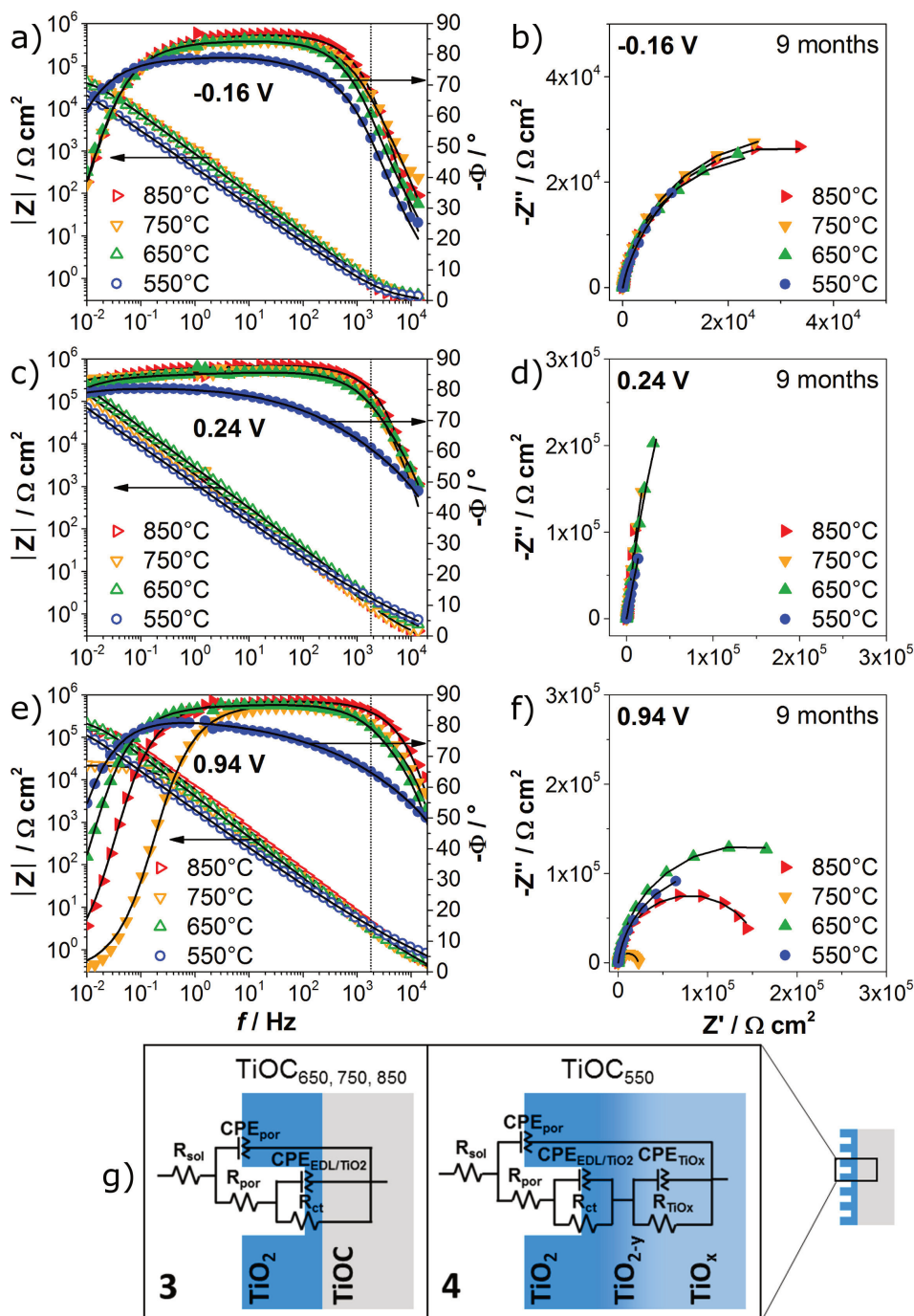


Fig. 77: EIS analysis of 9 months old TiOC in 1.0 M HClO₄. Bode (left) and Nyquist (right) diagrams of EIS data acquired at (a,b) -0.16 V, (c,d) 0.24 V and (e,f) 0.94 V with fit curves. Dotted lines in (a,c,e): $f = 1.8$ kHz, at which $-Z''$ was extracted to generate Mott-Schottky plots. g) EEC models used for the fits and schemes of the multi-layered film structure showing one nanopore of the outer oxide layer. Adapted from [251] © 2017 Wiley-VCH Verlag GmbH & Co. KGaA, Weinheim, and the associated supporting information.

aging for 12 days there is no TiC detected in TiOC₅₅₀ with XPS (Fig. 73), the additional time constant in the impedance spectra (represented by R_{TiOx} and CPE_{TiOx} in EEC 4) may be ascribed to a pronounced gradient in the concentration of oxygen vacancies, which is increasing from the near surface region towards the bulk of the film, as illustrated in the right scheme in Fig. 77g.

Fig. 78 depicts the polarization resistance-potential curves of TiOC films that have been exposed to air for ~ 9 months. They show similar trends as those obtained for the pristine TiOC electrodes (Fig. 71). In particular,

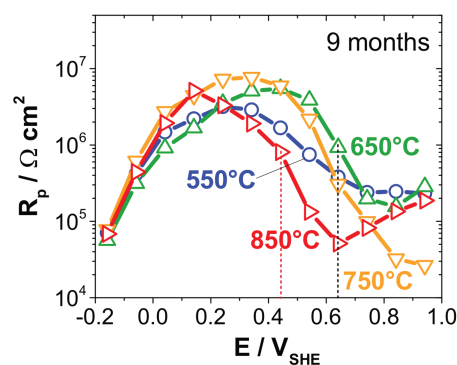


Fig. 78: Area specific polarization resistance of aged TiOC in 1.0 M HClO₄ versus dc potential, determined from EIS fits. Vertical dashed lines: threshold potentials up to which anodic current densities are $\leq 0.1 \mu\text{A cm}^{-2}$. Adapted from [251] © 2017 Wiley-VCH Verlag GmbH & Co. KGaA, Weinheim.

R_p of aged TiOC₈₅₀ increases again above ~ 0.64 V, the curve of aged TiOC₅₅₀ approaches a plateau toward the anodic potential limit, and the polarization resistance of aged TiOC₇₅₀ drops significantly at high anodic potentials, reaching a value of less than $\sim 3 \times 10^4 \Omega \text{ cm}^2$ at 0.94 V. Different from the trend found for pristine TiOC₆₅₀, the polarization resistance of aged TiOC₆₅₀ is increasing above ~ 0.84 V, indicating the formation of a more protective oxide film. At 0.94 V, the lowest R_p value among the aged films is observed for TiOC₇₅₀, and the polarization resistances of the other TiOC assume similar magnitudes. It should be remarked that even at potentials where the electrodes are most stable, and in particular where corrosion processes can be neglected, the polarization resistances of the aged TiOC do not show any correlation with the annealing temperature, as it was found for the pristine films (Fig. 71), nor with the chemical surface composition. This observation suggests that aging in air has a considerable impact on the films' physicochemical properties that determine their electrochemical stability, which is most likely not only the chemical composition.

Fig. 79 shows the Mott-Schottky diagrams of the interfacial capacitances of ~ 9 months old TiOC, measured at a frequency of $f = 1.8$ kHz. For comparison, the respective data of an as-grown anodic TiO₂ film are included in the graph. Similar to the observations made for the pristine TiOC films, the Mott-Schottky curves of all four aged TiOC films are flat compared to that of the as-grown anodic TiO₂. This is in agreement with the detected redox CVs, which show non-zero current densities in the cathodic and anodic going potential sweep, although the charge transfer resistance of all TiOC is considerably increased after aging (Fig. 75).

From the trends of the Mott-Schottky curves observed in Fig. 79b it can be inferred that at sufficiently anodic potentials beyond the onset of considerable anodic current densities, a semiconducting oxide film is growing on the aged TiOC, as in the case of the pristine TiOC. The slope of the Mott-Schottky curves of TiOC₆₅₀ and TiOC₈₅₀ starts to increase at somewhat lower anodic potentials after air exposure for ~ 9 months, which is in agreement with the trend of the polarization resistances. At 0.94 V, the current density measured at aged TiOC₇₅₀ does not reach steady state conditions so that it is difficult to ascribe the enhanced value of the inverse square capacitance to a considerably thicker passive film on the surface. EIS in presence of Fe(CN)₆³⁻/Fe(CN)₆⁴⁻ suggests that any oxide film that has electrochemically formed on aged TiOC₇₅₀ upon polarization to 0.9 V is sufficiently thin or highly doped so that it does not affect outer sphere electron transfer. The inverse square capacitances measured for aged TiOC₆₅₀, TiOC₇₅₀ and TiOC₈₅₀ are almost independent of potential in the respective potential ranges, where no steady state current densities are measured (Fig. 76). This observation corresponds to the findings made for all pristine TiOC. In contrast, the Mott-Schottky curve

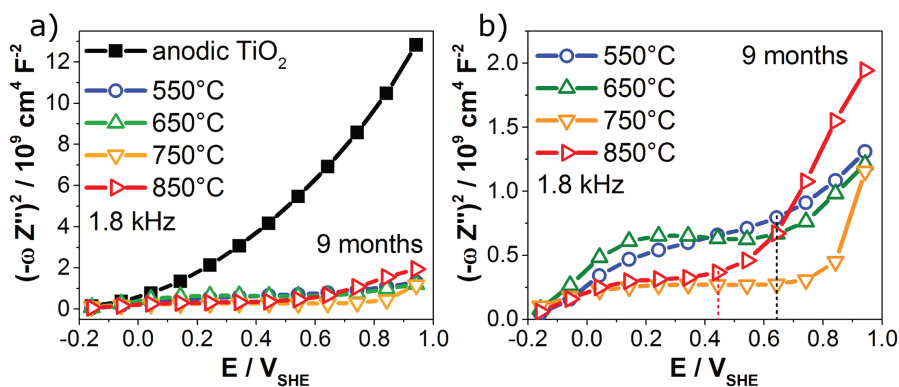


Fig. 79: Mott-Schottky diagrams of anodic TiO_2 and of 9 months old TiOC. Area specific $(-\omega Z''')$ values extracted from potential step EIS in 1.0 M HClO_4 at a frequency of 1.8 kHz (see dotted lines in Fig. 70), versus dc potential. b) Enlargement of a), showing only the data of TiOC. Vertical dashed lines in b): threshold potentials up to which anodic current densities are $\leq 0.1 \mu\text{A cm}^{-2}$.

of ~ 9 months old TiOC_{550} is slightly inclined over the entire potential range, which indicates semiconducting properties and therewith a lower conductivity of this film. This conclusion is in line with the exceptionally high polarization resistance against the redox reaction at aged TiOC_{550} (Fig. 75), and can be ascribed to the formation of a doped oxide layer on the surface upon air exposure, that is sufficiently thick, as suggested by XPS analysis (Fig. 73), to be detected electrochemically.

A comparison between the EC results obtained for pristine and aged TiOC in 1.0 M HClO_4 and those obtained in presence of $\text{Fe}(\text{CN})_6^{3-}/\text{Fe}(\text{CN})_6^{4-}$ reveals the effect of air aging on the passivation/corrosion behavior of the TiOC films and the consequent impact of the formed passive layers on the electrodes' activity towards outer sphere charge transfer.

As in the case of the pristine film, passivation/corrosion of aged TiOC_{850} sets in at relatively low anodic potentials leading to the formation of a considerably protective oxide film on the surface (Fig. 71, Fig. 72, Fig. 78, Fig. 79). On both, the pristine and aged electrode, the formation rate of this passive film at 0.9 V seems to be lower than the scan rate used to acquire the CVs in presence of $\text{Fe}(\text{CN})_6^{3-}/\text{Fe}(\text{CN})_6^{4-}$, which causes a successive increase of the redox peak separations during potential cycling (Fig. 66). The presented results indicate that the polarization resistance of TiOC_{850} against the redox reaction is affected by both aging in air and electrochemical passivation during the EC measurements.

Although stable redox CVs are detected for pristine and aged TiOC_{550} , TiOC_{650} and TiOC_{750} (Fig. 66, Fig. 75), the multilayered passive films that form on pristine and aged TiOC_{550} as well as on aged TiOC_{650} at potentials above ~ 0.84 V are sufficiently resistive (Fig. 71, Fig. 78) to affect the impedance response of these electrodes in presence of the redox probe (Fig. 74). However, since similar R_p -potential curves are obtained for pristine and aged TiOC_{550} (Fig. 71, Fig. 78), the high activity loss of TiOC_{550} upon aging mainly originates from the surface reoxidation in air and not from the anodic oxidation in the electrolyte. On the other hand, aging of TiOC_{650} appears to significantly affect its passivation/corrosion behavior, leading to the formation of a relatively protective passive film above ~ 0.84 V (Fig. 78). As a consequence, both reoxidation during air exposure and during anodic polarization in acidic electrolyte contribute to the lower electron transfer kinetics at aged TiOC_{650} (Fig. 74). Only in the case of TiOC_{750} , neither the pristine nor the aged film suffer from an additional activity loss due to passivation/corrosion. Any oxide layer that is forming on pristine and aged

TiOC₇₅₀ during the EC measurements is characterized by a low protection and resistivity, as evidenced by the low polarization resistances above 0.84 V (Fig. 71, Fig. 78), and does therewith not contribute to the electrodes' resistance against outer sphere charge transfer, as deduced from the EIS measurements with the redox couple (Fig. 74). Hence, the lower activity of aged TiOC₇₅₀ can be directly attributed to modifications of the physicochemical properties upon aging, in particular surface reoxidation in air.

5. Ti substrate grain effects on physicochemical properties of TiOC

So far, only the average physicochemical and electrochemical properties of TiOC films on polycrystalline Ti substrates have been investigated. From the SEM and AFM images shown in the last chapter it is apparent, that the grains of the polycrystalline Ti substrate affect the topography and morphology of the TiOC films. For applications in electrocatalysis, variations in the local physicochemical properties of TiOC materials can have significant effects on their behavior as catalyst supports. To analyze the chemical and crystalline phase composition of TiOC films on top of individual substrate grains, spectro-microscopic techniques are required. This chapter comprises the results of a detailed study, where the local properties of TiOC films, obtained through carbothermal treatments of anodic TiO_2 at different temperatures, are examined with SEM, scanning photoelectron microscopy (SPEM) and micro-Raman spectroscopy. Through comparison of these data with EBSD maps of the Ti substrate, substrate grain orientation effects on the carbothermal conversion of anodic TiO_2 into titanium oxycarbide phases are deduced.

In the first section, a study of TiOC films that are obtained through carbothermal treatment at 550°C is presented. As shown in the previous chapter, anodic film conversion at such a low annealing temperature yields highly instable oxycarbide phases that eventually decompose into a C/ TiO_2 composite. However, composite materials of titania and graphitic carbon, and their optimized synthesis are highly interesting for application in sustainable energy conversion and storage, so that a closer look on this system is considered to be of great value. It is found that the amount of generated carbon and the grade of anodic film crystallinity correlate with the crystallographic orientation of the Ti substrate grains. On top of Ti grains with the (0001) plane parallel to the substrate surface, the anodic TiO_2 exhibits the highest grade of crystallinity, and the C/ TiO_2 composite contains the highest fraction of graphitic carbon compared to Ti grains with other orientations. This indirect effect of the Ti substrate grain orientation yields new insights into the activity of TiO_2 towards the decomposition of carbon precursors.

In Chapter 4 it was found that the physicochemical and electrochemical properties of carbothermally produced TiOC films is crucially affected by the employed synthesis temperature. To gain a deeper understanding and control of the synthesis of such TiOC systems, it is therefore necessary to consider both substrate grain orientation and annealing temperature. For that purpose, a set of anodic films, carbothermally treated at 550, 650, 750 and 850°C , was investigated using the same microscopic multitechnique approach. The respective results are presented in the second section of this chapter. The different annealing temperatures are found to yield different substrate grain-dependent chemical compositions, structures, and morphologies. In particular, individual time scales for the carbothermal conversion and subsequent surface reoxidation on substrate grains of a given orientation are revealed.

5.1 Preparation of TiOC films and a $\text{TiO}_2^{\text{ref}}$ reference system

The samples that were prepared for SEM and the micro-Raman spectroscopy experiments had the same geometry, namely round disks of 1 mm thickness and 15 mm diameter, as those that were used for the electrochemical characterization reported in sections 4.3 and 4.4 of the previous chapter. For the SPEM experiments, the diameter of the Ti substrate disks had to be lowered to 10 mm to fit the sample holder. Both, the larger and smaller diameter disks were cut from the same precursor Ti rod. On the polished side, a disk of

8 mm (on the 10 mm samples) or 14 mm (on the 15 mm samples) was electrochemically polished and anodized. For the carbothermal treatments, two different reactor tubes were used and the gas flow rates were optimized for each reactor geometry to obtain comparable chemical surface composition of the films, as verified by XPS (not shown). To prepare the larger samples (15 mm diameter), a reactor tube of 40 mm diameter was used, and the following annealing procedure was applied:

- (i) purging for two hours with 750 sccm Ar to remove air,
- (ii) heating to the desired annealing temperature T during 90 min at a constant rate in 200 sccm Ar,
- (iii) dwelling for 60 min at T ,
- (iv) addition of 0.5 flow% (i.e. 1.0 sccm) of acetylene for 5 min,
- (v) dwelling for 60 min at T in Ar, and
- (vi) switching off the oven to let it cool down to room temperature.

To prepare the smaller samples (10 mm diameter), a reactor tube of 15 mm diameter was used, and the following annealing procedure was applied:

- (i) purging for one hour with 750 sccm Ar to remove air,
- (ii) heating to the desired annealing temperature T during 90 min at a constant rate in 50 sccm Ar,
- (iii) dwelling for 55 min at T ,
- (iv) addition of 0.2 flow% (i.e. 0.1 sccm) of acetylene for 10 min,
- (v) dwelling for 60 min at T in Ar, and
- (vi) switching off the oven to let it cool down to room temperature.

For the study presented in the first section, two types of films were synthesized and investigated: C/TiO₂ composite films and a reference film, TiO₂^{ref}. The composite films were obtained through carbothermal treatments at 550 °C. The reference film TiO₂^{ref} (15 mm substrate) was obtained through thermal treatment at 550 °C in 200 sccm Ar without C₂H₂ according to the sequence (i)-(ii)-(v)-(vi) in the larger reactor tube. For the study, presented in the second section, TiOC films were prepared at 550, 650, 750 and 850 °C.

5.2 Ti substrate grain dependent C/TiO₂ composites through carbothermal treatment of anodic TiO₂ at 550 °C

The study presented in this section was published by Rüdiger et al. in 2016.¹¹⁸ Note that the labels and definitions used here have been harmonized with those used in [259], the results of which are presented in the second section of this chapter.

5.2.1 Identification of substrate grain orientations from EBSD maps and optical appearance of anodic TiO₂ and thermally treated oxide films

The crystallographic orientations of the Ti substrate grains were determined with EBSD, which yields the three Euler angles φ_1 , Φ and φ_2 of the hexagonal unit cell with respect to the substrate surface (see Fig. 20). The obtained Euler angles were used to generate crystalline orientation maps of the Ti_{poly} substrates, which will be represented as surface-normal projected inverse pole figure (IPF) orientation maps (short EBSD maps) in the following. EBSD and optical microscopy were used to generate a correlation map between the Ti substrate grain orientation and the optical appearance of the anodic oxide film, as well as the optical appearance of the TiO₂^{ref} and C/TiO₂ films, which is illustrated in Fig. 80.

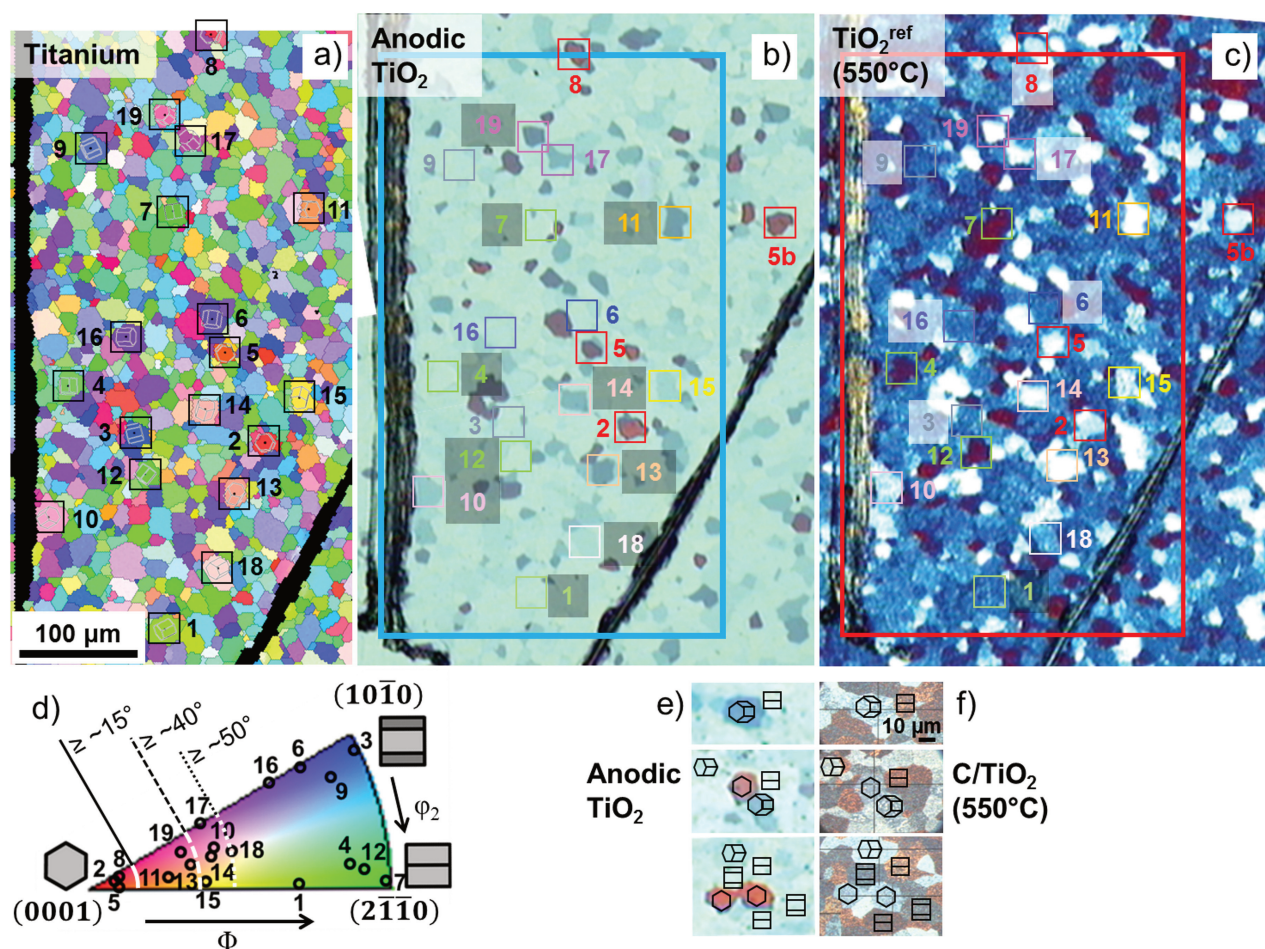


Fig. 80: Correlation between optical appearance of prepared films and substrate texture. a) EBSD map of a Ti substrate; optical micrographs of the surface area shown in a): b) after anodization, and c) after annealing at 550 °C without acetylene. d) standard triangle of the surface-normal projected inverse pole figure orientation map (EBSD map) with numbers of the studied grains, ranges of tilt-angles Φ and the low index projected hexagonal cells. Optical micrographs of anodic film e) prior to and f) after carbothermal treatment with acetylene, with projected hexagonal cells. Adapted from [118] and electronic supplementary information - Published by the PCCP Owner Societies.

According to ellipsometry measurements, the fresh anodic TiO₂ film has an average thickness of ~ 53 nm.²⁶⁰ The comparison between Fig. 80a and b reveals that the interference colors of the anodic TiO₂ are strongly affected by the orientation of the Ti substrate grains. In particular, the substrate tilt angle Φ has an important impact on the optical properties of the oxide film. Variations in interference properties are directly related to

variations in the TiO₂ film thickness. Under the applied synthesis conditions, dark colors correspond to thinner films (red), and bright colors to thicker TiO₂ films (bright blue).^{61,195} It is possible to identify four ranges of substrate tilt angles Φ that cause notably different interference colors of the pristine anodic oxide film. These are indicated in the standard triangle of the EBSD map in Fig. 80d. Due to the symmetry of the oxide film thickness on individual grains towards rotation about the surface normal, the corresponding orientation angle φ_1 does not affect the interference color of the anodic TiO₂. The azimuthal substrate orientation, described by φ_2 , seems to have only a minor effect on the interference colors of the anodic film. A close look to Fig. 80b reveals slightly different interference colors for the anodic films on top of some Ti grains with similar tilt angles Φ but very different azimuthal orientations (φ_2): grain 19 ($\Phi = 36.3^\circ$, $\varphi_2 = 8.8^\circ$), for example, appears darker than grain 11 ($\Phi = 30^\circ$, $\varphi_2 = 22.3^\circ$) although its tilt angle is slightly larger. The same observation holds for grain 17 ($\Phi = 46.4^\circ$, $\varphi_2 = 0.3^\circ$) when compared to grain 15 ($\Phi = 42.6^\circ$, $\varphi_2 = 27^\circ$). Since this color variation is very small, and due to the major impact of the tilt angle, it is not possible to deduce the azimuthal orientation from the optical appearance of the as-prepared anodic oxide film. However, the variation in interference colors due to an effect of φ_2 brings about an error for the Φ -values that are estimated only from the optical appearance of the oxide film, which is about $\pm 5^\circ$.

As can be seen from Fig. 80c and f, the optical appearance of the oxide film has changed significantly after the thermal treatments at 550 °C. This can be attributed to color centers in the TiO₂ caused by oxygen vacancies that are generated during the annealing in reducing atmosphere.²³ As a consequence of this effect, the two orientations $\sim\text{Ti}(10\bar{1}0)$ ($\varphi_2 \sim 0^\circ$) and $\sim\text{Ti}(2\bar{1}\bar{1}0)$ ($\varphi_2 \sim 30^\circ$) can be deduced by consideration of the optical appearance of the thermally treated oxide film. The comparison between Fig. 80c and e shows that both films, C/TiO₂ and TiO₂^{ref}, have the same optical characteristics. The thermally treated films have a red color on $\sim\text{Ti}(2\bar{1}\bar{1}0)$ oriented grains (see e.g. grains no. 4, 7 and 12 in Fig. 80c), which allows to differentiate these grains from all other grains with $\Phi \gtrsim 50^\circ$. On $\sim\text{Ti}(10\bar{1}0)$ oriented grains, the films appear dark blue.

Table 5.1: Ranges of Ti substrate orientations and assignment of labels and representative projected hexagonal cells. Based on the definitions in [118] and [259].






Ti tilt angle	$0^\circ \leq \Phi \leq 15^\circ$	$15^\circ \leq \Phi \leq 40^\circ$	$40^\circ \leq \Phi \leq 50^\circ$	$50^\circ \leq \Phi \leq 90^\circ$	
interference color TiO ₂	dark red (thin TiO ₂)	dark violet/ dark blue	blue	bright blue (thick TiO ₂)	
Ti azimuthal orientation		$0^\circ \leq \varphi_2 \leq 30^\circ$		$0^\circ \leq \varphi_2 \leq 15^\circ$	$15^\circ \leq \varphi_2 \leq 30^\circ$
color C/TiO ₂	bright blue	bright blue - white		dark blue	(dark) red
Ti(<i>hkil</i>)	$\sim\text{Ti}(0001)$			$\sim\text{Ti}(10\bar{1}0)$	$\sim\text{Ti}(2\bar{1}\bar{1}0)$
EBSD map colors	red	pink - orange	purple - yellow	blue	green
label	A	B	C	D	E
representative hexagonal cell					

Table 5.1 lists the identified ranges of Ti substrate orientations, which have a visible effect on the optical appearance of the anodic TiO₂ film and of the thermally treated films, and the assigned labels and representative surface projected hexagonal cells used in this study. This substrate grain effect allows an

estimation of the substrate orientation without the necessity of an EBSD measurement, as done in Fig. 80e and f.

In the following, the main focus will be on the correlation of local physicochemical properties of planar C/TiO₂/Ti_{poly}, obtained by (spectro-)microscopic techniques, with the tilt angle Φ of the Ti substrate grains. The restriction to Φ is motivated by studies of the TiO₂/Ti_{poly} system reported in the literature, which suggest that variations of the substrate tilt angle have a stronger influence on many physical and (electro-)chemical properties of anodic TiO₂ than the c-azimuthal orientation (represented by φ_2).^{57,58,60}

5.2.2 Potentials and limitations of micro-Raman spectrometry for chemical and structural analysis of thermally treated TiO₂ on polycrystalline Ti

For the present study, the crystalline phases and the chemical composition of C/TiO₂/Ti_{poly} and TiO₂^{ref}/Ti_{poly} films were investigated with micro-Raman spectroscopy. The focused laser beam had a lateral size of $\sim 5 \mu\text{m}$, whereas the studied grains had a size of 10–20 μm , which enabled to measure an averaged Raman response of the films on top of single substrate grains. Furthermore, with the used laser wavelength of 532 nm, the penetration depth was much larger than the C/TiO₂ and TiO₂^{ref} film thickness, so that the Raman signal originated from the entire films: Based on the extinction coefficient for anodic TiO₂ reported in [261], and using equation 2.102, the laser penetration depth into the thermally treated TiO₂ film can be estimated to be larger than 4 μm . The penetration depth into graphite was reported to be about 50 nm for $\lambda = 532 \text{ nm}$.²⁶² The herein analyzed C/TiO₂ composite film consists of a few nm thick layer of graphitic carbon (see below) on top of a $\sim 53 \text{ nm}$ thick thermally treated anodic TiO₂ film. The Ti substrate is not Raman active due to its metallic nature, where the free electrons undergo plasma-like oscillations under laser illumination, thus preventing lattice vibrations. Therefore, Raman spectroscopy allowed to extract structural and compositional information of the entire C/TiO₂ composite and the TiO₂^{ref} film on top of individual substrate grains. In particular, the Raman signal intensity is proportional to the amount of the detected species. However, care needs to be taken when attempting a quantitative interpretation of Raman spectra, since the number of Raman scatterers (e.g. a particular phase) is not the only quantity that affects Raman band intensities.

5.2.2.1 Effect of preferential orientation of crystalline phases in C/TiO₂ and TiO₂^{ref} on band intensities

Due to their tetragonal crystallographic structure, anatase and rutile TiO₂ are anisotropic Raman scatterers. Therefore, Raman bands of one symmetry are enhanced or suppressed compared to bands of other symmetry, depending on the orientation of the principal axis of the scatterer with respect to the polarization of the excitation laser beam.^{263,264} The excitation laser used in the present study was slightly polarized (note that no polarizer was used), so variations in relative band intensities are likely to occur in case of a locally varying preferential orientation of crystalline TiO₂ phases in the investigated films. To estimate the extent of preferential crystallite orientation in the thermally treated oxide films, and the consequent effects on the Raman response, two natural anatase TiO₂ crystals with polished surfaces oriented parallel to the (001) and to the (100) plane were studied as reference systems. Furthermore, they provided a standard for highly crystalline anatase TiO₂. In the case of the (100)-oriented crystal, two Raman spectra were acquired, whereby the crystal was positioned under the Raman microscope with two azimuthal orientations differing from each

other by $\sim 90^\circ$. The same was done for selected grains of the TiO₂^{ref} and the C/TiO₂ films.

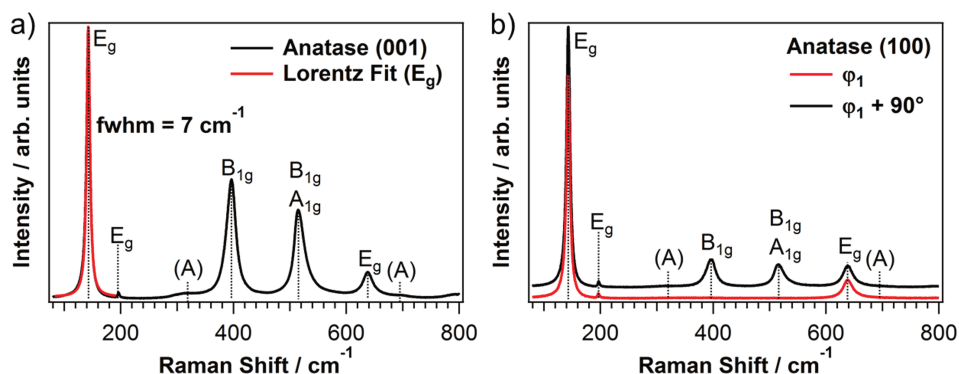


Fig. 81: Raman spectra of natural anatase crystals with oriented polished surfaces. The six Raman active modes are labeled with their irreducible representations, and the two combination bands with (A). a) incident laser normal to (001) surface; red: Lorentzian peak fit. b) incident laser normal to (100) surface; spectra taken at two azimuthal orientations with respect to the microscope that differ by $\sim 90^\circ$. For clarity, the black spectrum is shifted upwards. Laser wavelength: 532 nm. Adapted from [118] and electronic supplementary information - Published by the PCCP Owner Societies.

Fig. 81 depicts the Raman responses of the oriented anatase crystals, obtained with the polished (001) and (100) surfaces normal to the incident laser. Anatase TiO₂ has six Raman active modes.²⁶⁴ Due to the high proximity of the A_{1g} band and the high frequency B_{1g} band, they appear as one peak at 517 cm⁻¹. The weak shoulders at ~ 320 cm⁻¹ and ~ 695 cm⁻¹ can be attributed to combination bands of the anatase spectrum due to second-order Raman scattering.²⁶⁴ In Fig. 81a, the E_g band at 143 cm⁻¹ is fitted with a Lorentzian function which yields a FWHM of 7 cm⁻¹. Due to the rotational symmetry of anatase with respect to its c-axis, any rotation of the (001)-oriented crystal about its surface normal underneath the microscope does not change the relative peak heights in the Raman spectrum (not shown). Depending on the azimuthal orientation of the (100) plane of anatase TiO₂ with respect to the microscope, two different Raman spectra are obtained, where in one case, only the E_g bands are present. Furthermore, the relative intensities of the A_{1g} and B_{1g} bands, compared to the intensities of the E_g bands, are higher for (001)- than for (100)-oriented anatase. Independent of the crystal orientation with respect to the laser polarization and the incident laser beam, all spectra are characterized by intense and sharp peaks, typical for extended single crystals.

Fig. 82 shows the Raman responses of TiO₂^{ref} and C/TiO₂ acquired on top of differently oriented substrate grains, where the Ti substrate had each two different azimuthal orientations relative to the Raman microscope. From Fig. 82a, and taking into account the reference spectra in Fig. 81, it becomes clear that there is a preferential orientation of the anatase TiO₂ phase in the TiO₂^{ref} film, which is more emphasized on top of \sim Ti(0001) substrate grains (red curves in Fig. 82a) compared to \sim Ti(10 $\bar{1}$ 0) substrate grains. Yet, the inset in Fig. 82a shows that the intensity variations of the E_g band (at 143 cm⁻¹) due to variations of the preferential orientation of the anatase crystallites in the film can be neglected with respect to the intensity variations of the Raman signals detected on top of differently oriented Ti substrate grains. Hence, it is possible to extract qualitative trends of the anatase content in TiO₂^{ref} as a function of the substrate orientation from the relative intensity of the respective Raman bands.

Also in the case of the C/TiO₂ film, the spectral region associated with Raman scattering at titania species (i.e. between 100 and 830 cm⁻¹) is affected by the azimuthal orientation of the film relative to the laser polarization

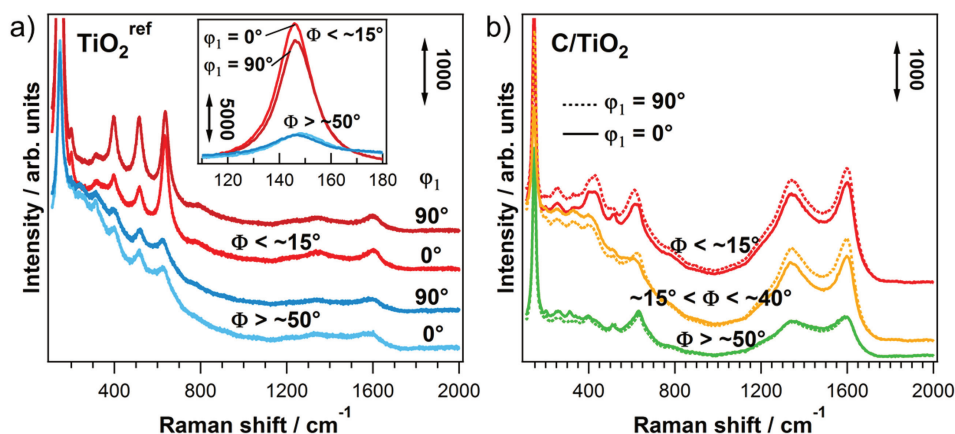


Fig. 82: a) Raman spectra of $\text{TiO}_2^{\text{ref}}$ acquired at two different azimuthal orientations of the substrate relative to the Raman microscope ($\varphi_1 = 0^\circ$ or 90°). Red: film on a $\sim\text{Ti}(0001)$ substrate grain; blue: film on a $\sim\text{Ti}(10\bar{1}0)$ substrate grain. Inset: magnification of the most intense E_g band. b) Raman spectra of C/TiO_2 acquired at $\varphi_1 = 0^\circ$ or 90° . Red: film on a Ti substrate grain with $\Phi \leq \sim 15^\circ$ ($\sim\text{Ti}(0001)$); orange: film on a Ti substrate grain with $\sim 15^\circ \leq \Phi \leq \sim 40^\circ$; green: film on a substrate grain with $\Phi \geq \sim 50^\circ$ ($\sim\text{Ti}(2\bar{1}\bar{1}0)$). Laser wavelength: 532 nm. Adapted from the electronic supplementary information of [118] - Published by the PCCP Owner Societies.

(Fig. 82b). Interestingly, the Raman signal of carbon-species, detected between 1000 and 1750 cm^{-1} ,²⁶⁵ appears to be slightly influenced by the azimuthal orientation of the substrate as well. One might speculate that this is due to a combined effect of surface topography (roughness) and anisotropic Raman scattering at disordered graphitic carbon.^{266,267} The exact reason cannot be clarified in the frame of this study. However, as can be seen in Fig. 82b, there is a pronounced variation in intensity of the carbon spectra detected for different substrate grain orientations, which cannot be explained by preferential orientation-effects and must instead be related to a varying amount of graphitic carbon on top of differently oriented substrate grains. In the following, the substrate grain effect on the amount of graphitic carbon on the surface of carbothermally treated anodic TiO_2 will be studied in detail.

5.2.3 Thermal treatment of anodic TiO_2 with acetylene at 550°C

Fig. 83 shows top-view scanning electron micrographs of the as-grown anodic TiO_2 and the C/TiO_2 composite film in the same area. Since the SEM images were acquired with a relatively high electron beam acceleration voltage (4 kV), a considerable fraction of the detected electrons originates from backscattering events at the Ti substrate underneath the films. Different substrate grain orientations become visible through contrast variations due to different backscattering efficiencies of differently oriented Ti. As a consequence, the grain boundaries of the underlying Ti substrate are clearly visible on both films (Fig. 83a and c). Morphological variations of the film surface are more apparent in the high magnification SEM images. The morphology of the anodic film varies for substrate grains with significantly different orientations (Fig. 83b), which is a well-studied phenomenon.⁶⁰ After the carbothermal treatment at 550°C , a granular film has formed on top of the anodic film (Fig. 83d). The morphology and the coverage of the deposit seem to be different on substrate grains with different orientations.

Fig. 84 shows micro-Raman spectra of C/TiO_2 for three ranges of Ti substrate tilt angles Φ . To exclude contributions from carbon contamination by secondary sources, no EBSD map was acquired of the electropolished Ti surface of this sample. In the spectral range between 100 and 830 cm^{-1} , all anatase

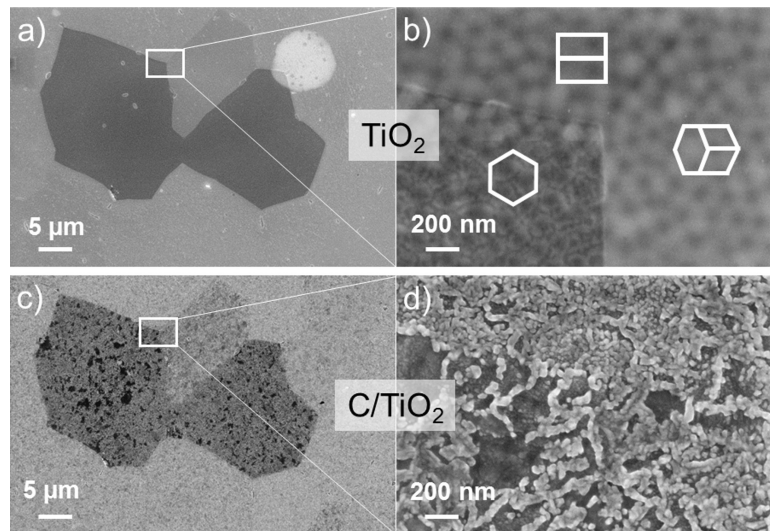


Fig. 83: SE micrographs of a selected area on the anodic TiO₂ film (a,b) and of the same area on the C/TiO₂ film (c,d), with hexagonal cells representing the Ti substrate grain orientations. SEM was performed with the InLens detector (electron beam acceleration voltage: 4 kV, working distance: 4–7 mm). Adapted from [118] - Published by the PCCP Owner Societies.

bands of first order Raman scattering and the two typically observed combination bands are detected (compare also with Fig. 81).²⁶⁴ The two most intense bands of rutile, E_g and A_{1g}, are present, as well as its most prominent combination band at ~ 235 cm⁻¹.²⁶³ Peaks found at ~ 267 cm⁻¹ and ~ 347 cm⁻¹ can be attributed to the most intense Raman signals of Ti₂O₃.^{268,269} The broad features between ~ 240 cm⁻¹ and ~ 395 cm⁻¹ cannot be clearly identified. The Raman spectra reveal that the oxide film contains crystalline domains of anatase and rutile and is partially reduced after the carbothermal treatment with C₂H₂.

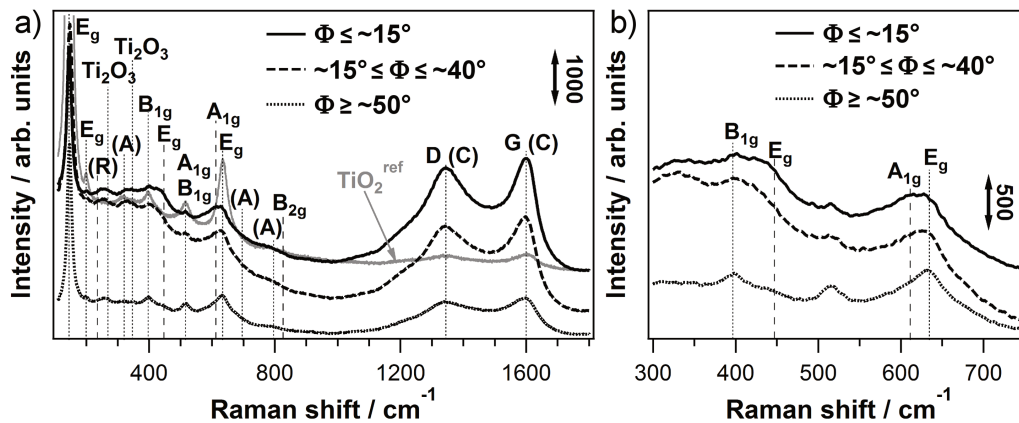


Fig. 84: Micro-Raman spectra of C/TiO₂/Ti_{poly} for different ranges of tilt angles Φ . For clarity, the spectra are shifted vertically. Gray spectrum in a): TiO₂^{ref} on Ti with $\Phi \leq 15^\circ$. Dashed lines: rutile bands, dotted lines: all other bands. D- and G-bands: from carbon (C). TiO₂ combination bands: (R) = rutile, (A) = anatase. b) Selected spectral range of a), where only each two neighboring anatase and rutile bands are indicated. Laser wavelength: 532 nm. a) Adapted from [118] - Published by the PCCP Owner Societies.

The spectra detected for different ranges of Φ clearly show that the phase composition of the C/TiO₂ film is affected by the underlying Ti substrate grain orientations. If preferential orientation effects can be neglected (see section 5.2.2.1), the fractions of crystalline anatase and rutile phases in the film can be deduced from the relative intensities of the corresponding Raman bands.²⁷⁰ A comparison between the most intense anatase

B_{1g} band ($\sim 399\text{ cm}^{-1}$) and the rutile E_g band ($\sim 447\text{ cm}^{-1}$), and between the rutile A_{1g} band ($\sim 612\text{ cm}^{-1}$) and the high frequency anatase E_g band ($\sim 639\text{ cm}^{-1}$), shown in Fig. 84b, indicates that there is considerably more rutile present in the thermally treated anodic TiO₂ film on top of grains with $\Phi \leq \sim 15^\circ$ than in the film on top of grains with $\Phi \geq \sim 50^\circ$. Grains with $\sim 15^\circ \leq \Phi \leq \sim 50^\circ$ exhibit mixed phase compositions.

All black spectra depicted in Fig. 84a show two strong broad peaks at $\sim 1348\text{ cm}^{-1}$ and $\sim 1600\text{ cm}^{-1}$ that are the characteristic D- and G-bands of carbon and can be attributed to nanocrystalline graphite (NCG).²⁶⁵ The Raman response of the C/TiO₂ composite film differs considerably from the spectrum of the reference sample (TiO₂^{ref}) that underwent a thermal treatment at 550 °C without addition of C₂H₂ (see gray spectrum in Fig. 84a). The intensities of the carbon bands are much lower in the case of TiO₂^{ref} than in the case of C/TiO₂, which evidences that the high amount of carbon in the latter film originates from the decomposition of acetylene and not from carbon contamination. Interestingly, the intensity of the carbon signals of C/TiO₂ appears to be influenced by the substrate grain orientation.

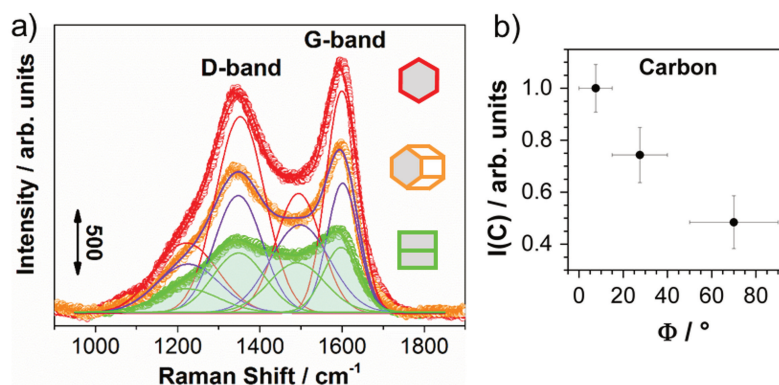


Fig. 85: a) Background-corrected micro-Raman spectra with four-peak Gaussian fits of carbon species detected in C/TiO₂ films on three differently tilted substrate grains. The signal intensity, $I(C)$, was determined by integration of the spectra, as indicated by the colored area in the green spectrum. b) Carbon signal intensity, normalized to the maximum value, versus substrate tilt angle Φ . Error bars of $I(C)$: standard deviations of $I(C)$ on grains within one Φ -range; error bars of Φ : ranges defined in table 5.1. Laser wavelength: 532 nm. Adapted from [118] and electronic supplementary information - Published by the PCCP Owner Societies.

Fig. 85a shows the background-corrected spectral regions of the carbon-related Raman signal of the C/TiO₂ film, that were acquired on top of three differently oriented substrate grains. A four-peak Gaussian fit was conducted and yields two peaks at $\sim 1348\text{ cm}^{-1}$ and $\sim 1600\text{ cm}^{-1}$ (D- and G-bands of carbon) and other two peaks at $\sim 1235\text{ cm}^{-1}$ and $\sim 1500\text{ cm}^{-1}$, which can be ascribed to minor modulations associated with the D- and G-bands,^{265,271} or to adsorbed long-chain polyenes with varying number of double bonds that can form upon interaction of C₂H₂ with TiO₂.²⁷²⁻²⁷⁴ The peak height ratio $H(D_1 + D_2)/H(G_1 + G_2)$ is about 0.7–0.8, independent of the substrate grain orientation, which corresponds to an average cluster size of about 6 nm according to the Tuinstra-Koenig relation.²⁶⁵ The overall intensity of the carbon-related signals, $I(C)$, determined by integration of the four corresponding Raman bands, provides a measurand for the quantity of carbon on the surface. In Fig. 85b the carbon band intensity is plotted versus the tilt angle Φ of the investigated Ti substrate grains. $I(C)$ decreases markedly with increasing substrate tilt angle. On top of substrate grains with $\Phi \leq \sim 15^\circ$, the intensity is about two times higher than on top of substrate grains with tilt angles $\Phi \geq \sim 50^\circ$.

SPEM was performed on the C/TiO₂ composite film to gain complementary information about the local chemical surface composition and its dependency on the Ti substrate grain orientation. The corresponding results are summarized in Fig. 86. It should be noted that only the region at the left of the dashed line in Fig. 86a coincides with the EBSD map that was acquired on the Ti substrate, which enables the identification of possible carbon contamination generated during the EBSD measurement. No change in contrast can be observed across the dashed line, which proves the absence of artefacts caused by the acquisition of the EBSD map. The grains investigated with SPEM are labeled according to the definitions in table 5.1. From Fig. 86 it can be seen that the chemical surface composition of the carbothermally treated film is considerably affected by the properties of the Ti substrate grains. In the chemical map shown in Fig. 86a brighter contrast corresponds to a relatively higher C 1s signal, evidencing an accordingly higher amount of carbon. The same areas that appear bright in the C/BG chemical map appear dark in the TiO₂/BG chemical map (Fig. 86b). This can be explained by the presence of a thicker carbon layer on top of the thermally treated anodic TiO₂ film in these areas, which attenuates the intensity of the Ti 2p_{3/2} core level photoelectrons. The film on the Ti substrate grain C, which is tilted by $\Phi = 46^\circ$, appears to be just at the transition from high to low carbon content, since it is barely distinguishable from the surrounding area of homogeneous shade in the chemical maps.

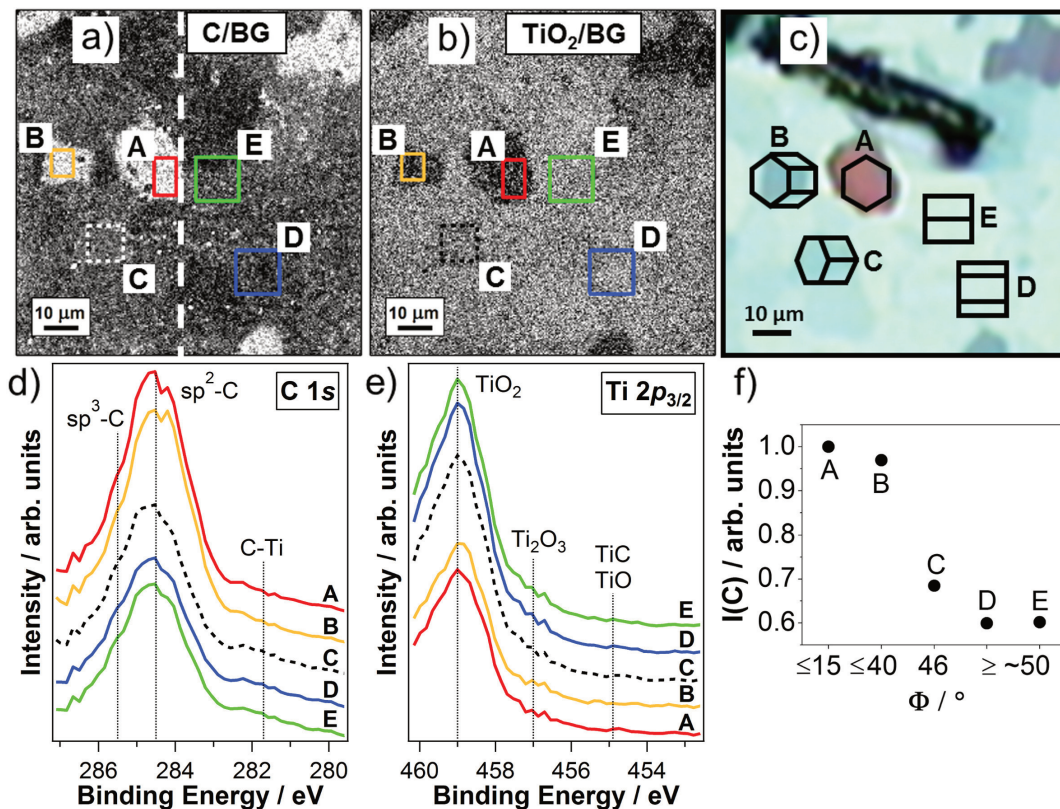


Fig. 86: Chemical maps of a) the C 1s and b) the Ti 2p_{3/2} core levels obtained by SPEM of a selected area of a C/TiO₂ film. c) Optical micrograph of the corresponding anodic TiO₂ film prior to the carbothermal treatment, with surface projected hexagonal cells representing the orientations (A–E) of the investigated substrate grains. Spectra extracted from the boxes in d) the C 1s and e) the Ti 2p_{3/2} chemical maps. For clarity, the spectra are shifted vertically. f) C 1s signal intensities, I(C), normalized to the maximum value, versus tilt angle Φ of Ti substrate grains. The intensity values correspond to the uncorrected absolute C 1s peak areas, which were obtained by integration of the spectra in d) after subtraction of a constant background. Adapted from [118] - Published by the PCCP Owner Societies.

Fig. 86d and e show the C 1s and Ti $2p_{3/2}$ spectra extracted from the indicated areas of the photoelectron micrographs. Using table 4.1 in Chapter 4, the chemical species that contribute to the XP signals can be identified. The C 1s peaks of all the studied grains are clearly dominated by the signal of graphite-like carbon (sp^2 hybridized carbon), detected at 284.5 eV. This is in accordance with the Raman response of the C/TiO₂ composite, which proves the presence of NCG. The weak shoulder occurring at 285.6 eV accounts for a small fraction of diamond-like carbon (sp^3 hybridized carbon). No defined peak of carbidic carbon (C–Ti bonds) is found at 281.7 eV (compare with SPEM results in the next section), hence only a negligible amount of this species is present at the C/TiO₂ interface. For all studied grains, the Ti $2p_{3/2}$ region is dominated by the TiO₂ peak at 459.0 eV that originates from the thermally treated anodic film. The small shoulder at the low binding energy tail of the peak reveals the presence of reduced titania species, such as Ti(III) in Ti₂O₃ at 457.0 eV, which confirms the Raman results. In accordance with the C 1s spectrum, no pronounced TiC (or TiO) component is detected at \sim 454.9 eV in the Ti $2p_{3/2}$ spectrum (compare with SPEM results in the next section). Fig. 86f shows the variation of the carbon signal intensities $I(C)$, extracted from the C 1s photoelectron micrograph, with substrate grain orientation, which gives an estimate of the differences in carbon content. As already indicated by the contrast in the chemical maps, there is an abrupt drop in the carbon intensity from grains with small tilt angles Φ (A, B) to grains with large tilt angles Φ (D, E) and a transition between these two types of substrate grains represented by grain C. The carbon signal intensity of grain A is about 1.7-times higher than the one of grain E. This trend is consistent with the Raman results (Fig. 85b). The complementary contrast in the chemical maps confirms a layered structure of the C/TiO₂ composite with a carbon layer on top of a weakly reduced TiO₂ film. Since SPEM yields a TiO₂ photoelectron signal on all substrate grains, the carbon layer should be less than \sim 2.3 nm thick, which is the photoelectron escape depth as defined in equation 2.118 derived for atomically planar graphitic carbon for the SPEM measurement geometry ($\theta = 30^\circ$). A close look at the chemical maps reveals that the film on top of individual substrate grains has no perfectly homogeneous composition (see black spots on grain A in Fig. 86a), which is supported by the inhomogeneous coverage of the deposit observed in the scanning electron micrographs (Fig. 83c,d). This finding is most likely related to the local properties of the anodic TiO₂ at the moment that C₂H₂ interacts with the surface during the carbothermal treatment, which motivates to take a closer look on the substrate grain dependent crystalline phase composition of TiO₂^{ref}.

5.2.4 Thermal treatment of anodic TiO₂ at 550 °C without acetylene

During the employed carbothermal treatment, acetylene is added to the process after one hour of annealing at 550 °C under an argon gas flow. It can be expected that prior to the addition of C₂H₂, the properties of the anodic TiO₂ film, in particular its crystallinity, are different from those of the pristine film and that these properties affect the interaction with acetylene. Hence, the investigation of the substrate grain-dependent properties of the anodic TiO₂ film prior to the addition of C₂H₂ may unravel the origin of the grain-dependent chemical composition of the final C/TiO₂/Ti_{poly} composite. A system, which approximates well the properties of the anodic film prior to addition of acetylene, is given by TiO₂^{ref}, which was prepared for this purpose. An EBSD map of the polycrystalline Ti substrate recorded after electropolishing allows a precise identification of the tilt angles Φ of the grains.

The substrate grain-dependent topography of TiO₂^{ref} was investigated with contact mode AFM. Roughness

analysis of AFM images of the TiO₂^{ref} film obtained on differently oriented substrate grains provides information about the grain-dependent topographic surface area that is available for carbon deposition. For that, image sections, the image root mean square height values (RMS) and roughness factors (RF = topographic area/projected area, where the topographic area is calculated by the sum of the area of three adjacent pixels) were extracted. The results of the AFM analysis are summarized in Fig. 87.

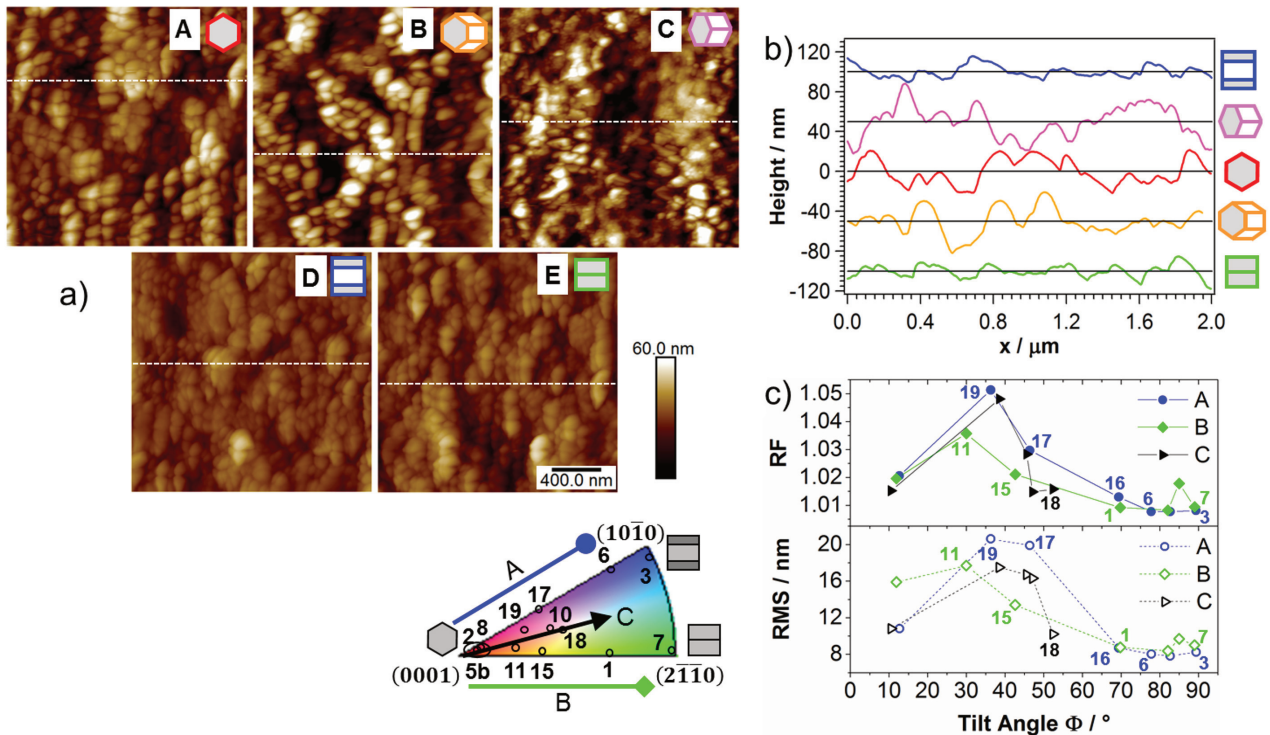


Fig. 87: a) $2 \times 2 \mu\text{m}^2$ AFM micrographs of TiO₂^{ref}, taken on top of substrate grains with different crystallographic orientations. Cross-sections in b) are taken along the dashed lines in a). c) Dependence of the roughness factor (RF) and the root mean square (RMS) height on the tilt angle Φ along three orientation paths, as indicated in the standard triangle. The number labels belong to the grains in Fig. 80. Adapted from the electronic supplementary information of [118] - Published by the PCCP Owner Societies.

As can be seen from Fig. 87a, the TiO₂^{ref} film has a particulate or granular surface morphology, which is affected by the tilt angle of the Ti substrate grains. High image contrast variations are observed on substrate grains A, B and C ($\Phi \leq 40^\circ$), while the film is relatively smooth on grains D and E ($\Phi \geq 50^\circ$). In the film on grain C, the dimples that are caused by electropolishing and preserved during anodization are still visible. Cross-sections along the dashed lines in the micrographs are depicted in Fig. 87b. It can be seen that relatively large protruding particulate features characterize the film surface on top of grains A, B and C. The width of the particulate shapes is about 50–200 nm. In contrast, the topography follows a relatively flat zigzag line with only weakly protruding particulate features on top of substrate grains D and E. These observations show that upon the thermal treatment, extensive structural reorganization has occurred in the film on grains with substrate tilt angles $\Phi \leq \sim 50^\circ$ which can be ascribed to an advanced film crystallization on these grains, as will be substantiated below.

To evaluate the average topography of the TiO₂^{ref} film on top of individual substrate grains, AFM-images of large scan size ($15 \times 15 \mu\text{m}^2$) were acquired (not shown). Roughness analysis was performed on rectangular areas within the grain boundaries of selected substrate grains. Fig. 87c depicts the obtained RMS and RF

values versus the substrate tilt angle Φ along three different orientation paths (A, B, C). For all three orientation paths, the surface roughness varies with Φ and follows a similar trend, which shows that the substrate tilt has an important influence on the topography of the thermally treated oxide film. Starting from mean values of $RF = (1.018 \pm 0.003)$ and $RMS = (12.5 \pm 2.9)$ nm at $\Phi \leq \sim 15^\circ$, the roughness of the TiO_2^{ref} film passes through a maximum between $\sim 30^\circ$ and $\sim 40^\circ$ (grain 19: $RF = 1.051$ and $RMS = 20.6$ nm) and drops to low values of $RF = (1.010 \pm 0.004)$ and $RMS = (8.6 \pm 2.9)$ nm for $\Phi \geq \sim 70^\circ$.

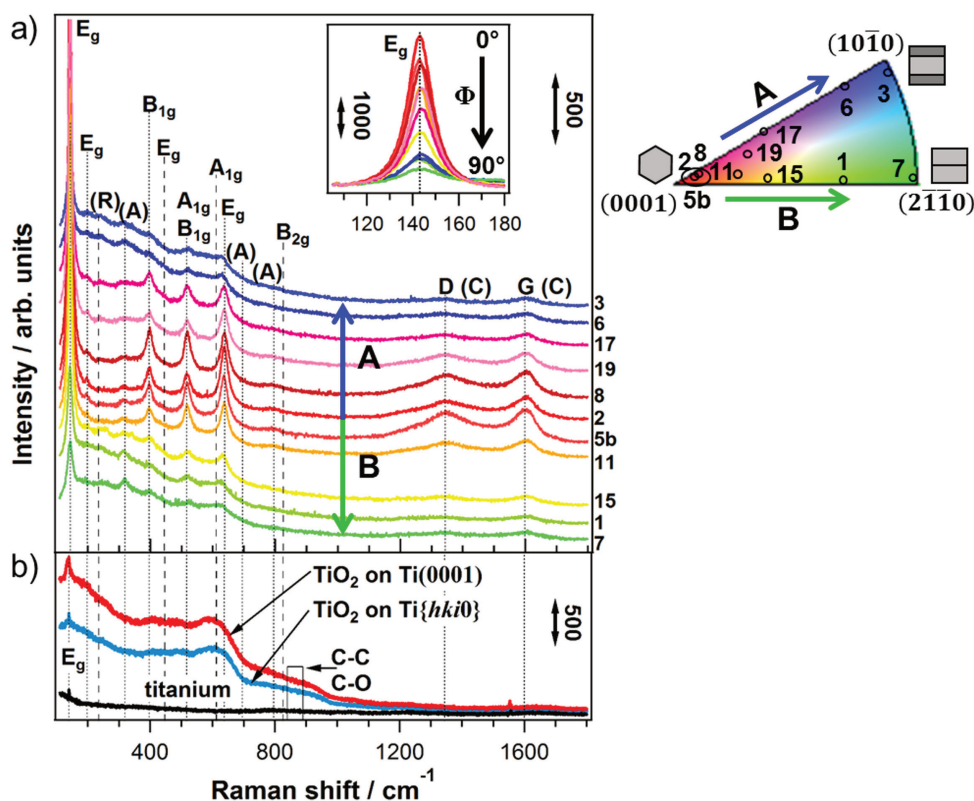


Fig. 88: a) Micro-Raman spectra of TiO_2^{ref} for different Φ . The colors correspond to the orientation-color code given by the standard triangle (the studied grains are depicted in Fig. 80). For clarity the spectra are shifted vertically. Dashed lines: rutile, dotted lines: anatase, carbon. D- and G-bands: carbon (C). TiO_2 combination bands: rutile (R), anatase (A). Inset: anatase E_g peak (143 cm^{-1}). Along the arrows (A and B), Φ varies from 0° to 90° . b) Micro-Raman spectrum of electropolished Ti (black) and an anodic TiO_2 film on $\sim Ti(0001)$ (red) and $\sim Ti\{hki0\}$ (blue). Laser wavelength: 532 nm. Adapted from [118] - Published by the PCCP Owner Societies.

Fig. 88a shows the Raman response of the TiO_2^{ref} film on differently tilted substrate grains. In all spectra, the characteristic bands of first-order Raman scattering of crystalline anatase TiO_2 are detected, and the weak peaks at 320 cm^{-1} and 769 cm^{-1} are combination bands of anatase.²⁶⁴ Apart from a weak feature at $\sim 235\text{ cm}^{-1}$, no distinct peaks in the spectrum can be attributed to rutile, which suggests a very low fraction of this phase in the TiO_2^{ref} film. All spectra show two peaks at $\sim 1340\text{ cm}^{-1}$ and $\sim 1600\text{ cm}^{-1}$ that are the characteristic D- and G-bands of carbon, which indicate the presence of NGC.²⁶⁵

Fig. 88b shows the spectra of an anodic TiO_2 film on top of two differently oriented Ti substrate grains. Apart from the weakly protruding E_g peak of anatase TiO_2 at 143 cm^{-1} , both Raman spectra are characterized by very broad and undefined features below $\sim 1000\text{ cm}^{-1}$, evidencing that the film is mainly amorphous.^{248,275,276} The intensity of the Raman signal of the TiO_2 film on $\sim Ti(0001)$ is slightly higher than that of the film on $\sim Ti\{hki0\}$, which indicates that the grain orientation of the Ti substrate influences the properties of the pristine

anodic TiO₂ film on top. The comparison between the Raman response of the TiO₂^{ref} film and the pristine anodic TiO₂ film discloses the changes that have occurred upon annealing: the thermal treatment at 550 °C leads to the crystallization of the anodic TiO₂ film. No graphitic carbon is detected on the pristine anodic TiO₂. The signal between 840 and 890 cm⁻¹, however, could be assigned to the Raman active C–C and C–O stretching of organic carbon contamination.^{248,276–280} The carbon detected on TiO₂^{ref} may therefore originate from organic contamination that adsorbed onto the surface of the anodic TiO₂ and was then converted to graphitic carbon during the thermal treatment in Ar. An electropolished titanium substrate yields a flat baseline signal with almost no features (black spectrum in Fig. 88b). Only at ~ 143 cm⁻¹ a small peak is detected which can be attributed to the corresponding E_g band of anatase TiO₂, arising most likely from the natural oxide film that is usually present on titanium. There is another small feature at ~ 1555 cm⁻¹, which might originate from carbon contamination as well and which is also present on the anodic TiO₂ film.

A strong influence of the substrate grain orientation on the Raman response of TiO₂^{ref} is found. While the anatase bands that are detected on top of grains with $\Phi \leq \sim 15^\circ$ (red spectra in Fig. 88a) are relatively intense and sharp, the same peaks are not only weaker and broader when detected on grains with $\Phi \geq \sim 50^\circ$ (green and blue spectra in Fig. 88a), but also embedded in a plateau-like background signal, which can be attributed to a considerable fraction of amorphous TiO₂ in these films. Well-defined, intense Raman bands of narrow FWHM are characteristic of an extended single crystal (see also Fig. 81)^{264,281} and are hence an indication of high crystallinity of the detected anatase phase. The more intense the characteristic bands of anatase are, the higher is the fraction of this crystalline phase in the probed volume of TiO₂^{ref}. Peaks of small FWHM indicate a high long-range order and thus sufficiently large crystalline domains. The features of the amorphous TiO₂ background are also present, but less pronounced, on grains with intermediate tilt angles, $\sim 15^\circ \leq \Phi \leq \sim 50^\circ$ (orange, yellow, light and dark purple spectra in Fig. 88a), suggesting that the anodic TiO₂ film is partially crystalline on these grains. The crystallinity of the anatase phase gradually improves with decreasing Φ , as can be inferred from the evolution of the E_g band at 143 cm⁻¹ (inset in Fig. 88a). A close comparison between the Raman spectra of grains 8, 2 and 5b (red in Fig. 88a) reveals a variation in relative peak heights of the three characteristic anatase bands detected between 350 and 650 cm⁻¹. This can be attributed to different preferential orientations of the anatase crystallites on these grains and is not related to varying crystallinity (see Fig. 81 and Fig. 82). Together with the improvement of crystallinity in the TiO₂^{ref} film, an increase in the intensity of the characteristic D- and G-bands of NCG is observed with decreasing Φ . This suggests that the amount of produced graphitic carbon depends on the crystallinity of anodic TiO₂, and in particular on its anatase content.

It is noteworthy that during the acquisition of the EBSD map of the electropolished Ti substrate of the TiO₂^{ref} sample, amorphous carbon may have formed due to contamination of the surface with organic carbon species present in the microscope chamber and their subsequent decomposition by the highly energetic electron beam. The Raman spectrum of grain 5b is taken outside the zone of the EBSD map and shows a carbon signal very similar to the ones detected on grains 2 and 8 which are within the mapped zone and have a similar tilt angle ($\Phi \leq \sim 15^\circ$). This observation shows that such contamination is negligible.

For a detailed analysis of the dependency of the TiO₂ crystallinity and the carbon content on the substrate tilt angle, the low frequency E_g (143 cm⁻¹), the B_{1g} (~ 396 cm⁻¹) and the high frequency E_g (~ 639 cm⁻¹) bands of anatase, as well as the Raman signal of carbon were fitted and integrated, as illustrated in Fig. 89. The

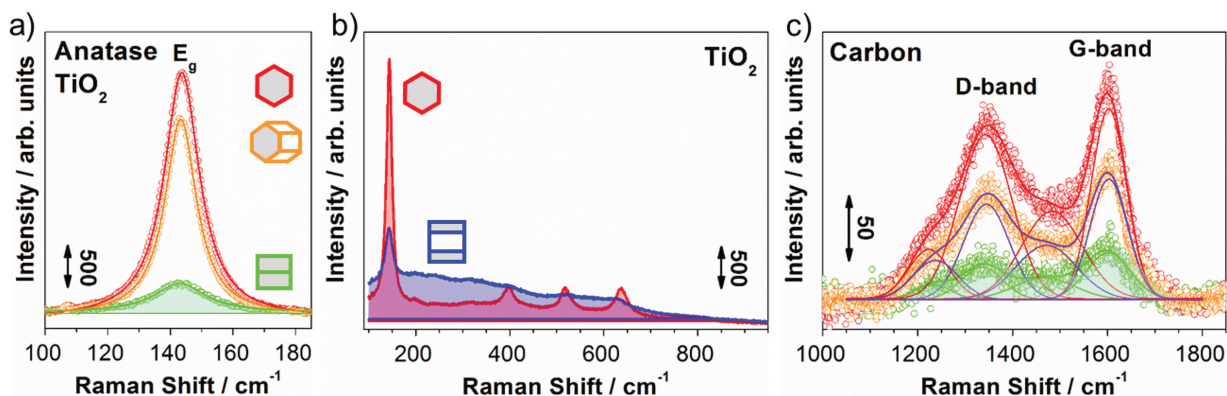


Fig. 89: Analysis of selected Raman signals detected in TiO₂^{ref} on top of substrate grains with the shown orientations. Integrated areas are colored. a) Lorentz-fit of anatase E_g-band at 143 cm⁻¹. b) Overall signal from thermally treated anodic TiO₂. c) Four-peak Gaussian fit of carbon signal. Laser wavelength: 532 nm. Adapted from the electronic supplementary information of [118] - Published by the PCCP Owner Societies.

anatase bands were fitted using a Lorentzian line shape, where the amorphous background signal served as baseline (Fig. 89a). The corresponding peak area reflects the relative content of crystalline anatase TiO₂ without the amorphous contribution. Also the FWHM of the anatase peaks, in particular that of the E_g band at 143 cm⁻¹, provides information about the crystallinity of the oxide film. As illustrated in Fig. 89b for two selected substrate grain orientations, the total fraction of amorphous and crystalline TiO₂ in the TiO₂^{ref} film is estimated by integration of the overall Raman signal between 100 and 830 cm⁻¹, covering the spectral range that contains all features associated with titania species, after subtraction of a constant background. The carbon signals were fitted with four Gaussian peaks at ~ 1340 and ~ 1600 cm⁻¹, as well as ~ 1227 and ~ 1480 cm⁻¹ (compare with the assignment in Fig. 85a) as depicted in Fig. 89c. Like in the case of C/TiO₂, the peak height ratio $H(D_1 + D_2)/H(G_1 + G_2)$ of the carbon bands in Fig. 89c is about 0.7–0.8, for all investigated substrate grains, which corresponds to an average cluster size of about 6 nm.²⁶⁵ To eliminate possible effects of grain-dependent surface roughness on the quantity of generated NCG, the carbon signal intensities $I_{\text{spec.}}(\text{C})$ are corrected for the respective topographic surface area of the TiO₂^{ref} film, using the RF values that were determined with AFM (see Fig. 87). From the trend of the RF values with Φ , reported in Fig. 87c, it becomes apparent that the variation in the film's topographic surface area from grain to grain is less than $\sim 5\%$. This is by far too low to explain the differences in carbon content that are observed for both films, TiO₂^{ref} and C/TiO₂, when comparing zones on top of substrate grains with $\Phi \leq \sim 15^\circ$ with zones on top of grains with $\Phi \geq \sim 50^\circ$.

The results obtained from the analysis of the anatase E_g band at 143 cm⁻¹, the overall Raman signal of the oxide, and the carbon bands are reported in Fig. 90. The fraction of crystalline anatase stays almost constant and low for $\Phi \geq \sim 50^\circ$ and abruptly increases below $\Phi \sim 50^\circ$ to five times higher values (Fig. 90a). The FWHM of the anatase E_g band drops linearly with decreasing Φ (Fig. 90b). For anatase TiO₂ nanocrystals, the FWHM of the E_g band was reported to be inversely related to their dimensions.^{131,281,282} Hence, this trend indicates a continuous increase of the size of the crystalline anatase domains with decreasing Φ . However, the smallest FWHM value is found to be ~ 12 cm⁻¹ and therewith still higher than the FWHM of 7 cm⁻¹ that is expected for bulk anatase TiO₂ (see Fig. 81).^{281,283} Therefore, the thermally treated anodic TiO₂ film can be considered polycrystalline, with different average crystallite sizes on top of differently oriented substrate grains. Similar

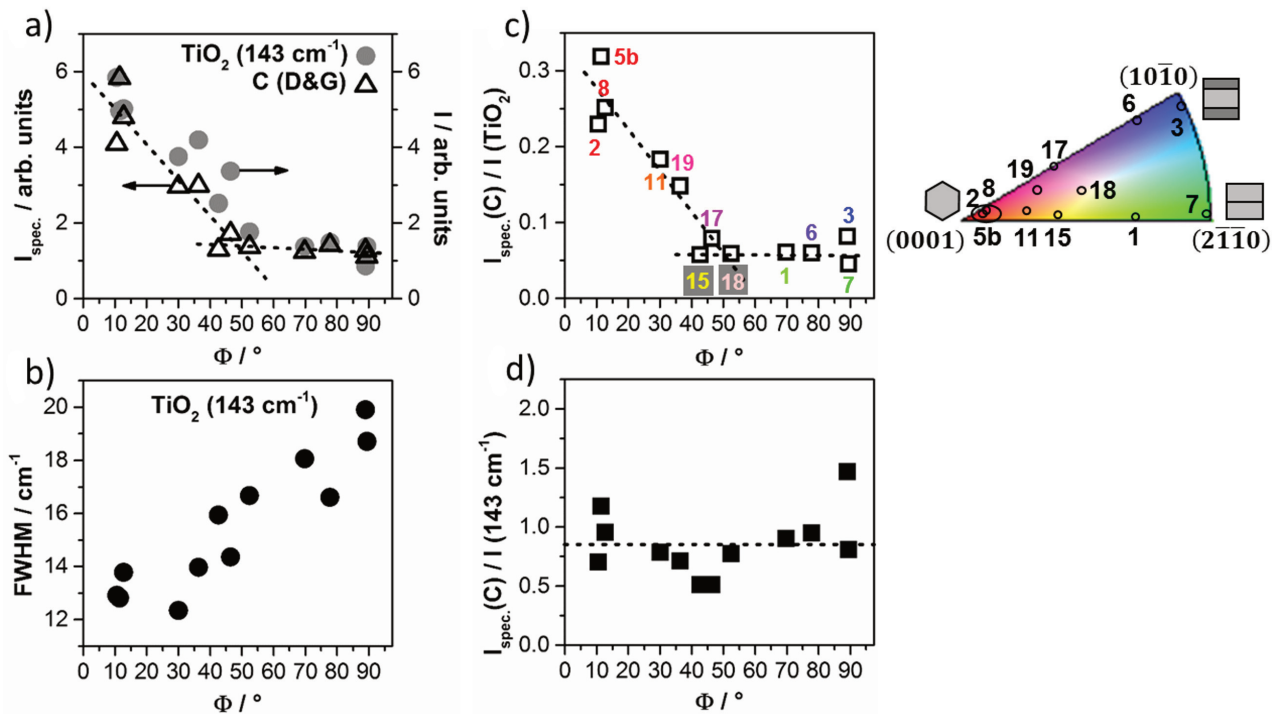


Fig. 90: Evaluation of Raman spectra of $\text{TiO}_2^{\text{ref}}$ as a function of the substrate tilt angle Φ . The studied grains are labeled with numbers and marked in the standard triangle. a) Anatase E_g band intensities at 143 cm^{-1} and area-specific carbon signal intensities ($I_{\text{spec}}(\text{C})$); b) FWHM of the anatase E_g band at 143 cm^{-1} . c) Ratio of $I_{\text{spec}}(\text{C})$ and the overall Raman response of crystalline and amorphous TiO_2 ($I(\text{TiO}_2)$). d) Ratio of $I_{\text{spec}}(\text{C})$ and the intensity of the anatase E_g band at 143 cm^{-1} . Dashed lines in a) and c): linear least squares fits of carbon band intensities below 55° and above 40° . Dashed line in d): arithmetic mean (0.85 ± 0.27). Adapted from [118] - Published by the PCCP Owner Societies.

FWHM values were obtained for anatase TiO_2 nanoparticles with a crystallite size of less than $\sim 20\text{ nm}$,¹³¹ which suggests that the size of the crystalline domains in thermally treated anodic TiO_2 are in the nanometer range. The area-specific carbon signal intensities, $I_{\text{spec}}(\text{C})$, give a qualitative measure of the amount of carbon on the thermally treated anodic film. From Fig. 90a it can be seen that $I_{\text{spec}}(\text{C})$ follows the same trend with Φ as the intensity of the anatase E_g band. In Fig. 90c, $I_{\text{spec}}(\text{C})$ is divided by the overall Raman response of the oxide film, $I(\text{TiO}_2)$, on individual substrate grains. As in Fig. 90a, two regions of different slopes can be identified and the crossing of the corresponding least squares linear fits (dashed lines) yields the tilt angle $\Phi \sim 50^\circ$ as a threshold value. At lower tilt angles, $I_{\text{spec}}(\text{C})/I(\text{TiO}_2)$, and therewith the amount of NCG that is produced on $\text{TiO}_2^{\text{ref}}$ upon thermal treatment, is increased substantially. When $I_{\text{spec}}(\text{C})$ is divided by the intensity of the anatase E_g band, a plot versus Φ yields an almost constant line (Fig. 90d). This evidences that the two quantities, i.e. the amount of NCG and crystalline TiO_2 , are closely linked.

Fig. 91 shows the peak intensities and the peak positions of the B_{1g} ($\sim 396\text{ cm}^{-1}$) band and the high frequency E_g band ($\sim 639\text{ cm}^{-1}$) of anatase, as a function of substrate tilt angle. For comparison, the intensities of the D- and G-band of graphitic carbon (detected at $\sim 1340\text{ cm}^{-1}$ and $\sim 1600\text{ cm}^{-1}$) are included in the graph. The intensities shown in Fig. 91a follow a very similar trend as those in Fig. 90a and c. In addition, a progressive blue-shift of the B_{1g} band from ~ 397 to $\sim 402\text{ cm}^{-1}$ and a parallel red-shift of the E_g band from ~ 637 to $\sim 628\text{ cm}^{-1}$ are observed when the tilt angle Φ increases from 0° to 90° , which can be attributed to an increasing fraction of amorphous TiO_2 (compare with Fig. 88b).

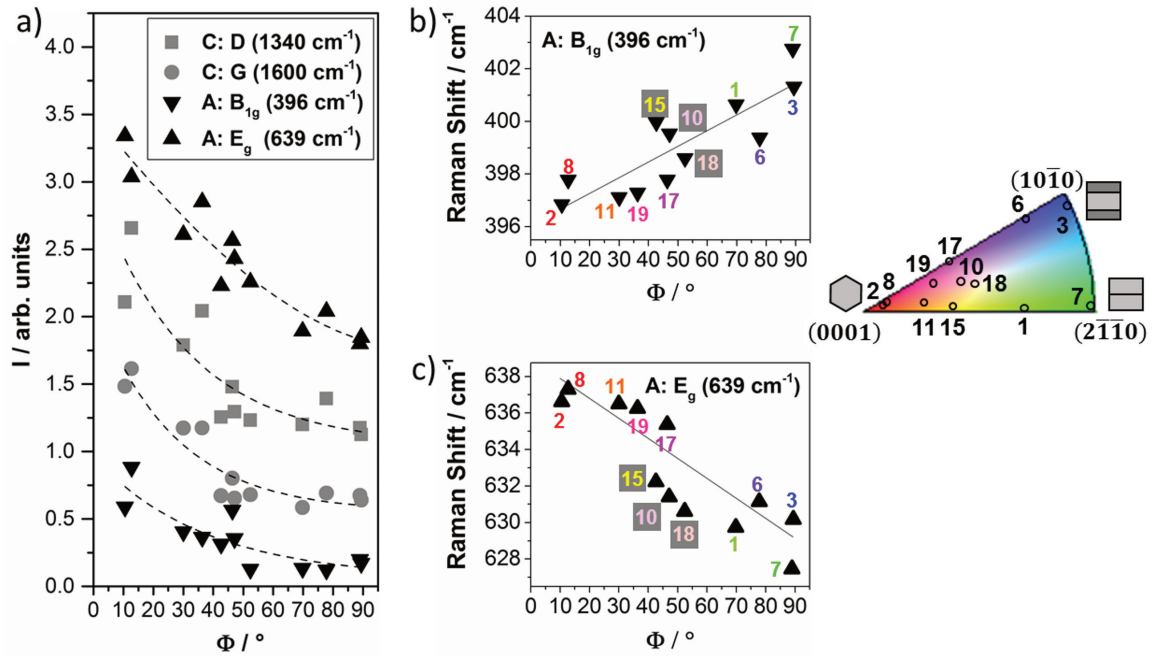


Fig. 91: Evaluation of the fitted Raman-spectra of TiO₂^{ref} on polycrystalline Ti. a) Peak areas of selected anatase and carbon Raman bands, and (b,c) band positions of two anatase bands are plotted *versus* the tilt angle Φ of the substrate grains. Dotted lines in a) serve as guide for the eye, solid lines in (b,c) are linear least squares fits. Adapted from the electronic supplementary information of [118] - Published by the PCCP Owner Societies.

5.2.5 Origin of the grain-dependent crystallinity of thermally treated anodic TiO₂

The phase evolution of anodic titania films during isothermal annealing proceeds from initially amorphous TiO₂ to phase pure anatase, over mixed phases of anatase and rutile towards phase pure rutile TiO₂, where the final phase composition depends on the annealing temperature, atmosphere and duration.^{247,248,276} A variation of the substrate tilt angle Φ from $\sim 50^\circ$ to 0° appears to have the same effect on the final crystallinity of TiO₂^{ref} as an enhancement of annealing temperature. This implies that the substrate grain orientation, and in particular the tilt angle Φ , has a strong impact on the kinetics of the phase transition. From the literature it is known that the compact anodic TiO₂ film on top of \sim Ti(0001) is thinner than that on \sim Ti{*hki*0}, and contains a higher concentration of donors, i.e. oxygen vacancies.^{56,59,61} This is likely to affect the atomic reorganization or diffusion processes during annealing and therewith yield a higher isothermal crystallization rate for TiO₂ on \sim Ti(0001) than for TiO₂ on \sim Ti{*hki*0}. In particular, a considerable increase of donor density, supported by a parallel increase in the electron transfer rate, oxygen evolution current and photocurrent, has been found for anodic TiO₂ films on top of Ti substrate grains with tilt angles $\Phi \leq \sim 45^\circ$,^{57,58} which is in very good agreement with the observed increase of the oxide film crystallinity for tilt angles $\Phi \leq \sim 50^\circ$ (see Fig. 90a).

The difference in phase composition of TiO₂^{ref} and TiO₂ is related to the annealing time, which is longer for the thermal treatment with C₂H₂, hence yielding a considerable fraction of rutile TiO₂. In addition, the carbon present on the TiO₂ may have an effect on the crystallization kinetics.^{284,285}

5.2.6 Origin of the grain-dependent carbon content in the C/TiO₂ composite film

SPEM, micro-Raman spectroscopy and SEM evidence that carbothermal treatment of a compact anodic TiO₂ film with C₂H₂ at 550 °C yields a C/TiO₂ composite material, consisting of a few nm thick nanocrystalline graphitic carbon layer on top of slightly reduced, polycrystalline TiO₂. On the reference sample TiO₂^{ref}, which is thermally treated without C₂H₂, a significantly less amount of carbon is detected, which originates only from organic or hydrocarbon contamination of the anodic TiO₂. The nature of the carbon film on TiO₂^{ref} and C/TiO₂ is very similar, as evidenced by the resembling shapes of the carbon Raman signals: from the height ratio of the carbon bands, a NCG cluster size of approximately 6 nm can be deduced, which is found to be independent of the substrate grain orientation and the carbon source.

The carbon signal intensity, extracted from SPEM and micro-Raman spectra, follows a very similar trend with Φ for both TiO₂^{ref} and C/TiO₂. There are mainly two classes of grains: class one comprises substrate grains with tilt angles of $0^\circ \leq \Phi \leq \sim 40^\circ$, where a relatively high amount of carbon is deposited on the oxide film; class two covers all grains with tilt angles $\Phi \geq \sim 50^\circ$ that exhibit a relatively low fraction of carbon after the carbothermal treatment of the anodic TiO₂. Grains with $40^\circ \leq \Phi \leq \sim 50^\circ$ belong to a transition zone, where an orientation of $\Phi \sim 50^\circ$ can be identified as the threshold value.

The formation of a grain-dependent carbon layer under the applied carbothermal treatment strongly suggests that C₂H₂ (and even organic contamination) is not thermally but catalytically decomposed at the surface of TiO₂.²⁸⁶ Furthermore, the presented results evidence that crystalline TiO₂, in particular the anatase phase, is able to decompose C₂H₂, since only a small amount of carbon is found on TiO₂ that is mainly amorphous. It has been reported that Ti⁴⁺-O²⁻ Lewis acid-base pairs on the surface of crystalline TiO₂ are the active centers for a heterolytic dissociation of C₂H₂, initiating self-assembly processes of acetylene to form polycyclic aromatic hydrocarbons at room temperature and graphitic carbon at sufficiently high temperatures (650 °C in ref. [286]).^{274,287} Anatase TiO₂ was found to be particularly efficient for the decomposition of acetylene, which is in line with our findings. The crystallinity of compact anodic films on polycrystalline Ti substrates is affected by the Ti substrate grain orientations. This causes the observed grain-dependent average chemical surface composition of the obtained C/TiO₂ composite film.

From the FWHM values of the anatase E_g (143 cm⁻¹) bands it is deduced that the TiO₂^{ref} film consists of polycrystalline anatase with nanometer size crystallites. This may explain why only nanocrystalline and no extended graphitic carbon layers are formed in the course of the thermal treatment. Furthermore, it gives an explanation for the inhomogeneous carbon coverage of TiO₂ on individual substrate grains as observed with SPEM and SEM, which is particularly emphasized on top of grains that are tilted by $\Phi \leq \sim 15^\circ$: A polycrystalline TiO₂ film consists of anatase domains that have different orientations exposing different faces at the surface, which in turn affects their activity towards C₂H₂ decomposition. The reason for this is that different anatase faces exhibit different fractions of active Ti⁴⁺-O²⁻ centers. According to the respective literature, a high fraction of these sites appears to be present on dehydroxylated, stoichiometric and extended (001) and/or (010) planes of crystalline anatase.^{287,288}

5.3 Ti substrate grain-dependent physicochemical properties of carburized anodic TiO₂ films prepared at different temperatures

The study presented in this section was published by Rüdiger et al. in 2017.²⁵⁹ Mind that in some figures of [259], the projected hexagonal cells indicating the substrate grain orientations $\sim\text{Ti}(10\bar{1}0)$ (blue, label D, $50^\circ \leq \Phi \leq 90^\circ$ and $0^\circ \leq \varphi_2 \leq 15^\circ$) and $\sim\text{Ti}(2\bar{1}\bar{1}0)$ (green, label E, $50^\circ \leq \Phi \leq 90^\circ$ and $15^\circ \leq \varphi_2 \leq 30^\circ$) are interchanged. An according correction will be published soon and has been taken into account in this thesis (see table 5.1). Following the notation used in Chapter 4, the carburized anodic films are termed TiOC_T throughout the text, where *T* represents the four employed annealing temperatures 550, 650, 750 and 850 °C. Note that TiOC₅₅₀ corresponds to the C/TiO₂ composite film analyzed in section 5.2.3 of this chapter.

5.3.1 Ti substrate grain-dependent surface morphology of TiOC

Fig. 92 shows scanning electron micrographs of TiOC, synthesized at different temperatures. After the thermal treatments at temperatures of up to 750 °C, the grain boundaries of the Ti substrate are still visible through the TiOC film. The morphology of TiOC₅₅₀ and TiOC₇₅₀ is clearly affected by the crystallographic orientation of the underlying Ti substrate grains. In particular, substrate grains with tilt angles $0^\circ \leq \Phi \leq \sim 40^\circ$ can be easily distinguished from substrate grains with tilt angles $\Phi \geq \sim 50^\circ$, due to apparent differences in the morphologies of the TiOC overlayers. TiOC₆₅₀ is characterized by a granular morphology with no pronounced substrate grain dependency; only the grain boundaries can be recognized. After carbothermal treatment at 850 °C, the initial grain boundaries of the substrate disappeared and extended areas of uniform morphology formed. No interdependence between morphology and the original substrate grain orientation is visible due to significant substrate grain growth at this temperature.¹⁵⁰ The comparison between the morphologies of

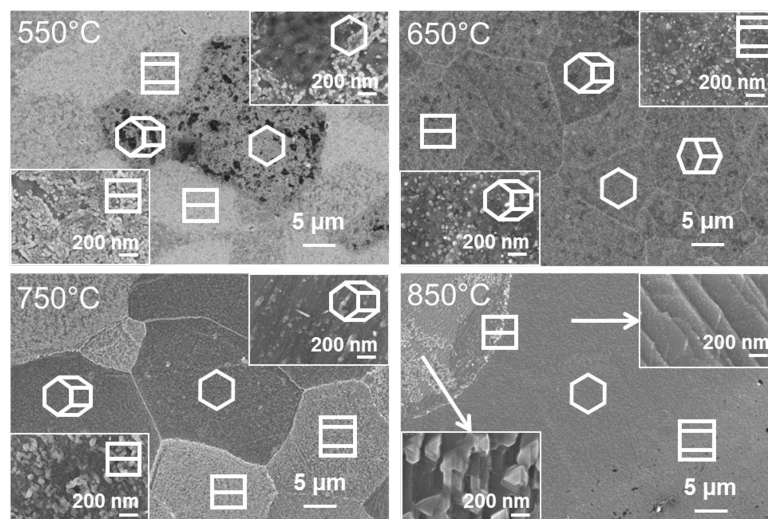


Fig. 92: SE micrographs of TiOC taken with the InLens detector (electron beam acceleration voltage: 4–6 kV, working distance: 3–5 mm). High-magnification insets: areas on differently oriented substrate grains (TiOC₅₅₀, TiOC₆₅₀, TiOC₇₅₀) or areas with different TiOC morphologies (TiOC₈₅₀). Projected hexagonal cells: approximate crystallographic orientation of the Ti substrate grains, according to table 5.1. Note that the substrate orientations were estimated from the optical appearance of the respective as-grown anodic TiO₂ films, so that type D and E grains cannot be distinguished. Reproduced from [259] © 2017 American Chemical Society.

TiOC₇₅₀ and TiOC₈₅₀ suggests that the surface undergoes an ordering at high annealing temperatures. The high-resolution micrographs (insets) of TiOC₈₅₀ show ordered morphologies, such as triangular shapes (left bottom) or stepped terraces (right top). The phase change of the Ti substrate from α Ti (hcp structure) to β Ti (bcc structure) does not happen below 882 °C and can therefore not be responsible for this ordering.¹⁷²

5.3.2 Ti substrate grain-dependent surface chemistry of TiOC

Fig. 93 depicts chemical maps of the Ti 2p_{3/2} and C 1s core level electrons extracted from SPEM of TiOC and the corresponding EBSD maps of the Ti substrate. Apparently, the surface chemistry of TiOC₅₅₀ and TiOC₇₅₀ is affected by the orientation of the substrate grains: TiOC films on type A and B grains (0° ≤ Φ ≤ ~40°, i.e. an orientation closer to ~Ti(0001)) show a clearly different average brightness in the chemical maps than that of films on type D and E grains (~50° ≤ Φ ≤ ~90°, ~Ti{hki0}). In the case of TiOC₇₅₀, several grain boundaries can be identified. On the other hand, the surface of TiOC₈₅₀ has a relatively homogeneous composition that is independent of the substrate grains that have been mapped in the same area prior to the anodization and carbothermal treatment. The chemical maps of TiOC₆₅₀ show several areas with dark spots and less pronounced grain boundaries.

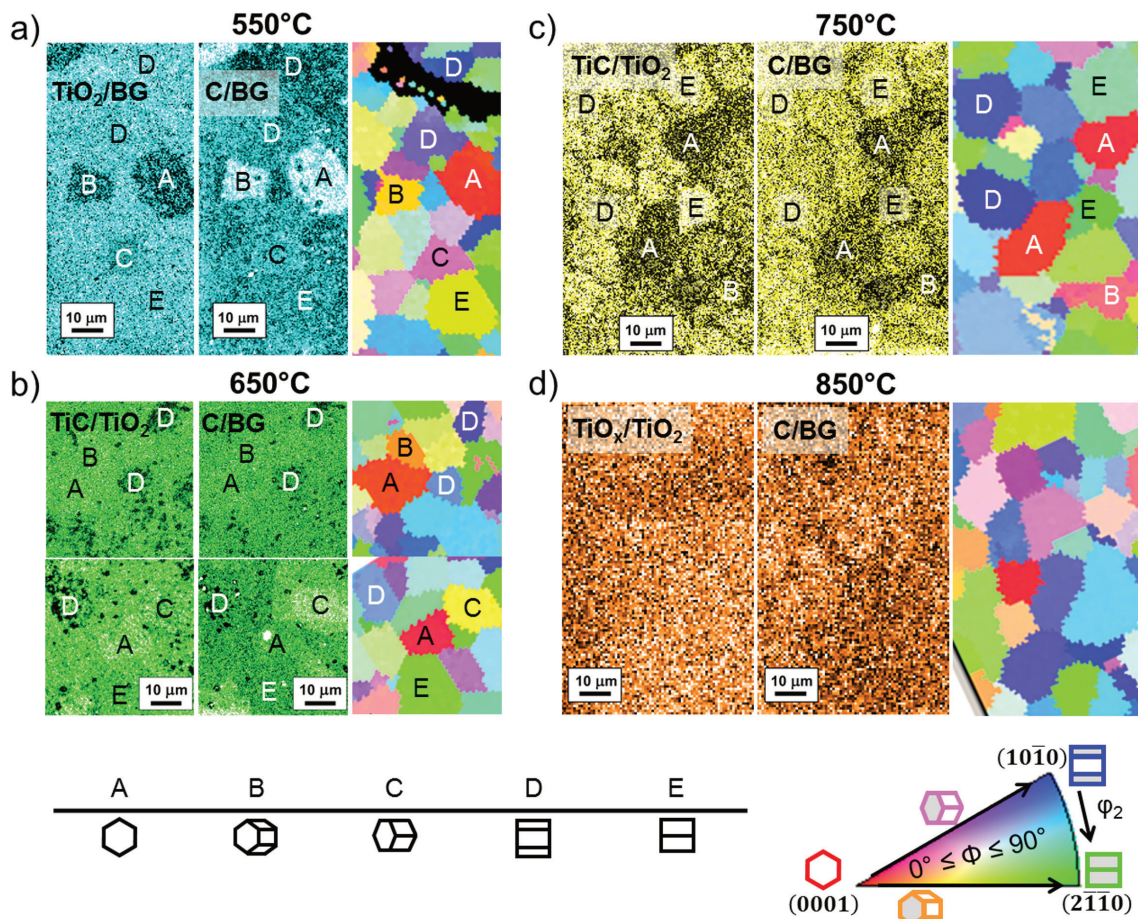


Fig. 93: Chemical maps from Ti 2p_{3/2} (always left) and C 1s (always center) photoelectron micrographs of TiOC, and EBSD maps (always right) of the corresponding Ti substrate. a) TiOC₅₅₀, b) TiOC₆₅₀, c) TiOC₇₅₀, and d) TiOC₈₅₀. To facilitate discrimination between the different TiOCs, the chemical maps are differently colored. Table: approximate orientations of labeled grains (see standard triangle and table 5.1). Adapted from [259] © 2017 American Chemical Society.

For each type of substrate grain, X-ray photoelectron (XP) spectra of the Ti $2p_{3/2}$ and C 1s core levels were extracted from the photoelectron maps and are plotted in Fig. 94. Each spectrum is obtained from a rectangular area on a substrate grain and represents the average surface composition of TiOC on that grain. An alternative representation of the XP spectra is given in Fig. 112 and Fig. 113 in Appendix A. The Ti $2p_{3/2}$ signals show that all TiOCs contain TiO₂ (459 eV) and that TiOC₆₅₀ and TiOC₇₅₀ additionally contain a considerable fraction of TiC and/or TiO species (454.9 eV) and some TiO_x sub-oxides (456–458 eV, $1 < x < 2$) at the surface. In the case of TiOC₅₅₀, TiOC₆₅₀, and TiOC₇₅₀, the pronounced peak in the C 1s spectra, centered at 284.5 eV, is attributed to an sp^2 -hybridized (graphite-like) carbon (C=C) (Fig. 94e-g). The C 1s peak found for TiOC₈₅₀ (Fig. 94h) is shifted toward the binding energy of an sp^3 -hybridized (diamond-like) carbon (C-C at 285.6 eV), indicating the presence of amorphous carbon on the surface.²⁸⁹ It can be seen that only TiOC₆₅₀ and TiOC₇₅₀ contain a notable amount of carbidic carbon (281.7 eV) within the film depth of ~ 1.4 – 2.3 nm (calculated for TiO₂ and graphite, using equation 2.118 and $\theta = 30^\circ$), which is analyzed with SPEM.

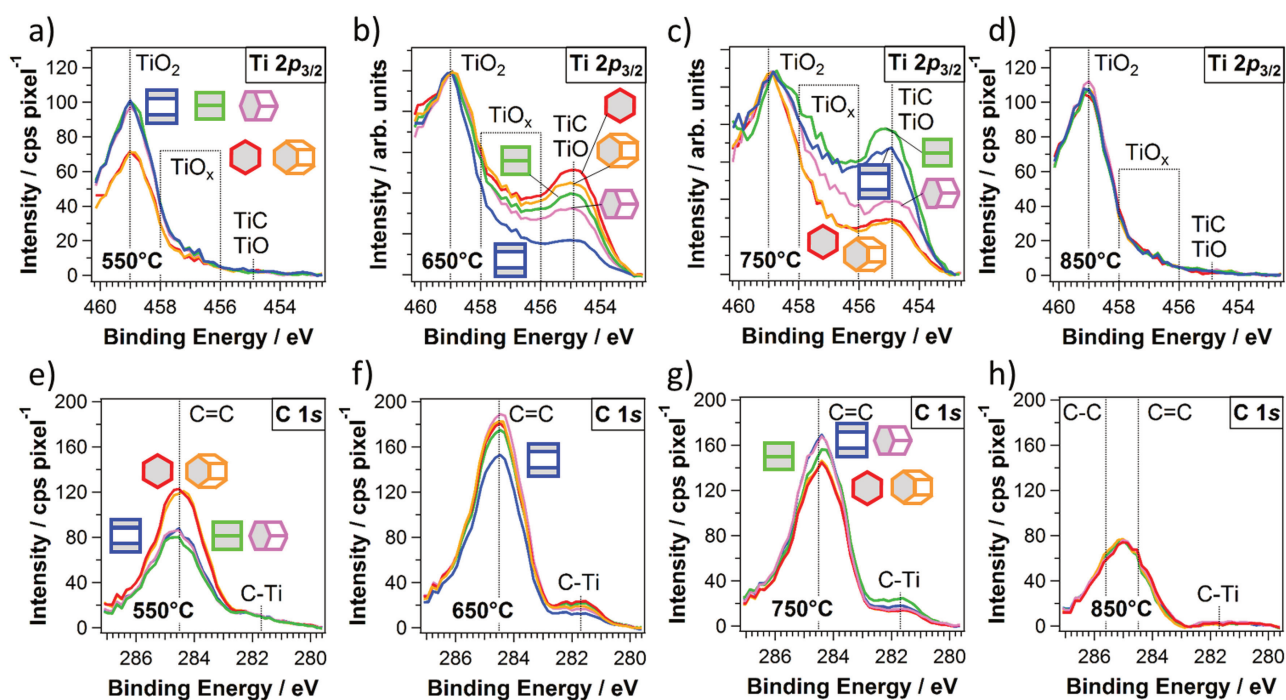


Fig. 94: Spectra from Ti $2p_{3/2}$ (top) and C 1s (bottom) core level maps of TiOC, acquired on top of substrate grains with five different orientations, as indicated by the hexagonal cells using the color-orientation code. (a,e) TiOC₅₅₀, (b,f) TiOC₆₅₀, (c,g) TiOC₇₅₀, and (d,h) TiOC₈₅₀. The spectra in (b,c) are scaled to the TiO₂ component height. Adapted from [259] © 2017 American Chemical Society.

Analysis of the XP spectra shows once more that a carbothermal treatment at 550 °C mainly yields graphitic carbon on top of TiO₂ (see section 5.2). A significant reduction of the anodic TiO₂ film is obtained through carbothermal treatments at 650 and 750 °C, generating TiC (TiO) and TiO_x species, and the resultant TiOC is covered by a relatively high amount of graphite-like carbon. The surface of TiOC₈₅₀ consists of TiO₂ covered by amorphous carbon. Both chemical maps (Fig. 93) and XP spectra (Fig. 94) show that the conversion from TiO₂ to TiC (TiO) and TiO_x depends both on the annealing temperature and substrate texture. On TiOC₅₅₀ (Fig. 93a and Fig. 94a,e), the relative amount of graphite-like carbon is significantly enhanced and the fraction of TiO₂ is small on top of substrate grains of types A and B (\sim Ti(0001)), with $0^\circ \leq \Phi \leq \sim 40^\circ$ (see section 5.2).

The XP spectra of TiOC₆₅₀ (Fig. 94b,f) suggest an exceptional surface chemistry on top of substrate grains of type D ($\sim\text{Ti}(10\bar{1}0)$), see table 5.1): on these grains, the conversion of the anodic film to TiC (TiO) and TiO_x phases is significantly lower, and slightly less graphite-like carbon is generated on the surface. This is in line with the TiC/TiO₂ and C/BG chemical maps (Fig. 93b), which show a high density of dark spots and thus a lower average content of TiC (TiO) and carbon in the TiOC on top of these grains. The variation in the surface chemistry of TiOC₆₅₀ on top of the other types of substrate grains is less strong. On TiOC₇₅₀, a pronounced substrate grain-dependent oxide film reduction can be observed, with the highest fraction of TiC (TiO) and TiO_x being present on top of substrate grains D and E, with $\sim 50^\circ \leq \Phi \leq 90^\circ$ ($\sim\text{Ti}\{hki0\}$), and the lowest, on substrate grains A and B, with $0^\circ \leq \Phi \leq \sim 40^\circ$ ($\sim\text{Ti}(0001)$), which is in accordance with the chemical maps (Fig. 94c,g and Fig. 93c). At the same time, the total amount of graphite-like and carbidic carbon species in TiOC₇₅₀ is slightly higher on substrate grains with $\sim 50^\circ \leq \Phi \leq 90^\circ$ ($\sim\text{Ti}\{hki0\}$) than that on substrate grains with $0^\circ \leq \Phi \leq \sim 40^\circ$ ($\sim\text{Ti}(0001)$). An intermediate composition is found on substrate grains C, with $\sim 40^\circ \leq \Phi \leq \sim 50^\circ$. No difference is visible in the XP spectra of TiOC₈₅₀ on differently oriented substrate grains, which confirms the homogeneous contrast of its chemical maps (Fig. 94d,h and Fig. 93d). The highest overall fraction of TiC is found in TiOC₇₅₀ on top of $\sim\text{Ti}\{hki0\}$ grains. The highest overall amount of diamond-like and graphite-like carbon is found in TiOC₆₅₀ on top of all substrate grains except for $\sim\text{Ti}(10\bar{1}0)$ (Fig. 94f). Considering only TiOC₆₅₀ and TiOC₇₅₀, an almost opposite chemical surface composition is observed on $\sim\text{Ti}(10\bar{1}0)$ and $\sim\text{Ti}(0001)$ substrate grains: TiOC₆₅₀ contains a high amount of TiC and C on $\sim\text{Ti}(0001)$ and a low amount on $\sim\text{Ti}(10\bar{1}0)$, whereas the contrary is found for TiOC₇₅₀.

The SPEM results reveal that both annealing temperature and substrate texture determine the TiOC surface chemistry. In accordance with the results presented in Chapter 4, TiC-rich TiOC can be synthesized through carburization of anodic TiO₂ at 650 or 750 °C. However, it depends on the substrate texture, whether a higher average TiC content is obtained in TiOC₆₅₀ or in TiOC₇₅₀ under the given annealing conditions (see Fig. 112 in Appendix A): in the case of a Ti substrate with a large fraction of $\sim\text{Ti}\{hki0\}$ grains, the average TiC content can be expected to be higher in TiOC₇₅₀ than that in TiOC₆₅₀; a Ti substrate with grain orientations restricted to $\sim 40^\circ \leq \Phi \leq \sim 50^\circ$ yields most likely a similar average TiC content in TiOC₆₅₀ and TiOC₇₅₀; finally, a Ti substrate with mainly $\sim\text{Ti}(0001)$ grains can be expected to yield a higher average TiC content in TiOC₆₅₀ than that in TiOC₇₅₀.

5.3.3 Ti substrate grain-dependent phase composition of TiOC

Micro-Raman spectroscopy was performed to gain information on the substrate grain-dependent structure and chemical composition of the entire anodic TiO₂ before and after carbothermal treatment at different temperatures. The laser used for this study had a wavelength of 514 nm, which gives rise to similar penetration depths into TiO₂ and graphitic carbon like those derived in section 5.2.2. Fig. 95 depicts the Raman spectra of as-anodized TiO₂ and of TiOC₅₅₀, TiOC₆₅₀, and TiOC₇₅₀ on top of $\sim\text{Ti}(10\bar{1}0)$ and $\sim\text{Ti}(0001)$ substrate grains, for which SPEM has revealed a clearly different chemical composition at the surface of TiOC. Since the initial grain boundaries of the titanium substrate have vanished after carbothermal treatment at 850 °C, Raman spectra of TiOC₈₅₀ were acquired on two spots of different appearance in the optical microscope (black and gray spectra in Fig. 95). The peaks at 1350 and 1600 cm⁻¹ in Fig. 95a,c correspond to the D- and G-bands of the (nanocrystalline) graphitic carbon.²⁶⁵ Fig. 95b,d depicts the spectral range of the bands

associated with Raman-active TiO_2 , TiO_x , or TiC_y phases. An alternative representation of these spectra is given in Fig. 114 in Appendix A. Anatase and rutile TiO_2 are characterized by vibrational bands marked with dashed lines and are labeled as A and R, respectively.^{263,264} Peaks at ~ 267 and $\sim 347 \text{ cm}^{-1}$, marked with dotted lines, can be attributed to the most intense Raman signals of Ti_2O_3 .^{268,269} Stoichiometric TiC has no Raman-active vibrational modes. However, the disorder in the cubic (NaCl) crystal structure of TiC_y (with $y < 1$) that is induced by carbon vacancies activates the A_{1g} , E_g , and T_{2g} modes for Raman scattering.²⁹⁰ The Raman spectrum of $\text{TiC}_{0.67}$ has been reported to contain five peaks at 265, 340, 372, 596, and 661 cm^{-1} ;²⁹¹ they are labeled in Fig. 95b,d.

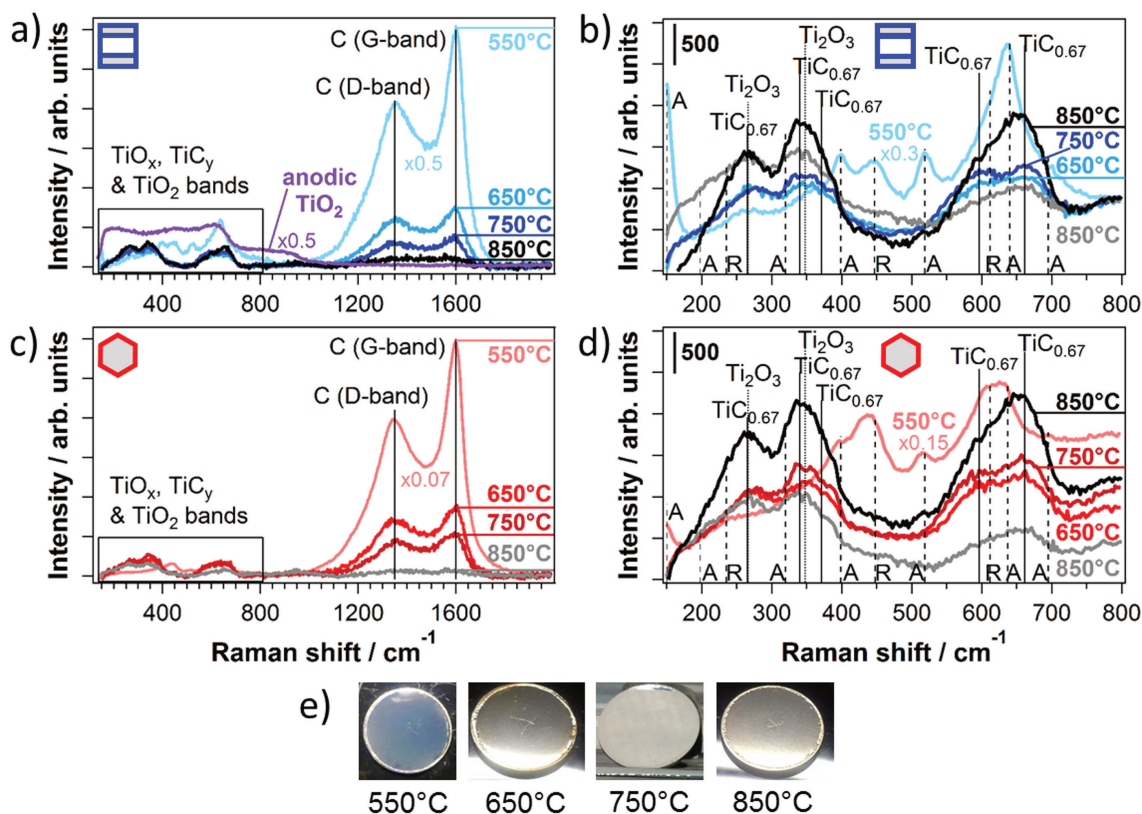


Fig. 95: Micro-Raman spectra of TiOC_{550} , TiOC_{650} , and TiOC_{750} on top of (a,b) $\sim\text{Ti}(10\bar{1}0)$ and (c,d) $\sim\text{Ti}(0001)$, and of two spots on TiOC_{850} with different optical appearance (black and gray spectra). Purple spectrum in a): as-grown anodic TiO_2 . (b,d) Spectral range within box in (a,c). Baseline correction: (a,c) subtraction of a fourth-order polynomial function; constant shift to a common level at b) 800 cm^{-1} and d) 150 cm^{-1} . Laser wavelength: 514 nm. e) Photographs of TiOC specimen. Adapted from [259] © 2017 American Chemical Society.

The absence of distinct bands associated with crystalline (rutile or anatase) TiO_2 evidences that the as-grown anodic film is amorphous (purple spectrum in Fig. 95a). Carbothermal treatment at 550°C leads to crystallization of the oxide, generating a mixed phase of rutile and anatase, and to a slight reduction, which is evidenced by the features ascribed to Ti_2O_3 . As already discussed in section 5.2, the highest fraction of rutile is detected on top of $\sim\text{Ti}(0001)$ (Fig. 95b,d, and Fig. 114a in Appendix A).²⁷⁰ There are no bands associated with TiC_y phases in the spectra of TiOC_{550} . The blue optical appearance of TiOC_{550} , which can be seen in Fig. 95e, indicates that the $\sim 53 \text{ nm}$ thick anodic oxide film is only slightly reduced. The color is most likely a result of interference effects in combination with color centers that are caused by oxygen vacancies in the bulk film.²³ Note that the as-grown anodic film has a different blue color, which arises from interference

effects only (see Fig. 80).

No graphitic carbon is detected prior to the carbothermal treatment. The carbon bands are intense for TiOC₅₅₀ and continuously decrease with increasing annealing temperature on both types of substrate grains (Fig. 95a,c). The Raman signal of the graphitic carbon is notably enhanced for TiOC₅₅₀ compared to that observed for TiOC₆₅₀ and TiOC₇₅₀, whereas the XP spectra suggest that there is less elemental carbon on TiOC₅₅₀ (Fig. 94). This enhancement of the carbon bands can be explained by resonant Raman scattering with the π -states of graphite, which is typical for thin graphite layers with a low content of defects.²⁹² The optically transparent anodic oxide underneath the graphite layer may contribute to this enhancement.²⁶²

The Raman spectra of the TiO₂, TiO_x, and TiC_y phases considerably change when the annealing temperature is enhanced from 550 to 650 °C (Fig. 95b,d). Whereas the anatase and rutile phases of TiO₂ are present in TiOC₅₅₀, the corresponding bands (in particular, the characteristic low-frequency band of anatase) are not visible in the spectra of TiOC₆₅₀, TiOC₇₅₀, and TiOC₈₅₀. Instead, Raman-active TiO_x and TiC_y phases appear and, at the same time, the optical appearance of TiOC changes to metallic gray (Fig. 95e). This indicates that the oxide film is completely converted to a (defective) TiO_{1-x}C_x phase when carbothermally treated at 650, 750, and 850 °C. TiO_{1-x}C_x is a solid solution of TiO and TiC and has been reported to have semi-metallic properties,^{38,252,293} which explains the metallic appearance of TiOC₆₅₀, TiOC₇₅₀ and TiOC₈₅₀. The fraction of TiO₂ on the surface, detected with SPEM, appears to be too small to considerably contribute to the Raman response. Only the slightly enhanced signal intensity at 447 cm⁻¹ (E_g band of rutile TiO₂) in the gray spectrum of TiOC₈₅₀ with respect to that in the black spectrum may be related to the presence of TiO₂ (Fig. 95b, and Fig. 114d in Appendix A). Without data on well-defined TiO_{1-x}C_x reference materials, it is not possible to quantify the phase composition and stoichiometry of the TiO_{1-x}C_x phase in the bulk of TiOC using Raman spectroscopy. Therefore, the observed differences between the Raman responses of TiOC₆₅₀, TiOC₇₅₀, and TiOC₈₅₀ can only be interpreted in a qualitative manner and suggest an effect of the annealing temperature on the stoichiometry and/or defectivity of the converted films.^{290,291} In the case of TiOC₆₅₀ and TiOC₇₅₀, a weak substrate grain orientation effect on the Raman response can be observed (Fig. 95b,d and Fig. 114b,c in Appendix A). A relation of the properties of TiOC₈₅₀ with the initial substrate grains is not possible, but local variations in phase composition are evidenced by notable differences between the black and gray spectra in Fig. 95b,d (see also Fig. 114d in Appendix A).

5.3.4 Representation of the cross-sectional composition of TiOC on differently oriented substrate grains

The presented results show that the final physicochemical properties of carbothermally produced TiOC on Ti_{poly}, such as the chemical composition, crystalline phase composition, and surface morphology, depend on the annealing temperature and underlying substrate grain orientations. It should be noted that the gas atmosphere during the carbothermal treatment constitutes an important synthesis parameter as well: very similar chemical maps to those of TiOC₇₅₀ are obtained by carburization of planar anodic TiO₂ films on Ti_{poly} under ultrahigh vacuum conditions using ethylene as a carbon source.²⁵²

To summarize the results obtained with SPEM and micro-Raman spectroscopy, Fig. 96 depicts simplified schematic models representing the cross-sectional compositions of TiOC on top of \sim Ti(10 $\bar{1}$ 0) and \sim Ti(0001) substrate grains for the different annealing temperatures. The different thicknesses of the compact, as-grown

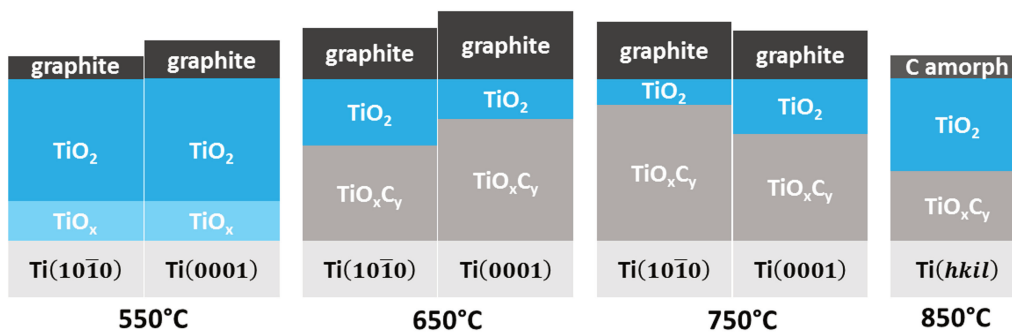


Fig. 96: Schematic representation of the cross-sectional composition of TiOC on top of \sim Ti(0001) and \sim Ti(1010) substrate grains for the different annealing temperatures. The substrate grain orientations of TiOC₈₅₀ are unknown due to grain growth during the thermal treatment. TiO_xC_y represents the solid solution of TiC and TiO, as well as TiO_x species. Reproduced from [259] © 2017 American Chemical Society.

anodic TiO₂ on top of differently oriented substrate grains, which have been reported in the literature,^{56,59,61} are neglected in the depicted models. The film thickness is assumed to remain constant for all carbothermal treatments. Compositional gradients are simplified to defined phase boundaries. Carburization at 650 and 750 °C is found to generate TiOC films with an inhomogeneous surface chemistry on individual grains: in the case of TiOC₆₅₀, SPEM reveals micrometer-sized spots on \sim Ti(1010), with compositions that differ from the average (Fig. 93b), and in the case of TiOC₇₅₀, a different chemical composition is observed at grain boundaries (Fig. 93c). Furthermore, on the nanometric scale, a patched surface composition of TiOC, with carbon, TiO₂, TiO_x and TiO_{1-x}C_x (if present) side by side, is possible.²⁵² For the sake of simplicity, only the grain area-averaged chemical composition is considered in Fig. 96. This gives rise to the layered film structure of the models, which is in line with the angle-resolved XPS measurements on TiOC, presented in Chapter 4, and is supported by the results of SPEM and micro-Raman spectroscopy, which reveal that the TiO_{1-x}C_x phase in TiOC₈₅₀ is covered by a TiO₂ film of at least \sim 1.4 nm (estimated from the $3\Lambda_e$ photoelectron escape depth in TiO₂).

Carbothermal treatment at 550 °C effectively yields a C/TiO₂ composite, with TiO_x species in the oxide film and a substrate grain-dependent amount of graphitic carbon on the surface, which is higher on top of \sim Ti(0001) than that on top of \sim Ti(1010), as reported in section 5.2. At 650, 750, and 850 °C, the anodic TiO₂ film is converted to TiO_{1-x}C_x in the bulk, as suggested by the Raman results (Fig. 90), but contains temperature- and substrate grain-dependent fractions of TiO₂ and carbon at the surface, as seen with SPEM (Fig. 93 and Fig. 94). The carbon is mainly graphitic (denoted by graphite in the model) on TiOC₅₅₀, TiOC₆₅₀ and TiOC₇₅₀, and amorphous (denoted by C amorph) on TiOC₈₅₀. In the case of TiOC₆₅₀, there is more TiO₂ and less carbon on \sim Ti(1010) than those on \sim Ti(0001). In the case of TiOC₇₅₀, there is less TiO₂ and more carbon on \sim Ti(1010) than those on \sim Ti(0001). The fractions of TiO₂ and carbon in TiOC₆₅₀ on \sim Ti(1010) are similar to the respective fractions in TiOC₇₅₀ on \sim Ti(0001), but there is more TiO₂ and C in TiOC₆₅₀ on \sim Ti(0001) than those in TiOC₇₅₀ on \sim Ti(1010)). After carburization at 850 °C, the amount of carbon is significantly lower and the amount of TiO₂ is significantly higher than those after carburization at 750 and 650 °C.

The physicochemical properties of TiOC can be understood as resulting from several parallel processes during and after carburization that are affected by temperature and substrate texture, which will be discussed in the following.

5.3.5 Effect of annealing temperature and Ti substrate texture on the crystallization of anodic TiO₂, and on the reactive decomposition of C₂H₂

During carbothermal treatments at high temperatures, the amorphous anodic TiO₂ crystallizes to anatase and/or rutile phases before C₂H₂ is added to the process. The crystallization kinetics depends on the temperature and orientation of the Ti substrate, which has consequences for the reaction of the surface with C₂H₂. This has been rationalized in the previous section based on the results obtained with the reference system TiO₂^{ref} (see sections 5.2.5 and 5.2.6). Because of the higher activity of anatase TiO₂ compared to that of amorphous TiO₂ toward the reactive decomposition of C₂H₂, the substrate grain-dependent crystallization results in a substrate grain-dependent amount of graphitic carbon on the surface of TiOC₅₅₀. Also, at higher temperatures, the substrate texture may affect the crystallization of anodic TiO₂ and thus the reactive decomposition of C₂H₂. In particular, the peculiar properties of TiOC₆₅₀ on top of $\sim\text{Ti}(10\bar{1}0)$, namely, the presence of spots with a lower carbon coverage and a lower fraction of TiC compared to the average, may be ascribed to the formation of a polycrystalline TiO₂ film on these grains, exposing facets of very different reactivities. Furthermore, the significantly lower amount of carbon on TiOC₈₅₀ could be related to a low reactivity of the rutile-rich TiO₂ film that most likely forms at the surface of the anodic film during the annealing at 850 °C prior to the addition of C₂H₂ (see Fig. 57 in Chapter 4).²⁸⁷ Besides the reactivity of the surface, the sticking coefficient of C₂H₂ on TiO₂ and the desorption probability of possible reaction intermediates, both of which depend on temperature and surface structure, may play a role in the substrate grain-dependent decomposition efficiency. Because of the concomitant diffusion of carbon into the bulk and generation of TiC at temperatures of 650 °C and higher, the final carbon content at the surface is not determined only by carbon layer formation.

5.3.6 Effect of annealing temperature and Ti substrate texture on the conversion of anodic TiO₂ to TiC, and on the material transport in TiO₂ and Ti

To explain the observed temperature-dependent average chemical composition of TiOC, thermodynamic considerations need to be taken into account, as described in Chapter 4. First, sufficiently high temperatures are required to convert TiO₂ into a solid solution of TiC and TiO.²⁵² Second, the final bulk composition is mostly determined by thermally activated diffusion of both carbon into the compact anodic TiO₂ and oxygen and carbon into the Ti substrate. The average amount of carbon on the surface decreases from 650 to 850 °C, which can be attributed mainly to the higher diffusion kinetics of carbon at higher temperatures, but partly also to the lower carbon-formation efficiency. It is noteworthy that the amorphous carbon found on TiOC₈₅₀ originates most likely from surface contamination after exposure of the carburized film to ambient air. The results obtained with micro-Raman spectroscopy suggest a temperature- and substrate grain-dependent stoichiometry and/or defectivity of the TiO_{1-x}C_x phase in TiOC, which can be understood on the basis of temperature- and substrate grain-dependent carbon supply and diffusion kinetics. The results shown in Chapter 4 have shown that at 850 °C, both oxygen and, in particular, carbon can diffuse into the Ti substrate, promoting the formation of a carbon-poor TiO_{1-x}C_x phase.²¹⁷

The main influence of the substrate grain orientation on the conversion can be conceived as an indirect effect controlled by the initial formation of polycrystalline TiO₂, with a substrate grain-dependent phase composition (anatase and rutile) and preferential orientation. First-principles calculations suggest anisotropic migration of

carbon in the tetragonal lattices of anatase ($c/a = 2.51$) and rutile TiO_2 ($c/a = 0.64$).^{294,295} Therefore, substrate grain-dependent material transport in TiO_2 , which brings about locally varying conversion time scales of the anodic TiO_2 at a given temperature, could be responsible for the substrate grain-dependent chemical compositions of TiOC_{650} and TiOC_{750} . When oxygen and carbon start to diffuse into the Ti substrate, which is activated at sufficiently high temperatures, the grain-dependent orientation of the hexagonal Ti lattice ($c/a = 1.58$) is likely to determine the diffusion kinetics,^{185,190} and therewith not only the fractions of C and O that remain in the $\text{TiO}_{1-x}\text{C}_x$ phase adjacent to the Ti substrate but also the thickness of the $\text{TiO}_{1-x}\text{C}_x$ layer. In addition, the substrate grain boundaries are likely to affect the conversion of the anodic TiO_2 . From the chemical maps of TiOC_{750} (Fig. 93c), a different conversion behavior of the anodic film at the boundaries compared to that in the area within the substrate grains can be inferred, suggesting a lower reactivity and/or faster carbon diffusion at the substrate grain boundaries. At 850°C , substrate grain growth becomes important, generating fresh grain boundaries in the oxide film, which facilitate diffusion of carbon into the bulk.

5.3.7 Effect of $\text{TiO}_{1-x}\text{C}_x$ surface reoxidation on the final composition of TiOC films

As shown in Chapter 4, the TiOC films reoxidize from the surface towards the bulk when exposed to air. In a work published together with Calvillo et al., the reoxidation of $\text{TiO}_{1-x}\text{C}_x$ -rich films, prepared under UHV conditions at 520°C , was found to happen even during cooling in reducing atmosphere at the end of a carbothermal treatment, when the temperature dropped below 475°C .²⁵² This was rationalized by DFT calculations, which revealed that $\text{TiO}_{1-x}\text{C}_x$ phases have a high tendency to decompose to TiO_2 and graphitic carbon near the surface, due to their relative thermodynamic instability at room temperature and in the presence of oxygen. The calculated intrinsic inertness toward reoxidation depended on the chemical composition of TiOC, in particular on the stoichiometry of the $\text{TiO}_{1-x}\text{C}_x$ phase. Consequently, a substrate grain effect on the reoxidation rate can be expected for TiOC_{650} and TiOC_{750} . In the TiOC_{850} film, local variations in chemical composition are observed that cannot be related to the initial substrate grain orientations. But also here, the intrinsic inertness is likely to vary accordingly on areas of different film compositions. The results on the aging behavior of TiOC films in air (Chapter 4), suggest that a high amount of graphitic carbon on the surface of TiOC after carburization does not retard the reoxidation process. Hence, a substrate-grain dependent carbon content, as observed for TiOC_{550} , TiOC_{650} and TiOC_{750} , should have no effect on the local reoxidation kinetics of the reduced titania species. In Chapter 4 it was concluded that the carbothermal treatment at 550°C yields an incomplete conversion of the anodic oxide film, with a highly instable oxycarbide phase initially present near the surface. After exposure to ambient air for several days, no $\text{TiO}_{1-x}\text{C}_x$ is detected with XPS anymore. This explains why the surface layers of the TiOC_{550} film, that has been analyzed with SPEM, contain almost stoichiometric TiO_2 on all substrate grains within the probed depth, and why no extended oxycarbide phases are detected with micro-Raman spectroscopy. To be able to observe possible substrate grain-dependent reoxidation rates on this type of film, time-resolved SPEM experiments should be performed on a freshly prepared TiOC_{550} sample, which still contains some oxycarbide species at the surface.

6. Ethanol electro-oxidation on Pt/TiO_{1-x}C_x

This chapter shows results of a study, in which the previously characterized planar TiOC films were applied as oxide-based model supports for Pt nanoparticles (NPs). The activity of this system towards the EOR and its stability in concentrated H₃PO₄ electrolyte were studied at temperatures ranging from 25 to 80 °C and compared to the performance and stability of glassy carbon (GC) supported Pt NPs in a half-cell electrochemical (EC) setup. TiOC films of different chemical composition were produced by carbothermal treatments at 750, 850, 950 and 1050 °C.

The relation between support properties and EOR activity of the Pt catalyst was investigated at room temperature and revealed a superior EOR activity for Pt NPs supported on TiOC films that were prepared at 750 °C. These were previously found to have a high TiC content on the surface and a low outer sphere electron transfer resistance (see Chapter 4). Compared to Pt/GC, this Pt/TiOC system showed a significantly enhanced activity towards the EOR at 80 °C in concentrated phosphoric acid and at potentials that are relevant for the DEFC anode. Although the TiOC support was found to be prone to anodic oxidation and corrosion, the Pt/TiOC system was outperforming Pt/GC in terms of its stability at reaction temperatures of ≤ 80 °C and potentials of < 0.8 V.

Most of the work presented here, in particular the high temperature EOR experiments, was performed in the frame of the Master thesis of F. Wiesinger,¹⁹⁴ and was published by Rüdiger et al. in 2013.²⁴⁶ At the end of this chapter, additional, unpublished results related to the stability of Pt/TiOC films and TiOC powders (provided by the Treibacher Industrie AG, Austria) in hot concentrated H₃PO₄ will be presented and discussed.

6.1 Preparation of the TiOC and GC electrodes

TiOC films were prepared on polycrystalline Ti disks with a thickness of 1.0 mm and a diameter of 15.5 mm, cut from the same precursor rod. For the EOR study performed at room temperature, TiOC films of different chemical composition were prepared by carbothermal treatments with 0.1 flow% C₂H₂ (i.e. 0.2 sccm) at annealing temperatures of 750, 850, 950 and 1050 °C, as described in section 4.2.1 of Chapter 4. For the EOR study at different reaction temperatures up to 90 °C, and for the stability tests in concentrated phosphoric acid at elevated temperatures, analogous TiOC supports with a higher fraction of TiC were synthesized at 750 °C with 0.5 flow% C₂H₂ (i.e. 1.0 sccm). As reference support, a polished GC disk of the same dimensions was used. Pt NPs were deposited *via* AAD as described in Chapter 3.

In accordance with the previous chapters, the catalyst/support model electrodes are labeled as Pt/TiOC_T, where *T* denotes the synthesis temperature of the TiOC films, and as Pt/GC.

6.2 EOR at room temperature using different TiOC supports

The electrochemical stability of freshly deposited Pt NPs on TiOC and GC supports at room temperature was investigated by monitoring the Pt ECSA during extended potentiodynamic cycling in 0.1 M HClO₄ at a scan rate of 400 mV s⁻¹ between 0.0 and two different anodic switching potentials, namely 1.2 and 1.35 V.

Fig. 97 shows the relative change of the Pt ECSA with cycling time for Pt/TiOC₇₅₀ and Pt/GC. During the first scans of all depicted measurements, the ECSA increases remarkably, which can be attributed to cleaning effects. In the smaller potential range, the ECSA value of Pt/TiOC₇₅₀ increases throughout all 200 cycles,

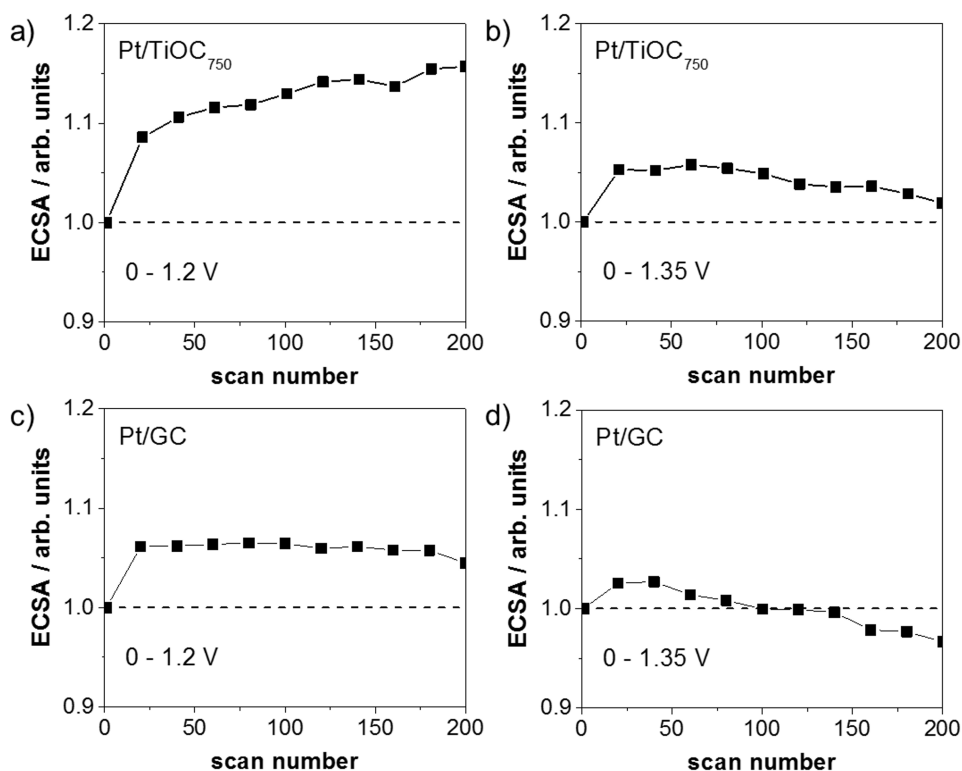


Fig. 97: Cycling stability of Pt ECSA in 0.1 M HClO₄ at room temperature. (a,b) Pt/TiOC₇₅₀ and (c,d) Pt/GC. 200 CVs were performed between (a,c) 0.0 and 1.2 V, and (b,d) 0.0 and 1.35 V at 400 mV s⁻¹. The ECSA is normalized to its initial values of 26.8 % (Pt/TiOC₇₅₀) and 48.4 % (Pt/GC) of the geometric area. Adapted from the supporting information of [246].

suggesting an ongoing activation of the Pt catalyst. The ECSA values of Pt/GC reach a plateau after ~ 20 cycles and stay unchanged. When cycling between 0.0 and 1.35 V, a decrease in the ECSA of both Pt/TiOC₇₅₀ and Pt/GC is observed after an initial increase up to cycle number 60 (Pt/TiOC₇₅₀) and number 40 (Pt/GC). After 200 cycles, the ECSA of Pt/TiOC₇₅₀ is still slightly above its initial value, while that of Pt/GC has decreased to 95 %. These observations demonstrate that both model systems have an excellent stability in 0.1 M HClO₄ at room temperature during cycling between 0.0 and 1.2 V, and a comparable and acceptable stability during cycling between 0.0 and 1.35 V.

Fig. 98 depicts CVs of the Pt/TiOC and Pt/GC electrodes that were acquired in 0.1 M HClO₄ with 0.5 M EtOH at room temperature. The general shape of the CVs is similar for all investigated electrodes, and is determined by the reaction mechanism of the EOR at the Pt catalyst (see section 2.1.4.3). The overall highest EOR activity of the Pt/TiOC systems is found for Pt/TiOC₇₅₀, which furthermore shows significantly higher current densities than Pt/GC. The EOR activity of the Pt/TiOC systems decreases with increasing synthesis temperature of the TiOC supports, and the overall lowest current densities are observed for Pt/TiOC₁₀₅₀. These observations are in line with the results obtained from the electrochemical characterization of TiOC films prepared at the same annealing temperatures (see Chapter 4). There, it was found that the TiOC film prepared at 750 °C had the lowest outer sphere charge transfer resistance (tested with the Fe(CN)₆³⁻/Fe(CN)₆⁴⁻ redox couple), which was similar to that of GC, and that it had the lowest overpotential towards the HER in comparison with the other studied TiOC. In particular, the charge transfer resistance increased and the HER activity decreased with an increasing fraction of TiO₂ on the surface, which in turn was related to an increasing TiOC synthesis

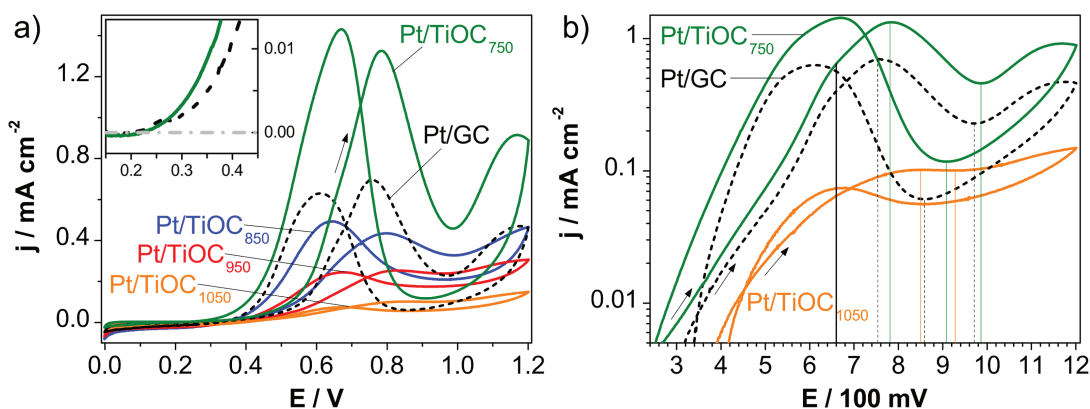


Fig. 98: CVs of Pt/TiOC and Pt/GC in 0.1 M HClO₄ with 0.5 M EtOH taken at a scan rate of 10 mV s⁻¹. b): logarithmic plot of a) showing the CVs of Pt/TiOC₇₅₀, Pt/TiOC₁₀₅₀ and Pt/GC. a) adapted from [246] © 2013 WILEY-VCH Verlag GmbH & Co. KGaA, Weinheim.

temperature.

As can be seen from the inset in Fig. 98a, the onset potential for the EOR at both Pt/TiOC₇₅₀ and Pt/GC is about 0.23 V. A more precise measure for the EOR onsets is given by the respective potentials at which notable anodic currents of a fixed value are observed. From the logarithmic plot in Fig. 98b it can be seen that during the anodic CV scan an EOR current density of 5 μA cm⁻² is first measured for Pt/TiOC₇₅₀ at 0.27 V, followed by Pt/GC at 0.32 V, and latest for Pt/TiOC₁₀₅₀ at 0.39 V. This indicates an earlier onset of the EOR at the Pt/TiOC₇₅₀ electrode. The shoulder at about 0.66 V that is clearly visible for both Pt/TiOC₇₅₀ and Pt/GC is most likely related to the current maximum of oxidative CO stripping, typically observed on Pt catalysts.^{10,92,101} Without DEMS measurements, it is however not possible to clearly identify the potential range in which complete oxidation of EtOH to CO₂ is the dominating reaction path. During the positive going potential sweeps, the CVs of Pt/TiOC₇₅₀ and Pt/GC show peak maxima of 1.33 mA cm⁻² at ~ 0.78 V and 0.70 mA cm⁻² at ~ 0.75 V, respectively. The higher peak potential observed for Pt/TiOC₇₅₀ may be related to a slightly later catalyst poisoning by adsorbed acetate.¹⁰¹ Above 0.8 V, the formation of adsorbed acetate causes the EOR rate to decrease until a minimum at ~ 0.98 V, beyond which oxidative removal of the adsorbate allows the EOR current to increase once more.¹⁰¹ This minimum is considerably less pronounced in the CV of Pt/TiOC₁₀₅₀ compared to Pt/TiOC₇₅₀ and Pt/GC (Fig. 98b). Furthermore the EOR current peak measured for Pt/TiOC₁₀₅₀ during the cathodic CV scan is notably lower than the respective anodic current peak. Based on the results presented in Chapter 4, both these observations may be explained by severe anodic passivation of the TiOC₁₀₅₀ support during the positive going potential sweep. Firstly, a contribution of the associated passivation current to the overall signal intensity during the anodic sweep could explain, why the current minimum at ~ 0.98 V is less pronounced in the CV of Pt/TiOC₁₀₅₀. Secondly, a passivation of the support during the positive going sweep enhances the interfacial electron transfer resistance, causing attenuated EOR currents in the cathodic CV scan, as it is observed. During the negative going potential sweep, EOR currents are recovered about 50 mV earlier on Pt/TiOC₇₅₀ than on Pt/GC, and the cathodic current peak is higher than the anodic current peak in the case of Pt/TiOC₇₅₀. The resulting potential separations between the current peaks in the anodic and cathodic sweeps are 0.11 V for Pt/TiOC₇₅₀ and 0.15 V for Pt/GC, suggesting a slightly improved reactivation of Pt/TiOC₇₅₀ during the cathodic CV scan. The reactivation of Pt catalysts during the negative going CV scan has been ascribed to the reductive dissolution

of Pt oxide.^{92,99,101} During this process, active catalyst sites for the adsorption of EtOH become available and, at the same time, the oxygen species that are still present on some Pt atoms can be used to oxidize the adsorbates. The observation of an earlier EOR onset in the cathodic CV branch of Pt/TiOC₇₅₀ may be related to a synergistic influence of the TiOC₇₅₀ support on the removal of oxide species from Pt or on the supply of oxide species for the oxidation of EtOH adsorbates.

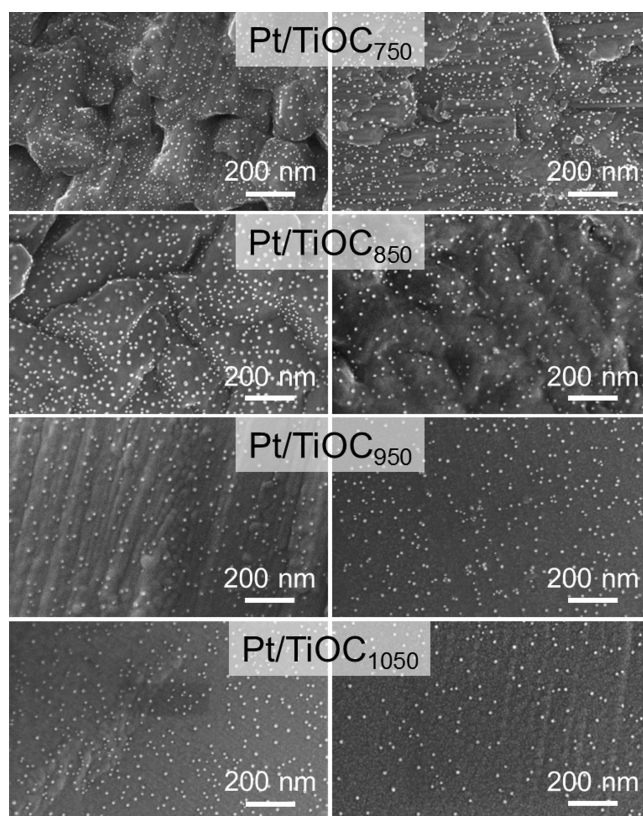


Fig. 99: Scanning electron micrographs of Pt/TiOC prior to (left) and after (right) CVs in 0.1 M HClO₄ with 0.5 M EtOH. Adapted from the supporting information of [246].

Table 6.1: Average diameter and particle planar density values of Pt NPs prior to and after electrochemistry on Pt/TiOC. Adapted from the supporting information of [246].

electrode	diameter (before EOR)	diameter (after EOR)	particle density (before EOR)	particle density (after EOR)	change in particle density
Pt/TiOC ₇₅₀	(6 ± 3) nm	(8 ± 4) nm	$1.59 \times 10^{11} \text{ cm}^{-2}$	$1.42 \times 10^{11} \text{ cm}^{-2}$	-10.43 %
Pt/TiOC ₈₅₀	(10 ± 4) nm	(7 ± 4) nm	$9.85 \times 10^{10} \text{ cm}^{-2}$	$4.94 \times 10^{10} \text{ cm}^{-2}$	-49.81 %
Pt/TiOC ₉₅₀	(8 ± 4) nm	(8 ± 3) nm	$3.79 \times 10^{10} \text{ cm}^{-2}$	$3.75 \times 10^{10} \text{ cm}^{-2}$	-0.97 %
Pt/TiOC ₁₀₅₀	(9 ± 5) nm	(9 ± 2) nm	$4.85 \times 10^{10} \text{ cm}^{-2}$	$1.79 \times 10^{10} \text{ cm}^{-2}$	-63.13 %

SE micrographs were taken of the Pt/TiOC electrodes before and after the electrochemical measurements to obtain information on the catalyst degradation and loss during the EOR at room temperature. From Fig. 99 it can be seen that before and after the CVs in EtOH containing electrolyte, the TiOC films are homogeneously covered with Pt NPs that have diameters of less than 10 nm. From a detailed image analysis, average particle diameters and planar particle densities were extracted. The obtained values are given in table 6.1.

While Pt agglomeration during EC conditions appears to be negligible, the analysis of the imaged electrode areas suggests a notable catalyst loss after the EOR experiments. It should be noted that SEM provides no information about the entire electrode area that was exposed to the electrolyte.

6.3 EOR on Pt/TiOC₇₅₀ and Pt/GC at elevated temperatures and in concentrated H₃PO₄

The EOR activity of the Pt/GC reference system and of the most promising Pt/TiOC system, that is Pt/TiOC₇₅₀ (termed Pt/TiOC in the following), was investigated in 14.6 M H₃PO₄ with 1.0 M EtOH by potentiodynamic cycling and subsequent current transient measurements at temperatures between 25 and 80 °C. To ensure reproducibility of the results, the electrochemical experiments were performed with five Pt/TiOC and three Pt/GC samples, which allowed to calculate average values and standard deviations from the measured currents and potentials.

Fig. 100 shows a representative set of CVs for Pt/TiOC and Pt/GC, acquired at different temperatures. At 90 °C, only one electrochemical experiment with Pt/TiOC yielded EOR currents (Fig. 100a). During other attempts to perform electrochemical measurements at this temperature, only negligible currents were detected, indicating a complete loss of the Pt catalyst. Therefore, the following experiments were limited to a maximum temperature of 80 °C.

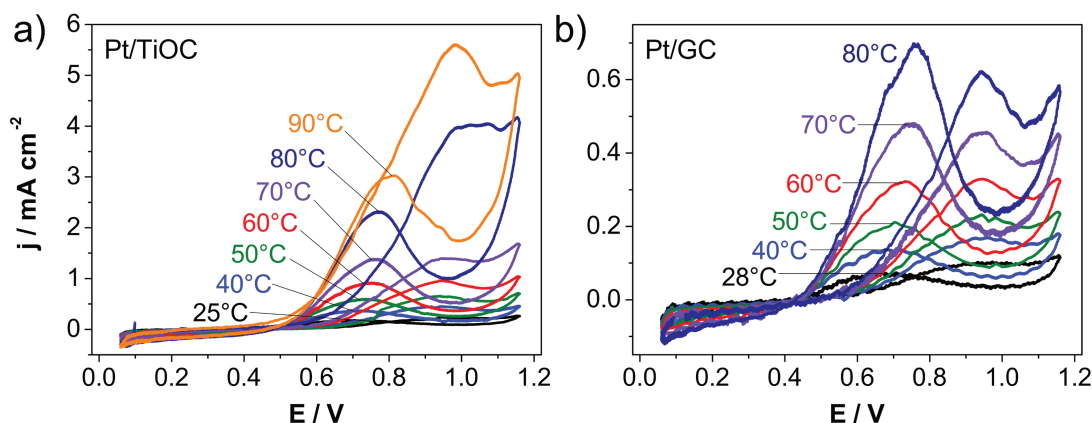


Fig. 100: CVs of a) Pt/TiOC and b) Pt/GC in 14.6 M H₃PO₄ with 1.0 M EtOH taken at a scan rate of 50 mV s⁻¹ and at temperatures between 25 and 90 °C, respective 80 °C. Adapted from the supporting information of [246].

As can be seen from the CVs, the EOR activity of both systems increases with increasing reaction temperature, which is a well-known trend for the Pt catalyzed EOR.^{10,76,99,100} More remarkably, however, is the observation of significantly enhanced EOR currents at the Pt/TiOC electrode compared to Pt/GC, which is in accordance with the findings obtained at room temperature (Fig. 98). The onset of EOR currents during the positive going potential sweep at room temperature is observed at ~ 0.57 V and ~ 0.55 V for Pt/TiOC and Pt/GC, respectively. These are considerably higher values than the onset potential of ~ 0.23 V, which was determined for the EOR at these electrodes in 0.1 M HClO₄ with 0.5 M EtOH (inset in Fig. 98). The reason for the anodically shifted onset potentials in concentrated H₃PO₄ is the (electrochemical) adsorption of impurities and anions from the supporting electrolyte, which block the electrode and inhibit the EOR at lower potentials.¹⁰⁰ The formation of phosphates or similar species on the Pt/TiOC electrode was confirmed with XPS analysis (see below). Despite the later current onset in the positive going sweep, the general shape of the CVs in

Fig. 100 is very similar to that reported for polycrystalline Pt electrodes in EtOH containing acidic supporting electrolytes.^{100,101} A closer look at the CVs acquired with the Pt/TiOC electrode (Fig. 100a) reveals that the current peak measured during the positive going sweep is significantly enhanced compared to the current peak observed in the cathodic CV scan, when the temperature is raised from 70 to 80 °C and subsequently to 90 °C. Furthermore, the current peak measured during the positive going sweep at 80 °C is notably broadened (additional CVs for Pt/TiOC electrodes at this temperature can be found in [194]). This suggests a change of the overall electrochemical reaction that is taking place at Pt/TiOC in ethanol containing concentrated H₃PO₄ electrolyte. In contrast, the respective ratio between the current peaks measured during the anodic and cathodic scans with the Pt/GC electrode is slightly lowered when the temperature is raised from 70 to 80 °C. This can be ascribed to an improved coupling between the thermally activated PtO reduction and EtOH oxidation at higher temperatures, leading to a higher peak in the cathodic scan.¹⁰⁰

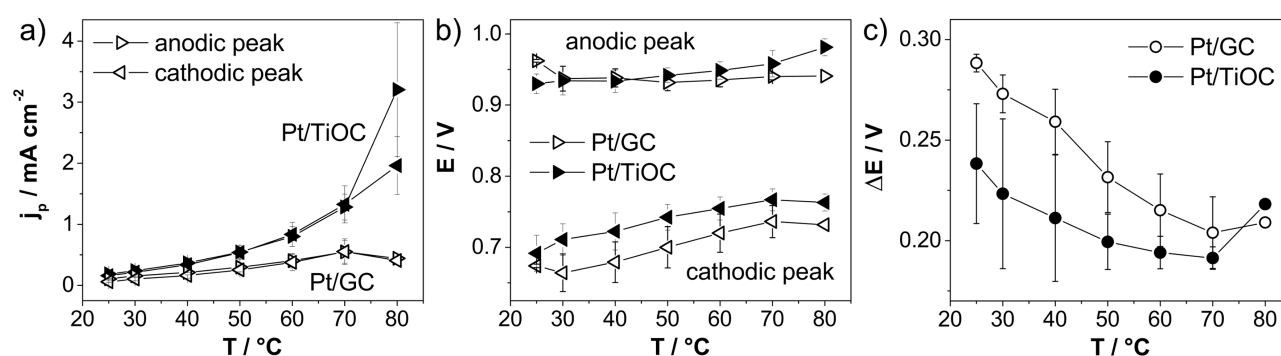


Fig. 101: Evaluation of CVs acquired with Pt/TiOC and Pt/GC electrodes in 14.6 M H₃PO₄ with 1.0 M EtOH: a) Peak-current densities, b) peak potentials, and c) peak separations (anodic/cathodic going potential sweeps). Error bars: standard deviation for different samples. Adapted from [246] © 2013 WILEY-VCH Verlag GmbH & Co. KGaA, Weinheim.

Fig. 101 shows the results of a detailed evaluation of all CVs, acquired with several Pt/TiOC and Pt/GC electrodes including those shown in Fig. 100. Thereby, the average peak current densities, peak potentials, and potential separations ΔE of the EOR peaks measured during the anodic and cathodic going potential sweeps were determined. As can be seen from Fig. 101a, the anodic and cathodic peak current densities of Pt/TiOC undergo a steeper increase with increasing temperature and are higher than those of Pt/GC for all investigated temperatures, evidencing an enhanced EOR activity of Pt/TiOC. In addition, the peak current densities obtained for Pt/GC drop again when the temperature is raised from 70 to 80 °C, which suggests catalyst loss and/or degradation.

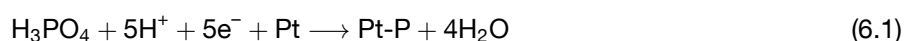
At room temperature, the current peak in the anodic CV scan (anodic peak in Fig. 101b) is observed at 0.962 V for Pt/GC and at 0.930 V for Pt/TiOC. Between 30 and 80 °C, the anodic peak detected for Pt/GC stays at a constant potential of 0.937 ± 0.003 V, whereas the anodic peak detected for Pt/TiOC shifts continuously towards higher potentials with increasing temperature, reaching a potential of 0.981 V at 80 °C.

Both these trends contradict with observations done by other research groups, which reported (for similar temperature ranges) a negative shift of the EOR peak in the anodic going CV scan with increasing temperature.^{10,76,99,100} A possible reason for this opposite result lies in the used reference electrodes and reference potentials. In the present work, potentials are reported versus the SHE (at 25 °C). A Hg|Hg₂SO₄|0.1 M H₂SO₄ RE was placed in an external compartment, filled with 0.1 M H₂SO₄ and kept at room temperature,

which was connected with the concentrated H₃PO₄ electrolyte in the main EC cell *via* an electrolyte bridge. Maybe the liquid junction in the electrolyte bridge caused a temperature-dependent potential drop, whose value is unknown. In the cited studies, the reference electrode, which was a reversible hydrogen electrode (RHE), a dynamic hydrogen electrode (DHE) or a saturated calomel electrode (SCE), was placed in the same (supporting) electrolyte as that used for the EOR measurements, and potentials are reported *versus* the temperature dependent RHE,^{10,76,99} or *versus* the DHE at room temperature after potential correction with the calculated thermodynamic temperature coefficient¹⁰⁰ (see equation 2.13). It should be remarked that this demonstrates the impact of the used methods and experimental conditions on the comparability of the results obtained in different studies. Well-defined and reproducible experimental conditions are essential to define benchmarks for EOR catalyst performances at elevated temperatures. At the time of the presented study, no commonly accepted agreement on standardized experiments was known. Nevertheless, deviations in the reference potential cannot explain the different temperature-dependent trends of the EOR CVs that are observed for Pt/TiOC and Pt/GC in the present study. Taking into account that Pt/GC should have comparable properties like the Pt/Vulcan powder catalysts that were investigated in the group of Behm,^{10,76} the different behavior of Pt/GC and Pt/TiOC point to peculiar electrocatalytic characteristics of the TiOC supported catalyst.

The current peaks in the cathodic CV scan (cathodic peak in Fig. 101b) shift in anodic direction with increasing temperature for both Pt/GC and Pt/TiOC, and are observed at more positive potentials in the case of Pt/TiOC at all investigated temperatures. Up to 70 °C, the resulting peak separations ΔE are smaller for Pt/TiOC compared to Pt/GC and decrease with increasing temperature for both electrodes (Fig. 101c). This is in accordance with literature reports on the EOR at Pt catalysts, where the vanishing hysteresis of the anodic and cathodic CV scans was explained by kinetically activated CO_{ads} oxidation (shift to lower potentials) and PtO reduction (shift to higher potentials).^{10,100,106,107} Consequently, the lower ΔE values of Pt/TiOC compared to Pt/GC up to 70 °C may be ascribed to an improved kinetic activation of either one or both of these reaction steps on Pt/TiOC. When the temperature is raised from 70 to 80 °C, the peak separations obtained for Pt/TiOC and Pt/GC increase again and attain a higher value for Pt/TiOC compared to Pt/GC. This observation suggests an activity loss of both catalyst systems at this temperature, which will be addressed in detail in the context of the performed electrochemical stability studies presented below.

Fig. 102 shows representative potentiostatic current density-time profiles (transients), measured at potentials between 0.5 and 0.9 V, for temperatures between room temperature and 90 °C (Pt/TiOC) or 80 °C (Pt/GC). At low anodic potentials and temperatures, negative current densities are observed for both electrodes. These may originate from the formation of platinum phosphide (Pt-P) via the electrochemical reaction:²⁹⁶



In the case of Pt/TiOC, the EOR currents are negligibly small up to potentials of 0.5 V, where the current starts to attain positive values at temperatures ≥ 60 °C (Fig. 102c). In the case of Pt/GC, small negative currents are detected at 0.5 V up to 80 °C (Fig. 102b,d).

At all investigated temperatures, the current transients obtained for Pt/TiOC show an instantaneous sharp increase at the beginning of each potential step, which is followed by an approximately exponential decay within the first 5–40 s. The magnitude of the initial current spike increases with increasing reaction temperature.

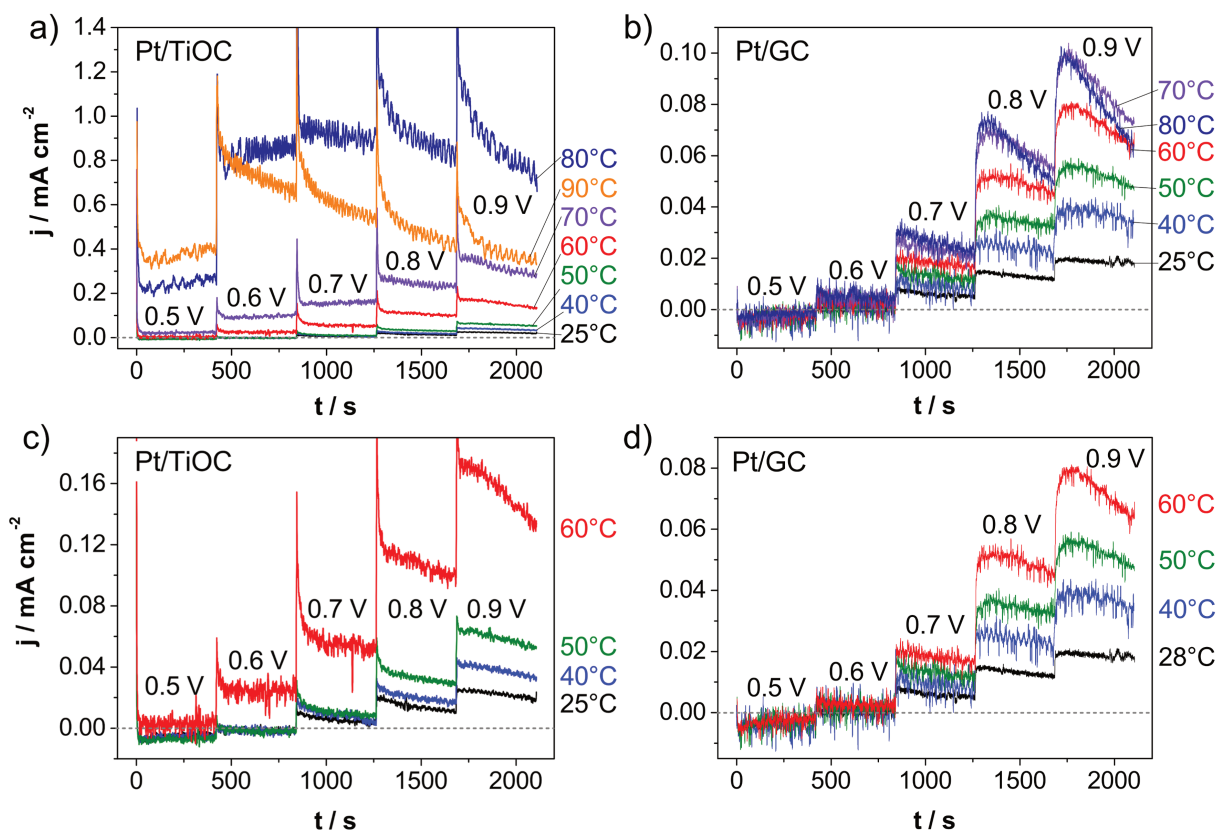


Fig. 102: Chronoamperometric profiles of (a,c) Pt/TiOC and (b,d) Pt/GC, acquired for 7 min each at potentials between 0.5 and 0.9 V after each CV in Fig. 100. (c,d): graphs from (a,b) with reduced current density scale. (a,b) adapted from [246] © 2013 WILEY-VCH Verlag GmbH & Co. KGaA, Weinheim.

Completely different transient profiles are found for Pt/GC (for additional data see [194]). In particular, current transients acquired at potentials of ≥ 0.8 V and temperatures ≥ 40 °C pass through a smooth maximum after the initial abrupt increase at the potential step, but show no sharp spike. Wang et al. studied current-time profiles of carbon supported Pt catalyst in 0.5 M sulfuric acid with 0.1 M EtOH.⁷⁶ They ascribed a slow and steady increase after the initial current step, as observed here for Pt/GC, to the relatively slow electrooxidation of adsorbed CO and CH_x species that have formed upon the dissociative adsorption of EtOH on Pt at low potentials. This process was proposed to dominate the initial current transient if no secondary faradaic reactions interfered, such as oxidative removal of adsorbed hydrogen from the Pt surface. On the other hand, the transient profiles observed for Pt/TiOC remind to the characteristic response that is observed during potentiostatic anodic oxide film growth on electropolished Ti.⁵⁴ Therefore it is likely that TiOC surface oxidation has a considerable contribution to the initial current transients.

For sufficiently small potentials and low temperatures, the currents obtained for Pt/TiOC attain stable steady-state values soon after the initial drop, or they increase or decrease at a very slow rate until the end of the transient. Considerably stable long-time currents are observed up to a potential of 0.7 V and up to 80 °C. At 80 °C, however, a steep current decrease is observed in the transients measured at potentials of ≥ 0.8 V, and at 90 °C, the long-time currents decrease continuously with time already for potentials of ≥ 0.6 V. In the case of Pt/GC, all of the chronoamperometric profiles show a steady current decrease with time at potentials ≥ 0.7 V, which is small at lower temperatures, but becomes more severe for temperatures of ≥ 70 °C, in particular at the two highest potentials.

The ongoing steep current decrease until the end of the transient measurements, observed for Pt/GC and Pt/TiOC at the higher potentials and temperatures, can be explained by electrode degradation and/or Pt loss, as will be substantiated below. As long as electrode stability is ensured, the steady-state EOR currents increase with increasing temperature, which is in line with the respective CVs (Fig. 100) and can be ascribed to the thermally activated reaction steps of the EOR. In the case of Pt/GC, the highest stable steady-state current was measured at 80 °C and 0.6 V ($\sim 0.005 \text{ mA cm}^{-2}$), and was by a factor of 170 lower than the corresponding current obtained for Pt/TiOC ($\sim 0.85 \text{ mA cm}^{-2}$). This observation clearly evidences a superior performance of Pt/TiOC in the electro-oxidation of EtOH under these conditions.

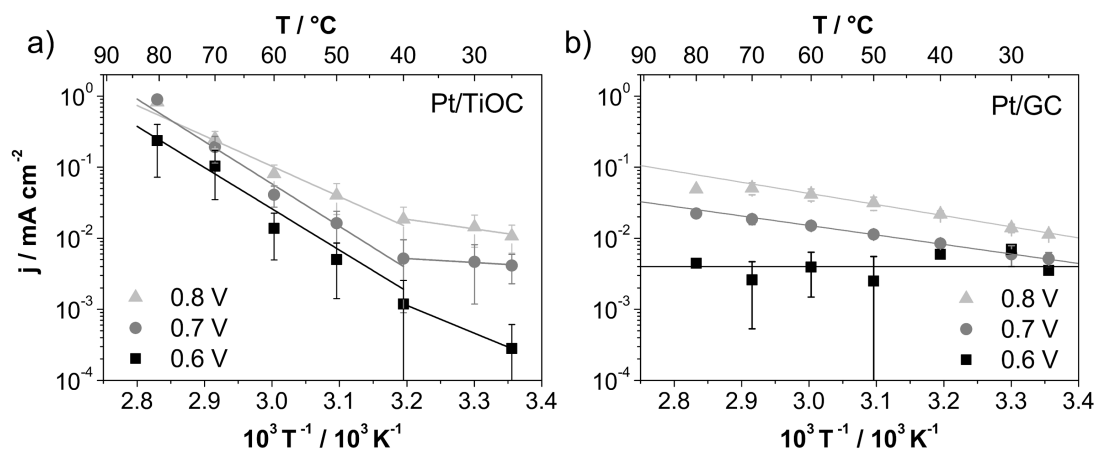


Fig. 103: Arrhenius plots obtained for a) Pt/TiOC and b) Pt/GC using the final steady-state current densities of chronoamperometric measurements at 0.6, 0.7 and 0.8 V. Adapted from [246] © 2013 WILEY-VCH Verlag GmbH & Co. KGaA, Weinheim.

The temperature-dependent steady-state values of the faradaic currents at the end of the transient curves (i.e. j at $t = 7 \text{ min}$) were used to construct Arrhenius plots. To compensate for the error in the current density due to noise during the measurement, a linear curve was fit to the last $\sim 3 \text{ min}$ of the transient curves, and its value at $t = 7 \text{ min}$ was used for the plots. From the Arrhenius plots, apparent activation energies (E_a) for the overall electro-oxidation of EtOH could be calculated for Pt/TiOC and Pt/GC. Fig. 103 shows Arrhenius plots that were obtained for potentials of 0.6, 0.7, and 0.8 V. Those transients that were affected by catalyst degradation were not used to calculate the activation energies, but the respective final current values are included in the Arrhenius plots to facilitate the identification of trends in the curves. In the case of Pt/TiOC, two linear branches of the logarithmic EtOH oxidation rates can be identified in the Arrhenius plots (Fig. 103a). The data points follow a steeper slope between 80 and 40 °C, and a shallower slope between 40 and 25 °C. This observation indicates a change in the rate-determining step of the EOR at Pt/TiOC at temperatures of $\sim 40 \text{ °C}$. At a potential of 0.7 V, the corresponding apparent activation energies are $E_a(T \geq 40 \text{ °C}) = 114.2 \pm 10.3 \text{ kJ mol}^{-1}$ and $E_a(T \leq 40 \text{ °C}) = 10.7 \pm 2.5 \text{ kJ mol}^{-1}$. For Pt/GC, the logarithmic oxidation rates decrease linearly with $1/T$ between 60 and 25 °C where degradation of the electrode is negligible (Fig. 103b). This suggests that there is no change in the rate limiting step of the EOR at Pt/GC in this range of temperatures. The slope yields an apparent activation energy of $E_a(T \leq 60 \text{ °C}) = 25.6 \pm 0.4 \text{ kJ mol}^{-1}$. No degradation effects are only visible at 0.6 V, but also no remarkable EOR activity is observed at this potential.

It is tempting to compare the obtained E_a with corresponding values reported in the literature. However, care needs to be taken when interpreting apparent activation energies. As pointed out by Cohen et al., several

factors influence the magnitude of the calculated E_a , such as surface poisoning from reaction intermediates, anion adsorption from the supporting electrolyte, pH effects and oxide formation processes on the surface of Pt catalysts.⁷⁸ Since all these factors are potential and temperature dependent, they must be kept in mind when comparing E_a values. At least two studies on the EOR at Pt catalysts are reported in the literature, where apparent activation energies have been determined in a similar way as in the present work and for comparable potentials. Sun et al., who studied the EOR on a carbon-supported Pt catalyst between room temperature and 100 °C, obtained an apparent activation energy of $40 \pm 2 \text{ kJ mol}^{-1}$ at a potential of 0.68 V (versus the RHE at the reaction temperature) in 0.1 M EtOH containing aqueous sulfuric acid solution.¹⁰ The authors conducted the electrochemical measurements in a pressurized flow cell and used the steady-state faradaic currents obtained from chronocoulometry to construct the Arrhenius plots. The resulting curves showed no change in slope over the studied temperature range. A direct comparison between the reported apparent activation energy and the value that was obtained for Pt/GC in the present work is difficult, since different supporting electrolytes were used. The EOR in 1.0 M EtOH containing concentrated phosphoric acid supporting electrolyte was studied by Camargo et al. under quasi-stationary conditions using a polycrystalline Pt electrode.¹⁰⁰ The authors constructed an Arrhenius plot from the final current values of 20 min long transient measurements at 0.65 V (versus the DHE at room temperature) and observed that the slope of the logarithmic current plot varied in different temperature ranges. In the range between 160 and 50 °C, the calculated apparent activation energy was 9.2 kJ mol^{-1} and from the significantly different slope of the two data points at 50 and 25 °C, they determined an E_a value of 90.6 kJ mol^{-1} . In the present work, temperature-dependent slopes in the Arrhenius plot were only found for Pt/TiOC and the respective E_a values highly disagree with those reported in the cited publication. Furthermore, the authors in [100] provide no information on whether or not the electrolyte was agitated to ensure kinetically controlled steady-state conditions. The discrepancies between the kinetic data reported in the literature and obtained in the present study highlight once more the importance of experimental aspects in the definition of activity benchmarks.

6.3.1 Origin of the enhanced EOR activity of the Pt/TiOC system

The results presented up to now evidence a superior activity of Pt/TiOC towards the EOR in acidic electrolytes at room temperature and at elevated temperatures compared to Pt/GC. To understand the exceptional behavior of the Pt/TiOC system, possible influences of the TiOC support on the overall catalytic activity need to be considered.

Several features in the electrochemical response of Pt/TiOC₇₅₀ point to a synergistic effect of the support on the EOR activity. At room temperature and in 0.1 M HClO₄ supporting electrolyte, notable EOR currents are observed at slightly lower potentials in the case of the Pt/TiOC₇₅₀ system than in the case of the Pt/GC reference system. Furthermore, the slightly earlier recovery of EOR currents at Pt/TiOC₇₅₀ during the cathodic sweep of the CVs suggests a positive influence of the TiOC support on the catalyst re-activation. Calvillo et al. found that EtOH molecules adsorb on the surface of the TiOC films (preferentially at TiO_x species),²⁵⁸ which substantiates the conclusion that the TiOC₇₅₀ support is actively involved in the reaction. Roca-Ayats observed an enhanced activity of Pt/TiC-based catalysts towards the electro-oxidation of adsorbed CO and of methanol after an anodic polarization of the electrode up to 1.0 V in 0.5 M H₂SO₄, which they ascribed to the formation of oxygenated species on the oxidized TiC support that promote the oxidation of CO and

methanol at lower anodic potentials.³² A similar effect can be expected for TiOC supported Pt in the EOR. Besides a co-catalytic effect, the TiOC support may directly influence the physicochemical properties of the deposited Pt NPs. It is well known, that group VIII noble metals that are supported on titanium oxide experience the so-called strong metal-support interaction (SMSI), which alters their chemisorption properties and therewith their catalytic activity.²⁵ The reason for the generally reduced chemisorption of e.g. H₂ on Pt was found to be an invasion of the catalyst surface by the oxide support, when the surface was exposed to thermal annealing in reducing atmosphere. Prerequisite was identified to be that the oxide support had to exhibit reduced species on the surface. Already at 200 °C, TiO_x was found to attack the supported Pt catalyst and cover part of its surface. A partial coverage of Pt with TiO_x can affect the geometry and the electronic properties of the Pt catalyst itself due to bonding interactions. In addition, the newly formed interfaces between Pt and TiO_x may act like a hybrid catalyst, where Ti or O species take over parts of the multi-step catalytic reaction, such as water activation (co-catalytic effect).

In this respect, the change in the slope of the Arrhenius plot at ~ 40 °C that has been observed for Pt/TiOC (Fig. 103a) during the EOR experiments in concentrated phosphoric acid at different temperatures, may be related to the activation of a specific co-catalytic contribution of the TiOC support or a changing catalyst support interaction, which influences the preferred reaction path and therewith the apparent rate determining step.

Furthermore, for the present Pt/TiOC system, a partial coverage of the Pt NPs with TiO_x is likely to happen during the deposition of the metal NPs *via* AAD at 350 °C. However, in the frame of this thesis, the nature of possible catalyst-support interactions or co-catalytic effects in the Pt/TiOC system could not be clarified and requires additional experiments. It should only be noted that from the XP spectra of the Pt 4f core level, recorded after the EC tests, no significant electronic effect of the support on the catalyst can be deduced.

6.4 Electrochemical stability of Pt/TiOC and Pt/GC in hot H₃PO₄

The current transient measurements revealed that both the Pt/TiOC and Pt/GC electrodes suffer from EOR activity loss at high anodic potentials and temperatures. This can be ascribed to a reduction of the active electrode area due to catalyst degradation or loss. Indeed, ESCA measurements before and after the EOR tests in concentrated H₃PO₄ point to a considerable loss of active Pt: The Pt ECSA of Pt/TiOC was reduced by about 50 % after EOR tests at temperatures between 25 and 70 °C, which included potentiodynamic cycling up to 1.16 V and potentiostatic steps up to 0.9 V. After the same experiment, the ECSA of Pt/GC was reduced by 54 %. When the EOR experiment was conducted up to 80 °C (with Pt/GC) or up to 90 °C (Pt/TiOC), no Pt CV could be detected anymore for the used electrodes, suggesting a loss of the entire catalyst.

SE micrographs of Pt/TiOC and Pt/GC were recorded before and after the EOR experiments to verify the Pt loss. Selected areas of the electrodes are depicted in Fig. 104. The freshly prepared samples show a uniform coverage with Pt NPs of similar sizes. The according ECSA was determined to be 28.6 % and 48.4 % of the geometric area for Pt/TiOC and Pt/GC, respectively. After the EOR tests up to 70 °C, random detachment and agglomeration of the Pt catalyst is observed on Pt/GC: Large areas on the surface appear darker, owing to Pt loss, and large Pt agglomerates are visible. Interestingly, in the case of Pt/TiOC, the stability of the Pt catalyst clearly depends on the local physicochemical properties, and in particular the electrochemical stability, of the TiOC support. The SE micrographs shown in the insets of Fig. 104 were taken on top of two

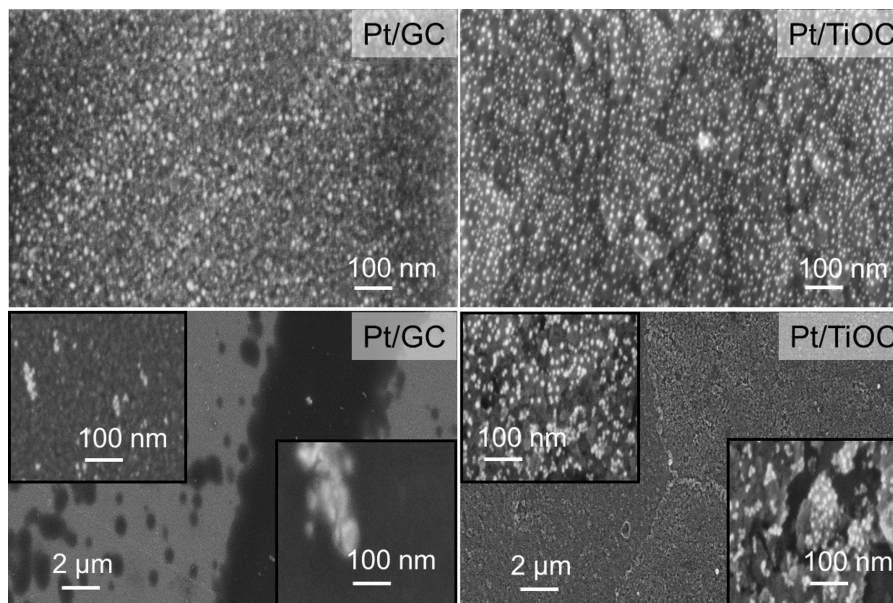


Fig. 104: SE micrographs of Pt/GC (left) and Pt/TiOC (right) before (top) and after (bottom) EOR tests at different temperatures. Before the EOR tests, the ECSA was 28.6 % of the geometric surface area for Pt/TiOC and 48.4 % for Pt/GC. Insets: two areas of higher (top) and lower (bottom) Pt coverage after EC. Adapted from [246] © 2013 WILEY-VCH Verlag GmbH & Co. KGaA, Weinheim.

different Ti substrate grains. It appears that on top of specific Ti substrate grains, the Pt coverage of the TiOC film remains almost unchanged after the EOR experiment, whereas on top of other grains, degradation of the TiOC support and concomitant Pt loss has taken place.

To study the influence of hot concentrated H₃PO₄ on the electrochemical degradation of Pt/TiOC and Pt/GC, EOR simulation experiments were performed at 50 and 80 °C in the absence of EtOH. In addition, a set of electrodes was exposed to the concentrated H₃PO₄ at room temperature for 6.5 h, which was comparable to the duration of an entire EOR experiment, and another set for 11 h. To quantify the catalyst degradation, the ECSA of Pt was determined from CVs at room temperature in 0.1 M HClO₄, which were acquired before and after the EOR simulation, as well as before and after the prolonged exposure to H₃PO₄. The EOR simulation test was performed with each two Pt/GC and Pt/TiOC samples. Fig. 105 shows selected CVs with the respective ECSA values.

After the electrochemical tests at 50 and 80 °C, the ECSA of the tested Pt/GC samples decreased on average by 61.5(±6.2)% of its initial value (Fig. 105b). In the case of Pt/TiOC, the two investigated surfaces showed remarkable differences in Pt loss: 65.6 % of the initial ECSA was lost in one case but only 21.4 % was lost in another (the CVs of the latter sample are shown in Fig. 105a). After exposure to 14.6 M H₃PO₄ at room temperature for 6.5 h, the ECSA of the tested Pt/TiOC electrode did not change, whereas that of Pt/GC decreased to half of its value before the stability test (not shown). An exposure to the acid for 11 h had an even more severe effect on Pt/GC, since no Pt could be detected electrochemically anymore (Fig. 105d). In contrast, the ECSA of the tested Pt/TiOC was still 72.7 % of its initial value (Fig. 105c).

The results of the stability tests show that both systems suffer from degradation in concentrated H₃PO₄ at elevated temperatures as well as at room temperature. But they also evidence that the Pt/TiOC system is more stable than Pt/GC, especially during long exposure to the acid at room temperature and without electrochemical polarization. The observation that the two Pt/TiOC samples, which underwent the

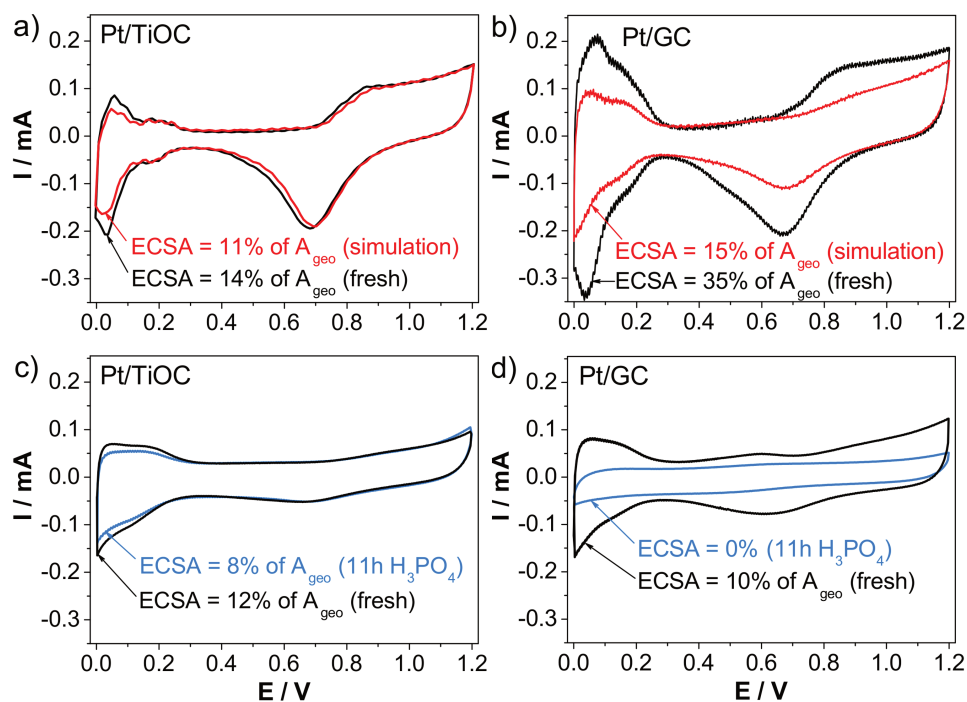


Fig. 105: CVs obtained for (a,c) Pt/TiOC and (b,d) Pt/GC before and after stability tests in 14.6 M H_3PO_4 . Red curves in (a,b): after CVs and transients at 50 and 80 °C (simulation). Blue curves in (c,d): after exposure to H_3PO_4 at room temperature for 11 h. Electrolyte: 0.1 M $HClO_4$ at room temperature; scan rate: 400 $mV s^{-1}$. ECSA values are given in % of the geometric surface area A_{geo} . Adapted from the supporting information of [246].

electrochemical simulation experiment at elevated temperatures, show very different losses in ECSA, is an indication for an influence of the average surface properties (morphology, structure and chemistry) of the TiOC films on the stability of the Pt/TiOC system. Recalling the results presented in Chapter 5, different average physicochemical properties of such TiOC films can originate from different textures (i.e. distributions of grain orientations) of the respective Ti substrates. It should be noted, however, that the deposition of Pt NPs *via* AAD caused a partial surface reoxidation on some TiOC films (visible as color changes) due to difficulties with the temperature control.¹⁹⁴ GC, on the other hand, has always the same surface properties and therefore the same degradation behavior can be expected. This interpretation is supported by the SE micrographs of Pt/TiOC and Pt/GC taken after electrochemical experiments in EtOH containing H_3PO_4 at different elevated temperatures (Fig. 104).

6.4.1 Electrochemical stability of Pt/TiOC in hot H_3PO_4

Due to the promising performance of the Pt/TiOC system during the EOR experiments, its electrochemical stability was studied in more detail with SEM and XPS. Fig. 106 shows SE micrographs of a freshly prepared Pt/TiOC electrode, a Pt/TiOC electrode after EOR tests up to 70 °C, and a Pt/TiOC electrode that underwent the electrochemical simulation test in the absence of EtOH up to a final temperature of 80 °C. The substrate grain effect on the morphology of thereon prepared TiOC films can be clearly seen in Fig. 106a1. The morphology of the TiOC film was not affected by AAD of Pt NPs, but the Pt particle size and coverage seems to depend on the nature of the underlying grains as can be seen in Fig. 106a2. From Fig. 106b1-b6 it can be deduced that different Ti substrate grains cause different Pt/TiOC degradation characteristics during the EOR

tests. It can be clearly seen that the TiOC film on the right grain (rough morphology) was strongly attacked during the EOR at elevated temperatures. Parts of the film were detached or dissolved. This degradation is accompanied by agglomeration and a severe loss of Pt NPs. The TiOC film on the left substrate grain (smooth morphology), on the other hand, appears intact, and the Pt NPs seem to be only slightly agglomerated. Fig. 106c1-c3 depicts SE micrographs of the Pt/TiOC surface that underwent the simulation test. In the analyzed areas the TiOC film shows no damage and it has a similar morphology as the film in Fig. 106b3. A possible explanation for this observation can be similar characteristics of the substrate grains underneath the film areas depicted in Fig. 106b3 and Fig. 106c2. The Pt NPs visible in Fig. 106c2 and c3 have larger diameters than those observed on the as-prepared Pt/TiOC surface, which indicates that, also here, catalyst agglomeration has taken place.

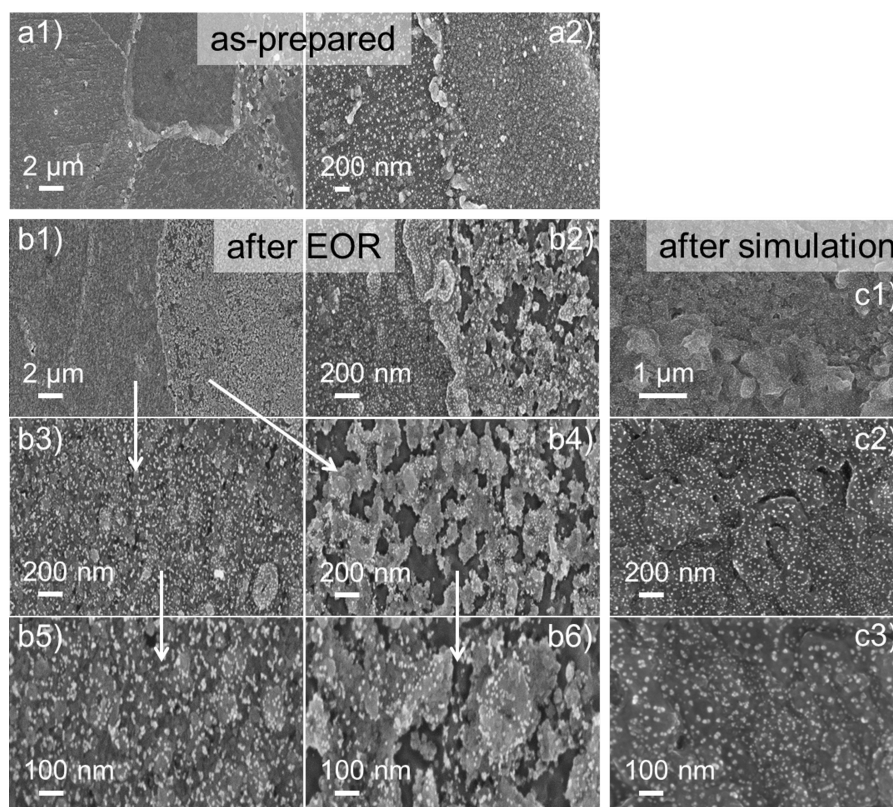


Fig. 106: SE micrographs of a) a freshly prepared Pt/TiOC electrode, b) a Pt/TiOC electrode that has been used for an EOR test up to 70 °C, and c) a Pt/TiOC electrode that underwent the electrochemical simulation test in the absence of EtOH up to a final temperature of 80 °C. The high magnification images in (b3-b6) show the tested Pt/TiOC on the left and right substrate grains in (b1,b2). a) and b) adapted from the supporting information of [246].

From the SE micrographs it can be concluded, that at least two mechanisms contribute to the degradation of Pt on the Pt/TiOC system: agglomeration of the Pt NP and dissolution of the supporting TiOC film accompanied by Pt loss. The latter mechanism however occurs only on distinct grains of the film. On certain substrate grains, the TiOC surface does not dissolve during EOR and can stabilize the Pt NP far better than the GC support at temperatures up to 80 °C. A third possible degradation mechanism may be a coverage of the Pt catalyst with titania species due to the SMSI between Pt and reduced titania.²⁵ However, such an effect could not be revealed with SEM.

Whether or not and to which extent the TiOC support suffers from electrochemical oxidation, can be verified

by the analysis of the electrochemical response of Pt/TiOC during potential cycling in concentrated H₃PO₄ at 50 and 80 °C without EtOH. The respective CVs are shown in Fig. 107. From the CVs that were measured with EtOH, it was deduced that oxidation/corrosion of the TiOC support becomes relevant at temperatures between 70 and 80 °C (Fig. 100 and Fig. 101), which is supported by the visible TiOC film degradation after an EOR experiment at 70 °C (Fig. 106b2,b4 and b6). Therefore, the EOR CVs obtained for Pt/TiOC at 70 and 80 °C are depicted in Fig. 107b together with the blank CVs, acquired without EtOH.

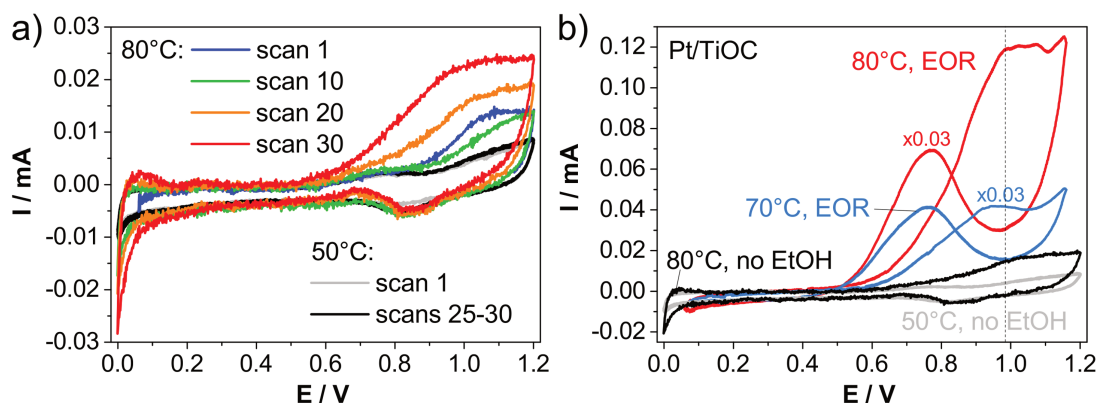


Fig. 107: a) CVs acquired with the Pt/TiOC electrode in 14.6 M H₃PO₄ at 50 and 80 °C. b) Comparison of the 20th CV scans in 14.6 M H₃PO₄ with 1.0 M EtOH (taken at 50 mV s⁻¹) and without EtOH (taken at 10 mV s⁻¹), acquired at the indicated temperatures.

From the black and gray CVs in Fig. 107a it can be inferred that the Pt/TiOC electrode is electrochemically stable in concentrated H₃PO₄ at 50 °C. After few potentiodynamic cycles, the CVs become stable and resemble the electrochemical fingerprint of Pt. During potentiodynamic cycling at 80 °C, new signatures appear at anodic potentials. In the first positive going sweep, the anodic current rises beyond that of the initial Pt CV at potentials $\geq \sim 0.8$ V and produces an enhanced oxidation peak at ~ 1.1 V. In the course of successive potentiodynamic cycles, the anodic current peak decreases at first (scan 10), but re-appears in later CV scans with increasing amplitude. During the 20th scan, an anodic excess current is observed already for potentials $\geq \sim 0.65$ V, and at 1.2 V the current assumes a more than twice as high value as that of the Pt CV measured at 50 °C. The onset potential of the additional oxidation current continuously shifts cathodic, reaching a value of ~ 0.55 V in the 30th CV scan. At the same time, an anodic current peak appears during the negative going potential sweep at ~ 0.7 V. This has been attributed to the oxidation of impurities in the supporting electrolyte (such as phosphorous acid), that derive from the reaction between the concentrated phosphoric acid and Pt at elevated temperatures.^{100,296,297}

Although the Pt-oxide formation current has been reported to increase with increasing temperature in concentrated H₃PO₄,¹⁰⁰ the progressively growing anodic currents in the positive sweep are most likely related to the electro-oxidation of the titanium oxycarbide phase in the TiOC support. Similar CV curves have been reported for TiC-based electrodes that were polarized in aqueous sulfuric acid solutions,^{33,37} and the anodic current increase above ~ 0.8 V was attributed to corrosion and passivation of TiC, where TiO²⁺ ions are initially released into solution until the surface is covered by TiO₂.¹⁹² In 2016, L. Calvillo et al. investigated the electrochemical stability of carbothermally reduced anodic TiO₂ films on Ti substrates, provided by the group of J. Kunze-Liebhäuser, and confirmed the electrochemical oxidation of the TiO_{1-x}C_x phase during polarization in 0.5 M H₂SO₄ by *in situ* XPS.²⁵⁸

The finding of considerable anodic currents at 80 °C due to the electro-oxidation of the TiOC support provides an explanation for the peculiar change in the shape of the EOR CVs that is observed for Pt/TiOC electrodes when the reaction temperature is raised from 70 to 80 °C. From the CVs compared in Fig. 107b it can be deduced that the positively shifted anodic current peak and the following current plateau that characterize the CVs measured at 80 °C in EtOH containing electrolyte result from the superposition of the EOR at Pt with the TiOC surface oxidation.

XPS was performed to verify the formation of surface TiO₂ during anodic polarization of Pt/TiOC in concentrated H₃PO₄ at elevated temperatures. Fig. 108 depicts XP spectra of the Ti 2*p*, O 1*s*, C 1*s*, P 2*p* and Pt 4*f* core levels, that were acquired of the freshly prepared TiOC surface, the Pt/TiOC surfaces after EOR experiments up to final temperatures of 70 and 90 °C, and of a Pt/TiOC surface that underwent the electrochemical simulation test up to 80 °C. Where Pt was detected, the binding energies were corrected for charging effects using the Pt 4*f*_{7/2} peak at 71.2 eV as reference.¹⁴¹ For the other samples, the binding energy of the C-Ti peak in the C 1*s* spectra (see inset in Fig. 108c) was fixed to 282.0 eV.²³⁵

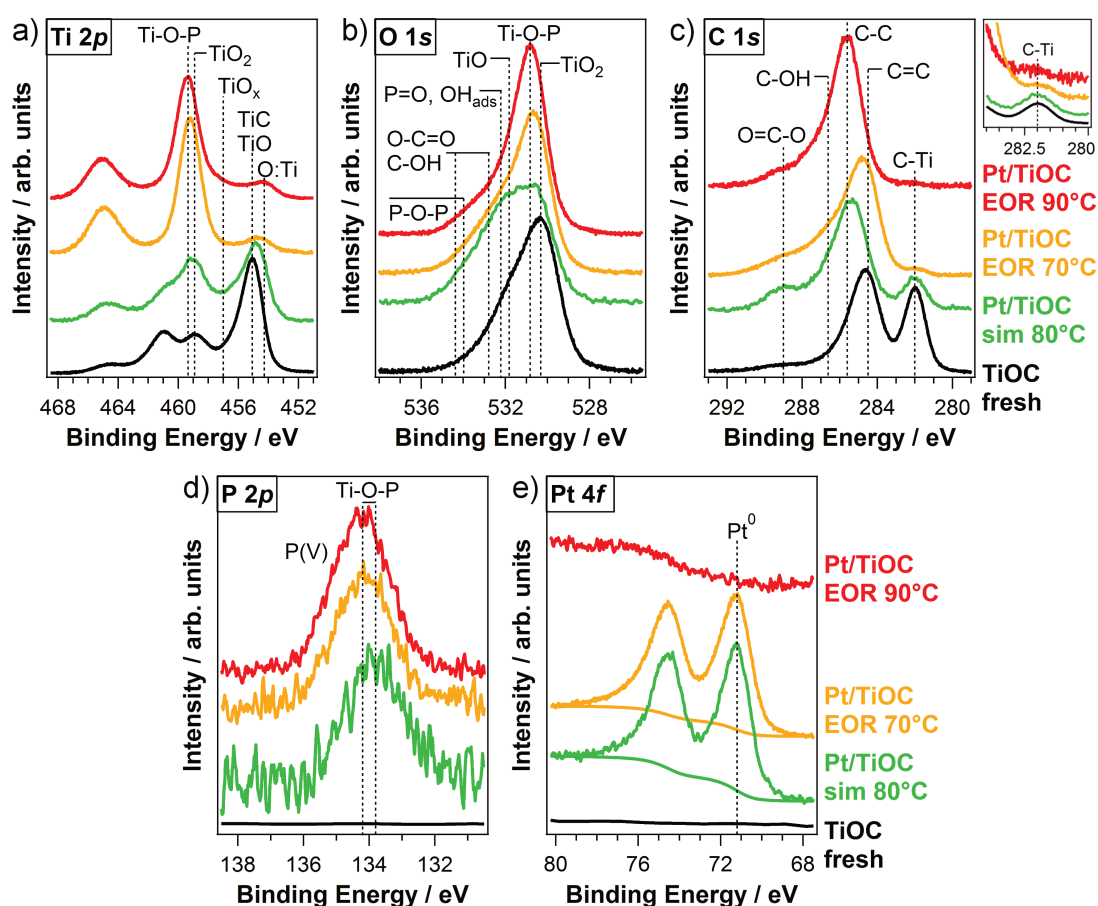


Fig. 108: XPS analysis of the as-prepared TiOC support (black) and of Pt/TiOC electrodes after electrochemical tests in 14.6 M H₃PO₄ with and without EtOH. a) Ti 2*p*, b) O 1*s*, c) C 1*s* (inset: arbitrary scaled C-Ti peaks) and d) P 2*p* spectra after subtraction of a Shirley-type background, and e) Pt 4*f* spectra with Shirley-type background. Green spectra: Pt/TiOC after electrochemical simulation tests without EtOH at 50 and 80 °C; yellow (red) spectra: Pt/TiOC after EOR tests at temperatures between room temperature and 70 °C (90 °C). X-ray source: Al K_α; acquisition normal to sample surface. For clarity, the spectra are shifted vertically.

In accordance with previously presented XPS analyses of TiOC films (prepared at 750 °C), the surface of the as-prepared TiOC film consists of a mixture of TiC-rich TiO_{1-x}C_x, TiO_{1<x<2} suboxides, TiO₂ and (mainly

graphite-like) carbon (Fig. 108a,b,c). The enhanced signal intensities on the high binding energy sides of the O 1s and C 1s spectra indicate that there is some adsorbed water (OH) and/or organic carbon contamination on the surface. From the yellow, green and red spectra in Fig. 108a,b and c it can be deduced that a considerable amount of the TiO_{1-x}C_x phase has been oxidized during the electrochemical tests in concentrated H₃PO₄ at elevated temperatures, which involved anodic polarization up to 1.2 V. This observation is in line with results published by Calvillo et al., who investigated the oxidation of (Pt-free) TiOC electrodes during anodic polarization up to 1.1 V_{RHE} in sulfuric acid solution (with and without EtOH) at room temperature and at 150 °C.²⁵⁸

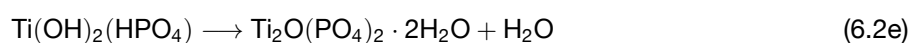
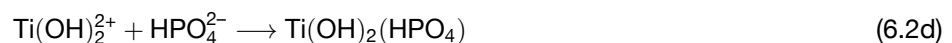
The decrease in the fraction of TiC and TiO species at the electrode surface appears to be smaller in the film that was used for the EC simulation test compared to those Pt/TiOC surfaces that were used for the two EOR experiments. The fact that the final temperature in the simulation test was higher than that in the EOR experiment up to 70 °C, suggests that the less severe support degradation is related to the shorter duration of the overall simulation test. Due to the considerably different durations of the three compared EC experiments it is not possible to extract information about the influence of EtOH on the TiOC oxidation. It is, however, unlikely that the absence of EtOH in the simulation test has helped to inhibit the oxidation of the oxycarbide phase, since the contrary was found by Calvillo et al..²⁵⁸

A severe oxidation of the TiO_{1-x}C_x phase at the surface of the Pt/TiOC electrodes is observed after the EOR experiments up to 70 and 90 °C (yellow and red spectra in Fig. 108a,b,c). In particular, almost no TiC is detected in the C 1s spectrum after the EOR experiment at 90 °C (red spectrum in Fig. 108c). Furthermore, the peak detected at 454.3 eV in the corresponding Ti 2p spectrum is shifted by -0.8 eV compared to that of the TiC (TiO) phase in the black spectrum, and can therefore not be ascribed to a Ti(II) species.²²¹ On the other hand, fully reduced titanium metal (Ti⁰) would cause a Ti 2p_{3/2} signal at binding energies of between 453.7 and 454.1 eV,²²¹ which are slightly too low to allow for an assignment of metallic Ti to the observed peak. Instead, the observed peak originates most likely from a solid solution of O in Ti metal (i.e. TiO_{x<1}), since Kuznetsov et al. reported an identical binding energy of 454.3 eV for the Ti 2p_{3/2} signal of such a phase.²⁴¹ These observations show that the TiC and TiO species in the TiOC films are particularly prone to oxidation during the EC tests, and that the TiO₂ layer that remains on the electrode surface after the EOR experiment up to 90 °C is, at least in parts, very thin, thus allowing for a detection of electrons from the transition layer between the oxide film and the Ti substrate. As will be demonstrated below, the thinning of the TiOC layer can be ascribed to severe Ti corrosion under the harsh reaction conditions.

After all three EC tests in phosphoric acid, a pronounced peak is observed at binding energies between 133.7 and 134.2 eV in the P 2p spectra, which indicates the presence of phosphorous in its highest oxidation state of +5.^{298,299} At the same time, the Ti 2p_{3/2} XP signal related to Ti(IV) species, as well as the main O 1s peak, are shifted to slightly higher binding energies (compared to the black spectra), and enhanced XP signal intensities are detected on the high binding energy side of the O 1s peak. The latter spectral change is particularly emphasized after the EC simulation test (green spectrum in Fig. 108b). These observations can be ascribed to the physis- or chemisorption of phosphoric acid and/or its anionic fragments on the Pt/TiOC surface, causing a variety of P-based chemical species. Similar shifts of the Ti 2p_{3/2} and of the O 1s peaks in comparison with pure TiO₂ have been reported for phosphated titania (denoted as T-O-P),^{300,301} titanium pyrophosphate (TiP₂O₇)³⁰² or other titanium phosphate compounds (Ti₃(PO₄)₄·nH₂O)³⁰³. Ghicov et al. observed a P 2p

peak at 133.8 eV for titania nanotubes that were anodically grown in a phosphate-based electrolyte,³⁰⁴ which can be ascribed to the incorporation of phosphorous (phosphate ions) from the electrolyte into the oxide film during anodic oxidation.^{45,305} This binding energy value compares well with those determined for the peaks in Fig. 108d. The fact that only P(V) is detected in the EC tested Pt/TiOC surfaces, indicates that the phosphorous is bound to oxygen. These bonds cause enhanced signal intensities on the high binding energy side of the O 1s spectra, and the particularly complex shape of the green O 1s peak. According to the literature, P=O bonds (e.g. in *ortho*- and *pyrophosphoric* acid and their anionic fragments) are expected to cause an O 1s signal at 532.2–532.5 eV.²⁹⁹ With respect to this peak, the XP signal related to P-O-H is shifted to higher binding energies,^{299,306} and O 1s core level electrons with a binding energy of 534.0 eV can be ascribed to P-O-P bonds.^{299,307} Ti-O-P bonds were reported to cause O 1s peaks at binding energies between 530.6 and 530.9 eV.^{298,300} The Pt-O-P bonds that build up when *ortho*- or *pyrophosphoric* acid and/or the respective anionic fragments are chemisorbed on Pt cause binding energy shifts of between +1.3 and +2.2 eV in comparison with the O 1s signal of the P=O bond in the respective free (desorbed) acid molecules, but have no notable effect on the position of the Pt 4f doublet.³⁰⁶ The XP spectra in Fig. 108e evidence that there is still Pt catalyst present after the simulation test up to 80 °C and after the EOR experiment at temperatures between room temperature and 70 °C. There is however no Pt detected on the Pt/TiOC surface that has been used for the EOR experiment at temperatures between room temperature and 90 °C. This is in accordance with the absence of the electrochemical Pt fingerprint in the CVs acquired after this EOR experiment in 0.1 M HClO₄, evidencing a complete loss of the catalyst.

The results obtained with the EC simulation tests and with XPS analysis of different EC tested Pt/TiOC surfaces provide a deeper insight into the degradation of the TiOC support. As confirmed by the chemical analysis, the anodic oxidation peak observed during the CVs in EtOH free H₃PO₄ at 80 °C arises from the oxidation of TiC and TiO to TiO₂ at the film surface. SEM has shown that on specific substrate grains, parts of the TiOC film were detached or dissolved during the EOR experiment up to 70 °C, which brought about severe catalyst loss in these spots. This observation points to corrosion of the TiOC film. Jalan and Frost tested Pt/TiC electrocatalysts as cathode in a phosphoric acid fuel cell at 200 °C and found, besides an enhanced current density compared to that obtained with a conventional Pt/C catalyst, a fairly good support stability at ORR potentials.³⁰⁸ On the other hand, metal titanium and any passive film thereon, are known to be prone to corrosion in hot concentrated phosphoric acid.^{167,168} Lu investigated the corrosion of titanium in aqueous phosphoric acid solutions at 250 °C using an autoclave, and found a considerable mass loss of the Ti sheet that was immersed into 1.0 M H₃PO₄ for 24 h. Furthermore, he observed a film of fibrous morphology on the surface of the corroded Ti sheet, which consisted mainly of hydrated titanium oxide phosphate (Ti₂O(PO₄)₂·2H₂O).³⁰⁹ He proposed that this film was produced *via* the reaction of Ti corrosion products with the doubly ionized phosphate anions:



or *via* the direct reaction of H₃PO₄ with TiO₂ on the surface:



Since the standard Gibbs free energy of the latter reaction has a considerably large negative value of $-225.74 \text{ kJ mol}^{-1}$, TiO₂ is thermodynamically unstable in phosphoric acid even at room temperature. This raises the question of how stable TiO_{1-x}C_x materials are in hot concentrated phosphoric acid without electrical polarization.

6.4.2 Chemical stability of TiOC powders in concentrated boiling H₃PO₄

To gain insight into the chemical stability of TiO_{1-x}C_x materials in hot concentrated phosphoric acid, a TiO_{1-x}C_x-rich powder, which was provided by the Treibacher Industrie AG (Austria) for test purposes, was boiled in 85 % H₃PO₄ at $145 \pm 5^\circ\text{C}$ for 2.5 h and analyzed with XPS prior to and after the chemical stability test. To distinguish the powder sample from the TiOC films, it will be denoted TiOC_{Trei}.

Experimental details

For the stability test, 1.005 g of the powder was mixed with 10 mL of the acid in a round bottom flask with a magnetic stirring bar. The flask was heated in a silicon oil bath on a hot plate, while the temperature was monitored with a Hg thermometer in the bath. The evaporating acid solution was recovered with a reflux condenser on the lid of the flask. After cooling down, the flask was filled with distilled water to dilute the slurry, and then sonicated for 30 min. The TiOC powder was recovered by repeated centrifugation and sonication of the slurry, where the separated acid solution was progressively replaced by distilled water. Therefore, the diluted slurry was equally filled in six centrifugation flasks of each 15 mL capacity and the following protocol was applied:

- 20 min centrifugation at 6000 rpm, exchange of separated solvent, sonication for 10 min
- 10 min centrifugation at 6000 rpm, exchange of separated solvent, sonication for 5 min
- 10 min centrifugation at 6000 rpm, exchange of separated solvent, sonication for 5 min

After the last dilution step, most of the solvent was removed with a pipette and the remaining slurry was filtered with filter paper and funnel. The filter paper with powder was allowed to dry in ambient air at room temperature.

Analysis of the TiOC powders

The compositional specification provided by Treibacher is given in table 6.2. Fig. 109 depicts SE micrographs and XRD patterns of the TiOC_{Trei} powder that were acquired in the frame of the present study. From the SEM images it can be seen that the powder consists of smooth, nearly oval shaped grains with sizes between 0.5 and $\sim 2.0 \mu\text{m}$. The 2θ angles, where X-ray diffraction peaks from pure TiC and TiO single crystals are expected, were calculated from the respective lattice constants (TiC: $a = 0.4331 \text{ nm}$, TiO: $a = 0.4177 \text{ nm}$), using the relation between lattice constant and lattice plane separation (equation 2.89) and Bragg's law (equation 2.87). As can be seen from Fig. 109c, the intense XRD peaks of TiOC_{Trei} are detected at angles

between those of TiC and TiO, which evidences the presence of a TiO-TiC solid solution (TiO_{1-x}C_x). Based on reference data obtained from the PDF-2 database (TiO_{1.51}, entry [00-073-1781]), the two low intensity peaks at 34.70° and 40.25° were assigned to a phase similar to Ti₂O₃. A closer look at the diffraction pattern of the TiO-TiC solid solution reveals that each XRD signal consists of a double peak (Fig. 109d), which suggests that the powder contains two distinct crystalline TiO_{1-x}C_x phases of differing stoichiometry. The respective stoichiometries were estimated using Vegard's law with the 2θ-values obtained from fits of the (331) peak with Gaussian profiles, and are denoted in Fig. 109d. In accordance with the compositional specifications provided by Treibacher, there is an excess of TiC.

Table 6.2: Composition of the TiOC_{Trei} powder, determined with hot-gas extraction (LECO). Provided by Treibacher Industrie AG.

C / tot. wt%	O / tot. wt%	C:O wt%	C:O / Mol%
LECO	LECO		calculated
11.35	8.74	56/44	63/37

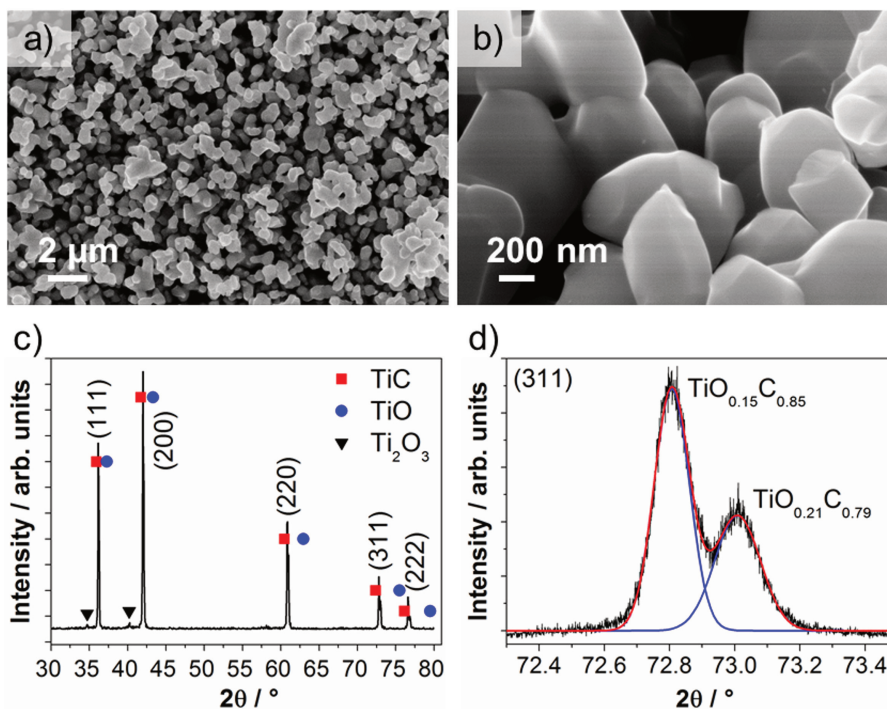


Fig. 109: Morphological and crystallographic analysis of the fresh TiOC_{Trei} powder. (a,b) SE micrographs taken at two magnifications with a beam acceleration voltage of 15 kV, c) XRD pattern and d) magnified (331) peak with fitted of Gaussian profiles and estimated stoichiometries. X-ray source: Cu K_α, λ = 1.541874 Å monochromatized.

Chemical surface modifications that were induced by the exposure of the TiOC_{Trei} powder to boiling concentrated H₃PO₄ were investigated with XPS. The XP spectra obtained for the as-received powder confirm the presence of a TiO_{1-x}C_x phase, but show as well a considerable fraction of TiO₂ on the surface (Fig. 110). Most likely, the oxide is not crystalline or constitutes only a very thin layer on the surface of the powder grains, so that it could not be detected with XRD. The C 1s and O 1s spectra furthermore evidence the presence of amorphous (free) carbon, as well as organic carbon contamination and adsorbed

water (OH) on the surface. After the chemical treatment in 145 °C hot H₃PO₄, a pronounced P(V) peak is observed in the P 2p spectrum, which is accompanied by a shift of the Ti 2p_{3/2} peak of Ti(IV) and of the O 1s peak maximum to higher binding energies. As explained in the previous section, these observations can be ascribed to the formation of titanium phosphate or similar species on the surface. Surprisingly, the Ti 2p and C 1s spectra point to a pronounced loss of the TiO₂ and free carbon on the surface, most likely due to corrosion.^{167,168,309,310} As a consequence, the fraction of TiO_{1-x}C_x at the surface is enhanced.

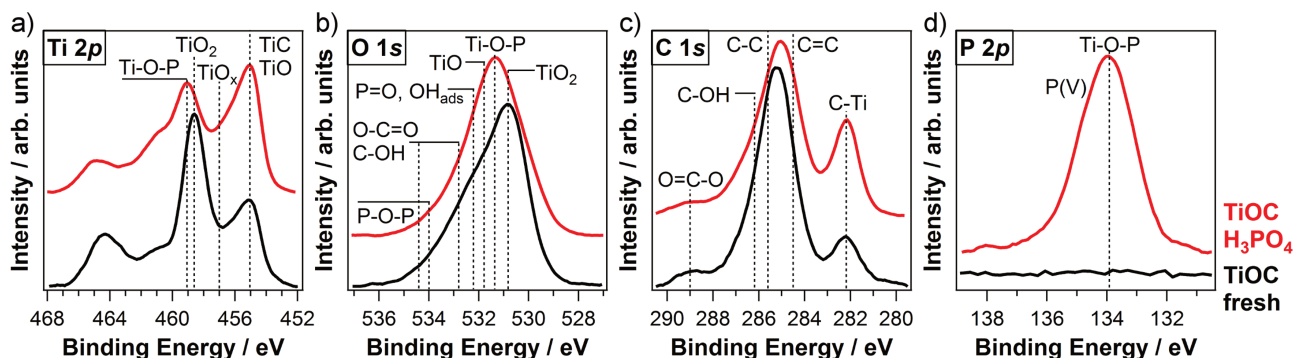


Fig. 110: Chemical analysis of the fresh and tested TiOC_{Trei} powder. XP spectra of a) Ti 2p, b) O 1s, c) C 1s and d) P 2p core levels before (black) and after (red) boiling in concentrated H₃PO₄. X-ray source: Mg K_α; acquisition normal to sample surface. For clarity, the spectra are shifted vertically.

6.4.3 The degradation mechanism of Pt/TiOC during the EOR in concentrated H₃PO₄ at elevated temperatures

The previously presented studies on the electrochemical stability of Pt/TiOC electrodes in H₃PO₄ with and without EtOH and at temperatures ≥ 70 °C suggest that the TiO_{1-x}C_x phase suffers from electrochemical oxidation to titania and carbon at sufficiently high positive potentials. From the stability experiments performed with the TiOC_{Trei} powder it can be deduced that TiO₂ and free carbon on the surface particularly suffer from corrosion when exposed to concentrated H₃PO₄ at elevated temperatures.

Based on these findings, the degradation mechanism of the Pt/TiOC system during EOR operating conditions can be understood as a two step process, consisting of anodic passivation and a subsequent corrosion step, which in combination give rise to a dissolution of the TiOC film and a concomitant Pt catalyst loss. The rate of the Pt/TiOC degradation depends on the temperature and on the substrate grains. After the EOR experiments up to 70 °C an attack of the TiOC support can be clearly observed with SEM on top of specific Ti substrate grains (Fig. 106), but several areas of the Pt/TiOC electrode have suffered less from degradation than the Pt/GC electrode. After the EOR experiment up to 90 °C, no Pt is detected on the Pt/TiOC electrode anymore, neither electrochemically nor with XPS. Furthermore, an XP signal that most likely originates from dissolved oxygen in titanium metal (TiO_{x<1}) is observed in the respective Ti 2p spectrum. Both these observations suggest that at this reaction temperature, most of the TiOC film is dissolved due to anodic passivation and subsequent corrosion. At least on top of specific Ti substrate grains, the remaining TiO₂ film appears to be very thin, allowing to detect parts of the transition layer between oxide and metal underneath. At even higher reaction temperatures, also the Ti substrate is likely to be attacked: Lu has shown that metallic Ti (and its passive film) corrodes at a considerably high rate in a 250 °C hot phosphoric acid solution, which causes a notable mass loss of the test material after only one day.³⁰⁹

As previously noted, it is possible that part of the TiOC supported Pt catalyst is covered with TiO_x.²⁵ The corrosive dissolution of this layer and the subsequent increase of the effective ECSA of the Pt catalyst would provide an explanation for the significant increase of the EOR currents that is observed in the CVs of Fig. 100a when the reaction temperature is raised from 70 to 80 °C. After removal of the covering oxide from the Pt catalyst, the effectively available ECSA, and therewith the EOR currents would be enhanced. However, after prolonged operation under the harsh reaction conditions also the TiOC support is attacked, which is accompanied by Pt loss and should cause an overall decrease of the EOR activity in the long term. Therefore, although the Pt/TiOC system has shown a higher electrochemical stability compared to Pt/GC, care should be taken in the choice of the operating conditions if a Pt/TiOC material is tested on the anode of a DEFC.

7. Summary and Conclusions

7.1 Synthesis and characterization of TiOC films

The studies presented in Chapter 4 have demonstrated that planar TiOC model electrodes, consisting of carbon-modified titania materials, can be synthesized through a carbothermal treatment of compact and amorphous anodic titania films on polycrystalline Ti substrates using acetylene as carbon source. The annealing temperature employed for the synthesis has been identified as a key parameter to promote the conversion of anodic TiO_2 into oxycarbide phases ($\text{TiO}_{1-x}\text{C}_x$). Topographic and morphological analyses with AFM and SEM have shown that a thorough preparation of the Ti substrate by optimized grinding and electropolishing procedures ensures a low roughness of the anodic film and of the produced TiOC films.

7.1.1 Understanding the carburization and reoxidation mechanisms of anodic TiO_2

To gain control of the carbothermal synthesis route of TiOC electrodes, anodic titania films have been carbothermally treated at different annealing temperatures, ranging from 550 to 1050 °C, and the obtained TiOC films have been studied with surface sensitive spectroscopic and diffractometric techniques (XPS, GID), as well as Raman spectroscopy (shown in Chapter 5), which allowed to study the phase composition of the (converted) anodic films. The results of this parameter study have led to a fundamental understanding of the conversion process of compact anodic TiO_2 films into $\text{TiO}_{1-x}\text{C}_x$ phases and of their subsequent reoxidation in air.

For a given acetylene concentration and temperature program, the composition and thickness of the converted film critically depends on the employed annealing temperature due to a temperature dependent acetylene decomposition and film conversion efficiency. As demonstrated in Chapter 5, the reactive decomposition of acetylene is facilitated on crystalline titania (in particular anatase TiO_2). Thus, the temperature-dependent deposition efficiency can be mainly ascribed to the temperature-dependent crystallization kinetics of the initially amorphous anodic film. The film conversion efficiency is mainly related to temperature activated solid state diffusion of carbon from the surface into the bulk of the anodic film (see the thermodynamic model in Fig. 60). For two acetylene concentrations, namely 0.2 and 1.0 sccm, the most efficient film conversion, yielding the highest fraction of TiC and TiO near the surface and an extended crystalline oxycarbide phase, is obtained at 750 °C. Apparently, both the carbon deposition rate and the rate of in-diffusion of carbon are optimal at this annealing temperature to generate a TiC-rich oxycarbide phase. At lower annealing temperatures, the slower carbon diffusion kinetics yield a lower fraction of TiC in the film and excess carbon on the surface. At higher annealing temperatures, carbon diffusion into the titanium substrate is activated giving rise to a depletion of carbon species in the anodic film, and in particular in the surface-near layers. The higher carbon in-diffusion rate at 850 °C could, however, be compensated by an enhancement of the acetylene concentration to 2.0 sccm, which yielded a higher fraction of TiC (and TiO) at the film surface.

When exposed to air, the reduced titania films reoxidize from their surface towards their bulk. In particular, an only partially converted anodic film, as obtained at low annealing temperatures (i.e. TiOC_{550}), is found to undergo fast passivation when exposed to air. These results are in line with the stability study of TiOC films, published by Calvillo et al. in 2014,²⁵² which revealed a generally lower thermodynamic stability of the $\text{TiO}_{1-x}\text{C}_x$ phase compared to the composite of carbon and TiO_2 . The rate of this oxidation process

decreases and hence the intrinsic stability of TiOC films improves with increasing synthesis temperature. This observation can be explained by an improved conversion of the entire anodic film at higher annealing temperatures and by a higher crystallinity of the thus obtained TiOC. An enhanced fraction of graphite-like carbon on the surface appears to have no positive impact on the intrinsic stability. After aging in air for ~ 9 months, the TiOC films prepared at 750°C still show the highest fraction of TiC (and TiO) species near the surface, which makes these films promising candidates for electrochemical applications that require a high electrode conductivity.

7.1.2 Understanding the interplay between synthesis conditions and electrochemical characteristics of TiOC films

The annealing temperature-dependent chemical and crystalline phase composition of the TiOC films has consequences for their electrochemical characteristics, which needs to be taken into account in view of their intended application as electrocatalyst supports. First HER studies have revealed that the electrocatalytic behavior is directly linked to the conductivity of the TiOC films and thus dependent on the surface electronic properties induced by carburization and annealing. This finding has great importance for the investigation of conductive and electrochemically stable flat TiOC films as model supports for electrocatalysis studies.

TiOC films with considerably different fractions of TiC, TiO, TiO_x , TiO_2 and graphite-like carbon have been prepared through carburization of anodic TiO_2 at different synthesis temperatures and investigated regarding their conductivity at the electrode/electrolyte interface and their resistance against passivation/corrosion during anodic polarization in acidic electrolyte. The results of this study allowed to identify advantages and limitations of the differently composed TiOC electrodes for their use as electrocatalyst supports in a low pH environment.

The resistance of TiOC electrodes against outer sphere electron transfer is decreasing with increasing TiOC synthesis temperature for films prepared at annealing temperatures between 550 and 750°C , but the resistance is increasing again with further increasing synthesis temperature. This trend can be mainly ascribed to the grade of reduction of the anodic films near the solid/liquid interface, obtained at the respective annealing temperature, since high fractions of Ti(II) and Ti(III) species enhance the interfacial conductivity (Fig. 68). Due to the high fraction of reduced titania species, the TiOC_{750} film prepared on a square Ti substrate by using 0.1 flow% acetylene during the carbothermal treatment has a charge transfer resistance similar to that of glassy carbon (GC), and the respective film prepared on a round Ti substrate with 0.5 flow% acetylene shows even nernstian charge transfer kinetics. Prolonged air exposure increases the fraction of TiO_2 on the surface of the TiOC films and thus decreases their interfacial conductivity.

EIS indicates that the investigated TiOC films form multilayered oxide films on the surface with a nanoporous outer layer on top of an inner compact layer when exposed to acidic aqueous electrolytes, due to passivation and corrosion processes. However, the electrochemical stability of TiOC films is affected by their synthesis temperature due to their temperature-dependent physicochemical properties, such as chemical and crystalline phase composition and the number of grain boundaries. A particularly low stability against passivation/corrosion is observed for an oxide covered carburized film with a low fraction of TiC that is prepared on a round substrate (TiOC_{850} of the second parameter study): this film is found to suffer from severe conductivity loss when polarized to 0.9 V , which is ascribed to the anodic formation of a highly resistive

passive layer on the surface. An enhanced fraction of graphite-like carbon on the surface appears to have no positive impact on the electrochemical stability nor on the interfacial conductivity of TiOC films.

In view of conductivity/stability requirements for electrocatalysis applications, a good compromise can be achieved through the synthesis of a TiC-rich film that is fully converted to $\text{TiO}_{1-x}\text{C}_x$ in the bulk and covered by a thin TiO_2 layer on the surface, as obtained through carbothermal treatment at 750°C . Such films are found to have a high stability against reoxidation in air and a high resistance against passivation/corrosion up to 0.74 V. They have a high outer sphere electron transfer activity during potential cycling in 0.1 M H_2SO_4 between 0.2 and 0.9 V, even after aging in air for ~ 9 months, and are therefore suited for electrocatalysis applications in this potential range.

Despite the annealing temperature, also the texture and quality (e.g. purity) of the used Ti substrate affects the physicochemical and electrochemical properties of TiOC films. Depending on the properties of the used polycrystalline Ti substrate, grain growth becomes relevant at annealing temperatures of 850°C (section 4.3) or of 950°C (section 4.2). The experimental results obtained in section 4.3 of Chapter 4 suggest that substrate grain growth during the carbothermal treatment at 850°C is responsible for the unexpectedly low fraction of TiC species in the TiOC_{850} film and the concomitant lower interfacial conductivity, as well as for its poor electrochemical stability during polarization to 0.9 V in 0.1 M H_2SO_4 .

7.2 The effect of the Ti substrate texture on the carbothermal conversion of anodic TiO_2

The results presented in Chapter 5 confirm that not only the synthesis temperature but also the substrate texture majorly influence the physicochemical properties of TiOC films, prepared from planar compact anodic TiO_2 on polycrystalline Ti *via* the carbothermal route, and using acetylene as carbon source. By means of a spectromicroscopic multimodal approach, employing EBSD, SEM, SPEM, and micro-Raman spectroscopy, it has been found that the anodic films on top of differently oriented substrate grains have individual time scales for the conversion to $\text{TiO}_{1-x}\text{C}_x$ phases and their subsequent reoxidation in ambient air. A combination of temperature- and substrate grain-dependent processes, such as anodic film crystallization, reactive carbon deposition, conversion to $\text{TiO}_{1-x}\text{C}_x$, and reoxidation of the surface, plays a major role in the definition of the heterogeneous physicochemical properties of TiOC films.

Particular efforts have been devoted to investigating the carbothermal treatment at 550°C , which effectively yields a C/ TiO_2 composite film, where the oxide is only slightly reduced in the bulk film. From the results presented in Chapter 4 it is known that already at such a low annealing temperature, a $\text{TiO}_{1-x}\text{C}_x$ phase can form, which is, however, highly instable in ambient air and completely re-oxidizes within few days to carbon and TiO_2 . A pronounced correlation between the amount of generated carbon and the Ti substrate grain orientations is observed: a significantly higher amount of graphite-like carbon is detected on top of $\sim\text{Ti}(0001)$ grains than on top of $\sim\text{Ti}\{hki0\}$ grains. The origin of this grain effect is identified as a substrate grain-dependent crystallization of the initially amorphous anodic TiO_2 film to nanocrystalline anatase during the thermal treatment, which in turn affects the activity of TiO_2 towards C_2H_2 decomposition to eventually form nanocrystalline graphite on the surface (most likely *via* the reoxidation of an initially formed unstable oxycarbide phase). This effect emphasizes the importance of TiO_2 precursor crystallinity for the synthesis of C/ TiO_2 functional materials *via* a carbothermal route with acetylene. To achieve the deposition of extended graphite layers on anodic TiO_2 films, their crystallization needs to be guided towards extended single crystalline

anatase domains exposing their most active facets, which may require a detailed knowledge and control of the substrate texture, as in the present case. In combination with the possibility of nanostructuring anodic TiO_2 , such composite systems provide a highly interesting functional material. Indeed, nanotubular $\text{C}/\text{TiO}_{2-x}$ composite layers, synthesized *via* the carbothermal route, have shown promising Li storage capacities,³¹¹ which may be further improved by means of an optimized synthesis, taking into account the crystallization characteristics of anodic films.

The physicochemical properties of TiOC films prepared at higher annealing temperatures are influenced by the substrate texture as well. Indirect and direct effects of the Ti substrate orientation and of grain boundaries on the anodic film conversion and subsequent reoxidation bring about $\text{TiO}_{1-x}\text{C}_x$ phases of locally varying stoichiometry, which are covered by locally varying amounts of TiO_2 and carbon. A deep understanding of such an interplay constitutes an essential point toward the development of novel transition metal oxycarbide-based synergistic supports for use in (electro)catalytic systems with improved performance. The obtained heterogeneous chemical composition and structure of TiOC films is likely to affect their overall performance when applied in electrocatalysis studies. For example, it is known that local variations in the charge transfer kinetics play a crucial role in the overall activity of electrocatalysts.²⁴⁵ In view of the potential applications of C/TiO_2 composite and $\text{TiO}_{1-x}\text{C}_x$ materials in energy conversion and storage, the herein introduced planar TiOC films are proposed as model systems for the investigation of property–performance relationships. Taking advantage of the substrate grain effect, two-dimensional property maps of the TiOC films that correlate (substrate grain-dependent) intrinsic physicochemical properties, such as chemical composition or morphology, and functional properties, such as electric conductivity, catalytic activity or (electro)chemical stability, will give valuable information about the material. This can be realized by means of local analysis tools, such as SPEM²¹³ and micro-electrochemistry³¹².

7.3 Application of TiOC films as Pt catalyst supports for the EOR

To test the performance of TiOC films as electrocatalyst supports, the activity of TiOC supported Pt catalysts towards the EOR has been investigated in two acidic electrolytes under different electrochemical conditions, i.e. different reaction temperatures and potentiodynamic or potentiostatic polarization. The obtained results were presented in Chapter 6 and have revealed a superior activity and electrochemical stability of $\text{Pt}/\text{TiOC}_{750}$ compared to Pt/GC .

7.3.1 Performance of the Pt/TiOC catalyst towards the EOR

In accordance with the attractive electrochemical properties of the TiOC_{750} film, such as a high interfacial conductivity and a high resistance against passivation/corrosion, Pt catalysts supported on this film yield a higher overall EOR current density during CVs in 0.1 M HClO_4 supporting electrolyte (with 0.5 M EtOH) at room temperature compared to the same catalyst supported on TiOC films prepared at higher annealing temperatures. Compared to Pt/GC , the $\text{Pt}/\text{TiOC}_{750}$ system yields furthermore higher EOR current densities during CVs in 14.6 M H_3PO_4 supporting electrolyte (with 1.0 M EtOH) at temperatures between room temperature and 80 °C. During current transient measurements, a 170 times higher faradaic steady state current has been found for $\text{Pt}/\text{TiOC}_{750}$ than for Pt/GC at a temperature of 80 °C and at a potential of 0.6 V, which are realistic operating conditions in a DEFC.

Several features in the electrochemical response of Pt/TiOC₇₅₀ point to a synergistic effect of the support on the EOR activity, which provides an explanation for the superior EOR activity of this system compared to Pt/GC. The detailed nature of the synergistic effect of TiOC, however, could not be clarified in the frame of this thesis. To gain a better understanding of possible catalyst support interactions in the Pt/TiOC system, investigations of the surface chemistry at the solid/liquid interface under EOR operating conditions are required, which may enable the identification of the active sites for water activation or of electronic effects of the support on the Pt catalyst.

It should not be forgotten that the desired EOR reaction path is the complete oxidation of EtOH to CO₂, which allows to take full advantage of the high specific energy density of EtOH. Therefore, in forthcoming studies of the Pt/TiOC system, DEMS measurements should be included to determine the CO₂ efficiency of the catalyst.

7.3.2 Electrochemical stability of TiOC in hot phosphoric acid

The study on the electrochemical stability of Pt/TiOC electrodes in concentrated H₃PO₄ with and without EtOH and at temperatures ≥ 70 °C has shown that the TiO_{1-x}C_x phase suffers from electrochemical oxidation at sufficiently high positive potentials, thereby generating TiO₂ and carbon on the surface (section 6.4.1). On the other hand, the investigation of the chemical stability of TiO_{1-x}C_x-rich powders (from the Treibacher Industrie AG, Austria) has revealed that TiO₂ and free carbon on the surface particularly suffer from corrosion when exposed to concentrated H₃PO₄ at 145 °C (section 6.4.2).

The presented results lead to the conclusion that TiO_{1-x}C_x-based electrodes suffer from a two-step degradation mechanism in hot phosphoric acid and under anodic polarization:

1. Anodic oxidation of the TiO_{1-x}C_x phase on the electrode surface to TiO₂ and amorphous/graphitic carbon at potentials $\geq \sim 0.8$ V.
2. Corrosive dissolution of TiO₂ and amorphous/graphitic carbon on the surface.

The degradation rate, in particular the dissolution rate, increases with increasing reaction temperature. Moreover, the electrochemical stability of the TiOC support is found to locally vary on a micrometer scale due to substrate grain effects on the physicochemical film properties.

To minimize the degradation of a TiOC supported Pt catalyst at the anode of an intermediate temperature PEM-DEFC (with a H₃PO₄-doped PBI-based membrane), it is therefore necessary to work at anodic potentials below 0.8 V, which is in any case desirable to enhance the CO₂ efficiency during the EOR on Pt.¹⁰ Furthermore, the phosphoric acid concentration at the interface with the catalyst support should be as low as possible, if high reaction temperatures are employed.³⁰⁹

In summary, the results obtained with the EOR studies on Pt/TiOC and Pt/GC model systems suggest that TiOC materials, and in particular those comprising a TiC-rich oxycarbide phase and some TiO₂ on the surface, are highly promising candidates to substitute carbon based catalyst supports for electrocatalysis applications that require harsh operating conditions such as low pH, anodic polarization and elevated temperatures.

A. Additional figures

A.1 Chapter 4

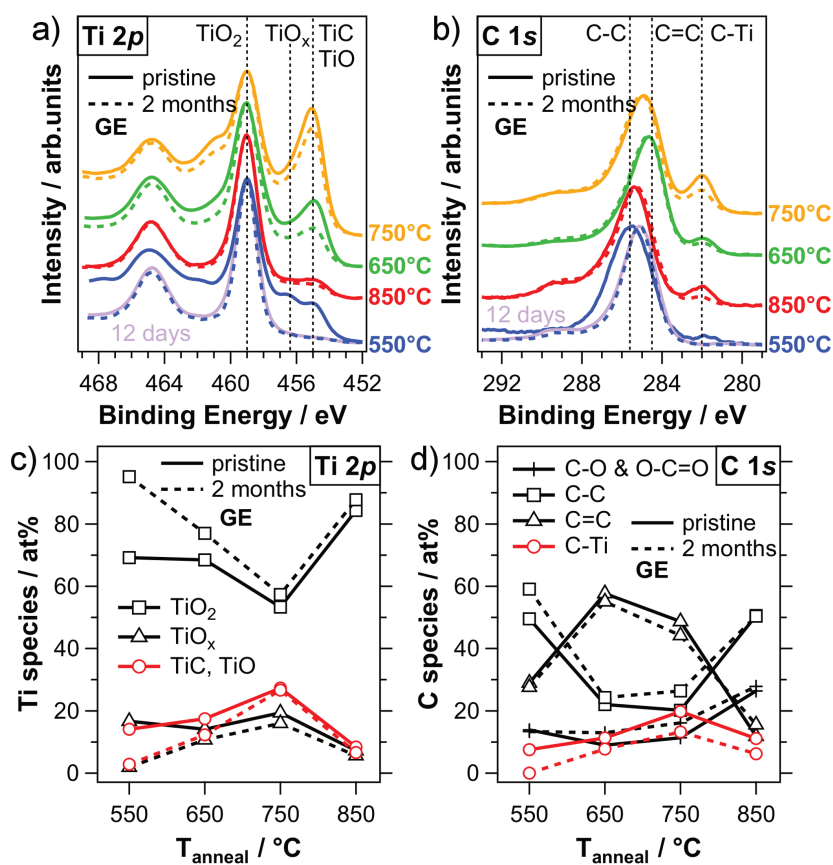


Fig. 111: XPS analysis of TiOC after different air exposure times. a) Ti 2p core level spectra, scaled to a common TiO₂ peak height, and b) C 1s core level spectra, scaled to a common height of the peak maximum, acquired at grazing emission (GE, $\theta = 30^\circ$). Solid lines: pristine TiOC, broken lines: two months old TiOC, violet spectra: 12 days old TiOC₅₅₀. For clarity, the spectra are shifted vertically. Results of multi-peak fitting for c) Ti 2p and d) C 1s spectra. Adapted from the supporting information of [251].

A.2 Chapter 5

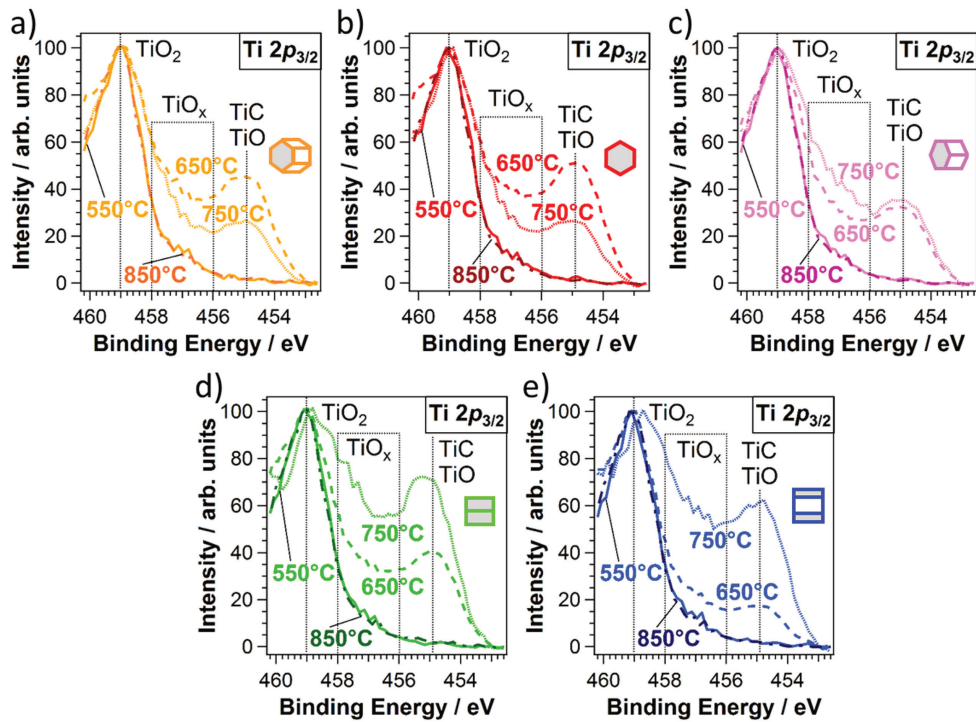


Fig. 112: XP spectra from Ti 2p_{3/2} photoelectron micrographs taken of TiOC on top of five differently oriented substrate grains for the four annealing temperatures. The substrate orientations are a) $\sim 15^\circ \leq \Phi \leq 40^\circ$, $0^\circ \leq \varphi_2 \leq 30^\circ$, b) $0^\circ \leq \Phi \leq \sim 15^\circ$, $0^\circ \leq \varphi_2 \leq 30^\circ$ c) $\sim 40^\circ \leq \Phi \leq \sim 50^\circ$, $0^\circ \leq \varphi_2 \leq 30^\circ$, d) $\sim 50^\circ \leq \Phi \leq 90^\circ$, $\sim 15^\circ \leq \varphi_2 \leq 30^\circ$ e) $\sim 50^\circ \leq \Phi \leq 90^\circ$, $0^\circ \leq \varphi_2 \leq \sim 15^\circ$. Adapted from the supporting information of [259].

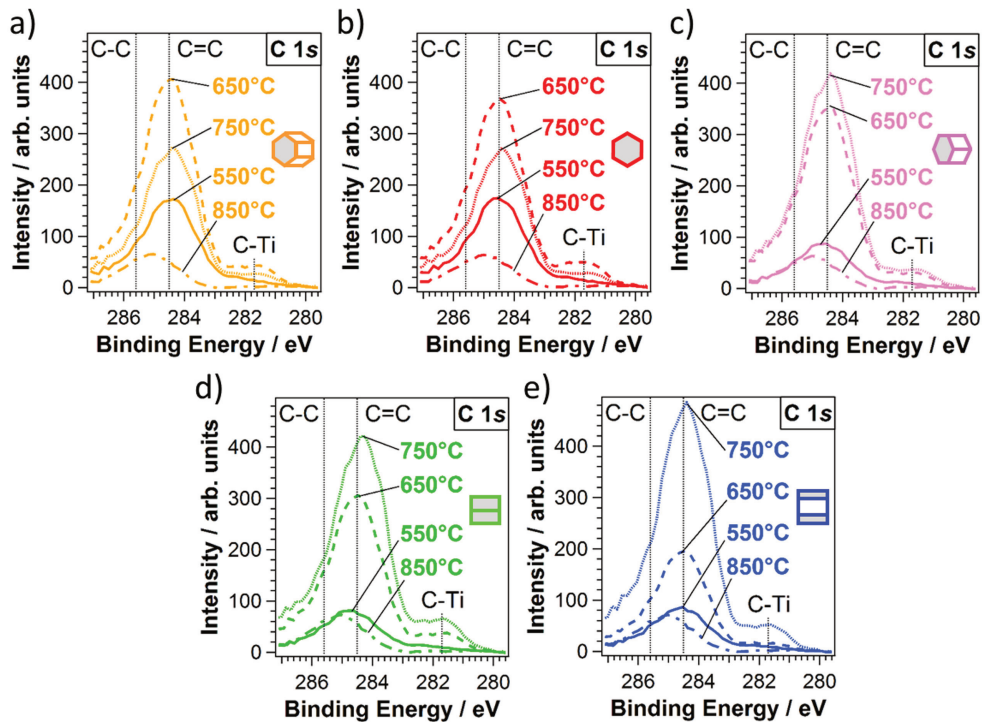


Fig. 113: XP spectra from C 1s photoelectron micrographs taken of TiOC on top of five differently oriented substrate grains for the four annealing temperatures. For the substrate orientations see Fig. 112. Adapted from the supporting information of [259].

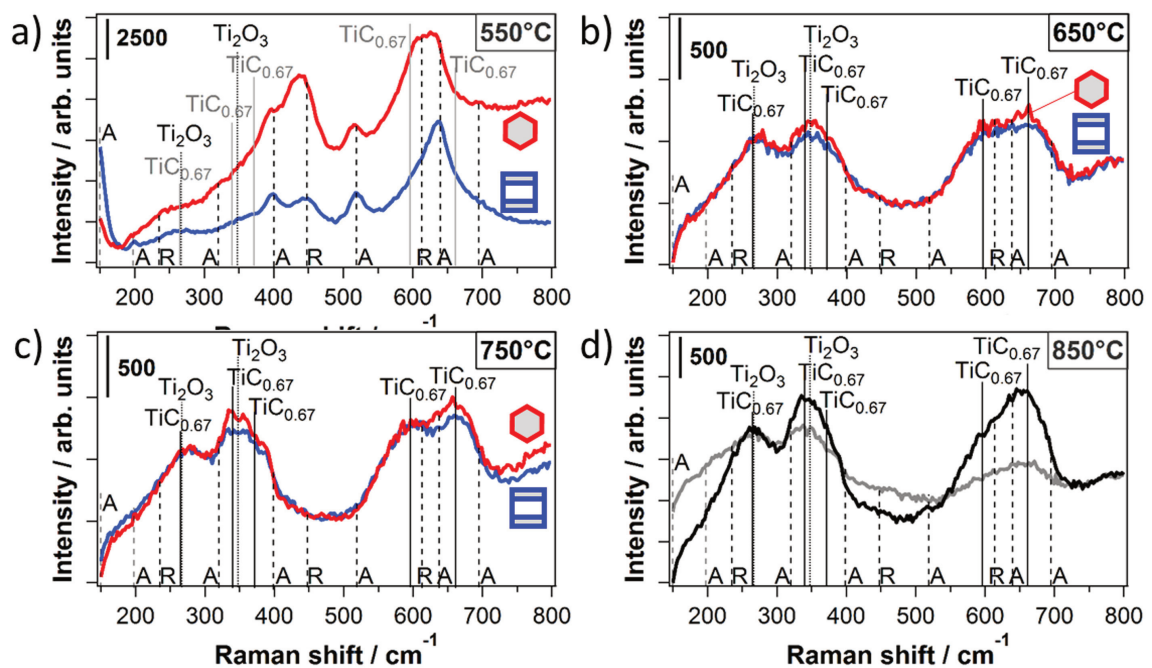


Fig. 114: Micro-Raman spectra of a) TiOC_{550} , b) TiOC_{650} , and c) TiOC_{750} on top of $\sim\text{Ti}(10\bar{1}0)$ and $\sim\text{Ti}(0001)$. d) Micro-Raman spectra of two spots on TiOC_{850} with different optical appearance. Baseline correction: constant shift to a common level. Laser wavelength: 514 nm. Adapted from the supporting information of [259].

B. Abbreviations

AAD	aerosol assisted deposition
ads (subscript)	adsorbed
AFM	atomic force microscopy/microscope
aq (subscript)	aqueous
BE	binding energy
BSE	backscattered electrons
CB	conduction band
CCD	charge-coupled device
CE	counter electrode
CPE	constant phase element
CPU	central processing unit
ct (subscript)	charge transfer
CV	cyclic voltammogram
DEFC	direct ethanol fuel cell
DHE	dynamic hydrogen electrode
DI	de-ionized
DLC	diamond-like carbon
EBSD	electron backscatter diffraction
EBSP	electron backscatter pattern
EC	electrochemical
ECSA	electrochemically active surface area
EDL	electrical double layer
EEC	electrical equivalent circuit
EIS	electrochemical impedance spectroscopy
EMF	electromotive force
EOR	ethanol oxidation reaction
eq (subscript)	equilibrium
EtOH	ethanol
ESCA	electron spectroscopy for chemical analysis
ETR	electron transfer reaction
FB, fb (subscript)	flat band
FE-SEM	field emission SEM
FRA	frequency response analyzer
FWHM	full width at half maximum
GC	glassy carbon (disks)
GL	Gaussian-Lorentzian (line shape)
GLC	graphite-like carbon
GID	grazing incidence diffraction

APPENDIX B. ABBREVIATIONS

H (subscript)	Helmholtz layer
HEA	hemispherical electron analyzer
HER	hydrogen evolution reaction
HOR	hydrogen oxidation reaction
H_{upd}	underpotential deposition of hydrogen
IHP	inner Helmholtz plane
IMFP	inelastic mean free path
IPF	inverse pole figure
ITR	ion transfer reaction
KE	kinetic energy
MFC	mass flow controller
MOR	methanol oxidation reaction
NPs	nanoparticles
OCP	open circuit potential
OER	oxygen evolution reaction
OHP	outer Helmholtz plane
ORR	oxygen reduction reaction
Ω	Ohm (unit), ohmic
PBI	polybenzimidazole
PEMFC	proton-exchange membrane fuel cell, polymer electrolyte membrane fuel cell
PES	photoelectron spectroscopy
RE	reference electrode
RF	roughness factor
RGB	red-green-blue
RHE	reversible hydrogen electrode
RMS	root mean square
rpm	rounds per minute
s (subscript)	solid
S (superscript)	surface
SC	semiconductor
SCE	saturated calomel electrode
SCL	space charge layer
SE	scanning electron, secondary electrons
SEM	scanning electron microscopy/microscope
SHE	standard hydrogen electrode ($E^0 = 0.0 \text{ V}$)
SMSI	strong metal-support interaction
SPEM	scanning photoelectron microscopy
SPM	scanning probe microscopy/microscope
SS	surface states
TiOC	carbon modified titania, containing TiO_2 , TiO_x , graphitic carbon (and TiC)

	TiOC films are prepared from anodic TiO ₂ films
TNT	titania nanotubes
UHV	ultra-high vacuum
UV	ultraviolet
VB	valence band
WE	working electrode
XP, XPS	X-ray photoelectron, X-ray photoelectron spectroscopy
2D	two-dimensional

C. List of Publications

- (1) **C. Rüdiger**, C. Valero-Vidal, M. Favaro, S. Agnoli, G. Granozzi, and J. Kunze-Liebhäuser, "Effect of air-aging on the electrochemical characteristics of TiO_xC_y films for electrocatalysis applications", *ChemElectroChem*, vol. 4, pp. 3100-3109, 2017. DOI: 10.1002/celec.201700912.
- (2) E. Portenkirchner, G. Neri, J. Lichtinger, J. Brumbarov, **C. Rüdiger**, R. Gernhäuser, and J. Kunze-Liebhäuser, "Tracking areal lithium densities from neutron activation – quantitative Li determination in self-organized TiO_2 nanotube anode materials for Li-ion batteries", *Physical Chemistry Chemical Physics*, vol. 19, pp. 8602-8611, 2017. DOI: 10.1039/C7CP00180K.
- (3) **C. Rüdiger**, M. Favaro, C. Valero-Vidal, L. Calvillo, N. Bozzolo, S. Jacomet, J. Hein, L. Gregoratti, S. Agnoli, G. Granozzi, and J. Kunze-Liebhäuser, "Substrate grain-dependent chemistry of carburized planar anodic TiO_2 on polycrystalline Ti", *ACS Omega*, vol. 2, pp. 631-640, 2017. DOI: 10.1021/acsomega.6b00472.
- (4) L. Calvillo, C. Valero-Vidal, S. Agnoli, H. Sezen, **C. Rüdiger**, J. Kunze-Liebhäuser, and G. Granozzi, "Combined photoemission spectroscopy and electrochemical study of a mixture of (oxy)carbides as potential innovative supports and electrocatalysts", *ACS Applied Materials and Interfaces*, vol. 8, pp. 19418-19427, 2016. DOI: 10.1021/acsomega.6b04414.
- (5) **C. Rüdiger**, M. Favaro, C. Valero-Vidal, L. Calvillo, N. Bozzolo, S. Jacomet, C. Hejny, L. Gregoratti, M. Amati, S. Agnoli, G. Granozzi, and J. Kunze-Liebhäuser, "Fabrication of Ti substrate grain dependent C/ TiO_2 composites through carbothermal treatment of anodic TiO_2 ", *Physical Chemistry Chemical Physics*, vol. 18, pp. 9220-9231, 2016. DOI: 10.1039/c5cp07727c.
- (6) I. Brand, C. Rüdiger, K. Hingerl, E. Portenkirchner, and J. Kunze-Liebhäuser, "Compact titanium oxycarbide: A new substrate for quantitative analysis of molecular films by means of infrared reflection absorption spectroscopy", *The Journal of Physical Chemistry C*, vol. 119, pp. 13767-13776, 2015. DOI: 10.1021/acs.jpcc.5b03570.
- (7) L. Calvillo, D. Fittipaldi, **C. Rüdiger**, S. Agnoli, M. Favaro, C. Valero-Vidal, C. Di Valentin, A. Vittadini, N. Bozzolo, S. Jacomet, L. Gregoratti, J. Kunze-Liebhäuser, G. Pacchioni, and G. Granozzi, "Carbothermal transformation of TiO_2 into TiO_xC_y in UHV: Tracking intrinsic stabilities", *The Journal of Physical Chemistry C*, vol. 118, pp. 22601-22610, 2014. DOI: 10.1021/jp506728w.
- (8) A. Zana, C. Rüdiger, J. Kunze-Liebhäuser, G. Granozzi, N. E. A. Reeler, T. Vosh, J. J. K. Kirkensgaard, and M. Arenz, "Core-shell $\text{TiO}_2@\text{C}$: Towards alternative supports as replacement for high surface area carbon for PEMFC catalysts", *Electrochimica Acta*, vol. 139, pp. 21-28, 2014. DOI: 10.1016/j.electacta.2014.07.002.
- (9) **C. Rüdiger**, J. Brumbarov, F. Wiesinger, S. Leonardi, O. Paschos, C. Valero Vidal, and J. Kunze-Liebhäuser, "Ethanol oxidation on TiO_xC_y -supported Pt nanoparticles", *ChemCatChem*, vol. 5, pp. 3219-3223, 2013. DOI: 10.1002/cctc.201300217.
- (10) **C. Rüdiger**, F. Maglia, S. Leonardi, M. Sachsenhauser, I. D. Sharp, O. Paschos, and J. Kunze, "Surface analytical study of carbothermally reduced titania films for electrocatalysis application", *Electrochimica Acta*, vol. 71, pp. 1-9, 2012. DOI: 10.1016/j.electacta.2012.02.044.

APPENDIX C. LIST OF PUBLICATIONS

This thesis contains results that have been previously published in (1),²⁵¹ (3),²⁵⁹ (5),¹¹⁸ (9),²⁴⁶ and (10).²¹⁷

List of Figures

Fig. 1	Guy-Chapman-Stern model of the EDL and according potential drop. Based on Fig. 3.16 in [65].	11
Fig. 2	Interface between n-type semiconductor (SC) and an electrolyte (EL) with redox couple. a) Before contact with indicated vacuum scale and electrochemical scale. b) After contact: depletion layer conditions, potential drop across space charge layer and accumulation of charge at interface. Applied potentials: c) flat-band conditions at $E = E_{fb}$, and d) accumulation layer conditions at $E < E_{fb}$ so that E_F lies within the conduction band. The donor level is not shown. Based on the theoretical treatments in [63, 67, 68].	13
Fig. 3	Scheme of the free energy change along the reaction coordinate.	16
Fig. 4	Scheme showing the modification of the free energy diagram caused by a change of the potential. Based on the theoretical treatments in [64] (Fig. 3.3.2) and [65] (Fig. 4.5).	18
Fig. 5	Simplified scheme of a potentiostat. Based on schemes in [74, 75].	23
Fig. 6	Potential step, current transient with indicated electrode processes at different times, and determination of electron transfer-limited current density from the plot of the current density versus \sqrt{t} .	25
Fig. 7	Arrhenius plot of the electron transfer-limited current density and extraction of the activation energy from the slope.	26
Fig. 8	Triangular voltage signal at working electrode and typical cyclic voltammogram of a reversible redox reaction. The scan direction is indicated by arrows.	28
Fig. 9	Sinusoidal potential signal that is applied to an electrochemical cell and sinusoidal current response with phase shift ϕ .	30
Fig. 10	Nyquist plot (left) and Bode plot (right) qualitatively presenting the impedance of an electrode reaction in presence of a redox couple. In the Nyquist plot, the frequency ω increases along the arrow. The plots are based on measured spectra reported in [80].	32
Fig. 11	EEC models representing typical non-faradaic and faradaic electrochemical processes: Charging of a) an ideal and b) a non-ideal EDL; faradaic process with c) irreversible charge transfer or d) charge transfer and mass transport control. The symbols denote: R = resistor, C = capacitor, CPE = constant phase element, Z_f = faradaic impedance, W = Warburg element. The labels denote: Ω = ohmic, EDL = electrical double layer, ct = charge transfer.	32
Fig. 12	Effect of a catalyst on the activation energy of a reaction.	35
Fig. 13	Sketch of a PEMFC fed with hydrogen gas or alcohols.	36
Fig. 14	Top views of the fcc crystal surfaces (111), (001) and (110) of Pt.	37
Fig. 15	CV of polycrystalline Pt wire in 0.1 M H_2SO_4 , scan rate 100 mV s^{-1} .	37
Fig. 16	Left: CV of polycrystalline Pt in 0.1 M $HClO_4$ with 0.5 M of ethanol, taken at a scan rate of 5 mV s^{-1} (reprinted from [101] © 2010, with permission from Elsevier Inc.). The potential of the original graph is reported vs. a saturated Ag/AgCl electrode. The corresponding SHE potential scale has been added on top of the graph. Right: Scheme of the EOR reaction pathways including the activation of water (box) (based on the considerations in [79, 101]).	40
Fig. 17	Bragg diffraction. A reflection is only observed at angles $2\vartheta_{\text{Bragg}}$ with respect to the incident X-ray beam. Based on the treatment in [108].	43
Fig. 18	Interaction volume of energetic electrons in a low-density, low-atomic-number specimen, and depths from which Auger, secondary and backscattered electrons, and X-rays emerge. Based on the treatment in [113]. The escape depth of Auger electrons was taken from [114].	45
Fig. 19	Definition of the Euler angles according to the Bunge convention. Based on the representation in [116].	49

LIST OF FIGURES

Fig. 20	Top-left to bottom-right: Orientation of hexagonal lattice with respect to surface normal (adapted from [118] - Published by the PCCP Owner Societies, and based on a similar sketch in [58]), standard triangle of surface-normal projected IPF orientation map with Euler angles, EBSD map with hexagonal lattice cells, and relation between low index directions and planes in the hexagonal system.	49
Fig. 21	Working principle of AFM.	51
Fig. 22	Energy level diagram for elastic, inelastic and resonant scattering processes of photons (visible to near UV regime) in a Raman active molecule, as well as absorption followed by fluorescence. The wavy arrows indicate radiation-less transitions. Based on [128].	52
Fig. 23	Scheme of core level photoelectron emission and the two de-excitation channels that cause the emission of radiation (fluorescence) or of an Auger electron (based on the treatments in [141] and [114]).	59
Fig. 24	Energy diagram of the sample and the spectrometer. Based on Fig. 3 in [138].	59
Fig. 25	Idealized geometry of X-ray source, solid sample and spectrometer. Based on Fig. 17 in [138].	63
Fig. 26	Inelastic mean free path of electrons as a function of their kinetic energy (printed with kind permission of M. Favaro).	65
Fig. 27	Escape depths of photoelectrons from a solid for normal emission (left) and tilted emission (right). Based on Fig. 43 in [138].	66
Fig. 28	Evolution of a) the cell potential, b) the cell current, and c) the oxide film thickness with time during potentiostatic anodization. Based on Fig. 3 in [54].	70
Fig. 29	Pourbaix diagram for Ti, extended by electronic data: U_{VB} : valence band potential, U_{CB} : conduction band potential, U_{FB} : flat band potential, U_{SS} : potential of surface states. E_g : band gap energy of anatase TiO_2 (3.2 eV). $\Delta\varphi_{ox} = U - U_{FB}$: potential drop in the oxide film. Reprinted from [53] © 2000, with permission from Elsevier Science Ltd..	73
Fig. 30	Equilibrium shape of a macroscopic TiO_2 crystal in the a) anatase and b) rutile phase, according to the presentation in [23].	75
Fig. 31	Bulk structures of anatase and rutile. Reprinted from [23] © 2002, with permission from Elsevier Science B.V..	75
Fig. 32	Calculated Pourbaix-diagram for the $TiC-H_2O$ system at 25 °C. The border lines are drawn for 10^0 , 10^{-2} , 10^{-4} , and 10^{-6} M solutions respectively. The points in the graph indicate: (P) theoretical passivation potential; measured (A) corrosion potential, (B) passivation potential and (C) passive potential during potentiodynamic anodic polarization in deaerated 1.0 M HCl at a scan rate of 0.1 mV s^{-1} . Reprinted from [191] © 1990, with permission from Elsevier Sequoia.	77
Fig. 33	Electropolishing setup. Adapted from [194] with kind permission of F. Wiesinger.	81
Fig. 34	a) Anodization cell (adapted from [194] with kind permission of F. Wiesinger). b) Anodic TiO_2 prepared at different potentials.	82
Fig. 35	Top: photograph of quartz boat with anodized Ti sheets; center: schematic of annealing setup; bottom: temperature and mass flow programs.	83
Fig. 36	Preparation steps of TiOC films: (0) raw Ti platelet/disk, (1) mechanically polished Ti surface, (2) electropolished Ti surface, (3) TiO_2 film on anodized Ti (4) carbothermally treated oxide film (TiOC). Top: square Ti platelets with an edge length of 12 mm; bottom: round Ti disks with a diameter of 15.5 mm.	84
Fig. 37	a) Scheme of AAD setup; b) physical and chemical processes during AAD of Pt using a H_2PtCl_6 precursor solution; c) TiOC film before and after impregnation with Pt <i>via</i> AAD. a) and b) are adapted from [198] with kind permission of J. Brumbarov.	86
Fig. 38	Left: Sketch of the three electrode glass EC cell; right: photograph of one of the used EC cells.	88
Fig. 39	Preparation of a working electrode for the room temperature EC cell, shown for a 15.5 mm diameter sample. See description in the text.	89

Fig. 40	Teflon [®] electrochemical cell for measurements at elevated temperatures. Adapted from [194] with kind permission of F. Wiesinger.	90
Fig. 41	Photographs of the used Autolab potentiostats. a) PGSTAT 30, b) PGSTAT 302N.	91
Fig. 42	Photographs of the Bruker (previously Veeco) MultiMode 8 SPM with AFM head, the sample holder on the scanner, a sample attached to the magnetic disk, the AFM probe holder, and the top view of a tapping mode cantilever on top of a sample surface (seen through the optical microscope with camera, which was mounted on top of the AFM head). The pictures of the equipment are taken from [203], with permission of the Bruker Corporation.	95
Fig. 43	Photograph of the sample stage of the Zeiss CrossBeam [®] NVision 40 system with five attached samples of each 15.5 mm diameter.	96
Fig. 44	Schematic drawing of a typical XPS setup with photon source (X-rays, UV-light, laser or Synchrotron radiation), a sample manipulation with different linear and rotational degrees of freedom, electron optics, an energy dispersive analyzer and detector. XP spectra (intensity vs. binding energy) are shown for four different metals with their element specific distribution of core level photoemission. Adapted from [205], with kind permission of F. Müller.	97
Fig. 45	Photograph of the UHV system of the <i>Surface Science and Catalysis Group</i> at UNIPD and of the manipulator head with attached sample. Reprinted from [207] with kind permission of M. Favaro.	99
Fig. 46	Scetch of the backscattering geometry of the used Raman equipment.	101
Fig. 47	Square Ti platelet (cut from metal sheet) after electropolishing at -30°C by applying five times 60 V for each 5 min. a) SE micrograph taken at a tilt angle of 2° , b) optical micrograph taken with crossed polarizers.	104
Fig. 48	Current transients during potentiostatic anodization of electropolished Ti substrates at a) 5 V and b) 10 V using a potentiostat. Insets: magnification of the current transients after the initial decrease.	104
Fig. 49	Oxide film on a square Ti platelet as that shown in Fig. 47, synthesized by anodization at 20 V for 10 min. a) Topographic contrast map acquired with tapping mode AFM, and line profiles A and B. Roughness analysis in the indicated boxes yields the following RMS height values: (1) 20 nm, (2) 15 nm, (3) 6 nm. SE micrograph taken at a tilt angle of b) 9.4° , and c) 45° . The AFM image shown in a) has been published in [217].	106
Fig. 50	AFM analysis of a round Ti disk after each electropolishing step. Electropolishing was performed at -33°C by repeatedly applying 60 V for 5 min. Topographic images after the a) first, b) second and (c,e) third repetition, and (d,f) height profiles along the respective arrows in c) and e).	107
Fig. 51	Morphology and topography of anodic TiO_2 on a round Ti substrate. (a,d) SE micrographs acquired with the inlens detector using an acceleration voltage of 4.0 kV and a working distance of 4.0 mm. Inset in a): optical micrograph of the analyzed film area. (b,e) Topographic images acquired with AFM and c) height profile along the arrow in b). Roughness analysis in the indicated boxes yields the following RMS height and RF values: (1) 5 nm, 1.016; (2) 4 nm, 1.007.	107
Fig. 52	AFM analysis of a) electropolished Ti substrate, and b) oxide film prepared by anodization at 20 V for 10 min.	108
Fig. 53	AFM analysis of TiOC films on square substrates prepared at a) 750, b) 850 and c) 1050 $^{\circ}\text{C}$. Top: height contrast images, bottom: height profiles along the arrows. Roughness analysis in the indicated boxes yields the following RMS height and RF values: (1) 14 nm, 1.024; (2) 11 nm, 1.025; (3) 8 nm, 1.011; (4) 14 nm, 1.012; (5) 6 nm, 1.012. The AFM image shown in b) has been published in [217].	110
Fig. 54	SE micrographs of TiOC films on square substrates prepared at different annealing temperatures. High magnification micrographs of different film areas are shown for TiOC_{750} , TiOC_{850} , and TiOC_{1050} . Similar SE micrographs have been published in [217].	111

- Fig. 55 XP spectra of TiOC films on square substrates prepared at different annealing temperatures. Reference spectra: as-grown anodic TiO₂ (black) and a TiC-rich film, that was prepared at 850 °C with a ten times higher flow fraction of C₂H₂ (green). High resolution spectra of the a) Ti 2*p*, b) O 1*s* and c) C 1*s* core level regions with multi-peak fits. The spectra in a) and b) are scaled to a common Ti 2*p*_{3/2} peak height of the TiO₂ component; the spectra in c) are scaled to a common height of the peak maximum, which originates from *sp*² (C=C) and/or *sp*³ (C-C) carbon. For clarity, the spectra are shifted vertically. X-ray source: Al K_α, normal emission. a) and c): re-analyzed spectra that have been published in [217]. 112
- Fig. 56 Fractions of photoelectrons from a) TiO₂, TiO_{*x*} and TiC (TiO) species in the Ti 2*p* spectral range and of those from b) carbidic carbon (C-Ti), carbon-carbon bonds (C=C, C-C) and carbon-oxygen groups (C-O, O-C=O) in the C 1*s* spectral range. Solid symbols: as-grown anodic TiO₂ and TiOC films prepared at different annealing temperatures with 0.1 flow% acetylene; open symbols: reference film, prepared at 850 °C with 1.0 flow% acetylene. 115
- Fig. 57 Grazing incidence X-ray diffraction patterns of TiOC films on square substrates prepared at different annealing temperatures. Assignment of the phases was done using the PDF-2 database. The XRD patterns of TiOC₇₅₀, TiOC₈₅₀ and TiOC₁₀₅₀ have been published in [217]. . . 116
- Fig. 58 Electrochemical oxidation and reduction of the ferro-/ferricyanide redox couple at TiOC films, and GC and anodic TiO₂ references. EIS spectra and EEC fits, represented in a) a Nyquist and b) a Bode plot. EIS was performed at the formal equilibrium potential 0.54 V_{SHE} in a frequency range of 100 kHz–1 mHz. Inset in a): EEC used to fit the spectra. c) Last CVs of 100 potentiodynamic cycles at 10 mV s⁻¹ prior to EIS. The indicated peak separation belongs to TiOC₇₅₀. d) Electron transfer resistance extracted from the EIS fits as a function of TiOC annealing temperature. Electrolyte: 0.1 M H₂SO₄ with each 2.5 M K₃[Fe(CN)₆] and K₄[Fe(CN)₆]. Currents and resistances are normalized to the geometric surface areas of the electrodes. The data have been published in [217]. 118
- Fig. 59 HER activity of TiOC prepared at different annealing temperatures. a) LSV in 0.1 M H₂SO₄, starting from 0.0 V and going cathodic with a scan rate of 10 mV s⁻¹ until a cathodic current density of ~ 4 mA cm⁻² is reached. b) HER current density at -0.8 V taken from a) vs. the area specific charge transfer resistance *r*_{ct} of the respective TiOC (determined by EIS with the ferro-/ferricyanide redox couple). The data in a) have been published in [217]; b) is adapted from [246] © 2013 WILEY-VCH Verlag GmbH & Co. KGaA, Weinheim. 119
- Fig. 60 Thermodynamic model of the phase evolution and temperature program of the annealing procedure. Adapted from [217]. 120
- Fig. 61 Photographs of as-grown anodic TiO₂ and TiOC films on round disk substrates prepared at different annealing temperatures. 122
- Fig. 62 SE micrographs of an anodic TiO₂ film prior to and after carbothermal treatment at 550 °C. Detector: inlens; acceleration voltage: 4 kV; working distance: 4 mm (TiO₂) and 5 mm (TiOC₅₅₀). . 123
- Fig. 63 SE micrographs of TiOC films on round disk substrates prepared at different annealing temperatures, as indicated. SE2: Everhart-Thornley detector, all others: inlens detector. For TiOC₈₅₀, high magnification micrographs are shown for two zones of different morphology. . . 123
- Fig. 64 XPS of TiOC films and of an as-grown anodic TiO₂ reference, prepared on round disk substrates. High resolution spectra with Shirley-type backgrounds and component fits (a,c,e,g,i) of the Ti 2*p* and (b,d,f,h,j) of the C 1*s* core levels. (a,b) As-grown anodic film, (c,d) TiOC₅₅₀, (e,f) TiOC₆₅₀, (g,h) TiOC₇₅₀ and (i,j) TiOC₈₅₀. X-ray source: Mg K_α, normal emission. The spectra with analysis have been published in the supporting information of [251]. 125

- Fig. 65 XPS analysis of TiOC films prepared on round disk substrates. a) Ti 2*p* and b) C 1*s* core level spectra acquired at $\theta = 90^\circ$ (solid lines: NE) and at $\theta = 30^\circ$ (broken lines: GE) of TiOC, and of an as-grown anodic TiO₂ reference (black, $\theta = 90^\circ$). Ti 2*p* spectra are scaled to a common TiO₂ peak height and C 1*s* spectra to a common height of the peak maximum. For clarity, the spectra are shifted vertically. Results of multi-peak fitting for c) Ti 2*p* and d) C 1*s* spectra. e) Relative concentrations of C=C, C-C, C-O and O-C=O species on the film (surface C), and of the detected Ti species (Ti 2*p*) versus annealing temperature (NE). Adapted from [251] © 2017 Wiley-VCH Verlag GmbH & Co. KGaA, Weinheim. 127
- Fig. 66 Cyclic voltammetry of TiOC films prepared on round disk substrates. (a-c) Each 20th CV scan of TiOC₅₅₀, TiOC₆₅₀ and TiOC₇₅₀ acquired with different scan rates, and d) evolution of CV scans of TiOC₈₅₀ at a scan rate of 50 mV s⁻¹. Peak separations are indicated in the graphs. (e-g) Peak current densities of CVs in (a-c), determined as shown in c), versus square root of scan rate *v*. Electrolyte: 0.1 M H₂SO₄ with each 2.5 M K₃[Fe(CN)₆] and K₄[Fe(CN)₆]. Adapted from [251] © 2017 Wiley-VCH Verlag GmbH & Co. KGaA, Weinheim, and the associated supporting information. 128
- Fig. 67 EIS of outer sphere electron transfer at TiOC. a) Nyquist and b) Bode plots from EIS data, and c) EEC models **1** and **2** used for the least squares fits plotted in a) and b). Gray lines: EEC **1**, black lines: EEC **2**. Electrolyte: 0.1 M H₂SO₄ with each 2.5 M K₃[Fe(CN)₆] and K₄[Fe(CN)₆]. Potential: 0.59 ± 5 mV; frequency range: 10 kHz–20 mHz. (a,c) Adapted from [251] © 2017 Wiley-VCH Verlag GmbH & Co. KGaA, Weinheim. 129
- Fig. 68 Polarization resistance of TiOC against the Fe(CN)₆³⁻/Fe(CN)₆⁴⁻ redox reaction, versus chemical surface composition. a) Fraction of Ti species in the oxide film (from Ti 2*p* spectra). b) Concentration of *sp*², *sp*³ carbon and carbon-oxygen species on the surface (relative to all Ti species). XP spectra were acquired at NE. Adapted from [251] © 2017 Wiley-VCH Verlag GmbH & Co. KGaA, Weinheim. 130
- Fig. 69 Current density-time profiles of a) TiOC₅₅₀, b) TiOC₆₅₀, c) TiOC₇₅₀ and d) TiOC₈₅₀ acquired at each potential step prior to EIS. The values of the approximate onset potentials of corrosion are given in the graphs. Electrolyte: 1.0 M HClO₄. Adapted from the supporting information of [251]. 132
- Fig. 70 EIS analysis of TiOC in 1.0 M HClO₄. Bode (left) and Nyquist (right) diagrams of EIS data acquired at (a,b) -0.16 V, (c,d) 0.24 V and (e,f) 0.94 V with fit curves. Dotted lines in (a,c,e): *f* = 1.8 kHz, at which -*Z*'' was extracted to generate Mott-Schottky plots. g) EEC models used for the fits and schemes of the multi-layered film structure showing one nanopore of the outer oxide layer. Adapted from [251] © 2017 Wiley-VCH Verlag GmbH & Co. KGaA, Weinheim, and the associated supporting information. 134
- Fig. 71 Area specific polarization resistance of TiOC in 1.0 M HClO₄ versus dc potential, determined from EIS fits. Vertical dashed lines: threshold potentials up to which anodic current densities are ≤ 0.1 μA cm⁻². Adapted from [251] © 2017 Wiley-VCH Verlag GmbH & Co. KGaA, Weinheim. 135
- Fig. 72 Mott-Schottky diagrams of anodic TiO₂ and of TiOC. Area specific (-ω*Z*'')² values extracted from potential step EIS in 1.0 M HClO₄ at a frequency of 1.8 kHz (see dotted lines in Fig. 70), versus dc potential. b) Enlargement of a), showing only the data of TiOC. Vertical dashed lines in b): threshold potentials up to which anodic current densities are ≤ 0.1 μA cm⁻². 136
- Fig. 73 XPS analysis of TiOC after different air exposure times. a) Ti 2*p* core level spectra, scaled to a common TiO₂ peak height, and b) C 1*s* core level spectra, scaled to a common height of the peak maximum, acquired at normal emission (NE, $\theta = 90^\circ$). Solid lines: pristine TiOC, broken lines: two months old TiOC, violet spectra: 12 days old TiOC₅₅₀. For clarity, the spectra are shifted vertically. Results of multi-peak fitting for c) Ti 2*p* and d) C 1*s* spectra. Adapted from [251] © 2017 Wiley-VCH Verlag GmbH & Co. KGaA, Weinheim. 138

- Fig. 74 EIS of outer sphere electron transfer at pristine and air aged TiOC. Nyquist (left) and Bode (right) diagrams of EIS data acquired for (a,b) TiOC₅₅₀, (c,d) TiOC₆₅₀, (e,f) TiOC₇₅₀ and (g,h) TiOC₈₅₀ with fit curves. The data were fitted using the models EEC 1 (colored) and EEC 2 (black) shown in Fig. 67c. The duration of air aging is indicated in the legend of the Bode plots. Insets on the left: Nyquist plot of a) pristine TiOC₅₅₀, c) 6 months aged TiOC₆₅₀, e) 9 months aged TiOC₇₅₀ and g) pristine TiOC₈₅₀. Electrolyte: 0.1 M H₂SO₄ with each 2.5 mM K₃[Fe(CN)₆] and K₄[Fe(CN)₆]. Potential: 0.59 ± 5 mV; frequency range: 10 kHz–20 mHz. Adapted from the supporting information of [251]. 140
- Fig. 75 Outer sphere charge transfer kinetics at pristine TiOC, air aged TiOC and reference films. Each 20th CV scan acquired at a scan rate of 50 mV s⁻¹ for a) TiOC₅₅₀, as-grown anodic TiO₂ and TiO_{2-x}, b) TiOC₆₅₀, c) TiOC₇₅₀ and d) TiOC₈₅₀. The duration of air aging is indicated in the legends. e) Area specific polarization resistance against the redox reaction, $R_{p,redox} = R_{ct} + R_{por}$, versus TiOC annealing temperature. $R_{p,redox}$ is determined from EIS fits using the models EEC 1 and EEC 2 shown in Fig. 67. Electrolyte: 0.1 M H₂SO₄ with each 2.5 M K₃[Fe(CN)₆] and K₄[Fe(CN)₆]. Adapted from [251] © 2017 Wiley-VCH Verlag GmbH & Co. KGaA, Weinheim. 141
- Fig. 76 Current density-time profiles of 9 months old a) TiOC₅₅₀, b) TiOC₆₅₀, c) TiOC₇₅₀ and d) TiOC₈₅₀ acquired at each potential step prior to EIS. The values of the approximate onset potentials of corrosion are given in the graphs. Electrolyte: 1.0 M HClO₄. Adapted from the supporting information of [251]. 143
- Fig. 77 EIS analysis of 9 months old TiOC in 1.0 M HClO₄. Bode (left) and Nyquist (right) diagrams of EIS data acquired at (a,b) -0.16 V, (c,d) 0.24 V and (e,f) 0.94 V with fit curves. Dotted lines in (a,c,e): $f = 1.8$ kHz, at which $-Z''$ was extracted to generate Mott-Schottky plots. g) EEC models used for the fits and schemes of the multi-layered film structure showing one nanopore of the outer oxide layer. Adapted from [251] © 2017 Wiley-VCH Verlag GmbH & Co. KGaA, Weinheim, and the associated supporting information. 144
- Fig. 78 Area specific polarization resistance of aged TiOC in 1.0 M HClO₄ versus dc potential, determined from EIS fits. Vertical dashed lines: threshold potentials up to which anodic current densities are ≤ 0.1 μA cm⁻². Adapted from [251] © 2017 Wiley-VCH Verlag GmbH & Co. KGaA, Weinheim. 145
- Fig. 79 Mott-Schottky diagrams of anodic TiO₂ and of 9 months old TiOC. Area specific $(-\omega Z'')^2$ values extracted from potential step EIS in 1.0 M HClO₄ at a frequency of 1.8 kHz (see dotted lines in Fig. 70), versus dc potential. b) Enlargement of a), showing only the data of TiOC. Vertical dashed lines in b): threshold potentials up to which anodic current densities are ≤ 0.1 μA cm⁻². 146
- Fig. 80 Correlation between optical appearance of prepared films and substrate texture. a) EBSD map of a Ti substrate; optical micrographs of the surface area shown in a): b) after anodization, and c) after annealing at 550 °C without acetylene. d) standard triangle of the surface-normal projected inverse pole figure orientation map (EBSD map) with numbers of the studied grains, ranges of tilt-angles Φ and the low index projected hexagonal cells. Optical micrographs of anodic film e) prior to and f) after carbothermal treatment with acetylene, with projected hexagonal cells. Adapted from [118] and electronic supplementary information - Published by the PCCP Owner Societies. 151
- Fig. 81 Raman spectra of natural anatase crystals with oriented polished surfaces. The six Raman active modes are labeled with their irreducible representations, and the two combination bands with (A). a) incident laser normal to (001) surface; red: Lorentzian peak fit. b) incident laser normal to (100) surface; spectra taken at two azimuthal orientations with respect to the microscope that differ by ~ 90°. For clarity, the black spectrum is shifted upwards. Laser wavelength: 532 nm. Adapted from [118] and electronic supplementary information - Published by the PCCP Owner Societies. 154

- Fig. 82 a) Raman spectra of $\text{TiO}_2^{\text{ref}}$ acquired at two different azimuthal orientations of the substrate relative to the Raman microscope ($\varphi_1 = 0^\circ$ or 90°). Red: film on a $\sim\text{Ti}(0001)$ substrate grain; blue: film on a $\sim\text{Ti}(10\bar{1}0)$ substrate grain. Inset: magnification of the most intense E_g band. b) Raman spectra of C/TiO_2 acquired at $\varphi_1 = 0^\circ$ or 90° . Red: film on a Ti substrate grain with $\Phi \leq \sim 15^\circ$ ($\sim\text{Ti}(0001)$); orange: film on a Ti substrate grain with $\sim 15^\circ \leq \Phi \leq \sim 40^\circ$; green: film on a substrate grain with $\Phi \geq \sim 50^\circ$ ($\sim\text{Ti}(2\bar{1}\bar{1}0)$). Laser wavelength: 532 nm. Adapted from the electronic supplementary information of [118] - Published by the PCCP Owner Societies. 155
- Fig. 83 SE micrographs of a selected area on the anodic TiO_2 film (a,b) and of the same area on the C/TiO_2 film (c,d), with hexagonal cells representing the Ti substrate grain orientations. SEM was performed with the InLens detector (electron beam acceleration voltage: 4 kV, working distance: 4–7 mm). Adapted from [118] - Published by the PCCP Owner Societies. 156
- Fig. 84 Micro-Raman spectra of $\text{C}/\text{TiO}_2/\text{Ti}_{\text{poly}}$ for different ranges of tilt angles Φ . For clarity, the spectra are shifted vertically. Gray spectrum in a): $\text{TiO}_2^{\text{ref}}$ on Ti with $\Phi \leq 15^\circ$. Dashed lines: rutile bands, dotted lines: all other bands. D- and G-bands: from carbon (C). TiO_2 combination bands: (R) = rutile, (A) = anatase. b) Selected spectral range of a), where only each two neighboring anatase and rutile bands are indicated. Laser wavelength: 532 nm. a) Adapted from [118] - Published by the PCCP Owner Societies. 156
- Fig. 85 a) Background-corrected micro-Raman spectra with four-peak Gaussian fits of carbon species detected in C/TiO_2 films on three differently tilted substrate grains. The signal intensity, $I(\text{C})$, was determined by integration of the spectra, as indicated by the colored area in the green spectrum. b) Carbon signal intensity, normalized to the maximum value, *versus* substrate tilt angle Φ . Error bars of $I(\text{C})$: standard deviations of $I(\text{C})$ on grains within one Φ -range; error bars of Φ : ranges defined in table 5.1. Laser wavelength: 532 nm. Adapted from [118] and electronic supplementary information - Published by the PCCP Owner Societies. 157
- Fig. 86 Chemical maps of a) the C 1s and b) the Ti $2p_{3/2}$ core levels obtained by SPEM of a selected area of a C/TiO_2 film. c) Optical micrograph of the corresponding anodic TiO_2 film prior to the carbothermal treatment, with surface projected hexagonal cells representing the orientations (A–E) of the investigated substrate grains. Spectra extracted from the boxes in d) the C 1s and e) the Ti $2p_{3/2}$ chemical maps. For clarity, the spectra are shifted vertically. f) C 1s signal intensities, $I(\text{C})$, normalized to the maximum value, *versus* tilt angle Φ of Ti substrate grains. The intensity values correspond to the uncorrected absolute C 1s peak areas, which were obtained by integration of the spectra in d) after subtraction of a constant background. Adapted from [118] - Published by the PCCP Owner Societies. 158
- Fig. 87 a) $2 \times 2 \mu\text{m}^2$ AFM micrographs of $\text{TiO}_2^{\text{ref}}$, taken on top of substrate grains with different crystallographic orientations. Cross-sections in b) are taken along the dashed lines in a). c) Dependence of the roughness factor (RF) and the root mean square (RMS) height on the tilt angle Φ along three orientation paths, as indicated in the standard triangle. The number labels belong to the grains in Fig. 80. Adapted from the electronic supplementary information of [118] - Published by the PCCP Owner Societies. 160
- Fig. 88 a) Micro-Raman spectra of $\text{TiO}_2^{\text{ref}}$ for different Φ . The colors correspond to the orientation-color code given by the standard triangle (the studied grains are depicted in Fig. 80). For clarity the spectra are shifted vertically. Dashed lines: rutile, dotted lines: anatase, carbon. D- and G-bands: carbon (C). TiO_2 combination bands: rutile (R), anatase (A). Inset: anatase E_g peak (143 cm^{-1}). Along the arrows (A and B), Φ varies from 0° to 90° . b) Micro-Raman spectrum of electropolished Ti (black) and an anodic TiO_2 film on $\sim\text{Ti}(0001)$ (red) and $\sim\text{Ti}\{hki0\}$ (blue). Laser wavelength: 532 nm. Adapted from [118] - Published by the PCCP Owner Societies. . . . 161

LIST OF FIGURES

Fig. 89 Analysis of selected Raman signals detected in $\text{TiO}_2^{\text{ref}}$ on top of substrate grains with the shown orientations. Integrated areas are colored. a) Lorentz-fit of anatase E_g -band at 143 cm^{-1} . b) Overall signal from thermally treated anodic TiO_2 . c) Four-peak Gaussian fit of carbon signal. Laser wavelength: 532 nm. Adapted from the electronic supplementary information of [118] - Published by the PCCP Owner Societies. 163

Fig. 90 Evaluation of Raman spectra of $\text{TiO}_2^{\text{ref}}$ as a function of the substrate tilt angle Φ . The studied grains are labeled with numbers and marked in the standard triangle. a) Anatase E_g band intensities at 143 cm^{-1} and area-specific carbon signal intensities ($I_{\text{spec}}(\text{C})$); b) FWHM of the anatase E_g band at 143 cm^{-1} . c) Ratio of $I_{\text{spec}}(\text{C})$ and the overall Raman response of crystalline and amorphous TiO_2 ($I(\text{TiO}_2)$). d) Ratio of $I_{\text{spec}}(\text{C})$ and the intensity of the anatase E_g band at 143 cm^{-1} . Dashed lines in a) and c): linear least squares fits of carbon band intensities below 55° and above 40° . Dashed line in d): arithmetic mean (0.85 ± 0.27). Adapted from [118] - Published by the PCCP Owner Societies. 164

Fig. 91 Evaluation of the fitted Raman-spectra of $\text{TiO}_2^{\text{ref}}$ on polycrystalline Ti. a) Peak areas of selected anatase and carbon Raman bands, and (b,c) band positions of two anatase bands are plotted *versus* the tilt angle Φ of the substrate grains. Dotted lines in a) serve as guide for the eye, solid lines in (b,c) are linear least squares fits. Adapted from the electronic supplementary information of [118] - Published by the PCCP Owner Societies. 165

Fig. 92 SE micrographs of TiOC taken with the InLens detector (electron beam acceleration voltage: 4–6 kV, working distance: 3–5 mm). High-magnification insets: areas on differently oriented substrate grains (TiOC_{550} , TiOC_{650} , TiOC_{750}) or areas with different TiOC morphologies (TiOC_{850}). Projected hexagonal cells: approximate crystallographic orientation of the Ti substrate grains, according to table 5.1. Note that the substrate orientations were estimated from the optical appearance of the respective as-grown anodic TiO_2 films, so that type D and E grains cannot be distinguished. Reproduced from [259] © 2017 American Chemical Society. 167

Fig. 93 Chemical maps from Ti $2p_{3/2}$ (always left) and C 1s (always center) photoelectron micrographs of TiOC, and EBSD maps (always right) of the corresponding Ti substrate. a) TiOC_{550} , b) TiOC_{650} , c) TiOC_{750} , and d) TiOC_{850} . To facilitate discrimination between the different TiOCs, the chemical maps are differently colored. Table: approximate orientations of labeled grains (see standard triangle and table 5.1). Adapted from [259] © 2017 American Chemical Society. 168

Fig. 94 Spectra from Ti $2p_{3/2}$ (top) and C 1s (bottom) core level maps of TiOC, acquired on top of substrate grains with five different orientations, as indicated by the hexagonal cells using the color-orientation code. (a,e) TiOC_{550} , (b,f) TiOC_{650} , (c,g) TiOC_{750} , and (d,h) TiOC_{850} . The spectra in (b,c) are scaled to the TiO_2 component height. Adapted from [259] © 2017 American Chemical Society. 169

Fig. 95 Micro-Raman spectra of TiOC_{550} , TiOC_{650} , and TiOC_{750} on top of (a,b) $\sim\text{Ti}(10\bar{1}0)$ and (c,d) $\sim\text{Ti}(0001)$, and of two spots on TiOC_{850} with different optical appearance (black and gray spectra). Purple spectrum in a): as-grown anodic TiO_2 . (b,d) Spectral range within box in (a,c). Baseline correction: (a,c) subtraction of a fourth-order polynomial function; constant shift to a common level at b) 800 cm^{-1} and d) 150 cm^{-1} . Laser wavelength: 514 nm. e) Photographs of TiOC specimen. Adapted from [259] © 2017 American Chemical Society. 171

Fig. 96 Schematic representation of the cross-sectional composition of TiOC on top of $\sim\text{Ti}(0001)$ and $\sim\text{Ti}(10\bar{1}0)$ substrate grains for the different annealing temperatures. The substrate grain orientations of TiOC_{850} are unknown due to grain growth during the thermal treatment. TiO_xC_y represents the solid solution of TiC and TiO, as well as TiO_x species. Reproduced from [259] © 2017 American Chemical Society. 173

- Fig. 97 Cycling stability of Pt ECSA in 0.1 M HClO₄ at room temperature. (a,b) Pt/TiOC₇₅₀ and (c,d) Pt/GC. 200 CVs were performed between (a,c) 0.0 and 1.2 V, and (b,d) 0.0 and 1.35 V at 400 mV s⁻¹. The ECSA is normalized to its initial values of 26.8 % (Pt/TiOC₇₅₀) and 48.4 % (Pt/GC) of the geometric area. Adapted from the supporting information of [246]. 178
- Fig. 98 CVs of Pt/TiOC and Pt/GC in 0.1 M HClO₄ with 0.5 M EtOH taken at a scan rate of 10 mV s⁻¹. b): logarithmic plot of a) showing the CVs of Pt/TiOC₇₅₀, Pt/TiOC₁₀₅₀ and Pt/GC. a) adapted from [246] © 2013 WILEY-VCH Verlag GmbH & Co. KGaA, Weinheim. 179
- Fig. 99 Scanning electron micrographs of Pt/TiOC prior to (left) and after (right) CVs in 0.1 M HClO₄ with 0.5 M EtOH. Adapted from the supporting information of [246]. 180
- Fig. 100 CVs of a) Pt/TiOC and b) Pt/GC in 14.6 M H₃PO₄ with 1.0 M EtOH taken at a scan rate of 50 mV s⁻¹ and at temperatures between 25 and 90 °C, respective 80 °C. Adapted from the supporting information of [246]. 181
- Fig. 101 Evaluation of CVs acquired with Pt/TiOC and Pt/GC electrodes in 14.6 M H₃PO₄ with 1.0 M EtOH: a) Peak-current densities, b) peak potentials, and c) peak separations (anodic/cathodic going potential sweeps). Error bars: standard deviation for different samples. Adapted from [246] © 2013 WILEY-VCH Verlag GmbH & Co. KGaA, Weinheim. 182
- Fig. 102 Chronoamperometric profiles of (a,c) Pt/TiOC and (b,d) Pt/GC, acquired for 7 min each at potentials between 0.5 and 0.9 V after each CV in Fig. 100. (c,d): graphs from (a,b) with reduced current density scale. (a,b) adapted from [246] © 2013 WILEY-VCH Verlag GmbH & Co. KGaA, Weinheim. 184
- Fig. 103 Arrhenius plots obtained for a) Pt/TiOC and b) Pt/GC using the final steady-state current densities of chronoamperometric measurements at 0.6, 0.7 and 0.8 V. Adapted from [246] © 2013 WILEY-VCH Verlag GmbH & Co. KGaA, Weinheim. 185
- Fig. 104 SE micrographs of Pt/GC (left) and Pt/TiOC (right) before (top) and after (bottom) EOR tests at different temperatures. Before the EOR tests, the ECSA was 28.6 % of the geometric surface area for Pt/TiOC and 48.4 % for Pt/GC. Insets: two areas of higher (top) and lower (bottom) Pt coverage after EC. Adapted from [246] © 2013 WILEY-VCH Verlag GmbH & Co. KGaA, Weinheim. 188
- Fig. 105 CVs obtained for (a,c) Pt/TiOC and (b,d) Pt/GC before and after stability tests in 14.6 M H₃PO₄. Red curves in (a,b): after CVs and transients at 50 and 80 °C (simulation). Blue curves in (c,d): after exposure to H₃PO₄ at room temperature for 11 h. Electrolyte: 0.1 M HClO₄ at room temperature; scan rate: 400 mV s⁻¹. ESCA values are given in % of the geometric surface area A_{geo}. Adapted from the supporting information of [246]. 189
- Fig. 106 SE micrographs of a) a freshly prepared Pt/TiOC electrode, b) a Pt/TiOC electrode that has been used for an EOR test up to 70 °C, and c) a Pt/TiOC electrode that underwent the electrochemical simulation test in the absence of EtOH up to a final temperature of 80 °C. The high magnification images in (b3-b6) show the tested Pt/TiOC on the left and right substrate grains in (b1,b2). a) and b) adapted from the supporting information of [246]. 190
- Fig. 107 a) CVs acquired with the Pt/TiOC electrode in 14.6 M H₃PO₄ at 50 and 80 °C. b) Comparison of the 20th CV scans in 14.6 M H₃PO₄ with 1.0 M EtOH (taken at 50 mV s⁻¹) and without EtOH (taken at 10 mV s⁻¹), acquired at the indicated temperatures. 191
- Fig. 108 XPS analysis of the as-prepared TiOC support (black) and of Pt/TiOC electrodes after electrochemical tests in 14.6 M H₃PO₄ with and without EtOH. a) Ti 2p, b) O 1s, c) C 1s (inset: arbitrary scaled C-Ti peaks) and d) P 2p spectra after subtraction of a Shirley-type background, and e) Pt 4f spectra with Shirley-type background. Green spectra: Pt/TiOC after electrochemical simulation tests without EtOH at 50 and 80 °C; yellow (red) spectra: Pt/TiOC after EOR tests at temperatures between room temperature and 70 °C (90 °C). X-ray source: Al K_α; acquisition normal to sample surface. For clarity, the spectra are shifted vertically. 192

- Fig. 109 Morphological and crystallographic analysis of the fresh $\text{TiOC}_{\text{Trei}}$ powder. (a,b) SE micrographs taken at two magnifications with a beam acceleration voltage of 15 kV, c) XRD pattern and d) magnified (331) peak with fitted of Gaussian profiles and estimated stoichiometries. X-ray source: Cu K_{α} , $\lambda = 1.541874 \text{ \AA}$ monochromatized. 196
- Fig. 110 Chemical analysis of the fresh and tested $\text{TiOC}_{\text{Trei}}$ powder. XP spectra of a) Ti 2*p*, b) O 1*s*, c) C 1*s* and d) P 2*p* core levels before (black) and after (red) boiling in concentrated H_3PO_4 . X-ray source: Mg K_{α} ; acquisition normal to sample surface. For clarity, the spectra are shifted vertically. 197
- Fig. 111 XPS analysis of TiOC after different air exposure times. a) Ti 2*p* core level spectra, scaled to a common TiO_2 peak height, and b) C 1*s* core level spectra, scaled to a common height of the peak maximum, acquired at grazing emission (GE, $\theta = 30^\circ$). Solid lines: pristine TiOC , broken lines: two months old TiOC , violet spectra: 12 days old TiOC_{550} . For clarity, the spectra are shifted vertically. Results of multi-peak fitting for c) Ti 2*p* and d) C 1*s* spectra. Adapted from the supporting information of [251]. 205
- Fig. 112 XP spectra from Ti 2*p*_{3/2} photoelectron micrographs taken of TiOC on top of five differently oriented substrate grains for the four annealing temperatures. The substrate orientations are a) $\sim 15^\circ \leq \Phi \leq \sim 40^\circ$, $0^\circ \leq \varphi_2 \leq 30^\circ$, b) $0^\circ \leq \Phi \leq \sim 15^\circ$, $0^\circ \leq \varphi_2 \leq 30^\circ$ c) $\sim 40^\circ \leq \Phi \leq \sim 50^\circ$, $0^\circ \leq \varphi_2 \leq 30^\circ$, d) $\sim 50^\circ \leq \Phi \leq 90^\circ$, $\sim 15^\circ \leq \varphi_2 \leq 30^\circ$ e) $\sim 50^\circ \leq \Phi \leq 90^\circ$, $0^\circ \leq \varphi_2 \leq \sim 15^\circ$. Adapted from the supporting information of [259]. 206
- Fig. 113 XP spectra from C 1*s* photoelectron micrographs taken of TiOC on top of five differently oriented substrate grains for the four annealing temperatures. For the substrate orientations see Fig. 112. Adapted from the supporting information of [259]. 206
- Fig. 114 Micro-Raman spectra of a) TiOC_{550} , b) TiOC_{650} , and c) TiOC_{750} on top of $\sim\text{Ti}(10\bar{1}0)$ and $\sim\text{Ti}(0001)$. d) Micro-Raman spectra of two spots on TiOC_{850} with different optical appearance. Baseline correction: constant shift to a common level. Laser wavelength: 514 nm. Adapted from the supporting information of [259]. 207

Bibliography

- [1] International Energy Agency, "World energy outlook 2015 factsheet, Global energy trends to 2040", International Energy Agency, Paris Cedex, Tech. Rep., 2015, pp. 1–3.
- [2] F. Birol, "World energy outlook special report, Energy and climate change", International Energy Agency, Paris Cedex, Tech. Rep., 2015, pp. 1–196.
- [3] M. Winter and R. J. Brodd, "What are batteries, fuel cells, and supercapacitors?", *Chemical Reviews*, vol. 104, pp. 4245–4269, 2004. DOI: 10.1021/cr020730k.
- [4] U. Krewer, T. Vidakovic-Koch, and L. Rihko-Struckmann, "Electrochemical oxidation of carbon-containing fuels and their dynamics in low-temperature fuel cells", *ChemPhysChem*, vol. 12, pp. 2518–2544, 2011. DOI: 10.1002/cphc.201100095.
- [5] M. Z. F. Kamarudin, S. K. Kamarudin, M. S. Masdar, and W. R. W. Daud, "Review: Direct ethanol fuel cells", *International Journal of Hydrogen Energy*, vol. 38, pp. 9438–9453, 2013. DOI: 10.1016/j.ijhydene.2012.07.059.
- [6] Y.-J. Wang, D. P. Wilkinson, and J. Zhang, "Noncarbon support materials for polymer electrolyte membrane fuel cell electrocatalysts", *Chemical Reviews*, vol. 111, pp. 7625–7651, 2011. DOI: 10.1021/cr100060r.
- [7] E. Antolini, "Carbon supports for low-temperature fuel cell catalysts", *Applied Catalysis B: Environmental*, vol. 88, pp. 1–24, 2009. DOI: 10.1016/j.apcatb.2008.09.030.
- [8] E. Antolini and E. R. Gonzalez, "Ceramic materials as supports for low-temperature fuel cell catalysts", *Solid State Ionics*, vol. 180, pp. 746–763, 2009. DOI: 10.1016/j.ssi.2009.03.007.
- [9] E. Antolini, "Catalysts for direct ethanol fuel cells", *Journal of Power Sources*, vol. 170, pp. 1–12, 2007. DOI: 10.1016/j.jpowsour.2007.04.009.
- [10] S. Sun, M. C. Halseid, M. Heinen, Z. Jusys, and R. J. Behm, "Ethanol electrooxidation on a carbon-supported Pt catalyst at elevated temperature and pressure: A high-temperature/high-pressure DEMS study", *Journal of Power Sources*, vol. 190, pp. 2–13, 2009. DOI: 10.1016/j.jpowsour.2009.01.073.
- [11] Y. Shao, G. Yin, Z. Wang, and Y. Gao, "Proton exchange membrane fuel cell from low temperature to high temperature: Material challenges", *Journal of Power Sources*, vol. 167, pp. 235–242, 2007. DOI: 10.1016/j.jpowsour.2007.02.065.
- [12] S. R. Samms, S. Wasmus, and R. F. Savinell, "Thermal stability of proton conducting acid doped polybenzimidazole in simulated fuel cell environments", *Journal of The Electrochemical Society*, vol. 143, pp. 1225–1232, 1996. DOI: 10.1149/1.1836621.
- [13] Y.-L. Ma, J. S. Wainright, M. H. Litt, and R. F. Savinell, "Conductivity of PBI membranes for high-temperature polymer electrolyte fuel cells", *Journal of The Electrochemical Society*, vol. 151, A8–A16, 2004. DOI: 10.1149/1.1630037.
- [14] A. Fujishima and K. Honda, "Electrochemical photolysis of water at a semiconductor electrode", *Nature*, vol. 238, pp. 37–38, 1972. DOI: 10.1038/238037a0.
- [15] K. Hashimoto, H. Irie, and A. Fujishima, "TiO₂ photocatalysis: A historical overview and future prospects", *Japanese Journal of Applied Physics*, vol. 44, pp. 8269–8285, 2005. [Online]. Available: <http://iopscience.iop.org/article/10.1143/JJAP.44.8269/meta>.
- [16] A. Fujishima, X. Zhang, and D. Tryk, "TiO₂ photocatalysis and related surface phenomena", *Surface Science Reports*, vol. 63, pp. 515–582, 2008. DOI: 10.1016/j.surfrep.2008.10.001.
- [17] B. O'Regan and M. Grätzel, "A low-cost, high-efficiency solar cell based on dye-sensitized colloidal TiO₂ films", *Nature*, vol. 353, pp. 737–740, 1991. DOI: 10.1038/350055a0.

- [18] K. Zhu, N. R. Neale, A. Miedaner, and A. J. Frank, "Enhanced charge-collection efficiencies and light scattering in dye-sensitized solar cells using oriented TiO₂ nanotubes arrays.", *Nano Letters*, vol. 7, pp. 69–74, 2007. DOI: 10.1021/nl1062000o.
- [19] D. M. Brunette, P. Tengvall, M. Textor, and P. Thomsen, Eds., *Titanium in Medicine, Material Science, Surface Science, Engineering, Biological Responses and Medical Applications*. Berlin Heidelberg: Springer-Verlag, 2001. DOI: 10.1007/978-3-642-56486-4.
- [20] V. Sáenz de Viteri and E. Fuentes, "Titanium and titanium alloys as biomaterials", in *Tribology - Fundamentals and Advancements*, J. Gegner, Ed., InTech, 2013, ch. 5, pp. 155–181. DOI: 10.5772/55860.
- [21] V. Zwillling, E. Darque-Ceretti, A. Boutry-Forveille, D. David, M. Y. Perrin, and M. Aucouturier, "Structure and physicochemistry of anodic oxide films on titanium and TA6V alloy", *Surface and Interface Analysis*, vol. 27, pp. 629–637, 1999. DOI: 10.1016/0022-5088(77)90043-1.
- [22] J. M. Macak, H. Tsuchiya, A. Ghicov, K. Yasuda, R. Hahn, S. Bauer, and P. Schmuki, "TiO₂ nanotubes: Self-organized electrochemical formation, properties and applications", *Current Opinion in Solid State and Materials Science*, vol. 11, pp. 3–18, 2007. DOI: 10.1016/j.cossms.2007.08.004.
- [23] U. Diebold, "The surface science of titanium dioxide", *Surface Science Reports*, vol. 48, pp. 53–229, 2003. DOI: 10.1016/S0167-5729(02)00100-0.
- [24] M. Chen and D. W. Goodman, "Catalytically active gold on ordered titania supports", *Chemical Society reviews*, vol. 37, pp. 1860–1870, 2008. DOI: 10.1039/b707318f.
- [25] S. J. Tauster, "Strong metal-support interactions", *Accounts of Chemical Research*, vol. 20, pp. 389–394, 1987. DOI: 10.1021/ar00143a001.
- [26] S. Andersson, B. Collén, U. Kuylénstierna, and A. Magnéli, "Phase analysis studies on the titanium-oxygen system", *Acta Chemica Scandinavica*, vol. 11, pp. 1641–1652, 1957. DOI: 10.3891/acta.chem.scand.11-1641.
- [27] J. R. Smith, F. C. Walsh, and R. L. Clarke, "Electrodes based on Magnéli phase titanium oxides: The properties and applications of Ebonex® materials", *Journal of applied electrochemistry*, vol. 28, pp. 1021–1033, 1998. DOI: 10.1023/A:1003469427858.
- [28] M. Zweynert, H. Doering, J. Garcke, K. Enghardt, and K. Wiesener, "Anwendung von Magnéli-Phasen des Titandioxids in der elektrochemischen Technologie", *Chemie Ingenieur Technik*, vol. 7, pp. 827–841, 1998. DOI: 10.1002/cite.330700705.
- [29] T. Ioroi, H. Senoh, S.-I. Yamazaki, Z. Siroma, N. Fujiwara, and K. Yasuda, "Stability of corrosion-resistant Magnéli-phase Ti₄O₇-supported PEMFC catalysts at high potentials", *Journal of The Electrochemical Society*, vol. 155, B321–B326, 2008. DOI: 10.1149/1.2833310.
- [30] L. Xiong and A. Manthiram, "Synthesis and characterization of methanol tolerant Pt/TiO_x/C nanocomposites for oxygen reduction in direct methanol fuel cells", *Electrochimica Acta*, vol. 49, pp. 4163–4170, 2004. DOI: 10.1016/j.electacta.2004.04.011.
- [31] Y. Liu, T. G. Kelly, J. G. Chen, and W. E. Mustain, "Metal carbides as alternative electrocatalyst supports", *ACS Catalysis*, vol. 3, pp. 1184–1194, 2013. DOI: 10.1021/cs4001249.
- [32] M. Roca-Ayats, G. Garcia, M. A. Pena, and M. V. Martínez-Huerta, "Titanium carbide and carbonitride electrocatalyst supports: Modifying Pt-Ti interface properties by electrochemical potential cycling", *Journal of Materials Chemistry A: Materials for Energy and Sustainability*, vol. 2, pp. 18786–18790, 2014. DOI: 10.1039/C4TA03782K.
- [33] A. Ignaszak, C. Song, W. Zhu, J. Zhang, A. Bauer, R. Baker, V. Neburchilov, S. Ye, and S. Campbell, "Titanium carbide and its core-shelled derivative TiC@TiO₂ as catalyst supports for proton exchange membrane fuel cells", *Electrochimica Acta*, vol. 69, pp. 397–405, 2012. DOI: 10.1016/j.electacta.2012.03.039.

- [34] D.-Y. Kim, S.-B. Han, Y.-W. Lee, and K.-W. Park, "Core-shell nanostructure supported Pt catalyst with improved electrocatalytic stability in oxygen reduction reaction", *Materials Chemistry and Physics*, vol. 137, pp. 704–708, 2013. DOI: 10.1016/j.matchemphys.2012.11.006.
- [35] J. Shim, C.-R. Lee, H.-K. Lee, J.-S. Lee, and E. J. Cairns, "Electrochemical characteristics of Pt-WO₃/C and Pt-TiO₂/C electrocatalysts in a polymer electrolyte fuel cell", *Journal of Power Sources*, vol. 102, pp. 172–177, 2001. DOI: 10.1016/S0378-7753(01)00817-5.
- [36] J. Tian, G. Sun, M. Cai, Q. Mao, and Q. Xin, "PtTiO_x/C electrocatalysts with improved durability in H₂/O₂ PEMFCs without external humidification", *Journal of The Electrochemical Society*, vol. 155, B187–B193, 2008. DOI: 10.1149/1.2816290.
- [37] Y. Ou, X. Cui, X. Zhang, and Z. Jiang, "Titanium carbide nanoparticles supported Pt catalysts for methanol electrooxidation in acidic media", *Journal of Power Sources*, vol. 195, pp. 1365–1369, 2010. DOI: 10.1016/j.jpowsour.2009.09.031.
- [38] R. Hahn, F. Schmidt-Stein, J. Salonen, S. Thiemann, Y. Y. Song, J. Kunze, V.-P. Lehto, and P. Schmuki, "Semimetallic TiO₂ nanotubes", *Angewandte Chemie (International ed. in English)*, vol. 48, pp. 7236–7239, 2009. DOI: 10.1002/anie.200902207.
- [39] R. Koc and J. S. Folmer, "Carbothermal synthesis of titanium carbide using ultrafine titania powders", *Journal of Materials Science*, vol. 32, pp. 3101–3111, 1997. DOI: 10.1023/A:1018634214088.
- [40] R. Koc, "Kinetics and phase evolution during carbothermal synthesis of titanium carbide from carbon-coated titania powder", *Journal of the European Ceramic Society*, vol. 17, pp. 1309–1315, 1997. DOI: 10.1016/S0955-2219(96)00241-5.
- [41] P. Lefort, A. Maitre, and P. Tristant, "Influence of the grain size on the reactivity of TiO₂/C mixtures", *Journal of Alloys and Compounds*, vol. 302, pp. 287–298, 2000. DOI: 10.1016/S0925-8388(00)00683-6.
- [42] Y. Gotoh, K. Fujimura, M. Koike, Y. Ohkoshi, M. Nagura, K. Akamatsu, and S. Deki, "Synthesis of titanium carbide from a composite of TiO₂ nanoparticles/methyl cellulose by carbothermal reduction", *Materials Research Bulletin*, vol. 36, pp. 2263–2275, 2001. DOI: 10.1016/S0025-5408(01)00713-9.
- [43] M. A. R. Dewan, G. Zhang, and O. Ostrovski, "Carbothermal reduction of titania in different gas atmospheres", *Metallurgical and Materials Transactions B*, vol. 40, pp. 62–69, 2009. DOI: 10.1007/s11663-008-9205-z.
- [44] G. Zhang and O. Ostrovski, "Reduction of titania by methane-hydrogen-argon gas mixture", *Metallurgical and Materials Transactions B*, vol. 31, pp. 129–139, 2000. DOI: 10.1007/s11663-000-0138-4.
- [45] A. Aladjem, "Review, Anodic oxidation of titanium and its alloys", *Journal of Materials Science*, vol. 8, pp. 688–704, 1973. DOI: 10.1007/BF00561225.
- [46] P. Roy, S. Berger, and P. Schmuki, "TiO₂ nanotubes: Synthesis and applications.", *Angewandte Chemie (International ed. in English)*, vol. 50, pp. 2904–2939, 2011. DOI: 10.1002/anie.201001374.
- [47] M. E. Sibert, "Electrochemical oxidation of titanium surfaces", *Journal of The Electrochemical Society*, vol. 110, pp. 65–72, 1963. DOI: 10.1149/1.2425674.
- [48] J.-L. Delplancke and R. Winand, "Galvanostatic anodization of titanium - I. Structures and compositions of the anodic films", *Electrochimica Acta*, vol. 33, pp. 1539–1549, 1988. DOI: 10.1016/0013-4686(88)80223-8.
- [49] M. V. Diamanti and M. P. Pedferri, "Effect of anodic oxidation parameters on the titanium oxides formation", *Corrosion Science*, vol. 49, pp. 939–948, 2007. DOI: 10.1016/j.corsci.2006.04.002.
- [50] B. Roh, "Defect properties of anodic oxide films on titanium and impact of oxygen vacancy on oxygen electrode reactions", Dissertation, Pennsylvania State University, 2007. [Online]. Available: <https://etda.libraries.psu.edu/catalog/7574>.

BIBLIOGRAPHY

- [51] F. Kover and M. J. Musselin, "A comparative study of anodic oxide films on titanium, niobium and tantalum", *Thin Solid Films*, vol. 2, pp. 211–234, 1968. DOI: 10.1016/0040-6090(68)90003-5.
- [52] M. M. Lohrengel, "Thin anodic oxide layers on aluminium and other valve metals: High field regime", *Materials Science and Engineering*, vol. R11, pp. 243–294, 1993. DOI: 10.1016/0927-796X(93)90005-N.
- [53] J. W. Schultze and M. M. Lohrengel, "Stability, reactivity and breakdown of passive films. Problems of recent and future research", *Electrochimica Acta*, vol. 45, pp. 2499–2513, 2000. DOI: 10.1016/S0013-4686(00)00347-9.
- [54] J.-F. Vanhumbecq and J. Proost, "Current understanding of Ti anodisation: Functional, morphological, chemical and mechanical aspects", *Corrosion Reviews*, vol. 27, pp. 117–204, 2009. DOI: 10.1515/CORRREV.2009.27.3.117.
- [55] C.-H. Paik, M. R. Kozlowski, P. S. Tyler, and W. H. Smyrl, "Metal decoration of surface defect structure on thin anodic TiO₂ films", *Journal of The Electrochemical Society*, vol. 135, pp. 2395–2396, 1988. DOI: 10.1149/1.2096283.
- [56] S. Kudelka, A. Michaelis, and J. W. Schultze, "Effect of texture and formation rate on ionic and electronic properties of passive layers on Ti single crystals", *Electrochimica Acta*, vol. 41, pp. 863–870, 1996. DOI: 10.1016/0013-4686(95)00375-4.
- [57] S. Kudelka and J. W. Schultze, "Photoelectrochemical imaging and microscopic reactivity of oxidised Ti", *Electrochimica Acta*, vol. 42, pp. 2817–2825, 1997. DOI: 10.1016/S0013-4686(97)00085-6.
- [58] U. König and B. Davepon, "Microstructure of polycrystalline Ti and its microelectrochemical properties by means of electron-backscattering diffraction (EBSD)", *Electrochimica Acta*, vol. 47, pp. 149–160, 2001. DOI: 10.1016/S0013-4686(01)00572-2.
- [59] B. Davepon, J. W. Schultze, U. König, and C. Rosenkranz, "Crystallographic orientation of single grains of polycrystalline titanium and their influence on electrochemical processes", *Surface and Coatings Technology*, vol. 169-170, pp. 85–90, 2003. DOI: 10.1016/S0257-8972(03)00163-4.
- [60] J. W. Schultze, B. Davepon, F. Karman, C. Rosenkranz, A. Schreiber, and O. Voigt, "Corrosion and passivation in nanoscopic and microscopic dimensions: The influence of grains and grain boundaries", *Corrosion Engineering, Science and Technology*, vol. 39, pp. 45–52, 2004. DOI: 10.1179/147842204225016813.
- [61] M. V. Diamanti, M. P. Pedferri, and C. A. Schuh, "Thickness of anodic titanium oxides as a function of crystallographic orientation of the substrate", *Metallurgical and Materials Transactions A*, vol. 39, pp. 2143–2147, 2008. DOI: 10.1007/s11661-008-9558-6.
- [62] S. Leonardi, A. Li Bassi, V. Russo, F. Di Fonzo, O. Paschos, T. M. Murray, H. Efstathiadis, and J. Kunze, "TiO₂ nanotubes: Interdependence of substrate grain orientation and growth characteristics", *Journal of Physical Chemistry C*, vol. 116, pp. 384–392, 2012. DOI: 10.1021/jp209418n.
- [63] N. Sato, *Electrochemistry at Metal and Semiconductor Electrodes*. Amsterdam: Elsevier Science B.V., 1998.
- [64] A. J. Bard and L. R. Faulkner, *Electrochemical Methods, Fundamentals and Applications*, 2nd ed., D. Harris, E. Swain, and E. Aiello, Eds. New York, NY: John Wiley & Sons, Inc., 2001.
- [65] C. H. Hamann, A. Hamnett, and W. Vielstich, *Electrochemistry*, 2nd ed. Weinheim: Wiley-VCH Verlag GmbH & Co. KGaA, 2007.
- [66] M. E. Orazem and B. Tribollet, *Electrochemical Impedance Spectroscopy*. Hoboken, NJ: John Wiley & Sons, Inc., 2008.
- [67] A. W. Bott, "Electrochemistry of semiconductors", *Current Separations*, vol. 17, pp. 87–91, 1998. [Online]. Available: <http://www.currentseparations.com/issues/17-3/cs-17-3d.pdf>.

- [68] K. Rajeshwar, "Fundamentals of semiconductor electrochemistry and photoelectrochemistry", in *Encyclopedia of Electrochemistry*, A. J. Bard, M. Stratmann, and S. Licht, Eds., vol. 6, John Wiley & Sons, Inc., 2007, ch. 1, pp. 1–51. DOI: 10.1002/9783527610426.bard060001.
- [69] K. Gelderman, L. Lee, and S. W. Donne, "Flat-band potential of a semiconductor: Using the Mott–Schottky equation", *Journal of Chemical Education*, vol. 84, pp. 685–688, 2007. DOI: 10.1021/ed084p685.
- [70] R. De Gryse, W. P. Gomes, F. Cardon, and J. Vennik, "On the interpretation of Mott-Schottky plots determined at semiconductor/electrolyte systems", *Journal of The Electrochemical Society*, vol. 122, pp. 711–712, 1975. DOI: 10.1149/1.2134298.
- [71] J. W. Schultze, U. Stimming, and J. Weise, "Capacity and photocurrent measurements at passive titanium electrodes", *Berichte der Bunsengesellschaft für Physikalische Chemie*, vol. 86, pp. 276–282, 1982. DOI: 10.1002/bbpc.19820860404.
- [72] M. H. Dean and U. Stimming, "Capacity of semiconductor electrodes with multiple bulk electronic states. 2. Applications to amorphous semiconductor electrodes", *The Journal of Physical Chemistry*, vol. 93, pp. 8053–8059, 1989. DOI: 10.1021/j100361a018.
- [73] E.-J. Lee and S.-I. Pyun, "Analysis of nonlinear Mott-Schottky plots obtained from anodically passivating amorphous and polycrystalline TiO₂ films", *Journal of Applied Electrochemistry*, vol. 22, pp. 156–160, 1992. DOI: 10.1007/BF01023817.
- [74] *Autolab application note EC08, Basic overview of the working principle of a potentiostat/galvanostat (PGSTAT) - Electrochemical cell setup*, Metrohm Autolab B.V., Utrecht, 2011, pp. 1–3. [Online]. Available: http://www.ecochemie.nl/download/Applicationnotes/Autolab_Application_Note_EC08.pdf.
- [75] *Understanding the specifications of your potentiostat*, GAMRY INSTRUMENTS, Warminster, PA, 2017. [Online]. Available: <https://www.gamry.com/application-notes/instrumentation/understanding-specs-of-potentiostat/>.
- [76] H. Wang, Z. Jusys, and R. J. Behm, "Ethanol electrooxidation on a carbon-supported Pt catalyst: Reaction kinetics and product yields", *The Journal of Physical Chemistry B*, vol. 108, pp. 19413–19424, 2004. DOI: 10.1021/jp046561k.
- [77] C. A. Angelucci, H. Varela, E. Herrero, and J. M. Feliu, "Activation energies of the electrooxidation of formic acid on Pt (100)", *Journal of Physical Chemistry C*, vol. 113, pp. 18835–18841, 2009. DOI: Doi10.1021/Jp907723k.
- [78] J. L. Cohen, D. J. Volpe, and H. D. Abruña, "Electrochemical determination of activation energies for methanol oxidation on polycrystalline platinum in acidic and alkaline electrolytes.", *Physical Chemistry Chemical Physics*, vol. 9, pp. 49–77, 2007. DOI: 10.1039/b612040g.
- [79] M. T. M. Koper, C. S. S. Lai, and E. Herrero, "Mechanisms of the oxidation of carbon monoxide and small organic molecules at metal electrodes", in *Fuel Cell Catalysis, A Surface Science Approach*, M. T. M. Koper, Ed., Hoboken, NJ: John Wiley & Sons, Inc., 2009, ch. 6, pp. 159–207. DOI: 10.1002/9780470463772.ch6.
- [80] A. Lasia, "Electrochemical impedance spectroscopy and its applications", in *Modern Aspects of Electrochemistry*, B. E. Conway, J. Bockris, and R. E. White, Eds., vol. 32, New York, NY: Kluwer Academic Publishers, 1999, pp. 143–248.
- [81] G. J. Brug, A. L. G. van den Eeden, M. Sluyters-Rehbach, and J. H. Sluyters, "The analysis of electrode impedances complicated by the presence of constant phase element", *Journal of Electroanalytical Chemistry and Interfacial Electrochemistry*, vol. 176, pp. 275–295, 1984. DOI: 10.1016/S0022-0728(84)80324-1.
- [82] J. Larminie and A. Dicks, *Fuel Cell Systems Explained*, 2nd ed. Chichester: John Wiley & Sons Ltd., 2003.

- [83] M. Bron, "Electrocatalysts for acid proton exchange membrane (PEM) fuel cells - an overview", in *Non-Noble Metal Fuel Cell Catalysts*, Z. Chen, J.-P. Dodelet, and J. Zhang, Eds., Weinheim: Wiley-VCH Verlag GmbH & Co. KGaA, 2014, ch. 1, pp. 1–28. DOI: 10.1002/9783527664900.ch1.
- [84] S. Song and P. Tsiakaras, "Recent progress in direct ethanol proton exchange membrane fuel cells (DE-PEMFCs)", *Applied Catalysis B: Environmental*, vol. 63, pp. 187–193, 2006. DOI: 10.1016/j.apcatb.2005.09.018.
- [85] C. Lamy and C. Coutanceau, "Electrocatalysis of alcohol oxidation reactions at platinum group metals", in *Catalysts for Alcohol-Fuelled Direct Oxidation Fuel Cells*, Z. X. Liang and T. S. Zhao, Eds., Cambridge: The Royal Society of Chemistry, 2012, ch. 1, pp. 1–70. DOI: 10.1039/9781849734783-00001.
- [86] S. Song, Y. Wang, and P. Shen, "Thermodynamic and kinetic considerations for ethanol electrooxidation in direct ethanol fuel cells", *Chinese Journal of Catalysis*, vol. 28, pp. 752–754, 2007. DOI: 10.1016/S1872-2067(07)60063-1.
- [87] N. M. Markovic and P. N. Ross Jr., "Surface science studies of model fuel cell electrocatalysts", *Surface Science Reports*, vol. 45, pp. 117–229, 2002. DOI: 10.1016/S0167-5729(01)00022-X.
- [88] J. Zhang, H. Zhang, J. Wu, and J. Zhang, "Techniques for PEM fuel cell testing and diagnosis", in *PEM Fuel Cell Testing and Diagnosis*, Oxford: Elsevier B.V., 2013, ch. 3, pp. 81–119. DOI: 10.1016/B978-0-444-53688-4.00003-6.
- [89] A. Brouzgou, S. Q. Song, and P. Tsiakaras, "Low and non-platinum electrocatalysts for PEMFCs: Current status, challenges and prospects", *Applied Catalysis B: Environmental*, vol. 127, pp. 371–388, 2012. DOI: 10.1016/j.apcatb.2012.08.031.
- [90] M. T. M. Koper, "Structure sensitivity and nanoscale effects in electrocatalysis", *Nanoscale*, vol. 3, pp. 2054–2073, 2011. DOI: 10.1039/c0nr00857e.
- [91] T. Biegler, D. A. J. Rand, and R. Woods, "Limiting oxygen coverage on platinized platinum; Relevance to determination of real platinum area by hydrogen adsorption", *Journal of Electroanalytical Chemistry and Interfacial Electrochemistry*, vol. 29, pp. 269–277, 1971. DOI: 10.1016/S0022-0728(71)80089-X.
- [92] H. Wang, Z. Jusys, and R. J. Behm, "Ethanol electro-oxidation on carbon-supported Pt, PtRu and Pt₃Sn catalysts: A quantitative DEMS study", *Journal of Power Sources*, vol. 154, pp. 351–359, 2006. DOI: 10.1016/j.jpowsour.2005.10.034.
- [93] V. Rao, C. Cremers, U. Stimming, L. Cao, S. Sun, S. Yan, G. Sun, and Q. Xin, "Electro-oxidation of ethanol at gas diffusion electrodes, A DEMS study", *Journal of The Electrochemical Society*, vol. 154, B1138–B1147, 2007. DOI: 10.1149/1.2777108.
- [94] E. Antolini, "A simple model to assess the contribution of alloyed and non-alloyed platinum and tin to the ethanol oxidation reaction on Pt–Sn/C catalysts: Application to direct ethanol fuel cell performance", *Electrochimica Acta*, vol. 55, pp. 6485–6490, 2010. DOI: 10.1016/j.electacta.2010.06.035.
- [95] J. Souza-Garcia, E. Herrero, and J. M. Feliu, "Breaking the C–C bond in the ethanol oxidation reaction on platinum electrodes: Effect of steps and ruthenium adatoms", *ChemPhysChem*, vol. 11, pp. 1391–1394, 2010. DOI: 10.1002/cphc.201000139.
- [96] A. Rabis, P. Rodriguez, and T. J. Schmidt, "Electrocatalysis for polymer electrolyte fuel cells: Recent achievements and future challenges", *ACS Catalysis*, vol. 2, pp. 864–890, 2012. DOI: 10.1021/cs3000864.
- [97] A. Kowal, M. Li, M. Shao, K. Sasaki, M. B. Vukmirovic, J. Zhang, N. S. Marinkovic, P. Liu, A. I. Frenkel, and R. R. Adzic, "Ternary Pt/Rh/SnO₂ electrocatalysts for oxidizing ethanol to CO₂", *Nature Materials*, vol. 8, pp. 325–330, 2009. DOI: 10.1038/nmat2359.
- [98] M. Li, A. Kowal, K. Sasaki, N. Marinkovic, D. Su, E. Korach, P. Liu, and R. R. Adzic, "Ethanol oxidation on the ternary Pt–Rh–SnO₂/C electrocatalysts with varied Pt:Rh:Sn ratios", *Electrochimica Acta*, vol. 55, pp. 4331–4338, May 2010. DOI: 10.1016/j.electacta.2009.12.071.

- [99] D. A. Cantane, W. F. Ambrosio, M. Chatenet, and F. H. B. Lima, "Electro-oxidation of ethanol on Pt/C, Rh/C, and Pt/Rh/C-based electrocatalysts investigated by on-line DEMS", *Journal of Electroanalytical Chemistry*, vol. 681, pp. 56–65, 2012. DOI: 10.1016/j.jelechem.2012.05.024.
- [100] A. P. M. Camargo, B. A. F. Previdello, H. Varela, and E. R. Gonzalez, "Effect of temperature on the electro-oxidation of ethanol on platinum", *Quim. Nova*, vol. 33, pp. 2143–2147, 2010. DOI: 10.1590/S0100-40422010001000026.
- [101] R. B. Kutz, B. Braunschweig, P. Mukherjee, R. L. Behrens, D. D. Dlott, and A. Wieckowski, "Reaction pathways of ethanol electrooxidation on polycrystalline platinum catalysts in acidic electrolytes", *Journal of Catalysis*, vol. 278, pp. 181–188, 2011. DOI: 10.1016/j.jcat.2010.11.018.
- [102] T. Iwasita and E. Pastor, "A DEMS and FTIR spectroscopic investigation of adsorbed ethanol on polycrystalline platinum", *Electrochimica Acta*, vol. 39, pp. 531–537, 1994. DOI: 10.1016/0013-4686(94)80097-9.
- [103] H. Wang, Z. Jusys, and R. J. Behm, "Ethanol and acetaldehyde adsorption on a carbon-supported Pt catalyst: A comparative DEMS study", *Fuel Cells*, vol. 4, pp. 113–125, 2004. DOI: 10.1002/fuce.200400014.
- [104] M. J. N. Pourbaix, J. Van Muylder, and N. de Zoubov, "Electrochemical properties of the platinum metals", *Platinum Metals Review*, vol. 3, pp. 47–53, 1959.
- [105] Y. Zhu, H. Uchida, T. Yajima, and M. Watanabe, "Attenuated total reflection - Fourier transform infrared study of methanol oxidation on sputtered Pt film electrode", *Langmuir*, vol. 17, pp. 146–154, 2001. DOI: 10.1021/1a000457m.
- [106] D. Kardash, J. Huang, and C. Korzeniewski, "Surface electrochemistry of CO and methanol at 25 - 75 °C probed in situ by infrared spectroscopy", *Langmuir*, vol. 16, pp. 2019–2023, 2000. DOI: 10.1021/1a990855t.
- [107] E. Herrero, B. Álvarez, J. M. Feliu, S. Blais, Z. Radovic-Hrapovic, and G. Jerkiewicz, "Temperature dependence of the CO_{ads} oxidation process on Pt(111), Pt(100), and Pt(110) electrodes", *Journal of Electroanalytical Chemistry*, vol. 567, pp. 139–149, 2004. DOI: 10.1016/j.jelechem.2003.12.019.
- [108] W. Demtröder, *Experimentalphysik 3, Atome, Moleküle und Festkörper*, 2nd ed. Berlin Heidelberg: Springer-Verlag, 2004.
- [109] C. Kittel, *Introduction to Solid State Physics*, 8th ed. New York, NY: John Wiley & Sons, Inc., 2005, trans. by S. Hunklinger as *Einführung in die Festkörperphysik* (München: Oldenbourg Wissenschaftsverlag GmbH, 2006).
- [110] K. T. Jacob, S. Raj, and L. Rannesh, "Vegard's law: A fundamental relation or an approximation?", *International Journal of Materials Research*, vol. 98, pp. 776–779, 2007. DOI: 10.3139/146.101545.
- [111] T. Mitsunaga, "X-ray thin-film measurement techniques II. Out-of-plane diffraction measurements", *The Rigaku Journal*, vol. 25, pp. 7–12, 2009. DOI: 10.1097/01.ss.0000026967.27546.82.
- [112] M. Bouroushian and T. Kosanovic, "Characterization of thin films by low incidence X-ray diffraction", *Crystal Structure Theory and Applications*, vol. 1, pp. 35–39, 2012. DOI: 10.4236/csta.2012.13007.
- [113] J. Goldstein, D. Newbury, D. Joy, C. Lyman, P. Echlin, E. Lifshin, L. Sawyer, and J. Michael, *Scanning Electron Microscopy and X-ray Microanalysis*, 3rd ed. New York, NY: Springer Science+Business Media, LLC, 2003. DOI: 10.1007/978-1-4615-0215-9.
- [114] J. M. Hollas, *Modern Spectroscopy*, 4th ed. Chichester: John Wiley & Sons, Ltd., 2004.
- [115] O. C. Wells, "Comparison of different models for the generation of electron backscattering patterns in the scanning electron microscope", *Scanning*, vol. 21, pp. 368–371, 1999. DOI: 10.1002/sca.4950210602.

BIBLIOGRAPHY

- [116] T. Maitland and S. Sitzman, “Electron backscatter diffraction (EBSD) technique and materials characterization examples”, in *Scanning Microscopy for Nanotechnology, Techniques and Applications*, W. Zhou and Z. L. Wang, Eds., New York, NY: Springer Science+Business Media, LLC, 2007, ch. 2, pp. 41–75. DOI: 10.1007/978-0-387-39620-0.
- [117] H.-J. Bunge, *Texture Analysis in Materials Science: Mathematical Methods*, 2nd ed. London: Butterworths & Co, 1982. [Online]. Available: https://www.ebsd.info/pdf/Bunge_TextureAnalysis.pdf.
- [118] C. Rüdiger, M. Favaro, C. Valero-Vidal, L. Calvillo, N. Bozzolo, S. Jacomet, C. Hejny, L. Gregoratti, M. Amati, S. Agnoli, G. Granozzi, and J. Kunze-Liebhäuser, “Fabrication of Ti substrate grain dependent C/TiO₂ composites through carbothermal treatment of anodic TiO₂”, *Physical Chemistry Chemical Physics*, vol. 18, pp. 9220–9231, 2016. DOI: 10.1039/c5cp07727c.
- [119] K. S. Birdi, *Scanning Probe Microscopes, Applications in Science and Technology*. Boca Raton, FL: CRC Press, LLC, 2003.
- [120] K. W. Kolasinski, *Surface Science: Foundations of Catalysis and Nanoscience*, 2nd ed. Chichester: John Wiley & Sons, Ltd., 2008.
- [121] R. Loudon, “The Raman effect in crystals”, *Advances in Physics*, vol. 13, pp. 423–482, 1964. DOI: 10.1080/00018736400101051.
- [122] L. A. Nafie, “Theory of Raman scattering”, in *Handbook of Raman Spectroscopy, From the Research Laboratory to the Process Line*, I. R. Lewis and H. G. M. Edwards, Eds., New York, NY: Marcel Dekker, Inc., 2001, ch. 1, pp. 1–10.
- [123] M. S. Dresselhaus, G. Dresselhaus, and A. Jorio, *Group Theory, Application to the Physics of Condensed Matter*. Berlin Heidelberg: Springer-Verlag, 2008. DOI: 10.1007/978-3-540-32899-5.
- [124] F. Siebert and P. Hildebrandt, “Theory of infrared absorption and Raman spectroscopy”, in *Vibrational Spectroscopy in Life Science*, Weinheim: Wiley-VCH Verlag GmbH & Co. KGaA, 2008, ch. 2, pp. 11–61. DOI: 10.1002/9783527621347.ch2.
- [125] D. Tuschel, “Raman crystallography, in theory and in practice”, *Spectroscopy*, vol. 27, pp. 2–6, 2012. [Online]. Available: https://www.lbt-scientific.com/uploads/6/0/1/3/60131373/raman_crystallography.pdf.
- [126] P. Vandenabeele, *Practical Raman Spectroscopy, An Introduction*. Chichester: John Wiley & Sons, Ltd., 2013. DOI: 10.1002/9781119961284.
- [127] R. Merlin, A. Pinczuk, and W. H. Weber, “Overview of phonon Raman scattering in solids”, in *Raman Scattering in Materials Science*, W. H. Weber and R. Merlin, Eds., Berlin Heidelberg: Springer-Verlag, 2000, ch. 1, pp. 1–29. DOI: 10.1007/978-3-662-04221-2.
- [128] *Raman scattering and fluorescence emission*, HORIBA Scientific, 2005. [Online]. Available: <https://www.azom.com/article.aspx?ArticleID=2950#>.
- [129] H. Richter, Z. P. Wang, and L. Ley, “The one phonon Raman spectrum in microcrystalline silicon”, *Solid State Communications*, vol. 39, pp. 625–629, 1981. DOI: 10.1016/0038-1098(81)90337-9.
- [130] I. H. Campbell and P. M. Fauchet, “The effects of microcrystal size and shape on the one phonon Raman spectra of crystalline semiconductors”, *Solid State Communications*, vol. 58, pp. 739–741, 1986. DOI: 10.1016/0038-1098(86)90513-2.
- [131] A. Li Bassi, D. Cattaneo, V. Russo, C. E. Bottani, E. Barborini, T. Mazza, P. Piseri, P. Milani, F. O. Ernst, K. Wegner, and S. E. Pratsinis, “Raman spectroscopy characterization of titania nanoparticles produced by flame pyrolysis: The influence of size and stoichiometry”, *Journal of Applied Physics*, vol. 98, p. 0743051, 2005. DOI: 10.1063/1.2061894.
- [132] G. Gouadec and P. Colomban, “Raman spectroscopy of nanomaterials: How spectra relate to disorder, particle size and mechanical properties”, *Progress in Crystal Growth and Characterization of Materials*, vol. 53, pp. 1–56, 2007. DOI: 10.1016/j.pcrysgrow.2007.01.001.

- [133] R. P. Feynman, R. B. Leighton, and M. Sands, "Refractive index of dense materials", in *The Feynman Lectures on Physics, Vol. II, Mainly Electromagnetism and Matter*, A. M. Gottlieb and R. Pfeiffer, Eds., Pasadena, CA: California Institute of Technology, 1963, 2006, 2013, ch. 32. [Online]. Available: http://www.feynmanlectures.caltech.edu/II_32.html.
- [134] M. J. Pelletier, "Quantitative analysis using Raman spectrometry", *Applied Spectroscopy*, vol. 57, 20A–42A, 2003. DOI: 10.1366/000370203321165133.
- [135] R. L. McCreery, "Photometric standards for Raman spectroscopy", in *Handbook of Vibrational Spectroscopy*, J. M. Chalmers and P. R. Griffiths, Eds., Chichester: John Wiley & Sons, Ltd., 2002, pp. 1–13.
- [136] M. Bradley, "Curve fitting in Raman and IR spectroscopy: Basic theory of line shapes and applications", *Thermo Scientific Application Note*, no. 50733, pp. 1–4, 2007.
- [137] P. M. Fauchet and I. H. Campbell, "Raman spectroscopy of low-dimensional semiconductors", *Critical Reviews in Solid State and Materials Sciences*, vol. 14, S79–S101, 1988. DOI: 10.1080/10408438808244783.
- [138] C. S. Fadley, "Basic concepts of X-ray photoelectron spectroscopy", in *Electron Spectroscopy: Theory, Techniques, and Applications*, C. R. Brundle and A. D. Baker, Eds., vol. 2, London: Academic Press, 1978, ch. 1, pp. 1–156. [Online]. Available: <http://fadley.physics.ucdavis.edu/BasicConceptsofXPS.pdf>.
- [139] A. B. Christie, "X-ray photoelectron spectroscopy", in *Methods of Surface Analysis, Techniques and Applications*, J. M. Walls, Ed., Cambridge: Cambridge University Press, 1989, ch. 5, pp. 127–168.
- [140] S. Hüfner, *Photoelectron Spectroscopy, Principles and Applications*, 3rd ed. Berlin Heidelberg: Springer-Verlag, 2003. DOI: 10.1006/rwsp.2000.0406.
- [141] J. F. Moulder, W. F. Stickle, P. E. Sobol, and K. D. Bomben, *Handbook of X-ray Photoelectron Spectroscopy, A Reference Book of Standard Spectra for Identification and Interpretation of XPS Data*, 3rd ed., J. Chastain and R. C. King Jr., Eds. Eden Prairie, MN: Physical Electronics, Inc., 1995.
- [142] *XPS reference table of elements*, Thermo Fisher Scientific Inc., 2013-2017. [Online]. Available: <http://xpssimplified.com/periodictable.php>.
- [143] A. V. Naumkin, A. Kraut-Vass, S. W. Gaarenstroom, and C. J. Powell, *NIST X-ray photoelectron spectroscopy database*, U.S. Secretary of Commerce on behalf of the United States of America, 2012. [Online]. Available: <http://srdata.nist.gov/xps/default.aspx>.
- [144] J. H. Scofield, "Theoretical photoionization cross sections from 1 to 1500 keV", Master's thesis, University of California/Livermore, 1973. DOI: 10.2172/4545040.
- [145] —, "Hartree-Slater subshell photoionization cross-sections at 1254 and 1487 eV", *Journal of Electron Spectroscopy and Related Phenomena*, vol. 8, pp. 129–137, 1976. DOI: 10.1016/0368-2048(76)80015-1.
- [146] *Atomic calculation of photoionization cross-sections and asymmetry parameters*, Elettra-Sincrotrone Trieste S.C.p.A. [Online]. Available: <https://vuo.elettra.eu/services/elements/WebElements.html>.
- [147] M. P. Seah and W. A. Dench, "Quantitative electron spectroscopy of surfaces: A standard data base for electron inelastic mean free paths in solids", *Surface and Interface Analysis*, vol. 1, pp. 2–11, 1979. DOI: 10.1002/sia.740010103.
- [148] S. Tanuma, C. J. Powell, and D. R. Penn, "Calculations of electron inelastic mean free paths. V. Data for 14 organic compounds over the 50-2000 eV range", *Surface and Interface Analysis*, vol. 21, pp. 165–176, 1994. DOI: 10.1002/sia.740210302.
- [149] G. Lütjering and J. C. Williams, "Fundamental aspects", in *Titanium*, 2nd ed., Berlin Heidelberg: Springer-Verlag, 2007, ch. 2, pp. 15–52. DOI: 10.1007/978-3-540-73036-1.

BIBLIOGRAPHY

- [150] K. Okazaki and H. Conrad, "Recrystallization and grain growth in titanium: I. Characterization of the structure", *Metallurgical Transactions*, vol. 3, pp. 2411–2421, 1972. DOI: 10.1007/BF02647044.
- [151] N. Bozzolo, N. Dewobroto, T. Grosdidier, and F. Wagner, "Texture evolution during grain growth in recrystallized commercially pure titanium", *Materials Science and Engineering A*, vol. 397, pp. 346–355, 2005. DOI: 10.1016/j.msea.2005.02.049.
- [152] R. Boyer, G. Welsch, and E. W. Collings, Eds., *Materials Properties Handbook, Titanium Alloys*. Materials Park, OH: ASM International, 1994.
- [153] J.-F. Vanhumbecq, "In-situ monitoring of the internal stress evolution during titanium thin film anodising", Dissertation, Université Catholique de Louvain, 2008. [Online]. Available: <https://dial.uclouvain.be/pr/boreal/en/object/boreal:20866/datastreams>.
- [154] R. J. D. Tilley, "Intrinsic and extrinsic defects in insulators: Ionic conductivity", in *Defects in Solids*, John Wiley & Sons, Inc., 2008, ch. 6, pp. 251–295. DOI: 10.1002/9780470380758.ch6.
- [155] D. D. MacDonald, "The history of the point defect model for the passive state: A brief review of film growth aspects", *Electrochimica Acta*, vol. 56, pp. 1761–1772, 2011. DOI: 10.1016/j.electacta.2010.11.005.
- [156] D. D. Macdonald, "Some personal adventures in passivity - A review of the point defect model for film growth", *Russian Journal of Electrochemistry*, vol. 48, pp. 235–258, 2012. DOI: 10.1134/S1023193512030068.
- [157] J. W. Schultze and A. W. Hassel, "Passivity of metals, alloys, and semiconductors", in *Encyclopedia of Electrochemistry*, A. J. Bard and M. Stratmann, Eds., John Wiley & Sons, Inc., 2007, ch. 3, pp. 216–270. DOI: 10.1002/9783527610426.bard040302.
- [158] I. A. Ammar and I. Kamal, "Kinetics of anodic oxide-film growth on titanium – I. Acid media", *Electrochimica Acta*, vol. 16, pp. 1539–1553, 1971. DOI: 10.1016/0013-4686(71)80024-5.
- [159] E. Zhuravlyova, L. Iglesias-Rubianes, A. Pakes, P. Skeldon, G. E. Thompson, X. Zhou, T. Quance, M. J. Graham, H. Habazaki, and K. Shimizu, "Oxygen evolution within barrier oxide films", *Corrosion Science*, vol. 44, pp. 2153–2159, 2002. DOI: 10.1016/S0010-938X(02)00025-2.
- [160] H. Habazaki, M. Uozumi, H. Konno, K. Shimizu, P. Skeldon, and G. E. Thompson, "Crystallization of anodic titania on titanium and its alloys", *Corrosion Science*, vol. 45, pp. 2063–2073, 2003. DOI: 10.1016/S0010-938X(03)00040-4.
- [161] E. Matykina, R. Arrabal, P. Skeldon, G. E. Thompson, and H. Habazaki, "Influence of grain orientation on oxygen generation in anodic titania", *Thin Solid Films*, vol. 516, pp. 2296–2305, 2008. DOI: 10.1016/j.tsf.2007.08.104.
- [162] Z. J. Liu, X. Zhong, J. Walton, and G. E. Thompson, "Anodic film growth of titanium oxide using the 3-electrode electrochemical technique: Effects of oxygen evolution and morphological characterizations", *Journal of the Electrochemical Society*, vol. 163, E71–E82, 2016. DOI: 10.1149/2.0181603jes.
- [163] J. Kunze, A. Seyeux, and P. Schmuki, "Anodic TiO₂ layer conversion: Fluoride-induced rutile formation at room temperature", *Electrochemical and Solid-State Letters*, vol. 11, K11–K13, 2008. DOI: 10.1149/1.2811722.
- [164] S. Berger, S. P. Albu, F. Schmidt-Stein, H. Hildebrand, P. Schmuki, J. S. Hammond, D. F. Paul, and S. Reichlmaier, "The origin for tubular growth of TiO₂ nanotubes: A fluoride rich layer between tube-walls", *Surface Science*, vol. 605, pp. L57–L60, 2011. DOI: 10.1016/j.susc.2011.06.019.
- [165] D. J. Blackwood, L. M. Peter, and D. E. Williams, "Stability and open circuit breakdown of the passive oxide film on titanium", *Electrochimica Acta*, vol. 33, pp. 1143–1149, 1988. DOI: 10.1016/0013-4686(88)80206-8.
- [166] J.-L. Delplancke, A. Garnier, Y. Massiani, and R. Winand, "Influence of the anodizing procedure on the structure and the properties of titanium oxide films and its effect on copper nucleation", *Electrochimica Acta*, vol. 39, pp. 1281–1289, 1994. DOI: 10.1016/0013-4686(94)E0048-5.

- [167] M. J. Donachie Jr., “Corrosion resistance”, in *Titanium, A Technical Guide*, 2nd ed., Materials Park, OH: ASM International, 2000, ch. 13, pp. 123–130.
- [168] Matthew J. Donachie Jr., “Corrosion data”, in *Titanium, A Technical Guide*, 2nd ed., Materials Park, OH: ASM International, 2000, ch. Appendix F, pp. 307–310.
- [169] D. L. Arsov, “Dissolution electrochimique des films anodiques du titane dans l’acide sulfurique”, *Electrochimica Acta*, vol. 30, pp. 1645–1657, 1985. DOI: 10.1016/0013-4686(85)87011-0.
- [170] L. Kavan, M. Grätzel, S. E. Gilbert, C. Klemenz, and H. J. Scheel, “Electrochemical and photoelectrochemical investigation of single-crystal anatase”, *Journal of the American Chemical Society*, vol. 118, pp. 6716–6723, 1996. DOI: 10.1021/ja9541721.
- [171] U. Diebold, M. Li, O. Dulub, E. L. D. Hebenstreit, and W. Hebenstreit, “The relationship between bulk and surface properties of rutile TiO₂ (110)”, *Surface Review and Letters*, vol. 7, pp. 613–617, 2000. DOI: 10.1142/S0218625X0000052X.
- [172] J. L. Murray and H. A. Wriedt, “The O-Ti (oxygen-titanium) system”, *Bulletin of Alloy Phase Diagrams*, vol. 8, pp. 148–165, 1987. DOI: 10.1007/BF02873201.
- [173] A. Seeber, A. N. Klein, C. V. Speller, P. Egert, F. A. Weber, and A. Lago, “Sintering unalloyed titanium in dc electrical abnormal glow discharge”, *Materials Research*, vol. 13, pp. 99–106, 2010. DOI: 10.1590/S1516-14392010000100020.
- [174] H. W. Li, “Lattice constants, thermal expansion coefficients and perfection of the phase TiO”, Master’s thesis, Missouri School of Mines and Metallurgy, 1959. [Online]. Available: http://scholarsmine.mst.edu/masters_theses/2544/.
- [175] D. N. Miller, A. K. Azad, H. Delpouve, L. Quazuguel, J. Zhou, A. Sinha, P. Wormald, and J. T. S. Irvine, “Studies on the crystal structure, magnetic and conductivity properties of titanium oxycarbide solid solution (TiO_{1-x}C_x)”, *Journal of Materials Chemistry A*, vol. 4, pp. 5730–5736, 2016. DOI: 10.1039/C6TA00042H.
- [176] Y. G. Zainulin, S. I. Alyamovsky, and G. P. Shveikin, “Concerning the structural mechanism of oxygen inclusion into the lattice of titanium carbide”, *Journal of Physics and Chemistry of Solids*, vol. 39, pp. 29–31, 1978. DOI: 10.1016/0022-3697(78)90195-6.
- [177] S. T. Oyama, Ed., *The Chemistry of Transition Metal Carbides and Nitrides*. Glasgow: Blackie Academic & Professional, an imprint of Chapman & Hall, 1996. DOI: 10.1007/978-94-009-1565-7.
- [178] A. D. Mazzoni and M. S. Conconi, “Synthesis of group IVB metals oxycarbides by carboreduction reactions”, *Materials Research*, vol. 5, pp. 459–466, 2002. DOI: 10.1590/S1516-14392002000400011.
- [179] A. C. Fernandes, P. Carvalho, F. Vaz, S. Lanceros-Méndez, A. V. Machado, N. M. G. Parreira, J. F. Pierson, and N. Martin, “Property change in multifunctional TiC_xO_y thin films: Effect of the O/Ti ratio”, *Thin Solid Films*, vol. 515, pp. 866–871, 2006. DOI: 10.1016/j.tsf.2006.07.047.
- [180] J. M. Chappé, A. C. Fernandes, C. Moura, E. Alves, N. P. Barradas, N. Martin, J. P. Espinós, and F. Vaz, “Analysis of multifunctional titanium oxycarbide films as a function of oxygen addition”, *Surface and Coatings Technology*, vol. 206, pp. 2525–2534, 2011. DOI: 10.1016/j.surfcoat.2011.11.005.
- [181] C. Sousa and F. Illas, “Ionic-covalent transition in titanium oxides”, *Physical Review B*, vol. 50, pp. 13974–13980, 1994. DOI: 10.1103/PhysRevB.50.13974.
- [182] K. Chen and S. Kamran, “Bonding characteristics of TiC and TiN”, *Modeling and Numerical Simulation of Material Science*, vol. 3, pp. 7–11, 2013. DOI: 10.4236/mnsms.2013.31002.
- [183] A. Paul and S. Divinski, Eds., *Handbook of Solid State Diffusion, Diffusion Fundamentals and Techniques*. Amsterdam: Elsevier Inc., 2017, vol. 1.
- [184] K. Hoshino, N. L. Peterson, and C. L. Wiley, “Diffusion and point defects in TiO_{2-x}”, *Journal of Physics and Chemistry of Solids*, vol. 46, pp. 1397–1411, 1985. DOI: 10.1016/0022-3697(85)90079-4.

BIBLIOGRAPHY

- [185] V. B. Vykhodets, T. E. Kurennykh, and A. Y. Fishman, "Identification of heterogeneous state and trajectories of interstitials in the titanium-oxygen system using precise diffusion experiment", *Defect and Diffusion Forum*, vol. 143-147, pp. 79–84, 1997. DOI: 10.4028/www.scientific.net/DDF.143-147.79.
- [186] H. Wu, "Oxygen diffusion through titanium and other hcp metals", Dissertation, University of Illinois at Urbana-Champaign, 2013.
- [187] E. K. Storms, "The titanium-titanium carbide system", in *Refractory Materials, Vol. 2. The Refractory Carbides*, New York, NY: Academic Press Inc., 1967, ch. 1, pp. 1–17. [Online]. Available: <https://doi.org/10.1016/B978-1-4832-3070-2.50006-9>.
- [188] W. Lengauer, "Transition metal carbides, nitrides, and carbonitrides", in *Handbook of Ceramic Hard Materials*, R. Riedel, Ed., Weinheim: Wiley-VCH Verlag GmbH, 2000, ch. 7, pp. 202–252. DOI: 10.1002/9783527618217.ch7.
- [189] Y. Zhong, X. Xia, F. Shi, J. Zhan, J. Tu, and H. J. Fan, "Transition metal carbides and nitrides in energy storage and conversion", *Advanced Science*, vol. 3, pp. 1500286–1500313, 2016. DOI: 10.1002/advs.201500286.
- [190] C. J. Quinn and D. L. Kohlstedt, "Solid-state reaction between titanium carbide and titanium metal", *Journal of the American Ceramic Society*, vol. 67, pp. 305–310, 1984. DOI: 10.1111/j.1151-2916.1984.tb19527.x.
- [191] B. Beverskog, J.-O. Carlsson, A. D. Bauer, C. V. Deshpandey, H. J. Doerr, R. F. Bunshah, and B. P. O'Brien, "Corrosion properties of TiC films prepared by activated reactive evaporation", *Surface and Coatings Technology*, vol. 41, pp. 221–229, 1990. DOI: 10.1016/0257-8972(90)90170-H.
- [192] H. E. Hintermann, A. C. Riddiford, R. D. Cowling, and J. Malyszko, "The anodic behaviour of titanium carbide in sulphuric acid solutions", *Electrodeposition and Surface Treatment*, vol. 1, pp. 59–69, 1972. DOI: 10.1016/0300-9416(72)90015-6.
- [193] A. D. Vlasov, J. S. Rez, and M. L. Fil'chenkov, "Beilby layers on crystal surfaces", *Crystal Research and Technology*, vol. 23, pp. 1093–1100, 1988. DOI: 10.1002/crat.2170230908.
- [194] F. Wiesinger, "Alcohol oxidation at elevated temperatures on planar Pt/TiO_xC_y model systems", Master's thesis, Technische Universität München, 2013.
- [195] A. K. Sharma, "Anodizing titanium for space applications", *Thin Solid Films*, vol. 208, pp. 48–54, 1992. DOI: 10.1016/0040-6090(92)90946-9.
- [196] J. Landesfeind, "Electrochemical deposition of noble metal particles on TiO_xC_y films", Bachelor's thesis, Technische Universität München, 2011.
- [197] O. Paschos, P. Choi, H. Efstathiadis, and P. Haldar, "Synthesis of platinum nanoparticles by aerosol assisted deposition method", *Thin Solid Films*, vol. 516, pp. 3796–3801, 2008. DOI: 10.1016/j.tsf.2007.06.123.
- [198] J. Brumbarov, "Aerosol assisted deposition of Pt nanoparticles on planar model TiO_xC_y surfaces", Master's thesis, Technische Universität München, 2011.
- [199] J. O. Hernández and E. A. Choren, "Thermal stability of platinum complexes", *Thermochimica Acta*, vol. 71, pp. 265–272, 1983. DOI: 10.1016/0040-6031(83)80059-8.
- [200] *Autolab modules*, Metrohm Autolab B.V., 2010-2018. [Online]. Available: <http://www.metrohm-autolab.com/Products/Echem/ModulesFolder/Modules.html>.
- [201] *OriginPro 9.1.0*, Northampton, MA: OriginLab Corporation, 1991-2013. [Online]. Available: <http://www.OriginLab.com>.
- [202] *NOVA 1.10.3*, Utrecht: Metrohm Autolab B.V., 2005-2013. [Online]. Available: <http://www.metrohm-autolab.com>.

- [203] *Bruker MultiMode 8 with ScanAsyst, Instruction Manual*, Rev. B, 004-1033-000, Bruker Corporation, Santa Barbara, CA, 2009, 2010, 2011.
- [204] I. Horcas, R. Fernandez, J. M. Gomez-Rodriguez, J. Colchero, J. Gomez-Herrero, and A. M. Baro, "WSXM: A software for scanning probe microscopy and a tool for nanotechnology", *Review of Scientific Instruments*, vol. 78, p. 013705, 2007. DOI: 10.1063/1.2432410.
- [205] F. Müller, "Epitaktisches Wachstum von Graphen und Boronitren auf Übergangsmetallen", Habilitationsschrift, Universität des Saarlandes, 2014.
- [206] P. A. Redhead, J. P. Hobson, and E. V. Kornelsen, *The Physical Basis of Ultrahigh Vacuum*. Melville, NY: American Institute of Physics, 1993.
- [207] M. Favaro, "A rational approach to the optimization of efficient electrocatalysts for the next generation fuel cells", Dissertation, Università degli Studi di Padova, 2015.
- [208] *IGOR Pro 6.37*, Lake Oswego, OR: WaveMetrics Inc., 1988-2014. [Online]. Available: <http://www.wavemetrics.com/>.
- [209] N. Fairley, *CasaXPS*, Casa Software Ltd., 2007. [Online]. Available: <http://www.casaxps.com/>.
- [210] S. Tougaard, *QUASES-IMFP-TPP2M*, Odense: Quases-Tougaard Inc., 2000-2002. [Online]. Available: <http://www.quases.com/>.
- [211] P. Vandenabeele, "Raman spectroscopy in daily lab-life", in *Practical Raman Spectroscopy – An Introduction*, P. Vandenabeele, Ed., Chichester: John Wiley & Sons, Ltd., 2013, ch. 5, pp. 101–148. DOI: 10.1002/9781119961284.ch5.
- [212] *ESCA Microscopy beamline description*, Elettra-Sincrotrone Trieste S.C.p.A. [Online]. Available: <https://www.elettra.trieste.it/it/lightsources/elettra/elettra-beamlines/esca-microscopy/beamline-description-test.html>.
- [213] M. K. Abyaneh, L. Gregoratti, M. Amati, M. Dalmiglio, and M. Kiskinova, "Scanning photoelectron microscopy: A powerful technique for probing micro and nano-structures", *e-Journal of Surface Science and Nanotechnology*, vol. 9, pp. 158–162, 2011. DOI: 10.1380/ejssnt.2011.158.
- [214] L. Gregoratti, A. Barinov, E. Benfatto, G. Cautero, C. Fava, P. Lacovig, D. Lonza, M. Kiskinova, R. Tommasini, S. Mähl, and W. Heichler, "48-Channel electron detector for photoemission spectroscopy and microscopy", *Review of Scientific Instruments*, vol. 75, pp. 64–68, 2004. DOI: 10.1063/1.1630837.
- [215] N. F. Fahim, T. Sekino, M. F. Morks, and T. Kusunose, "Electrochemical growth of vertically-oriented high aspect ratio titania nanotubes by rapid anodization in fluoride-free media", *Journal of Nanoscience and Nanotechnology*, vol. 9, pp. 1803–1818, 2009. DOI: 10.1166/jnn.2009.440.
- [216] D. Regonini, C. R. Bowen, A. Jaroenworoluck, and R. Stevens, "A review of growth mechanism, structure and crystallinity of anodized TiO₂ nanotubes", *Materials Science and Engineering R: Reports*, vol. 74, pp. 377–406, 2013. DOI: 10.1016/j.mser.2013.10.001.
- [217] C. Rüdiger, F. Maglia, S. Leonardi, M. Sachsenhauser, I. D. Sharp, O. Paschos, and J. Kunze, "Surface analytical study of carbothermally reduced titania films for electrocatalysis application", *Electrochimica Acta*, vol. 71, pp. 1–9, 2012. DOI: 10.1016/j.electacta.2012.02.044.
- [218] G. Zhang, H. Huang, Y. Zhang, H. L. W. Chan, and L. Zhou, "Highly ordered nanoporous TiO₂ and its photocatalytic properties", *Electrochemistry Communications*, vol. 9, pp. 2854–2858, 2007. DOI: 10.1016/j.elecom.2007.10.014.
- [219] R. Hahn, J. M. Macak, and P. Schmuki, "Rapid anodic growth of TiO₂ and WO₃ nanotubes in fluoride free electrolytes", *Electrochemistry Communications*, vol. 9, pp. 947–952, 2007. DOI: 10.1016/j.elecom.2006.11.037. [Online]. Available: <http://linkinghub.elsevier.com/retrieve/pii/S1388248106005613>.

BIBLIOGRAPHY

- [220] K. Okada and A. Kotani, "Theory of core level X-ray photoemission and photoabsorption in Ti compounds", *Journal of Electron Spectroscopy and Related Phenomena*, vol. 62, pp. 131–140, 1993. DOI: 10.1016/0368-2048(93)80010-J.
- [221] L. Ramqvist, K. Hamrin, G. Johansson, A. Fahlman, and C. Nordling, "Charge transfer in transition metal carbides and related compounds studied by ESCA", *Journal of Physics and Chemistry of Solids*, vol. 30, pp. 1835–1847, 1969. DOI: 10.1016/0022-3697(69)90252-2.
- [222] M. C. Biesinger, L. W. M. Lau, A. R. Gerson, and R. St. C. Smart, "Resolving surface chemical states in XPS analysis of first row transition metals, oxides and hydroxides: Sc, Ti, V, Cu and Zn", *Applied Surface Science*, vol. 257, pp. 887–898, 2010. DOI: 10.1016/j.apsusc.2010.07.086.
- [223] J. Pouilleau, D. Devilliers, H. Groult, and P. Marcus, "Surface study of a titanium-based ceramic electrode material by X-ray photoelectron spectroscopy", *Journal of Materials Science*, vol. 32, pp. 5645–5651, 1997. DOI: 10.1023/A:1018645112465.
- [224] Y. Mizokawa, T. Miyasato, S. Nakamura, K. M. Geib, and C. W. Wilmsen, "The C KLL first derivative X-ray photoelectron spectroscopy spectra as a fingerprint of the carbon state and the characterization of diamondlike carbon films", *Journal of Vacuum Science & Technology A: Vacuum, Surfaces, and Films*, vol. 5, pp. 2809–2813, 1987. DOI: 10.1116/1.574312.
- [225] J. C. Lascovich, R. Giorgi, and S. Scaglione, "Evaluation of the sp^2/sp^3 ratio in amorphous carbon structure by XPS and XAES", *Applied Surface Science*, vol. 47, pp. 17–21, 1991. DOI: 10.1016/0169-4332(91)90098-5.
- [226] S. T. Jackson and R. G. Nuzzo, "Determining hybridization differences for amorphous carbon from the XPS C 1s envelope", *Applied Surface Science*, vol. 90, pp. 195–203, 1995. DOI: 10.1016/0169-4332(95)00079-8.
- [227] J. Díaz, G. Paolicelli, S. Ferrer, and F. Comin, "Separation of the sp^3 and sp^2 components in the C 1s photoemission spectra of amorphous carbon films", *Physical Review B*, vol. 54, pp. 8064–8069, 1996. DOI: 10.1103/PhysRevB.54.8064.
- [228] Y. Taki and O. Takai, "XPS structural characterization of hydrogenated amorphous carbon thin films prepared by shielded arc ion plating", *Thin Solid Films*, vol. 316, pp. 45–50, 1998. DOI: 10.1016/S0040-6090(98)00386-1.
- [229] S. K. Sen, J. Riga, and J. Verbist, "2s and 2p X-ray photoelectron spectra of Ti^{4+} ion in TiO_2 ", *Chemical Physics Letters*, vol. 39, pp. 560–564, 1976. DOI: 10.1016/0009-2614(76)80329-6.
- [230] A. F. Carley, P. R. Chalker, J. C. Riviere, and M. W. Roberts, "The identification and characterisation of mixed oxidation states at oxidised titanium surfaces by analysis of X-ray photoelectron spectra", *Journal of the Chemical Society, Faraday Transactions 1: Physical Chemistry in Condensed Phases*, vol. 83, pp. 351–370, 1987. DOI: 10.1039/f19878300351.
- [231] E. McCafferty and J. P. Wightman, "Determination of the concentration of surface hydroxyl groups on metal oxide films by a quantitative XPS method", *Surface and Interface Analysis*, vol. 26, pp. 549–564, 1998. DOI: 10.1002/(SICI)1096-9918(199807)26:8<549::AID-SIA396>3.0.CO;2-Q.
- [232] S. Hashimoto and A. Tanaka, "Alteration of Ti 2p XPS spectrum for titanium oxide by low-energy Ar ion bombardment", *Surface and Interface Analysis*, vol. 34, pp. 262–265, 2002. DOI: 10.1002/sia.1296.
- [233] I. Milošev, T. Kosec, and H.-H. Strehblow, "XPS and EIS study of the passive film formed on orthopaedic Ti–6Al–7Nb alloy in Hank's physiological solution", *Electrochimica Acta*, vol. 53, pp. 3547–3558, 2008. DOI: 10.1016/j.electacta.2007.12.041.
- [234] M. V. Kuznetsov, J. F. Zhuravlev, V. A. Zhilyaev, and V. A. Gubanov, "XPS study of the nitrides, oxides and oxynitrides of titanium", *Journal of Electron Spectroscopy and Related Phenomena*, vol. 58, pp. 1–9, 1992. DOI: 10.1016/0368-2048(92)80001-0.

- [235] H. Ihara, Y. Kumashiro, A. Itoh, and K. Maeda, "Some aspects of ESCA spectra of single crystals and thin films of titanium carbide", *Japanese Journal of Applied Physics*, vol. 12, pp. 1462–1463, 1973. DOI: 10.1143/JJAP.12.1462.
- [236] L. Zhang and R. V. Koka, "A study on the oxidation and carbon diffusion of TiC in alumina – titanium carbide ceramics using XPS and Raman spectroscopy", *Materials Chemistry and Physics*, vol. 57, pp. 23–32, 1998. DOI: 10.1016/S0254-0584(98)00187-4.
- [237] G. Li and L. F. Xia, "Structural characterization of TiC_x films prepared by plasma based ion implantation", *Thin Solid Films*, vol. 396, pp. 16–22, 2001. DOI: 10.1016/S0040-6090(01)01227-5.
- [238] D. M. Phase and V. Sathe, "In situ photoelectron spectroscopy study of TiC_xN_y films synthesized through reactive ion beam mixing", *Journal of Physics D: Applied Physics*, vol. 37, pp. 1696–1700, 2004. DOI: 10.1088/0022-3727/37/12/015.
- [239] M. Hassan, R. S. Rawat, P. Lee, S. M. Hassan, A. Qayyum, R. Ahmad, G. Murtaza, and M. Zakallah, "Synthesis of nanocrystalline multiphase titanium oxycarbide (TiC_xO_y) thin films by UNU/ICTP and NX2 plasma focus devices", *Applied Physics A*, vol. 90, pp. 669–677, 2008. DOI: 10.1007/s00339-007-4335-8.
- [240] D. T. Clark and A. Dilks, "ESCA applied to polymers. XXIII. RF glow discharge modification of polymers in pure oxygen and helium-oxygen mixtures", *Journal of Polymer Science: Polymer Chemistry Edition*, vol. 17, pp. 957–976, 1979. DOI: 10.1002/pol.1978.170160506.
- [241] M. V. Kuznetsov, J. F. Zhuravlev, and V. A. Gubanov, "XPS analysis of adsorption of oxygen molecules on the surface of Ti and TiN_x films in vacuum", *Journal of Electron Spectroscopy and Related Phenomena*, vol. 58, pp. 169–176, 1992. DOI: 10.1016/0368-2048(92)80016-2.
- [242] J. F. Morar, F. J. Himpsel, J. L. Jordan, G. Hughes, and F. R. McFeely, "C 1s excitation studies of diamond (111)", *Physical Review B*, vol. 33, pp. 1340–1345, 1986. DOI: 10.1103/PhysRevB.33.1340.
- [243] A. Barinov, O. B. Malcioğlu, S. Fabris, T. Sun, L. Gregoratti, M. Dalmiglio, and M. Kiskinova, "Initial stages of oxidation on graphitic surfaces: Photoemission study and density functional theory calculations", *The Journal of Physical Chemistry C*, vol. 113, pp. 9009–9013, 2009. DOI: 10.1021/jp902051d.
- [244] L. M. Torres, A. F. Gil, L. Galicia, and I. González, "Understanding the difference between inner- and outer-sphere mechanisms", *Journal of Chemical Education*, vol. 73, pp. 808–810, 1996. DOI: 10.1021/ed073p808.
- [245] A. N. Patel, M. G. Collignon, M. A. O'Connell, W. O. Y. Hung, K. McKelvey, J. V. MacPherson, and P. R. Unwin, "A new view of electrochemistry at highly oriented pyrolytic graphite", *Journal of the American Chemical Society*, vol. 134, pp. 20117–20130, 2012. DOI: 10.1021/ja308615h.
- [246] C. Rüdiger, J. Brumbarov, F. Wiesinger, S. Leonardi, O. Paschos, C. Valero Vidal, and J. Kunze-Liebhäuser, "Ethanol oxidation on TiO_xC_y-supported Pt nanoparticles", *ChemCatChem*, vol. 5, pp. 3219–3223, 2013. DOI: 10.1002/cctc.201300217.
- [247] D. Regonini, A. Jaroenworuluck, R. Stevens, and C. R. Bowen, "Effect of heat treatment on the properties and structure of TiO₂ nanotubes: Phase composition and chemical composition", *Surface and Interface Analysis*, vol. 42, pp. 139–144, 2010. DOI: 10.1002/sia.3183.
- [248] F. D. Hardcastle, H. Ishihara, R. Sharma, and A. S. Biris, "Photoelectroactivity and Raman spectroscopy of anodized titania (TiO₂) photoactive water-splitting catalysts as a function of oxygen-annealing temperature", *Journal of Materials Chemistry*, vol. 21, pp. 6337–6345, 2011. DOI: 10.1039/c0jm03106b.
- [249] S. Otani, T. Tanaka, and Y. Ishizawa, "Electrical resistivities in single crystals of TiC_x and VC_x", *Journal of Materials Science*, vol. 21, pp. 1011–1014, 1986. DOI: 10.1007/BF01117387.
- [250] D.C. Cronmeyer, "Infrared absorption of reduced rutile TiO₂ single crystals", *Physical Review*, vol. 113, pp. 1222–1226, 1959. DOI: 10.1103/PhysRev.113.1222.

BIBLIOGRAPHY

- [251] C. Rüdiger, C. Valero-Vidal, M. Favaro, S. Agnoli, G. Granozzi, and J. Kunze-Liebhäuser, "Effect of air-aging on the electrochemical characteristics of TiO_xC_y films for electrocatalysis applications", *ChemElectroChem*, vol. 4, pp. 3100–3109, 2017. DOI: 10.1002/ce1c.201700912.
- [252] L. Calvillo, D. Fittipaldi, C. Rüdiger, S. Agnoli, M. Favaro, C. Valero-Vidal, C. Di Valentin, A. Vittadini, N. Bozzolo, S. Jacomet, L. Gregoratti, J. Kunze-Liebhäuser, G. Pacchioni, and G. Granozzi, "Carboth-ermal transformation of TiO_2 into TiO_xC_y in UHV: Tracking intrinsic chemical stabilities", *The Journal of Physical Chemistry C*, vol. 118, pp. 22 601–22 610, 2014. DOI: 10.1021/jp506728w.
- [253] J. Pan, D. Thierry, and C. Leygraf, "Electrochemical impedance spectroscopy study of the passive oxide film on titanium for implant application", *Electrochimica Acta*, vol. 41, pp. 1143–1153, 1996. DOI: 10.1016/0013-4686(95)00465-3.
- [254] M. Aziz-Kerrzo, K. G. Conroy, A. M. Fenelon, S. T. Farrell, and C. B. Breslin, "Electrochemical studies on the stability and corrosion resistance of titanium-based implant materials", *Biomaterials*, vol. 22, pp. 1531–1539, 2001. DOI: 10.1016/s0142-9612(00)00309-4.
- [255] S. V. Gnedenkov, S. L. Sinebryukhov, and V. I. Sergienko, "Electrochemical impedance simulation of a metal oxide heterostructure/electrolyte interface: A review", *Russian Journal of Electrochemistry*, vol. 42, pp. 197–211, 2006. DOI: 10.1134/S1023193506030013.
- [256] S. K. Poznyak, A. D. Lisenkov, M. G. S. Ferreira, A. I. Kulak, and M. L. Zheludkevich, "Impedance behaviour of anodic TiO_2 films prepared by galvanostatic anodisation and powerful pulsed discharge in electrolyte", *Electrochimica Acta*, vol. 76, pp. 453–461, 2012. DOI: 10.1016/j.electacta.2012.05.064.
- [257] A. G. Pandolfo and A. F. Hollenkamp, "Carbon properties and their role in supercapacitors", *Journal of Power Sources*, vol. 157, pp. 11–27, 2006. DOI: 10.1016/j.jpowsour.2006.02.065.
- [258] L. Calvillo, G. García, A. Paduano, O. Guillen-Villafuerte, C. Valero-Vidal, A. Vittadini, M. Bellini, A. Lavacchi, S. Agnoli, A. Martucci, J. Kunze-Liebhäuser, E. Pastor, and G. Granozzi, "Electrochemical behavior of TiO_xC_y as catalyst support for direct ethanol fuel cells at intermediate temperature: From planar systems to powders", *ACS Applied Materials & Interfaces*, vol. 8, pp. 716–725, 2016. DOI: 10.1021/acsmami.5b09861.
- [259] C. Rüdiger, M. Favaro, C. Valero-Vidal, L. Calvillo, N. Bozzolo, S. Jacomet, J. Hein, L. Gregoratti, S. Agnoli, G. Granozzi, and J. Kunze-Liebhäuser, "Substrate grain-dependent chemistry of carburized planar anodic TiO_2 on polycrystalline Ti", *ACS Omega*, vol. 2, pp. 631–640, 2017. DOI: 10.1021/acsomega.6b00472. [Online]. Available: <http://pubs.acs.org/articlesonrequest/A0R-sfJnx44JpUJ5kNXvGMfc>.
- [260] I. Brand, C. Rüdiger, K. Hingerl, E. Portenkirchner, and J. Kunze-Liebhäuser, "Compact titanium oxycarbide: A new substrate for quantitative analysis of molecular films by means of infrared reflection absorption spectroscopy", *The Journal of Physical Chemistry C*, vol. 119, pp. 13 767–13 776, 2015. DOI: 10.1021/acs.jpcc.5b03570.
- [261] J. Joseph and A. Gagnaire, "Ellipsometric study of anodic oxide growth: Application to the titanium oxide systems", *Thin Solid Films*, vol. 103, pp. 257–265, 1983. DOI: 10.1016/0040-6090(83)90442-X.
- [262] Y. Y. Wang, Z. H. Ni, Z. X. Shen, H. M. Wang, and Y. H. Wu, "Interference enhancement of Raman signal of graphene", *Applied Physics Letters*, vol. 92, p. 043 121, 2008. DOI: 10.1063/1.2838745.
- [263] S. P. S. Porto, P. A. Fleury, and T. C. Damen, "Raman spectra of TiO_2 , MgF_2 , ZnF_2 , FeF_2 , and MnF_2 ", *Physical Review*, vol. 154, pp. 522–526, 1967. DOI: 10.1103/PhysRev.154.522.
- [264] T. Ohsaka, F. Izumi, and Y. Fujiki, "Raman spectrum of anatase, TiO_2 ", *Journal of Raman Spectroscopy*, vol. 7, pp. 321–324, 1978. DOI: 10.1002/jrs.1250070606.
- [265] A. C. Ferrari and J. Robertson, "Interpretation of Raman spectra of disordered and amorphous carbon", *Physical Review B*, vol. 61, pp. 14 095–14 107, 2000. DOI: 10.1103/PhysRevB.61.14095.

- [266] S. Reich and C. Thomsen, "Raman spectroscopy of graphite", *Philosophical Transactions of the Royal Society of London A*, vol. 362, pp. 2271–2288, 2004. DOI: 10.1098/rsta.2004.1454.
- [267] A. C. Ferrari and D. M. Basko, "Raman spectroscopy as a versatile tool for studying the properties of graphene", *Nature Nanotechnology*, vol. 8, pp. 235–246, 2013. DOI: 10.1038/nnano.2013.46.
- [268] A. Mooradian and P. M. Raccach, "Raman study of the semiconductor-metal transition in Ti_2O_3 ", *Physical Review B*, vol. 3, pp. 4253–4256, 1971. DOI: 10.1103/PhysRevB.3.4253.
- [269] S.-W. Hsu, T.-S. Yang, T.-K. Chen, and M.-S. Wong, "Ion-assisted electron-beam evaporation of carbon-doped titanium oxide films as visible-light photocatalyst", *Thin Solid Films*, vol. 515, pp. 3521–3526, 2007. DOI: 10.1016/j.tsf.2006.10.113.
- [270] J. Zhang, M. Li, Z. Feng, J. Chen, and C. Li, "UV Raman spectroscopic study on TiO_2 . I. Phase transformation at the surface and in the bulk", *Journal of Physical Chemistry B*, vol. 110, pp. 927–935, 2006. DOI: 10.1021/jp0552473.
- [271] F. C. Tai, S. C. Lee, J. Chen, C. Wei, and S. H. Chang, "Multipeak fitting analysis of Raman spectra on DLCH film", *Journal of Raman Spectroscopy*, vol. 40, pp. 1055–1059, 2009. DOI: 10.1002/jrs.2234.
- [272] C. Tric, "Planar vibrations of carbon skeleton of polyenes", *The Journal of Chemical Physics*, vol. 51, pp. 4778–4786, 1969. DOI: 10.1063/1.1671866.
- [273] V. Rives-Arnau and N. Sheppard, "Raman spectroscopic study of the polymerization of acetylene on titanium dioxide (rutile)", *Journal of the Chemical Society, Faraday Transactions 1: Physical Chemistry in Condensed Phases*, vol. 76, pp. 394–402, 1980. DOI: 10.1039/f19807600394.
- [274] S. M. Jain, J. J. Biedrzycki, V. Maurino, A. Zecchina, L. Mino, and G. Spoto, "Acetylene oligomerization on the surface of TiO_2 : A step forward in the in situ synthesis of nanostructured carbonaceous structures on the surface of photoactive oxides", *Journal of Materials Chemistry A*, vol. 2, pp. 12 247–12 254, 2014. DOI: 10.1039/c4ta01581a.
- [275] M. Fernández-García, X. Wang, C. Belver, J. C. Hanson, and J. A. Rodriguez, "Anatase- TiO_2 nanomaterials: Morphological/size dependence of the crystallization and phase behavior phenomena", *Journal of Physical Chemistry C*, vol. 111, pp. 674–682, 2007. DOI: 10.1021/jp065661i.
- [276] V. Likodimos, T. Stergiopoulos, P. Falaras, J. Kunze, and P. Schmuki, "Phase composition, size, orientation, and antenna effects of self-assembled anodized titania nanotube arrays: A polarized micro-Raman investigation", *Journal of Physical Chemistry C*, vol. 112, pp. 12 687–12 696, 2008. DOI: 10.1021/jp8027462.
- [277] H. Matsuura, M. Hiraiishi, and T. Miyazawa, "Raman spectra and energy difference between rotational isomers of ethylene glycol", *Spectrochimica Acta Part A: Molecular Spectroscopy*, vol. 28, pp. 2299–2304, 1972. DOI: 10.1016/0584-8539(72)80209-5.
- [278] J. F. Mammone, S. K. Sharma, and M. Nicol, "Raman spectra of methanol and ethanol at pressures up to 100 kbar", *Journal of Physical Chemistry*, vol. 84, pp. 3130–3134, 1980. DOI: 10.1021/j100460a032.
- [279] N. Ito, T. Fujiyama, and Y. Udagawa, "A study of local structure formation in binary solutions of 2-butoxyethanol and water by Rayleigh scattering and Raman spectra", *Bulletin of the Chemical Society of Japan*, vol. 56, pp. 379–385, 1983. DOI: 10.1246/bcsj.56.379.
- [280] I. H. Boyaci, H. E. Genis, B. Guven, U. Tamer, and N. Alper, "A novel method for quantification of ethanol and methanol in distilled alcoholic beverages using Raman spectroscopy", *Journal of Raman Spectroscopy*, vol. 43, pp. 1171–1176, 2012. DOI: 10.1002/jrs.3159.
- [281] D. Bersani, P. P. Lottici, and X.-Z. Ding, "Phonon confinement effects in the Raman scattering by TiO_2 nanocrystals", *Applied Physics Letters*, vol. 72, pp. 73–75, 1998. DOI: 10.1063/1.120648.
- [282] W. F. Zhang, Y. L. He, M. S. Zhang, Z. Yin, and Q. Chen, "Raman scattering study on anatase TiO_2 nanocrystals", *Journal of Physics D: Applied Physics*, vol. 33, pp. 912–916, 2000. DOI: 10.1088/0022-3727/33/8/305.

BIBLIOGRAPHY

- [283] T. Ohsaka, "Temperature dependence of the Raman spectrum in anatase TiO₂", *Journal of the Physical Society of Japan*, vol. 48, pp. 1661–1668, 1980. DOI: 10.1143/JPSJ.48.1661.
- [284] T. Tsumura, N. Kojitani, I. Izumi, N. Iwashita, M. Toyoda, and M. Inagaki, "Carbon coating of anatase-type TiO₂ and photoactivity", *Journal of Materials Chemistry*, vol. 12, pp. 1391–1396, 2002. DOI: 10.1039/b201942f.
- [285] M. Pfanzelt, P. Kubiak, U. Hörmann, U. Kaiser, and M. Wohlfahrt-Mehrens, "Preparation, characterization, and electrochemical performances of carbon-coated TiO₂ anatase", *Ionics*, vol. 15, pp. 657–663, 2009. DOI: 10.1007/s11581-009-0364-y.
- [286] I. Eswaramoorthi and L.-P. Hwang, "Anodic titanium oxide: A new template for the synthesis of larger diameter multi-walled carbon nanotubes", *Diamond and Related Materials*, vol. 16, pp. 1571–1578, Aug. 2007. DOI: 10.1016/j.diamond.2006.12.035.
- [287] J. J. Biedrzycki, S. Livraghi, I. Corazzari, L. Mino, G. Spoto, and E. Giamello, "On the redox mechanism operating along C₂H₂ self-assembly at the surface of TiO₂", *Langmuir*, vol. 31, pp. 569–577, 2015. DOI: 10.1021/la504290d.
- [288] G. Martra, "Lewis acid and base sites at the surface of microcrystalline TiO₂ anatase: Relationships between surface morphology and chemical behaviour", *Applied Catalysis A: General*, vol. 200, pp. 275–285, 2000. DOI: 10.1016/S0926-860X(00)00641-4.
- [289] P. K. Chu and L. Li, "Characterization of amorphous and nanocrystalline carbon films", *Materials Chemistry and Physics*, vol. 96, pp. 253–277, 2006. DOI: 10.1016/j.matchemphys.2005.07.048.
- [290] M. V. Klein, J. A. Holy, and W. S. Williams, "Raman scattering induced by carbon vacancies in TiC_x", *Physical Review B*, vol. 17, pp. 1546–1556, 1978. DOI: 10.1103/PhysRevB.17.1546.
- [291] M. Amer, M. W. Barsoum, T. El-Raghy, I. Weiss, S. Leclair, and D. Liptak, "The Raman spectrum of Ti₃SiC₂", *Journal of Applied Physics*, vol. 84, pp. 5817–5819, 1998. DOI: 10.1063/1.368849.
- [292] A. C. Ferrari, "Raman spectroscopy of graphene and graphite: Disorder, electron–phonon coupling, doping and nonadiabatic effects", *Solid State Communications*, vol. 143, pp. 47–57, 2007. DOI: 10.1016/j.ssc.2007.03.052.
- [293] M. Favaro, S. Leonardi, C. Valero-Vidal, S. Nappini, M. Hanzlik, S. Agnoli, J. Kunze-Liebhäuser, and G. Granozzi, "In-situ carbon doping of TiO₂ nanotubes via anodization in graphene oxide quantum dot containing electrolyte and carburization to TiO_xC_y nanotubes", *Advanced Materials Interfaces*, vol. 2, pp. 1400462–1400472, 2015. DOI: 10.1002/admi.201400462.
- [294] L. Tsetseris, "Stability and dynamics of carbon and nitrogen dopants in anatase TiO₂: A density functional theory study", *Physical Review B*, vol. 81, p. 165205, 2010. DOI: 10.1103/PhysRevB.81.165205.
- [295] —, "Configurations, electronic properties, and diffusion of carbon and nitrogen dopants in rutile TiO₂: A density functional theory study", *Physical Review B*, vol. 84, p. 165201, 2011. DOI: 10.1103/PhysRevB.84.165201.
- [296] W. M. Vogel and J. M. Baris, "Changes in the surface of platinum in hot concentrated phosphoric acid at low potentials", *Electrochimica Acta*, vol. 23, pp. 463–466, 1978. DOI: 10.1016/0013-4686(78)87047-9.
- [297] J. C. Huang, R. K. Sen, and E. Yeager, "Oxygen reduction on platinum in 85% orthophosphoric acid", *Journal of The Electrochemical Society*, vol. 126, pp. 786–792, 1979. DOI: 10.1149/1.2129139.
- [298] H. U. Lee, S. C. Lee, J. Won, B.-C. Son, S. Choi, Y. Kim, S. Y. Park, H.-S. Kim, Y.-C. Lee, and J. Lee, "Stable semiconductor black phosphorus (BP)@titanium dioxide (TiO₂) hybrid photocatalysts", *Scientific Reports*, vol. 5, pp. 8691–8696, 2015. DOI: 10.1038/srep08691.
- [299] W. Luo, D. Y. Zemlyanov, C. a Milligan, Y. Du, L. Yang, Y. Wu, and P. D. Ye, "Surface chemistry of black phosphorus under a controlled oxidative environment", *Nanotechnology*, vol. 27, p. 434002, 2016. DOI: 10.1088/0957-4484/27/43/434002.

- [300] J. C. Yu, L. Zhang, Z. Zheng, and J. Zhao, "Synthesis and characterization of phosphated mesoporous titanium dioxide with high photocatalytic activity", *Chemistry of Materials*, vol. 15, pp. 2280–2286, 2003. DOI: 10.1021/cm0340781.
- [301] K. J. A. Raj, R. Shanmugam, R. Mahalakshmi, and B. Viswanathan, "XPS and IR spectral studies on the structure of phosphate and sulphate modified titania - A combined DFT and experimental study", *Indian Journal of Chemistry A*, vol. 49, pp. 9–17, 2010. [Online]. Available: <http://nopr.niscair.res.in/handle/123456789/7185>.
- [302] Z. Shi, Q. Wang, W. Ye, Y. Li, and Y. Yang, "Synthesis and characterization of mesoporous titanium pyrophosphate as lithium intercalation electrode materials", *Microporous and Mesoporous Materials*, vol. 88, pp. 232–237, 2006. DOI: 10.1016/j.micromeso.2005.09.013.
- [303] T. Hanawa and M. Ota, "Calcium phosphate naturally formed on titanium in electrolyte solution", *Biomaterials*, vol. 12, pp. 767–774, 1991. DOI: 10.1016/0142-9612(91)90028-9.
- [304] A. Ghicov, H. Tsuchiya, J. M. Macak, and P. Schmuki, "Titanium oxide nanotubes prepared in phosphate electrolytes", *Electrochemistry Communications*, vol. 7, pp. 505–509, 2005. DOI: 10.1016/j.elecom.2005.03.007.
- [305] H. Habazaki, K. Shimizu, S. Nagata, P. Skeldon, G. E. Thompson, and G. C. Wood, "Ionic transport in amorphous anodic titania stabilised by incorporation of silicon species", *Corrosion Science*, vol. 44, pp. 1047–1055, 2002. DOI: 10.1016/S0010-938X(01)00111-1.
- [306] Y. T. Law, S. Zafeiratos, S. G. Neophytides, A. Orfanidi, D. Costa, T. Dintzer, R. Arrigo, A. Knop-Gericke, R. Schlögl, and E. R. Savinova, "In situ investigation of dissociation and migration phenomena at the Pt/electrolyte interface of an electrochemical cell", *Chemical Science*, vol. 6, pp. 5635–5642, 2015. DOI: 10.1039/C5SC01421B.
- [307] R. Nishitani, H. Iwasaki, Y. Mizokawa, and S. Nakamura, "An XPS analysis of thermally grown oxide film on GaP", *Japanese Journal of Applied Physics*, vol. 17, pp. 321–327, 1978. DOI: 10.1143/JJAP.17.321.
- [308] V. Jalan and D. G. Frost, "Fuel cell electrocatalyst support comprising an ultra-fine chainy-structured titanium carbide", Patent US 4795684, Jan. 1989.
- [309] J.-S. Lu, "Corrosion of titanium in phosphoric acid at 250 °C", *Transactions of Nonferrous Metals Society of China (English Edition)*, vol. 19, pp. 552–556, 2009. DOI: 10.1016/S1003-6326(08)60311-8.
- [310] P. Stonehart, "Carbon substrates for phosphoric acid fuel cell cathodes", *Carbon*, vol. 22, pp. 423–431, 1984. DOI: 10.1016/0008-6223(84)90015-0.
- [311] J. Brumbarov, J. P. Vivek, S. Leonardi, C. Valero-Vidal, E. Portenkirchner, and J. Kunze-Liebhäuser, "Oxygen deficient, carbon coated self-organized TiO₂ nanotubes as anode material for Li-ion intercalation", *Journal of Materials Chemistry A*, vol. 3, pp. 16469–16477, 2015. DOI: 10.1039/C5TA03621F.
- [312] S. O. Klemm, J.-C. Schauer, B. Schuhmacher, and A. W. Hassel, "A microelectrochemical scanning flow cell with downstream analytics", *Electrochimica Acta*, vol. 56, pp. 4315–4321, 2011. DOI: 10.1016/j.electacta.2011.01.052.